THE UNIVERSITY of ADELAIDE

Integration of advanced remote sensing and geospatial methodologies to enhance mineral exploration: An example from the southern Gawler Ranges, South Australia

Alicia Sophia Caruso

School of Biological Sciences
Department of Ecology and Evolutionary Biology

This thesis is submitted in fulfilment of the requirements for the degree of Doctor of Philosophy

July 2020

Cover Image: View east along the northern boundary fence line track for Buckleboo and Mt. Ive stations.

Table of Contents

List of Figures

List of Tables

Abstract

The world's demand for metals is increasing and there is a growing need for mineral explorers to locate new ore deposits. Globally, discovery of economic mineral deposits is becoming more challenging due to the increasing depths where exploration is being conducted to discover mineral deposits. Most surficial deposits have been discovered, driving exploration into terrains with substantial weathered regolith cover, and requiring new exploration methods. Current traditional exploration methods including geophysics, high density soil sampling and geochemical analysis can be expensive, time consuming and limited in geographic extent. Although remote sensing methods have been applied to regional-scale mineral exploration, there is potential for them to be used more fully in regions where regolith is a continuing challenge. The overarching aim of this multidisciplinary thesis is to develop methods that integrate forms of remote sensing and geospatial information to reduce the risk and cost of exploration in weathered terrains by identifying and mapping surface alteration related to buried mineralisation.

The study area used to develop and test these methodologies was the southern Gawler Ranges, South Australia, a region prospective for gold, porphyry-copper and epithermal-silver mineralisation. This semi-arid environment is moderately vegetated with limited geological exposures. Most basement rocks are overlain by approximately 100 m of weathered cover materials presenting challenges for both exploration and remote sensing methods.

The broad research aim was addressed through three more specific objectives:

1. Development of an objective regolith-landform map using geospatial data and a repeatable methodology that can be used to guide the early stages of exploration potential assessment;
2. Characterisation of surface expressions of alteration mineralogy and interpretation of landscape processes using airborne hyperspectral imagery and mineralogical data; and
3. Integration of surface geochemistry, mineralogy and regolith-landform mapping to understand and map surface signatures of potential buried mineralisation.

An unsupervised classification was applied to geospatial data layers including a Digital Elevation Model, Topographic Position Index and potassium, thorium and uranium gamma-ray radiometrics. This was clustered to generate an objective regolith-landform map representing the main regolith-landform types. This map captured many of the features typically mapped by traditional regolith-landform mapping as assessed by a statistical goodness of fit measure. While not a replacement for the resource-intensive traditional regolith maps derived from extensive field work, this method used freely available geospatial data an objective, repeatable methodology to produce a map that has potential to increase understanding

of the landscape and assist targeting of areas of alteration and mineralisation for more detailed exploration.

Airborne hyperspectral imagery was analysed by Spectral Feature Fitting, matching image spectra to reference spectra to identify alteration mineralogy. X-ray diffraction was used to independently validate mineralogy present in the landscape providing insight into unclear spatial distributions of some minerals and confirming the presence of key alteration minerals. Landscape processes were interpreted by integrating the spatial distribution of minerals with the objective regolith-landform map. Advanced argillic and argillic alteration were identified in the study area, focused around an exposed alunite breccia at Nankivel Hill. The results placed the central topographic feature, Nankivel Hill, proximal to potential porphyry mineralisation, with Peterlumbo Hill distal to mineralisation as possible chloritic alteration expressed at the surface in this region.

Definition of lithologies from major element geochemistry identified ten rock and cover sequence types within the study area. A region-specific pathfinder element suite was defined using interpretation and thresholds of the Nankivel and Peterlumbo Hill rock exposures. The mineral hosts of these pathfinder elements were proposed from interpretation of semi-quantitative X-ray diffraction to determine the influence of weathering on dispersion of pathfinder elements from rock exposure to cover sequence materials. This suggested that most pathfinder elements were hosted in a variety of minerals including alunite, jarosite, microcline, muscovite, orthoclase and hematite in rock exposures and a broader range of feldspars, clays, micas, carbonates and iron oxides associated with cover sequence materials.

Definitions of proximal and distal geochemical and mineralogical footprints of a porphyry deposit were delineated using the surface geochemistry, X-ray diffraction and hyperspectral mineralogical data. The landscape position of pathfinder elements was interpreted to recommend sample media with the most potential for identification of pathfinders at higher concentrations.

The outcomes of this research demonstrate several encouraging approaches for use of land surface remote sensing and geospatial analysis in the context of mineral exploration in highly weathered and covered terrains. These methods can be integrated easily with more traditional methods and data to improve mineral exploration outcomes for the industry. The increasing need to explore terrains with extensive depths of cover in order to discover new ore deposits suggests that the industry would benefit from integrating these tools to enhance future exploration.

Declaration

I certify that this work contains no material which has been accepted for the award of any other degree or diploma in my name, in any university or other tertiary institution and, to the best of my knowledge and belief, contains no material previously published or written by another person, except where due reference has been made in the text. In addition, I certify that no part of this work will, in the future, be used in a submission in my name, for any other degree or diploma in any university or other tertiary institution without the prior approval of the University of Adelaide and where applicable, any partner institution responsible for the joint-award of this degree.

The author acknowledges that copyright of published works contained within this thesis resides with the copyright holder(s) of those works.

I also give permission for the digital version of my thesis to be made available on the web, via the University's digital research repository, the Library Search and also through web search engines, unless permission has been granted by the University to restrict access for a period of time.

I acknowledge the support I have received for my research through the provision of an Australian Government Research Training Program Scholarship.

19/07/2020

Alicia Sophia Caruso Date

Publications arising from the thesis

Journal Articles

Caruso, A. S., Clarke, K. D., Tiddy, C. J., Lewis, M. M. (*in review*). Airborne hyperspectral characterisation of hydrothermal alteration in a regolith dominated terrain, southern Gawler Ranges, SA.

Caruso, A. S., Clarke, K. D., Tiddy, C. J., Delean, S. & Lewis, M. M. (2018). Objective Regolith-Landform Mapping in a Regolith Dominated Terrain to Inform Mineral Exploration. *Geosciences*, *8*, 318. doi: 10.3390/geosciences8090318

Conference Presentations

Caruso, A. S., Clarke. K. D., Tiddy, C. J., Lewis. M. M. (2019). Integrating hyperspectral and radiometric remote sensing, spatial topographic analysis and surface geochemistry to assist mineral exploration. In *Australasian Exploration Geoscience Conference 2019* (p 1-3). Perth, Australia. doi: 10.1080/22020586.2019.12072996

Caruso, A. S., Clarke, K. D., Tiddy, C. J., Lewis, M. M. (2019). Integrating hyperspectral and radiometric remote sensing, spatial topographic analysis and surface geochemistry to assist mineral exploration in southern Australia. In, *2019 IEEE International Geoscience and Remote Sensing Symposium* (pp. 6783-6786). Yokohama, Japan: Institute of Electronic and Electrical Engineers. doi: 10.1109/IGARSS.2019.8900280

Caruso, A., Tiddy, C., Clarke, K., Lewis, M. (2018). Initial evaluation of soil geochemistry and regolith mapping in the southern Gawler Ranges. In, *15th South Australian Exploration and Mining Conference*. Adelaide, Australia

Caruso, A., Clarke, K., Tiddy, C., Delean, S., Lewis, M. (2018). Linking regolith-landform mapping with surface geochemistry in a regolith dominated terrain to inform mineral exploration. In, *Australian Geoscience Council Convention 2018: Big Issues and Ideas in Geoscience* (pp. 494). Adelaide, Australia: Australian Geoscience Council

Caruso, A. S., Tiddy, C. J., Clarke, K. D., Lewis, M. M. (2017). Hyperspectral characterisation of alteration in a covered terrain in the Southern Gawler Ranges, South Australia. In, *Tenth International Mining Geology Conference 2017*. (pp. 447-449). Hobart, Australia: The Australasian Institute of Mining and Metallurgy. doi: 10.4225/55/59ed274d3f6d1

Caruso, A., Clarke, K., Forbes, C., Lewis, M. (2016). Hyperspectral characterisation of alteration zones in the southern Gawler Range Volcanics margin. In, *13th South Australian Exploration and Mining Conference*. Adelaide, Australia

Acknowledgements

Firstly, I would like to thank my supervisors, Professor Megan Lewis, Dr Ken Clarke and Dr Caroline Tiddy for their guidance and encouragement throughout the course of my PhD. Special thank you to Megan for questioning the logic and my thought process regularly and being available when your calendar was very full! Thanks to Ken for answering every inane question I had and asking why so many times! (Frustrating, but definitely worth it.) A big thank you to Caroline for providing geological support and getting that geochemistry to the finish line, it's never as simple as it seems and you don't realise how challenging it is until you're right in the middle of it! I'm so grateful I've gotten to work with you all, I've thoroughly enjoyed learning with and from all of you over the last four years.

This project would not have been possible without the support of Investigator Resources, particularly John Anderson (former Managing Director) whose infectious enthusiasm and drive got this project off the ground and Andrew Alesci and Jason Murray for all of their assistance providing data throughout the project and a place to camp for field work. Part of the data analysis for this project would not have been possible without the support of a Minerals Council of Australia 'Australian Minerals Industry Research Scholarship'. Thank you to the station owners and managers of Buckleboo and Mt. Ive for letting us drive around and collect samples, and thanks to Anthony Gray (Alliance Resources) for allowing access for sample collection and providing some historical data for me to interpret.

A big thank you to Ben McKay from University of Adelaide Legal Services. Without your help we would have most certainly been stranded in a precarious situation, your mediation abilities saved all of us a huge amount of stress! Thank you to Dr Tony Hall for your help getting the XRD analysis up and running, showing me the joys of RockJock, and just how slow it is - the hours waiting for Excel macros in the Mawson basement was worth it!

Thank you to Dr Alan Mauger, Dr John Keeling and Georgina Gordon (GSSA) for Paris, hyperspectral and clay conversations to clarify understanding geological understanding of the area and maybe how outcomes were going askew. Also a thank you to Alan and Georgina for taking the time to discuss opening high resolution hyperspectral data in TSG, a future project perhaps?!

A huge thanks must to go to the Spatial Sciences Group (SIG/SSG) for providing a welcoming, friendly and positive environment over the years. I have loved the tea room conversations about literally any topic (even if it was whinging about work and data!) with online demonstrations when necessary (but not when Ken played 'lock-pick lawyer'). Thank you to PhD/Hons floor-mates, Aakash, Alan (and Peri), Amelie, Andrew, Angus, Brooke, Claire, Claire, Dillion, Grace, Hannah, Jarrod, Matt, Tasya and now Drs Gennady, Sofi and Sreekar plus staff, A/Prof Bertram Ostendorf, Dr Dot Turner, Molly

Hennekam and Dr Ramesh Raja Segaran. I could not have made it to the end without all of your encouragement and support (and I'm not just saying that).

Thank you to my friends, Jade, Eliza and Nepheli and other UCB friends for being excited for me when I achieved things, even though you didn't necessarily know what some of those things were and to other PhD friends Kate and (now) Dr James for PhD and/or life discussions over a coffee throughout these last few years.

Thank you to my parents for their endless support, understanding and weekly coffees and/or cake/lunch, depending on which campus I was based at. (PS: Just so you know, this is the 'final thing' for all this! – Finally!)

My last thank you is to Sean who has been so supportive even though this PhD felt like it would never end. Thanks for reminding me this is actually important, cooking me food when I was late (to everything) or working on Sundays, being a sounding board while letting me relentlessly discuss (or complain about) work and being my biggest cheerleader throughout (but especially at the end), it's all so appreciated.

Chapter 1

INTRODUCTION

1.1 Research Motivation

There is an increasing discrepancy between the global demand for metals, which doubles every 20 – 30 years, and the rate of large mineral discoveries (Schodde 2017b). A proportional increase in discoveries of major mineral resources would be necessary to meet this demand but discoveries of this magnitude are increasingly uncommon due to the challenge of exploration in prospective regions obscured by deep cover (Hillis *et al.* 2014). These challenges are posed by the increased risk and cost involved to use traditional exploration methods in unexplored terrains. More recently, mineral exploration has increasingly focused on targets near existing mines that have typically required deeper drilling for successful discovery (Guj and Schodde 2013). Location of new economic deposits will require increased exploration in prospective but unexplored regions which involves higher risk but potentially high reward deposits (Cairns *et al.* 2010). More than half of all mineral exploration in Australia is conducted by junior exploration companies (Schodde 2019) that typically have smaller budgets and fewer technical staff than large mining companies. Consequently, these companies need to conduct efficient exploration and obtain maximum value from their data.

The majority of mineral exploration at the district and target scales uses extrapolated prior knowledge or a range of geophysical and geochemical methods (Schodde 2017a). These methods are expensive and can be time consuming. However, remote sensing and geospatial data have demonstrated potential for a variety of mineral exploration applications (e.g. Shives *et al.* 2000; Hewson *et al.* 2006; Kreuzer *et al.* 2015; Graham *et al.* 2018). There is an increasing practice for multidisciplinary exploration integrating traditional exploration data to provide multiple lines of evidence to inform targeting through surface and subsurface identification of alteration and mineralisation (e.g. Haest *et al.* 2012; Harraden *et al.* 2013; Wells *et al.* 2016). This type of research is also proving valuable in regions of extensive surface cover (e.g. Eppinger *et al.* 2013; van der Wielen *et al.* 2013; Forbes *et al.* 2015; Lampinen *et al.* 2017).

This thesis combines innovative geospatial and remote sensing methods with more traditional geological exploration approaches to demonstrate potential improvements to early stage mineral exploration under cover. The research was conducted in the southern Gawler Ranges, South Australia, a highly prospective region for silver, base metals and copper (Nicolson *et al.* 2017) with cover sediments of up to 150 m (Gordon *et al.* 2016). This region provided a test case to assess the application and results of a suite of multi-disciplinary methods. Three distinct approaches integrating remotely sensed and geospatial data are demonstrated here, each widely applicable to enhance mineral exploration outcomes. The methods applied in this research are potentially applicable to other locations dominated by regolith and which may contain buried mineralisation. The following sections summarise background research relating to the topics that are the focus of the thesis.

1.2 Background

1.2.1 Regolith

Defined by Eggleton *et al.* (2001), regolith is the surface expression of unconsolidated or secondarily re-cemented cover overlying bedrock formed through weathering, erosion, transport or deposition of older material. Processes that produce regolith are complex and vary with landscape based on the type of underlying bedrock, formation and weathering processes (Anand 2016).

Areas where the basement rock is overlain by younger cover sequences are termed regolith dominated terrains (RDTs) (Anand and Paine 2002; Bierwirth *et al.* 2002). Australian RDTs developed following a period of tectonic stability during the Phanerozoic (Anand 2005). They were deemed 'the new exploration frontiers' (Smith 1996) in the mid-1990s as many of these terrains were effectively unexplored and were a problem not only confined to Australia but also to a majority of regions typically around the equator (Figure 1.1). Most regolith research incorporates a variety of analysis techniques such as petrology, multi-element geochemistry, X-ray diffraction (XRD) and X-ray fluorescence (XRF). A majority of the literature presents case studies with general conclusions applicable to other RDTs.

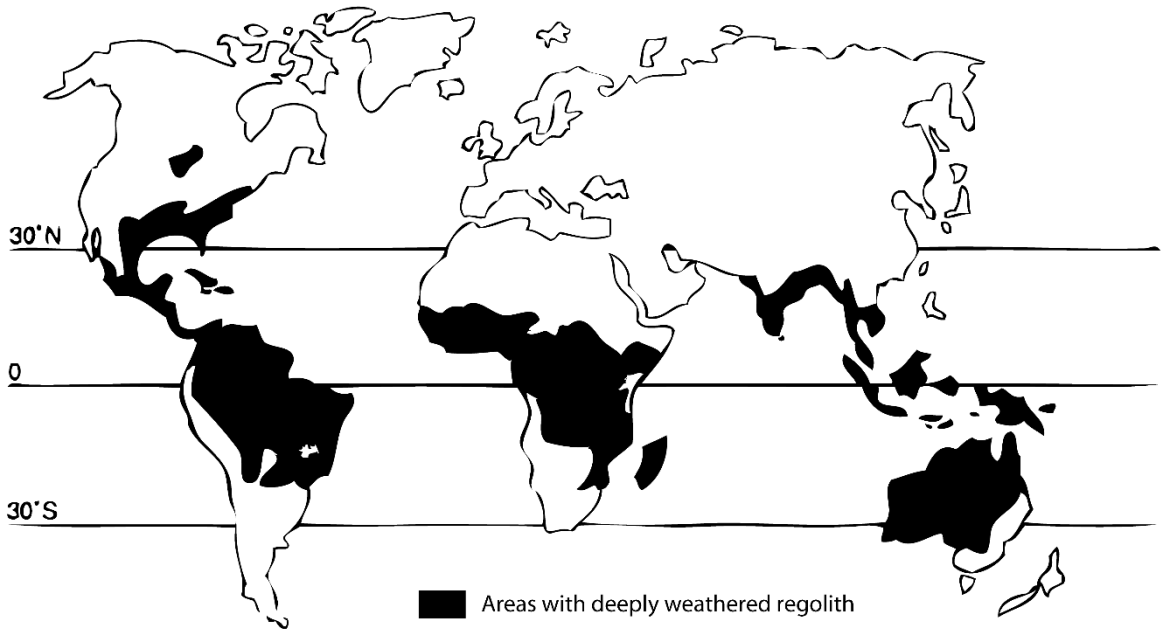

Figure 1.1: Global distribution of deeply weathered regolith, reproduced from Smith (1996).

In Australia, research on regolith geology has primarily concentrated on the development of appropriate exploration methods in these landscapes, which are widespread across much of Australia (Figure 1.1) (e.g. Butt *et al.* 2000; Anand *et al.* 2001; Anand and Paine 2002; Lintern *et al.* 2011; González-Álvarez *et al.* 2016). A majority of this work was conducted within programs of the Cooperative Research Centre for Landscape Evolution and Mineral Exploration and CRC Landscape Environments and Mineral Exploration (CRC LEME) from 1995 to 2008. CRC LEME research examined geochemical dispersion

of elements in regolith profiles and the characterisation of regolith prior to commencing mineral exploration (e.g. Anand *et al.* 2001; Craig 2001; Lintern 2002). Research in this field has continued since CRC LEME to present day (e.g. Anand and Robertson 2012; Anand *et al.* 2016; McHarg and Aspandiar 2019). The spatial and genetic associations between geology, topography and regolith can be summarised in a regolith-landform map (Dehaan and Taylor 2004). Regolith-landform mapping is recommended as an initial step for mineral exploration in RDTs (Taylor and Butt 1998) but is still undervalued and not necessarily conducted prior to exploration activities (Anand and Butt 2010).

1.2.2 Remote Sensing

Remote sensing is the science of acquiring, processing and interpreting data that remotely records the interaction between matter and electromagnetic energy (Sabins 1999). In recent years, optical remote sensing has found broad applications within environmental monitoring and geological mapping. Satellite remote sensing first became operational in the 1960s and 1970s with instruments such as the Landsat Multispectral Scanner (MSS) with four broad bands across the visible and near infrared (Goetz 2009). One of the best-known and frequently used sensors within the Landsat program is the Landsat Thematic Mapper (TM) launched in 1982 (Rumerman 1999). This sensor contained six spectral bands across the visible, near infrared and shortwave infrared parts of the spectrum plus one band in the thermal infrared. The spatial and spectral resolution of the imagery means this sensor is still an attractive option for remote sensing products. Landsat 8 is the current operational satellite of the program with the launch of Landsat 9 scheduled for December 2020 (National Aeronautics and Space Administration 2019). The success of the Landsat program has seen over 40 years of constant Earth observation.

Another relevant multispectral satellite-borne sensor was the Advanced Spaceborne Thermal Emission and Reflectance Radiometer (ASTER), launched in 1999. This imager was designed with Shortwave Infrared (SWIR) and Thermal Infrared (TIR) band placement appropriate for geological applications including the characterisation of minerals (Yamaguchi *et al.* 1998). Although the SWIR sensor ceased operation in 2008, the Visible Near-Infrared (VNIR) and TIR sensors are still in operation and are used for successful identification of broad scale geological applications (e.g. Mars and Rowan 2006; Mulder *et al.* 2013; Cudahy *et al.* 2016; Abrams 2019). In general, multispectral imagery is still used extensively for temporal, environmental and some geological applications with access via government and commercial satellite-based sensors with repeat times ranging from daily to fortnightly at a range of spatial and spectral resolutions.

Hyperspectral imaging was developed in the 1980s and over the following decades has become used primarily for targeted applications. Hyperspectral imagery has a number of advantages over multispectral imagery including 100 or more contiguous, narrow wavebands allowing for more accurate

characterisation and analysis of spectral signatures. Although there are these benefits to airborne hyperspectral imagery, the cost of collecting this data can be much greater than that of satellite-borne multispectral data and the feasibility of using this imagery is project and application dependent. There are a number of airborne hyperspectral imaging sensors including Airborne Visible Infrared Imaging Spectrometer (AVIRIS) developed by Jet Propulsion Laboratory (JPL) and the Australian HyMap™ (Vane *et al.* 1984; Cocks *et al.* 1998). These sensors have high spatial resolutions up to 2.5 – 10 m and spectral bandwidths of approximately 20 nm (Figure 1.2). VNIR-SWIR airborne hyperspectral imagery has been used across environmental and geological applications (e.g. Mustard 1993; Crósta *et al.* 1998; Andrew and Ustin 2008; Ong and Cudahy 2014).

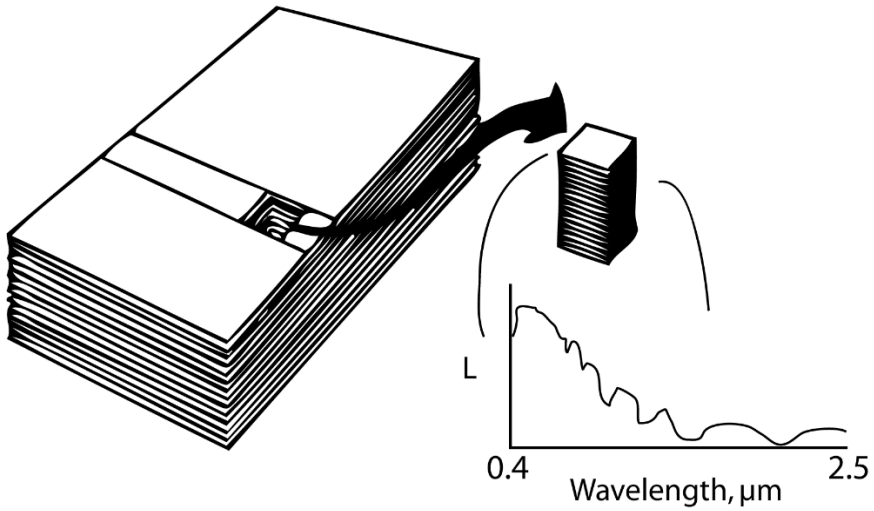

Figure 1.2: Illustrating the numerous contiguous spectral bands to create a near continuous radiance spectrum that is the basis for hyperspectral imaging systems. Reproduced from Goetz (2009).

Airborne hyperspectral remote sensing has been moving into the TIR part of the electromagnetic spectrum over a number of decades. Sensors include the Spatially-Enhanced Broadband Array Spectrograph System (SEBASS) (Hackwell *et al.* 1996), Hyperspectral Thermal Emission Spectrometer (HyTES) (Johnson *et al.* 2011) and AisaOWL (Specim 2019) ranging from approximately 8000 - 12000 nm, primarily used for geological and geothermal mapping (e.g. Cudahy *et al.* 2001a, b; Hecker 2006; Kruse and McDowell 2015; Tappert *et al.* 2015; Aslett *et al.* 2018; Lorenz *et al.* 2018; Laakso *et al.* 2019) and some vegetation mapping (e.g. Ullah *et al.* 2012; Rock *et al.* 2016; Harrison *et al.* 2018).

One successful satellite-borne sensor, Hyperion aboard the Earth Observing-1 satellite, was launched by NASA in 2000 and although it was expected to function for 12 months, remained in operation until 2017 (United States Geological Survey 2018). More recently, several hyperspectral sensors have launched, with two attached to the International Space Station: the German Aerospace Centre (DLR) Earth Sensing Imaging Spectrometer (DESIS) launched in June 2018 (Carmona *et al.* 2019) and the Hyperspectral Imager Suite (HISUI) (Mastunaga *et al.* 2019) developed by the Japanese Ministry of Economy, Trade

and Industry (METI). Other standalone hyperspectral satellites have recently been launched, the Precursore Iperspettrale della Missione Applicativa (PRISMA) (Agenzia Spaziale Italiana 2019) and Hyperspectral Imaging Satellite (HySIS) (Indian Space Research Organisation 2017) were launched in November 2018 and March 2019 respectively by the Italian and Indian Space Agencies. These satellites are in initial testing phases with no imagery currently available for general users and applications. From the 2007 NASA Decadal Survey, an imaging spectrometer covering VNIR, SWIR and multiband TIR to be attached to a low Earth orbit satellite was proposed as the HyspIRI Mission, but this did not eventuate (Jet Propulsion Laboratory and California Institute of Technology 2018). Discussions are now underway following the 2017 NASA Decadal Survey regarding a new satellite hyperspectral mission designed for geological applications to launch during the 2020s (National Academies of Sciences 2018). Another future satellite is the German Aerospace Centre (DLR) managed Environmental Mapping and Analysis Program (EnMAP) satellite which is scheduled to launch in 2020 (Earth Observation Center of DLR 2018).

Geological remote sensing has spanned over 50 years of research and has included applications such as surface mapping of mineralogy (Kruse 2012). The identification of minerals and other geological materials using VNIR, SWIR and some TIR spectroscopy is well-established and widely reported (e.g. Kruse 1988; Sabins 1999; Cudahy *et al.* 2001a; Hewson *et al.* 2009; Haest *et al.* 2012). Globally, research has focused on prominent mineral-rich regions in the United States, Canada and Australia (Vaughan *et al.* 2005; Laukamp *et al.* 2011a; Rogge *et al.* 2014). The focus on ore deposits has included hydrothermal (e.g. Kruse *et al.* 2003) and porphyry deposits (e.g. Cudahy *et al.* 2001a). Lithological mapping using hyperspectral imagery has been successfully achieved in a number of locations (e.g. Clark *et al.* 1992; Rowan *et al.* 2004), including a HyMap™ survey across almost the full extent of Afghanistan (King *et al.* 2011) and the challenging northern high-latitude environments including Greenland and northern Canada (Harris *et al.* 2005; Bedini 2009; Feng *et al.* 2018) where geological exposures are often covered with abundant vegetation and lichen. Surface mineralogical mapping can provide detail on differing regolith mineralogy or zones of alteration in a landscape (e.g. Eggleton 2009; Laukamp *et al.* 2011b). Both of these conditions are more precisely mapped using higher spatial and spectral resolution hyperspectral imagery.

1.2.3 Gamma-Ray Spectrometry

Gamma-Ray spectrometry, or radiometrics, is a passive remote sensing technique that detects gamma-rays emitted from the natural radioactive isotopes of potassium (^{40}K), uranium (^{238}U, ^{235}U) and thorium (^{232}Th) from the top 30 - 45 cm of material at the Earth's surface (Gregory and Horwood 1961; Dickson and Scott 1997; Wilford *et al.* 1997). A number of environmental effects such as soil moisture, vegetation, rainfall and non-radioactive overburden can attenuate the detection of the gamma-rays

(Minty 1997). This data has been used since the 1970s for geological interpretation of the landscape, mapping soils and regolith materials and for mineral exploration (e.g. Schwarzer *et al.* 1972; Darnley and Ford 1989; Wilford *et al.* 1992; Cook *et al.* 1996; Dauth 1997). Radiometric maps have been produced in a number of countries including Tanzania (Batterham *et al.* 1983), the United States (Duval 1990) and New Zealand (Stagpoole *et al.* 2012). In Australia, a radiometric map was produced by Minty *et al.* (2009) encompassing most of the continent.

Many studies that employ radiometrics focus on mapping discrete lithologies (e.g. Galbraith and Saunders 1983; Graham and Bonham-Carter 1993; Anderson and Nash 1997). However, some research has used radiometrics for interpreting geomorphic landscape processes and demonstrating the variation in radiometric response of regolith materials above weathered bedrock compared to transported materials (Dickson and Scott 1997; Wilford *et al.* 1997). Radiometrics have also been used for uranium and tin-tungsten exploration (e.g. Foote and Humphrey 1976; Ward 1981; Yeates *et al.* 1982; Webster 1984) as well as identifying alteration related to mineralisation (e.g. Shives *et al.* 2000). Other applications for this data include agriculture where radiometrics have been integrated with traditional soil analyses to interpret surficial soils (e.g. Taylor e*t al.* 2002; Pracilio 2007).

1.2.4 Applied Geochemistry

Applied geochemistry is an integral part of mineral exploration and is used to determine processes by which elements migrate towards the Earth's surface (Kyser *et al.* 2015). Selection of appropriate sample media, horizon or lithology is important to optimise the use of this data, with extensive research conducted over decades illustrating the outcomes of these choices (e.g. McQueen *et al.* 1999; McClenaghan *et al.* 2000; Anand and Butt 2010; Sadeghi *et al.* 2015; Noble *et al.* 2019). Integrating regolith, climate and landscape evolution data with mineralogy and geochemistry is critical for effective mineral exploration (Salama *et al.* 2016). Correct interpretation of the regolith profile structure is essential for understanding geochemical expressions at the surface and their links to underlying geology (González-Álvarez *et al.* 2016). Typically, exploration samples for geochemical analysis are collected on a regular grid spacing dependent on the targeted feature (Mann *et al.* 1998). This data is collected early in the exploration process, allowing for evaluation of background and elevated levels of major and trace elements (Cohen *et al.* 2010). It is also vital in a new area to develop an extensive database to inform prospectivity of the region as well as confidently define background and elevated elemental concentrations (Tiddy *et al.* 2019). Recent research has focused primarily on rapid geochemical analysis, novel lab-based and in-field rapid data acquisition methods, data access, integration and interoperability (Winterburn *et al.* 2019).

There are two main ways that geochemical data analysis can be examined. The first is an interpretative method using cumulative probability plots derived by Garrett (1991), while the other is compositional data analysis that primarily focuses on multivariate analysis to recognise patterns within geochemical data (Grunsky 2010). Compositional analysis can be achieved in specialist software such as ioGAS™ (IMDEX 2019) or freely available statistical software such as *R* or Python (e.g. van den Boogaart and Tolosana-Delgado 2008; Williams 2019).

1.2.5 Multidisciplinary Research for Mineral Exploration

Integrated assessment of multiple data sets has become a valuable approach in recent years for mineral exploration. A range of traditionally collected data types including geophysics, multi-element geochemistry, petrology, core logging and assay results have been successfully used with a variety of remote sensing data in a number of terrains (e.g. van Ruitenbeek *et al.* 2012; Laakso *et al.* 2016; Lampinen *et al.* 2017). Examining and mapping variation in wavelength position for diagnostic absorption features (e.g. Al-OH or Fe-OH) has been achieved using HyMap™ airborne imagery (e.g. Laukamp *et al.* 2011b; Graham *et al.* 2018) and is commonly performed on sub-surface HyLogger™ hyperspectral data typically from drill core (e.g. Huntington *et al.* 2004; Duuring *et al.* 2016; Wang *et al.* 2017; Lypaczewski *et al.* 2019). This type of analysis has also been applied to laboratory spectra to identify alteration intensity in sub-surface data (e.g. Laakso *et al.* 2016). This style of spectral analysis has been integrated with geochemical or petrological data resulting in mineralogical and geochemical footprints of alteration that indicate potential vectors for mineralisation (e.g. Travers and Wilson 2015; Wells *et al.* 2016). Recent research has also used HyLogger™ mineralogy with geochemistry and geochronology to determine the provenance of regolith materials in the Eromanga Basin (Baudet *et al.* 2020).

Other multidisciplinary methods for mineral exploration include prospectivity mapping and machine learning (e.g. Kreuzer *et al.* 2010; Cracknell and de Caritat 2017; Kuhn *et al.* 2018; Ferrier *et al.* 2019). These maps have become more popular due to their regional or continental spatial scales and integration of a wide range of datasets including traditional geological, geophysical and remotely sensed data available via geological surveys or mineral exploration companies. However, there has been slow uptake of these methods by industry for mineral exploration (Hronsky and Kreuzer 2019).

1.3 Study Area

The study area for this research is part of the southern margin of the Gawler Ranges Volcanics, northern Eyre Peninsula in South Australia, approximately 60 km north west of Kimba (Figure 1.3). This region hosts the Paris silver deposit with a resource of 9.3 Mt @ 139 g/t Ag, 0.6% Pb (42 Moz Ag, 55 kt Pb) and a number of prospective copper and silver exploration targets (Investigator Resources 2017a). Paris

is an epithermal silver deposit consisting of a series of laterally extensive hydrothermal and volcanic breccias hosted within the Hutchison Group (Paul *et al.* 2015). Exploration in recent years has focused on the potential porphyry copper deposit located at Nankivel Hill and other nearby silver targets.

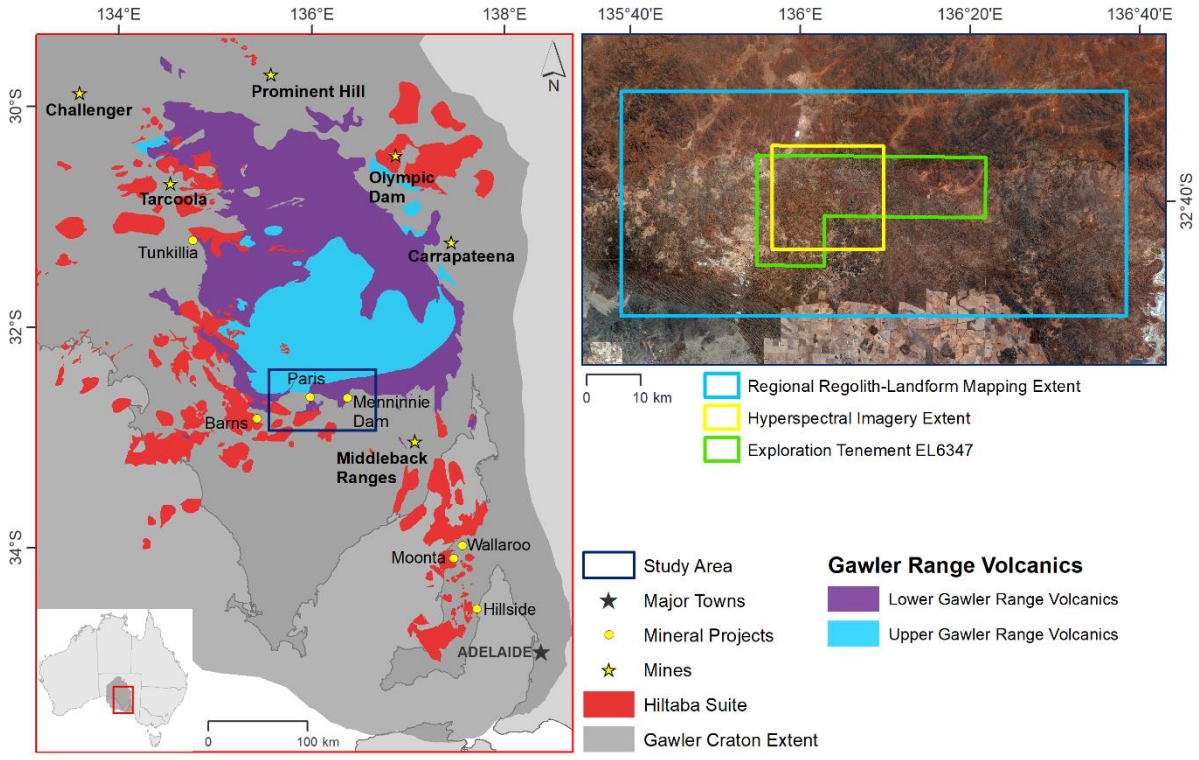

Figure 1.3: Context and study area maps. Left: The Gawler Craton showing major geological units relevant to this work, and the major mines and mineral projects in the Gawler Craton. Right: The spatial extents of each study area examined in the thesis placed in context with the main Investigator Resources tenement EL6347.

The study area is within the 'Arid, Desert, Cold' (BWk) climate classification (Beck *et al.* 2018) receiving approximately 300 mm of rainfall annually and mean minimum and maximum temperatures of 10.4 °C and 23.6 °C respectively (Bureau of Meterology 2019). The area is within the Interim Biogeographic Regionalisation for Australia (IBRA) 'Gawler' and 'Eyre Yorke Block' region and is separated into the 'Eyre Hills', 'Eyre Mallee', 'Myall Plains' and 'Gawler Volcanics' subregions (Department of the Environment and Energy 2012). This region is typically dominated by arid, shrubland vegetation with some larger trees across the landscape. The vegetation comprises low open woodlands of western myall (*Acacia papyrocarpa*) and black oak (*Casuarina pauper*) trees over sparse shrub understoreys of bluebush (*Maireana* spp.), saltbush (*Atriplex* spp.) and spinifex (*Triodia* spp.).

1.3.1 Geological Setting

The Gawler Craton is defined as a region of Archean to Mesoproterozoic crystalline basement that has undergone substantial deformation during the *ca.* 2450 - 2420 Ma Sleafordian Orogeny (Daly and Fanning 1993), *ca.* 1730 - 1670 Ma Kimban Orogeny (Daly *et al.* 1998; Ferris *et al.* 2002), *ca.* 1610 - 1580 Ma

Wartakan Orogeny/Hiltaba Event (Stewart and Betts 2010) and the *ca.* 1570 - 1540 Ma Kararan Orogeny (Daly *et al.* 1998; Hand *et al.* 2007). There is evidence of intense tectonothermal activity associated with voluminous magmatism and generation of Iron Oxide - Copper - Gold (IOCG) mineralisation at *ca.* 1600 - 1580 Ma (Fanning *et al.* 2007; Cutts *et al.* 2011; Reid *et al.* 2011; Forbes *et al.* 2012). The Gawler Craton has a number of unique geological terrains including the Olympic Province, the Gawler Range Volcanics, and the Central Gawler Gold Province (Ferris and Schwarz 2003). These regions host a number of economic mineral deposits including Prominent Hill (IOCG), Carrapateena (IOCG), Hillside (IOCG), Challenger (Au), Middleback Ranges (Fe_2O_3), historical Wallaroo and Moonta mines (Cu), and most notably, Olympic Dam (IOCG) (Johnson and Cross 1995; Belperio *et al.* 2007; Conor *et al.* 2010).

The Gawler Range Volcanics (GRV) are a volcanic province primarily comprised of felsic extrusive igneous rocks extending 25,000 km^2 across the central region of the Gawler Craton (Blissett *et al.* 1993; Garner and McPhie 1999). The volcanics have been defined as representing a Silicic Large Igneous Province (SLIP) (Allen *et al.* 2008; Agangi 2011). The GRV overlies Archaean and Palaeoproterozoic granitoids and is overlain by Proterozoic and Phanerozoic cover sequences towards its eastern extent (Blissett *et al.* 1993; Garner and McPhie 1999). The GRV is divided into Upper and Lower units with predominantly felsic strata in the Upper GRV and extrusive mafic rocks within the Lower GRV (Allen *et al.* 2003; Agangi *et al.* 2012). The Lower GRV are heterogeneous, lower volume and erupted at *ca.* 1591 $\pm$ 3 Ma (Fanning *et al.* 1988). The Upper GRV are dominated rhyolites and ignimbrites, high volume and were erupted during a period of rapid volcanism. The timing of volcanism of the Upper GRV is constrained by ages of the two uppermost units, the Eucarro Rhyolite and the Moonaree Dacite (top member of Yardea Dacite) to 1587.5 $\pm$ 0.6 Ma and 1587.2 $\pm$ 0.5 Ma respectively (Jagodzinski *et al.* 2016). The GRV are co-magmatic with shallow intrusives of the Hiltaba Suite that were emplaced throughout the Gawler Craton *ca.* 1595 - 1575 Ma (Flint 1993).

The geomorphology and surface regolith materials have been recently identified and mapped by Krapf (2016), illustrating the variety of materials across the southern Gawler Ranges margin. The most prominent regolith units within the study area are transported sand dune deposits and the Gawler Range Volcanics and associated colluvium (Krapf 2016). The main regions of in-situ regolith identified using the TI (transported or in-situ) scheme, devised by Pain *et al.* (2007), are the GRV geological exposures that extend across the northern half of the southern Gawler Ranges margin. These have significant relief of approximately 200 AMSL compared to the remainder of the study area. The other major geomorphological features in the landscape include the Hutchinson Group geological exposures and the lacustrine playa lake deposits demonstrating modern drainage through the salt lakes north east of Peterlumbo Hill (Krapf 2016).

1.3.2 Regional Exploration History

Numerous generations of geochemical, geophysical and geological exploration have been conducted in the southern Gawler Ranges since the early 1980s by several exploration companies (Davies *et al.* 1988; Gerakiteys 1996; Drown *et al.* 2000; Garsed 2003; Pigott *et al.* 2008). In the 1990s, the focus was to discover a prospect similar to Menninnie Dam (Pb-Zn-Ag), with little success. Projects likely hosting gold were preferentially examined in 1991 (Drown *et al.* 2003). Following successful gold-in-calcrete analysis nearby, this method was applied to the Peterlumbo tenement with limited success. Focus shifted to the development of the nearby Death Adder (Au) prospect before returning to the Peterlumbo Hill and Nankivel Dam region (Drown *et al.* 2003). Mount Isa Mines exploration collected a variety of data in 1995/96 at Nankivel Hill from three Reverse Circulation (RC) holes and spectral analysis of surface samples using a SWIR Portable Infrared Mineral Analyser (PIMA). No mineralisation was identified in the drilling and assay results were disappointing, but the spectral analysis identified alunite, pyrophyllite, dickite and illite at Nankivel Hill which led to deeper drilling to locate mineralisation and any indications of an epithermal system present (Gerakiteys 1996).

More recent research in this region has focused primarily on the Paris silver deposit discovered in 2011 by Investigator Resources (Investigator Resources, 2017a). Studies at Paris have concentrated on ore mineralogy, ore genesis (Paul *et al.* 2015, 2016) and sub-surface spectral analysis for mineralogical understanding of lithology from diamond drill core using the HyLogger™ (Gordon *et al.* 2016). Other research in the area has focused on the potential porphyry copper mineralisation at Nankivel Hill. A unique alunite breccia exists at Nankivel Hill and is proximal to high-sulphidation epithermal mineralisation (Nicolson *et al.* 2017). Dating using $^{40}Ar/^{39}Ar$ of alunite within the breccia identified a minimum age for hydrothermal crystallisation, hence the acid sulphate event producing the breccia of 1586 $\pm$ 8 Ma (Nicolson *et al.* 2017). This date largely corresponds with the emplacement of the Hiltaba Suite and eruption of the GRV in the Gawler Craton (Nicolson *et al.* 2017).

This area was chosen for this research because it is considered prospective for base metal and copper mineralisation (e.g. Gerakiteys 1996; Investigator Resources 2017a, b; Nicolson *et al.* 2017), but carries substantial regolith cover, posing a challenge to traditional exploration methods. The South Australian Geological Survey has acquired airborne hyperspectral imagery within the area, while Investigator Resources has conducted considerable drilling and geochemical sampling mainly related to the Paris silver deposit. Hence, several datasets were available for comparison and integration in this study.

1.4 Thesis Aims

Multidisciplinary methods that utilise the potential of available data while reducing risk and cost of mineral exploration is the primary theme of this thesis. The research aims to use and integrate spatial

and spectral methods to advance understanding of the landscape to enhance mineral exploration, intending to reduce risk and cost. The approaches developed and applied focus on data and products which provide information about surface materials and terrain over broad areas and which can be cost effective. They have potential to guide and inform traditional geological data collection such as drilling in early phases of exploration. In the southern Gawler Ranges study area, these approaches provide new insights into the surface expression of mineralisation. The approaches demonstrated in this thesis also have potential for application in other regolith dominated terrains that are unexplored or underexplored. The overarching aim is pursued through three research components, each with specific objectives.

Component 1 – Objective regolith-landform mapping

Creation of regolith-landform maps is considered an important step prior to conducting traditional mineral exploration in a new region (e.g. Anand and Butt 2010). However, these maps typically require expert knowledge to produce and can be subjective. The objective of this component was to develop a more objective method to map regional regolith-landforms using remotely sensed and geospatial data in a methodology that is repeatable and not operator-specific.

Component 2 – Characterising alteration using airborne hyperspectral imagery

Airborne hyperspectral imagery has the potential to be used to examine a wide range of viable deposit models and also reduce initial exploration costs. This is especially beneficial in new and underexplored terrain to locate potential target regions. Hence, the objective of this component was to characterise mineralogical surface expressions of high sulphidation epithermal alteration in a regolith dominated terrain using airborne hyperspectral imagery and to identify potential landscape processes that influenced these surface expressions.

Component 3 – Geochemical and mineralogical characterisation

Exploration geochemistry is commonly collected by exploration companies and its integration with other available data can provide multiple lines of evidence towards a potential buried deposit. The objective of this component of the research was to integrate surface geochemistry, mineralogical alteration mapping and regolith-landform mapping to identify a surface footprint of potential buried mineralisation in the southern Gawler Ranges.

1.5 Thesis Outline

Following this introduction, **Chapters 2 – 5** present new research and results while **Chapter 6** synthesises and summarises this research.

Chapter 2 develops an alternative regolith-landform mapping method using freely available remote sensing products including a Digital Elevation Model (DEM) and gamma-ray spectrometry, applying objective criteria in a reproducible method. An unsupervised classification and hierarchical clustering

are used to create an objective regolith-landform map. This is then statistically compared with a traditionally derived regolith-landform map using the Mapcurves Goodness of Fit measure in *R* (Hargrove *et al.* 2006). This chapter is published as Caruso, A. S., Clarke, K. D., Tiddy, C. J., Delean, S., Lewis, M. M. (2018). Objective Regolith-Landform Mapping in a Regolith Dominated Terrain to Inform Mineral Exploration. *Geosciences*, *8*, 318.

Chapter 3 uses airborne hyperspectral imagery and X-ray diffraction (XRD) to characterise zones of epithermal and porphyry alteration. Hyperspectral analysis is used to map key alteration minerals illustrating the surface expression of advanced argillic alteration. Mineralogy is validated using semi-quantitative XRD analysis of rock exposure and surface soil samples. The integration of airborne hyperspectral and XRD characterisation allows for interpretation of mineralogical landscape patterns to assist with identifying surface alteration that may be related to potential buried mineralisation. This chapter has been peer-reviewed and resubmitted for publication as Caruso, A. S., Clarke, K. D., Tiddy, C. J., Lewis, M. M. (*in review*). Airborne hyperspectral characterisation of hydrothermal alteration in a regolith dominated terrain, southern Gawler Ranges, SA. *Australian Journal of Earth Sciences*.

Chapter 4 examines surface soil geochemistry and mineralogical deportment of pathfinder elements in the study area. This work examines the major and trace element geochemistry as well as defining a relevant pathfinder element suite and investigating the mineralogical deportment of these elements. Mineralogy in the form of XRD analysis from **Chapter 3** is used to provide further interpretation of the geochemistry for each lithology and the potential landscape processes that have occurred in this region.

Chapter 5 integrates the outcomes from **Chapter 4** with results from **Chapter 2** and **Chapter 3** to examine the spatial distribution of pathfinder elements and identify a mineralogical and geochemical footprint of buried mineralisation. This is followed by a discussion of selection of appropriate sample media and the benefits of integrating data for mineral exploration for positive mineral exploration outcomes. Materials from **Chapters 4** and **5** will be used to prepare a journal article for future publication.

These research chapters are followed by a summary of the outcomes of each chapter and discussion of how they could be used to reduce risk and cost for mineral exploration as well as a summary of future research directions for work on this topic (**Chapter 6**).

1.6 References

Abrams, M. (2019). ASTER 20th Anniversary: Achievements and geologic contributions to mineral and lithologic mapping. In, *2019 IEEE International Geoscience and Remote Sensing Symposium* (pp. 5571-5574). Yokohama, Japan: Institute of Electrical and Electronics Engineers

Agangi, A. (2011). Magmatic and volcanic evolution of a silicic large igneous province (SLIP): the Gawler Range Volcanics and Hiltaba Suite, South Australia. *PhD Thesis (Unpublished),* University of Tasmania

Agangi, A., Kamenetsky, V.S., & McPhie, J. (2012). Evolution and emplacement of high fluorine rhyolites in the Mesoproterozoic Gawler silicic large igneous province, South Australia. *Precambrian Research, 208*, 124-144. doi: 10.1016/j.precamres.2012.03.011

Agenzia Spaziale Italiana (2019). PRISMA: small Innovative Earth Observation mission, http://www.prisma-i.it/index.php/en/: Agenzia Spaziale Italiana. Access Date: September 2019

Allen, S.R., McPhie, J., Ferris, G., & Simpson, C. (2008). Evolution and architecture of a large felsic Igneous Province in western Laurentia: The 1.6 Ga Gawler Range Volcanics, South Australia. *Journal of Volcanology and Geothermal Research, 172*, 132-147. doi: 10.1016/j.jvolgeores.2005.09.027

Allen, S.R., Simpson, C.J., McPhie, J., & Daly, S.J. (2003). Stratigraphy, distribution and geochemistry of widespread felsic volcanic units in the Mesoproterozoic Gawler Range Volcanics, South Australia. *Australian Journal of Earth Sciences, 50*, 97-112. doi: 10.1046/j.1440-0952.2003.00980.x

Anand, R.R. (2005). Weathering history, landscape evolution and implications for exploration. In R.R. Anand, & P. De Broekert (Eds.), *Regolith Landscape Evolution Across Australia: A Compilation of Regolith Landscape Case Studies With Regolith Landscape Evolution Models* (pp. 2-40): CRC LEME. ISBN: 978-1-92-103928-7

Anand, R.R. (2016). Regolith-landform processes and geochemical exploration for base metal deposits in regolith-dominated terrains of the Mt Isa region, northwest Queensland, Australia. *Ore Geology Reviews, 73, Part 3*, 451-474. doi: 10.1016/j.oregeorev.2015.08.014

Anand, R.R., Aspandiar, M.F., & Noble, R.R.P. (2016). A review of metal transfer mechanisms through transported cover with emphasis on the vadose zone within the Australian regolith. *Ore Geology Reviews, 73*, 394-416. doi: 10.1016/j.oregeorev.2015.06.018

Anand, R.R., & Butt, C.R.M. (2010). A guide for mineral exploration through the regolith in the Yilgarn Craton, Western Australia. *Australian Journal of Earth Sciences, 57*, 1015-1114. doi: 10.1080/08120099.2010.522823

Anand, R.R., & Paine, M. (2002). Regolith geology of the Yilgarn Craton, Western Australia: implications for exploration. *Australian Journal of Earth Sciences, 49*, 3-162. doi: 10.1046/j.1440-0952.2002.00912.x

Anand, R.R., & Robertson, I.D.M. (2012). The role of mineralogy and geochemistry in forming anomalies on interfaces and in areas of deep basin cover: implications for exploration. *Geochemistry: Exploration, Environment, Analysis, 12*, 45-66. doi: 10.1144/1467-7873/10-ra-067

Anand, R.R., Wildman, J.E., Varga, Z.S., & Phang, C. (2001). Regolith evolution and geochemical dispersion in transported and residual regolith–Bronzewing gold deposit. *Geochemistry: Exploration, Environment, Analysis, 1*, 265-276. doi: 10.1144/geochem.1.3.265

Anderson, H., & Nash, C. (1997). Integrated lithostructural mapping of the Rössing area, Namibia using high resolution aeromagnetic, radiometric, Landsat data and aerial photographs. *Exploration Geophysics, 28*, 185-191. doi: 10.1071/EG997185

Andrew, M.E., & Ustin, S.L. (2008). The role of environmental context in mapping invasive plants with hyperspectral image data. *Remote Sensing of Environment, 112*, 4301-4317. doi: 10.1016/j.rse.2008.07.016

Aslett, Z., Taranik, J.V., & Riley, D.N. (2018). Mapping rock forming minerals at Boundary Canyon, Death Valey National Park, California, using aerial SEBASS thermal infrared hyperspectral image data. *International Journal of Applied Earth Observation and Geoinformation, 64*, 326-339. doi: 10.1016/j.jag.2017.08.001

Batterham, P.M., Bullock, S.J., & Hopgood, D.N. (1983). Tanzania: integrated interpretation of aeromagnetic and radiometric maps for mineral exploration. *Transactions of the Institution of Mining and Metallurgy. Section B, Applied Earth Science, 92*, 83-92

Baudet, E., Tiddy, C., Giles, D., Hill, S., & Gordon, G. (2020). Diverse provenance of the Early Cretaceous sediments of the Eromanga Basin, South Australia: Constraints on basin evolution. *Australian Journal of Earth Sciences,* doi: 10.1080/08120099.2020.1772367

Beck, H.E., Zimmermann, N.E., McVicar, T.R., Vergopolan, N., Berg, A., & Wood, E.F. (2018). Present and future Köppen-Geiger climate classification maps at 1-km resolution. *Scientific Data, 5*, 180214. doi: 10.1038/sdata.2018.214

Bedini, E. (2009). Mapping lithology of the Sarfartoq carbonatite complex, southern West Greenland, using HyMap imaging spectrometer data. *Remote Sensing of Environment, 113*, 1208-1219. doi: 10.1016/j.rse.2009.02.007

Belperio, A., Flint, R., & Freeman, H. (2007). Prominent Hill: A hematite-dominated, iron oxide copper-gold system. *Economic Geology, 102*, 1499-1510. doi: 10.2113/gsecongeo.102.8.1499

Bierwirth, P., Huston, D., & Blewett, R. (2002). Hyperspectral mapping of mineral assemblages associated with gold mineralization in the Central Pilbara, Western Australia. *Economic Geology, 97*, 819-826. doi: 10.2113/97.4.819

Blissett, A.H., Creaser, R.A., Daly, S.J., Flint, R.B., & Parker, A.J. (1993). Gawler Range Volcanics. In J.F. Drexel, W.V. Preiss, & A.J. Parker (Eds.), *Bulletin 54, The geology of South Australia; Volume 1: The Precambrian* (pp. 107-124). Adelaide, South Australia: Geological Survey of South Australia. ISBN: 978-0-73-084146-3

Bureau of Meterology (2019). Climate Data Online, http://www.bom.gov.au/climate/data/: Australian Government. Access Date: January 2019

Butt, C.R.M., Lintern, M.J., & Anand, R.R. (2000). Evolution of regoliths and landscapes in deeply weathered terrain - implications for geochemical exploration. *Ore Geology Reviews, 16*, 167-183. doi: 10.1016/s0169-1368(99)00029-3

Cairns, C., Hronsky, J., & Schodde, R. (2010). Market Failure in the Australian Mineral Exploration Industry: The Case for Fiscal Incentives: Australian Institute of Geoscientists

Carmona, E., Alonso-Gonzalez, K., Bachmann, M., Cerra, D., Dietrich, D., Heiden, U., Knodt, U., Krutz, D., Muller, R., de los Reyes, R., Tegler, M., & Ziel, V. (2019). First results of the DESIS imaging spectrometer on board the International Space Station. In, *2019 IEEE International Geoscience and Remote Sensing Symposium* (pp. 4499-4502). Yokohama, Japan: Institute of Electrical and Electronics Engineers

Clark, R.N., Swayze, G.A., & Gallagher, A. (1992). Mapping the mineralogy and lithology of Canyonlands, Utah with imaging spectrometer data and the multiple spectral feature mapping algorithm. In, *Summaries of the Third Annual JPL Airborne Geoscience Workshop* (pp. 11-13): Jet Propulsion Laboratory

Cocks, T., Jenssen, R., Stewart, A., Wilson, I., & Shields, T. (1998). The HyMap™ airborne hyperspectral sensor: The system, calibration and performance. In M. Schaepman, D. Schlapfer, & K. Itten (Eds.), *1st EARSeL Workshop on Imaging Spectroscopy* (pp. 37-42). Zurich, Switzerland: EARSeL

Cohen, D.R., Kelley, D.L., Anand, R., & Coker, W.B. (2010). Major advances in exploration geochemistry, 1998–2007. *Geochemistry: Exploration, Environment, Analysis, 10*, 3. doi: 10.1144/1467-7873/09-215

Conor, C.H.H., Raymond, O., Baker, T., Teale, G.S., Say, P., & Lowe, G. (2010). Alteration and mineralisation in the Moonta-Wallaroo copper-gold mining field region, Olympic Domain, South Australia. In T.M. Porter (Ed.), *Hydrothermal Iron Oxide Copper - Gold and Related Deposits: A Global Perspective. Advances in the Understanding of IOCG Deposits Vol. 3* (pp. 147-170). Adelaide, Australia: Porter Geological Consulting Publishing

Cook, S.E., Corner, R.J., Groves, P.R., & Grealish, G.J. (1996). Use of airborne gamma radiometric data for soil mapping. *Australian Journal of Soil Research, 34*, 183-194. doi: 10.1071/sr9960183

Cracknell, M.J., & de Caritat, P. (2017). Catchment-based gold prospectivity analysis combining geochemical, geophysical and geological data across northern Australia. *Geochemistry: Exploration, Environment, Analysis, 17*, 204-216. doi: 10.1144/geochem2016-012

Craig, M.A. (2001). Regolith mapping for geochemical exploration in the Yilgarn Craton, Western Australia. *Geochemistry: Exploration, Environment, Analysis, 1*, 383-390. doi: 10.1144/geochem.1.4.383

Crósta, A.P., Sabine, C., & Taranik, J.V. (1998). Hydrothermal Alteration Mapping at Bodie, California, Using AVIRIS Hyperspectral Data. *Remote Sensing of Environment, 65*, 309-319. doi: 10.1016/S0034-4257(98)00040-6

Cudahy, T., Caccetta, M., Thomas, M., Hewson, R., Abrams, M., Kato, M., Kashimura, O., Ninomiya, Y., Yamaguchi, Y., Collings, S., Laukamp, C., Ong, C., Lau, I., Rodger, A., Chia, J., Warren, P., Woodcock, R., Fraser, R., Rankine, T., Vote, J., de Caritat, P., English, P., Meyer, D., Doescher, C., Fu, B.H., Shi, P.L., & Mitchell, R. (2016). Satellite-derived mineral mapping and monitoring of weathering, deposition and erosion. *Scientific Reports, 6*. doi: 10.1038/srep23702

Cudahy, T.J., Wilson, J., Hewson, R., Linton, P., Harris, P., Sears, M., Okada, K., & Hackwell, J.A. (2001a). Mapping porphyry-skarn alteration at Yerington, Nevada, using airborne hyperspectral VNIR-SWIR-TIR imaging data. In, *2001 IEEE International Geoscience and Remote Sensing Symposium* (pp. 631-633). Sydney, Australia: Institute of Electrical and Electronics Engineers

Cudahy, T.J., Wilson, J., Hewson, R., Linton, P., Harris, P., Sears, M., Okada, K., & Hackwell, J.A. (2001b). Mapping variations in plagioclase felspar mineralogy using airborne hyperspectral TIR imaging data. In, *2001 IEEE International Geoscience and Remote Sensing Symposium* (pp. 730-732). Sydney, Australia: Institute of Electrical and Electronics Engineers

Cutts, K., Hand, M., & Kelsey, D.E. (2011). Evidence for early Mesoproterozoic (ca. 1590 Ma) ultrahigh-temperature metamorphism in southern Australia. *Lithos, 124*, 1-16. doi: 10.1016/j.lithos.2010.10.014

Daly, S.J., & Fanning, C.M. (1993). Archean. In J.F. Drexel, W.V. Preiss, & A.J. Parker (Eds.), *Bulletin 54, The geology of South Australia; Volume 1: The Precambrian* (pp. 33-50). Adelaide, South Australia: Geological Survey of South Australia. ISBN: 978-0-73-084146-3

Daly, S.J., Fanning, G.M., & Fairclough, M.C. (1998). Tectonic evolution and exploration potential of the Gawler Craton, South Australia. *AGSO Journal of Australian Geology and Geophysics, 17*, 145-168

Darnley, A.G., & Ford, K.L. (1989). Regional airborne gamma-ray surveys: A review. In G.D. Garland (Ed.), *Proceedings of Exploration '87: Third Decennial International Conference on Geophysical and Geochemical Exploration for Minerals and Groundwater* (pp. 229-240). Toronto, Canada: Ontario Ministry of Northern Development and Mines, Mines and Minerals Division

Dauth, C. (1997). Airborne magnetic, radiometric and satellite imagery for regolith mapping in the Yilgarn Craton of Western Australian. *Exploration Geophysics, 28*, 199-203. doi: 10.1071/EG997199

Davies, P.R., Robison, H.R., & Fethers, G.H. (1988). Open File Envelope No. 4267, Gawler Range Volcanics Project. Adelaide, South Australia. Stockdale Prospecting, The Shell Co. of Australia, Billiton Austraila, Western Mining Corporation.

Dehaan, R.L., & Taylor, G.R. (2004). A remote-sensing method of mapping soils and surficial lags from a deeply weathered and region, near Cobar, NSW, Australia. *Geochemistry: Exploration, Environment, Analysis, 4*, 99-112. doi: 10.1144/1467-7873/03-026

Department of the Environment and Energy (2012). *Interim Biogeographic Regionalisation for Australia, Version 7*. Canberra, Australia: Department of the Environment and Energy

Dickson, B.L., & Scott, K.M. (1997). Interpretation of aerial gamma-ray surveys – adding the geochemical factors. *AGSO Journal of Australian Geology and Geophysics, 17*, 187-200

Drown, C.G., Gerakiteys, C., Ashley, P.M., Joyce, R.M., Mackay, C.R., & Standish, T.R. (2000). Open File Envelope No. 8811, Mount Ive Gate. Adelaide, South Australia. Aberfoyle Resources, Acacia Resources, Anglogold Australasia.

Drown, C.G., Humphries, B.G., Curran, C.A., Pontifex, I.R., Gerakiteys, C., Joyce, R.M., Mackay, C.R., Standish, T.R., Beckwith, A., Lithgow, N., & Smith, R.N. (2003). Open File Envelope No. 8169, Carpie Puntha and Peterlumbo. Adelaide, South Australia. Aberfoyle Resources, MIM Exploration, Acacia Resources, Anglogold Australasia, Aquila Resources.

Duuring, P., Hassan, L., Zelic, M., & Gessner, K. (2016). Geochemical and Spectral Footprint of Metamorphosed and Deformed VMS-Style Mineralization in the Quinns District, Yilgarn Craton, Western Australia. *Economic Geology, 111*, 1411-1438. doi: 10.2113/econgeo.111.6.1411

Duval, J.S. (1990). Modern aerial gamma-ray spectrometry and regional potassium map of the conterminous United States. *Journal of Geochemical Exploration, 39*, 249-253. doi: 10.1016/0375-6742(90)90076-M

Earth Observation Center of DLR (2018). EnMAP Hyperspectral Imager Mission, http://www.enmap.org/mission.html: Earth Observation Center of DLR. Access Date: October 2019

Eggleton, R.A. (2009). Regolith mineralogy. In K.M. Scott, & C.F. Pain (Eds.), *Regolith Science* (pp. 66-102): CSIRO Publishing. ISBN: 978-0-64-309826-8

Eggleton, R.A., Anand, R.R., Butt, C.R.M., Chen, X.Y., Craig, M.A., de Caritat, P., Field, J.B., Gibson, D.L., Greene, R., Hill, S.M., Jones, M., Lintern, M.J., McQueen, K.G., Pain, C.F., Pillans, B.J., Robertson, I.D.M., Smith, K., & Taylor, G.F. (Eds.) (2001). *The Regolith Glossary: surficial geology, soils and landscapes*. Perth, Australia: CRC LEME. ISBN: 978-0-73-153343-5

Eppinger, R.G., Fey, D.L., Giles, S.A., Grunsky, E.C., Kelley, K.D., Minsley, B.J., Munk, L., & Smith, S.M. (2013). Summary of Exploration Geochemical and Mineralogical Studies at the Giant Pebble

Porphyry Cu-Au-Mo Deposit, Alaska: Implications for Exploration Under Cover. *Economic Geology*, *108*, 495-527. doi: 10.2113/econgeo.108.3.495

Fanning, C.M., Flint, R.B., Parker, A.J., Ludwig, K.R., & Blissett, A.H. (1988). Refined proterozoic evolution of the Gawler Craton, South Australia, through U-Pb zircon geochronology. *Precambrian Research, 40/41*, 363-386. doi: 10.1016/0301-9268(88)90076-9

Fanning, C.M., Reid, A.J., & Teale, G.S. (Eds.) (2007). *A geochronological framework for the Gawler Craton, South Australia*. Bulletin 55. Adelaide, South Australia: Department of Primary Industries and Resources. ISBN: 978-0-75-901392-6

Feng, J., Rogge, D., & Rivard, B. (2018). Comparison of lithological mapping results from airborne hyperspectral VNIR-SWIR, LWIR and combined data. *International Journal of Applied Earth Observation and Geoinformation, 64*, 340-353. doi: 10.1016/j.jag.2017.03.003

Ferrier, G., Ganas, A., & Pope, R. (2019). Prospectivity mapping for high sulfidation epithermal porphyry deposits using an integrated compositional and topographic remote sensing dataset. *Ore Geology Reviews, 107*, 353-363. doi: 10.1016/j.oregeorev.2019.02.029

Ferris, G., & Schwarz, M. (2003). Proterozoic gold province of the central Gawler Craton. *MESA Journal, 30*, 4-12

Ferris, G.M., Schwarz, M.P., & Heithersay, P. (2002). The geological framework, distribution and controls of Fe-oxide Cu–Au mineralisation in the Gawler Craton, South Australia. Part 1: Geological and tectonic framework. In T.M. Porter (Ed.), *Hydrothermal Iron Oxide Copper - Gold and Related Deposits: A Global Perspective Vol. 2* (pp. 9-31). Adelaide, South Australia: Porter Geological Consulting Publishing. ISBN: 978-0-95-805741-7

Flint, R.B. (1993). Hiltaba Suite. In J.F. Drexel, W.V. Preiss, & A.J. Parker (Eds.), *Bulletin 54, The geology of South Australia, Volume 1: The Precambrian* (pp. 127-130). Adelaide, South Australia: The Geological Survey of South Australia. ISBN: 978-0-73-084146-3

Foote, R., & Humphrey, N. (1976). Airborne radiometric techniques and applications to U exploration. In, *Exploration for U ore deposits* (pp. 17-34). Vienna, Austria: International Atomic Energy Agency

Forbes, C.J., Giles, D., Jourdan, F., Sato, K., Omori, S., & Bunch, M. (2012). Cooling and exhumation history of the northeastern Gawler Craton, South Australia. *Precambrian Research, 200*, 209-238. doi: 10.1016/j.precamres.2011.11.003

Forbes, C., Giles, D., Freeman, H., Sawyer, M., & Normington, V. (2015). Glacial dispersion of hydrothermal monazite in the Prominent Hill deposit: An exploration tool. *Journal of Geochemical Exploration*, *156*, 10-33. doi: 10.1016/j.gexplo.2015.04.011

Galbraith, J.H., & Saunders, D.F. (1983). Rock classification by characteristics of aerial gamma-ray measurements. *Journal of Geochemical Exploration, 18*, 49-73. doi: 10.1016/0375-6742(83)90080-8

Garner, A., & McPhie, J. (1999). Partially melted lithic megablocks in the Yardea Dacite, Gawler Range Volcanics, Australia: implications for eruption and emplacement mechanisms. *Bulletin of Volcanology, 61*, 396-410. doi: 10.1007/s004450050281

Garrett, R.G. (1991). The management, analysis and display of exploration geochemical data. Ottawa, Canada: Geological Survey of Canada. Document Number: Open File 2390

Garsed, I. (2003). Open File Envelope, No. 9910, Mount Ive Gate. Adelaide, South Australia. MIM Exploration.

Gerakiteys, C. (1996). Technical Report No. 2718, EL 1841 "Mt Ive Gate". Adelaide, Australia. MIM Exploration. Document Number: R96/02406

Goetz, A.F.H. (2009). Three decades of hyperspectral remote sensing of the Earth: A personal view. *Remote Sensing of Environment, 113*, S5-S16. doi: 10.1016/j.rse.2007.12.014

González-Álvarez, I., Ley-Cooper, A.Y., & Salama, W. (2016). A geological assessment of airborne electromagnetics for mineral exploration through deeply weathered profiles in the southeast Yilgarn Cratonic margin, Western Australia. *Ore Geology Reviews, 73, Part 3*, 522-539. doi: 10.1016/j.oregeorev.2015.10.029

Gordon, G., Murray, J., & Mauger, A. (2016). Infrared analysis of drill cores from the Paris Silver Prospect, South Australia. In, *AESC 2016 - Australian Earth Sciences Convention*. Adelaide, Australia: Geological Society of Australia

Graham, D.F., & Bonham-Carter, G.F. (1993). Airborne radiometric data - a tool for reconnaissance geological mapping using a GIS. *Photogrammetric Engineering and Remote Sensing, 59*, 1243-1249

Graham, G.E., Kokaly, R.F., Kelley, K.D., Hoefen, T.M., Johnson, M.R., & Hubbard, B.E. (2018). Application of Imaging Spectroscopy for Mineral Exploration in Alaska: A Study over Porphyry Cu Deposits in the Eastern Alaska Range. *Economic Geology, 113*, 489-510. doi: 10.5382/econgeo.2018.4559

Gregory, A.F., & Horwood, J.L. (1961). A laboratory study of gamma-ray spectra at the surface of rocks. Ottawa, Canada. Department of Energy, Mines & Resources. Document Number: Mines Branch Research Report R85

Grunsky, E.C. (2010). The interpretation of geochemical survey data. *Geochemistry: Exploration, Environment, Analysis, 10*, 27-74. doi: 10.1144/1467-7873/09-210

Guj, P., & Schodde, R. (2013). Where are Australia's mines of tomorrow? *AusIMM Bulletin, June 2013*, 76-82

Hackwell, J.A., Warren, D.W., Bongiovi, R.P., Hansel, S.J., Hayhurst, T.L., Mabry, D.J., Sivjee, M.G., & Skinner, J.W. (1996). *LWIR/MWIR imaging hyperspectral sensor for airborne and ground-based remote sensing*. ISBN: 978-0-81-942207-1

Haest, M., Cudahy, T., Laukamp, C., & Gregory, S. (2012). Quantitative Mineralogy from Infrared Spectroscopic Data. II. Three-Dimensional Mineralogical Characterization of the Rocklea Channel Iron Deposit, Western Australia. *Economic Geology, 107*, 229-249. doi: 10.2113/econgeo.107.2.229

Hand, M., Reid, A., & Jagodzinski, L. (2007). Tectonic framework and evolution of the Gawler Craton, Southern Australia. *Economic Geology, 102*, 1377-1395. doi: 10.2113/gsecongeo.102.8.1377

Hargrove, W.W., Hoffman, F.M., & Hessburg, P.F. (2006). Mapcurves: a quantitative method for comparing categorical maps. *Journal of Geographical Systems, 8*, 187-208. doi: 10.1007/s10109-006-0025-x

Harraden, C.L., McNulty, B.A., Gregory, M.J., & Lang, J.R. (2013). Shortwave Infrared Spectral Analysis of Hydrothermal Alteration Associated with the Pebble Porphyry Copper-Gold-Molybdenum Deposit, Iliamna, Alaska. *Economic Geology, 108*, 483-494. doi: 10.2113/econgeo.108.3.483

Harris, J.R., Rogge, D., Hitchcock, R., Ijewliw, O., & Wright, D. (2005). Mapping lithology in Canada's Arctic: application of hyperspectral data using the minimum noise fraction transformation and matched filtering. *Canadian Journal of Earth Sciences, 42*, 2173-2193. doi: 10.1139/e05-064

Harrison, D., Rivard, B., & Sanchez-Azofeifa, A. (2018). Classification of tree species based on longwave hyperspectral data from leaves, a case study for a tropical dry forest. *International Journal of Applied Earth Observation and Geoinformation, 66*, 93-105. doi: 10.1016/j.jag.2017.11.009

Hecker, C.A. (2006). Geologic Surface Compositional Mapping from Thermal Infrared SEBASS Data. In N. Kerle, & A. Skidmore (Eds.), *ISPRS Commission VII Symposium, 'Remote Sensing: From Pixels to Processes'* (p. 3). Enschede, The Netherlands: International Society for Photogrammetry and Remote Sensing

Hewson, R.D., Cudahy, T.J., Caccetta, M., Rodger, A., Jones, M., & Ong, C. (2009). Advances in hyperspectral processing for province- and continental- wide mineral mapping. In, *2009 International Geoscience and Remote Sensing Symposium* (pp. 701-704): Institute of Electrical and Electronics Engineers

Hewson, R.D., Cudahy, T.J., Drake-Brockman, J., Meyers, J., & Hashemi, A. (2006). Mapping geology associated with manganese mineralisation using spectral sensing techniques at Woodie Woodie, East Pilbara. *Exploration Geophysics, 37*, 389-400. doi: 10.1071/eg06389

Hillis, R.R., Giles, D., Van Der Wielen, S.E., Baensch, A., Cleverley, J.S., Fabris, A., Halley, S.W., Harris, B.D., Hill, S.M., Kanck, P.A., Kepic, A., Soe, S.P., Stewart, G., & Uvarova, Y. (2014). Coiled

Tubing Drilling and Real-Time Sensing-Enabling Prospecting Drilling in the 21st Century? In K.D. Kelley, & H.C. Golden (Eds.), *Society of Economic Geologists Special Publication Number 18* (pp. 243-259): Society of Economic Geologists. ISBN: 978-1-62-949637-5

Hronsky, J.M.A., & Kreuzer, O.P. (2019). Applying spatial prospectivity mapping to exploration targeting: Fundamental practical issues and suggested solutions for the future. *Ore Geology Reviews, 107*, 647-653. doi: 10.1016/j.oregeorev.2019.03.016

Huntington, J., Mauger, A., Skirrow, R., Bastrakov, E., Connor, P., Mason, P., Keeling, J., Coward, D., Berman, M., Phillips, R., Whitbourn, L., & Heithersay, P. (2004). Automated mineralogical logging of core from the Emmie Bluff, iron oxide copper-gold prospect, South Australia. In, *PACRIM 2004 Congress* (pp. 223-230). Adelaide, Australia: The Australasian Institute of Mining and Metallurgy

IMDEX, (2019). ioGAS 7.1

Indian Space Research Organisation (2017). HySIS, https://www.isro.gov.in/Spacecraft/hysis: Indian Space Research Organisation. Access Date: September 2019

Investigator Resources (2017a). Paris Silver Project. In J. Anderson, & J. Murray (Eds.). Adelaide, Australia: Investigator Resources

Investigator Resources (2017b). New drilling and advanced exploration techniques upgrade porphyry copper target at Nankivel. In J. Anderson, & J. Murray (Eds.). Adelaide, Australia: Investigator Resources

Jagodzinski, E.A., Reid, A.J., Crowley, J.L., McAvaney, S., & Wade, C.E. (2016). Precise zircon U-Pb dating of a Mesoproterozoic silicic large igneous province: the Gawler Range Volcanics and Benagerie Volcanic Suite, South Australia. In, *AESC 2016 - Australian Earth Sciences Convention*. Adelaide, Australia: Geological Society of Australia

Jet Propulsion Laboratory, & California Institute of Technology (2018). HyspIRI Final Report. Pasadena, California: Jet Propulsion Laboratory

Johnson, J.P., & Cross, K.C. (1995). U-Pb geochronological constraints on the genesis of the Olympic Dam Cu-U-Au-Ag deposit, South Australia. *Economic Geology, 90*, 1046-1063

Johnson, W.R., Hook, S.J., Mouroulis, P., Wilson, D.W., Gunapala, S.D., Realmuto, V., Lamborn, A., Paine, C., Mumolo, J.M., & Eng, B.T. (2011). HyTES: Thermal imaging spectrometer development. In, *2011 IEEE Aerospace Conference* (pp. 1803 - 1810). Big Sky, MA: Institute of Electrical and Electronics Engineers

King, T.V.V., Johnson, M.R., Hubbard, B.E., & Drenth, B.J. (Eds.) (2011). *Identification of mineral resources in Afghanistan-Detecting and mapping resource anomalies in prioritized areas using geophysical and remote sensing (ASTER and HyMap) data*. Virginia, USA: United States Geological Survey

Krapf, C.B.E. (2016). Regolith Map of the Southern Gawler Ranges Margin (YARDEA and PORT AUGUSTA 1:250 000 map sheets). Adelaide, South Australia: Geological Survey of South Australia

Kreuzer, O.P., Markwitz, V., Porwal, A.K., & McCuaig, T.C. (2010). A continent-wide study of Australia's uranium potential Part I: GIS-assisted manual prospectivity analysis. *Ore Geology Reviews, 38*, 334-366. doi: 10.1016/j.oregeorev.2010.08.003

Kreuzer, O.P., Miller, A.V.M., Peters, K.J., Payne, C., Wildman, C., Partington, G.A., Puccioni, E., McMahon, M.E., & Etheridge, M.A. (2015). Comparing prospectivity modelling results and past exploration data: A case study of porphyry Cu-Au mineral systems in the Macquarie Arc, Lachlan Fold Belt, New South Wales. *Ore Geology Reviews, 71*, 516-544. doi: 10.1016/j.oregeorev.2014.09.001

Kruse, F.A. (1988). Use of airborne imaging spectrometer data to map minerals associated with hydrothermally altered rocks in the northern Grapevine mountains, Nevada, and California. *Remote Sensing of Environment, 24*, 31-51. doi: 10.1016/0034-4257(88)90004-1

Kruse, F.A. (2012). Mapping surface mineralogy using imaging spectrometry. *Geomorphology, 137*, 41-56. doi: 10.1016/j.geomorph.2010.09.032

Kruse, F.A., Boardman, J.W., & Huntington, J.F. (2003). Comparison of airborne hyperspectral data and EO-1 Hyperion for mineral mapping. *IEEE Transactions on Geoscience and Remote Sensing, 41*, 1388-1400. doi: 10.1109/TGRS.2003.812908

Kruse, F.A., & McDowell, M. (2015). Analysis of multispectral and hyperspectral longwave infrared (LWIR) data for geologic mapping. In M. VelezReyes, & F.A. Kruse (Eds.), *Algorithms and Technologies for Multispectral, Hyperspectral, and Ultraspectral Imagery XXI*. Baltimore, Maryland: SPIE

Kuhn, S., Cracknell, M.J., & Reading, A.M. (2018). Lithologic mapping using Random Forests applied to geophysical and remote-sensing data: A demonstration study from the Eastern Goldfields of Australia. *Geophysics, 83*, B183-B193. doi: 10.1190/geo2017-0590.1

Kyser, K., Barr, J., & Ihlenfeld, C. (2015). Applied Geochemistry in Mineral Exploration and Mining. *Elements, 11*, 241-246. doi: 10.2113/gselements.11.4.241

Laakso, K., Peter, J.M., Rivard, B., & White, H.P. (2016). Short-Wave Infrared Spectral and Geochemical Characteristics of Hydrothermal Alteration at the Archean Izok Lake Zn-Cu-Pb-Ag Volcanogenic Massive Sulfide Deposit, Nunavut, Canada: Application in Exploration Target Vectoring. *Economic Geology, 111*, 1223-1239. doi: 10.2113/econgeo.111.5.1223

Laakso, K., Turner, D.J., Rivard, B., & Sanchez-Azofeifa, A. (2019). The long-wave infrared (8-12 mu m) spectral features of selected rare earth element-Bearing carbonate, phosphate and silicate minerals. *International Journal of Applied Earth Observation and Geoinformation, 76*, 77-83. doi: 10.1016/j.jag.2018.11.005

Lampinen, H.M., Laukamp, C., Occhipinti, S.A., Metelka, V., & Spinks, S.C. (2017). Delineating Alteration Footprints from Field and ASTER SWIR Spectra, Geochemistry, and Gamma-Ray Spectrometry above Regolith-Covered Base Metal Deposits—An Example from Abra, Western Australia. *Economic Geology, 112*, 1977-2003. doi: 10.5382/econgeo.2017.4537

Laukamp, C., Cudahy, T., Cleverley, J.S., Oliver, N.H.S., & Hewson, R. (2011a). Airborne hyperspectral imaging of hydrothermal alteration zones in granitoids of the Eastern Fold Belt, Mount Isa Inlier, Australia. *Geochemistry: Exploration, Environment, Analysis, 11*, 3-24. doi: 10.1144/1467-7873/09-231

Laukamp, C., Cudahy, T., Thomas, M., Jones, M., Cleverley, J.S., & Oliver, N.H.S. (2011b). Hydrothermal mineral alteration patterns in the Mount Isa Inlier revealed by airborne hyperspectral data. *Australian Journal of Earth Sciences, 58*, 917-936. doi: 10.1080/08120099.2011.571287

Lintern, M., Sheard, M., & Buller, N. (2011). The gold-in-calcrete anomaly at the ET gold prospect, Gawler Craton, South Australia. *Applied Geochemistry, 26*, 2027-2043. doi: 10.1016/j.apgeochem.2011.06.032

Lintern, M.J. (2002). Calcrete sampling for mineral exploration. In X.Y. Chen, M.J. Lintern, & I.C. Roach (Eds.), *Calcrete: characteristics, distribution and use in mineral exploration* (pp. 31-109). Perth, Australia: CSIRO, CRC LEME. ISBN: 978-0-95-811450-9

Lorenz, S., Kirsch, M., Zimmermann, R., Tusa, L., Mockel, R., Chamberland, M., & Gloaguen, R. (2018). Long-wave Hyperspectral Imaging For Lithological Mapping: A Case Study. In, *2018 IEEE International Geoscience and Remote Sensing Symposium* (pp. 1620-1623). Valencia, Spain: Institute of Electrical and Electronics Engineers

Lypaczewski, P., Rivard, B., Gaillard, N., Perrouty, S., Piette-Lauzière, N., Bérubé, C.L., & Linnen, R.L. (2019). Using hyperspectral imaging to vector towards mineralization at the Canadian Malartic gold deposit, Québec, Canada. *Ore Geology Reviews, 111*, 102945. doi: 10.1016/j.oregeorev.2019.102945

Mann, A.W., Birrell, R.D., Mann, A.T., Humphreys, D.B., & Perdrix, J.L. (1998). Application of the mobile metal ion technique to routine geochemical exploration. *Journal of Geochemical Exploration, 61*, 87-102. doi: 10.1016/s0375-6742(97)00037-x

Mars, J.C., & Rowan, L.C. (2006). Regional mapping of phyllic- and argillic-altered rocks in the Zagros magmatic arc, Iran, using Advanced Spaceborne Thermal Emission and Reflection Radiometer (ASTER) data and logical operator algorithms. *Geosphere, 2*, 161-186. doi: 10.1130/ges00044.1

Mastunaga, T., Iwasaki, A., Tsuchida, S., Iwao, K., Tanii, J., Kashimura, O., Nakamura, R., Yamamoto, H., Kato, S., Obata, K., Mouri, K., & Tachikawa, T. (2019). HiSUI status toward 2020 launch. In, *2019 IEEE International Geoscience and Remote Sensing Symposium* (pp. 4495-4498). Yokohama, Japan: Institute of Electrical and Electronics Engineers

McClenaghan, M.B., Thorleifson, L.H., & DiLabio, R.N.W. (2000). Till geochemical and indicator mineral methods in mineral exploration. *Ore Geology Reviews, 16*, 145-166. doi: 10.1016/S0169-1368(99)00028-1

McHarg, S., & Aspandiar, M.F. (2019). Gold distribution and lithogeochemical discrimination of residual regolith and transported overburden, Minotaur gold deposit, Lake Lefroy, Western Australia. *Australian Journal of Earth Sciences*, 1-16. doi: 10.1080/08120099.2019.1611663

McQueen, K.G., Hill, S.M., & Foster, K.A. (1999). The nature and distribution of regolith carbonate accumulations in southeastern Australia and their potential as a sampling medium in geochemical exploration. *Journal of Geochemical Exploration, 67*, 67-82. doi: 10.1016/s0375-6742(99)00071-0

Minty, B., Franklin, R., Milligan, P., Richardson, M., & Wilford, J. (2009). The Radiometric Map of Australia. *Exploration Geophysics, 40*, 325-333. doi: 10.1071/eg09025

Minty, B.R.S. (1997). Fundamentals of airborne gamma-ray spectrometry. *AGSO Journal of Australian Geology and Geophysics, 17*, 39-50

Mulder, V.L., de Bruin, S., Weyermann, J., Kokaly, R.F., & Schaepman, M.E. (2013). Characterizing regional soil mineral composition using spectroscopy and geostatistics. *Remote Sensing of Environment, 139*, 415-429. doi: 10.1016/j.rse.2013.08.018

Mustard, J.F. (1993). Relationships of soil, grass, and bedrock over the Kaweah Serpentinite Melange through spectral mixture analysis of AVIRIS data. *Remote Sensing of Environment, 44*, 293-308. doi: 10.1016/0034-4257(93)90023-Q

National Academies of Sciences, Engineering, and Medicine, (2018). *Thriving on Our Changing Planet: A Decadal Strategy for Earth Observation from Space*. Washington DC: The National Acadamies of Sciences, Engineering, Medicine. ISBN: 978-0-30-946757-5

National Aeronautics and Space Administration (2019). Landsat 9, https://landsat.gsfc.nasa.gov/landsat-9/: National Aeronautics and Space Administration. Access Date: October 2019

Nicolson, B., Reid, A., McAvaney, S., Keeling, J., Fraser, G., & Vasconcelos, P. (2017). A Mesoproterozoic advanced argillic alteration system: $^{40}Ar/^{39}Ar$ thermochronology from Nankivel Hill, Gawler Craton. Adelaide, South Australia: Department of Premier and Cabinet. Geological Survey of South Australia. Document Number: Report Book 2017/00011

Noble, R.R.P., Morris, P.A., Anand, R.R., Lau, I.C., & Pinchand, G.T. (2019). Application of ultrafine fraction soil extraction and analysis for mineral exploration. *Geochemistry: Exploration, Environment, Analysis*, *20*, 129-154. doi: 10.1144/geochem2019-009

Ong, C.C.H., & Cudahy, T.J. (2014). Mapping contaminated soils: using remotely-sensed hyperspectral data to predict pH. *European Journal of Soil Science, 65*, 897-906. doi: 10.1111/ejss.12160

Pain, C.F., Chan, R., Craig, M.A., Gibson, D., Kilgour, P., & Wilford, J. (2007). RTMAP Regolith Database Field Book and Users Guide (Second Edition): CRC LEME Open File Report 231

Paul, M.W., Cook, N.J., Ciobanu, C.L., Anderson, J., & Murray, J. (2015). Preliminary mineralogical investigations of the Paris silver deposit, northern Eyre Peninsula, South Australia. In, *Society for Geology Applied to Mineral Deposits 13th Biennial Meeting* (pp. 181-184). Nancy, France: Society for Geology Applied to Mineral Deposits

Paul, M.W., Cook, N.J., Ciobanu, C.L., Anderson, J., & Murray, J. (2016). Balance of precious metals in the Paris silver deposit, South Australia. In, *AESC 2016- Australian Earth Sciences Convention*. Adelaide, Australia: Geological Society of Australia

Pigott, G.F., Derriman, M.D., Thorne, L., Rankin, L.R., Wilson, P., Purvis, A.C., Clent, W., Coopes, G.A., Falk, M., Jochymek, K., Hanson, J., Matonia, K., & Freeman, R. (2008). Open File Envelope No. 10493, Wilcherry Hill Project. Adelaide, Australia. Aquila Resources, Trafford Resources, IronClad Mining.

Pracilio, G. (2007). The utilisation of gamma ray spectrometry, a soil mapping technology, to improve dryland crop production. *PhD Thesis (Unpublished),* University of Western Australia

Reid, A.J., Swain, G., Mason, D., & Maas, R. (2011). Nature and timing Cu-Au-Zn-Pb mineralisation at Punt Hill, eastern Gawler Craton. *MESA Journal, 60*, 7-17

Rock, G., Gerhards, M., Schlerf, M., Hecker, C., & Udelhoven, T. (2016). Plant species discrimination using emissive thermal infrared imaging spectroscopy. *International Journal of Applied Earth Observation and Geoinformation, 53*, 16-26. doi: doi.org/10.1016/j.jag.2016.08.005

Rogge, D., Rivard, B., Segl, K., Grant, B., & Feng, J. (2014). Mapping of Ni-Cu-PGE ore hosting ultramafic rocks using airborne and simulated EnMAP hyperspectral imagery, Nunavik, Canada. *Remote Sensing of Environment, 152*, 302-317. doi: 10.1016/j.rse.2014.06.024

Rowan, L.C., Simpson, C.J., & Mars, J.C. (2004). Hyperspectral analysis of the ultramafic complex and adjacent lithologies at Mordor, NT, Australia. *Remote Sensing of Environment, 91*, 419-431. doi: 10.1016/j.rse.2004.04.007

Rumerman, J.A. (1999). Space Applications. In J.A. Rumerman (Ed.), *NASA Historical Data Book Volume VI* (pp. 11-173). Washington DC, USA: NASA

Sabins, F.F. (1999). Remote sensing for mineral exploration. *Ore Geology Reviews, 14*, 157-183. doi: 10.1016/s0169-1368(99)00007-4

Sadeghi, M., Billay, A., & Carranza, E.J.M. (2015). Analysis and mapping of soil geochemical anomalies: Implications for bedrock mapping and gold exploration in Giyani area, South Africa. *Journal of Geochemical Exploration, 154*, 180-193. doi: 10.1016/j.gexplo.2014.11.018

Salama, W., González-Álvarez, I., & Anand, R.R. (2016). Significance of weathering and regolith/landscape evolution for mineral exploration in the NE Albany-Fraser Orogen, Western Australia. *Ore Geology Reviews, 73, Part 3*, 500-521. doi: 10.1016/j.oregeorev.2015.07.024

Schodde, R.C. (2017a). Challenges of Exploring Under Deep Cover. In, *AMIRA International's 11th Biennial Exploration Managers Conference* (p. 43). Healesville, Australia: MinEx Consulting

Schodde, R.C. (2017b). The National State of Exploration. In, *Copper to the World Conference*. (p. 31). Adelaide, Australia: MinEx Consulting

Schodde, R.C. (2019). Trends in exploration. In, *International Mining and Resource Conference* (p. 30). Melbourne, Australia: MinEx Consulting

Schwarzer, T.F., Cook, B.G., & Adams, J.A.S. (1972). Low altitude gamma-spectrometric surveys from helicopters in Puerto Rico as an example of the remote sensing of thorium, uranium, and potassium in soils and rocks. *Remote Sensing of Environment, 2*, 83-94. doi: 10.1016/0034-4257(71)90081-2

Shives, R.B.K., Charbonneau, B.W., & Ford, K.L. (2000). The detection of potassic alteration by gamma-ray spectrometry—Recognition of alteration related to mineralization. *Geophysics, 65*, 2001-2011. doi: 10.1190/1.1444884

Smith, R.E. (1996). Regolith research in support of mineral exploration in Australia. *Journal of Geochemical Exploration, 57*, 159-173. doi: 10.1016/s0375-6742(96)00032-5

Specim (2019). AisaOWL Hyperspectral Sensor, http://www.specim.fi/products/aisaowl/: Specim. Access Date: April 2019

Stagpoole, V.M., Edbrooke, S.W., Christie, A.B., Davy, B.W., Caratori Tontini, F., Soengkono, S., Cox, S.C., & Isaac, M.J. (2012). Northland airborne magnetic and radiometric survey: a geological interpretation. Lower Hutt NZ: GNS Science. Document Number: GNS Science Report 2011/54

Stewart, J.R., & Betts, P.G. (2010). Late Paleo-Mesoproterozoic plate margin deformation in the southern Gawler Craton: Insights from structural and aeromagnetic analysis. *Precambrian Research, 177*, 55-72. doi: 10.1016/j.precamres.2009.11.004

Tappert, M.C., Rivard, B., Fulop, A., Rogge, D., Feng, J., Tappert, R., & Stalder, R. (2015). Characterizing Kimberlite Dilution by Crustal Rocks at the Snap Lake Diamond Mine (Northwest Territories, Canada) using SWIR (1.90-2.36 mu m) and LWIR (8.1-11.1 mu m) Hyperspectral Imagery Collected from Drill Core. *Economic Geology, 110*, 1375-1387. doi: 10.2113/econgeo.110.6.1375

Taylor, G., & Butt, C.R.M. (1998). The Australian regolith and mineral exploration. *AGSO Journal of Australian Geology and Geophysics, 17*, 55-67

Taylor, M.J., Smettem, K., Pracilio, G., & Verboom, W. (2002). Relationships between soil properties and high-resolution radiometrics, central eastern Wheatbelt, Western Australia. *Exploration Geophysics, 33*, 95-102. doi: 10.1071/eg02095

Tiddy, C.J., Hill, S.M., Giles, D., van der Hoek, B.G., Normington, V.J., Anand, R.R., Baudet, E., Custance, K., Hill, R., Johnson, A., McLennan, S., Mitchell, C., Zivak, D., Salama, W., Stoate, K., & Wolff, K. (2019). Utilising geochemical data for the identification and characterisation of mineral exploration sample media within cover sequence materials. *Australian Journal of Earth Sciences*, 1-29. doi: 10.1080/08120099.2019.1673484

Travers, S.J., & Wilson, C.J.L. (2015). Reflectance spectroscopy and alteration assemblages at the Leven Star gold deposit, Victoria, Australia. *Australian Journal of Earth Sciences, 62*, 873-882. doi: 10.1080/08120099.2015.1114525

Ullah, S., Schlerf, M., Skidmore, A.K., & Hecker, C. (2012). Indentifying plant species using mid-wave infrared (2.5-6 um) and thermal infrared (8-14 um) emissivity spectra. *Remote Sensing of Environment, 118*, 95-102. doi: 10.1016/j.rse.2011.11.008

United States Geological Survey (2018). Earth Observing 1 (EO-1), https://archive.usgs.gov/archive/sites/eo1.usgs.gov/index.html: United States Geological Survey. Access Date: October 2019

van den Boogaart, K.G., & Tolosana-Delgado, R. (2008). "compositions": A unified R package to analyze compositional data. *Computers & Geosciences, 34*, 320-338. doi: 10.1016/j.cageo.2006.11.017

van der Wielen, S., Fabris, A., Keeling, J., Mauger, A., Gordon, G., Keeping, T., Heath, P., Reed, G., Katona, L., Fairclough, M., Hill, S., Giles, D., & Halley, S. (2013). Integrated 3D mineral systems maps for iron oxide copper gold (IOCG) Deposits, Eastern Gawler Craton, South Australia. In E. Jonsson (Ed.), *12th SGA Biennial Meeting - "Mineral Deposit Research for a High-Tech World"* (pp. 108-111). Uppsala, Sweden: Society of Geology Applied to Mineral Deposits

van Ruitenbeek, F.J.A., Cudahy, T.J., van der Meer, F.D., & Hale, M. (2012). Characterization of the hydrothermal systems associated with Archean VMS-mineralization at Panorama, Western Australia, using hyperspectral, geochemical and geothermometric data. *Ore Geology Reviews, 45*, 33-46. doi: 10.1016/j.oregeorev.2011.07.001

Vane, G., Chrisp, M., Enmark, H., Macenka, S., & Solomon, J. (1984). Airborne Visible/Infrared Imaging Spectrometer (AVIRIS): an advanced tool for Earth remote sensing. In, *IGARSS '84: Remote Sensing - From Research Towards Operational Use* (pp. 751-757). Strasbourg, France: Institute of Electrical and Electronics Engineers

Vaughan, R.G., Hook, S.J., Calvin, W.M., & Taranik, J.V. (2005). Surface mineral mapping at Steamboat Springs, Nevada, USA, with multi-wavelength thermal infrared images. *Remote Sensing of Environment, 99*, 140-158. doi: 10.1016/j.rse.2005.04.030

Wang, R., Cudahy, T., Laukamp, C., Walshe, J.L., Bath, A., Mei, Y., Young, C., Roache, T.J., Jenkins, A., Roberts, M., Barker, A., & Laird, J. (2017). White Mica as a Hyperspectral Tool in Exploration for the Sunrise Dam and Kanowna Belle Gold Deposits, Western Australia. *Economic Geology, 112*, 1153-1176. doi: 10.5382/econgeo.2017.4505

Ward, S.H. (1981). Gamma-ray spectrometry in geological mapping and uranium exploration. *Economic Geology, 75th Anniversary Volume*, 840-849

Webster, S.S. (1984). Comments on the use of gamma-ray spectrometry for tin prospecting. *Exploration Geophysics, 15*, 61-63. doi: 10.1071/EG984061

Wells, M., Laukamp, C., & Hancock, E. (2016). Reflectance spectroscopic characterisation of mineral alteration footprints associated with sediment-hosted gold mineralisation at Mt Olympus (Ashburton Basin, Western Australia). *Australian Journal of Earth Sciences, 63*, 987-1002. doi: 10.1080/08120099.2017.1281077

Wilford, J.R., Pain, C.F., & Dohrenwend, J.C. (1992). Enhancement and integration of airborne gamma-ray spectrometric and Landsat imagery for regolith mapping - Cape York Peninsula. *Exploration Geophysics, 23*, 441-446. doi: 10.1071/EG992441

Wilford, J.R., Bierwirth, P.N., & Craig, M.A. (1997). Application of airborne gamma-ray spectrometry in soil/regolith mapping and applied geomorphology. *AGSO Journal of Australian Geology and Geophysics, 17*, 201-216

Williams, M.J., (2019). pyrolite. doi: 10.5281/zenodo.2545106

Winterburn, P.A., Noble, R.R.P., & Lawie, D. (2019). Advances in exploration geochemistry, 2007 to 2017 and beyond. *Geochemistry: Exploration, Environment, Analysis*, *20*, 157-166. doi: 10.1144/geochem2019-030

Yamaguchi, Y., Kahle, A.B., Tsu, H., Kawakami, T., & Pniel, M. (1998). Overview of Advanced Spaceborne Thermal Emission and Reflection Radiometer (ASTER). *IEEE Transactions on Geoscience and Remote Sensing, 36*, 1062-1071. doi: 10.1109/36.700991

Yeates, A.N., Wyatt, B.W., & Tucker, D.H. (1982). Application of gamma-ray spectrometry to prospecting for tin and tungsten granites, particularly within the Lachlan Fold Belt, New South Wales. *Economic Geology, 77*, 1725-1738. doi: 10.2113/gsecongeo.77.7.1725

Chapter 2

This chapter is published as:

Caruso, A. S., Clarke, K. D., Tiddy, C. J., Delean, S., Lewis, M. M., 2018. Objective regolith-landform mapping in a regolith dominated terrain to inform mineral exploration. *Geosciences*, 8 (9), 318.

This chapter appears as published with minor modifications to reference style and formatting of figure and table captions for consistency with the remainder of the thesis

Statement of Authorship

Title of Paper	Objective Regolith-Landform Mapping in a Regolith Dominated Terrain to Inform Mineral Exploration
Publication Status	✓ Published ☐ Accepted for Publication ☐ Submitted for Publication ☐ Unpublished and unsubmitted work written in manuscript style
Publication Details	Caruso, A. S., Clarke, K. D., Tiddy, C. J., Delean, S. & Lewis, M. M. (2018). Objective Regolith-Landform Mapping in a Regolith Dominated Terrain to Inform Mineral Exploration. Geosciences, 8, 318. doi: 10.3390/geosciences8090318

Principal Author

Name of Principal Author (Candidate)	Alicia Caruso		
Contribution to the Paper	Conceptual study design, data collection, data analysis and interpretation, statistical processing and writing and editing of figures and manuscript		
Overall Percentage	75%		
Certification	This paper reports on original research I conducted during the period of my Higher Degree by Research candidature and is not subject to any obligations or contractual agreements with a third party that would constrain its inclusion in this thesis. I am the primary author of this paper.		
Signature		Date	09/10/19

Co-Author Contributions

By signing the Statement of Authorship, each author certifies that:

i. the candidate's stated contribution to the publication is accurate (as detailed above);

ii. permission is granted for the candidate to include the publication in the thesis; and

iii. the sum of all co-author contributions is equal to 100% less the candidate's stated contribution.

Name of Co-Author	Kenneth Clarke		
Contribution to the Paper	Contributed to conceptual study design, assistance with data and statistical interpretation and manuscript review.		
Signature		Date	15/10/2019

Name of Co-Author	Caroline Tiddy		
Contribution to the Paper	Contributed to conceptual study design, assistance with data and statistical interpretation and manuscript review.		
Signature		Date	16/10/2019

Name of Co-Author	Steven Delean		
Contribution to the Paper	Contributed to statistical concept design, processing and interpretation.		
Signature		Date	09/10/2019

Name of Co-Author	Megan Lewis		
Contribution to the Paper	Contributed to conceptual study design, assistance with data and statistical interpretation and manuscript review.		
Signature		Date	14/10/2019

ABSTRACT

An objective method for generating statistically sound objective regolith-landform maps using widely accessible digital topographic and geophysical data without requiring specific regional knowledge is demonstrated and has application as a first pass tool for mineral exploration in regolith dominated terrains. This method differs from traditional regolith-landform mapping methods in that it is not subject to interpretation and bias of the mapper. This study was undertaken in a location where mineral exploration has occurred for over 20 years and traditional regolith mapping had recently been completed using a standardised subjective methodology. An unsupervised classification was performed using a Digital Elevation Model, Topographic Position Index, and airborne gamma-ray spectrometry as data inputs resulting in 30 classes that were clustered to eight groups representing regolith types. The association between objective and traditional mapping classes was tested using the 'Mapcurves' algorithm to determine the 'Goodness-of-Fit', resulting in a mean score of 26.4 % between methods. This Goodness-of-Fit indicates that this objective map may be used for initial mineral exploration in regolith dominated terrains.

2.1 Introduction

Regolith is the surface expression of the entire unconsolidated or secondarily recemented cover that overlies coherent bedrock that has been formed by weathering, erosion, transport, and/or deposition of older material (Eggleton *et al.* 2001). Regolith is also known as the 'Critical Zone', the combination of chemical, geological, biological, and physical processes at the Earth's surface preserved as sediments above bedrock (Brantley *et al.* 2007; Brantley and Lebedeva 2011). Regolith connects to the underlying geology through weathering and commonly alters the surface expression of a buried ore body in a prospective region (e.g. Wilford *et al.* 1992; Taylor and Eggleton 2001; Anand and Paine 2002; Anand and Butt 2010). Approximately 80 % of basement rocks in Australia are covered by regolith (Smith 1996; Pain *et al.* 2012). Given that these basement rocks are known to host numerous economically viable ore deposits of various commodities in South Australia (e.g. Olympic Dam Cu-Au-REE-U; Carrapateena Cu-Au; Middleback Ranges Fe_2O_3: Figure 2.1), they are highly prospective for mineral exploration. Therefore, regolith mapping is becoming an increasingly used tool to assist in identifying key regions for mineral exploration (e.g. Anand and Smith 1993; Butt *et al.* 2005).

Regolith mapping contributes to understanding the geomorphology and landscape evolution of a region, but it is not a wholly objective method (Anand and Paine 2002; Anand and Butt 2010) and there are known spatial and compositional inconsistencies arising from differences in subjective interpretations of experts (Craig *et al.* 1999). Significant progress has been made in standardising regolith-landform mapping techniques within Australia (e.g. Lintern 2002; Worrall and Gray 2004; Pain *et al.* 2007) –

although are subject to the preferred interpretation of the mapper. Some forms of remotely sensed data are used when creating traditional regolith-landform maps but are usually utilised as an interpretative tool (Saadat *et al.* 2008; Mulder *et al.* 2011). Similarly, landform mapping has traditionally been performed through visual interpretation of aerial photography and field surveys (Dent and Young 1981; Blaszczynski 1997; Mulder *et al.* 2011). Landforms provide an understanding of past geologic and geomorphic processes and can also be used as a surrogate for regolith mapping due to genetic and spatial links (Pain *et al.* 1991; Craig *et al.* 1999; Dehn *et al.* 2001). Although landforms can improve the understanding of previous processes, similar landforms can represent differing regolith domains (Dehn *et al.* 2001). To assist in this discrimination, the use of scale is vital as well as examining the relationship between other regolith-landform features and field validation (Irvin *et al.* 1997).

Spatial GIS methods have evolved to enrich geomorphological maps (Seijmonsbergen *et al.* 2011) but there are few standards established for digital regolith mapping. An objective regolith map using a standard set of spatial analytical methods may therefore provide higher consistency across a region or continent (Burrough *et al.* 2000). The work in Wilford *et al.* (1992) provides an example of digital regolith mapping in a tropical environment, successfully mapping regolith and basement geology using an unsupervised classification of radiometric data and Landsat TM imagery followed by an interpretation of the weathering and geomorphic history. Integrating regolith and landforms spatially has been beneficial for mineral exploration success by identifying appropriate target regions or sampling media (e.g. Craig *et al.* 1999; Salama *et al.* 2016a; Salama *et al.* 2016b).

Recent work (Cracknell and Reading 2014; Cracknell *et al.* 2014; Wilford *et al.* 2015; Kuhn *et al.* 2018; Metelka *et al.* 2018) has used a variety of machine learning methods to digitally map lithology and regolith using a range of geophysical and remote sensing data. A majority of this work has been done at regional scales, but machine learning methods have also been applied at a continental scale (Cracknell *et al.* 2015). Although these machine learning methods have been shown to be beneficial in a range of settings, they are all advanced forms of supervised classifications. To the best of our knowledge, an unsupervised classification using geophysical and remote sensing data has not been used to produce a useful regolith-landform map in Australia.

In this paper, we create an objective mapping method to map broad regolith-landforms based on readily available digital landform and gamma-ray spectrometry data. The example is from the southern Gawler Ranges in South Australia, which is host to several prospective targets including the Paris silver deposit and the Nankivel porphyry copper prospect (Figure 2.1). We present and discuss a statistical comparison between the newly proposed objective mapping method and traditional regolith-landform mapping followed by the examination of this application of this technique to mineral exploration.

2.2 Background

2.2.1 Geological Setting

The area used in this study covers 3866 km^2 within the southern region of the Gawler Craton (Figure 2.1) and includes a variety of landscape and vegetation features. The study area includes the 'Gawler' region and 'Gawler volcanics' and 'Myall Plains' sub-regions of the Interim Biogeographic Regionalisation for Australia (IBRA) (Department of the Environment and Energy 2012). The landscape is broadly characterised by hills, hill foot slopes, and sandy plains (Kenny 2008). The vegetation varies across the sub-regions but mainly comprises low open woodlands of western myall (*Acacia papyrocarpa*) and black oak (*Casuarina pauper*) trees over sparse shrub understoreys of bluebush (*Maireana* spp.), saltbush (*Atriplex* spp.), and spinifex (*Triodia* spp.).

The oldest basement rocks are preserved in the south of the study area and are poorly exposed. These rocks are part of the Sleaford Complex (*ca.* 2550 - 2440 Ma) and the unconformably overlying Palaeoproterozoic Hutchinson Group (Daly *et al.* 1998; Hoek and Schaefer 1998; Hand *et al.* 2007). The Warrow Quartzite is the oldest unit of the Hutchinson Group within the study area and has an age of *ca.* 2008 Ma (Jagodzinski 2005; Fanning *et al.* 2007). The Gawler Range Volcanics (GRV) are well exposed in the north of the study area and variably exposed throughout the southern and central thirds of the study area. Within the study area, the GRV is defined as the Lower GRV (Figure 2.1) which has an extrusion age of *ca.* 1591 - 1588 Ma (Jagodzinski *et al.* 2016). The Hiltaba Suite is co-magmatic to the GRV but has a longer extrusion time of *ca.* 1598 - 1574 Ma (Fanning *et al.* 2007; Allen *et al.* 2008). It occurs widely throughout the Gawler Craton and is known to be associated with the major tectonothermal and metallogenic episode that impacted much of the Gawler Craton (e.g. Daly *et al.* 1998; Hand *et al.* 2007) (Figure 2.1).

The composition and formation of the regolith in the study area is described in detail by Krapf (2016). Archean and Palaeoproterozoic basement rocks are uncomfortably overlain by much younger Cenozoic sediments. Limited regolith was deposited throughout the Paleogene and Neogene, and mostly comprises ferricrete, silcrete, some colluvial sediments, and palaeochannel sediments of the Garford Formation. The Garford Formation occurs in low relief areas and includes carbonaceous clay and silt with other fluvial and lacustrine sediments.

Development of ferricrete and silcrete continued into the Quaternary, cementing host lithologies and fragments of quartz and other material. A variety of sediments were deposited including aeolian, terrestrial, colluvial, and lacustrine. Colluvial sediments comprise ferruginous and poorly sorted pebbly conglomerate and sandstone. Calcrete formed throughout the Quaternary as laminated sheets of nodular aggregates now generally exposed in erosional terrains near alluvial channels and in areas of deflation.

During the Pleistocene, aeolian sediments dominated and are characterised by fine to medium grained sands, some of which formed ridges and swales. The most recent sediments deposited were aeolian quartzose sands draped over lacustrine and other aeolian deposits on the leeward side of playas (Krapf 2016).

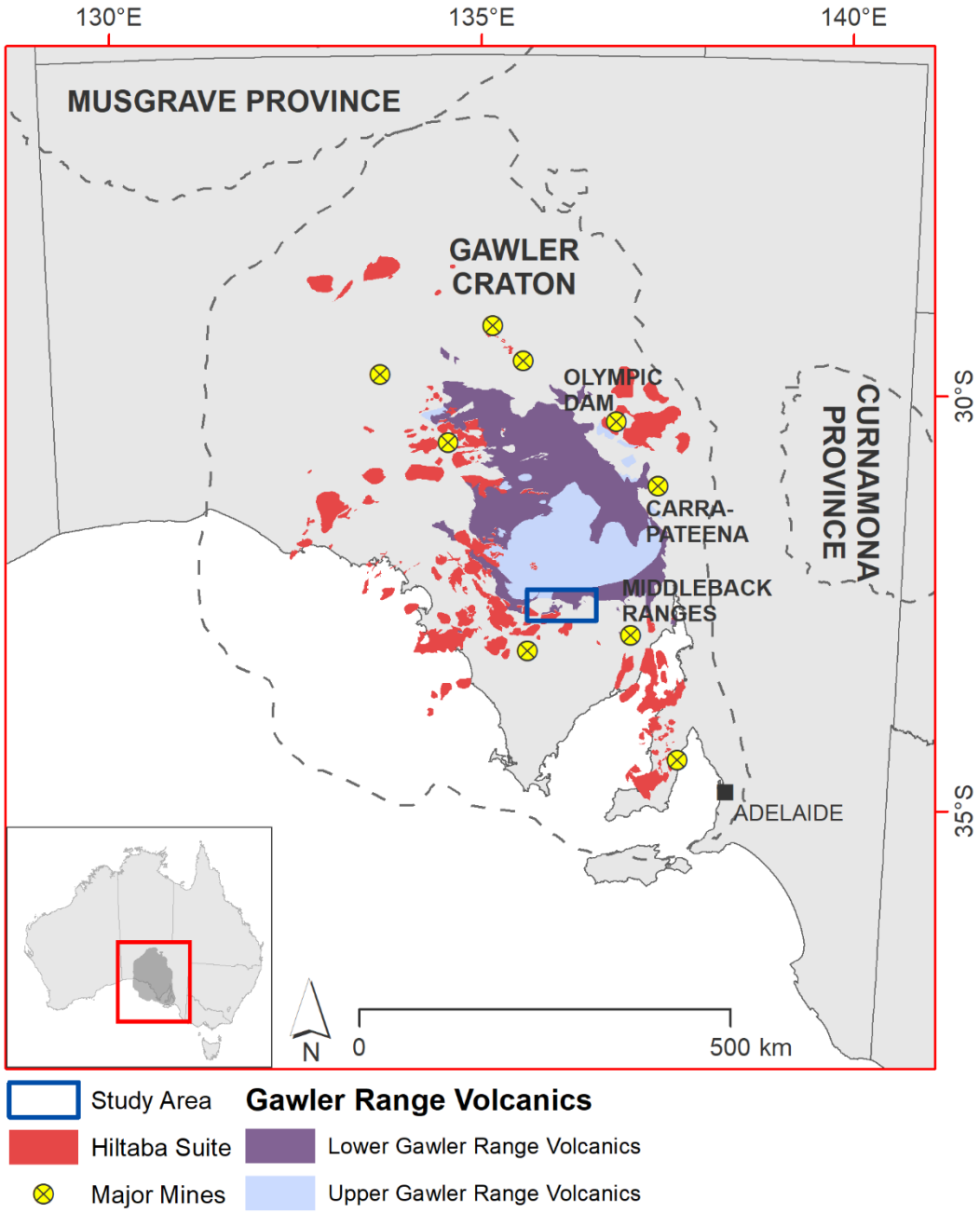

Figure 2.1: Simplified geological map showing the location of the study area and other known major deposits throughout the Gawler Craton. The dark grey area in inset map corresponds to the extent of the Gawler Craton. Modified after Forbes *et al.* (2015).

2.2.2 Regolith Mapping

A regolith unit is a subdivision of the regolith with visibly distinguishable boundaries at a mappable scale. The term can also be used for zones or horizons of weathering profiles (Eggleton *et al.* 2001). There are many ways regolith unit are classified but the most common schemes are TI (Transported or In-situ) or RED (Relict, Erosional, or Depositional) (Anand and Smith 1993; Smith 1993). Following this classification, the units may be categorised according to sediment origin e.g. marine or terrestrial. Then units may be distinguished based on physical attributes such as grain size, thickness, composition, to create detailed descriptions. If possible, age will also be included in the definition to provide an understanding of landscape formation processes that occurred in the region. Some units also include information on predominant vegetation cover.

Traditional regolith mapping of the Yardea and Port Augusta 1:250,000 map sheets was completed in 2016 by Krapf (2016), and the study area for this work is a small section of this mapping area where there are known exploration targets. The original mapping involved a combination of visual interpretation and some field assessment of a number of available data sets including: state geological mapping, Landsat TM5 and ETM7 imagery, 1 and 3 sec Digital Elevation Models (DEMs), and gamma-ray spectrometry data (Department of State Development 2016). Ten attributes were assigned to mapping units including regolith materials, landform names, Regolith Terrain Map (RTMAP) code, and TI scheme. Bedrock weathering intensity and regolith thickness were not able to be inferred from the data used but are available as individual products from the Geological Survey of South Australia. The final product was based on the 1:100,000 geology mapping using the RTMAP scheme developed by (Pain *et al.* 2007).

2.3 Materials and Methods

The methods for this work were multi-faceted and are detailed in the following subsections with an overview presented in Figure 2.2.

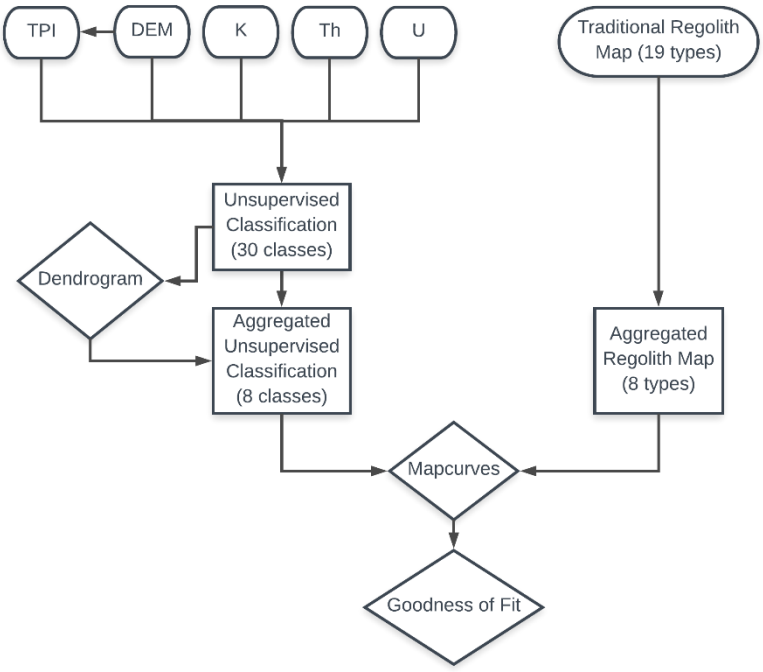

Figure 2.2: Flowchart illustrating the methodology workflow.

2.3.1 Clustering of Traditional Regolith Map

Figure 2.3 shows the regolith map of Krapf (2016) for the study area. This map shows 19 regolith-landform units that depict the fine scale detail throughout the map area. The landscape is clearly dominated by a few regolith types with a majority of others sparsely distributed and limited in extent (Figure 2.3). Due to the limited extent of some regolith units, the 19 regolith map units were aggregated into eight types based on their spatial distribution and description of regolith material origin. The topological integrity of the mapping was retained although the number of overall regolith classes was reduced. An example of this was aggregating silcrete, calcrete, and ferricrete together (Duricrusts) to retain topology as they are expressed with the same landform at surface. Similarly, the palaeochannel deposits and playa lake deposits were also spatially limited and were clustered together to preserve map topology and include these regolith types as an exclusive class, water related formation processes (Lake/Palaeochannel sediments, Table 2.1). The accuracy of the DEM methodology that is applied in this work does not allow to discriminate them.

Although this aggregation retained some types of regolith, others were clustered to provide greater clarity. For example, the Sandplains/dunes, mostly aeolian origin regolith type (herein referred to as 'Sandplains/dunes') includes sediments formed by wind formation processes, longitudinal sief dune field deposits and aeolian sand sheet deposits (Table 2.1). Colluvial sediments occurring in the north and south of the study area were clustered together as they are derived from the same formation processes (erosion–weathering–transport–deposition sediments).

Some regolith types were particularly distinctive and were not aggregated in the Clustered Regolith Mapping Unit (CRMU) map (Figure 2.4) as they were considered to be unrelated to other regolith types. These included Alluvial sediments, GRV bedrock, and Undifferentiated Quartz. It is known that GRV and Non-GRV bedrock are compositionally different (Daly *et al.* 1998; Blissett *et al.* 2017) and undergo differing formation processes, therefore it was reasonable to keep these regolith types separate in the clustering process (Figure 2.4, Table 2.1) shows the clustering of the original 19 regolith types of Krapf (2016) to form the CRMU map shown in Figure 2.4. The reduction of detail in the CRMU map has simplified regolith primarily in the southern two-thirds of the study area (Figure 2.4). Clustering the traditional regolith map based on formation processes alone can introduce some bias and subjectivity in this method.

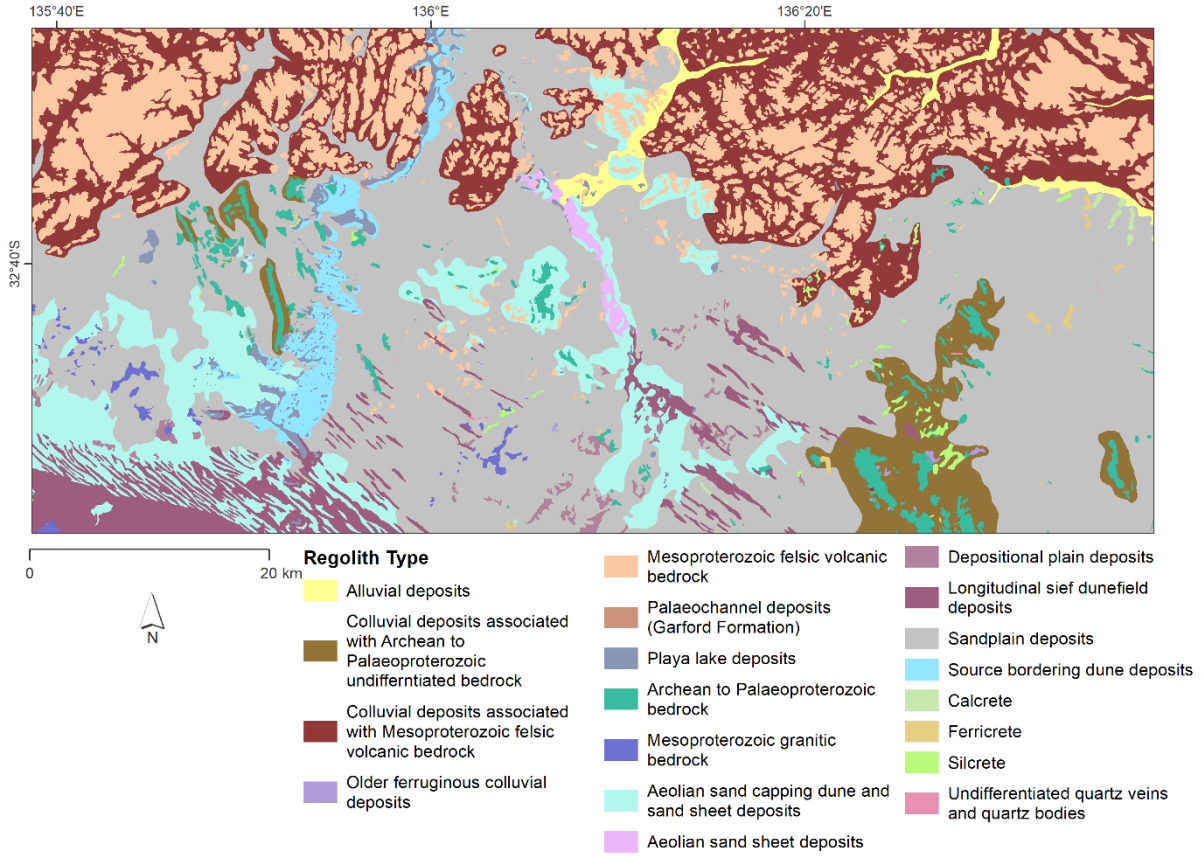

Figure 2.3: Regolith map of the study area. Regolith spatial data from Krapf (2016).

Table 2.1: Matrix showing aggregation of 19 regolith types from Figure 2.3 into 8 Clustered Regolith Mapping Units (CRMU) in Figure 2.4. Each colour represents the colour of the aggregated class displayed in Figure 2.4.

Traditional Regolith Types (Figure 2.2)	**CRMU Regolith Types (Figure 2.6)**								
	Alluvial Sediments	**Colluvial Sediments**	**Gawler Range Volcanics**	**Lake / Palaeochannel Sediments**	**Non- Gawler Range Volcanics Bedrock**	**Sandplains/ dunes, mostly aeolian origin**	**Duricrusts**	**Undifferentiated Quartz**
Alluvial deposits								
Colluvial deposits associated with Archean to Palaeoproterozoic undifferentiated bedrock								
Colluvial deposits associated with Mesoproterozoic felsic volcanic bedrock								
Older ferruginous colluvial deposits								
Mesoproterozoic felsic volcanic bedrock								
Palaeochannel deposits (Garford Formation)								
Playa lake deposits								
Archean Palaeoproterozoic bedrock								
Mesoproterozoic granitic bedrock								
Aeolian sand capping dune and sand sheet deposits								
Aeolian sand sheet deposits								
Depositional plain deposits								
Longitudinal sief dune field deposits								
Sandplain deposits								
Source bordering dune deposits								
Calcrete								
Ferricrete								
Silcrete								
Undifferentiated quartz veins and quartz bodies								

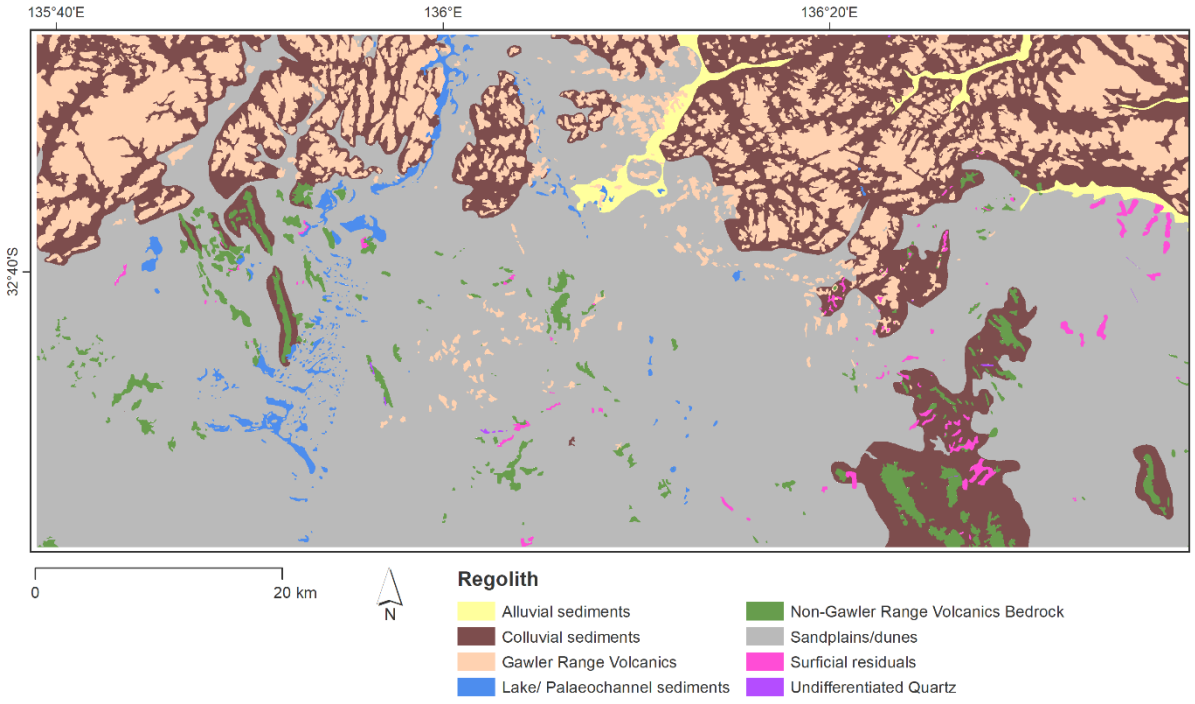

Figure 2.4: Clustered Regolith Mapping Unit (CRMU) map of the study area after aggregation based on the description of regolith material.

2.3.2 Regolith-Landform Analysis

The data used to perform the regolith-landform analysis was selected for its comprehensive extent and high spatial resolution. This data is also of high quality for this remote region of South Australia. All data and data transformations used in this work are freely available, produced by Geoscience Australia and cover the entirety or vast majority of Australia providing the ability to replicate this method.

2.3.2.1 Spatial Data and Transforms

Spatial data used in the analysis includes a Digital Elevation Model (DEM), Topographic Position Index (TPI), and Slope Position Classification (SPC) derived from the smoothed DEM (DEM-S) derived by Geoscience Australia from the 1-second Shuttle Radar Topography Mission (SRTM) of NASA in 2000 with a spatial resolution of 30 m (Gallant *et al.* 2011) (Figure 2.5).

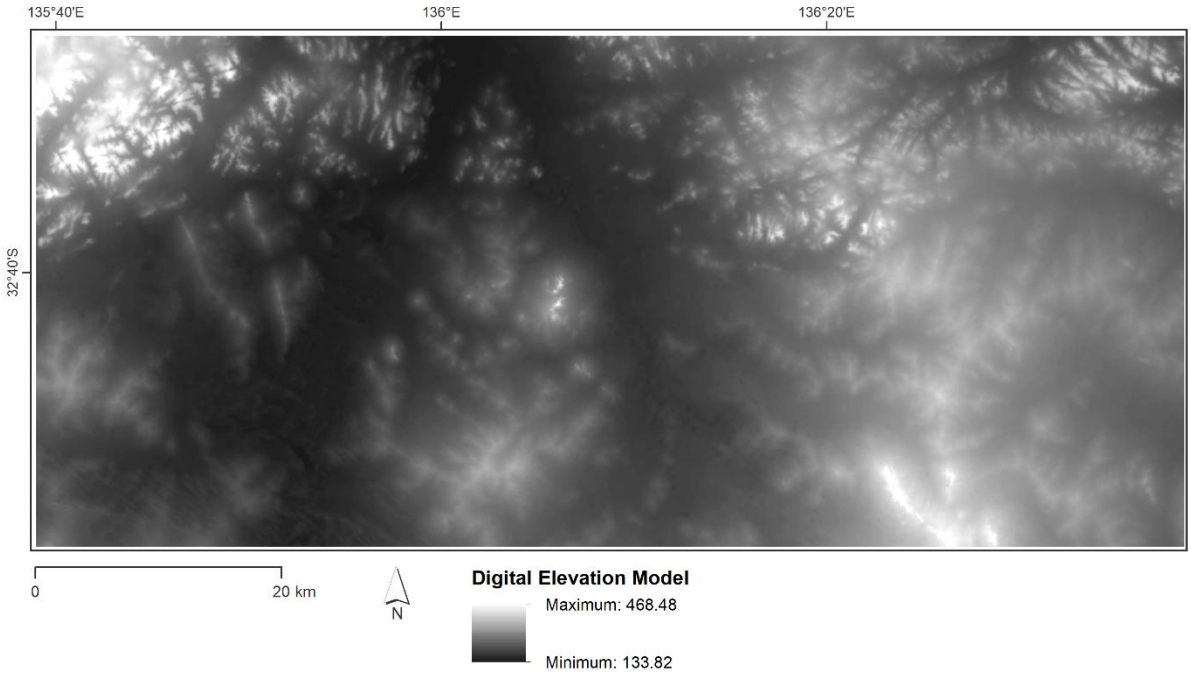

Figure 2.5: 1-second Digital Elevation Model (DEM) used as an input for the unsupervised classification, sourced from Geoscience Australia.

The TPI developed by Weiss (2001); Jenness (2006) has been used to interpret numerous landscapes globally and across disciplines (e.g. Guisan *et al.* 1999; De Reu *et al.* 2013). TPI is calculated as the mean elevation within a focal window of a specified radius around each cell in a DEM (Weiss 2001). This index is scale dependent, with fine scales more appropriate for exploring soil erosion and coarse scales appropriate for studying regional landforms. The study area was analysed at a coarse (2000 m radius) and fine (300 m radius) scale using ArcGIS 10.3 Toolbox (Dilts 2015).

The TPI is an index of curvature and while mathematically meaningful is not easily interpreted. However, the SPC classifies this index into a more interpretable form that describes the slopes in the study area. SPC is not a geometric classification of a landscape, it uses the local elevation and slope conditions for each point based on the TPI using standard deviation thresholds listed in Table 2.2, as defined by Weiss (2001). These thresholds are appropriate across different terrains, as shown by De Reu *et al.* (2013); Singh *et al.* (2016). The SPC algorithm applied to both TPI grids to visualise the landscape patterns at the different scales (Figure 2.6).

Table 2.2: Slope position classification thresholds. Reproduced from Weiss (2001).

Class	Description	Breakpoints (Standard Deviation Units)	Slope (Degrees)
1	Ridge	> 1	N/A
2	Upper slope	> 0.5 ≤ 1	N/A
3	Middle slope	> -0.5 < 0.5	> 5
4	Flats slope	≥ -0.5 ≤ 0.5	≤ 5
5	Lower slopes	≥ -1 < 0.5	N/A
6	Valleys	< -1	N/A

Figure 2.6a shows the fine scale SPC at 300 m radius, illustrating many local ridge formations across the landscape and flat slopes with some valleys apparent in the north of the study area, whereas Figure 2.6b (2000 m radius) highlights the ridge and valley features with only some intermediate slopes.

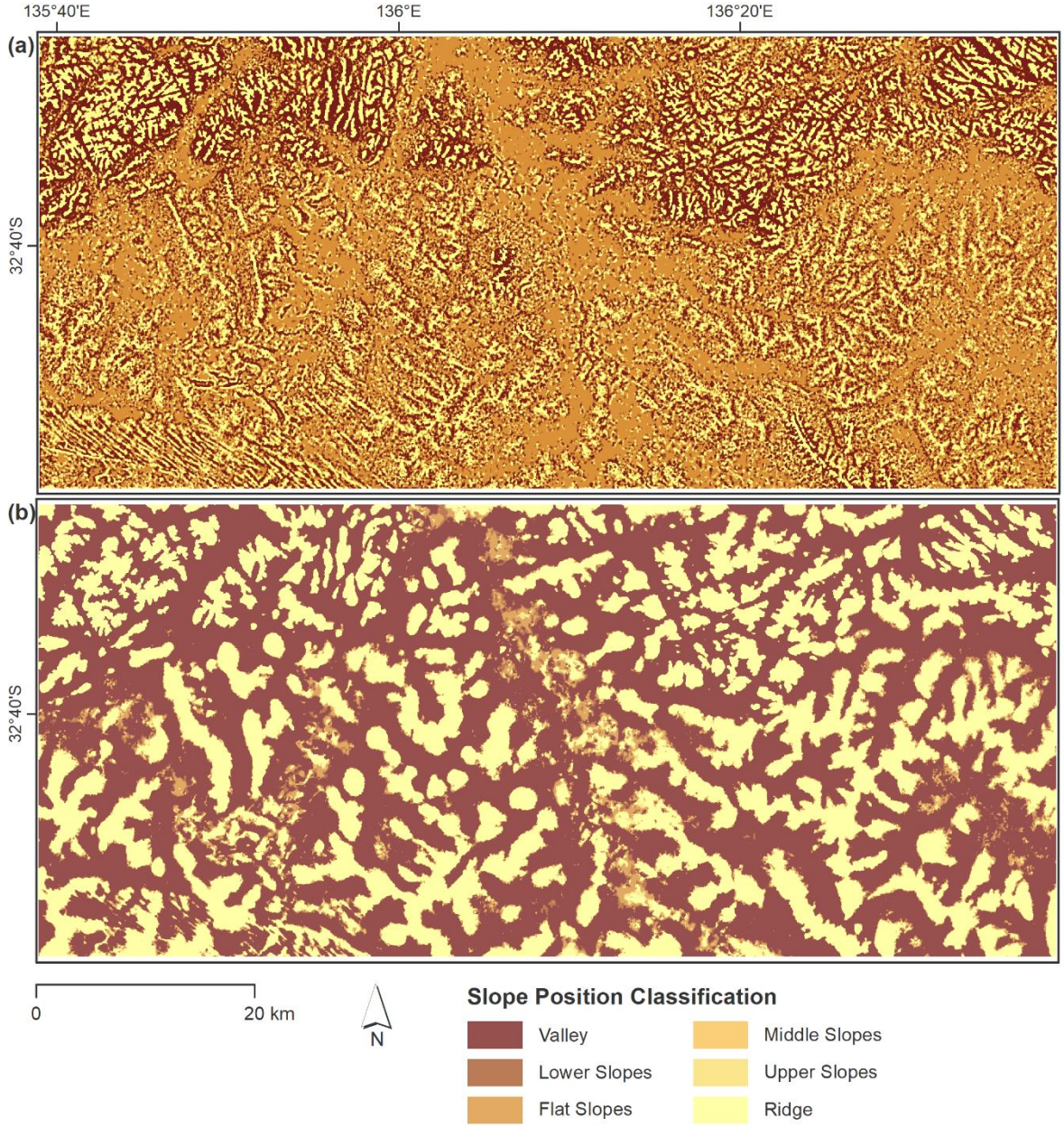

Figure 2.6: Slope Position Classification at (**a**) fine scale (300 m); and (**b**) coarse scale (2000 m) derived using Dilts (2015) ArcGIS 10.3 Toolbox. SPC is based on the local elevation and slope of each point.

2.3.2.2 Gamma-Ray Spectrometry

Digital maps of potassium, thorium, and uranium emissions were obtained through the South Australian Resources Information Gateway (SARIG: https://map.sarig.sa.gov.au/) with a spatial resolution of 100 m (Figure 2.7). The data were derived through interpolating data of previously flown airborne radiometric surveys based on methods from the Australia Wide Airborne Geophysical Survey (Savitzky and Golay 1964; Minty *et al.* 2009).

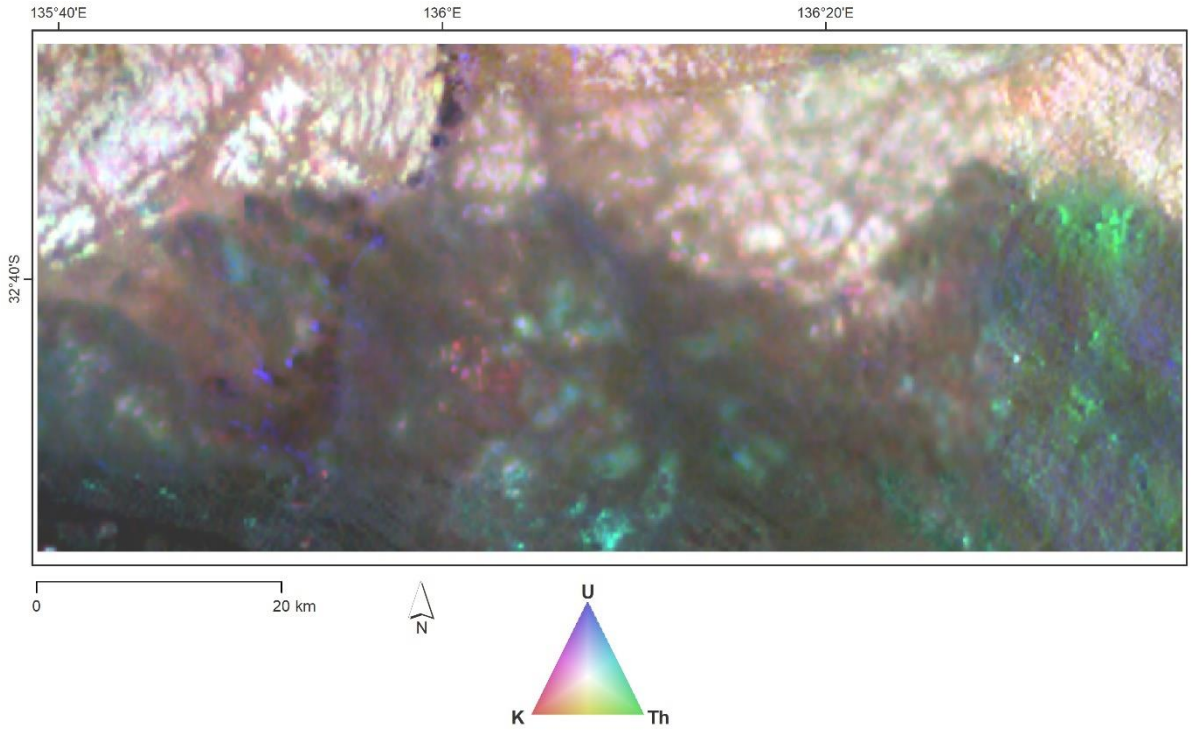

Figure 2.7: Ternary composite gamma-ray spectrometry map of the study area, sourced from SARIG.

2.3.3 Unsupervised Classification

An unsupervised classification was used to cluster and identify spatial patterns in the input data sets. Inputs for the unsupervised classification were elevation from the DEM; two TPIs of different radii (2000 m and 300 m); and gamma-ray spectrometry grids for potassium, equivalent thorium, and equivalent uranium (Figures 2.5 - 2.7). An Iso Cluster Unsupervised Classification was performed classifying the gridded data into 30 classes. These were clustered to eight classes using a class similarity threshold applied to a dendrogram of between-class distance of sequentially merged classes. This threshold was informed by visual interpretations of the spatial distribution and coherence of the classes produced.

2.3.4 Relationship between Mapping Methods

The relationship between the aggregated unsupervised classification and the CRMU map classes was evaluated using the Mapcurves 'Goodness-of-Fit' (GOF) measure developed by Hargrove *et al.* (2006). This measure evaluates the spatial concordance between the two maps (Equation 2.1).

$$Goodness\ of\ Fit = \sum \left[\left(\frac{C}{B + C} \right) \left(\frac{C}{A + C} \right) \right] \quad (2.1)$$

where A is the total area of the category on the compared map, B is the total area of the category on a reference map, and C is the amount of intersection of a category between two maps.

This method was selected because of its ability to be applied to maps with differing numbers of categories and as it is independent of resolution (Hargrove *et al.* 2006; Williams *et al.* 2008). Mapcurves analysis

has been successfully used to compare categorical maps in a variety of disciplines including species distribution and biogeographical region modelling (e.g. Moore and Messina 2010; Edler *et al.* 2017). Mapcurves analysis was implemented using 5000 points generated randomly across the study area. For each of these points, the mapped class and regolith type was sampled for each mapping method. The Mapcurves implementation of van Loon (2011) was applied using 400 iterations of the algorithm using a random subsample of 500 of the 5000 points. Finally, we considered the sensitivity of the statistics from the 400 Mapcurves outputs.

2.4 Results

2.4.1 Aggregation of Traditional Regolith-Landform Map

With the number of regolith mapping units of the traditional regolith map reduced to eight, it becomes much easier to visualise the distribution of broad regolith types. Figure 2.4 shows that the landscape is dominated by Sandplains/dunes and the Gawler Range Volcanics in the north of the study area. The landscape also contains a large proportion of Colluvial sediments, generally surrounding bedrock, mostly around the Gawler Range Volcanics in the north of the study area. Figure 2.4 also highlights the prevalence of Non-Gawler Range Volcanics bedrock in the south and western regions of the study area. There are smaller units of Duricrusts and Lake/Palaeochannel sediments across the study area. Duricrusts mostly occur in the eastern portion of the study area and are in proximity of Colluvial sediments and Non-GRV bedrock. Alluvial sediments appear as they did in Figure 2.3, as they were not aggregated with other regolith types.

2.4.2 Aggregated Unsupervised Classification

The unsupervised classification produced 30 classes which were clustered hierarchically into eight broad groups. Figure 2.8 shows the aggregation of the classes, indicating the threshold used to establish the aggregated unsupervised objective mapping (herein referred to as 'the image map') classes displayed in Figure 2.9. Table 2.3 displays the average values of input variables for each derived class with the average crustal abundances of radiometric variables included for comparison. The distribution of Slope Position Classes, both coarse and fine scale for each mapping class are shown in Figure 2.10.

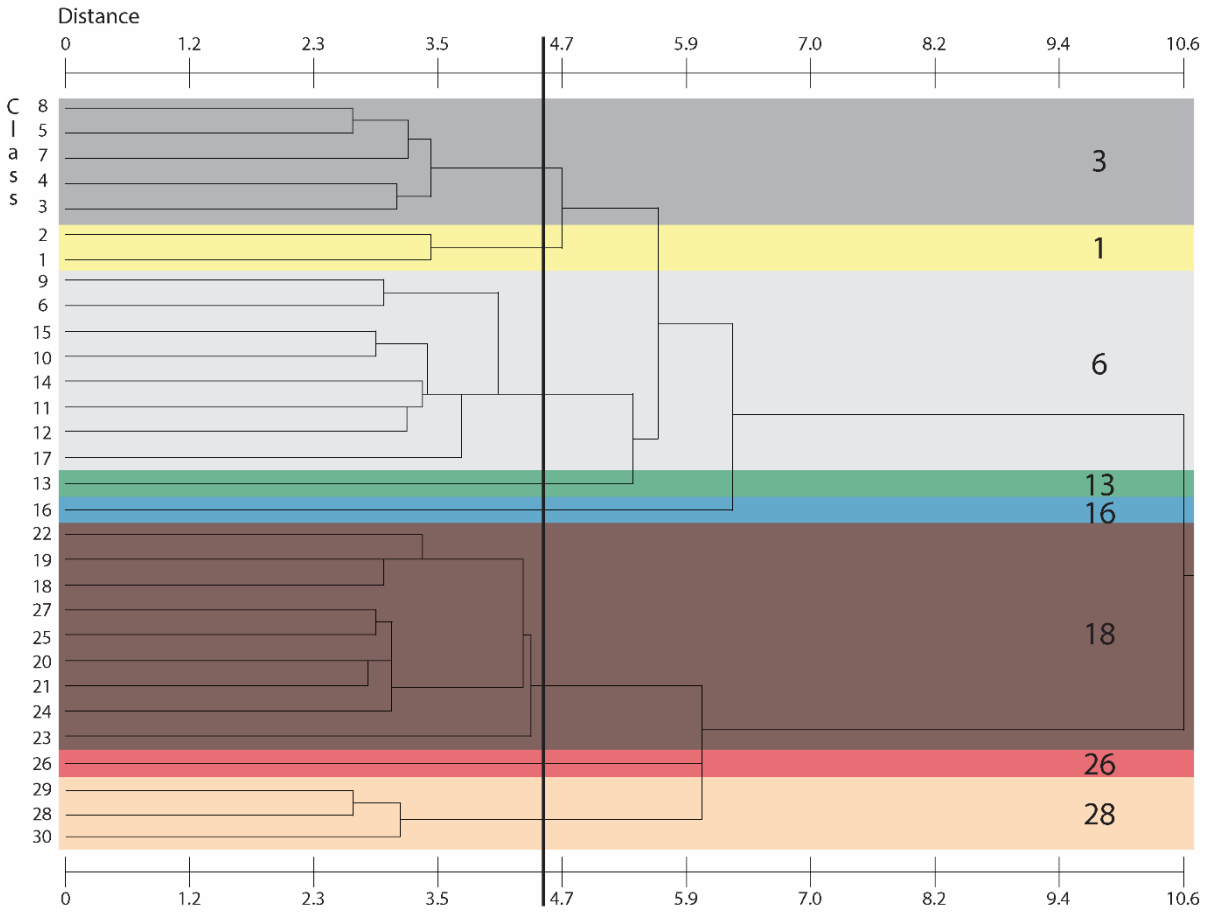

Figure 2.8: Dendrogram produced from the initial unsupervised classification illustrating the 30 classes that were hierarchically clustered to eight for the image mapping product. Each colour represents the colour of the final aggregated class displayed in Figure 2.9, the black line indicates the threshold used for aggregation.

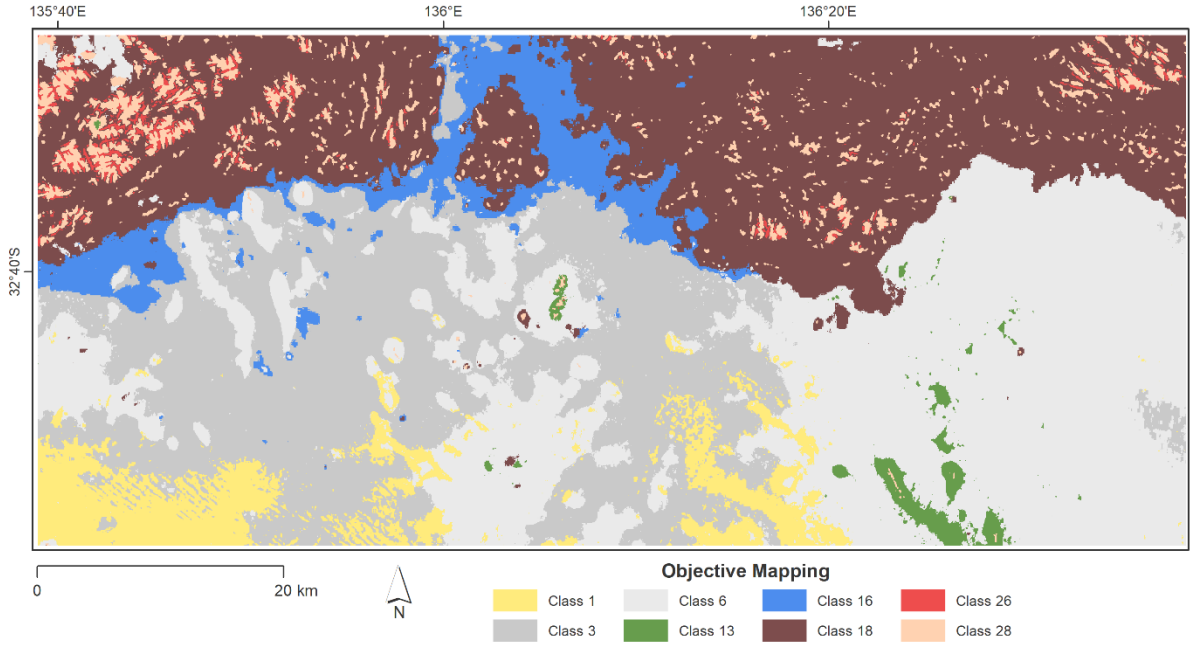

Figure 2.9: Image map of eight classes resulting from the unsupervised classification. Each class is based on a common topographic and radiometric signature.

Table 2.3: Summary statistics for each defined class derived from input data. Average crustal abundance for radiometric elements are provided here for reference (data from Minty (1997) and Rudnick and Gao (2003)).

Class	Average Values	1	3	6	13	16	18	26	28
DEM (m)	NA	202.73	177.13	250.03	346.91	165.14	229.41	293.46	306.80
K (%)	1.90	0.59	1.08	1.26	0.93	2.20	3.17	3.69	3.67
Th (ppm)	8.50	1.08	7.38	10.41	10.46	13.22	21.44	26.36	26.86
U (ppm)	2.70	1.26	1.01	1.31	1.20	1.81	2.90	3.99	3.87

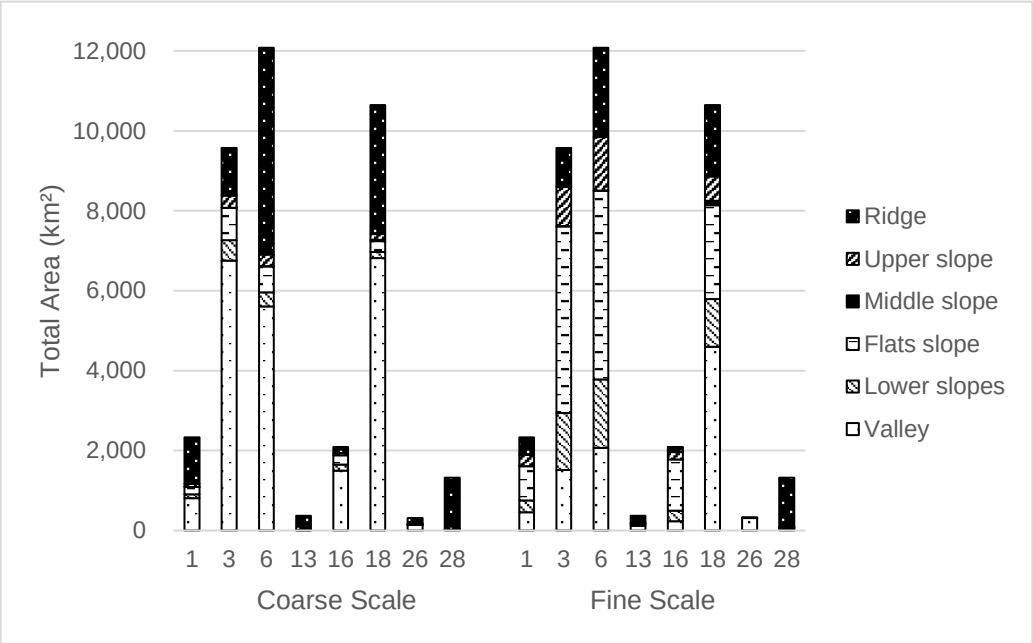

Figure 2.10: The proportion of SPC of the total area for each class, for both coarse and fine scales of slope analysis.

2.4.3 Composition and Distribution of the Image Mapping Classes

Class 3 accounts for 24.7 % of the study area. It is mostly located across the western-central region of the study area with some small areas located in the far east and north. The raw radiometric data (Figure 2.7) indicates that this region is rich in thorium, confirmed in Table 2.3 with approximately average crustal abundance values for thorium and below average abundances for potassium and uranium. At the coarse SPC analysis, this class is predominantly made up of valley features; whereas at the fine scale, a higher proportion of flat slopes and upper and lower slopes are evident.

Class 1 is distributed in the south east and across some of the southern margin of the study area and makes up 6 % of the study area. It has an average elevation of 202 m, with below-average abundance of all radiometric elements. At the coarse scale of topographic analysis, this class comprises mostly ridge features with 35 % valley features (Figure 2.10). At the fine scale, much of this is identified as flat slopes, accounting for 36 % of the terrain.

Class 6 is the largest class, making up 31.2 % of the study area but more commonly in the east. This class has an average elevation of 250 m with some enrichment in thorium and uranium. This class has above-average abundance of thorium but below-average values of potassium and uranium. Class 6 contains approximately half ridge and half valley features at the coarse scale with the fine scale illustrating upper, flat, and lower slopes forming 64 % of this class.

Class 13 is the most geographically restricted class at < 1 % of the total area, confined to high ridges in the southern and central regions. This class contains the highest mean elevation at 346 m above average thorium and approximately half the average abundance of potassium and uranium. The coarse SPC shows this class has 95 % ridge features but 45 % ridge features combined with valley and other slope features at the fine scale.

Class 16 is restricted to the north and the southern boundary of class 18 in the west of the study area. This class contains the lowest average elevation at 165 m. Figure 2.7 suggests that this class would be high in uranium, but the abundance in Table 2.3 indicates that this class contains 1.81 ppm, below average. Thorium and potassium are both above average crustal abundance. Valley features make up over 70 % of the coarse SPC, whereas the fine scale indicates contains a higher occurrence of flat slopes at 61 %.

Class 18 is the second largest class derived, making up 27.5 % of the study area. It is mostly located in the central to western region of the study area with some small areas located in the north. Figure 2.7 indicates that this class is high in all three radiometric elements and Table 2.3 attests that this class contains average or clearly above average abundances. The coarse scale highlights the large proportion of valley features for this class with approximately 30 % ridge features. At the fine scale, intermediate slope types make up a large proportion of the SPC result and ridge and valley features are reduced in their proportion.

Class 26 is the smallest of all classes at 0.85 % of the area and it is spatially restricted, likely due to its representation of specific landscape features. It contains above-average radiometric values across all elements with all three elements, with potassium and uranium being the greatest of all classes. The coarse scale indicates an approximately equal division between ridge and valley features whereas the fine scale clearly shows the high proportion of valley features within this class. This class also has one of the highest average elevations of all classes at 293 m.

Class 28 makes up 3.4 % of the total area and is distributed across the northern region with exceptions in the central and southern margins. This class has the second-highest average elevation at 306 m with Figure 2.7 and Table 2.3 in agreement that this class is high in all three radiometric elements. This class is represented by primarily ridge features at the coarse and fine scale. Class 28 illustrates the most

dominant relationship with one slope type compared to all other classes identified in the final mapping method.

Classes 13, 16, and 26 were not aggregated with other classes and are noticeably distinct (Figure 2.8, Table 2.3). Class 1 is a relatively unique class as it is formed from two classes during aggregation but has some similarity to Classes 3 and 6 in the thorium and uranium content. Coincidentally, Classes 1, 3, and 6 are adjacent across the southern two-thirds of the study area (Figure 2.9).

2.4.4 Spatial Concordance between Mapping Methods

The iterative Mapcurves function produced Goodness-of-Fit (GOF) scores between map classes ranging from 22.4 - 38.5 % with a mean GOF of 26.4 %. Table 2.4 shows the mean GOF for each intersection between the CRMU and the image mapping classes, indicating the highest GOF scores for each image mapping class. The intersection of Class 3 and Sandplains/dunes has the largest GOF score at 35.98 %, followed by Class 18 and Colluvial sediments at 31.8 %. Other large GOF scores also occur between Class 28 and 18 and Gawler Range Volcanics and Class 13 and Non-Gawler Range Volcanics CRMU regolith types.

When comparing the image map to the CRMU map, Classes 1, 3, 6, and 16 have the highest GOF with Sandplains/dunes. The Gawler Range Volcanics CRMU regolith type has multiple correspondences with Classes 26 and 28. None of the 5000 randomly generated points fell within the Undifferentiated Quartz regolith type due to its small area, therefore it was not included in the Mapcurves analysis.

Table 2.4: Mean GOF (%) from Mapcurves analysis: bold values are the highest GOF for the comparison of image mapping with the CRMU regolith type, and italicised values are the highest GOF for the comparison of CRMU regolith type with the image mapping classes. Values bold and italicised are the highest GOF for both comparison directions.

CRMU Regolith Type	**Image Mapping Class**							
	1	**3**	**6**	**13**	**16**	**18**	**26**	**28**
Alluvial sediments	0	0	0.21	0	1.21	*2.29*	0	0
Colluvial sediments	0	0	3.57	0.93	0.37	***31.8***	0.14	0
Gawler Range Volcanics	0	0	0.07	0.03	0.01	23.3	***35.98***	***25.71***
Lake/Palaeochannel sediments	0	1.61	0.01	0	*2.37*	0.04	0	0
Non-Gawler Ranges Volcanics	0.03	0.23	2.90	***11.66***	0.07	0	0	0.11
Sandplains/dunes	**9.24**	***35.98***	**30.41**	0.03	***5.97***	1.04	0	0
Duricrusts	0	0.03	1.17	*1.59*	0	0.03	0	0

2.5 Discussion

2.5.1 Relationship between Maps and Input Variables

Sandplains/dunes has two large GOF scores with Classes 3 and 6 at 35.98 % and 30.41 % respectively. When examining Figure 2.9 in conjunction with Table 2.4, it can be seen that Classes 3 and 6 make up a majority of the central region of the study area. Comparison with Figure 2.4 demonstrates that both classes have high GOF scores with this CRMU regolith type due to the majority of the CRMU map comprising Sandplains/dunes with other regolith types scattered throughout the central region of the study area. The image map shows two different classes (Classes 3 and 6) that make up approximately the same area (Figure 2.9). It is likely that this is due to elevation and SPC input data. It can be seen in Figure 5 that an area of high elevation on the eastern side and centre of the study area, corresponds with Sandplains/dunes in Figure 2.4. From Table 2.3, elevation and radiometric thorium content will likely explain the separation of Classes 3 and 6 and hence their similar GOF scores.

Although there are strong relationships between Sandplains/dunes and Classes 3 and 6, there are much smaller GOF scores with this CRMU regolith type and Classes 1 and 16 (Table 2.4). Figure 2.4 shows that the south western corner and central northern portion of the study area are sandplains/dunes but these have been separated in the image mapping as Classes 1 and 16 respectively likely due to the differences in both radiometric response and elevation from Figure 2.4 and 2.6 and Table 2.3. This means that Classes 1 and 16 are not as well predicted from Sandplains/dunes and they make up a smaller proportion of this CRMU regolith type, explaining their low GOF scores.

Class 18 has strong correspondence with both Colluvial sediments and the Gawler Range Volcanics (Table 2.4). The northern regolith types are distinct in the radiometric input data (Figure 2.7) as they are high in all radiometric elements, confirmed in Table 2.3. Figure 2.4 shows the extent of the GRV in the north of the study area and when comparing this to Figure 2.9, it can be seen that Class 28 is not as extensive. The strong similarities of the radiometric responses explain the separation of classes and therefore high GOF scores for both Colluvial sediments and GRV with Class 18.

While there are areas of higher GOF, there are also many minor GOF values which still indicate some relationship between map classes (Table 2.4). The GOF between Colluvial sediments and Class 6 at 3.57 % is due to the aggregation of the unsupervised classification. Class 6 includes some Colluvial sediments in the eastern half of the study area when comparing Figure 2.3 and 2.8. This type of interaction between mapping methods also occurs with Class 18 and Alluvial sediments.

2.5.2 Mapcurves for Comparison of Regolith-Landform Maps

The choice of map to use as the reference is subjective and will produce differing outcomes. Mapcurves analysis permits the comparison of mapping methods to be made in both directions, i.e. using the traditional map or the image map as the reference for the comparison between classes. The comparison that produces the greatest GOF is considered to be the best direction of concordance between the maps and may also indicate which map is finer scale (Hargrove *et al.* 2006). It has been suggested by Antonetti *et al.* (2016) that the coarser map would be advantaged when selecting the highest Mapcurve result. However, given the similarity in scales of the two maps compared in this study this seems unlikely to be an influencing factor in the results.

The Mapcurves result suggests that in this case the traditional map should be used as the reference as the greatest GOF score (26.4 %) is for the comparison of the image map to the traditional map. This Goodness-of-Fit indicates that our objective regolith-landform map describes some of the same pattern as the traditional subjective map, but also contains significant additional information, probably resulting from the topographic indices and radiometric data. An unsupervised regolith-landform map is easily evaluated using Mapcurves as shown in this study. Mapcurves can provide confidence in this mapping method due to its numerous advantages, such as application beyond a pair-wise comparison with multiple maps and resolution independence. This work has identified, analysed, and interpreted the GOF scores and intersections between classes (Table 2.4) to bring greater interpretation to the objective regolith-landform map and how it relates to the traditional map.

2.5.3 Regolith-Landform Mapping without Prior Knowledge

The generation of an objective map from digital data that is comparable to the pre-existing regolith-landform map demonstrates that it is not necessary to have extensive knowledge of a site prior to using this method. This is because the image map is data driven and the methodology identifies meaningful patterns in the data. The characteristics of the image mapping classes have been derived from summary measures of the input variables. When used as a first-pass analysis tool, the objective mapping method can provide a basis for targeted field work to further describe and characterise regolith units.

Although most classifications of landforms are attempting to replicate a manual classification (MacMillan and Shary 2009), an objective method that provides similarities to a traditional map does have its place. In this case, the objective mapping method illustrates the effectiveness of using easily and freely accessible data and simple methodology. The image mapping could also be accomplished on open source software such as QGIS. It can be argued that this method is faster, taking only days versus weeks of field work followed by quality control, meaning turnaround time of a regional regolith-landform product is reduced

and that publication of products to be used in a number of applications, such as mineral exploration, are more accessible.

While this method results in faster production of regolith-landform maps, it is not intended to be a replacement for 'boots on ground' mapping. The objective mapping method presented here gives an indication of the distribution of broad scale regolith-landform features. Therefore, if the traditional mapping method were to be discarded detailed descriptions and interpretations of regolith and soil types would be lost. This highlights why 'boots on ground' mapping and regolith expertise will always be useful and could be incorporated into a data-driven methodology. Other research comparable to this study primarily focused on providing descriptive attributes for each defined class rather than an overview and statistical measure of fit (e.g. Blaszczynski 1997; Summerell *et al.* 2005; Prima *et al.* 2006). Supervised classification methods, including machine learning methods such as fuzzy k-means or Self-Organising Maps, provide continuity between classes and are described as more of a continuous classification method (Burrough *et al.* 2000; Carneiro *et al.* 2012; Cracknell *et al.* 2015). However, they require training data or an accuracy assessment to verify their resulting product unlike this study which used a statistical measure to evaluate the objective method.

The relationships between the image map classes and regolith types mapped by traditional methods for the southern Gawler Ranges study area demonstrates that this mapping method based on digital data analysis could be implemented in other regolith dominated terrains. In regions of sporadic or no coverage of regolith mapping, this method could be used prior to a field campaign to gain insight and understanding of the landscape without the time or expense required for traditional mapping. Digital data including geology and high-resolution satellite imagery that provide insights to alternative landform features are example avenues that could be considered as additional input datasets.

2.5.4 Application for Mineral Exploration

Objective mapping methods can be beneficial in expanding geological understanding prior to entering an area for purposes such as mineral exploration. As knowledge of the geomorphology and landscape is improved with mapping, exploration models can be adapted to be better suited for the environment of the explorer (Craig 2001). The extensive, and in places very deep, sedimentary cover across regions such as the Gawler Craton can be a huge barrier to explorers considering exploration targets. This method could assist in identifying a specific regolith-landform type and identifying areas of rock exposure with negligible time and monetary expense.

It is advantageous to integrate both regolith and landforms to enhance possible geochemical exploration success by identifying appropriate sampling media once a regolith-landform map has been produced (Craig *et al.* 1999; Salama *et al.* 2016a; Salama *et al.* 2016b). For some initial geochemical soil sampling,

this image mapping could provide an intuitive guide to the regolith-landform characteristics and highlight where sampling could take place. For example, if a company wanted to employ a stream-sediment geochemical survey within the study area, this objective regolith-landform map could indicate that Class 16 might be the most appropriate sampling unit.

Other types of remotely sensed data at a variety of spatial and spectral resolutions are also becoming increasingly available, including ASTER imagery at a national and state level plus a range of standard spectral data products that are regularly used in mineral exploration. These data have the potential to be incorporated into an objective mapping method such as the one presented here.

2.6 Conclusions

Characterising and interpreting regolith and landforms is vital for exploration success. This work has shown that an unsupervised objective mapping method can produce a regolith-landform map with a relationship to a traditionally derived map that could be used for first-pass mineral exploration. The Goodness-of-Fit indicates the similarity of mapping methods but also highlights the additional information that is possible to interpret from the objective regolith-landform map. Using open access data and an accessible unsupervised classification makes this method is easily useable for a variety of applications. This objective method has the advantage of removing much of the subjectivity in regolith-landform mapping. The spatial extent of the data used suggests that this method could be used across much of Australia with traditional regolith and additional remote sensing data being integrated to create a final product.

2.7 References

Allen, S.R., McPhie, J., Ferris, G., & Simpson, C. (2008). Evolution and architecture of a large felsic Igneous Province in western Laurentia: The 1.6 Ga Gawler Range Volcanics, South Australia. *Journal of Volcanology and Geothermal Research, 172*, 132-147. doi: 10.1016/j.jvolgeores.2005.09.027

Anand, R., & Smith, R. (1993). Regolith distribution, stratigraphy and evolution in the Yilgarn Craton-implications for exploration. In P.R. Williams, & J.A. Haldane (Eds.), *An International Conference on Crustal Evolution, Metallogeny and Exploration of the Eastern Goldfields: Kalgoorlie '93 Abstracts* (pp. 187-193). Kalgoorlie, Western Australia: Australian Geological Survey Organisation

Anand, R.R., & Butt, C.R.M. (2010). A guide for mineral exploration through the regolith in the Yilgarn Craton, Western Australia. *Australian Journal of Earth Sciences, 57*, 1015-1114. doi: 10.1080/08120099.2010.522823

Anand, R.R., & Paine, M. (2002). Regolith geology of the Yilgarn Craton, Western Australia: implications for exploration. *Australian Journal of Earth Sciences, 49*, 3-162. doi: 10.1046/j.1440-0952.2002.00912.x

Antonetti, M., Buss, R., Scherrer, S., Margreth, M., & Zappa, M. (2016). Mapping dominant runoff processes: An evaluation of different approaches using similarity measures and synthetic runoff simulations. *Hydrology and Earth System Sciences, 20*, 2929-2945. doi: 10.5194/hess-20-2929-2016

Blaszczynski, J.S. (1997). Landform characterization with Geographic Information Systems. *Photogrammetric Engineering and Remote Sensing, 63*, 183-191

Blissett, A.H., Parker, A.J., Crooks, A.F., Allen, S.R., Simpson, C.J., McPhie, J., Daly, S.J., Benbow, M.C., Giles, C.W., Ambrose, G.J., McAvaney, S.O., Wade, C.E., & Cowley, W.M. (2017). *Yardea,* Adelaide, South Australia: Geological Survey of South Australia

Brantley, S.L., Goldhaber, M.B., & Ragnarsdottir, K.V. (2007). Crossing disciplines and scales to understand the Critical Zone. *Elements, 3*, 307-314. doi: 10.2113/gselements.3.5.307

Brantley, S.L., & Lebedeva, M. (2011). Learning to Read the Chemistry of Regolith to Understand the Critical Zone. *Annual Review of Earth and Planetary Sciences, 39*, 387-416. doi: 10.1146/annurev-earth-040809-152321

Burrough, P.A., van Gaans, P.F.M., & MacMillan, R.A. (2000). High-resolution landform classification using fuzzy k-means. *Fuzzy Sets and Systems, 113*, 37-52. doi: 10.1016/s0165-0114(99)00011-1

Butt, C.R.M., Robertson, I.D.M., Scott, K.M., & Cornelius, M. (Eds.) (2005). *Regolith expression of Australian ore systems*. Perth, Australia: CRC LEME. ISBN: 978-1-92-103928-7

Carneiro, C. C., Fraser, S.J., Crósta, A.P., Silva, A.M., & Barros, C.E. de M. (2012). Semiautomated geologic mapping using self-organizing maps and airborne geophysics in the Brazilian Amazon. *Geophysics, 77*, K17-K24. doi: 10.1190/geo2011-0302.1

Cracknell, M.J., & Reading, A.M. (2014). Geological mapping using remote sensing data: A comparison of five machine learning algorithms, their response to variations in the spatial distribution of training data and the use of explicit spatial information. *Computers & Geosciences, 63*, 22-33. doi: 10.1016/j.cageo.2013.10.008

Cracknell, M.J., Reading, A.M., & de Caritat, P. (2015). Multiple influences on regolith characteristics from continental-scale geophysical and mineralogical remote sensing data using Self-Organizing Maps. *Remote Sensing of Environment, 165*, 86-99. doi: 10.1016/j.rse.2015.04.029

Cracknell, M.J., Reading, A.M., & McNeill, A.W. (2014). Mapping geology and volcanic-hosted massive sulfide alteration in the Hellyer–Mt Charter region, Tasmania, using Random Forests™ and Self-Organising Maps. *Australian Journal of Earth Sciences, 61*, 287-304. doi: 10.1080/08120099.2014.858081

Craig, M.A. (2001). Regolith mapping for geochemical exploration in the Yilgarn Craton, Western Australia. *Geochemistry: Exploration, Environment, Analysis, 1*, 383-390. doi: 10.1144/geochem.1.4.383

Craig, M.A., Wilford, J.R., & Tapley, I.J. (1999). Regolith-landform mapping in the Gawler Craton. *MESA Journal, 12*, 17-21

Daly, S.J., Fanning, G.M., & Fairclough, M.C. (1998). Tectonic evolution and exploration potential of the Gawler Craton, South Australia. *AGSO Journal of Australian Geology and Geophysics, 17*, 145-168

De Reu, J., Bourgeois, J., Bats, M., Zwertvaegher, A., Gelorini, V., De Smedt, P., Chu, W., Antrop, M., De Maeyer, P., Finke, P., Van Meirvenne, M., Verniers, J., & Crombe, P. (2013). Application of the topographic position index to heterogeneous landscapes. *Geomorphology, 186*, 39-49. doi: 10.1016/j.geomorph.2012.12.015

Dehn, M., Gartner, H., & Dikau, R. (2001). Principles of semantic modeling of landform structures. *Computers & Geosciences, 27*, 1005-1010. doi: 10.1016/s0098-3004(00)00138-2

Dent, D., & Young, A. (1981). *Soil survey and land evaluation*. London, UK: George Allen & Unwin. ISBN: 978-0-04-631013-4

Department of State Development (2016). Metadata: Regolith map of the Southern Gawler Ranges Margin (YARDEA and PORT AUGUSTA 1:250 000 map sheets). Adelaide, South Australia: Geological Survey of South Australia

Department of the Environment and Energy (2012). *Interim Biogeographic Regionalisation for Australia, Version 7*. Canberra, Australia: Department of the Environment and Energy

Dilts, T.E. (2015). Topography Tools for ArcGis 10.1, http://arcgis.com/home/item.html?id=b13b3b40fa3c43d4a23a1a09c5fe96b9: University of Nevada Reno. Access Date: November 2016

Edler, D., Guedes, T., Zizka, A., Rosvall, M., & Antonelli, A. (2017). Infomap bioregions: Interactive mapping of biogeographical regions from species distributions. *Systematic Biology, 66*, 197-204. doi: 10.1093/sysbio/syw087

Eggleton, R.A., Anand, R.R., Butt, C.R.M., Chen, X.Y., Craig, M.A., de Caritat, P., Field, J.B., Gibson, D.L., Greene, R., Hill, S.M., Jones, M., Lintern, M.J., McQueen, K.G., Pain, C.F., Pillans, B.J., Robertson, I.D.M., Smith, K., & Taylor, G.F. (Eds.) (2001). *The Regolith Glossary: surficial geology, soils and landscapes*. Perth, Australia: CRC LEME. ISBN: 978-0-73-153343-5

Fanning, C.M., Reid, A.J., & Teale, G.S. (Eds.) (2007). *A geochronological framework for the Gawler Craton, South Australia*. Bulletin 55. Adelaide, South Australia: Department of Primary Industries and Resources. ISBN: 978-0-75-901392-6

Forbes, C., Giles, D., Freeman, H., Sawyer, M., & Normington, V. (2015). Glacial dispersion of hydrothermal monazite in the Prominent Hill deposit: An exploration tool. *Journal of Geochemical Exploration, 156*, 10-33. doi: 10.1016/j.gexplo.2015.04.011

Gallant, J.C., Dowling, T.I., Read, A.M., Wilson, N., Tickle, P., & Inskeep, C. (2011). 1 second SRTM Derived Digital Elevation Models User Guide. Canberra, Australia. Geoscience Australia.

Guisan, A., Weiss, S.B., & Weiss, A.D. (1999). GLM versus CCA spatial modeling of plant species distribution. *Plant Ecology, 143*, 107-122. doi: 10.1023/a:1009841519580

Hand, M., Reid, A., & Jagodzinski, L. (2007). Tectonic framework and evolution of the Gawler Craton, Southern Australia. *Economic Geology, 102*, 1377-1395. doi: 10.2113/gsecongeo.102.8.1377

Hargrove, W.W., Hoffman, F.M., & Hessburg, P.F. (2006). Mapcurves: a quantitative method for comparing categorical maps. *Journal of Geographical Systems, 8*, 187-208. doi: 10.1007/s10109-006-0025-x

Hoek, J.D., & Schaefer, B.F. (1998). Palaeoproterozoic Kimban mobile belt, Eyre Peninsula: timing and significance of felsic and mafic magmatism and deformation. *Australian Journal of Earth Sciences, 45*, 305-313. doi: 10.1080/08120099808728389

Irvin, B.J., Ventura, S.J., & Slater, B.K. (1997). Fuzzy and isodata classification of landform elements from digital terrain data in Pleasant Valley, Wisconsin. *Geoderma, 77*, 137-154. doi: 10.1016/S0016-7061(97)00019-0

Jagodzinski, E.A. (2005). Compilation of SHRIMP U-Pb geochronological data, Olympic Domain, Gawler Craton, South Australia, 2001-2003. Canberra, Australia: Geoscience Australia. Document Number: Record 2005/20

Jagodzinski, E.A., Reid, A.J., Crowley, J.L., McAvaney, S., & Wade, C.E. (2016). Precise zircon U-Pb dating of a Mesoproterozoic silicic large igneous province: the Gawler Range Volcanics and Benagerie Volcanic Suite, South Australia. In, *AESC 2016 - Australian Earth Sciences Convention*. Adelaide, Australia: Geological Society of Australia

Jenness, J. (2006). Topographic Position Index (tpi_jen.avx) extension for ArcView 3.x, v 1.2, http://jennessent.com/arcview/tpi.htm: Jenness Enterprises. Access Date: November 2016

Kenny, S.D. (2008). A Vegetation Map of the Gawler Craton Region South Australia. Adelaide, South Australia: Department for Environment and Heritage.

Krapf, C.B.E. (2016). Regolith Map of the Southern Gawler Ranges Margin (YARDEA and PORT AUGUSTA 1:250 000 map sheets). Adelaide, South Australia: Geological Survey of South Australia

Kuhn, S., Cracknell, M.J., & Reading, A.M. (2018). Lithologic mapping using Random Forests applied to geophysical and remote-sensing data: A demonstration study from the Eastern Goldfields of Australia. *Geophysics, 83*, B183-B193. doi: 10.1190/geo2017-0590.1

Lintern, M.J. (2002). Calcrete sampling for mineral exploration. In X.Y. Chen, M.J. Lintern, & I.C. Roach (Eds.), *Calcrete: characteristics, distribution and use in mineral exploration* (pp. 31-109). Perth, Australia: CSIRO, CRC LEME. ISBN: 978-0-95-811450-9

MacMillan, R.A., & Shary, P.A. (2009). Landforms and Landform Elements in Geomorphometry. In T. Hengl, & H.I. Reuter (Eds.), *Geomorphometry: Concepts, Software, Applications* (pp. 227-254). Oxford, UK: Elsevier. ISBN: 978-0-12-374345-9

Metelka, V., Baratoux, L., Jessell, M.W., Barth, A., Jezek, J., & Naba, S. (2018). Automated regolith landform mapping using airborne geophysics and remote sensing data, Burkina Faso, West Africa. *Remote Sensing of Environment, 204*, 964-978. doi: 10.1016/j.rse.2017.08.004

Minty, B., Franklin, R., Milligan, P., Richardson, M., & Wilford, J. (2009). The Radiometric Map of Australia. *Exploration Geophysics, 40*, 325-333. doi: 10.1071/eg09025

Minty, B.R.S. (1997). Fundamentals of airborne gamma-ray spectrometry. *AGSO Journal of Australian Geology and Geophysics, 17*, 39-50

Moore, N., & Messina, J. (2010). A Landscape and Climate Data Logistic Model of Tsetse Distribution in Kenya. *PLoS One, 5*. doi: 10.1371/journal.pone.0011809

Mulder, V.L., de Bruin, S., Schaepman, M.E., & Mayr, T.R. (2011). The use of remote sensing in soil and terrain mapping - A review. *Geoderma, 162*, 1-19. doi: 10.1016/j.geoderma.2010.12.018

Pain, C.F., Chan, R., Craig, M.A., Gibson, D., Kilgour, P., & Wilford, J. (2007). RTMAP Regolith Database Field Book and Users Guide (Second Edition): CRC LEME. Document Number: Open File Report 231

Pain, C.F., Chan, R., Craig, M.A., Hazell, M., Kamprad, J., & Wilford, J. (1991). *RTMAP BMR regolith database field handbook*.

Pain, C.F., Pillans, B.J., Roach, I.C., Worrall, L., & Wilford, J.R. (2012). Old, flat and red - Australia's distinctive landscape. In R.S. Blewett (Ed.), *Shaping a nation: A geology of Australia* (pp. 227-275). Canberra, Australia: Geoscience Australia and ANU E-Press. ISBN: 978-1-92-186282-3

Prima, O.D.A., Echigo, A., Yokoyama, R., & Yoshida, T. (2006). Supervised landform classification of Northeast Honshu from DEM-derived thematic maps. *Geomorphology, 78*, 373-386. doi: 10.1016/j.geomorph.2006.02.005

Rudnick, R.L., & Gao, S. (2003). Composition of the Continental Crust. In R.L. Rudnick (Ed.), *Treatise on Geochemistry, Volume 3: The Crust* (pp. 1-64). Oxford, UK: Elsevier - Pergamon. ISBN: 978-0-08-044847-3

Saadat, H., Bonnell, R., Sharifi, F., Mehuys, G., Namdar, M., & Ale-Ebrahim, S. (2008). Landform classification from a digital elevation model and satellite imagery. *Geomorphology, 100*, 453-464. doi: 10.1016/j.geomorph.2008.01.011

Salama, W., Gazley, M.F., & Bonnett, L.C. (2016a). Geochemical exploration for supergene copper oxide deposits, Mount Isa Inlier, NW Queensland, Australia. *Journal of Geochemical Exploration, 168*, 72-102. doi: 10.1016/j.gexplo.2016.05.008

Salama, W., González-Álvarez, I., & Anand, R.R. (2016b). Significance of weathering and regolith/landscape evolution for mineral exploration in the NE Albany-Fraser Orogen, Western Australia. *Ore Geology Reviews, 73, Part 3*, 500-521. doi: 10.1016/j.oregeorev.2015.07.024

Savitzky, A., & Golay, M.J.E. (1964). Smoothing and differentiation of data by simplified least squares procedures. *Analytical Chemistry, 36*, 1627-1639. doi: 10.1021/ac60214a047

Seijmonsbergen, A.C., Hengl, T., & Anders, N.S. (2011). Semi-Automated Identification and Extraction of Geomorphological Features Using Digital Elevation Data. In M.J. Smith, P. Paron, & J.S. Griffiths (Eds.), *Geomorphological Mapping: Methods and Applications* (pp. 297-335). Oxford, UK: Elsevier Science. ISBN: 978-0-44-453446-0

Singh, G., Williard, K.J., & Schoonover, J.E. (2016). Spatial Relation of Apparent Soil Electrical Conductivity with Crop Yields and Soil Properties at Different Topographic Positions in a Small Agricultural Watershed. *Agronomy, 6*. doi: 10.3390/agronomy6040057

Smith, R.E. (1993). Regolith evolution and exploration significance. In P.R. Williams, & J.A. Haldane (Eds.), *An International Conference on Crustal Evolution, Metallogeny and Exploration of the Eastern Goldfields: Kalgoorlie '93 Abstracts* (pp. 181-186). Kalgoorlie, Western Australia: Australian Geological Survey Organisation

Smith, R.E. (1996). Regolith research in support of mineral exploration in Australia. *Journal of Geochemical Exploration, 57*, 159-173. doi: 10.1016/s0375-6742(96)00032-5

Summerell, G.K., Vaze, J., Tuteja, N.K., Grayson, R.B., Beale, G., & Dowling, T.I. (2005). Delineating the major landforms of catchments using an objective hydrological terrain analysis method. *Water Resources Research, 41*. doi: 10.1029/2005wr004013

Taylor, G., & Eggleton, R.A. (2001). *Regolith geology and geomorphology*. John Wiley & Sons. ISBN: 978-0-47-197454-3

van Loon, E. (2011). Mapcurves algorithm, https://staff.fnwi.uva.nl/e.e.vanloon/paco.html Access Date: May 2018

Weiss, A.D. (2001). Topographic Position and Landforms Analysis. Poster Presentation, ESRI User Conference, San Diego, CA. Poster Presentation, ESRI User Conference, San Diego, CA.

Wilford, J., de Caritat, P., & Bui, E. (2015). Modelling the abundance of soil calcium carbonate across Australia using geochemical survey data and environmental predictors. *Geoderma, 259*, 81-92. doi: 10.1016/j.geoderma.2015.05.003

Wilford, J.R., Pain, C.F., & Dohrenwend, J.C. (1992). Enhancement and integration of airborne gamma-ray spectrometric and Landsat imagery for regolith mapping - Cape York Peninsula. *Exploration Geophysics, 23*, 441-446. doi: 10.1071/EG992441

Williams, C.L., Hargrove, W.W., Liebman, M., & James, D.E. (2008). Agro-ecoregionalization of Iowa using multivariate geographical clustering. *Agriculture Ecosystems & Environment, 123*, 161-174. doi: 10.1016/j.agee.2007.06.006

Worrall, L., & Gray, D.J. (2004). Regolith in the central Gawler, through and through. In, *Gawler Craton 2004: State of Play*. Adelaide, Australia: CRC LEME

Chapter 3

This chapter has been submitted to *Australian Journal of Earth Sciences* as:

Caruso, A. S., Clarke, K. D., Tiddy, C. J., Lewis, M. M. Airborne hyperspectral characterisation of hydrothermal alteration in a regolith dominated terrain, southern Gawler Ranges, SA.

This chapter appears as submitted with minor modifications to reference style and formatting of figure and table captions for consistency with the remainder of the thesis

Statement of Authorship

Title of Paper	Airborne hyperspectral characterisation of hydrothermal alteration in a regolith dominated terrain, southern Gawler Ranges, SA
Publication Status	☐ Published ☐ Accepted for Publication ✓ Submitted for Publication ☐ Unpublished and unsubmitted work written in manuscript style

Principal Author

Name of Principal Author (Candidate)	Alicia Caruso		
Contribution to the Paper	Conceptual study design, data collection, data analysis and interpretation, writing and editing of figures and manuscript.		
Overall Percentage	75%		
Certification	This paper reports on original research I conducted during the period of my Higher Degree by Research candidature and is not subject to any obligations or contractual agreements with a third party that would constrain its inclusion in this thesis. I am the primary author of this paper.		
Signature		Date	09/10/19

Co-Author Contributions

By signing the Statement of Authorship, each author certifies that:

i. the candidate's stated contribution to the publication is accurate (as detailed above);

ii. permission is granted for the candidate to include the publication in the thesis; and

iii. the sum of all co-author contributions is equal to 100% less the candidate's stated contribution.

Name of Co-Author	Kenneth Clarke		
Contribution to the Paper	Contributed to conceptual study design, assistance with data interpretation and manuscript review.		
Signature		Date	15/10/2019

Name of Co-Author	Caroline Tiddy		
Contribution to the Paper	Contributed to conceptual study design, assistance with data interpretation and manuscript review.		
Signature		Date	16/10/2019

Name of Co-Author	Megan Lewis		
Contribution to the Paper	Contributed to conceptual study design, assistance with data interpretation and manuscript review.		
Signature		Date	14/10/2019

ABSTRACT

Key alteration minerals associated with epithermal and porphyry Cu-Au mineralisation have been successfully identified using HyMap airborne hyperspectral imagery in a regolith dominated terrain in the southern Gawler Ranges, South Australia. Alteration assemblages were mapped using Spectral Feature Fitting, a spectral matching algorithm, identifying the spatial distribution of localised advanced argillic and broader argillic alteration. X-ray diffraction (XRD) analysis was undertaken to independently identify the mineralogy of 57 surface soil and rock samples collected from the study area. This analysis confirmed the presence of key alteration minerals including alunite, pyrophyllite and dickite. The integration of spectral and XRD analytical techniques allowed interpretation of mineralogical patterns across the landscape. This study demonstrates that it is possible to identify surface alteration related to potential mineralisation using airborne hyperspectral imagery and semi-quantitative XRD even in a weathered regolith dominated terrain.

3.1 Introduction

Deeply weathered environments, commonly referred to as regolith dominated terrains (RDTs), regularly coincide with major geomorphological features such as cratons and shields (González-Álvarez *et al.* 2016). RDTs occur naturally across a number of continents including Australia and are considered challenging environments for mineral exploration, as deeply weathered regolith can reduce or prevent the surface expression of buried mineral systems (Smith 1996). There has been considerable research on appropriate strategies for mineral exploration in RDTs across Australia (e.g. Butt *et al.* 2000; McQueen 2008; Anand and Butt 2010; Salama *et al.* 2016). There is an increasing need to explore to greater depths as the majority of surficial deposits in Australia have already been discovered (e.g. Hillis *et al.* 2014). Discovering an ore deposit using traditional exploration methods requires considerable time, effort and financial investment (Schodde 2017). Generally, specific geological knowledge is required of a particular region, including understanding the types of mineral systems that may be present within an area. Typical methods employed to locate economic ore deposits include geological mapping, drilling and a variety of geochemical and geophysical surveys. Remote sensing of land surface reflectance has been shown to be an effective tool for mineral exploration (e.g. Sabins 1999; Kruse *et al.* 2002; Cudahy 2016), but this method is currently underutilised in RDTs. It is generally assumed that widespread cover inhibits spectral mineral detection, although such regions can include subcrop or residual soils containing relics of weathered in situ rock that can be identified at the surface due to dispersion processes and be remotely sensed with high spatial and spectral resolution systems.

Remote sensing has numerous applications that may be used to understand a diversity of spatial and temporal characteristics of Earth's surface. Multispectral imagery from satellite-based imagers, Landsat

and Advanced Spaceborne Thermal Emission and Reflection Radiometer (ASTER), has been used over the last 30 years for mineral exploration (e.g. Goetz and Rowan 1981; Yamaguchi *et al.* 1998; Carranza and Hale 2002; Rowan *et al.* 2003; Cudahy 2012). These multispectral sensors have produced informative results in mineral exploration for numerous ore deposit types (e.g. Duuring *et al.* 2012; Pour and Hashim 2012; Witt *et al.* 2014) but are somewhat limited in their spatial and spectral resolutions (Goetz and Rowan 1981; Clark 1999). Hyperspectral remote sensing has a higher spectral resolution usually with 100 or more contiguous wavebands across the 400-2500 nm visible, near infrared and shortwave infrared spectrum (Kruse *et al.* 2002). This type of imagery has been in commercial use for over 20 years with great success for landscape, vegetation and mineral mapping (e.g. Cocks *et al.* 1998; Lewis *et al.* 2001; Andrew and Ustin 2008). Unlike Landsat and ASTER, airborne hyperspectral remote sensing can provide higher spectral resolution spectral signatures to assist with spectral mineral identification and surface mapping. Discrimination of mineral signatures using satellite or airborne hyperspectral data has been shown to be effective for mapping minerals (e.g. Kruse 1988; Quigley *et al.* 2005; Brown *et al.* 2006; Kruse 2012; Swayze *et al.* 2014; Cudahy 2016). Generally, surface characterisation using hyperspectral remote sensing is most effective in semi-arid to arid regions with well exposed geology and minimal vegetation cover (e.g. Kruse *et al.* 2002; Laukamp *et al.* 2011). Australian mineral exploration studies have utilised the considerable coverage of both satellite and airborne hyperspectral imagery available across the continent (e.g. Hewson *et al.* 2001; Bierwirth *et al.* 2002; Mahoney *et al.* 2003; Mauger *et al.* 2007; Laukamp *et al.* 2011), although RDTs in the southern margin of the Gawler Ranges in South Australia have not been examined in detail. This region preserves evidence of known and potential mineralisation and associated alteration (Nicolson *et al.* 2017a) providing an opportunity to evaluate the application of airborne hyperspectral remote sensing for exploration-focused mineral mapping.

This paper aims to identify and characterise surface expressions of alteration mineralogy in a known prospective region of the southern Gawler Ranges using HyMap airborne hyperspectral imagery (Cocks *et al.* 1998). Mineralogical data collected by X-ray diffraction (XRD) is used as an independent validation of surface mineralogy, assisting with interpretations of whether alteration or other geological processes such as weathering have influenced their occurrence.

3.1.1 Background Geology and Setting

The area for this study is 415 km^2 located in the southern Gawler Ranges within the Gawler Craton in South Australia (Figure 3.1). Detailed reviews of the prolonged and complex history of the Gawler Craton can be found in Daly *et al.* (1998) and Hand *et al.* (2007). Within the study area the oldest basement rocks form part of the Palaeoproterozoic Hutchinson Group. These rocks are preserved in the south but with limited exposure in this area: the only unit exposed at the surface is Warrow Quartzite,

with an age of *ca.* 2008 Ma (Jagodzinski 2005; Fanning *et al.* 2007). The Gawler Range Volcanics (GRV) are well exposed in the north and sporadically exposed throughout the remainder of the study area. In this region, the GRV is defined as the Lower GRV (Figure 3.1) which has an extrusion age of *ca.* 1591 - 1589 Ma (Jagodzinski *et al.* 2016). The GRV are equivalent to the *ca.* 1595 - 1575 Ma Hiltaba Suite (Blissett *et al.* 1993; Daly *et al.* 1998) that is extensive throughout the Gawler Craton (Figure 3.1), however is not exposed within the study area.

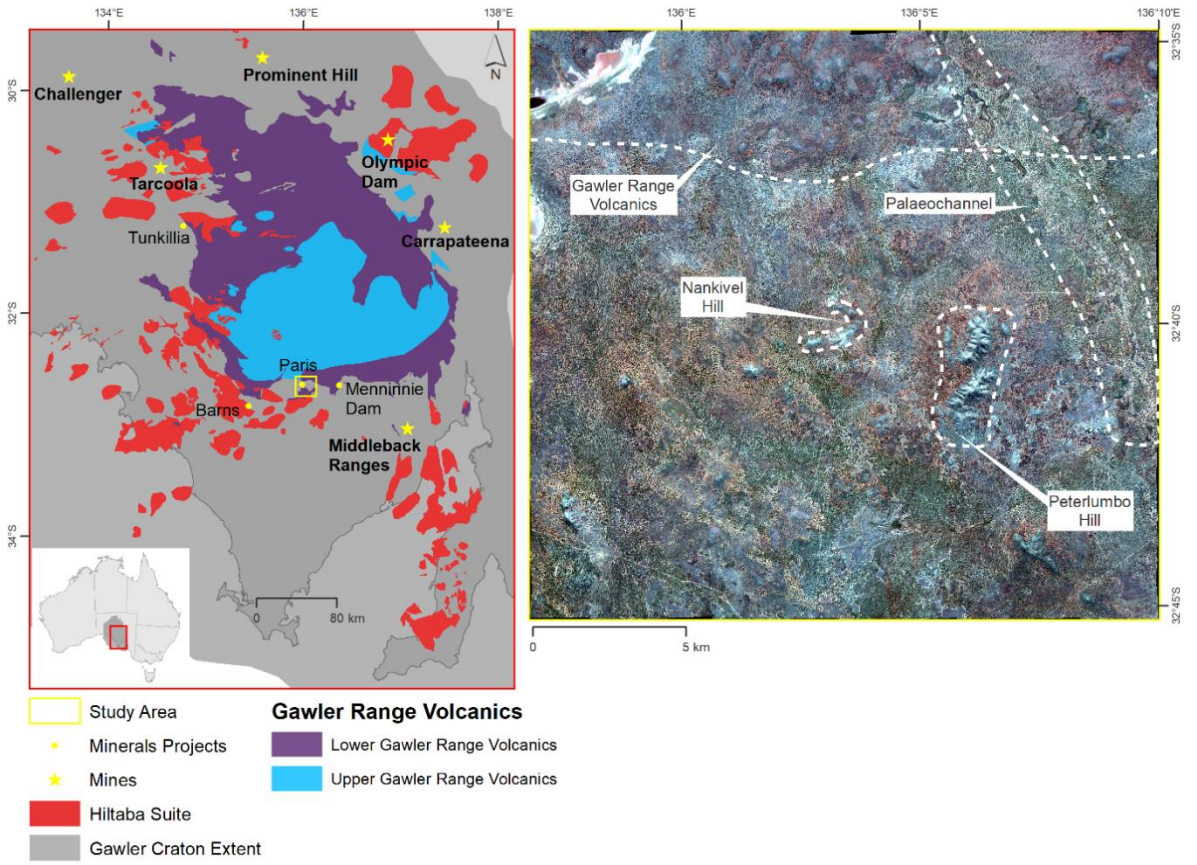

Figure 3.1: Context and study area. Left: The Gawler Craton showing the major geological units relevant to this study and major mines and mineral projects in the region. Right: HyMap true colour image (Red: Band 13 (637.7 nm), Green: Band 7 (546 nm), Blue: Band 2 (467.3 nm)) of the study area highlighting four key regions of this work.

The southern Gawler Ranges area is considered to be prospective for high-sulphidation epithermal silver and porphyry copper-gold mineralisation that formed contemporaneously with the GRV and Hiltaba Suite magmatism (e.g. Ferris *et al.* 2002; Ferris and Schwarz 2003; Werner *et al.* 2018). Investigator Resources Ltd. holds tenements in this region with their primary focus on the Paris silver project and exploration focusing on the potential Nankivel Hill porphyry copper-gold prospect (Investigator Resources 2018) (Figure 3.1). Over the last 20 years, numerous companies have undertaken geological drilling and associated test work (Drown *et al.* 2000). This included early spectral characterisation of rock-chip samples using a Portable Infrared Mineral Analyser (PIMA) in the mid-1990s (Gerakiteys 1996), and recent exploration drilling and research by Nicolson *et al.* (2017a) identifying alunite, topaz,

dickite, diaspore, kaolinite and pyrophyllite as key alteration minerals focused around Nankivel Hill. The primary result from Nicolson *et al.* (2017a) demonstrated a $^{40}Ar/^{39}Ar$ interpreted crystallisation age and therefore, timing of the acid sulphate event at Nankivel Hill at 1586 ± 6 Ma. Extensive regolith, mostly comprising sand plains, duricrusts and colluvial sediments, overlies the basement geology and has been fully described by Krapf (2016).

The study area has a warm, semi-arid climate (Peel *et al.* 2007), receiving approximately 300 mm of rainfall annually with mean minimum and maximum temperatures of 10.4°C and 23.6°C respectively (Bureau of Meterology 2018). It lies within the Interim Biogeographic Regionalisation for Australia (IBRA) 'Gawler' region (Department of the Environment and Energy 2012). Surface exposures and land covers in the region include an altered alunite breccia (Figure 3.2A), Warrow quartzite exposures at Peterlumbo Hill (Figure 3.2B), and sparse to moderate vegetation cover over clay-dominated soil (Figure 3.2C and 3.2D). The vegetation comprises low open woodlands of western myall (*Acacia papyrocarpa*) and black oak (*Casuarina pauper*) trees over sparse shrub understoreys of bluebush (*Maireana* spp.), saltbush (*Atriplex* spp.) and spinifex (*Triodia* spp.).

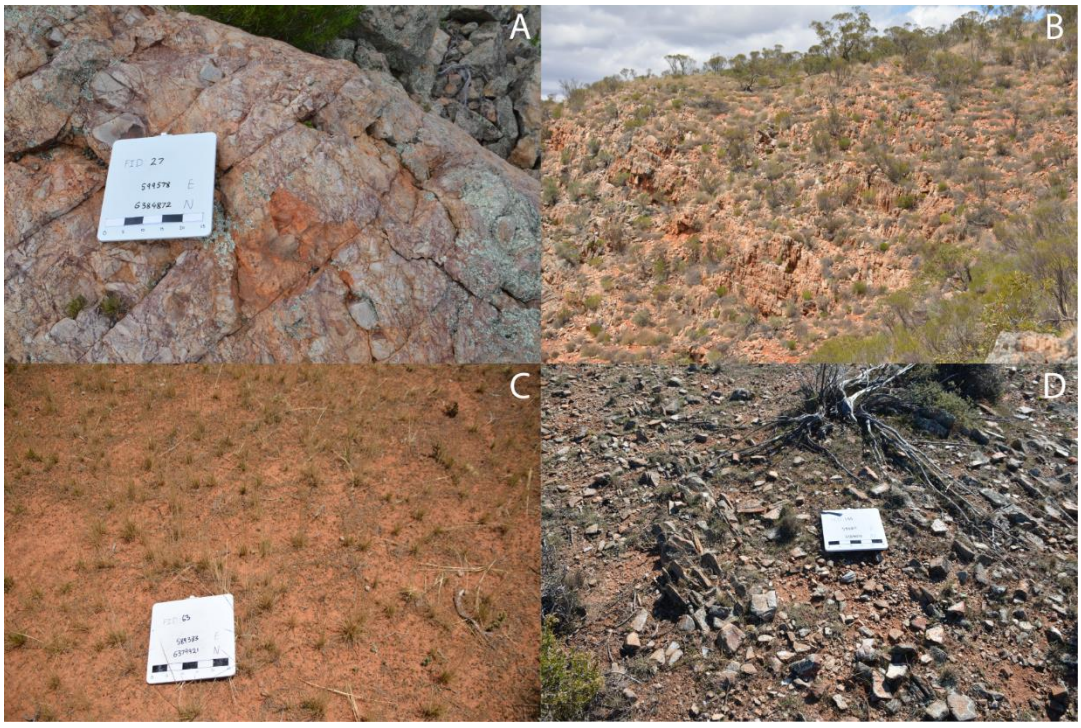

Figure 3.2: Examples of exposures and land surfaces in the study area, A: Silicified and altered alunite breccia at Nankivel Hill; B: Exposures of Warrow Quartzite on Peterlumbo Hill; C: Soil with lightly vegetated ground cover; D: Mix of low relief exposure, colluvium, soil and some green and dead vegetation.

The landscape is broadly low relief with limited geological exposures. The highest features are the GRV exposures in the north, Nankivel and Peterlumbo Hills in the centre and other smaller, dispersed relief features throughout the study area (Figure 3.1). Salt lakes are prominent in the north west and there is a palaeochannel in the north east of the study area (Figure 3.1).

3.2 Methods

This study used a masked hyperspectral image, spectral library reference signatures and spectral matching algorithms to produce alteration mineral maps to characterise surface alteration mineralogy and assess mineral distribution relative to known alteration zonation patterns of the expected mineral systems present. Mineral assemblages selected for this analysis had been previously determined through understanding of the mineral system and its associated alteration mineralogy by Investigator Resources (2017a, 2017b) and Nicolson *et al.* (2017b). X-ray diffraction analysis was conducted to provide an independent assessment of mineralogy across the study area and validate the hyperspectral alteration mineral maps. An overview of the methodology of this study is presented in Figure 3.3, with details in the following subsections.

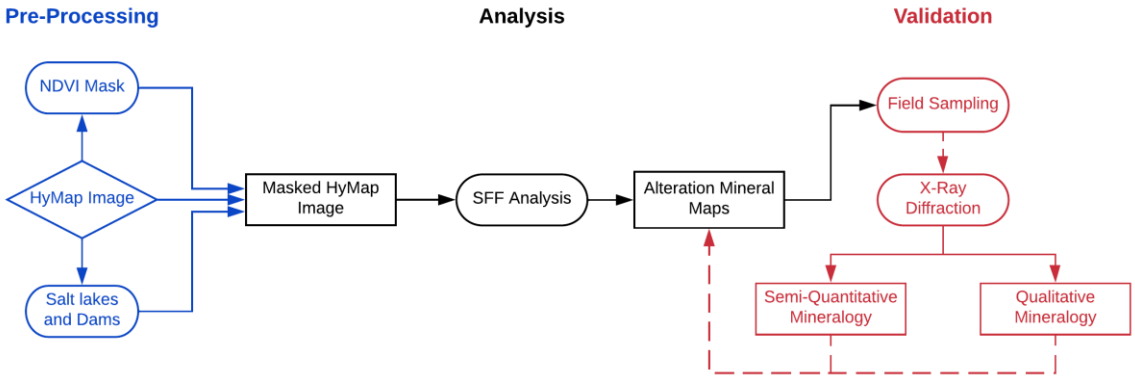

Figure 3.3: Flowchart of the methodology undertaken for this study.

3.2.1 Hyperspectral Imagery

HyMap airborne hyperspectral imagery was collected by HyVista Corporation in 2011 as part of a South Australian Government program to obtain hyperspectral data from prospective regions across South Australia. The HyMap sensor contains 124 bands across the visible, near-infrared and shortwave infrared regions of the electromagnetic spectrum (420 – 2450 nm) (Table 3.1). This imagery comprised ten swaths, each approximately 2.5 km wide, over 415 km^2 (136°0' – 136°9' E; 33°44' – 32°42' S). Atmospheric corrections were performed by HyVista using HyCORR software followed by EFFORT (Empirical Flat Field Optimal Reflectance Transformation) polishing pass (HyVista Corporation 2003). The imagery was delivered as a georeferenced image mosaic calibrated to apparent surface reflectance with a spatial resolution of 4.6 m (Cocks *et al.* 1998; Hussey 2015).

Table 3.1: Spectral configuration of the HyMap (modified from Cocks *et al.* (1998)).

Detector	Spectral Range (nm)	Number of bands	Bandwidth (nm)	Average spectral sampling interval (nm)
VIS	450 - 890	30	15 - 16	15
NIR	890 - 1350	31	15 - 16	15
SWIR1	1400 - 1800	30	15 - 16	13
SWIR2	1950 - 2480	33	18 - 20	17

3.2.1.1 Pre-Processing

Extensively noisy bands containing little spectral information were excluded prior to pre-processing, reducing the number of bands from 124 to 113. Excluded bands were those at the interface between the four sensor detectors, and near 1400 nm and 1900 nm where strong atmospheric water vapour absorption reduces radiance levels. Table 3.2 lists the remaining bands and their wavelengths used in the spectral analysis.

Table 3.2: HyMap sensor bands and wavelengths used in spectral analysis.

Detector	Remaining Bands	Wavelengths (nm)
VIS	2 - 31	467.3 - 895.1
NIR	32 - 60	901.3 - 1318.5
SWIR1	65 - 90	1460.8 - 1783.3
SWIR2	96 - 123	1996.1 - 2459

The imagery was masked to exclude the most green and dense vegetation cover using the Normalised Difference Vegetation Index (NDVI) (Rouse *et al.* 1974). This was produced using wavelengths 683.2 nm and 1073.6 nm and applied with a moderate threshold to restrict the mask to the most photosynthetically active vegetation, removing as little surrounding soil as possible for further analysis. Other features such as salt lakes and dams were digitised using ENVI® version 5.3 image analysis software (Exelis Visual Information Solutions 2015) following visual and geological map descriptions and incorporated in the mask to exclude areas not relevant to the analysis. (Figure 3.3).

3.2.2 Spectral Feature Fitting

Spectrally active minerals within alteration types have been well studied (e.g. Hunt and Ashley 1979), with Hauff (2008) classifying spectrally active minerals for specific alteration styles and environments. The spectrally active minerals investigated in this study are related to advanced argillic, argillic and propylitic alteration types associated with high-sulphidation epithermal alteration (Nicolson *et al.* 2017b) (Table 3.3). From this information, relevant United States Geological Survey (USGS) visible-shortwave infrared spectral reflectance signatures (Kokaly *et al.* 2017) were selected for initial analysis (Figure 3.4)

using Spectral Feature Fitting (SFF) in ENVI® software. SFF analysis, widely used in spectral mineral mapping, compares the fit of image spectra to a reference spectrum over a selected wavelength range using a least-squares technique (Clark *et al.* 1990; Clark *et al.* 1991) and was selected to focus on the diagnostic features of each mineral. Key diagnostic features for each mineral were identified using the GMEX Spectral Analysis Guides for Mineral Exploration (AusSpec International Ltd 2008) (Table 3.4). Minerals such as zunyite and diaspore were not included in the analysis as their diagnostic spectral features are not within the spectral regions available in usable HyMap bands.

Table 3.3: Spectrally active minerals characteristic of advanced argillic, argillic and propylitic alteration associated with hydrothermal mineral systems. Adapted from Hauff (2008).

Alteration Type	**SWIR active mineral assemblage (key minerals in bold)**
Advanced argillic	**Kaolinite**, **dickite**, **alunite**, diaspore, pyrophyllite, zunyite
Argillic	**Kaolinite**, **dickite**, **montmorillonite**, **illite-smectite**
Propylitic	**Calcite**, **chlorite**, **epidote**, sericite, clay

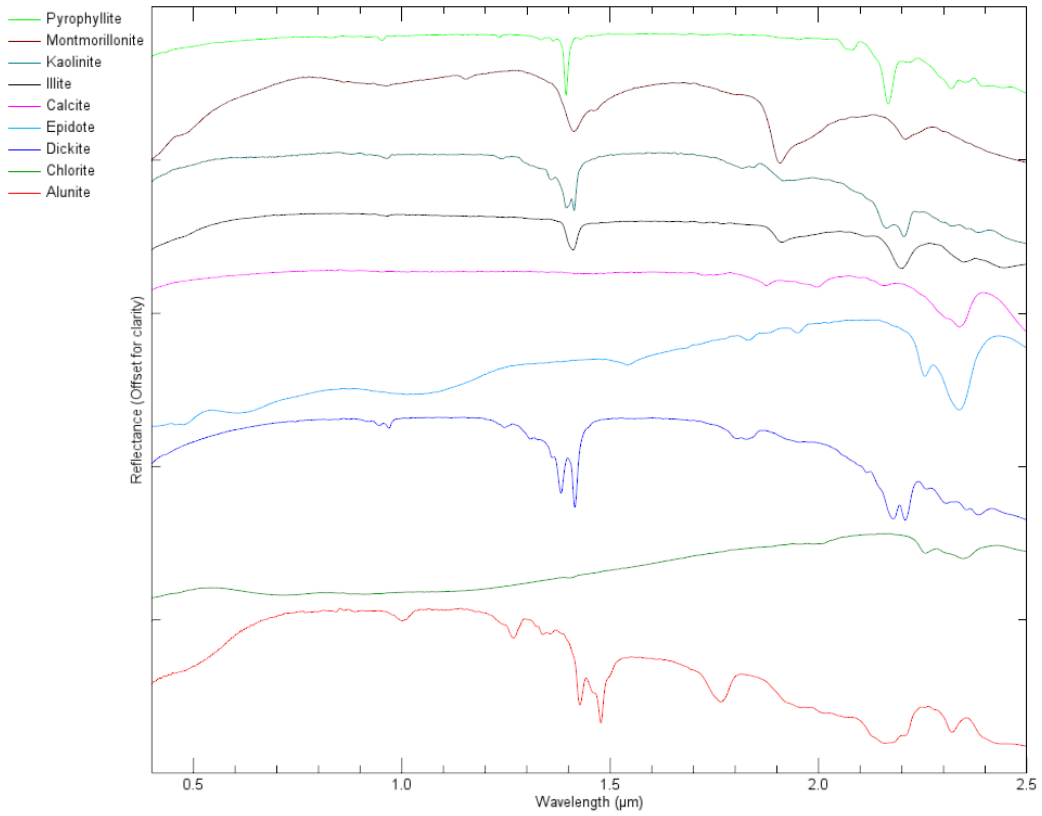

Figure 3.4: USGS spectral library signatures for the minerals used in this analysis.

Table 3.4: Mineral species, their chemistry, diagnostic absorption features and the wavelength ranges used in SFF analysis.

Mineral	Chemical Formula	Diagnostic absorption feature wavelength(s) (nm)	Chemical bond	Wavelengths used in SFF (nm)
Alunite	$KAl_3(SO_4)_2(OH)_6$	~1400 ~1760	H_2O OH	1460.8 – 1543.1 1710.2 – 1783.3
Calcite	$CaCO_3$	~2340 - 2345	CO_3	2194.2 – 2396.2
Chlorite	$(Mg,Fe)_3(Si,Al)_4O_{10}(OH)_2$ $(Mg,Fe)_3(OH)_6$	~2245 – 2256 ~2325 - 2365	Fe-OH Mg-OH	2194.2 – 2427.8
Dickite	$Al_2Si_2O_5(OH)_4$	~1384 - 1420 ~2178 - 2204	OH Al-OH	1262.7 – 1474.9 2124.9 – 2247.5
Epidote	$Ca_2(Al,Fe)_2(SiO_4)_3(OH)$	~2256 ~2335 - 2342	Fe-OH	2142.7 – 2427.8
Illite	$K_{0.65}Al_2[Al_{0.65}Si_{3.35}O_{10}]$ $(OH)_2$	~2180 – 2228 ~2350 ~2440	Al-OH Mg-OH	2142.7 – 2265.0 2298.5 – 2380.3 2412.0 – 2474.4
Kaolinite	$Al_2Si_2O_5(OH)_4$	~2160 ~2206 ~2350?	Al-OH -OH	2124.9 – 2230.4 2298.5 – 2412.0
Montmorillonite	$(Na,Ca)_{0.33}(Al,Mg)_2Si_4O_{10}$ $(OH)_2 \cdot nH_2O$	2205 - 2212	Al-OH	2160.4 – 2265.0
Pyrophyllite	$Al_2Si_4O_{10}(OH)_2$	~2166	Al-OH	2106.9 – 2194.7

The maps created from the SFF analysis showed absorption feature depths that can be interpreted as indicating relative similarity to the reference spectra and hence, likelihood of a mineral occurring in each pixel in the image. Histograms of the SFF results were evaluated to determine an appropriate threshold level for each mineral map to show the regions of best spectral match (Figure 3.5). Finally, the maps were smoothed and isolated pixels aggregated using spatial 3x3 majority filter.

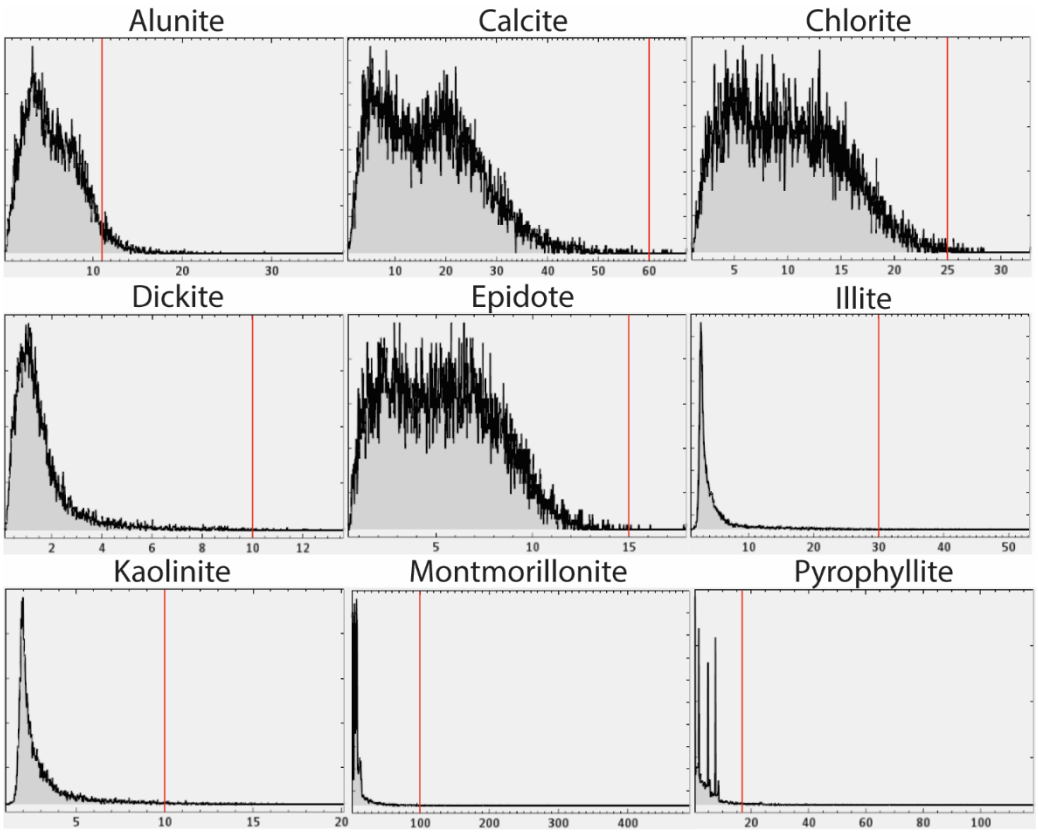

Figure 3.5: Histogram of SFF result for each mineral analysed. The red line indicates the threshold used to create the alteration mineral maps.

3.2.3 X-Ray Diffraction

Qualitative and semi-quantitative XRD analysis was conducted on 57 soil and geological exposure samples collected in July and November 2017, to validate the alteration mineral maps (Figure 3.6). Samples were finely milled to <75 µm prior to analysis. Measurements were undertaken using a Bruker D8 Advance with a Cu X-ray tube, with a 1.5406 Å wavelength of radiation. Samples were measured between 5° - 65.02° degrees (2θ) with steps of 0.02°. Mineralogy was identified using the Bruker Diffrac.EVA V4.2.1 software. Semi-quantitative analysis was done using the RockJock11 macro through Microsoft Excel 2007 (Eberl 2003) providing a result within ± 5 %.

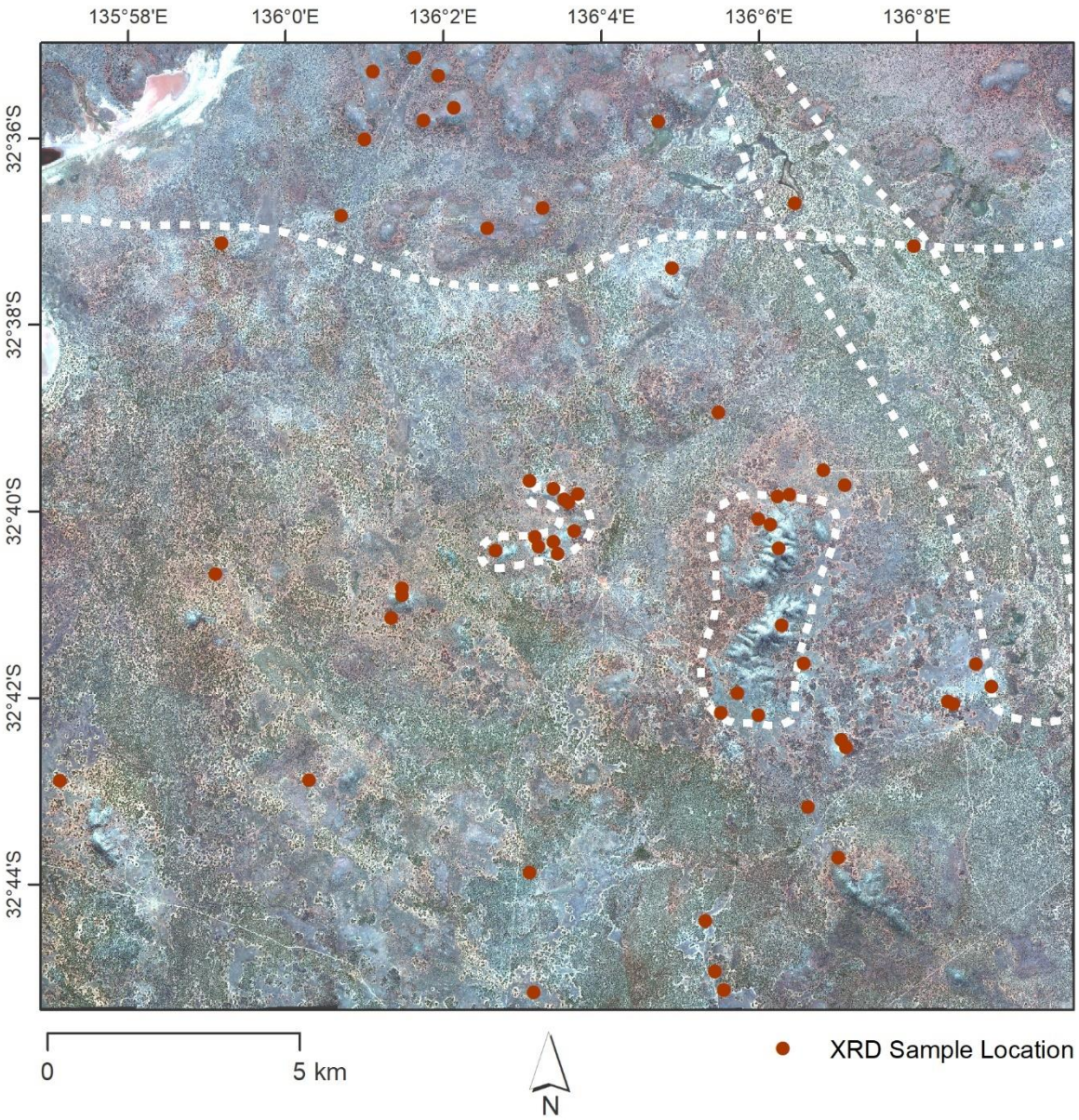

Figure 3.6: Location and distribution of XRD samples with landscape features as shown in Figure 3.1. Base image: HyMap true colour image (Red: 637.7 nm, Green: 546 nm, Blue: 467.3 nm).

3.3 Results

3.3.1 Hyperspectral Alteration Mineral Mapping

Spatial distributions of mineral occurrences resulting from the SFF analysis for each type of alteration understood to occur in the region are shown in Figure 3.7 and 3.8.

Kaolinite is the most spatially extensive mineral across the geological exposures, palaeochannel in the north east and the general landscape (Figure 3.7a). Dickite has a relatively similar surface expression but it is less widely distributed than kaolinite (Figure 3.7c). Alunite and pyrophyllite both have localised surface expressions at Nankivel Hill (Figure 3.7b and 3.7d).

Montmorillonite has a different surface expression to other clay minerals with limited distribution across the landscape within soils and no presence on geological exposures (Figure 3.8c) while illite has a similar spatial distribution to dickite but is slightly more pervasive on Peterlumbo Hill (Figure 3.8d).

The hyperspectral mineral maps were interpreted in conjunction with XRD results evaluate the spatial distribution of hydrothermal alteration around Nankivel and Peterlumbo Hills (Figure 3.9 – 3.11). A geological exposure south west of Nankivel Hill has distinctive surface expressions of kaolinite and dickite on its northern slopes (Figure 3.9a and 3.9b). Kaolinite occurs more broadly across the landscape, especially surrounding and to the east of Peterlumbo Hill (Figure 3.9a). Dickite is present on the southern slopes of Peterlumbo Hill and is slightly more extensive than kaolinite (Figure 3.9c). There are localised areas of Nankivel Hill that have surface expressions of alunite and pyrophyllite (Figure 3.9b and 3.9d).

Minor occurrences of dickite and illite are evident at Nankivel Hill with similar surface expressions apparent south west of Nankivel Hill (Figure 3.10b and 3.10c). Illite occurs sparsely at Peterlumbo Hill, similar to kaolinite and dickite but has a restricted surface expression further south. Montmorillonite is recognised to the north of Nankivel Hill but does not appear to be spatially extensive (Figure 3.10c).

Propylitic alteration was not extensively or obviously recognised in the Peterlumbo or Nankivel Hill areas (Figure 3.11). A localised occurrence of chlorite is seen to the south of Peterlumbo Hill (Figure 3.11b). Clear surface expressions of epidote and calcite were not observed through analysis of the HyMap imagery.

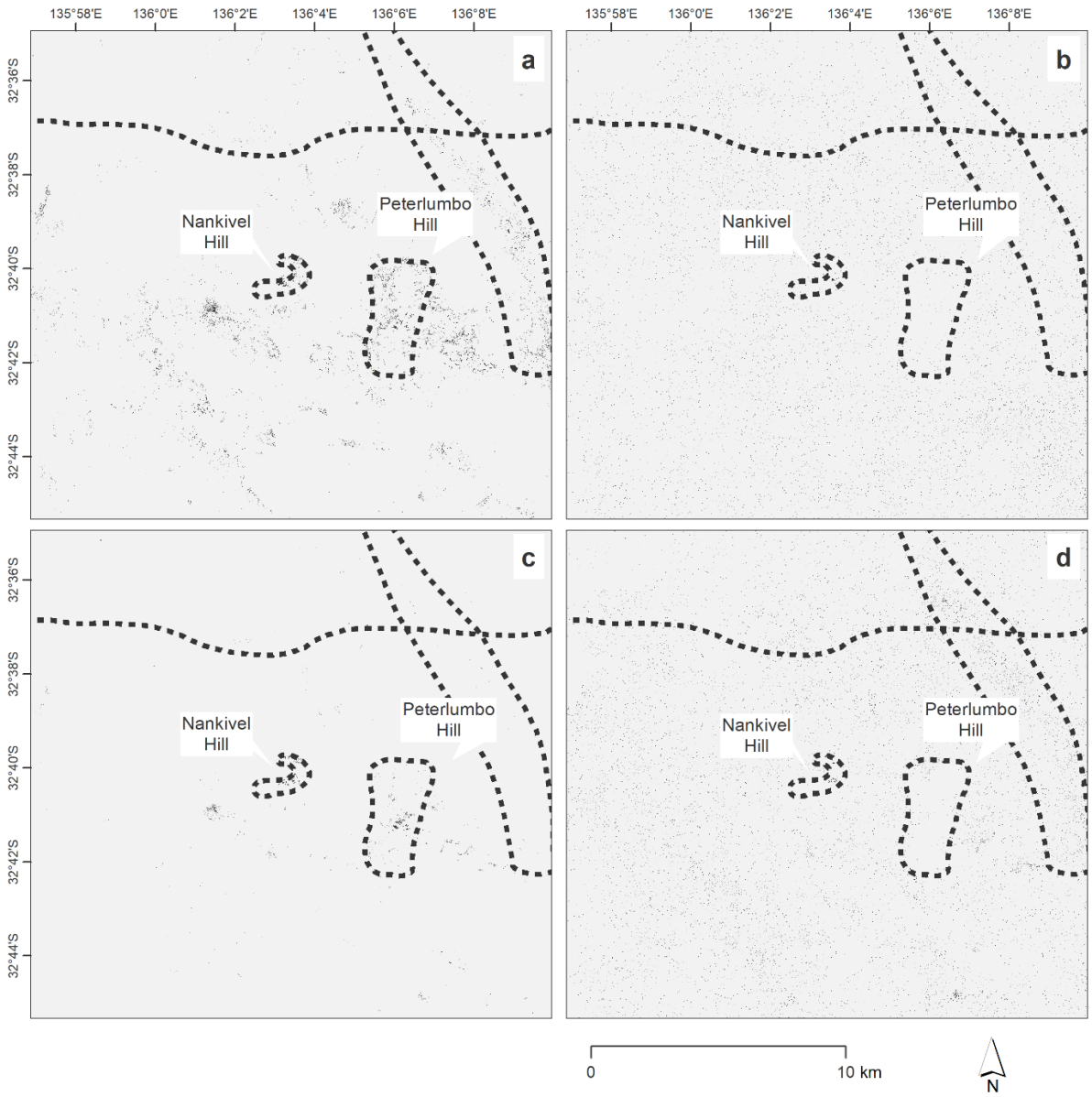

Figure 3.7: Surface expressions of minerals that form the advanced argillic alteration style. a: Kaolinite; b: Alunite; c: Dickite; d: Pyrophyllite.

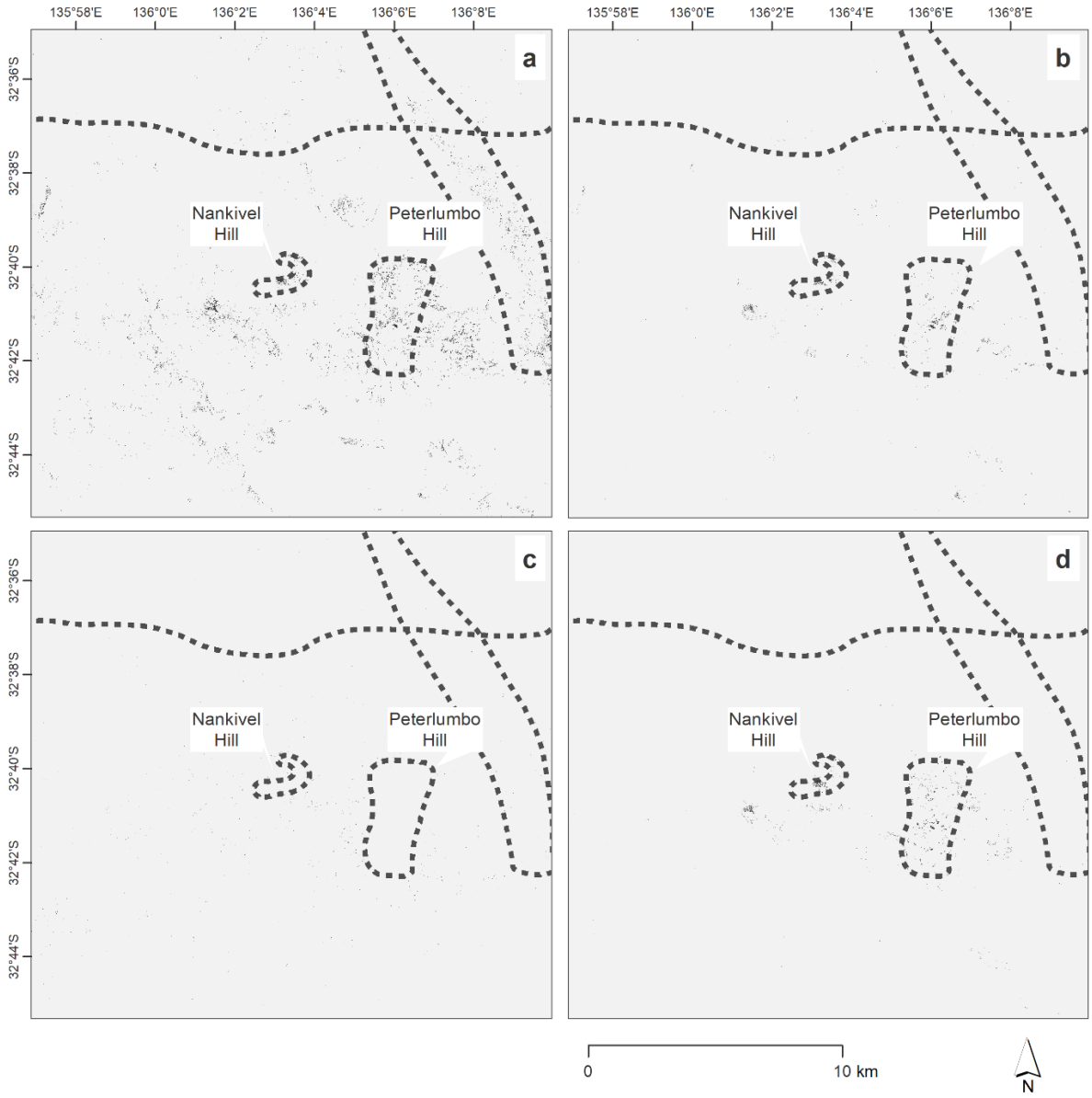

Figure 3.8: Surface expressions of minerals that form the argillic alteration style. a: Kaolinite, b: Dickite, c: Montmorillonite, d: Illite.

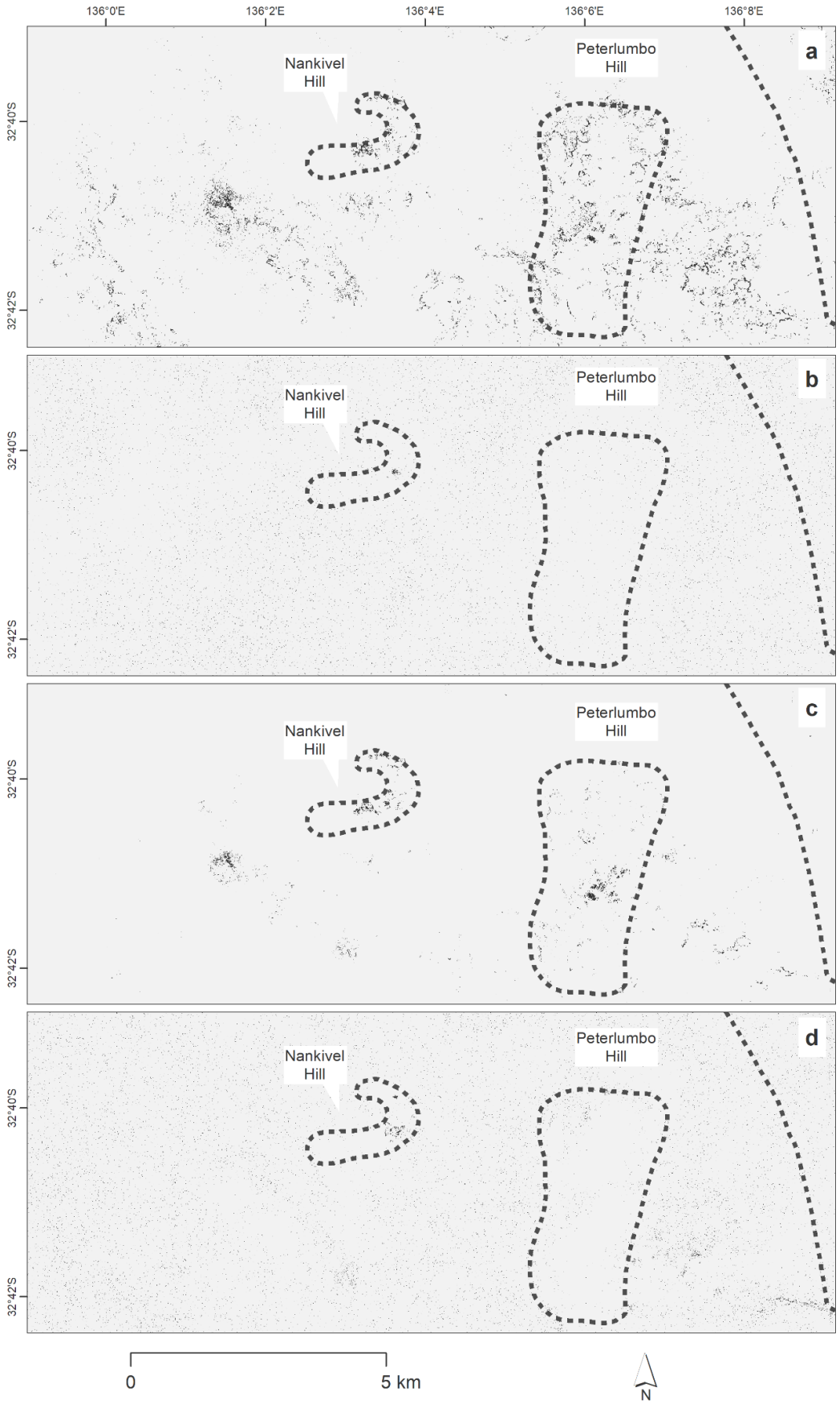

Figure 3.9: Surface expressions of minerals that form the advanced argillic alteration style focused on Nankivel and Peterlumbo Hills to illustrate alteration in these prominent regions of geological exposures, a: Kaolinite, b: Alunite, c: Dickite, d: Pyrophyllite.

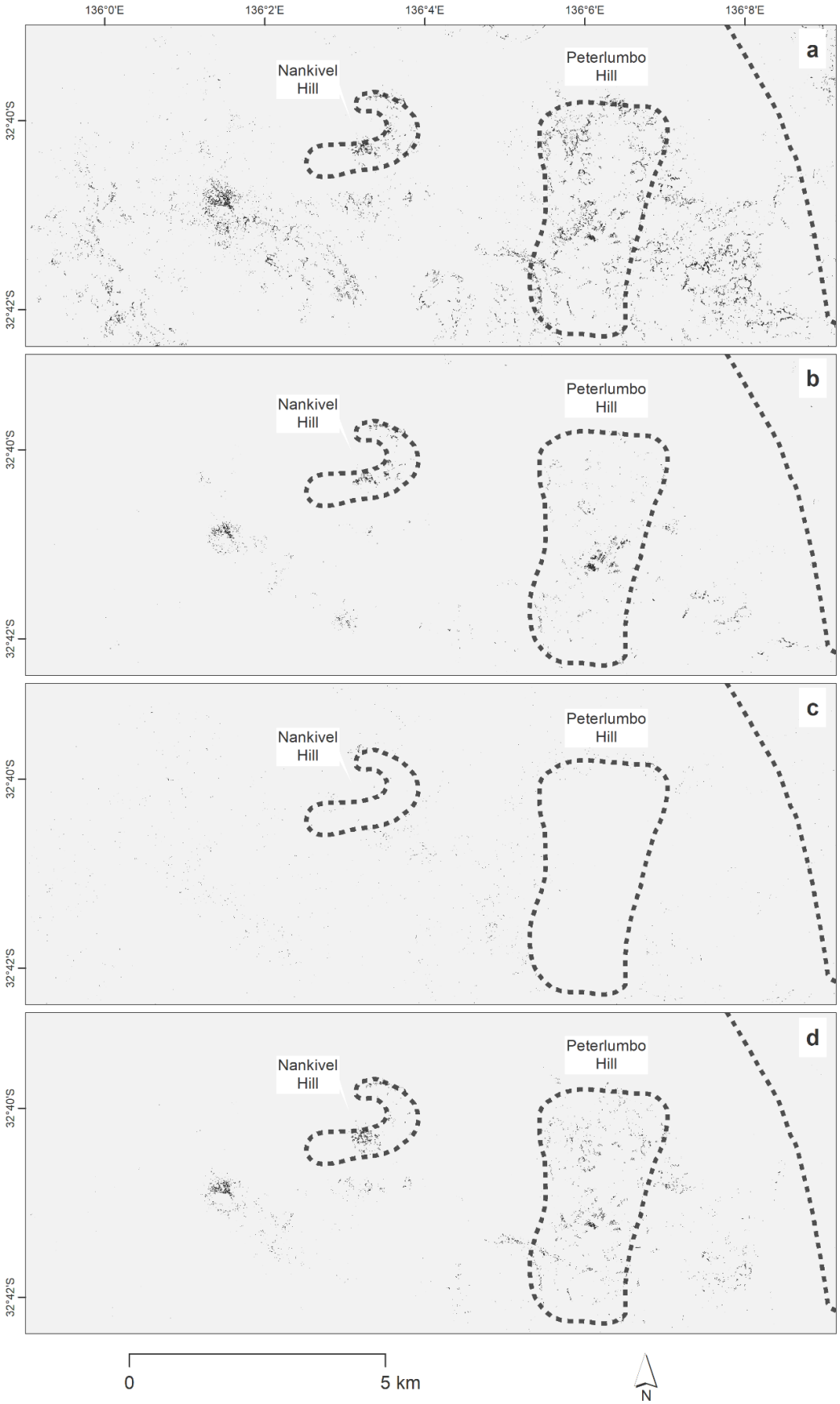

Figure 3.10: Surface expressions of minerals that form the argillic alteration style focused on Nankivel and Peterlumbo Hills to illustrate alteration in these prominent regions of geological exposures, a: Kaolinite, b: Dickite, c: Montmorillonite, d: Illite.

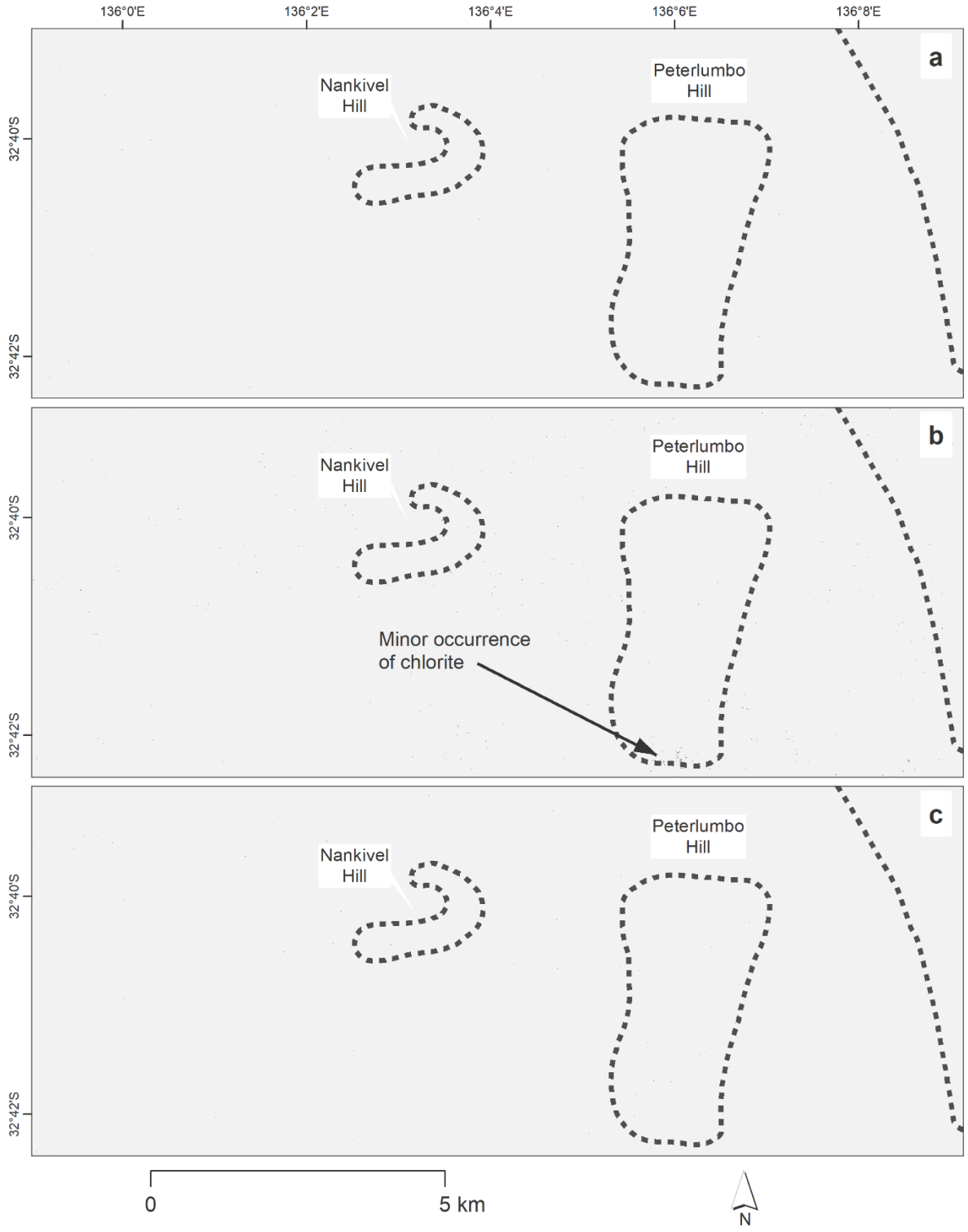

Figure 3.11:Surface expressions of minerals that form the propylitic alteration style focused on Nankivel and Peterlumbo Hills to illustrate alteration in these prominent regions of geological exposures, a: Epidote, b: Chlorite, c: Calcite.

3.3.2 Distribution of X-Ray Diffraction Mineralogy

The main mineralogy identified across both exposure and soil samples was quartz, kaolinite, muscovite, microcline and calcite. Full XRD semi-quantitative results for each sample can be found in Appendix B. The spatial distribution of XRD results for six key minerals; kaolinite, alunite, pyrophyllite, dickite, illite and chamosite (Fe-chlorite) are shown in Figure 3.12. The most widespread mineral was kaolinite, recognised within 41 samples that range from 4.5 to 23.3 % (Figure 3.12a). Alunite occurs within two samples, one with 0.90 % and the other with 24 % both located at Nankivel Hill (Figure 3.12b). Pyrophyllite occurs in three samples, containing 22 %, 30.7 % and 98.4 % (Figure 3.12c). Dickite was identified in two samples at 7.6 % and 45.8 % (Figure 3.12d). Illite occurs in five samples, which are distributed across the centre of the study area (Figure 3.12e) with proportions ranging from 17.4 to 30 %. Chamosite was recognised in four samples in the north of the study area and one sample south of Peterlumbo Hill (Figure 3.12f). The proportion of chamosite ranges from 9.7 to 22.3 %.

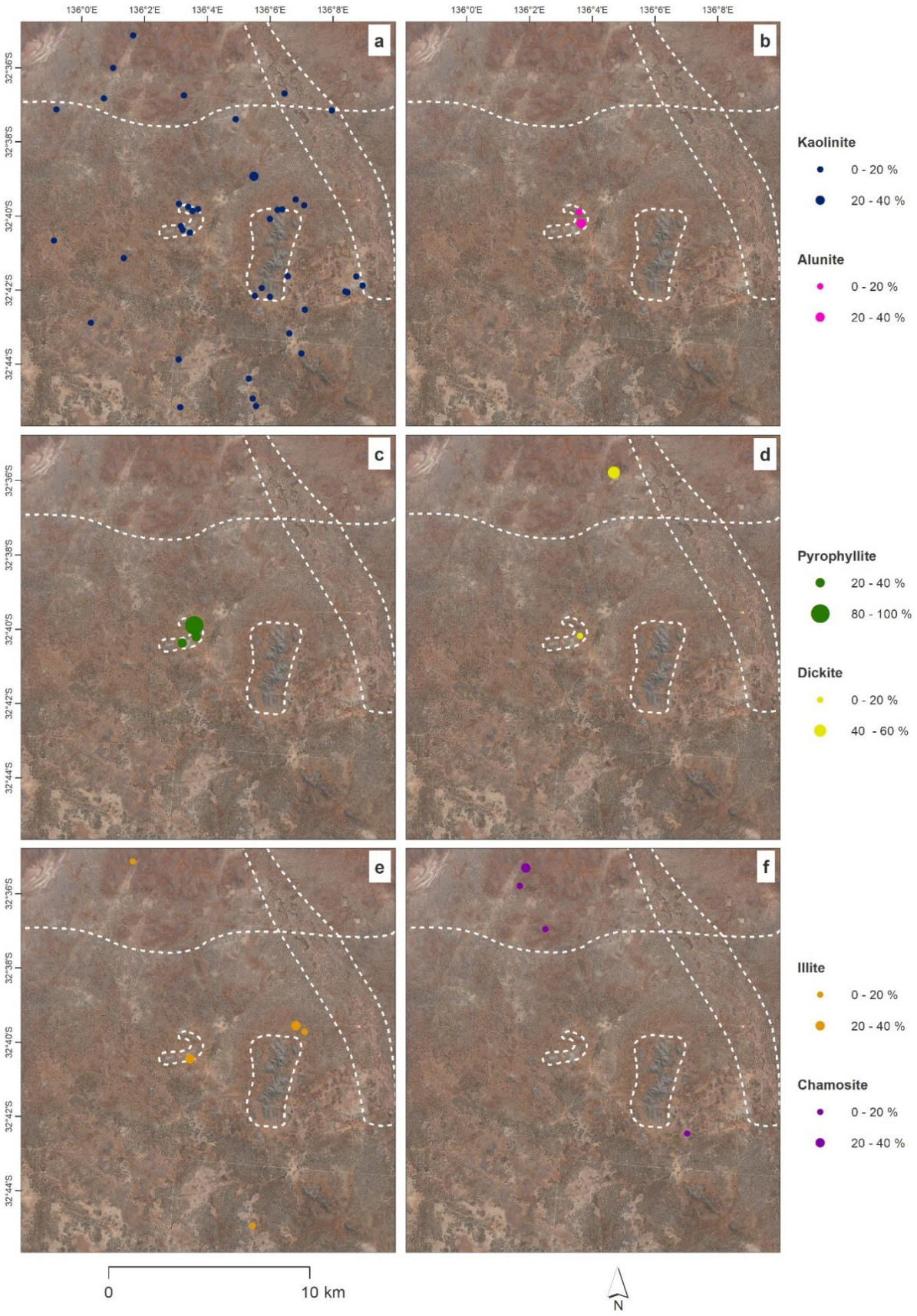

Figure 3.12: Distribution of six relevant alteration minerals identified in XRD analysis, a: Kaolinite, b: Alunite, c: Pyrophyllite, d: Dickite, e: Illite, f: Chamosite. For clarity, only samples that contain each mineral are shown.

3.4 Discussion

3.4.1 Limitations of Hyperspectral Mapping

Although hyperspectral mapping has been used here to produce several mineral distribution maps, there are some limitations that should be considered. Firstly, there is the absence of usable spectral information in the hyperspectral imagery around 1400 nm and 1900 nm, respectively related to OH and H_2O. The low signal to noise ratio in these spectral regions in the HyMap data is due to strong absorption of radiation by atmospheric water vapour. These wavelength regions can contain absorption features for some minerals, in which case alternative diagnostic absorption features are used for analysis where possible. This may also account for the noise in the alunite mineral map as only the edge of the diagnostic feature was able to be used for spectral analysis and those bands may inherently contain noise due to proximity to 'bad bands' (Figure 3.6 and 3.9, Table 3.2 and 3.4). Another limitation is that several minerals contain diagnostic absorption features in similar wavelength regions (Table 3.4). Although absorption features may differ slightly for each mineral, the spectral bandwidth of the HyMap sensor, at 15 – 20 nm (Table 3.1), can limit the unambiguous discrimination of minerals with similar spectral characteristics.

The presence of vegetation can limit the detection of the underlying soil in optical remote sensing. Masking was used to remove the most photosynthetically active vegetation from the hyperspectral image but influences of sparse green and non-photosynthetic vegetation may remain within the pixels analysed. Using a lower NDVI threshold to mask vegetation would considerably reduce the number of pixels available for analysis. Spectral features for non-photosynthetic vegetation and some Australian arid zone plants between 2090 nm and 2400 nm overlap with mineral absorption features that also occur in this range (Elvidge 1990). Without unmixing each pixel, the contribution of dry vegetation to overall pixel spectral response cannot be determined. Considering the size of most plants and vegetation clumps in this region, the image spatial resolution of 4 m is too large to successfully mask all vegetation, especially woody shrub vegetation.

3.4.2 Mineralogical Alteration Mapping

The minerals discussed here may have formed in a number of ways: they may comprise the primary or secondary rock mineralogy as a result of weathering, regional metamorphism or alteration associated with the mineralising system. In this study area, the alteration is considered to be epithermal-porphyry in nature from the conclusions of previous research including Investigator Resources (2017a); Nicolson *et al.* (2017a).

3.4.2.1 Nankivel Hill

Surface expressions of minerals associated with high-sulphidation epithermal alteration assemblages were recognised here using airborne hyperspectral mineral mapping. The preservation of an advanced argillic alteration mineral assemblage has previously been reported in the Nankivel Hill area (Gerakiteys 1996; Nicolson *et al.* 2017b). XRD analysis confirms the presence of alunite, pyrophyllite and dickite at Nankivel Hill, supporting current understanding that this region preserves evidence of advanced argillic alteration (Figure 3.9 and 3.12). Minerals potentially ascribed to argillic alteration are also detected in the region with kaolinite, dickite and illite observable at Nankivel Hill from spectral and XRD analysis (Figure 3.10 and 3.12). Samples that contain illite identified by XRD correspond with the spectral analysis, with the largest proportions of illite observed at Nankivel Hill (Figure 3.12). The spatial association of mineral assemblages that may be attributed to advanced argillic and argillic alteration at Nankivel Hill are consistent with current models of porphyry systems by Sillitoe (2010) and Corbett (2018). However, it is possible that kaolinite is not necessarily attributable to alteration and may be present due to weathering. This highlights the significance of the presence of dickite and illite in this region as they form at higher temperatures than kaolinite and hence are more likely to be associated with alteration (Corbett 2018).

3.4.2.2 Peterlumbo Hill

Minerals present at Peterlumbo Hill are primarily dickite and illite (Figure 3.9 and 3.10). XRD results highlight the presence of illite just north of Peterlumbo Hill but did not identify dickite at Peterlumbo Hill (Figure 3.12d). Further analysis regarding crystallinity would be required to identify if illite is present due to metamorphism or alteration processes. As at Nankivel Hill, dickite is a higher temperature mineral (Corbett 2018) and is more likely to be associated with alteration. However, its presence is not validated by the XRD analysis at Peterlumbo Hill and could be a misidentification of another mineral with a strong 2200 nm feature in the SFF analysis (Table 3.4).

In this study area, the Fe-rich chlorite endmember, chamosite, was identified south east of Peterlumbo Hill within a sampled exposure of GRV. Chamosite is not uncommon within the study area and is also observed in the GRV exposures in the north of the study area (Figure 3.12). Chlorite within GRV samples taken from within the study area have been interpreted to represent alteration associated with a mineralising system, potentially the *ca.* 1590 Ma magmatic-hydrothermal event that effected the Gawler Craton (Reid and Jagodzinski 2012; Wade *et al.* 2014). On a broader scale, chlorite in general is reported as being a common mineralogical constituent of the GRV (e.g. Garner and McPhie 1999; Allen and McPhie 2002; Agangi 2011) and is interpreted to represent alteration of primary ferromagnesian mineralogy such as pyroxene (e.g. Morrow and McPhie 2000; Allen *et al.* 2008). Propylitic alteration

also commonly includes calcite and epidote ((Sillitoe 2010); Table 3.3) and as neither of these minerals were observed within the GRV exposure sample at Peterlumbo Hill, it is unlikely that this style of alteration has occurred in this geological exposure. Therefore, this alteration could be deemed chloritic alteration and be more generic in nature as similar alteration has impacted other GRV units. It cannot be strictly determined what the mode of occurrence of chamosite is from the results in this study without further analysis beyond the scope of this current work.

3.4.3 Landscape Processes

Mapping surface expressions of alteration patterns that are known to be present and associated with epithermal-porphyry mineralisation within the southern Gawler Ranges study area (e.g. Nicolson *et al.* 2017b; Werner *et al.* 2018) is difficult, which is likely due to transportation and redistribution of material during broad scale landscape processes. From the HyMap and XRD results, the spatial distribution of alunite, pyrophyllite, dickite and illite at Nankivel Hill and Peterlumbo suggest advanced argillic alteration and argillic alteration primarily preserved at geological exposures (Figure 3.9 and 3.10). Preservation of minerals associated with the alteration in the wider landscape is limited and it is not possible to see spatial distributions of advanced argillic and argillic alteration beyond the geological exposures. Minerals such as pyrophyllite, chamosite and dickite are susceptible to weathering due to their crystal structure and weak chemical bonds (e.g. Brigatti *et al.* 2011). This suggests that there has been significant weathering in this landscape also demonstrated by the XRD results that indicate the surface soils are quartz and clay (kaolinite) rich in nature (see supplementary material).

Conversely, kaolinite is pervasive across this RDT (Figure 3.12a). Kaolinite is known to be a common product of granitic weathering, due to the breakdown of feldspar, or hydrothermal alteration (Robertson and Eggleton 1991). Kaolinite present at Nankivel and Peterlumbo Hill is within soil samples and not geological exposures, indicating its formation by weathering. On a landscape scale, kaolinite and quartz are the dominant constituents of samples taken throughout the study area. This suggests that kaolinite observed has primarily originated as a product of weathering and not alteration. However, further XRD analysis would be necessary to explicitly clarify this.

The analyses undertaken in this study suggests that any propylitic alteration mineralogy did not survive weathering in this landscape. Calcite is only identified in the XRD analysis within soil samples and chamosite is the only mineral from the propylitic mineral assemblage to be identified within geological exposure samples. However chamosite was not recognised in any proximal or distal soil samples from these GRV exposures across the study area. As with other alteration minerals in this study, chamosite is easily weathered and breaks down to kaolinite (Anand 2005), depending on its specific chemical composition. There is some debate concerning epidote weathering mechanisms but it is considered to

be a common constituent of the residual mineral fraction of soils (cf. Price *et al.* 2005). Therefore, if there was epidote present in the geological exposures, it is likely to be identifiable in soils, even after weathering. There was no epidote identified by XRD or image analysis, which implies that neither chloritic nor propylitic alteration is present in this study area.

Overall, the highly weathered nature of this RDT in the southern Gawler Ranges area presents challenges in identifying mineralogical alteration associated with potential epithermal – porphyry mineral systems. The easily weathered nature of key alteration phases means if and when they undergo redistribution within the landscape, they are likely to breakdown to common clays (e.g. kaolinite or smectite). This process reduces the mineralogical footprint of alteration that may be identified using airborne hyperspectral imagery. Challenges such as this may be overcome by using higher spatial and spectral resolution airborne data. Higher spatial resolution would reduce the potential for pixel-scale vegetation and soil mixing therefore allowing for purer spectral signatures of ground surface materials. Higher spectral resolution would also allow for more specific identification of wavelength shifts based on mineral chemistry of relevant mineralogy such as white micas or clays (e.g. Post and Noble 1993).

3.4.4 Relationship with a Mineral System

Although there is limited published information regarding this porphyry-epithermal system, there is evidence of a mineral system present in this region from previous research and exploration (e.g. Gerakiteys 1996; Drown *et al.* 2000). The alunite breccia exposure at Nankivel Hill has been described as sulphide bearing (e.g. pyrite: Nicolson *et al.* (2017b)). However, Nankivel Hill is considered to be barren of mineralisation and therefore may represent the 'barren shoulder' of a porphyry system (J. Keeling, G. Corbett; pers. comm). The alunite breccia exposure could possibly form part of a lithocap, which are voluminous zones of topographically prominent advanced argillic-argillic alteration that can occur some distance from a porphyry copper deposit (Sillitoe 1995). However, without further geological and petrographic analysis it is not possible to ascertain whether Nankivel Hill is an exposed part of a lithocap. These results at Nankivel Hill identify similar alteration mineralogy associated with advanced argillic alteration as has been identified by Nicolson *et al.* (2017a) and Gerakiteys (1996) which supports the inference that Nankivel Hill preserves evidence of advanced argillic alteration. If the interpretation of a barren shoulder is correct, then Nankivel Hill could be associated with a blind porphyry system. The 'N' in Figure 13 illustrates the approximate position of Nankivel Hill in a porphyry system based on prior knowledge and results from this study.

The presence of chamosite around Peterlumbo Hill may be suggestive of chloritic alteration associated with epithermal-porphyry systems (Sillitoe 2010) (Figure 3.13). Therefore, the region just south of Peterlumbo Hill area would be located at the position marked 'P' in the porphyry-epithermal system

alteration model shown in Figure 3.13, distal to mineralisation. Placement of Nankivel Hill and Peterlumbo Hill within the porphyry-epithermal model may indicate a progression of alteration from proximal (advanced argillic alteration) to distal (chloritic alteration) within the mineralisation system.

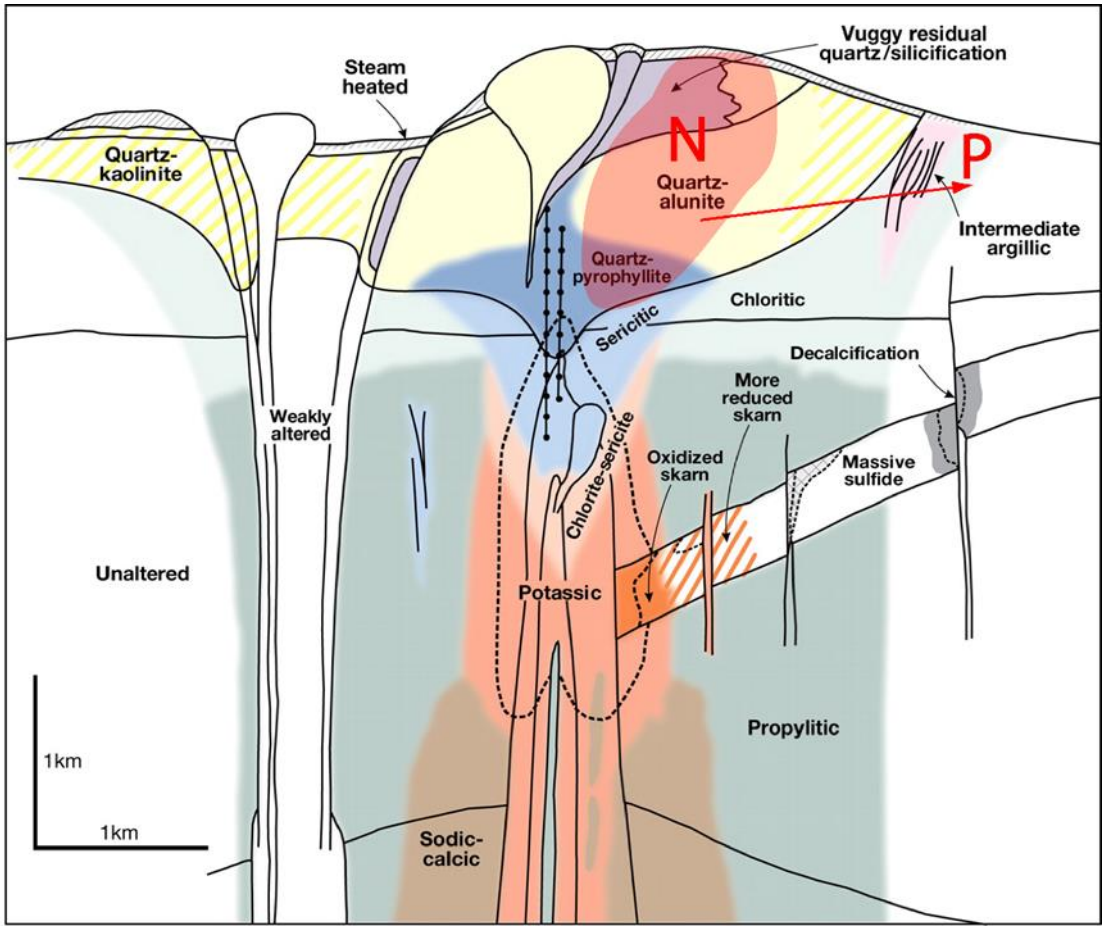

Figure 3.13: Generalised alteration-mineralisation zoning patterns for telescoped porphyry Cu deposits, modified from Sillitoe (2010).

Topography can play a role in locating porphyry mineralisation as it can illustrate conditions at the time of formation and current conditions to inform appropriate exploration methods (White and Hedenquist 1995). From current understanding of barren shoulders and alteration seen in the study area, mineralisation may be located to the south/ south-west of Nankivel Hill, consistent with suggestions by Corbett (2018) that regions of lower topography contain mineralisation. There are other cases where deposits have been discovered at lower elevations, lateral to barren shoulders (e.g. Halilaga, Turkey, Bilimoia Papua New Guinea) (Corbett 2018). There are also lowlands to the west of Nankivel Hill but these have previously been drilled by Investigator Resources with limited success in identifying economic mineralisation but did highlight relevant alteration at depth (Investigator Resources 2017b).

3.4.5 Application to Mineral Exploration

Traditional mineral exploration is an expensive and high-risk process. Using airborne hyperspectral imagery to understand the distribution of key minerals in a landscape prior to undertaking a detailed field campaign is likely to be significantly faster and cheaper than extensive sampling and drilling campaigns. Of most value to mineral exploration is the substantial spatial coverage that can be achieved by an airborne hyperspectral survey, although there are pre- and post-acquisition costs that also need to be considered.

Other RDTs in Australia where work similar to this has been implemented include the Mt Isa Inlier (e.g. Laukamp *et al.* 2011) and research similar to this could be possible in other known RDTs including the Yilgarn Craton and central NSW.

XRD analysis provides a validation method but is limited to soil and rock samples and can be expensive and time consuming. As demonstrated in this study, it is difficult to clearly identify alteration in highly weathered areas with limited geological exposures using airborne hyperspectral remote sensing alone, therefore, other methodologies should be considered to supplement this data. Analysis and interpretation of any geological exposures in the landscape is crucial as they can provide a primary source of mineralogy. In regions without geological exposures, regolith-landform maps (e.g. Krapf 2016; Caruso *et al.* 2018) can provide insight to understand material types and their origins to assist with interpretation hyperspectral imagery.

Opportunities for rapid and cost-effective collection of very high resolution airborne hyperspectral data are beginning to be realised through new technologies such as drones with shortwave infrared (SWIR) hyperspectral sensors (e.g. Dering *et al.* 2019). Data across the visible- near infrared (VNIR) part of the spectrum collected from these platforms has been shown to have advantages across a number of research areas including acid mine drainage monitoring and outcrop mapping (e.g. Jackisch *et al.* 2018; Kirsch *et al.* 2018). This technology has potential for use in mineral exploration to identify localised occurrences of alteration at geological exposures and distinctive vegetation occurrences that could assist with biogeochemical analysis.

Although this work has focused on a porphyry-epithermal deposit model, the general method using airborne hyperspectral imagery could be used across a wider range of RDTs. In addition to reducing initial costs, airborne hyperspectral remote sensing methods for mineral exploration could provide insight into unknown or underexplored terrains to locate prospective areas and discount barren regions early in the exploration cycle.

3.5 Conclusions

This study has demonstrated that hyperspectral imagery can be used to identify some key alteration minerals that relate to porphyry-epithermal alteration in a RDT, despite challenges including vegetation cover, extensive weathering and RDT processes. XRD analysis was successfully used to validate the mineralogical interpretations made from image analysis. Advanced argillic (alunite, pyrophyllite, dickite) and argillic (kaolinite, dickite, illite) alteration assemblages are concentrated around the limited rock exposures within the southern Gawler Ranges study area. The lack of redistribution of these minerals throughout the landscape is attributed to prolonged weathering within the current arid environment. Conversely, kaolinite is widely distributed throughout the study area and is deemed a product of weathering.

Overall, this study demonstrates that airborne hyperspectral imagery could be considered as an early analytical technique within a RDT to understand the occurrence and distribution of alteration across a landscape. The use of this imagery would allow rapid assessment of prospectivity prior to undertaking a more expensive exploration campaign. In the case of the southern Gawler Ranges, image analysis was able to identify mineral assemblages associated with advanced argillic and argillic alteration, consistent with previous claims that this area is prospective for porphyry mineralisation. The surface expressions mapped in this study show that some mineralogical signatures related to an epithermal- porphyry system are preserved in this area.

3.6 References

Agangi, A. (2011). Magmatic and volcanic evolution of a silicic large igneous province (SLIP): the Gawler Range Volcanics and Hiltaba Suite, South Australia. *PhD Thesis (Unpublished),* University of Tasmania

Allen, S.R., & McPhie, J. (2002). The Eucarro Rhyolite, Gawler Range Volcanics, South Australia: A >675 km^3, compositionally zoned lava of Mesoproterozoic age. *Geological Society of America Bulletin, 114*, 1592-1609

Allen, S.R., McPhie, J., Ferris, G., & Simpson, C. (2008). Evolution and architecture of a large felsic Igneous Province in western Laurentia: The 1.6 Ga Gawler Range Volcanics, South Australia. *Journal of Volcanology and Geothermal Research, 172*, 132-147. doi: 10.1016/j.jvolgeores.2005.09.027

Anand, R.R. (2005). Weathering history, landscape evolution and implications for exploration. In R.R. Anand, & P. De Broekert (Eds.), *Regolith Landscape Evolution Across Australia: A Compilation of Regolith Landscape Case Studies With Regolith Landscape Evolution Models* (pp. 2-40): CRC LEME. ISBN: 978-1-92-103928-7

Anand, R.R., & Butt, C.R.M. (2010). A guide for mineral exploration through the regolith in the Yilgarn Craton, Western Australia. *Australian Journal of Earth Sciences, 57*, 1015-1114. doi: 10.1080/08120099.2010.522823

Andrew, M.E., & Ustin, S.L. (2008). The role of environmental context in mapping invasive plants with hyperspectral image data. *Remote Sensing of Environment, 112*, 4301-4317. doi: 10.1016/j.rse.2008.07.016

AusSpec International Ltd (2008). *GMEX Spectral Analysis Guides for Mineral Exploration*. (3rd ed.). AusSpec International

Bierwirth, P., Huston, D., & Blewett, R. (2002). Hyperspectral mapping of mineral assemblages associated with gold mineralization in the Central Pilbara, Western Australia. *Economic Geology, 97*, 819-826. doi: 10.2113/97.4.819

Blissett, A.H., Creaser, R.A., Daly, S.J., Flint, R.B., & Parker, A.J. (1993). Gawler Range Volcanics. In J.F. Drexel, W.V. Preiss, & A.J. Parker (Eds.), *Bulletin 54, The geology of South Australia; Volume 1: The Precambrian* (pp. 107-124). South Australia: Geological Survey of South Australia. ISBN: 978-0-73-084146-3

Brigatti, M.F., Malferrari, D., Laurora, A., & Elmi, C. (2011). Structure and mineralogy of layer silicates: recent perspectives and new trends. In M.F. Brigatti, & A. Mottana (Eds.), *Layered Mineral Structures and their Application in Advanced Technologies* (pp. 1-71): Mineralogical Society of Great Britain and Ireland. ISBN: 978-0-90-305645-8

Brown, A.J., Cudahy, T.J., & Walter, M.R. (2006). Hydrothermal alteration at the Panorama Formation, North Pole Dome, Pilbara Craton, Western Australia. *Precambrian Research, 151*, 211-223. doi: 10.1016/j.precamres.2006.08.014

Bureau of Meterology (2018). Climate Data Online, http://www.bom.gov.au/climate/data/: Australian Government. Access Date: August 2018

Butt, C.R.M., Lintern, M.J., & Anand, R.R. (2000). Evolution of regoliths and landscapes in deeply weathered terrain – implications for geochemical exploration. *Ore Geology Reviews, 16*, 167-183. doi: 10.1016/s0169-1368(99)00029-3

Carranza, E.J.M., & Hale, M. (2002). Mineral imaging with Landsat Thematic Mapper data for hydrothermal alteration mapping in heavily vegetated terrane. *International Journal of Remote Sensing, 23*, 4827-4852. doi: 10.1080/01431160110115014

Caruso, A.S., Clarke, K.D., Tiddy, C.J., Delean, S., & Lewis, M.M. (2018). Objective regolith-landform mapping in a regolith dominated terrain to inform mineral exploration. *Geosciences, 8*, 318. doi: 10.3390/geosciences8090318

Clark, R.N. (1999). Chapter 1: Spectroscopy of Rocks and Minerals, and Principles of Spectroscopy. In A.N. Rencz (Ed.), *Manual of Remote Sensing, Volume 3, Remote Sensing for the Earth Sciences* (pp. 3-58). New York: John Wiley and Sons

Clark, R.N., Gallagher, A.J., & Swayze, G.A. (1990). Material absorption band depth mapping of imaging spectrometer data using a complete band shape least-squares fit with library reference spectra. USA: National Aeronautics and Space Administration. Jet Propulsion Laboratory.

Clark, R.N., Swayze, G.A., Gallagher, A., Gorelick, N., & Kruse, F.A. (1991). Mapping with imaging spectrometer data using the complete band shape least-squares algorithm simultaneously fit to multiple spectral features from multiple materials. In, *Proceedings of the third airborne visible/infrared imaging spectrometer (AVIRIS) workshop* (pp. 2-3): Jet Propulsion Laboratory Publication

Cocks, T., Jenssen, R., Stewart, A., Wilson, I., & Shields, T. (1998). The HyMap™ airborne hyperspectral sensor: The system, calibration and performance. In M. Schaepman, D. Schlapfer, & K. Itten (Eds.), *1st EARSeL Workshop on Imaging Spectroscopy* (pp. 37-42). Zurich, Switzerland: EARSeL. ISBN: 978-2-908885-22-0

Corbett, G.J. (2018). Chapter 2 – Alteration. *Epithermal Gold-Silver and Porphyry Copper-Gold Exploration-Short Course Manual* (p. 51): Corbett Geological Services

Cudahy, T. (2012). Satellite ASTER Geoscience Product Notes for Australia. Canberra, Australia: CSIRO. Document Number: EP-30-07-12-44

Cudahy, T. (2016). Mineral Mapping for Exploration: An Australian Journey of Evolving Spectral Sensing Technologies and Industry Collaboration. *Geosciences, 6*, 52. doi: 10.3390/geosciences6040052

Daly, S.J., Fanning, G.M., & Fairclough, M.C. (1998). Tectonic evolution and exploration potential of the Gawler Craton, South Australia. *AGSO Journal of Australian Geology and Geophysics, 17*, 145-168

Department of the Environment and Energy (2012). *Interim Biogeographic Regionalisation for Australia, Version 7*. Canberra, Australia: Department of the Environment and Energy

Dering, G.M., Micklethwaite, S., Thiele, S.T., Vollgger, S.A., & Cruden, A.R. (2019). Review of drones, photogrammetry and emerging sensor technology for the study of dykes: Best practises and future potential. *Journal of Volcanology and Geothermal Research, 373*, 148-166. doi: 10.1016/j.jvolgeores.2019.01.018

Drown, C.G., Gerakiteys, C., Ashley, P.M., Joyce, R.M., Mackay, C.R., & Standish, T.R. (2000). Open File Envelope No. 8811, Mount Ive Gate. Adelaide, Australia. Aberfoyle Resources, Acacia Resources, Anglogold Australasia.

Duuring, P., Hagemann, S.G., Novikova, Y., Cudahy, T., & Laukamp, C. (2012). Targeting Iron Ore in Banded Iron Formations Using ASTER Data: Weld Range Greenstone Belt, Yilgarn Craton, Western Australia. *Economic Geology, 107*, 585-597. doi: 10.2113/econgeo.107.4.585

Eberl, D.D. (2003). User's Guide to RockJock – A program for determining quantitative mineralogy from powder X-Ray Diffraction data. Boulder, Colorado: United States Geological Survey. Document Number: Open File Report 03-78

Elvidge, C.D. (1990). Visible and near infrared reflectance characteristics of dry plant materials. *International Journal of Remote Sensing, 11*, 1775-1795. doi: 10.1080/01431169008955129

Exelis Visual Information Solutions, (2015). ENVI 5.3

Fanning, C.M., Reid, A.J., & Teale, G.S. (Eds.) (2007). *A geochronological framework for the Gawler Craton, South Australia*. Bulletin 55. Adelaide, Australia: South Australian Department of Primary Industries and Resources. ISBN: 978-0-75-901392-6

Ferris, G., & Schwarz, M. (2003). Proterozoic gold province of the central Gawler Craton. *MESA Journal, 30*, 4-12

Ferris, G.M., Schwarz, M.P., & Heithersay, P. (2002). The geological framework, distribution and controls of Fe-oxide Cu–Au mineralisation in the Gawler Craton, South Australia. Part 1: Geological and tectonic framework. In T.M. Porter (Ed.), *Hydrothermal Iron Oxide Copper – Gold and Related Deposits: A Global Perspective Vol. 2* (pp. 9-31). Adelaide, Australia: Porter Geological Consulting Publishing. ISBN: 978-0-95-805741-7

Garner, A., & McPhie, J. (1999). Partially melted lithic megablocks in the Yardea Dacite, Gawler Range Volcanics, Australia: implications for eruption and emplacement mechanisms. *Bulletin of Volcanology, 61*, 396-410. doi: 10.1007/s004450050281

Gerakiteys, C. (1996). Technical Report No. 2718, EL 1841 "Mt Ive Gate". Adelaide, Australia. MIM Exploration. Document Number: R96/02406

Goetz, A.F.H., & Rowan, L.C. (1981). Geologic Remote Sensing. *Science, 211*, 781-791. doi: 10.1126/science.211.4484.781

González-Álvarez, I., Boni, M., & Anand, R.R. (2016). Mineral exploration in regolith-dominated terrains: Global considerations and challenges. *Ore Geology Reviews, 73, Part 3*, 375-379. doi: 10.1016/j.oregeorev.2015.11.017

Hand, M., Reid, A., & Jagodzinski, L. (2007). Tectonic framework and evolution of the Gawler Craton, Southern Australia. *Economic Geology, 102*, 1377-1395. doi: 10.2113/gsecongeo.102.8.1377

Hauff, P.L. (2008). An overview of VIS-NIR-SWIR field spectroscopy as applied to precious metals exploration. Colorado, USA: Spectral International Inc.

Hewson, R.D., Cudahy, T.J., & Huntington, J.F. (2001). Geologic and alteration mapping at Mt Fitton, South Australia, using ASTER satellite-borne data. In, *IGARSS 2001: Scanning the Present and Resolving the Future* (pp. 724-726). Sydney, Australia: Institute of Electrical and Electronics Engineers

Hillis, R.R., Giles, D., Van Der Wielen, S.E., Baensch, A., Cleverley, J.S., Fabris, A., Halley, S.W., Harris, B.D., Hill, S.M., Kanck, P.A., Kepic, A., Soe, S.P., Stewart, G., & Uvarova, Y. (2014). Coiled Tubing Drilling and Real-Time Sensing-Enabling Prospecting Drilling in the 21st Century? In K.D. Kelley, & H.C. Golden (Eds.), *Society of Economic Geologists Special Publication Number 18* (pp. 243-259): Society of Economic Geologists. ISBN: 978-1-62-949637-5

Hunt, G.R., & Ashley, R.P. (1979). Spectra of altered rocks in the visible and near infrared. *Economic Geology, 74*, 1613-1629. doi: 10.2113/gsecongeo.74.7.1613

Hussey, M. (2015). March 2011 Peterlumbo area HyMap survey. Mineral maps Data Package. Adelaide, Australia: Department of State Development. Geological Survey of South Australia. Document Number: GDP00028

HyVista Corporation (2003). HyMap Data Products: HyVista Corporation

Investigator Resources (2017a). Large altered porphyry system with enhanced copper-gold potential confirmed at the Nankivel Prospect. In J. Anderson, & J. Murray (Eds.). Adelaide, Australia: Investigator Resources

Investigator Resources (2017b). New drilling and advanced exploration techniques upgrade porphyry copper target at Nankivel. In J. Anderson, & J. Murray (Eds.). Adelaide, Australia: Investigator Resources

Investigator Resources (2018). Projects, http://www.investres.com.au/cms/page.asp?ID=1002: Investigator Resources Access Date: August 2018

Jackisch, R., Lorenz, S., Zimmermann, R., Möckel, R., & Gloaguen, R. (2018). Drone-Borne Hyperspectral Monitoring of Acid Mine Drainage: An Example from the Sokolov Lignite District. *Remote Sensing, 10*, 385. doi: 10.3390/rs10030385

Jagodzinski, E.A. (2005). Compilation of SHRIMP U-Pb geochronological data, Olympic Domain, Gawler Craton, South Australia, 2001-2003. Canberra, Australia: Geoscience Australia. Document Number: Record 2005/20

Jagodzinski, E.A., Reid, A.J., Crowley, J.L., McAvaney, S., & Wade, C.E. (2016). Precise zircon U-Pb dating of a Mesoproterozoic silicic large igneous province: the Gawler Range Volcanics and Benagerie Volcanic Suite, South Australia. In, *AESC 2016 - Australian Earth Sciences Convention*. Adelaide, Australia: Geological Society of Australia

Kirsch, M., Lorenz, S., Zimmermann, R., Tusa, L., Mockel, R., Hodl, P., Booysen, R., Khodadadzadeh, M., & Gloaguen, R. (2018). Integration of terrestrial and drone-borne hyperspectral and photogrammetric sensing methods for exploration mapping and mining monitoring. *Remote Sensing, 10*. doi: 10.3390/rs10091366

Kokaly, R.F., Clark, R.N., Swayze, G.A., Livo, K.E., Hoefen, T.M., Pearson, N.C., Wise, R.A., Benzel, W.M., Lowers, H.A., Driscoll, R.L., & Klein, A.J. (2017). USGS Spectral Library Version 7.

Krapf, C.B.E. (2016). Regolith Map of the Southern Gawler Ranges Margin (YARDEA and PORT AUGUSTA 1:250 000 map sheets). Adelaide, South Australia: Geological Survey of South Australia

Kruse, F.A. (1988). Use of airborne imaging spectrometer data to map minerals associated with hydrothermally altered rocks in the northern Grapevine mountains, Nevada, and California. *Remote Sensing of Environment, 24*, 31-51. doi: 10.1016/0034-4257(88)90004-1

Kruse, F.A. (2012). Mapping surface mineralogy using imaging spectrometry. *Geomorphology, 137*, 41-56. doi: 10.1016/j.geomorph.2010.09.032

Kruse, F.A., Boardman, J.W., & Huntington, J.F. (2002). Comparison of airborne and satellite hyperspectral data for geologic mapping. *Proceedings of SPIE - The International Society for Optical Engineering, 4725*, 128-139. doi: 10.1117/12.478743

Laukamp, C., Cudahy, T., Cleverley, J.S., Oliver, N.H.S., & Hewson, R. (2011). Airborne hyperspectral imaging of hydrothermal alteration zones in granitoids of the Eastern Fold Belt, Mount Isa

Inlier, Australia. *Geochemistry: Exploration, Environment, Analysis, 11*, 3-24. doi: 10.1144/1467-7873/09-231

Lewis, M., Jooste, V., & De Gasparis, A.A. (2001). Discrimination of arid vegetation with airborne multispectral scanner hyperspectral imagery. *IEEE Transactions on Geoscience and Remote Sensing, 39*, 1471-1479. doi: 10.1109/36.934078

Mahoney, S., James, P., Mauger, A., & Heinson, G. (2003). Geologic and regolith mapping for mineral exploration in the Gawler Craton of South Australia using Hyperion and other remote sensing techniques. In, *International Geoscience and Remote Sensing Symposium 2003* (pp. 1779-1781). Toulouse, France: Institute for Electrical and Electronics Engineers

Mauger, A.J., Keeling, J.L., & Huntington, J.F. (2007). Alteration mapping of the Tarcoola Goldfield (South Australia) using a suite of hyperspectral methods. *Applied Earth Science, 116*, 2-12. doi: 10.1179/174327507x167028

McQueen, K.G. (2008). *A guide for mineral exploration through the regolith in the Cobar Region, Lachlan Orogen, New South Wales*. CRC LEME. ISBN: 978-1-921039-85-0

Morrow, N., & McPhie, J. (2000). Mingled silicic lavas in the Mesoproterozoic Gawler Range Volcanics, South Australia. *Journal of Volcanology and Geothermal Research, 96*, 1-13. doi: 10.1016/s0377-0273(99)00143-2

Nicolson, B., Reid, A., McAvaney, S., Keeling, J., Fraser, G., & Vasconcelos, P. (2017a). A Mesoproterozoic advanced argillic alteration system: $^{40}Ar/^{39}Ar$ thermochronology from Nankivel Hill, Gawler Craton. Adelaide, South Australia: Department of State Development. Geological Survey of South Australia. Document Number: Report Book 2017/00011

Nicolson, B.E., Reid, A., McAvaney, S., Keeling, J., Fraser, G., & Vasconcelos, P.M. (2017b). Timing of advanced argillic alteration at Nankivel Hill, SE of Paris silver deposit, northern Eyre Peninsula. *MESA Journal, 83*, 20-26

Peel, M.C., Finlayson, B.L., & McMahon, T.A. (2007). Updated world map of the Köppen-Geiger climate classification. *Hydrology and earth system sciences discussions, 4*, 439-473. doi: 10.5194/hess-11-1633-2007

Post, J.L., & Noble, P.N. (1993). The near-infrared combination band frequencies of dioctahedral smectites, micas, and illites. *Clays and Clay Minerals, 41*, 639-644. doi: 10.1346/ccmn.1993.0410601

Pour, A.B., & Hashim, M. (2012). The application of ASTER remote sensing data to porphyry copper and epithermal gold deposits. *Ore Geology Reviews, 44*, 1-9. doi: 10.1016/j.oregeorev.2011.09.009

Price, J.R., Velbel, M.A., & Patino, L.C. (2005). Allanite and epidote weathering at the Coweeta Hydrologic Laboratory, western North Caroline, U.S.A. *American Mineralogist, 90*, 101-114. doi: 10.2138/am.2005.1444

Quigley, M.A., Ridley, J.R., & Huntington, J.F. (2005). Airborne hyperspectral mineral mapping in regolith and variably weathered high-grade metamorphic sequences of the mineralized West Pinnacles area, Broken Hill, Australia. In H.N. Rhoden, R.C. Steininger, & P.G. Vikre (Eds.), *Geological Society of Nevada Symposium 2005: Window to the World* (pp. 981-998). Reno, Nevada

Reid, A., & Jagodzinski, E. (2012). PACE Geochronology: Results of collaborative geochronology projects 2011-12. Adelaide, South Australia: Department of Manufacturing, Innovation, Trade, Resources and Energy. Geological Survey of South Australia. Document Number: Report Book 2012/00012

Robertson, I.D.M., & Eggleton, R.A. (1991). Weathering of granitic muscovite to kaolinite and halloysite and of plagioclase-derived kaolinite to halloysite. *Clays and Clay Minerals, 39*, 113-126. doi: 10.1346/ccmn.1991.0390201

Rouse, J.W., Haas, R.H., Schell, J.A., & Deering, D.W. (1974). Monitoring vegetation systems in the Great Plains with ERTS. *NASA special publication, 351*, 309-313

Rowan, L.C., Hook, S.J., Abrams, M.J., & Mars, J.C. (2003). Mapping hydrothermally altered rocks at Cuprite, Nevada, using the Advanced Spaceborne Thermal Emission and Reflection Radiometer (ASTER), a new satellite-imaging system. *Economic Geology and the Bulletin of the Society of Economic Geologists, 98*, 1019-1027. doi: 10.2113/98.5.1019

Sabins, F.F. (1999). Remote sensing for mineral exploration. *Ore Geology Reviews, 14*, 157-183. doi: 10.1016/s0169-1368(99)00007-4

Salama, W., González-Álvarez, I., & Anand, R.R. (2016). Significance of weathering and regolith/landscape evolution for mineral exploration in the NE Albany-Fraser Orogen, Western Australia. *Ore Geology Reviews, 73, Part 3*, 500-521. doi: 10.1016/j.oregeorev.2015.07.024

Schodde, R.C. (2017). The National State of Exploration. In, *Copper to the World Conference*. Adelaide, Australia: MinEx Consulting

Sillitoe, R.H. (1995). Exploration of porphyry copper lithocaps. In J.L. Mauk, & J.D. St. George (Eds.), *PACRIM Congress* (pp. 527-532): Australasian Institute of Mining and Metallurgy

Sillitoe, R.H. (2010). Porphyry Copper Systems. *Economic Geology, 105*, 3-41. doi: 10.2113/gsecongeo.105.1.3

Smith, R.E. (1996). Regolith research in support of mineral exploration in Australia. *Journal of Geochemical Exploration, 57*, 159-173. doi: 10.1016/s0375-6742(96)00032-5

Swayze, G.A., Clark, R.N., Goetz, A.F.H., Livo, K.E., Breit, G.N., Kruse, F.A., Sutley, S.J., Snee, L.W., Lowers, H.A., Post, J.L., Stoffregen, R.E., & Ashley, R.P. (2014). Mapping Advanced Argillic Alteration at Cuprite, Nevada, Using Imaging Spectroscopy. *Economic Geology, 109*, 1179-1221. doi: 10.2113/econgeo.109.5.1179

Wade, C.E., McAvaney, S.O., & Gordon, G.A. (2014). Epithermal-style mineral textures, brecciation, veining & alteration, southern Gawler Ranges, SA. *MESA Journal, 74*, 31-43

Werner, M., Krapf, C., Curtis, S., Pawley, M., & Fabris, A. (2018). Boots on the ground: release of Peltabinna maps and explanatory notes, southwestern Gawler Ranges margin. *MESA Journal, 86*, 14-29

White, N., & Hedenquist, J. (1995). Epithermal gold deposits. Styles, characteristics and exploration. *Society of Economic Geologists, Newsletter, 23*, 1, 9-13

Witt, W.K., Hagemann, S.G., Ojala, J., Laukamp, C., Vennemann, T., Villanes, C., & Nykanen, V. (2014). Multiple methods for regional-to mine-scale targeting, Pataz gold field, northern Peru. *Australian Journal of Earth Sciences, 61*, 43-58. doi: 10.1080/08120099.2013.763859

Yamaguchi, Y., Kahle, A.B., Tsu, H., Kawakami, T., & Pniel, M. (1998). Overview of Advanced Spaceborne Thermal Emission and Reflection Radiometer (ASTER). *IEEE Transactions on Geoscience and Remote Sensing, 36*, 1062-1071. doi: 10.1109/36.700991

Chapter 4

SOIL GEOCHEMISTRY & INTERPRETATION

4.1 Introduction

Recent research efforts have focused on understanding how regolith can be used as a valuable exploration tool (e.g. Butt *et al.* 2000; Anand *et al.* 2001; Forbes *et al.* 2015; Baudet *et al.* 2018; Wolff *et al.* 2018). Regional geochemical soil sampling is a commonly used exploration method, although it is expensive and time consuming to collect and analyse thousands of samples required for moderate or high-resolution coverage depending on target scale. Soil geochemical samples are typically collected from a particular depth or horizon (e.g. Mann *et al.* 1998). Surface soils can also be considered as a sample medium as they can contain valuable information, even if it is predominantly transported material (de Caritat *et al.* 2016).

Selection of relevant geochemical pathfinders for particular mineralisation styles is commonly used to identify vectors towards mineralisation which usually includes assessment at depth to examine variation of geochemistry (e.g. Scott and Howard 2001; Anand and Butt 2010; Salama *et al.* 2016; Anand *et al.* 2019). Two commonly collected data sets from exploration drilling are geochemistry and mineralogy. At depth, this data can provide valuable assessment of alteration and potential mineralisation processes at depth (e.g. Haest *et al.* 2012; Duuring *et al.* 2016). This is regularly integrated with surface geochemistry to interpret mineralisation at depth and to focus future mineral exploration drilling. The influence of weathering and how it affects the geochemistry and mineralogy of surficial materials in a landscape is vital when conducting mineral exploration (e.g. González-Álvarez *et al.* 2019). These interpretations can impact target selection and future drill planning by recognising that there may be a limited surface expression of buried mineralisation, which can be the case in Australia.

The aim of this chapter is to examine major and trace element geochemistry and define a suite of pathfinder elements relevant to local and regional mineralisation in the southern Gawler Ranges RDT which contains some alteration. The mineralogical deportment of pathfinder elements is assessed using geochemistry and X-ray diffraction (XRD) data. A discussion on the effects of weathering on abundance of pathfinder elements in the landscape is then given. This work is presented as a thesis chapter rather than a submitted or published manuscript and therefore a description of background geology of the study area is provided in Chapter 1.

4.2 Methodology

4.2.1 Geochemical Data Collection, Preparation and Analysis

Fifty-seven soil and rock exposure samples were collected during field work conducted in July and November 2017 across the study area (Figure 4.1). These were analysed by Intertek Genalysis for Four Acid Digest (4A/MS48R), 10g Aqua Regia digest for Au (AR10/aMS) and Peroxide Fusion (FP1/OM)

to obtain Si elemental data following standard sample preparation methods. Both aqua regia and four acid digest were finished with Inductively Coupled Plasma - Mass Spectrometry (ICP-MS) while peroxide fusion was finished with Inductively Coupled Plasma – Optical Emission Spectrometry (ICP-OES).

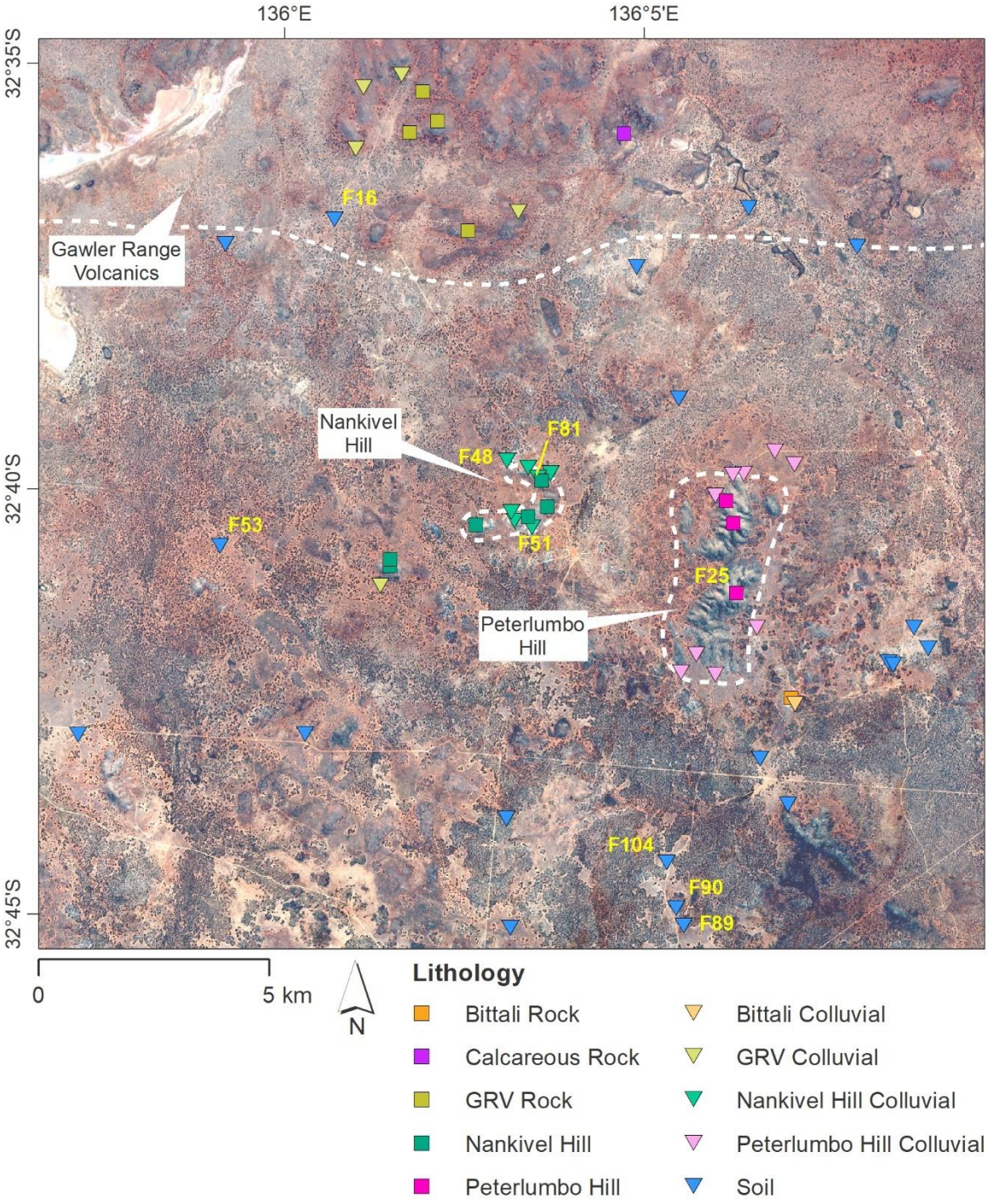

Figure 4.1: Locations of geochemical samples, their lithology and distribution in relation to landscape features, labelled samples are mentioned in text. Background image: Sentinel 2A satellite true colour image

4.2.1.1 Lithogeochemistry

Lithologies were initially identified using the 1:100,000 geological map of the study area (Blissett *et al.* 2017). Major elements were assessed using part of the workflow derived by Tiddy *et al.* (2019) to identify samples of similar lithology that could then be geochemically compared. Spearman's Rank Correlations were used to assess the relationships between major elements using their ranked variables to avoid inaccurate correlations produced from significantly elevated raw data (Spearman 1904). Another component of the major element chemistry analysis used Al_2O_3 - CaO + Na_2O - K_2O (A-CN-K) and Al_2O_3 - CaO + Na_2O + K_2O - Fe_2O_3 + MgO (A-CNK-FM) ternary diagrams (Nesbitt and Young 1984, 1989) to broadly examine the weathering trends of the samples. More specifically, the A-CN-K diagram illustrates the separability between rock and soil samples as well as the differences between rock and soil from differing origins. A SiO_2 vs Al_2O_3 scatterplot was used to assist with identification of the chemical composition of sample materials.

4.2.1.2 Trace Elements

Background concentrations of trace element geochemistry were assessed to identify elevated concentrations using the ioGAS 7.1 software (IMDEX 2019). Data below detection limit was replaced throughout the dataset with a value of half of the detection limit for the respective element. Thresholds of elevated geochemistry were quantified relative to element abundance in average Upper Continental Crust (UCC) (Rudnick and Gao 2003). Pathfinder elements were selected based on prior knowledge of the mineralisation systems expected in the region (Roache 1996; Halley *et al.* 2015; Nicolson *et al.* 2017).

4.2.2 X-Ray Diffraction

X-ray diffraction (XRD) was conducted on the 57 samples used for geochemical analysis using a Bruker D8 Advance with a Cu X-ray tube and a 1.5406 Å wavelength of radiation. Qualitative analysis was identified using Bruker Diffrac.EVA V4.2.1 software while semi-quantitative analysis was achieved using the RockJock11 macro in Microsoft Excel 2007 (Eberl 2003). Refer to Chapter 3 for further detail on the XRD data collection methodology.

4.3 Results

Representative geochemical data is presented in Table 4.1 and 4.2. All data is given in Appendix C. Silver, Au, Re, Se and Te were excluded from analysis due to the significant proportion of data below detection limit.

Table 4.1: Representative whole-rock geochemical results for Rock lithologies. (Coordinates in GDA94 MGA Zone 53S) (Raw data in Appendix C)

Sample	**F98**	**F03**	**F97**	**F76B**	**F27**	**F41**	**F23**	**F25**
Sample Type	Rock	Rock	Rock	Rock	Rock	Rock	Rock	Rock
Easting	601249	596880	597197	604878	599577	596167	603472	603699
Northing	6392991	6393898	6393264	6380727	6384873	6383739	6385004	6382997
Lithology	Calcareous Rock	GRV Rock	GRV Rock	Bittali Rock	Nankivel Hill	Nankivel Hill	Peterlumbo Hill	Peterlumbo Hill
Major elements (wt%)								
SiO_2	44.93	67.17	66.53	60.11	65.46	78.09	93.06	83.86
TiO_2	0.44	0.64	0.66	0.55	0.16	0.09	0.17	0.14
Al_2O_3	14.84	12.52	13.37	15.78	14.28	14.24	5.76	9.86
Fe_2O_3	2.92	4.99	4.52	3.63	1.49	0.89	1.06	0.94
MnO	0.01	0.11	0.07	0.09	0.00	0.01	0.01	0.01
MgO	2.57	0.76	0.29	0.71	0.02	0.20	0.09	0.06
CaO	11.97	1.47	1.17	1.90	0.06	0.07	0.03	0.02
Na_2O	0.10	2.79	2.48	3.43	0.67	0.07	0.03	0.20
K_2O	0.34	5.07	5.10	6.09	1.77	4.24	1.71	2.85
P_2O_5	0.02	0.15	0.15	0.16	0.20	0.06	0.01	0.02
Trace and Rare Earth Elements (ppm)								
Li	16.9	21.3	8	16.4	3.3	16.3	3.9	14.1
Be	0.46	3.39	3.39	1.75	0.73	5.08	0.5	3.58
Ga	20.95	19.95	21.4	18.99	14.87	20.74	6.94	12.85
Ge	0.8	1.1	1.3	1.1	0.7	1.3	0.8	1.6
S	600	250	250	250	36800	250	250	250
As	4.5	1.7	1.2	2.4	3.4	6.8	1.2	1.2
Cr	17	14	10	10	49	14	18	8
Ni	3.6	2.9	2.7	4	1.4	1.2	2.5	2.1
Co	1.9	4.2	3.2	4.3	0.5	0.7	0.8	0.5
Sc	7.3	11.2	11.5	7.6	4	3.4	1.6	1.4
V	19	17	18	24	36	7	17	10
Mo	0.7	1	1.2	0.8	3.2	0.2	0.1	0.1
W	1.1	1.7	1.1	0.7	2.2	1.6	1.7	9
Cu	7.9	10.8	7	6.3	8.1	3	1.9	2.2
Zn	7	101	74	68	4	7	7	13
Cd	0.04	0.13	0.07	0.09	0.03	0.01	0.01	0.01
Y	14.36	56.09	58.8	23.16	5.26	6.45	5.51	8.09
Rb	15.74	208.84	224.25	124.86	6.48	260.77	71.41	403.85
Sr	303.59	136.64	126.54	215.67	639.62	129.75	18.66	21.36
Cs	1.02	2.49	4.69	2.09	0.32	4.22	1.63	45.33
Ba	543.3	1387.3	2284.8	1898.1	481.5	127	112	66.9
Th	21.93	28.6	27.87	16.56	13.53	6.92	13.07	28.89
U	2.9	6.12	5.65	2.68	3.01	3.31	2.04	3.35
In	0.04	0.09	0.08	0.05	0.005	0.17	0.02	0.02
Sb	0.24	0.21	0.42	0.08	1.13	0.2	0.09	0.025
Sn	3.5	3.7	3.9	2.2	3.5	11.7	1.1	12.3
Tl	0.14	1	1.05	0.74	0.08	1.89	0.54	1.89
Pb	6.5	29.2	17.6	28.5	38.9	14.1	9	10.4
Bi	0.11	0.13	0.15	0.11	0.11	2.03	0.08	0.1

Sample	F98	F03	F97	F76B	F27	F41	F23	F25
Zr	252.5	351	354.5	231.8	165.7	50.8	107.4	111.2
Hf	7.23	10.01	9.82	6.45	5.2	1.91	3.28	3.5
Nb	13.22	21.04	21.5	12.87	6.32	11.88	3.47	12.11
Ta	0.88	1.38	1.4	0.68	0.63	2.28	0.28	4.07
La	7.75	77.69	75.87	77.56	66.93	14.96	32.52	32.39
Ce	15.17	156.33	151.23	147.58	109.11	23.8	65.47	71.08
Pr	1.47	17.63	17.44	16.16	9.38	3.03	7.41	8.29
Nd	4.98	65.41	65.67	58.89	25.66	9.82	26.44	31.52
Sm	1.22	12.29	12.07	8.77	2.59	1.64	4.63	6.11
Eu	0.3	2.38	2.41	2.48	0.4	0.16	0.5	0.34
Gd	1.5	10.92	10.95	6.62	1.35	1.06	3.21	4.3
Tb	0.32	1.68	1.64	0.8	0.16	0.18	0.36	0.48
Dy	2.47	10.44	10.53	4.67	0.99	1.15	1.57	2.15
Ho	0.57	2.18	2.17	0.9	0.22	0.21	0.24	0.33
Er	1.85	6.24	6.33	2.52	0.71	0.57	0.57	0.7
Tm	0.29	0.88	0.87	0.33	0.12	0.08	0.06	0.08
Yb	2.13	5.97	5.86	2.25	0.92	0.48	0.38	0.48
Lu	0.31	0.84	0.86	0.32	0.14	0.06	0.05	0.07

Table 4.2: Representative whole-rock geochemical results for Soil lithologies, continued over page. (Raw data in Appendix C)

Sample	F17	F42	F47	F80	F31	F62	F38	F99
Sample Type	Soil	Soil	Soil	Soil	Soil	Soil	Soil	Soil
Easting	595415	595951	599649	599161	604129	604522	603612	598687
Northing	6392640	6383149	6385600	6385710	6382245	6386077	6385559	6378092
Lithology	GRV Colluvial	GRV Colluvial	Nankivel Hill Colluvial	Nankivel Hill Colluvial	Peterlumbo Hill Colluvial	Peterlumbo Hill Colluvial	Soil	Soil
Major Elements (wt%)								
SiO_2	81.51	82.58	82.58	79.80	86.00	79.37	91.13	69.53
TiO_2	0.34	0.25	0.35	0.33	0.27	0.33	0.24	0.49
Al_2O_3	7.04	6.16	7.23	9.74	4.42	7.10	4.08	8.42
Fe_2O_3	3.56	2.13	2.43	3.06	2.60	2.63	1.73	4.68
MnO	0.02	0.02	0.02	0.03	0.01	0.02	0.02	0.04
MgO	0.27	0.33	0.38	0.39	0.11	0.77	0.17	0.87
CaO	0.18	0.24	0.49	0.15	0.06	2.27	0.22	2.64
Na_2O	0.44	0.17	0.17	0.16	0.05	0.46	0.08	0.61
K_2O	2.85	1.70	1.83	2.25	0.43	1.77	0.65	2.62
P_2O_5	0.03	0.03	0.03	0.04	0.03	0.03	0.03	0.06
Trace and Rare Earth Elements (ppm)								
Li	13.8	16.5	15.5	17.2	11.3	18.7	11.1	16.2
Be	1.1	1.24	1.11	1.51	0.65	1.1	0.6	1.69
Ga	9.18	7.4	8.78	12.76	6.6	8.58	5.24	9.77
Ge	0.9	0.9	1	1.2	0.9	0.8	0.8	0.9
S	250	250	250	250	250	250	250	500
As	2.9	2	2.9	8.1	4.6	2.2	1.9	6.8
Cr	45	24	36	41	45	39	34	35
Ni	7.6	7.9	8.5	8.9	7.6	11.9	6.9	9.3
Co	2.8	3.5	3.2	3.5	3	4.8	2.5	5.2

Sample	F17	F42	F47	F80	F31	F62	F38	F99
Sc	5.4	4.3	5.1	6.6	4.4	6	3.7	6.6
V	49	30	38	40	46	35	25	54
Mo	0.7	0.4	0.5	0.8	0.7	0.4	0.4	0.7
W	0.8	0.5	0.9	0.9	0.9	0.7	0.8	2.2
Cu	9.5	8.9	9.6	11.7	8.1	14.6	8.2	9
Zn	27	22	24	26	12	32	16	41
Cd	0.04	0.01	0.03	0.03	0.01	0.04	0.01	0.05
Y	25.53	11.71	12.11	13.6	6.58	16.75	7.29	12.11
Rb	119.49	74.99	80.63	97.89	24.42	73.11	31.34	93.52
Sr	53.73	40.04	47.8	40.1	23.63	92.09	25.42	141.34
Cs	2.37	1.73	2.14	2.43	1.41	2.13	1.27	4.29
Ba	817.3	374.3	436	414.9	96.2	374.2	150.1	1508.8
Th	15.24	8.6	8.54	11.83	7.69	9.57	7	8.02
U	2.24	1.38	1.15	1.59	0.96	1.21	0.78	1.18
In	0.03	0.02	0.03	0.03	0.02	0.03	0.02	0.08
Sb	0.33	0.2	0.33	0.57	0.18	0.23	0.33	0.19
Sn	1.6	1.7	1.5	1.5	1	1.3	0.9	6.1
Tl	0.61	0.43	0.47	0.65	0.16	0.37	0.19	0.93
Pb	14.1	12.7	13.2	20.9	7.7	12.1	7	12.9
Bi	0.2	0.18	0.31	0.75	0.12	0.15	0.1	0.38
Zr	168.8	75.3	91	109.1	93.3	95.9	82	75.3
Hf	4.44	2.09	2.57	3.28	3.25	2.96	2.35	2.2
Nb	9.91	6.07	8.1	7.39	5.07	6.63	4.11	7.27
Ta	0.77	0.46	0.74	0.55	0.39	0.48	0.33	0.51
La	18.25	13.44	14.64	25.19	10.9	18.4	11.01	18.46
Ce	35.13	27.97	29.13	49.68	22.31	36.58	23.37	38.67
Pr	4.38	3.22	3.33	5.41	2.49	4.45	2.62	4.52
Nd	15.89	11.86	12.35	19.23	9.41	17.07	10.08	16.78
Sm	3.43	2.3	2.43	3.38	1.86	3.33	2	3.22
Eu	0.86	0.49	0.49	0.66	0.35	0.73	0.36	0.99
Gd	3.53	2.22	2.1	2.99	1.44	3.83	1.74	2.67
Tb	0.63	0.33	0.32	0.43	0.23	0.47	0.25	0.37
Dy	4.36	2.1	2.17	2.55	1.32	2.96	1.46	2.22
Ho	0.94	0.44	0.45	0.53	0.25	0.63	0.28	0.45
Er	2.89	1.34	1.3	1.52	0.75	1.84	0.81	1.35
Tm	0.41	0.19	0.21	0.21	0.1	0.26	0.12	0.17
Yb	2.93	1.36	1.37	1.52	0.77	1.73	0.81	1.14
Lu	0.41	0.19	0.2	0.22	0.1	0.25	0.12	0.17

4.3.1 Major Elements

Representative data for major elements for each rock and soil lithology is shown in Table 4.3. This data demonstrates variation in major element chemistry across the landscape. GRV Rock samples from the two geological units are presented on a Total Alkali Silica (SiO_2 vs $Na_2O + K_2O$) diagram (Le Maitre *et al.* 2002) (Figure 4.2) to demonstrate the chemistry of the different GRV units compared to prior published geochemistry for these units. The Spearman's Rank Correlations for all major elements are shown in Table 4.4 and 4.5 for Rock and Soil samples respectively and scatterplots of major elements with the greatest absolute Spearman's Rank Correlations ≤ -0.8 and ≥ 0.8, shown in Figure 4.3 and 4.4 respectively.

Table 4.3: Summary statistics on major element chemistry of each lithological unit

Lithology and Statistic, N = 59	SiO_2 (%)	TiO_2 (%)	Al_2O_3 (%)	Fe_2O_3 (%)	MnO (%)	MgO (%)	CaO (%)	Na_2O (%)	K_2O (%)	P_2O_5 (%)
GRV Rock: Minimum (*n* = 4)	66.53	0.39	12.44	4.02	0.07	0.18	0.99	2.33	4.84	0.05
GRV Rock: Maximum	71.03	0.66	13.37	4.99	0.11	0.76	1.47	2.85	6.22	0.15
GRV Rock: Mean	68.24	0.58	12.83	4.63	0.09	0.45	1.24	2.61	5.30	0.12
GRV Rock: Median	67.71	0.63	12.75	4.75	0.09	0.43	1.25	2.63	5.08	0.14
GRV Rock: Standard Deviation	1.98	0.13	0.43	0.46	0.02	0.26	0.20	0.25	0.62	0.05
Nankivel Hill: Minimum (*n* = 6)	65.46	0.06	6.97	0.73	0.00	0.02	0.05	0.07	0.63	0.02
Nankivel Hill: Maximum	83.22	0.34	14.28	2.44	0.02	0.69	0.93	0.67	4.24	0.20
Nankivel Hill: Mean	77.32	0.16	11.75	1.68	0.01	0.26	0.20	0.17	2.42	0.10
Nankivel Hill: Median	78.51	0.12	12.12	1.96	0.01	0.20	0.07	0.08	2.00	0.06
Nankivel Hill: Standard Deviation	5.95	0.10	2.51	0.66	0.00	0.26	0.32	0.22	1.54	0.08
Peterlumbo Hill: Minimum (*n* = 3)	83.86	0.09	1.78	0.66	0.00	0.03	0.02	0.02	0.63	0.01
Peterlumbo Hill: Maximum	94.34	0.17	9.86	1.06	0.01	0.09	0.07	0.20	2.85	0.02
Peterlumbo Hill: Mean	90.42	0.13	5.80	0.89	0.01	0.06	0.04	0.08	1.73	0.02
Peterlumbo Hill: Median	93.06	0.14	5.76	0.94	0.01	0.06	0.03	0.03	1.71	0.01
Peterlumbo Hill: Standard Deviation	5.72	0.04	4.04	0.21	0.00	0.03	0.03	0.10	1.11	0.00
GRV Colluvial: Minimum (*n* = 5)	71.67	0.25	6.16	2.13	0.02	0.27	0.17	0.17	1.70	0.03
GRV Colluvial: Maximum	82.58	0.58	10.94	4.43	0.05	0.48	0.37	0.59	3.48	0.05
GRV Colluvial: Mean	77.10	0.39	8.43	3.50	0.03	0.33	0.23	0.46	2.84	0.04
GRV Colluvial: Median	75.30	0.34	7.55	3.56	0.03	0.28	0.18	0.53	2.85	0.03
GRV Colluvial: Standard Deviation	4.72	0.14	2.14	0.85	0.01	0.09	0.09	0.17	0.71	0.01
Nankivel Hill Colluvial: Minimum (*n* = 7)	70.60	0.25	6.32	2.19	0.02	0.38	0.12	0.07	1.66	0.03
Nankivel Hill Colluvial: Maximum	82.58	0.35	13.03	3.06	0.03	0.93	5.05	0.28	3.47	0.06
Nankivel Hill Colluvial: Mean	76.22	0.31	9.54	2.71	0.02	0.60	1.57	0.18	2.35	0.04
Nankivel Hill Colluvial: Median	75.30	0.33	9.74	2.82	0.02	0.53	0.49	0.17	2.25	0.04
Nankivel Hill Colluvial: Standard Deviation	4.11	0.05	2.23	0.36	0.00	0.21	1.84	0.07	0.59	0.01

Lithology and Statistic, N = 59	SiO_2 (%)	TiO_2 (%)	Al_2O_3 (%)	Fe_2O_3 (%)	MnO (%)	MgO (%)	CaO (%)	Na_2O (%)	K_2O (%)	P_2O_5 (%)
Peterlumbo Hill Colluvial: Minimum (*n* = 9)	75.09	0.24	4.08	1.60	0.01	0.11	0.06	0.05	0.43	0.02
Peterlumbo Hill Colluvial: Maximum	91.13	0.34	7.16	2.63	0.02	0.77	2.27	0.46	1.80	0.16
Peterlumbo Hill Colluvial: Mean	83.46	0.28	5.70	2.17	0.02	0.33	0.49	0.14	1.13	0.04
Peterlumbo Hill Colluvial: Median	84.72	0.27	5.93	2.09	0.02	0.23	0.22	0.10	1.19	0.03
Peterlumbo Hill Colluvial: Standard Deviation	4.59	0.04	1.11	0.39	0.00	0.23	0.72	0.12	0.51	0.04
Soil: Minimum (*n* = 21)	54.77	0.19	4.61	1.80	0.01	0.15	0.07	0.09	0.81	0.02
Soil: Maximum	89.42	0.50	12.62	23.16	0.07	1.25	8.06	1.42	2.62	0.06
Soil: Mean	73.76	0.34	7.45	3.98	0.03	0.64	2.67	0.26	1.60	0.04
Soil: Median	71.24	0.34	7.53	2.90	0.03	0.64	2.64	0.16	1.62	0.04
Soil: Standard Deviation	8.75	0.09	2.01	4.50	0.02	0.28	2.08	0.29	0.44	0.01
Bittali Rock (*n* = 1)	60.11	0.55	15.78	3.63	0.09	0.71	1.90	3.43	6.09	0.16
Bittali Colluvial (*n* = 1)	72.31	0.54	10.97	3.16	0.05	0.46	0.51	1.10	3.38	0.04
Calcareous Rock (*n* = 1)	44.93	0.44	14.84	2.92	0.01	2.57	11.97	0.10	0.34	0.02

GRV Rock samples plotted on a Total Alkali Silica (SiO_2 vs $Na_2O + K_2O$) diagram (Le Maitre *et al.* 2002) show that these units are not geochemically similar (Figure 4.2). The Pondanna Dacite unit preserves higher SiO_2 abundances relative to the Bittali Rock (66 – 71 vs 60 wt%), however the proportion of $Na_2O + K_2O$ is similar (7.5 – 8.5 vs 9.5 wt%) (Figure 4.2).

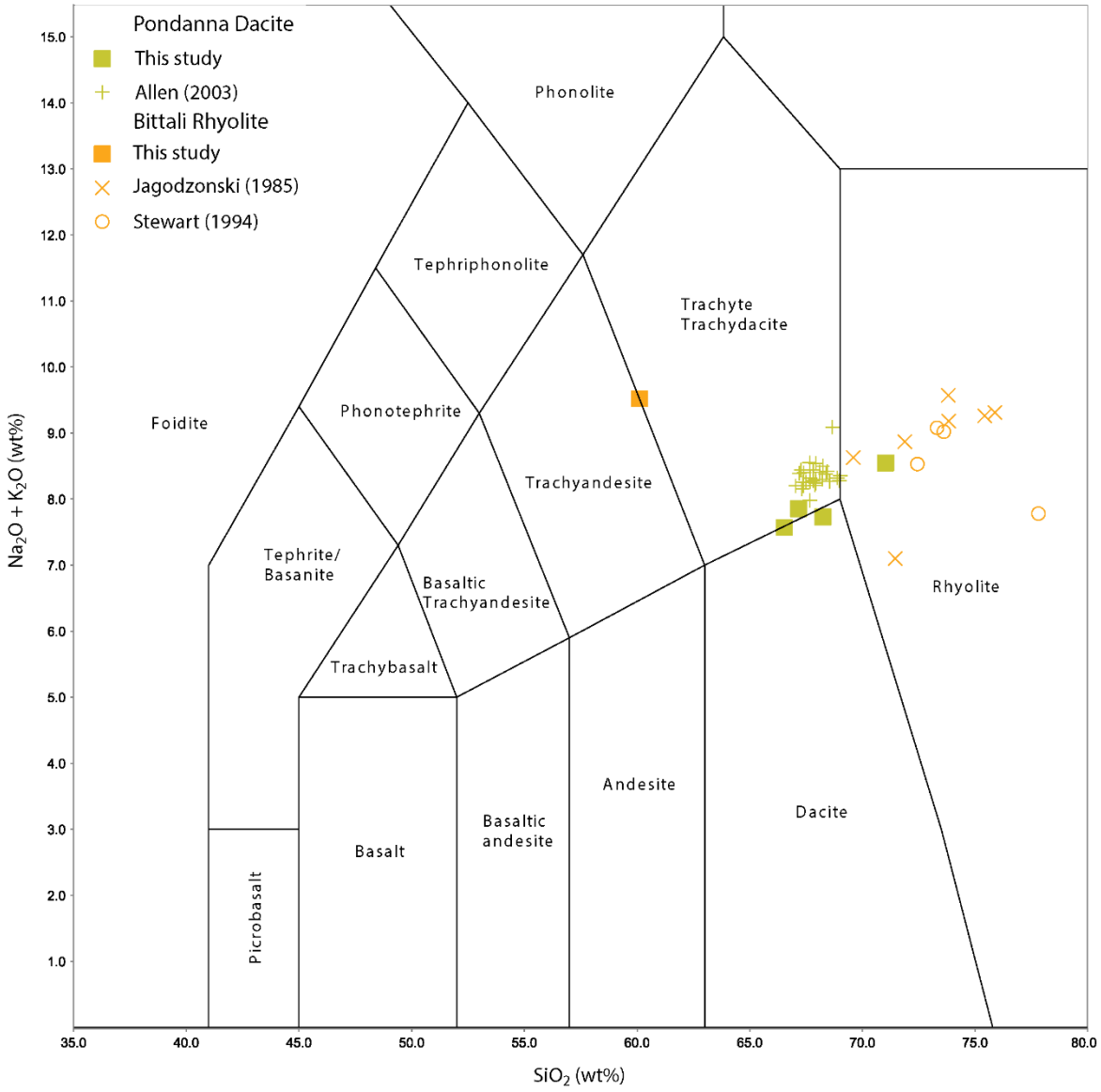

Figure 4.2: Comparison of Pondanna Dacite and Bittali Rhyolite geochemistry on a total alkalis vs silica diagram. Data sourced from this study, Allen *et al.* (2003), Stewart (1994) and Jagodzinski (1985). Base diagram from Le Maitre *et al.* (2002).

Table 4.4: Spearman's Rank Correlations of major elements for all Rock samples, significant relationships (≤ -0.8, ≥ 0.8) are in bold

Rock Samples, N = 16

	SiO_2 (%)	**TiO_2 (%)**	**Al_2O_3 (%)**	**Fe_2O_3 (%)**	**MnO (%)**	**MgO (%)**	**CaO (%)**	**K_2O (%)**	**Na_2O (%)**	**P_2O_5 (%)**
SiO_2 (%)	1	-	-	-	-	-	-	-	-	-
TiO_2 (%)	-0.66	1	-	-	-	-	-	-	-	-
Al_2O_3 (%)	**-0.92**	0.44	1	-	-	-	-	-	-	-
Fe_2O_3 (%)	-0.68	**0.83**	0.45	1	-	-	-	-	-	-
MnO (%)	-0.38	0.66	0.31	0.68	1	-	-	-	-	-
MgO (%)	-0.5	0.7	0.41	0.52	0.58	1	-	-	-	-
CaO (%)	-0.69	0.62	0.52	0.77	0.4	0.58	1	-	-	-
K_2O (%)	-0.41	0.59	0.44	0.53	**0.89**	0.39	0.29	1	-	-
Na_2O (%)	-0.69	0.66	0.53	**0.81**	0.67	0.25	0.6	0.62	1	-
P_2O_5 (%)	-0.55	0.16	0.49	0.5	0.3	-0.12	0.39	0.31	0.71	1

Table 4.5: Spearman's Rank Correlations of major elements for all Soil samples, significant relationships (≤ -0.8, ≥ 0.8) are in bold

Soil Samples, N = 43

	SiO_2 (%)	**TiO_2 (%)**	**Al_2O_3 (%)**	**Fe_2O_3 (%)**	**MnO (%)**	**MgO (%)**	**CaO (%)**	**K_2O (%)**	**Na_2O (%)**	**P_2O_5 (%)**
SiO_2 (%)	1	-	-	-	-	-	-	-	-	-
TiO_2 (%)	-0.54	1	-	-	-	-	-	-	-	-
Al_2O_3 (%)	-0.64	0.72	1	-	-	-	-	-	-	-
Fe_2O_3 (%)	-0.68	**0.84**	0.74	1	-	-	-	-	-	-
MnO (%)	-0.66	0.69	0.54	0.64	1	-	-	-	-	-
MgO (%)	-0.69	0.51	0.56	0.51	0.6	1	-	-	-	-
CaO (%)	-0.6	0.3	0.22	0.36	0.46	**0.8**	1	-	-	-
K_2O (%)	-0.35	0.41	0.66	0.42	0.47	0.26	0.004	1	-	-
Na_2O (%)	-0.3	0.38	0.29	0.31	0.61	0.27	0.21	0.68	1	-
P_2O_5 (%)	-0.66	0.54	0.69	0.63	0.42	0.61	0.48	0.39	0.15	1

Major element concentrations demonstrate strong relationships for each lithology separated by sample type. For the rock lithologies (Calcareous Rock, Bittali Rock, GRV Rock, Nankivel Hill Rock, Peterlumbo Hill Rock) there is a strong negative correlation for SiO_2 vs Al_2O_3 while there are positive correlations for Fe_2O_3 vs CaO, Na_2O, TiO_2 and MnO vs K_2O (Figure 4.3; Table 4.4). The soil lithologies (Bittali Colluvial, GRV Colluvial Nankivel Hill Colluvial, Peterlumbo Hill Colluvial and Soil) have positive correlations between MgO and CaO and TiO_2 and Fe_2O_3 (Figure 4.4A, B; Table 4.5). For the Soil lithologies, there is a negative relationship for almost all samples with five samples (F89, F16, F90, F104, F53, Figure 4.1) containing lower SiO_2 and Al_2O_3, not following the same trend as the remainder of the samples (Figure 4.4C).

Compared to the Nankivel and Peterlumbo Hill lithologies, the GRV Rock and Bittali Rock lithologies contain less Al_2O_3 (70 – 100 wt% vs. 50 – 55 wt%) but greater CaO + Na_2O (0 – 10 wt% vs. 20 – 30 wt%) while containing approximately the same proportion of K_2O (Figure 4.5A). The GRV Rock lithology shows little variation in CaO + Na_2O + K_2O (~40 wt%), FeO + MgO (~20 wt%) and Al_2O_3 (~40 wt%) (Figure 4.5B). Nankivel and Peterlumbo Hill contain significantly less CaO + Na_2O + K_2O (10 – 30 wt%), a range of FeO + MgO (10 – 25 wt%) and more Al_2O_3 than GRV Rock and Bittali Rock lithologies (Figure 4.5B). The CaO + Na_2O + K_2O axis indicates that there is some variation between Nankivel and Peterlumbo Hills due to K_2O (Figure 4.5B). Nankivel Hill generally has higher Al_2O_3 concentrations compared to Peterlumbo Hill which has a much greater SiO_2 concentration and lower Al_2O_3 (Figure 4.6). These two lithologies also follow the SiO_2 – Al_2O_3 trend excluding one sample, F27, from the Nankivel Hill lithology (Figure 4.6).

Nankivel Hill Colluvial has the greatest range of CaO + Na_2O + K_2O and Al_2O_3 with values from 20 – 50 wt% and 30 – 60 wt% respectively (Figure 4.5B). Peterlumbo Hill Colluvial samples have less Al_2O_3 and a greater proportion of FeO + MgO than their associated rock exposures (Figure 4.5B). Three Peterlumbo Hill Colluvial samples follow the same trend as the Nankivel Hill Colluvial lithology with increased concentrations of CaO + Na_2O + K_2O at 35, 25 and 20 wt% (Figure 4.5B). The most SiO_2 rich material (75 – 91 wt%) is the Peterlumbo Hill Colluvial lithology however, Nankivel Hill Colluvial contains more Al_2O_3 (6.3 – 13 wt%) but less SiO_2 compared to Peterlumbo Hill Colluvial (70.5 – 82.5 wt%) (Figure 4.6). A majority of the Nankivel and Peterlumbo Hill Colluvial samples follow the SiO_2 – Al_2O_3 trend but three samples from these lithologies plot under that trend and within the 'Altered Siliciclastic Material' area (Figure 4.6). The GRV Colluvial samples plot along 10 wt% CaO + Na_2O and have similar Al_2O_3 values to the Soil lithology (Figure 4.5A). GRV Colluvial contains more Al_2O_3 than its rock exposure counterpart and has less CaO + Na_2O + K_2O at approximately 20 – 30 wt% (Figure 4.5B).

The Soil lithology ranges in major element composition from increased CaO + Na_2O (<60 wt%) and low Al_2O_3 (30 wt%) to >70 wt% Al_2O_3 and limited CaO + Na_2O (0 – 10 wt%) (Figure 4.5A). This variation of major element composition continues in the A-CNK-FM diagram with CaO + Na_2O + K_2O ranging from 10 – 50 wt%, Al_2O_3 from 20 – 60 wt% and FeO + MgO containing 20 – 50 wt% (Figure 4.5B). The Soil lithology plots across the SiO_2 - Al_2O_3 trend but also into the 'Altered Siliciclastic Material' area where the SiO_2 content is lower (Figure 4.6). One sample (F89) is unique in this data set, containing the greatest FeO + MgO proportions at approximately 70 wt% (red circle, Figure 4.5B). The major element concentrations of the Colluvial and Soil lithologies are relatively comparable.

Figure 4.6 shows SiO_2 vs Al_2O_3 to class these lithologies into siliciclastic and non-siliciclastic material. As described by Tiddy *et al.* (2019), non-siliciclastic lithologies will plot as SiO_2 <50 wt%. Samples that plot in the area underneath the Al_2O_3 – SiO_2 linear trend and with SiO_2 >50 wt% may be indicative of a degree of alteration (e.g. carbonate or ferruginous alteration, Figure 4.4and 4.5).

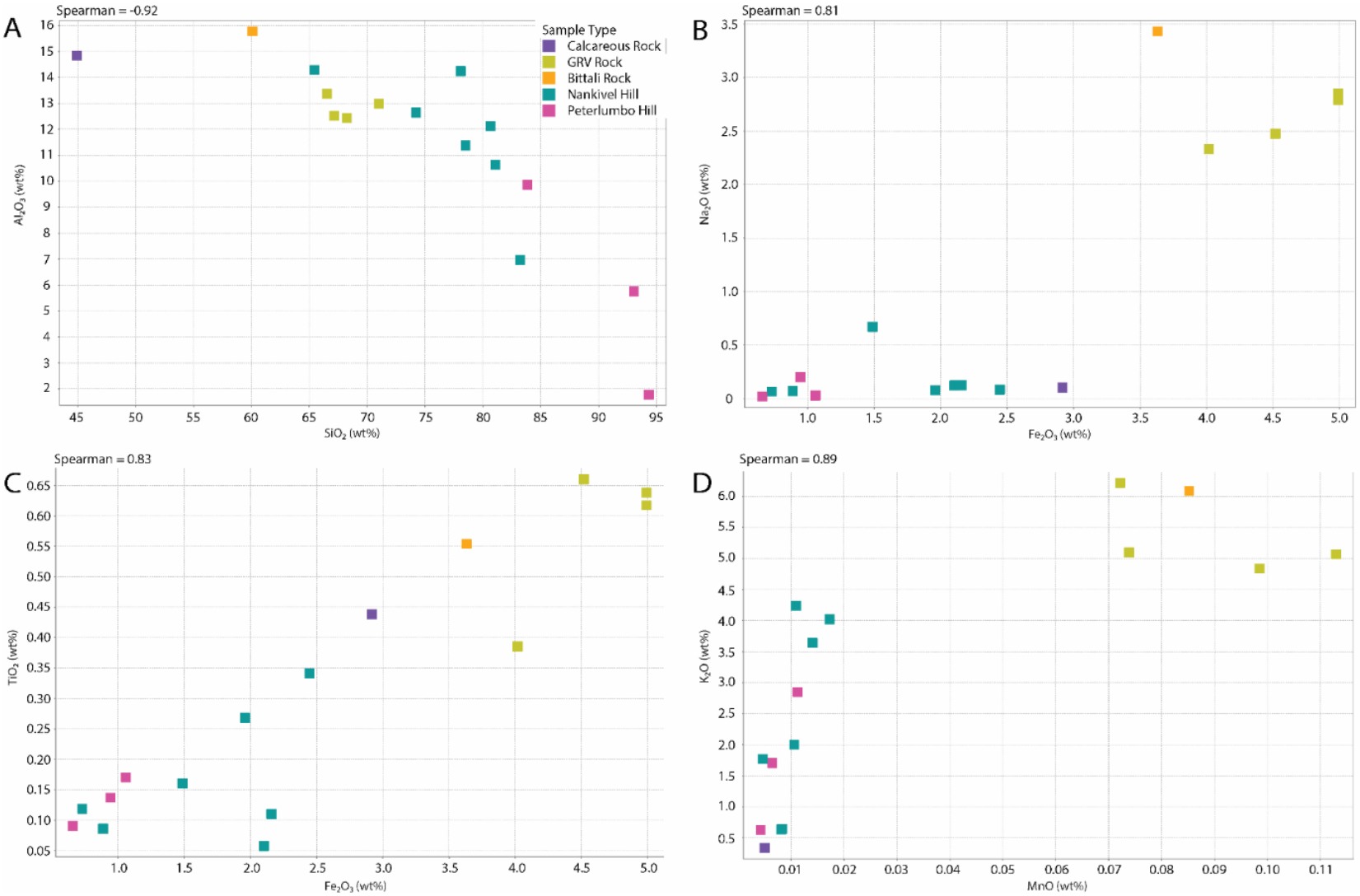

Figure 4.3: Scatterplots of major elements for Rock lithologies; A: SiO_2 vs Al_2O_3; B: Fe_2O_3 vs Na_2O; C: Fe_2O_3 vs TiO_2; D: MnO vs K_2O.

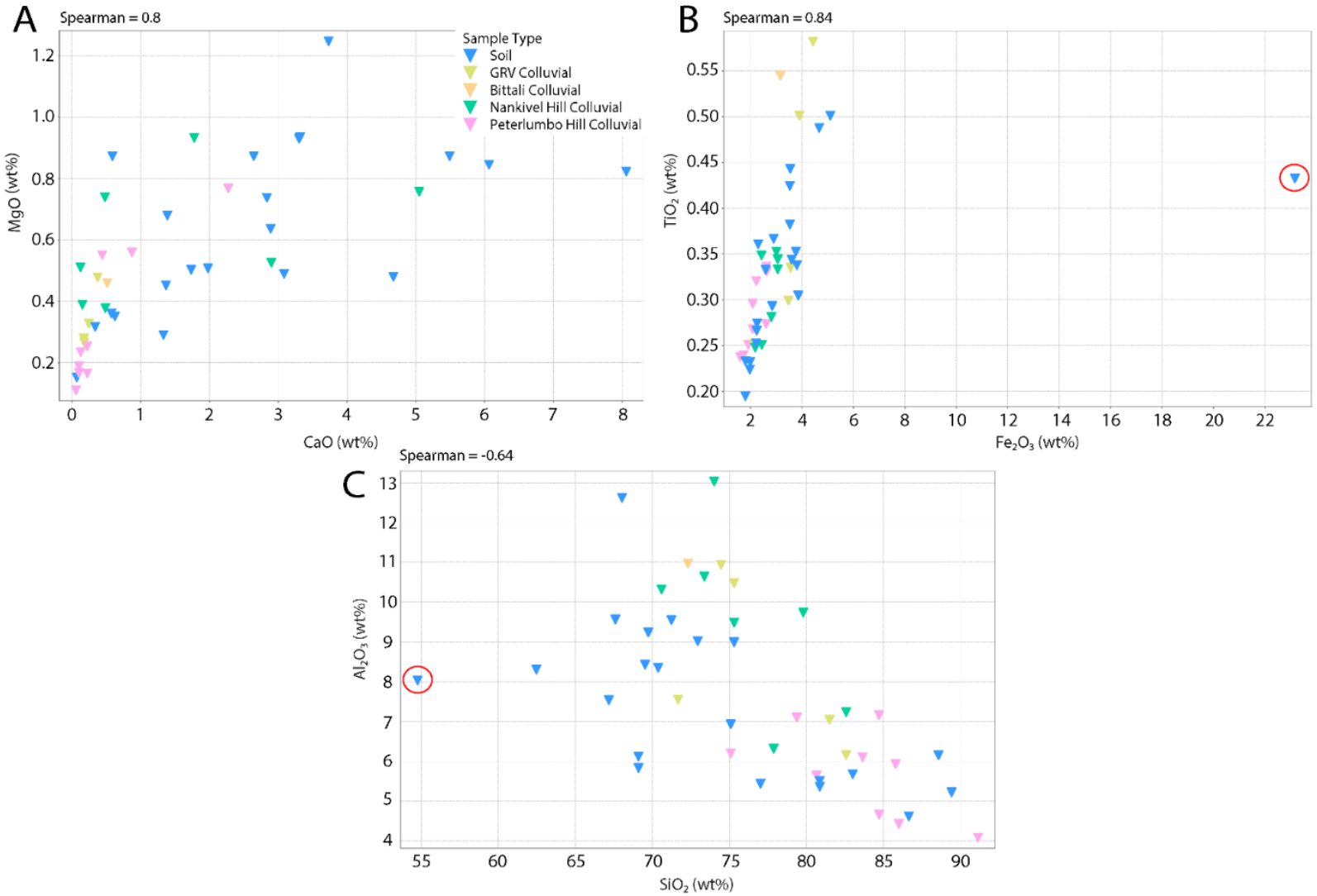

Figure 4.4: Scatterplots of major elements for Soil lithologies; A: CaO vs MgO; B: Fe_2O_3 vs TiO_2; C: SiO_2 vs Al_2O_3. The red circle in 4.4B and 4.4C indicates sample F89.

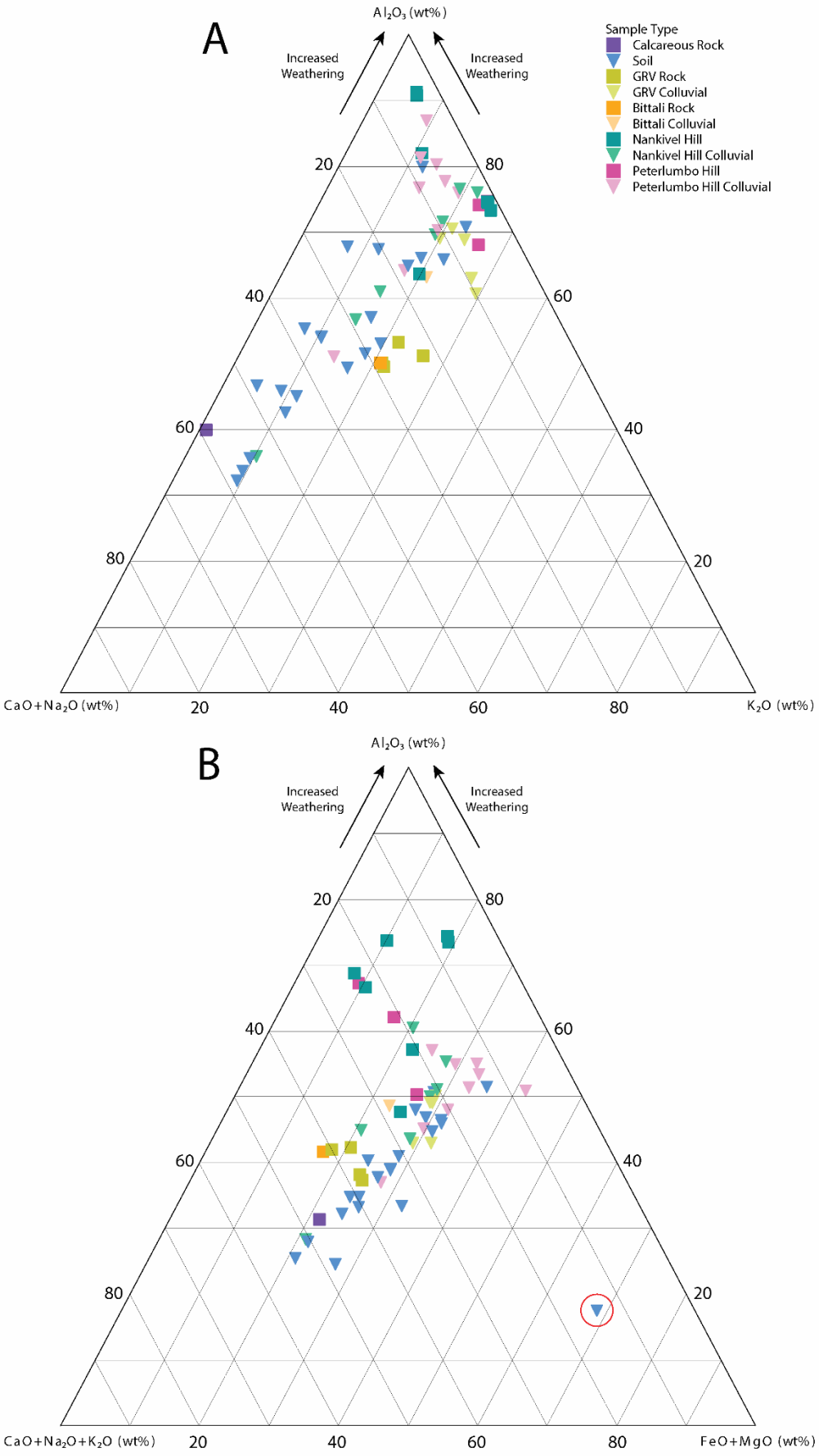

Figure 4.5: A: A-CN-K diagram, B: A-CNK-FM diagram both defined by Nesbitt and Young (1984, 1989). The red circle highlights sample F89.

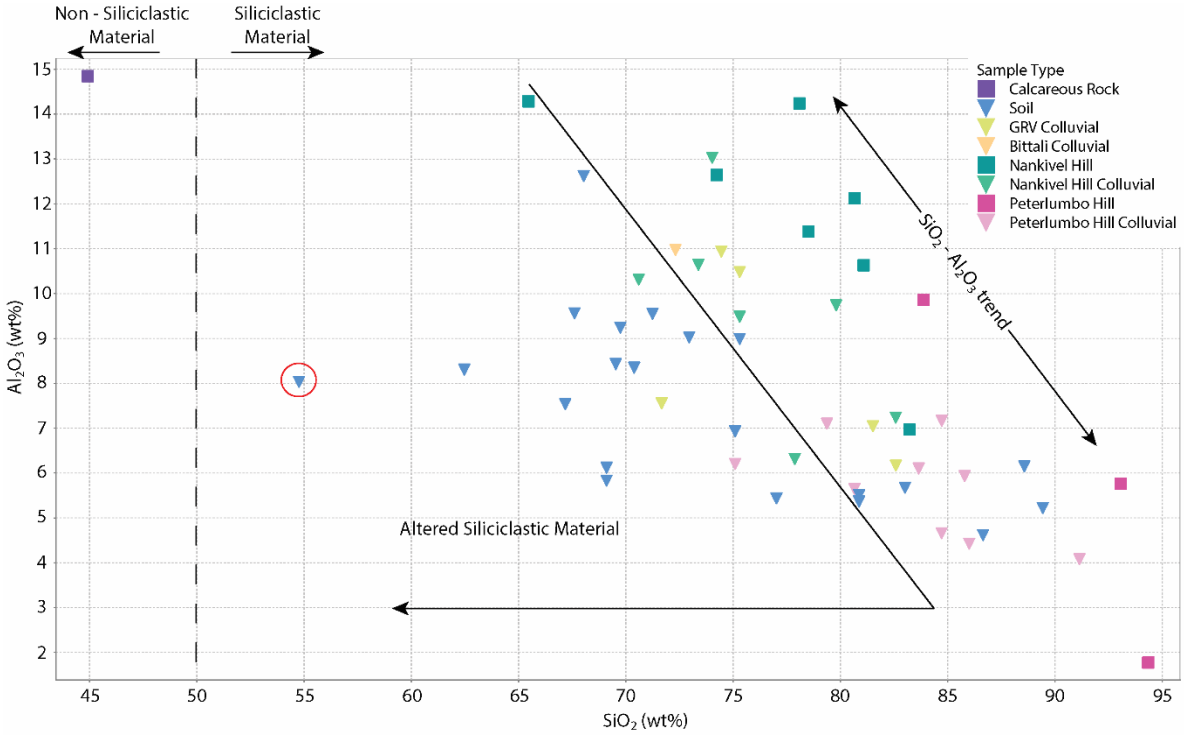

Figure 4.6: SiO_2 vs Al_2O_3 plot with annotations to indicate the approximate definitions of 'siliciclastic material' and 'altered siliciclastic material' as described by Tiddy *et al.* (2019). The red circle highlights sample F89.

4.3.2 Trace Elements

Cumulative probability plots are used for examining the distribution of trace element data, assisting definition of background geochemistry (Reimann 2005) and illustrating the distribution of concentrations for each trace element (Figure 4.7). For trace elements As, Bi, Co, Cu, Li, Mo, Sb, and Sc, the Peterlumbo Hill lithology contains some of their lowest values with the exception of sample F25 that has high concentrations of Cs, Rb, Sn, Ta, Tl and W. Peterlumbo Hill contains low concentrations for Heavy Rare Earth Elements (HREEs) (Figure 4.8). The lowest trace element concentrations for Nankivel Hill are for Cd, Co, Cr, Cs, In, Li, Ni, Pb, Rb, Sc, Sr, Ta, Tl, V and Zn. Nankivel Hill also has trace elements distributed across both the low and high values for Bi, Cr, Cs, Cu, Mo, Pb, Rb, Sc, Ta and Tl (Figure 4.7). Other trace elements display a range of intermediate values for this lithology. Antinomy and S have a slightly different distribution for Nankivel Hill where almost all samples contain the highest values for these elements. Rare Earth Elements (REEs) for this lithology are generally of intermediate concentrations with Nankivel Hill containing the lowest concentrations for some HREEs (Figure 4.8).

GRV Rock (Pondanna Dacite) contains higher concentrations of Cu, Mo, Pb, Sc, Tl and Zn but also has low As (Figure 4.7). The Bittali Rock lithology has similar concentrations of trace elements as GRV Rock but contains higher As and lower Sb, Sn and W compared to GRV Rock (Figure 4.7). GRV Rock contains the highest concentrations of all REEs with the Bittali Rock sample also containing very high concentrations of Light Rare Earth Elements (LREEs) (Figure 4.8). The trace and REE concentrations

for the Pondanna Dacite are relatively consistent (Figure 4.7), therefore this unit was used as the GRV Rock average to normalise other lithologies.

Nankivel Hill Colluvial typically has intermediate concentrations for trace elements but has higher concentrations of As, Bi and Sb (Figure 4.7). Similar to its rock exposure lithology, it has higher concentrations of LREEs but it also has greater HREE concentrations compared to the rock exposure (Figure 4.8). Peterlumbo Hill Colluvial contains low concentrations of As, Bi, Cd, In, Mo, Rb, S, Sn, Sr, Ta, Tl, U and W (Figure 4.7). However, this lithology does contain intermediate concentrations of Co, Cr, Cu, Li, Ni and Zn, which are typically higher trace element concentrations than Peterlumbo Hill (Figure 4.7). The Peterlumbo Hill Colluvial lithology has generally low to intermediate concentrations for the LREEs and predominantly low concentrations for HREEs (Figure 4.8). The GRV Colluvial lithology contains a range of concentrations for all pathfinder elements and these are predominantly intermediate concentrations (Figure 4.7). The concentrations for LREEs are variable, while concentrations for HREEs are typically higher, just below that of GRV Rock (Figure 4.8).

The Soil lithology contains the greatest variation across all trace elements, due to the number of samples available for analysis in this unit. Generally, the soil samples have intermediate concentrations with Sample F89 noticeably higher in concentration for As, Bi, Co, Cr, Mo, Sn and W (Figure 4.1). However, there are also some low values for this lithology within Bi, Mo, Sn, W (Figure 4.7). There is a wide range of REEs concentrations across Light and Heavy Rare Earths for the soils (Figure 4.8).

There is an interesting pattern present for Ni and V trace elements, with all rock samples containing the lowest concentrations and the soil lithologies containing the highest concentrations for these two elements (Figure 4.7). Similar patterns are evident for Li, Co and Cr, although there are some rock samples contain higher concentrations of these elements (Figure 4.7).

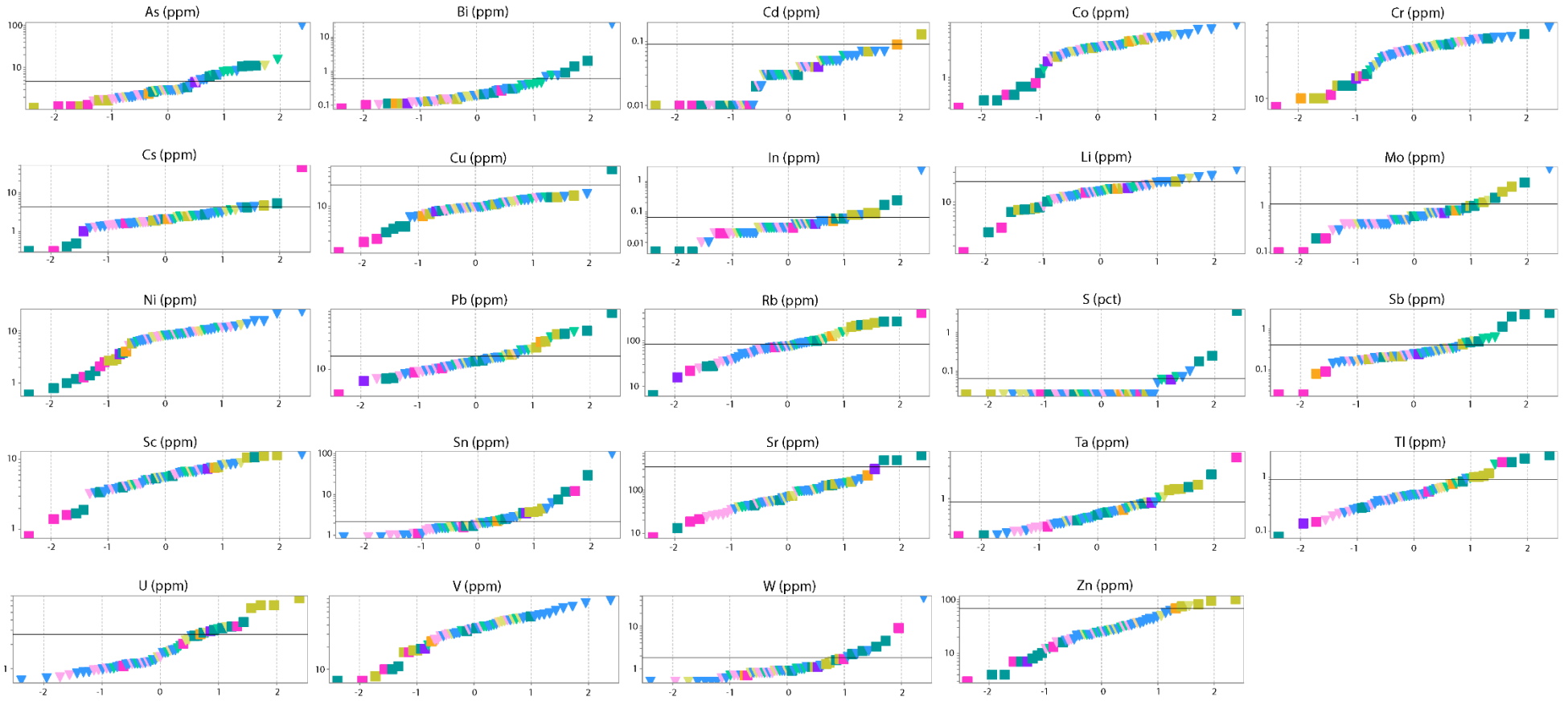

Figure 4.7: Cumulative probability plots for a selection of trace elements, black lines indicate Upper Continental Crust from Rudnick and Gao (2003). Elements with no black line indicates that all samples are below Upper Continental Crust concentrations.

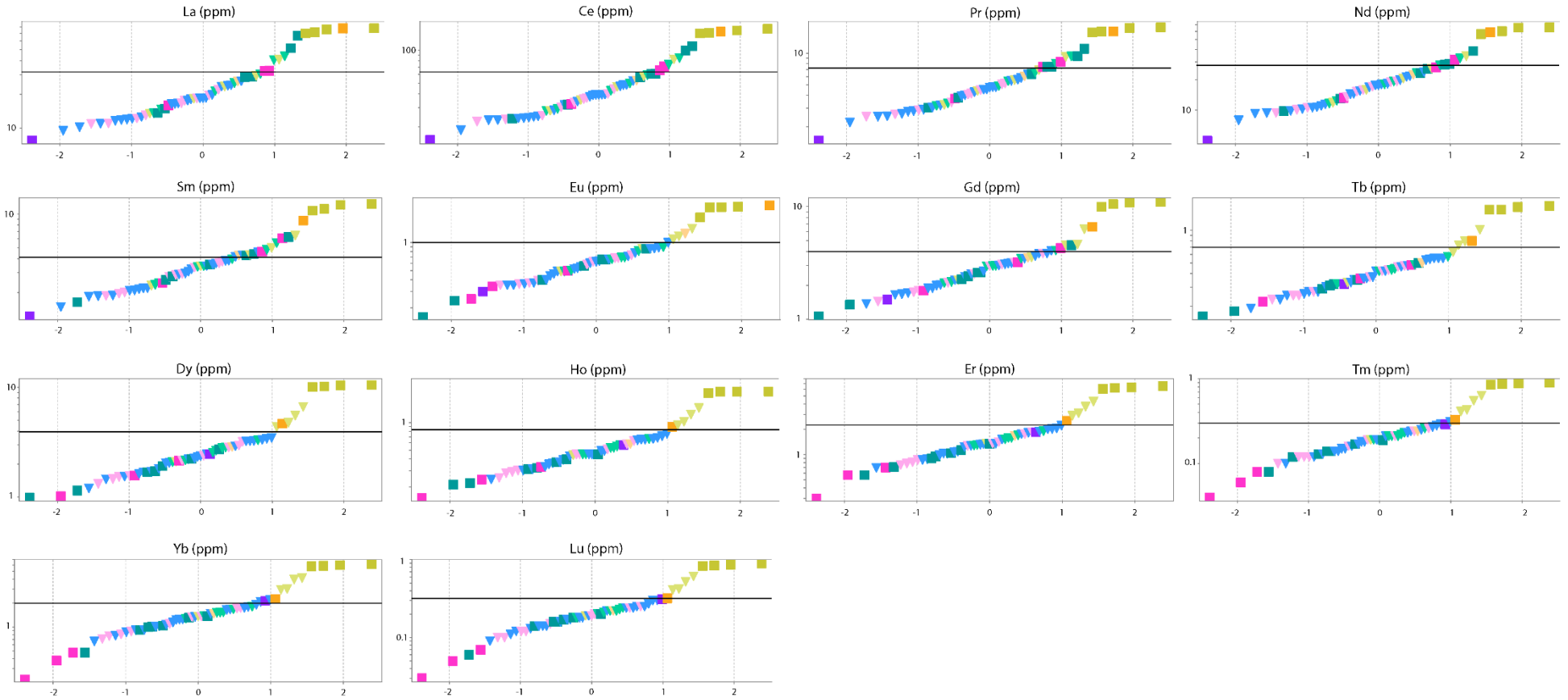

Figure 4.8: Cumulative probability plots for Rare Earth Elements, black line indicates Upper Continental Crust (Rudnick and Gao 2003).

4.3.3 Mineralogy

Average proportions of mineralogical results from semi-quantitative XRD are shown in Table 4.6. Raw semi-quantitative data is given in Appendix B. The rock lithologies indicate a differing mineralogical composition compared to the soil based lithologies. The GRV Rock and Bittali Rock lithologies contain a similar composition that includes albite, chamosite, microcline and quartz. Nankivel Hill contains several unique minerals including alunite, dickite, jarosite and pyrophyllite as well as common minerals such as calcite, microcline and muscovite. Peterlumbo Hill preserves a noticeably different mineralogically with a limited number of minerals present, hematite, microcline, phengite and quartz. The Calcareous Rock sample had a unique mineralogical result with the highest proportion of calcite and dickite as well as containing some dolomite and quartz.

The colluvial soil lithologies contain a similar mineralogical composition as their rock exposure equivalents (Table 4.6). Bittali Colluvial notably also contains actinolite, similar to its rock counterpart but also contains kaolinite, muscovite and less microcline. GRV Colluvial is again mineralogically similar to the GRV Rock lithology but with smaller proportions of feldspars (Table 4.6). Nankivel Hill Colluvial contains no alunite, dickite and significantly less pyrophyllite compared to the Nankivel Hill rock exposure but does contain kaolinite, phengite and significant illite (Table 4.6). Peterlumbo Hill Colluvial is more mineralogically diverse compared to the Peterlumbo Hill rock exposure including albite, calcite, dolomite, illite, kaolinite, muscovite and orthoclase (Table 4.6). The Soil lithology contains a range of micas, clays and feldspars (Table 4.6). Further interpretation of these results can be found in Chapter 3.

Table 4.6: Average proportions for each mineral identified in X-ray diffraction analysis delineated by lithology, continued over page. (Raw data in Appendix B)

		Lithology									
Mineral	**Chemical Formula**	**Calcareous Rock (*n* = 1)**	**GRV Rock (*n* = 4)**	**GRV Colluvial (*n* = 5)**	**Bittali Rock (*n* = 1)**	**Bittali Colluvial (*n* = 1)**	**Nankivel Hill (*n* = 6)**	**Nankivel Hill Colluvial (*n* = 7)**	**Peterlumbo Hill (*n* = 3)**	**Peterlumbo Hill Colluvial (*n* = 9)**	**Soil (*n* = 20)**
Actinolite (%)	$Ca_2Mg_{2.5}Fe_{2.5}[Si_8O_{22}](OH_2)$	-	-	-	3.9	4.2	-	-	-	-	-
Albite (%)	$NaAlSi_3O_8$	-	26	6	31	12	-	-	-	2.7	4.2
Alunite (%)	$K_2Al_6(OH)_{12}(SO_4)_4$	-	-	-	-	-	12.5	-	-	-	-
Calcite (%)	$CaCO_3$	28.4	1.5	-	-	-	1.8	5.8	-	2.5	6
Chamosite (%)	$(Fe^{2+})_{10}Al_2[Al_2Si_6O_{20}](OH)_{16}$	-	16.9	-	11.3	-	-	-	-	-	-
Dickite (%)	$Al_2Si_2O_5(OH)_4$	45.8	-	-	-	-	7.6	-	-	-	-
Dolomite (%)	$CaMg(CO_3)_2$	3.2	-	-	-	-	-	-	-	1.2	0.9
Hematite (%)	Fe_2O_3	-	1	1.3	-	-	0.5	0.8	0.3	0.7	1.3
Illite (%)	$K1_{.5\text{-}1}Al_4[S_{i6.5\text{-}7}Al_{1.5\text{-}1}O_{20}](OH)_4$	-	-	18.1	-	-	-	30	-	19.4	18.1

		Lithology									
Mineral	**Chemical Formula**	**Calcareous Rock (n = 1)**	**GRV Rock (n = 4)**	**GRV Colluvial (n = 5)**	**Bittali Rock (n = 1)**	**Bittali Colluvial (n = 1)**	**Nankivel Hill (n = 6)**	**Nankivel Hill Colluvial (n = 7)**	**Peterlumbo Hill (n = 3)**	**Peterlumbo Hill Colluvial (n = 9)**	**Soil (n = 20)**
Jarosite (%)	$KFe^{3+}_3(OH)_6(SO_4)_2$	-	0	-	-	-	1	-	-	-	-
Kaolinite (%)	$Al_2Si_2O_5(OH)_4$	-	-	9.9	-	8.1	-	8.7	-	7.8	11.3
Microcline (%)	$KAlSi_3O_8$	-	21.8	13.2	33.5	18.2	2	5.8	2.4	5.2	9.2
Muscovite (%)	$K_2Al_4[Si_6Al_2O_{20}](OH,F)_4$	-	11.7	11.8	6.5	12.3	38.8	20.7	-	13.1	14.1
Oligoclase (%)	$Na_{0.8}Ca_{0.2}Al_{1.2}Si_{2.8}O_8$	-	12.9	-	-	-	-	-	-	-	3.4
Orthoclase (%)	$KAlSi_3O_8$	-	41.8	17.1	-	-	3.3	8.6	-	6.9	12
Phengite (%)	$K(AlMg)_2(OH)_2(SiAl)_4O_{10}$	-	-	11.8	-	-	-	17.9	17.3	-	21.3
Phlogopite (%)	$K_2Mg_6[Al_2Si_6O_{20}](OH)4$	-	-	-	-	-	-	-	-	-	3.4
Pyrophyllite (%)	$Al_4[Si_8O_{20}](OH)_4$	-	-	-	-	-	64.6	22	-	-	-
Quartz (%)	SiO_2	22.6	27.3	58.6	13.8	45.1	48.2	59.5	81.8	74.8	59.5

4.4 Discussion

4.4.1 Lithogeochemistry

Samples within the GRV Rock lithology do have geochemical variation as shown by the distribution of the data on the igneous extrusive rock classification diagram (Figure 4.2). The samples that comprise the Pondanna Dacite are considered relatively similar, and hence of the same lithology (Figure 4.2). However, these two GRV units are not geochemically similar. Compared to previously published geochemistry for these GRV units, the major element concentrations for the Bittali Rhyolite sample is not consistent with data analysed by Stewart (1994), but this unit has been described as forming from multiple rhyolitic and rhyodacitic magmas (Stewart 1994) and is demonstrated as such within the 100K surface geology map (Blissett *et al.* 2017) (Figure 4.2). The Pondanna Dacite samples from this study are broadly consistent with Pondanna Dacite samples from Allen *et al.* (2003) with similar $Na_2O + K_2O$ concentrations although there is a greater range of SiO_2 (Figure 4.2). The Pondanna Dacite is deemed to be mostly consistent with samples from other research and hence will be referred to herein as GRV Rock, it is the most prominent GRV unit in the study area. The Bittali Rhyolite is not consistent with samples from other research and hence is considered separately from the GRV Rock lithology and referred to as Bittali Rock as named in the 1:100,000 surface geology map.

Nankivel Hill and Peterlumbo Hill are known to contain altered rocks (Chapter 3, Nicolson *et al.* 2017) and hence are treated differently from GRV Rock. Nankivel and Peterlumbo Hill lithologies contain different major element chemistry. Figure 4.3 indicates that Nankivel Hill has a range of concentrations for SiO_2, Fe_2O_3, TiO_2 and K_2O. However, Peterlumbo Hill contains limited concentrations of Fe_2O_3 (Figure 4.3B) and higher concentrations of SiO_2 (Figure 4.3A; Figure 4.6). The A-CN-K-FM diagram also highlights the differences of the major elements for Nankivel and Peterlumbo Hill lithologies as Nankivel Hill contains a range of concentrations for $CaO + Na_2O + K_2O$ unlike Peterlumbo Hill (Figure 4.5B). Figure 4.6 also demonstrates how these two lithologies are different and why they should be separated for examination of trace elements.

As GRV Rock and Bittali Rock have been classified as individual lithologies (Figure 4.2), the colluvium should also be treated similarly. The geochemistry of these colluvial lithologies shows higher concentrations of Al_2O_3, indicating weathering of these lithologies compared to their rock exposure equivalents (Nesbitt and Young 1989; Tiddy *et al.* 2019) (Figure 4.5). There are also some geochemical differences between Bittali Colluvial from GRV Colluvial (Figure 4.6). Nankivel Hill Colluvial and Peterlumbo Hill Colluvial are also distinctly different, with both Nankivel and Peterlumbo Hill colluvium primarily containing less Al_2O_3 than their respective rock exposure samples, and they are approximately clustered together (Figure 4.6). The Soil lithology does not appear to have any spatial relationships to

GRV, Nankivel Hill or Peterlumbo Hill rock exposures and this is also true geochemically as this lithology has a wide range of major element concentrations meaning that this lithology is not associated directly with any rock exposure lithology (Figure 4.5 and 4.6). The ability to separate these lithologies using lithogeochemistry indicates that they should be examined separately when interpreting trace element concentrations.

4.4.2 Distribution of Pathfinder Elements

4.4.2.1 Nankivel Hill, Peterlumbo Hill and Gawler Range Volcanics

The mineral system predicted in the study area are porphyry-epithermal deposits (Wade *et al.* 2014; Nicolson *et al.* 2017) which can be used to inform the suite of pathfinder elements to consider here. The known pathfinder element suite for porphyry deposits includes Ag, As, Au, Bi, Co, Cs, Cu, Li, Mo, Ni, Pb, Sb, Se, Sn, Te, Tl, W and Zn (Halley *et al.* 2015). Silver, Au, Se and Te were excluded from analysis due to the number of samples in the dataset that were below detection limit. Elevated concentrations of trace elements may be identified using log normalised histograms (e.g. Baudet *et al.* 2018; Wolff *et al.* 2018). However, for this study, identification of anomalous populations using this method was not possible due to the small number of samples and limited number of elements at significant concentrations (Figure 4.9).

Elevated element concentrations were assessed here following Fabris *et al.* (2013), who defined elevated concentrations for basement rock proximal to mineral occurrences based on comparison with average Upper Continental Crust (UCC). The UCC values determined by Rudnick and Gao (2003) are used here. For Nankivel Hill, some of the elements in the known pathfinder suite such as Bi, Sn, Sb, Pb, As, Tl, W and Mo occur at concentrations 4.6 – 1.06 x above UCC (Figure 4.9). Cobalt and Ni are significantly depleted at >10 x below UCC (Figure 4.9). Concentrations for Cs, Sn and W are also significantly elevated at Peterlumbo Hill at 3.2 – 2 x above UCC (Figure 4.9). However, most pathfinder elements are depleted compared to UCC, with Sc, Cu, Ni and Co significantly depleted at >10 x below UCC for Peterlumbo Hill lithology (Figure 4.9). From the known pathfinder suite, GRV Rock has Sn, Pb, Mo, Zn and Tl occurring at concentrations 1.8 – 1.1 x above UCC (Figure 4.9). The remaining pathfinder elements are below UCC with concentrations of 0.84 – 0.2 x UCC and Ni is particularly depleted at >10 x below UCC (Figure 4.9). Bittali Rock follows similar patterns to GRV Rock but only has Pb, Sn and Zn above UCC at 1.6 – 1 x UCC with the other pathfinders below UCC and Ni depleted >10 x below UCC (Figure 4.9).

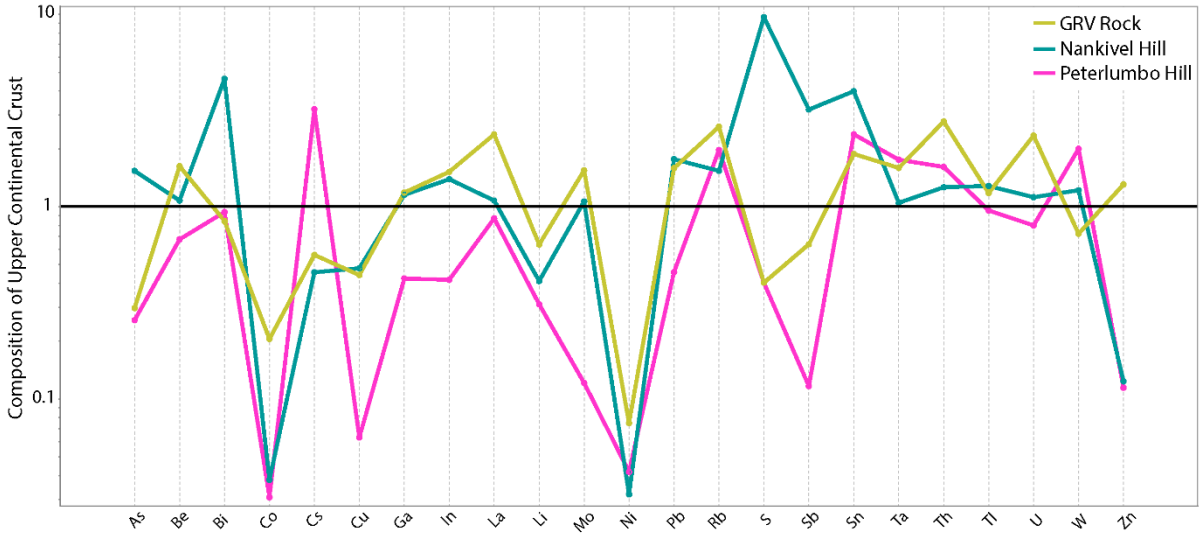

Figure 4.9: Examples of elevated and depleted concentrations of trace elements for Rock lithologies. All normalised to Rudnick and Gao (2003) Upper Continental Crust concentrations.

Trace elements that are not within the predefined porphyry-epithermal pathfinder element suite but that are significantly above UCC are also considered here. Nankivel Hill has above UCC concentrations of S, Rb, In, Th, Ga, U, Be, La, Mo and Ta ranging from 9.6 – 1 x UCC (Figure 4.9). Peterlumbo Hill has concentrations of Rb, Ta and Th elevated at 2 – 1.6 x above UCC (Figure 4.9). GRV Rock has almost all REEs above UCC occurring at concentrations of 3 - 1.8 x. These elements are of interest, however, the Hiltaba Suite and GRV in the Olympic Domain system is known to contain considerably elevated REEs and elements such as U and Th (e.g. Allen and McPhie 2002; Agangi 2011). Given that the Nankivel and Peterlumbo Hill system is spatially associated with the intrusion and extrusion of the Hiltaba Suite and GRV (Paul *et al.* 2015; Nicolson *et al.* 2017), the concentrations of U and Th are likely due to the influence of the GRV and Hiltaba Suite on this region (e.g. Pollard 2000; Allen and McPhie 2002; Betts *et al.* 2007). However, LREEs are worth retaining in a pathfinder suite as they have been shown to be linked with mineral systems in the Olympic Domain (e.g. Forbes *et al.* 2015; Baudet *et al.* 2018). A limited number of samples within Nankivel Hill and Peterlumbo Hill contain above UCC concentrations of LREEs but on average, these lithologies have below UCC concentrations of all REEs (Figure 4.8).

Due to the limited number of significantly elevated pathfinder elements from the known pathfinder suite and lack of elevated trace elements proximal to ore deposits (e.g. Fabris *et al.* 2013) it is necessary to reassess pathfinder element thresholds for this region. Generally, the elevated element concentrations observed in the Nankivel and Peterlumbo Hill exposures are comparable for some elements (Figure 4.9). Rubidium, Sn, W and Ta are elevated within both exposures at 1.04 x above UCC (Figure 4.9) and both Ni and Co are significantly depleted (0.04 – 0.03 x below UCC) for Nankivel and Peterlumbo Hills (Figure 4.9). New pathfinder element thresholds for the rock lithologies in this region are defined as elevated if they are ≥1.5 x UCC and depleted if they are ≤0.1 x UCC. The differences in the thresholds

set for elevated concentrations between Fabris *et al.* (2013) and this study are primarily due to this research being limited by using rock exposure samples that had been impacted by weathering rather than fresh drill core. When applied, this produces a pathfinder element suite that identify elevated Pb, Rb, Sn and Ta ± As, Bi, Cs, In, Mo, S, Sb and W and depleted Ni, Co ± Cu, Sc, Sr. However, it is known that Rb is naturally elevated in feldspars and micas (e.g. Scott and Smith 1987) and is also retained in stable minerals (Butt *et al.* 2000). As this landscape is dominated by feldspars and micas and is relatively stable, Rb is excluded from the pathfinder element suite.

Most elements within the pathfinder element suite identified were expected due to the current knowledge of potential mineralisation in the region. The region-specific pathfinder suite defined here is predominantly a subset of the well-known porphyry pathfinder suite by Halley *et al.* (2015). It is noted that Ni and Co are included in the published pathfinder suite for porphyry mineralisation, however in the samples used here they are significantly depleted.

The pathfinder elements defined above are primarily associated with Nankivel Hill and to a lesser extent, Peterlumbo Hill. The only pathfinders where the concentrations are greater for Peterlumbo Hill compared to Nankivel Hill is Cs, Ta and W (Figure 4.9). Although there are some pathfinder elements above the 1.5 x UCC threshold, these are limited and there are more pathfinders identified in the Nankivel Hill lithology (Figure 4.9). GRV Rock is also a very different lithology to Nankivel and Peterlumbo Hill and any potential alteration may manifest differently. The differing protoliths, sediments versus volcanics, would impact the travel and expression of alteration fluids.

4.4.2.2 Colluvium and Soils

In general, the concentration of pathfinder elements within cover sequence materials is expected to be lower relative to altered or mineralised basement lithologies that host a mineral occurrence (e.g. Anand *et al.* 2002). This implies that the threshold for what is considered elevated pathfinder element concentrations will be lower relative to those defined for basement materials (e.g. Hill 2015). The thresholds for elevated concentrations in the colluvial and soil lithologies in this study area is therefore considered here. Hill (2015) defined the threshold for elevated pathfinder element concentrations for cover sequence materials in the Yorke Peninsula area as being 3 x UCC. The only trace elements above a threshold of 3 x UCC in the soil or colluvium in this study area is Bi and Sn at approximately 9 and 3 x UCC respectively (Figure 4.10). Similar to the rock lithologies, there are limited elevated concentrations above a previously defined threshold and hence, a new threshold should be determined for this region.

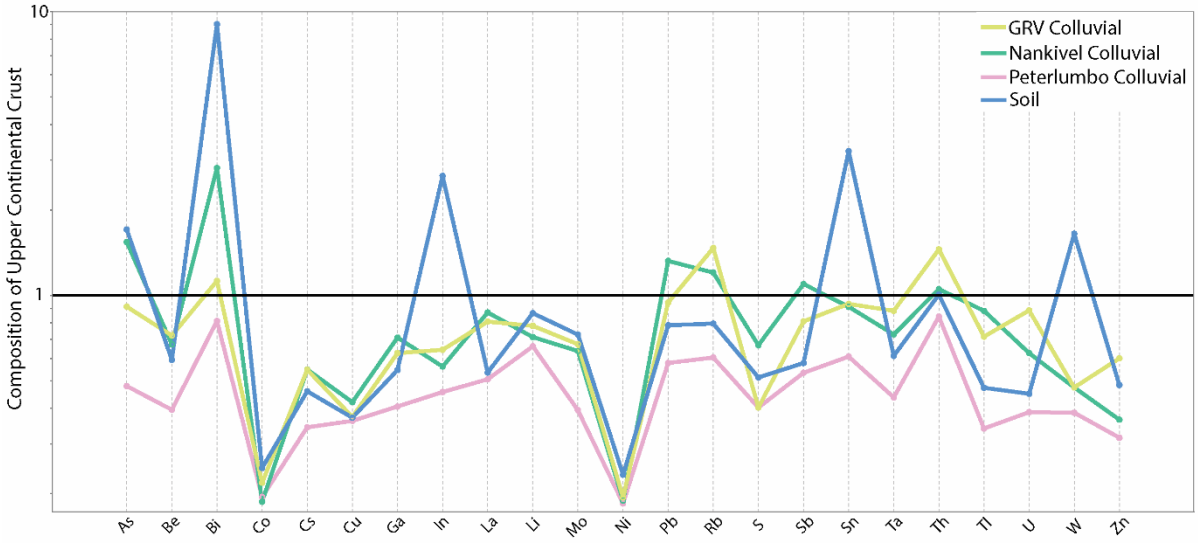

Figure 4.10: Examples of elevated and depleted concentrations of trace elements for Soil and Colluvial lithologies. All normalised to Rudnick and Gao (2003) Upper Continental Crust concentrations.

When applying the threshold defined by Hill (2015) to the Nankivel Hill Colluvial lithology, there are no elements 3 x above UCC (Figure 4.10). However, there are a number of elements above UCC including Bi, Th, As, Pb and Sb from 2.8 – 1.1 x UCC. Peterlumbo Hill also has no elements above the 3 x UCC threshold but also has no elements above UCC. GRV Colluvial only contains Th and Bi above UCC, with no pathfinders 3 x above UCC and Bittali Colluvial has the same pathfinders as GRV Colluvial but also contains Pb (Figure 4.10). The Soil lithology is different from the colluvial lithologies with Bi and Sn above the 3 x UCC threshold, defined as elevated as well as above UCC concentrations of In, As, W and Th (Figure 4.10). Figure 4.7 shows one sample (F89) for this lithology with concentrations significantly above the rest of the lithology for As, Bi, Mo, In, Sn and W. Across all of these cover sequence lithologies, Co and Ni have had the lowest concentrations ranging from 0.27 – 0.18 x UCC (Figure 4.10).

Across the majority of these cover sequence lithologies, the concentrations of pathfinder elements are relatively low and generally below the UCC concentrations. Therefore, it can be determined that the 3 x threshold is inappropriate for these lithologies and a lower concentration should be delineated to define elevated pathfinders. The thresholds for the pathfinder element suite within the cover sequence lithologies is defined as ≥0.75 x UCC and ≤0.25 x UCC for elevated and depleted elements respectively. The lower threshold in this region is due to the highly weathered and transported nature of the soil and colluvial sediments.

4.4.3 Mineralogical Deportment of Pathfinder Elements

Pathfinder elements can be accommodated in primary minerals by isomorphic substitution for major elements in the crystal structure, random incorporation non-isomorphically or as essential structural

constituents in accessory minerals (McQueen 2009). Therefore, it is important to distinguish mineralogical deportment as it assists with interpretation of the migration paths and current location of pathfinder elements in rock exposures and cover sequence materials (e.g. Baudet *et al.* 2020).

4.4.3.1 Rock Exposures

Nankivel Hill

The dominant mineralogy for Nankivel Hill is pyrophyllite, quartz, muscovite and alunite with other minor minerals present (Table 4.6). Considering these mineralogical constituents, the geochemistry would be expected to be dominated by Al, Si, K and S. The variation of Al_2O_3 across this lithology (Figure 4.5) can be somewhat attributed to the proportion of Al-rich minerals present in each sample such as alunite, dickite, muscovite and pyrophyllite (Table 4.6). From Table 4.3, the average major element geochemistry reflects these suggestions and this lithology does contain substantial Al_2O_3, K_2O and SiO_2. There are no strong relationships between pathfinder elements and Al_2O_3 or SiO_2 (Table 4.7). Therefore, Al-rich minerals are not considered to host pathfinder elements in this lithology. However, strong positive relationships are observed between K_2O and Ta, Bi, Cs and In (Table 4.7). Potassium bearing minerals within the Nankivel Hill lithology include alunite, muscovite, microcline and orthoclase (Table 4.6). As none of these elements have correlations with S, it can be suggested that Ta, Bi, Cs and In are not hosted by alunite and may be hosted within microcline, muscovite or orthoclase. Due to the opposing correlations of Bi and In with K_2O and Na_2O (Table 4.7) and the known solid solution for feldspars (e.g. Deer *et al.* 2013) it is more likely that Bi and In are within a feldspar rather than muscovite.

Strong positive correlations also exist for Sb and Fe_2O_3. Sb may therefore be interpreted to be hosted within hematite or jarosite (Table 4.7). The absence of a correlation between Sb and S (Table 4.7) suggests that Sb could be hosted in hematite rather than jarosite. Lead, Ni and Cu show correlations with TiO_2 (Table 4.7) although there are no Ti-bearing minerals identified in the XRD analysis, Ti can be substituted in hematite and these pathfinders could therefore be hosted in hematite (McQueen 2009; Deer *et al.* 2013). Strong correlations also exist for Sr and Na_2O (Table 4.7), Sr is known to substitute into feldspars (e.g. Deer *et al.* 2013) and Cs with MgO which could be attributed to small amounts of MgO substituted in muscovite (e.g. Deer *et al.* 2013). Bismuth, Cs, In have an association with MnO (Table 4.7) but due to its very low concentrations, it will be excluded from further interpretation as it is not possible to identify any potential substitution with the mineralogy identified. Copper and Mo have strong positive relationships with S indicating that they may be hosted in alunite or jarosite (Table 4.7).

Peterlumbo Hill

The mineralogy for Peterlumbo Hill is limited to quartz, phengite (white mica), microcline and hematite (Table 4.6). As expected, this lithology is SiO_2 rich (Figure 4.6, Table 4.3) and the concentration of all other major elements is relatively low apart from Al_2O_3 and K_2O (Table 4.3). It is possible that these two elements are present due to microcline and phengite (Table 4.6). The concentrations of Fe_2O_3 and MgO are potentially related to phengite with Tschermak substitutions possibly accounting for some positive correlations (Table 4.8; Deer *et al.* 2013).

The pathfinder and major element relationships are conceivably influenced by the limited number of samples and mineralogy identified from XRD analysis for the Peterlumbo Hill exposure (Table 4.8). Lead, Cs, W, Cu and Sr have positive relationships with both Al_2O_3 and K_2O, but do not have any correlations with MgO (Table 4.8). This may indicate that instead of a relationship with phengite, these pathfinders have a relationship with microcline. Elements that have a positive relationship with MgO, such as Sb, Ni, Co and Sc, do not have any relationship with Al_2O_3 or K_2O (Table 4.8) meaning they could be hosted within a mineral that has substituted some MgO. It is likely that most mineralogical deportment of the pathfinders will be associated with white mica as they are known to potentially contain a variety of trace elements in their crystal structure (Deer *et al.* 2013) (e.g. phengite; Table 4.6). There are positive relationships for Sb, Ni, Co and Sc with TiO_2 and Fe_2O_3 (Table 4.8). These could be attributed to hematite as Ti can be substituted in hematite (e.g. Droubay *et al.* 2007; Li *et al.* 2016).

Gawler Range Volcanics

The dominant mineralogy of this lithology includes orthoclase, quartz, albite, microcline, chamosite, oligoclase and muscovite (Table 4.6). This lithology contains the greatest proportion of feldspars in the study area and hence the concentrations of their major constituents such as Al_2O_3, Na_2O and K_2O is higher than the other lithologies (Table 4.3). The higher concentrations of MgO and Fe_2O_3 could be attributed to the presence of chamosite and hematite in this lithology (Table 4.6).

Indium and Pb correlate with Na_2O suggesting that these elements are possibly hosted within albite or oligoclase (Table 4.6 and 4.8). Tantalum has a positive correlation with Al_2O_3 and K_2O indicating that it may be hosted in feldspars or micas (Table 4.9). Antinomy has a positive relationship with only Al_2O_3 meaning it could be within a number of Al-rich minerals but due to a moderate relationship with K_2O, it could be hosted in Al- and K-rich minerals (Table 4.9). There are positive correlations for In, Ni, Co and Sr with Fe_2O_3, and In, Co and Sr with MgO (Table 4.9). Based on mineralogy for this lithology, In, Co and Sr are possibly within chamosite while Ni would be within hematite (Table 4.6). Molybdenum and Cu have strong positive correlations with SiO_2 while Sn only has a positive relationship with K_2O linking Sn with feldspars or micas with a moderate correlation of Al_2O_3 (Table 4.9).

Table 4.7: Major and pathfinder element Spearman's Rank Correlation Coefficients for Nankivel Hill lithology. Significant relationships (≤ -0.8, ≥ 0.8) are in bold

	Pb	**Sn**	**Ta**	**As**	**Bi**	**Cs**	**In**	**Mo**	**S**	**Sb**	**W**	**Ni**	**Co**	**Cu**	**Sc**	**Sr**
SiO_2	-0.18	-0.49	-0.54	0.07	0.04	-0.07	0.13	-0.39	-0.51	-0.21	-0.5	-0.18	0.19	-0.05	-0.14	-0.32
TiO_2	**0.86**	0.09	0.11	-0.36	0.07	0.32	0.17	0.71	0.79	0.29	0	**0.86**	0.6	**0.85**	0.79	-0.36
Al_2O_3	0.14	0.67	0.71	-0.32	0.11	0.11	0.11	0.14	0.37	-0.14	0.21	0.14	-0.06	-0.11	0.18	0.21
Fe_2O_3	0.04	-0.52	-0.5	0.79	-0.18	0.04	-0.58	0.5	0.24	**0.93**	0.79	0.04	-0.32	0.4	-0.11	0.18
MnO	0.32	0.61	0.61	-0.14	**0.86**	**0.96**	**0.8**	-0.29	-0.12	-0.07	0	0.32	0.62	0.18	0.68	**-0.89**
MgO	0.56	0.23	0.25	-0.13	0.74	**0.85**	0.66	-0.05	0.08	0.02	-0.13	0.56	0.77	0.48	0.74	**-0.88**
CaO	-0.04	**-0.88**	-0.75	0.46	-0.29	-0.39	-0.47	0	-0.16	0.04	-0.18	-0.04	-0.09	-0.09	-0.57	0.39
K_2O	0.54	0.74	**0.86**	-0.39	**0.86**	**0.86**	**0.82**	-0.25	0.1	-0.43	-0.21	0.54	0.73	0.04	0.61	-0.61
Na_2O	-0.14	-0.54	-0.54	0.43	**-0.82**	-0.71	**-0.95**	0.68	0.43	0.64	0.57	-0.14	-0.69	0.14	-0.46	**0.86**
P_2O_5	-0.36	-0.4	-0.36	0.39	-0.64	-0.71	**-0.84**	0.32	0.2	0.32	0.46	-0.36	-0.77	-0.2	-0.64	**0.93**
S	0.75	-0.11	-0.06	-0.32	-0.26	-0.12	-0.25	**0.91**	-	0.32	0.12	0.75	0.27	**0.8**	0.51	0.16

Table 4.8: Major and pathfinder element Spearman's Rank Correlation Coefficients for Peterlumbo Hill lithology. Significant relationships (≤ -0.8, ≥ 0.8) are in bold

	Pb	**Sn**	**Ta**	**As**	**Bi**	**Cs**	**In**	**Mo**	**Sb**	**W**	**Ni**	**Co**	**Cu**	**Sc**	**Sr**
SiO_2	**-1**	-0.5	-0.5	**0.87**	0.5	**-1**	**0.87**	**0.87**	0	**-1**	-0.5	-0.5	**-1**	-0.5	**-1**
TiO_2	0.5	-0.5	-0.5	**-0.87**	**-1**	0.5	**-0.87**	**-0.87**	**0.87**	0.5	**1**	**1**	0.5	**1**	0.5
Al_2O_3	**1**	0.5	0.5	**-0.87**	-0.5	**1**	**-0.87**	**-0.87**	0	**1**	0.5	0.5	**1**	0.5	**1**
Fe_2O_3	0.5	-0.5	-0.5	**-0.87**	**-1**	0.5	**-0.87**	**-0.87**	**0.87**	0.5	**1**	**1**	0.5	**1**	0.5
MnO	**1**	0.5	0.5	**-0.87**	-0.5	**1**	**-0.87**	**-0.87**	0	**1**	0.5	0.5	**1**	0.5	**1**
MgO	0.5	-0.5	-0.5	**-0.87**	**-1**	0.5	**-0.87**	**-0.87**	**0.87**	0.5	**1**	**1**	0.5	**1**	0.5
CaO	**-1**	-0.5	-0.5	**0.87**	0.5	**-1**	**0.87**	**0.87**	0	**-1**	-0.5	-0.5	**-1**	-0.5	**-1**
K_2O	**1**	0.5	0.5	**-0.87**	-0.5	**1**	**-0.87**	**-0.87**	0	**1**	0.5	0.5	**1**	0.5	**1**
Na_2O	**1**	0.5	0.5	**-0.87**	-0.5	**1**	**-0.87**	**-0.87**	0	**1**	0.5	0.5	**1**	0.5	**1**
P_2O_5	**1**	0.5	0.5	**-0.87**	-0.5	**1**	**-0.87**	**-0.87**	0	**1**	0.5	0.5	**1**	0.5	**1**

Table 4.9: Major and pathfinder element Spearman's Rank Correlation Coefficients for GRV Rock lithology. Significant relationships (≤ -0.8, ≥ 0.8) are in bold

	Pb	**Sn**	**Ta**	**As**	**Bi**	**Cs**	**In**	**Mo**	**Sb**	**W**	**Ni**	**Co**	**Cu**	**Sc**	**Sr**
SiO_2	0.4	0.32	0.2	0.21	-0.63	**-0.95**	0	**0.8**	-0.63	0.4	0.11	-0.2	**1**	**-1**	-0.2
TiO_2	-0.4	-0.32	-0.2	-0.21	0.63	**0.95**	0	**-0.8**	0.63	-0.4	-0.11	0.2	**-1**	**1**	0.2
Al_2O_3	**-1**	0.74	**0.8**	0.32	-0.11	0.63	**-0.89**	0	**0.95**	-0.4	**-0.95**	**-0.8**	-0.4	0.4	**-0.8**
Fe_2O_3	0.74	**-1**	**-0.95**	-0.39	0.5	0.06	**0.94**	-0.63	-0.5	0.21	**0.89**	**0.95**	-0.32	0.32	**0.95**
MnO	0.6	**-0.95**	**-0.8**	-0.11	0.32	0.21	**0.89**	**-0.8**	-0.32	0.4	0.74	**0.8**	-0.4	0.4	**0.8**
MgO	0.6	**-0.95**	**-0.8**	-0.11	0.32	0.21	**0.89**	**-0.8**	-0.32	0.4	0.74	**0.8**	-0.4	0.4	**0.8**
CaO	0.6	**-0.95**	**-0.8**	-0.11	0.32	0.21	**0.89**	**-0.8**	-0.32	0.4	0.74	**0.8**	-0.4	0.4	**0.8**
K_2O	**-0.8**	**0.95**	**1**	0.63	-0.63	0.11	**-0.89**	0.4	0.63	0	**-0.95**	**-1**	0.2	-0.2	**-1**
Na_2O	**0.8**	**-0.95**	**-1**	-0.63	0.63	-0.11	**0.89**	-0.4	-0.63	0	**0.95**	**1**	-0.2	0.2	**1**
P_2O_5	0	-0.63	-0.4	0.11	0.32	0.74	0.45	**-1**	0.32	0.2	0.21	0.4	**-0.8**	**0.8**	0.4

4.4.3.2 Transported Lithologies

Colluvial material is derived from the nearby rock exposures and has generally not undergone significant transport (Eggleton *et al.* 2001). Comparison of the geochemistry of rock exposure and the nearby samples of colluvium is used here to understand the redistribution of pathfinder elements during processes associated with generation of the colluvial material.

Nankivel Hill Colluvium

Nickel and Co have significantly higher concentrations (≥4.9 x) in the Nankivel Hill Colluvium compared to Nankivel Hill, while Sc, Cs, As and Cu are above the cover materials threshold (0.75 x) and therefore considered elevated (Figure 4.11). Sulphur and Sn are depleted in the colluvium at ≤0.25 x below Nankivel Hill concentrations (Figure 4.11). It could be inferred from Figure 4.11 that the Nankivel Hill Colluvium contains more mineralogy hosting Ni, Co, Sc, Cs and As and there is a smaller mineralogical component hosting S and Sn compared to Nankivel Hill. There is no alunite or jarosite present in the Nankivel Hill Colluvial lithology (Table 4.6) and this is evident geochemically by the significant depletion of S (Figure 4.11). Nickel is the only element with a correlation with TiO_2 (Table 4.10), indicating potential Ti within hematite as Ni also has a moderate relationship with Fe_2O_3. Strontium and Cs have no strong correlations with any major elements for the colluvium (Table 4.10).

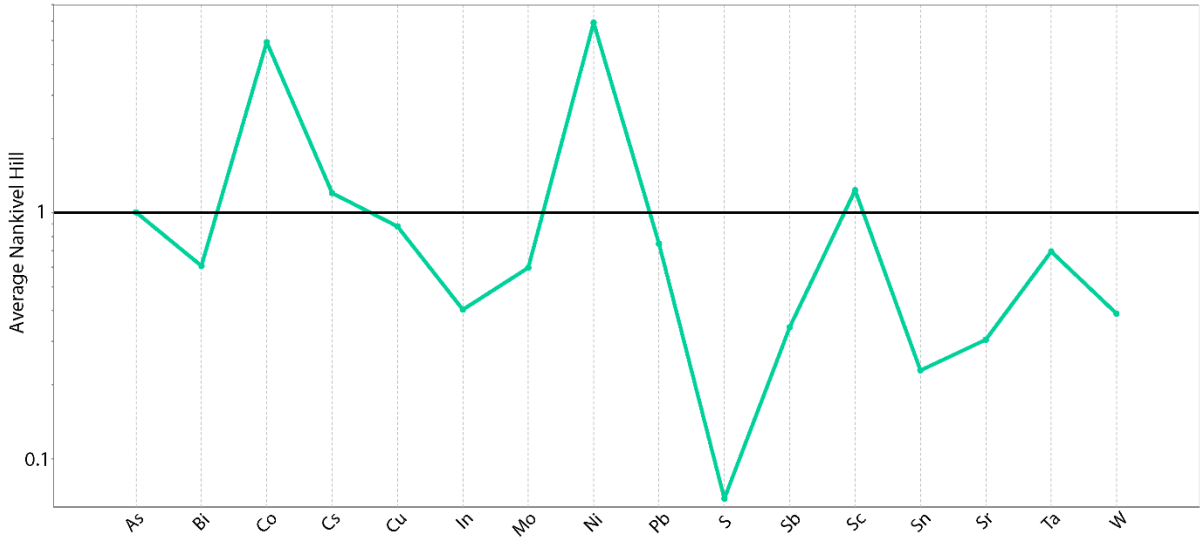

Figure 4.11: Pathfinder elements for Nankivel Hill Colluvial normalised to Nankivel Hill

Arsenic has a strong correlation with Al_2O_3 and K_2O so it is potentially hosted within illite, microcline, muscovite, orthoclase or phengite (Table 4.6). However, the negative relationship between As and MgO indicates that phengite is not hosting As (Table 4.10). Sc may be hosted within hematite due to its relationship with Fe_2O_3. Copper has strong positive correlation with MgO (Table 4.10). Based on the correlation with MgO, it could be suggested that Cu is associated with phengite, however as the

relationships of Cu with Al_2O_3 and K_2O are moderately negative, phengite is not likely to be hosting Cu. It is possible that Cu is hosted within a mineral such as calcite due to its moderate relationship with CaO (Table 4.10). Since significant concentrations of Cu can be found in calcrete in other regions of South Australia, the relationship between Cu and CaO in this region is plausible.

Molybdenum and Sb only have strong correlations for Al_2O_3, meaning they could be hosted within kaolinite or pyrophyllite (Table 4.6). There is only one negative relationship identified in this lithology for Sn and SiO_2 (Table 4.10). Therefore, it can be said that the concentration of Sn would decrease with the increase of SiO_2. There are moderate relationships for Sn with Al_2O_3 and K_2O (Table 4.10) indicating the potential that Sn is hosted in micas or feldspars.

Peterlumbo Hill Colluvial

There are a number of elevated trace elements in Peterlumbo Hill Colluvial compared to Peterlumbo Hill, including Co, Cu, Sb, Ni, Sc, Mo, Sr, As, Pb, In, Bi and S (Figure 4.12). Sulphur was excluded from this analysis as it was not identified above detection limit for the Peterlumbo Hill and Colluvial lithologies (Table 4.1, Table 4.2). Similar to Peterlumbo Hill, the colluvium has positive relationships for Pb, Cs and Sr with Al_2O_3 and K_2O, indicating that these elements are possibly hosted within minerals such as illite, kaolinite, microcline, muscovite and orthoclase (Table 4.6). However, the colluvium also has positive relationships of Al_2O_3 and K_2O with Ni and Co (Table 4.11) meaning that they could also be hosted in these minerals. There is a strong positive relationship between Sr with CaO (Table 4.11) which would indicate that Sr is hosted in calcite and there is a known association of Ca and Sr (e.g Dart *et al.* 2012). Strontium also has a relationship with MgO (Table 4.11), likely related to dolomite in this lithology (Table 4.6). As well as Sr, Ni and Cu both have positive relationships with CaO and MgO (Table 4.11), indicating that they could be hosted within dolomite, while Pb and Cs have positive relationships with CaO, meaning they are hosted within calcite (Table 4.11).

There are positive relationships of Pb, Cs and Sr with Na_2O, potentially associated with albite (Table 4.6). There are also strong relationships for Ta, Ni, Co and Sc with Fe_2O_3 (Table 4.11). Based on the mineralogy in Table 4.6, it could be implied that these pathfinders are hosted in hematite as well as the other minerals they have been identified in such as dolomite.

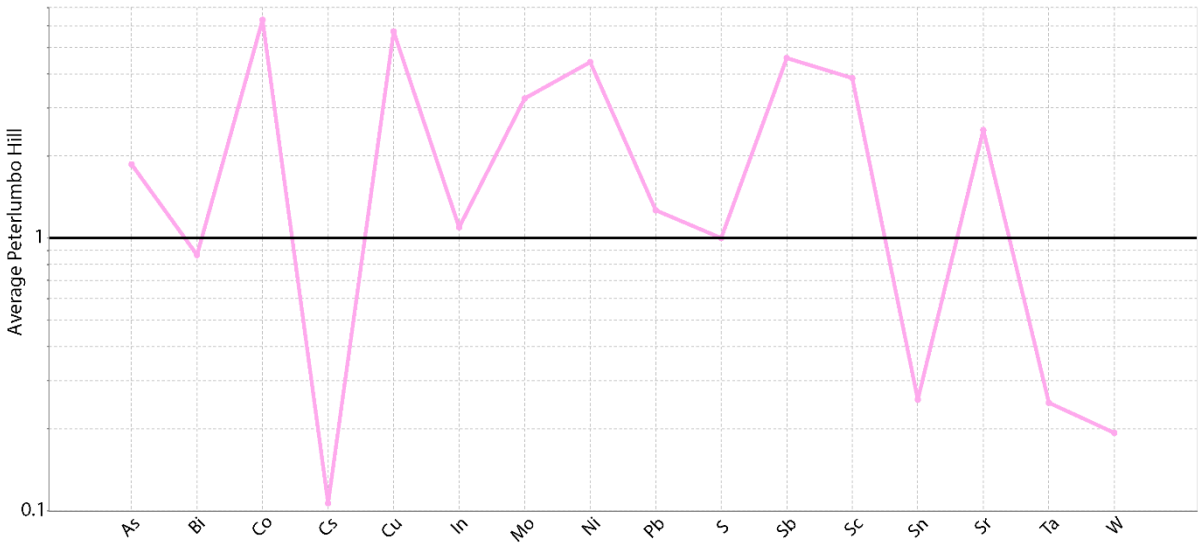

Figure 4.12: Pathfinder elements for Peterlumbo Hill Colluvial normalised to Peterlumbo Hill

Gawler Range Volcanics Colluvial

GRV Colluvial contains more As, Ni, Bi, Sb and Co compared to GRV Rock (Figure 4.13). Nickel and Co have strong relationships with MgO indicating they are possibly hosted within phengite in the colluvium (Table 4.12). There were no strong relationships for As in GRV Rock, however for GRV Colluvial, there are a number of strong relationships for As and Al_2O_3, Fe_2O_3 and TiO_2 (Table 4.12). This indicates hematite, potentially with some Ti substitution, or kaolinite hosts As (Table 4.6). There are other pathfinder element relationships for this lithology including Pb, Ta, Cs, In, W, Cu, Sc and Sr with Al_2O_3 (Table 4.12). From this suite of relationships, Ta is the only element that also has a positive correlation with K_2O indicating that this pathfinder is possibly hosted within minerals such as illite, microcline, muscovite and orthoclase (Table 4.6; Table 4.12). Lead, Cs, In, Sb, W, Cu, Sc and Sr also have strong positive correlations with Fe_2O_3, likely hosted in hematite (Table 4.6).

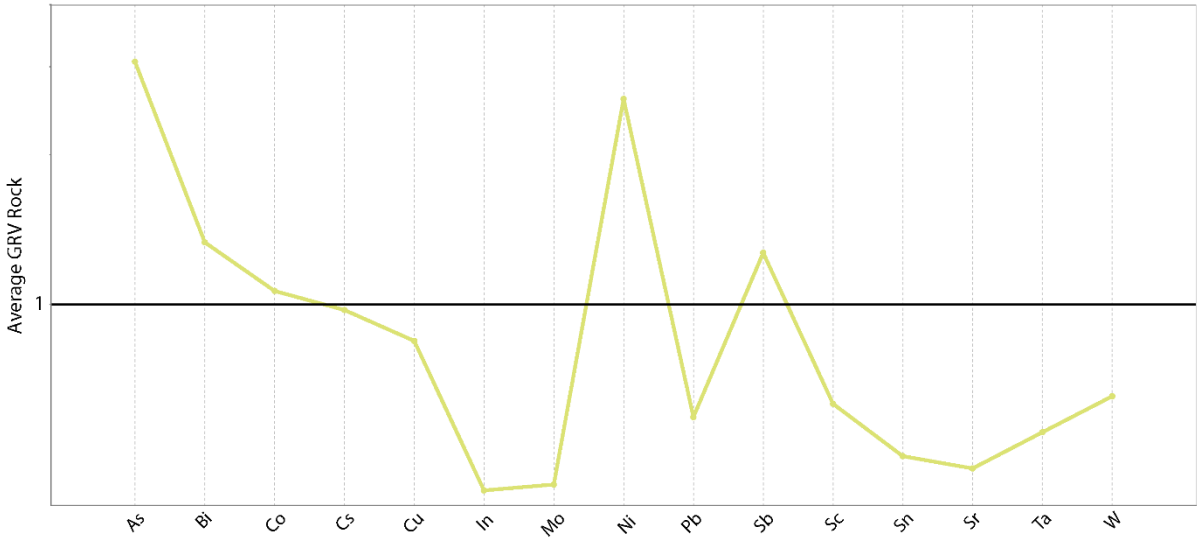

Figure 4.13: Pathfinder elements for GRV Colluvial normalised to GRV Rock

Distal Soils

The major element concentrations in this lithology have large ranges of Al_2O_3, CaO, K_2O and Na_2O (Figure 4.5). This variation in major element chemistry can be attributed to the varied mineralogy present, this lithology includes Al- and K-rich minerals such as kaolinite, microcline, muscovite, orthoclase and phengite while also including oligoclase, calcite and albite accounting for the variation in CaO and Na_2O (Table 4.6; Figure 4.5).

The Soil lithology, although quartz dominated, is one of the most mineralogically diverse but has limited correlations (Table 4.13). There are positive correlations of Al_2O_3 with Cs; Co with MgO and Sc with Fe_2O_3 (Table 4.13). From this, it can be determined that Cs may be within a mineral such as kaolinite, while Co and Ni are possibly hosted in phengite or phlogopite. Scandium could be within hematite or an Al-rich mineral such as kaolinite (Table 4.6).

Table 4.10: Major and pathfinder element Spearman's Rank Correlation Coefficients for Nankivel Hill Colluvial lithology. Significant relationships (≤ -0.8, ≥ 0.8) are in bold

	Pb	**Sn**	**Ta**	**As**	**Bi**	**Cs**	**In**	**Mo**	**S**	**Sb**	**W**	**Ni**	**Co**	**Cu**	**Sc**	**Sr**
SiO_2	-0.57	**-0.85**	0.29	-0.5	-0.18	-0.71	-0.34	-0.48	-0.6	-0.36	-0.06	-0.04	-0.21	-0.07	-0.37	-0.36
TiO_2	0.18	-0.32	-0.29	-0.21	-0.61	-0.07	0.54	-0.2	-0.42	-0.46	0.08	**0.86**	0.75	0.25	0.56	-0.07
Al_2O_3	0.71	0.79	-0.07	**0.96**	0.5	0.61	0.42	**0.84**	0.12	**0.86**	0.45	-0.21	-0.07	-0.54	0.37	-0.43
Fe_2O_3	0.76	0.05	-0.52	0.41	0.29	0.2	0.42	0.48	-0.06	0.16	-0.07	0.7	0.77	0.23	**0.97**	-0.23
MnO	0.18	-0.4	-0.43	-0.46	-0.32	0	0.12	-0.33	-0.12	-0.71	-0.37	**0.89**	**0.86**	**0.86**	0.63	0.39
MgO	-0.04	0.31	-0.39	-0.29	-0.18	0.54	0.16	-0.15	0.36	-0.54	-0.02	0.29	0.39	**0.82**	0.19	0.79
CaO	-0.79	-0.14	-0.43	-0.61	-0.21	-0.25	0.06	-0.33	0.6	-0.57	-0.08	0	0.07	0.54	-0.37	0.71
K_2O	**0.86**	0.76	0.04	**0.89**	0.39	0.64	0.3	0.72	0.06	0.79	0.26	-0.11	0	-0.46	0.44	-0.36
Na_2O	0.04	-0.31	-0.18	-0.68	-0.61	-0.04	-0.1	-0.62	0.12	-0.79	-0.62	0.71	0.64	0.79	0.3	0.71
P_2O_5	0.61	0.74	-0.43	0.79	0.57	0.5	0.44	**0.83**	0.54	0.68	0.21	-0.04	0.18	-0.18	0.48	-0.07
S	-0.18	0.36	-0.42	0	0.24	0	0.03	0.18	-	0.12	-0.25	-0.18	0	0.18	-0.12	0.6

Table 4.11: Major and pathfinder element Spearman's Rank Correlation Coefficients for Peterlumbo Hill Colluvial lithology. Significant relationships (≤ -0.8, ≥ 0.8) are in bold

	Pb	**Sn**	**Ta**	**As**	**Bi**	**Cs**	**In**	**Mo**	**Sb**	**W**	**Ni**	**Co**	**Cu**	**Sc**	**Sr**
SiO_2	-0.68	-0.68	-0.24	0.59	-0.33	-0.69	-0.6	0.34	0.21	0.29	-0.45	-0.33	-0.49	-0.11	-0.74
TiO_2	0.75	0.1	0.77	0.62	0.75	0.75	0.27	0.35	0.46	-0.25	**0.85**	**0.94**	0.67	**0.9**	0.62
Al_2O_3	**0.99**	0.6	0.66	-0.03	0.75	**0.97**	0.66	-0.13	0.29	-0.38	**0.87**	**0.83**	0.78	0.69	**0.92**
Fe_2O_3	0.64	0.02	**0.84**	0.72	0.69	0.66	0.27	0.42	0.39	-0.05	**0.8**	**0.84**	0.62	**0.82**	0.52
MnO	0.76	0.2	0.3	-0.23	0.3	0.75	0.36	-0.15	0.54	-0.51	0.63	0.65	0.73	0.25	0.78
MgO	**0.93**	0.5	0.56	-0.06	**0.8**	**0.95**	0.66	-0.22	0.34	-0.39	**0.92**	0.79	**0.87**	0.7	**0.98**
CaO	0.76	0.29	0.49	0.06	0.65	0.78	0.64	-0.22	0.67	-0.22	**0.85**	0.7	**0.82**	0.66	**0.87**
K_2O	**0.91**	0.7	0.57	-0.26	0.62	**0.87**	0.72	-0.43	0.28	-0.35	0.7	0.62	0.68	0.45	**0.85**
Na_2O	**0.91**	0.45	0.45	-0.27	0.54	**0.9**	0.45	-0.22	0.24	-0.6	0.72	0.73	0.77	0.37	**0.88**
P_2O_5	0.01	-0.06	0.13	0.11	-0.01	0.06	0.35	0.2	0.29	0.49	0.19	0.06	0.09	0.12	0.19

Table 4.12: Major and pathfinder element Spearman's Rank Correlation Coefficients for GRV Colluvial lithology. Significant relationships (≤ -0.8, ≥ 0.8) are in bold

	Pb	**Sn**	**Ta**	**As**	**Bi**	**Cs**	**In**	**Mo**	**Sb**	**W**	**Ni**	**Co**	**Cu**	**Sc**	**Sr**
SiO_2	-0.7	-0.05	**-0.9**	-0.4	0.67	-0.7	-0.56	-0.67	-0.3	-0.56	0.2	0.05	-0.4	-0.7	-0.6
TiO_2	**0.9**	0.67	0.7	**1**	0.22	**0.9**	**0.97**	0.67	**0.9**	**0.97**	0.6	0.56	**1**	**0.9**	**0.8**
Al_2O_3	**1**	0.67	**0.9**	**0.9**	-0.22	**1**	**0.97**	0.67	0.7	**0.97**	0.5	0.56	**0.9**	**1**	**0.9**
Fe_2O_3	**0.9**	0.67	0.7	**1**	0.22	**0.9**	**0.97**	0.67	**0.9**	**0.97**	0.6	0.56	**1**	**0.9**	**0.8**
MnO	**0.9**	0.56	0.7	0.8	-0.22	**0.9**	**0.87**	0.36	0.5	**0.87**	0.6	0.67	**0.8**	**0.9**	**1**
MgO	0.2	0.67	-0.1	0.1	-0.22	0.2	0.15	-0.56	-0.3	0.15	**0.8**	**0.87**	0.1	0.2	0.4
CaO	-0.4	-0.05	-0.7	-0.3	0.22	-0.4	-0.36	**-0.87**	-0.5	-0.36	0.4	0.36	-0.3	-0.4	0
K_2O	0.7	0.15	**0.9**	0.6	-0.22	0.7	0.67	**0.97**	0.7	0.67	-0.2	-0.15	0.6	0.7	0.4
Na_2O	0.7	0.21	0.6	0.5	-0.45	0.7	0.62	0.21	0.2	0.62	0.3	0.41	0.5	0.7	**0.9**
P_2O_5	0.6	0.72	0.2	**0.8**	0.45	0.6	0.72	0.1	0.6	0.72	**0.9**	**0.82**	**0.8**	0.6	0.7

Table 4.13: Major and pathfinder element Spearman's Rank Correlation Coefficients for Soil lithology. Significant relationships (≤ -0.8, ≥ 0.8) are in bold

	Pb	**Sn**	**Ta**	**As**	**Bi**	**Cs**	**In**	**Mo**	**S**	**Sb**	**W**	**Ni**	**Co**	**Cu**	**Sc**	**Sr**
SiO_2	-0.59	-0.62	-0.53	-0.63	-0.71	-0.54	-0.64	-0.67	-0.21	-0.47	-0.56	-0.73	-0.68	-0.75	-0.72	-0.6
TiO_2	0.76	0.7	0.71	0.64	0.61	0.73	0.77	0.64	0.18	0.63	0.73	0.73	0.72	0.64	**0.84**	0.39
Al_2O_3	0.63	0.63	0.66	0.57	0.51	**0.8**	0.64	0.53	0.19	0.63	0.53	0.78	**0.82**	0.63	**0.91**	0.22
Fe_2O_3	0.61	0.78	0.56	**0.9**	0.75	0.62	**0.88**	**0.89**	0.2	0.76	0.69	0.72	0.63	0.61	**0.85**	0.43
MnO	0.69	0.51	0.57	0.47	0.45	0.43	0.52	0.48	0.39	0.36	0.42	0.62	0.56	0.62	0.61	0.47
MgO	0.54	0.68	0.63	0.52	0.63	0.77	0.67	0.47	0.51	0.36	0.61	**0.83**	**0.91**	0.7	0.79	0.66
CaO	0.33	0.55	0.47	0.53	0.67	0.44	0.49	0.41	0.33	0.38	0.51	0.65	0.58	0.61	0.47	0.78
K_2O	0.42	-0.02	0.33	0.03	-0.08	0.54	0.08	0.13	0.2	-0.02	0.09	0.17	0.35	0.36	0.18	0.22
Na_2O	0.16	0.07	0.3	-0.04	0.08	0.18	-0.07	-0.01	0.49	-0.24	0.19	-0.11	0.04	0.03	-0.16	0.44
P_2O_5	0.45	0.54	0.38	0.68	0.54	0.69	0.75	0.72	0.29	0.5	0.46	0.7	0.67	0.69	0.74	0.55
S	0	0.52	0.23	0.29	0.47	0.39	0.31	0.19	-	-0.13	0.46	0.28	0.34	0.03	0.07	0.56

4.4.4 Effects of Weathering Processes

This section compares the geochemistry and mineralogy of the rock exposures with their surrounding colluvium to assess the effects of secondary processes such as erosion, weathering, transport and redeposition. This is to understand the effects of processes associated with weathering on the preservation of pathfinder elements within weathered and transported lithologies. Table 4.14 shows the mineralogy and potential mineralogical deportment for both rock, colluvium and soil lithologies.

Table 4.14: Summary of mineralogy within rock and colluvial lithologies and their associated pathfinder elements

Lithology Group	Minerals within Rock Exposure	Pathfinder Elements Hosted	Minerals within Colluvium	Pathfinder Elements Hosted
GRV	Albite, calcite, chamosite, hematite, microcline, muscovite, oligoclase, orthoclase, quartz	In, Pb, Sb, Ni, Co, Sr, Cu, Mo	Albite, hematite, illite, kaolinite, microcline, muscovite, orthoclase, phengite, quartz	As, Pb, Ta, Cs, In, W, Cu, Sc, Sr
Nankivel Hill	Alunite, calcite, dickite, hematite, jarosite, microcline, muscovite, orthoclase, pyrophyllite, quartz	Sb, Ta, Bi, Cs, In, Pb, Ni, Cu, Sr, Mo	Calcite, hematite, illite, kaolinite, microcline, muscovite, orthoclase, phengite, pyrophyllite, quartz	Mo, Sb, As, Sc, S, Sn, Ni, Co, Cs
Peterlumbo Hill	Hematite, microcline, phengite, quartz	Pb, Cs, W, Cu, Sr, Sb, Ni, Co, Sc	Albite, calcite, dolomite, hematite, illite, kaolinite, microcline, muscovite, orthoclase, quartz	Pb, Cs, Sr, Ta, Ni, Co, Sc
Soil	Albite, calcite, dolomite, hematite, illite, kaolinite, microcline, muscovite, oligoclase, orthoclase, phengite, phlogopite, quartz			Cs, Co, Sc

4.4.4.1 Nankivel Hill

There is less Al_2O_3 and K_2O but significantly increased CaO in Nankivel Hill Colluvial compared to Nankivel Hill (Table 4.3). Nankivel Hill Colluvial is as mineralogically diverse as Nankivel Hill but has more mineralogy containing Al_2O_3, K_2O and MgO, which can be attributed to the presence of illite, kaolinite and phengite (Table 4.6). There are reduced proportions of both muscovite and pyrophyllite while there is no alunite, dickite or jarosite in the colluvium (Table 4.6). There are higher proportions of calcite, hematite, microcline, orthoclase and quartz in the colluvium, accounting for the increased concentrations of CaO and Fe_2O_3 and conserved SiO_2 (Table 4.3). This points to increased quantities of calcite, hematite, microcline, orthoclase and quartz (Table 4.6). Due to the Al-rich nature of most of the minerals in this lithology, it is expected that there would be a number of correlations between pathfinder elements and Al_2O_3 (Table 4.10).

Pathfinder elements are hosted in a range of minerals that have been enriched in the Nankivel Hill colluvium. Some minerals do have distinct mineralogical deportment within both Nankivel Hill and the colluvium (Table 4.14). This includes Mo and Sb with these minerals potentially hosted within hematite, jarosite or alunite at Nankivel Hill but possibly hosted in kaolinite or pyrophyllite in the colluvium. Table 4.6 demonstrates that there was no preservation of alunite or jarosite in Nankivel Hill colluvial sediments, and the lack of S in the colluvium also indicates weathering of these minerals at Nankivel Hill (Figure 4.11). Arsenic did not have a clear relationship at Nankivel Hill but is potentially hosted within illite, microcline, muscovite or orthoclase within the colluvium (Table 4.10). The overwhelming proportion of Al-rich minerals within this lithology may indicate that it is not possible to identify if illite is a host of As (Table 4.10). There are also no minerals containing MgO within Nankivel Hill, indicating that MgO within the colluvium could be sourced by transport from other nearby material, potentially from the Soil lithology which contains a number of minerals that contain MgO (Table 4.6).

The main geochemical differences between the Nankivel Hill Rock lithology compared to its colluvium are the increased concentrations of Co and Ni (Figure 4.11). It was not possible to infer mineralogical hosts for Co and Ni at Nankivel Hill but it can be postulated that their elevated presence in the colluvium is due to host minerals surviving prolonged weathering. This could also be attributed to transport of material from other lithologies such as the Soil lithology (Table 4.14). Not all colluvial samples collected were close to Nankivel Hill Rock samples, and hence there may be other nearby or transported material in the landscape influencing the minerals in this lithology. The depletion of S can be directly related to the lack of sulphate minerals in the colluvium, alunite and jarosite (Table 4.6). As it is known that these minerals can break down easily due to their solubility (e.g. Anand and Paine 2002), it can be suggested that this landscape experienced conditions in which these minerals would weather as they do not persist in the Nankivel Hill colluvium.

4.4.4.2 Peterlumbo Hill

Peterlumbo Hill colluvium contains greater proportions of hematite and microcline compared to Peterlumbo Hill while albite, calcite, dolomite, illite, kaolinite, muscovite and orthoclase are present in the colluvium compared to the rock exposure (Table 4.14). This translates to a reduced concentration of SiO_2 and increased concentrations of Na_2O and Fe_2O_3 in the colluvium (Table 4.3). Al_2O_3 is conserved from Peterlumbo Hill to the colluvium as there is substantial Al-rich minerals within the colluvium (Table 4.3). Materials from elsewhere in the landscape have likely influenced the major element chemistry and the mineralogy of the colluvium as minerals that would weather to albite, calcite or dolomite were not identified at Peterlumbo Hill (Table 4.6).

Most of these pathfinders have had their mineralogical deportment inferred for both Peterlumbo Hill and within the colluvium. Lead, Cs, Sr and Cu were suggested to be hosted within microcline at Peterlumbo Hill and within the colluvium, minerals including illite, kaolinite, muscovite and orthoclase were possible hosts (Table 4.14). Lead, Sr and Cu are elevated in the colluvium (Figure 4.12), therefore it could be implied that there has been enrichment of these elements by weathering in the landscape. Therefore, these three elements may have been adsorbed to other Al-, K- and Na- rich minerals such as illite, kaolinite, muscovite or orthoclase within the colluvium (Table 4.6 and Table 4.11) Cobalt and Sc also have deportment inferred for both lithologies with these pathfinders as hematite at Peterlumbo Hill but possibly illite, kaolinite, microcline, muscovite, orthoclase and hematite in the colluvium. Nickel and Cu have relationships with MgO and CaO indicating they are likely hosted within calcite or dolomite in the colluvium (Table 4.11). As hematite is a resistive mineral (e.g. McQueen 2009), it would be expected that it would remain in the landscape and potentially contain greater concentrations of pathfinder elements. It could also be suggested that moderate relationships of Ni, Co and Sc with Al_2O_3, K_2O and Na_2O (Table 4.8) meant that these elements were also hosted in other minerals that were more susceptible to weathering.

Caesium, Ta and W are all depleted in the colluvium and the only element with deportment inferred for both Peterlumbo Hill and its colluvium is Cs. It is suggested that Cs was hosted in microcline at Peterlumbo Hill and potentially within microcline, kaolinite, illite, muscovite, orthoclase, albite, calcite or dolomite in the colluvium based on the correlation of Cs with K_2O, Al_2O_3, MgO and Na_2O (Table 4.11). The variability of deportment indicates that microcline was weathered at Peterlumbo Hill and dispersed Cs considering the depletion of this element in the colluvium (Figure 4.12). The inferred deportment of W is only at Peterlumbo Hill with microcline (Table 4.11). From the lack of possible mineralogical deportment within the colluvium, it may be inferred that this mineral was susceptible to weathering and the pathfinders hosted by this mineral were dispersed into the landscape, indicating that there is limited W within the colluvium around Peterlumbo Hill. This interpretation corresponds with the depleted concentration of W in the colluvium (Figure 4.12). The inferred mineralogical host of Ta within the colluvium is hematite (Table 4.11). As there are no strong correlations between Ta and any minerals in the Peterlumbo Hill lithology (Table 4.8), it is not possible to suggest any processes that possibly led to the depletion of Ta in the colluvium.

4.4.4.3 Gawler Range Volcanics

There is a decrease in the average concentration of all major elements for GRV Rock and GRV Colluvial but an increase in SiO_2 which is attributed to the increase of quartz in this lithology (Table 4.3; Table 4.6). GRV Colluvial contains noticeably less albite, microcline and orthoclase and contains no calcite, chamosite or oligoclase (Table 4.6). Across the GRV Colluvial lithology, there are lower concentrations

of all major elements apart from SiO_2 as compared to GRV Rock (Table 4.3) likely due to the increased quartz content in this lithology as it is resistive to weathering (Eggleton *et al.* 2001). Although there is less Al_2O_3 in the GRV Colluvial lithology compared to GRV Rock (Table 4.3), the proportion of Al_2O_3 for GRV Colluvial increases due to the weathering of GRV Rock (Nesbitt and Young 1984) (Figure 4.5). Feldspars are present in the GRV Colluvial lithology but in reduced concentrations compared to GRV Rock, as they are known to weather to kaolinite equating to lower concentrations of K_2O and Na_2O in the colluvium (Table 4.3; Table 4.6) (Anand 2005).

Arsenic, Ni, Bi, Sb, Co, Cs and Cu are elevated in GRV Colluvial compared to the rock exposure (Figure 4.13). Not all of these elevated pathfinders have clear mineralogical deportment, with potential hosts for Ni, Co and Sb identified in both the GRV Rock and colluvium. Within GRV Rock, Ni and Co were suggested to be within hematite or chamosite and Sb was possibly hosted in minerals such as microcline, muscovite and orthoclase (Table 4.9). In the colluvium, Ni and Co are inferred to be hosted within phengite and Sb in hematite (Table 4.12). Chamosite is known to weather to kaolinite (Anand 2005) and it is possible that this process led to the dispersion of both Ni and Co and their enrichment in the colluvium (Figure 4.13). The composition of chamosite can vary and include other major elements such as Mg, Mn and Cr (e.g. Deer *et al.* 2013) and as the association between Ni, Co and MgO is notable in the colluvium (Table 4.9), it is possible that Ni and Co have a preferable association with minerals containing MgO. This could be related to re-adsorption of these pathfinders with phengite in the colluvium. Weathering of microcline, muscovite and orthoclase from GRV Rock has allowed for distribution of Sb and re-adsorption of this element with hematite, which is known to be a relatively resistive mineral.

Arsenic, Cs and Cu had mineralogical hosts including hematite and kaolinite inferred in the colluvium. This is not unexpected as kaolinite and hematite are two main components of surface soil material (e.g. Anand 2005). Consequently, these pathfinders are elevated in the colluvium compared to GRV Rock (Figure 4.13). Although most pathfinders have had their mineralogical deportment interpreted, Bi does not have any strong major element relationships for GRV Rock (Table 4.9) and is only associated with MgO in colluvium (Table 4.12). From the mineralogy identified in this landscape, it cannot be determined which mineral may host Bi, and hence the method by which it is enriched within the colluvium. It is possible that other surface material has influenced the concentration of Bi in the GRV Colluvial lithology.

There are some interesting pathfinders present within GRV Rock (Sn, Ta, Pb, Mo and In) (Figure 4.9) but this is overwhelmed by the significant concentrations of REEs in the lithology (Figure 4.8). The colluvium contains higher concentrations of pathfinder elements than GRV Rock and Bi, Pb, Sn, As, Ta and Sb are above the 0.75 x UCC threshold defined for cover sequence materials. Therefore, it can be

said that there is some influence of the pathfinder elements within GRV Rock but the rock exposures are not visibly altered and these are in small concentrations. GRV Rock has very different composition and protolith which has likely led to the difference in alteration expression between GRV Rock and Nankivel and Peterlumbo Hills.

4.4.4.4 Distal Soils

Distal soils contain the largest proportion of kaolinite, hematite and phengite across all lithologies and uniquely contains phlogopite (Table 4.6). There are limited correlations for pathfinder elements in this lithology, Cs, Sc and Co suggested to be hosted within hematite, kaolinite, phengite or phlogopite (Table 4.13). This lithology is focused primarily in the south of the study area with some samples in the north of the area near GRV Rock and colluvium (Figure 4.1). It is expected that there would be some influence from these other lithological materials on the mineralogy and geochemistry of the Soil lithology. The proximity to the GRV likely explains the presence of albite, and oligoclase as Na-rich mineralogy are primarily associated with the GRV lithologies (Table 4.6). This could indicate material from GRV Colluvial has been transported, predominantly in the north of the study area. The presence of phengite is also potentially associated with GRV Colluvial but also may be related to Nankivel Hill colluvium and Peterlumbo Hill (Table 4.6) as there were a limited number of soil samples close to Nankivel Hill colluvium or Peterlumbo Hill (Figure 4.1). This could indicate either significant transport of phengite, which is somewhat unlikely due to the weathering potential of phengite, or that phengite is a common mineral in the Soil lithology. It is also notable that there are few correlations between pathfinder elements and MgO, this is potentially due to the significant influence of Al- and K-rich minerals on the overall chemistry of the regolith materials (Table 4.6).

4.4.4.5 Overall Effects

Overall, there is no preservation of pathfinder elements from Nankivel or Peterlumbo Hills within its associated colluvium (Figure 4.11 – 4.13). There are pathfinders that are elevated in the colluvium compared to their rock exposures but these are likely due to processes such as weathering and the influence of surrounding materials. There are a number of elevated elements within the colluvium surrounding Nankivel and Peterlumbo Hills that are also elevated in the Soil lithology, suggesting that this would be worth further investigation and interpretation of the source.

This landscape has undergone significant and prolonged weathering based on the kaolinite and quartz rich nature of these soils (Figure 4.6). Samples such as F89 and F104 that contain extremely elevated concentrations of pathfinder elements do not trace their concentrations back to a source such as Nankivel Hill, Peterlumbo Hill or the GRV as they are distant from all of these rock exposures. Sample F21 is

most likely to contain concentrations of Ni, Co, Sc due to its position in the landscape and the weathering processes that have led to the concentration of the minerals hosting these elements.

4.5 Conclusions

Using the known pathfinder element suite, this chapter quantified thresholds to create a region-specific pathfinder suite for epithermal and porphyry Cu-style mineralisation in the Nankivel and Peterlumbo Hills. The pathfinder suite includes elevated Pb, Sn and Ta ± As, Bi, Cs, In, Mo, S, Sb and W and depleted Ni, Co ± Cu, Sc, Sr. Relationships between major and pathfinder elements were determined using the Spearman's Correlation Coefficient and these relationships were related to XRD mineralogy using the major element chemistry, making it possible to suggest which minerals could be hosting pathfinders. Interpreting the variation of mineralogy between rock exposure and colluvial lithologies identified chemical and physical weathering processes occurring at Nankivel and Peterlumbo Hills. It also demonstrated the influence of surrounding soils on the colluvial lithologies with unexpected minerals present in some colluvium. The deportment of pathfinder elements highlighted hematite, kaolinite and phengite as being the main hosts of pathfinder elements in colluvial soils.

4.6 References

Agangi, A. (2011). Magmatic and volcanic evolution of a silicic large igneous province (SLIP): the Gawler Range Volcanics and Hiltaba Suite, South Australia. *PhD Thesis (Unpublished),* University of Tasmania

Allen, S.R., & McPhie, J. (2002). The Eucarro Rhyolite, Gawler Range Volcanics, South Australia: A >675 km^3, compositionally zoned lava of Mesoproterozoic age. *Geological Society of America Bulletin, 114*, 1592-1609

Allen, S.R., Simpson, C.J., McPhie, J., & Daly, S.J. (2003). Stratigraphy, distribution and geochemistry of widespread felsic volcanic units in the Mesoproterozoic Gawler Range Volcanics, South Australia. *Australian Journal of Earth Sciences, 50*, 97-112. doi: 10.1046/j.1440-0952.2003.00980.x

Anand, R.R. (2005). Weathering history, landscape evolution and implications for exploration. In R.R. Anand, & P. De Broekert (Eds.), *Regolith Landscape Evolution Across Australia: A Compilation of Regolith Landscape Case Studies With Regolith Landscape Evolution Models* (pp. 2-40): CRC LEME. ISBN: 978-1-92-103928-7

Anand, R.R., & Butt, C.R.M. (2010). A guide for mineral exploration through the regolith in the Yilgarn Craton, Western Australia. *Australian Journal of Earth Sciences, 57*, 1015-1114. doi: 10.1080/08120099.2010.522823

Anand, R.R., Fraser, S.J., Jones, M.R., Shu, L., Munday, T.J., Phang, C., Robertson, I.D.M., Scott, K.M., Vasconcelos, P., Wildman, J.E., & Wilford, J. (2002). Geochemical exploration in regolith-dominated terrain, North Queensland: CRC LEME. Document Number: Open File Report 120

Anand, R.R., Hough, R.M., Salama, W., Aspandiar, M.F., Butt, C.R.M., González-Álvarez, I., & Metelka, V. (2019). Gold and pathfinder elements in ferricrete gold deposits of the Yilgarn Craton of Western Australia: A review with new concepts. *Ore Geology Reviews, 104*, 294-355. doi: 10.1016/j.oregeorev.2018.11.003

Anand, R.R., & Paine, M. (2002). Regolith geology of the Yilgarn Craton, Western Australia: implications for exploration. *Australian Journal of Earth Sciences, 49*, 3-162. doi: 10.1046/j.1440-0952.2002.00912.x

Anand, R.R., Wildman, J.E., Varga, Z.S., & Phang, C. (2001). Regolith evolution and geochemical dispersion in transported and residual regolith–Bronzewing gold deposit. *Geochemistry: Exploration, Environment, Analysis, 1*, 265-276. doi: 10.1144/geochem.1.3.265

Baudet, E., Giles, D., Tiddy, C., Asamoah, R., & Hill, S. (2020). Mineralogy as a proxy to characterise geochemical dispersion processes: A study from the Eromanga Basin over the Prominent Hill IOCG deposit, South Australia. *Journal of Geochemical Exploration, 210*, 106447. doi: 10.1016/j.gexplo.2019.106447

Baudet, E., Giles, D., Tiddy, C., & Hill, S. (2018). Evaluation of cover sequence geochemical exploration sample media through assessment of element migration processes. *Ore Geology Reviews, 102*, 449-473. doi: 10.1016/j.oregeorev.2018.09.017

Betts, P.G., Giles, D., Schaefer, B.F., & Mark, G. (2007). 1600–1500 Ma hotspot track in eastern Australia: implications for Mesoproterozoic continental reconstructions. *Terra Nova, 19*, 496-501. doi: 10.1111/j.1365-3121.2007.00778.x

Blissett, A.H., Parker, A.J., Crooks, A.F., Allen, S.R., Simpson, C.J., McPhie, J., Daly, S.J., Benbow, M.C., Giles, C.W., Ambrose, G.J., McAvaney, S.O., Wade, C.E., & Cowley, W.M. (2017). *Buckleboo*. Adelaide, South Australia: Geological Survey of South Australia

Butt, C.R.M., Lintern, M.J., & Anand, R.R. (2000). Evolution of regoliths and landscapes in deeply weathered terrain - implications for geochemical exploration. *Ore Geology Reviews, 16*, 167-183. doi: 10.1016/s0169-1368(99)00029-3

Dart, R.C., Barovich, K.M., Hill, S.M., & Chittleborough, D.J. (2012). Sr-isotopes as a tracer of Ca sources and mobility in profiles hosting regolith carbonates from southern Australia. *Australian Journal of Earth Sciences, 59*, 373-382. doi: 10.1080/08120099.2012.662912

de Caritat, P., Main, P.T., Grunsky, E.C., & Mann, A.W. (2016). Recognition of geochemical footprints of mineral systems in the regolith at regional to continental scales. *Australian Journal of Earth Sciences*, 1-11. doi: 10.1080/08120099.2017.1259184

Deer, W.A., Howie, R.A., & Zussman, J. (Eds.) (2013). *An introduction to the Rock-Forming Minerals*. London: The Mineralogical Society. ISBN: 978-0-90-305633-5

Droubay, T., Rosso, K.M., Heald, S.M., McCready, D.E., Wang, C.M., & Chambers, S.A. (2007). Structure, magnetism, and conductivity in epitaxial Ti-doped α-Fe_2O_3 hematite: Experiment and density functional theory calculations. *Physical Review B, 75*, 104412. doi: 10.1103/PhysRevB.75.104412

Duuring, P., Hassan, L., Zelic, M., & Gessner, K. (2016). Geochemical and Spectral Footprint of Metamorphosed and Deformed VMS-Style Mineralization in the Quinns District, Yilgarn Craton, Western Australia. *Economic Geology, 111*, 1411-1438. doi: 10.2113/econgeo.111.6.1411

Eberl, D.D. (2003). User's Guide to RockJock - A program for determining quantitative mineralogy from powder X-Ray Diffraction data. Boulder, Colorado: United States Geological Survey. United States Geological Survey. Document Number: Open File Report 03-78

Eggleton, R.A., Anand, R.R., Butt, C.R.M., Chen, X.Y., Craig, M.A., de Caritat, P., Field, J.B., Gibson, D.L., Greene, R., Hill, S.M., Jones, M., Lintern, M.J., McQueen, K.G., Pain, C.F., Pillans, B.J., Robertson, I.D.M., Smith, K., & Taylor, G.F. (Eds.) (2001). *The Regolith Glossary: surficial geology, soils and landscapes*. Perth, Australia: CRC LEME. ISBN: 978-0-73-153343-5

Fabris, A.J., Halley, S., van der Wielen, S., Keeping, T., & Gordon, G. (2013). IOCG-style mineralisation in the central eastern Gawler Craton, SA; characterisation of alteration, geochemical associations and exploration vectors. Adelaide, South Australia: Department of Manufacturing, Innovation, Trade, Resources and Energy. Geological Survey of South Australia. Document Number: Report Book 2013/0014

Forbes, C., Giles, D., Freeman, H., Sawyer, M., & Normington, V. (2015). Glacial dispersion of hydrothermal monazite in the Prominent Hill deposit: An exploration tool. *Journal of Geochemical Exploration, 156*, 10-33. doi: 10.1016/j.gexplo.2015.04.011

González-Álvarez, I., Salama, W., Hilliard, P., Ibrahimi, T., LeGras, M., & Rondon-Gonzalez, O. (2019). Landscape evolution and geochemical dispersion of the DeGrussa Cu-Au deposit, Western Australia. *Ore Geology Reviews, 105*, 487-513. doi: 10.1016/j.oregeorev.2018.12.008

Haest, M., Cudahy, T., Laukamp, C., & Gregory, S. (2012). Quantitative Mineralogy from Infrared Spectroscopic Data. II. Three-Dimensional Mineralogical Characterization of the Rocklea Channel Iron Deposit, Western Australia. *Economic Geology, 107*, 229-249. doi: 10.2113/econgeo.107.2.229

Halley, S., Dilles, J., & Tosdal, R. (2015). Footprints: hydrothermal alteration and geochemical dispersion around porphyry copper deposits. *Society of Economic Geologists Newsletter, 100*, 12-17

Hill, R.L. (2015). Lithogeochemical characterisation of cover sequence on Yorke Peninsula, South Australia, and identification of pathfinder elements for IOCG exploration. *Honours Thesis (Unpublished),* University of Adelaide

IMDEX, (2019). ioGAS 7.1

Jagodzinski, E. (1985). The geology of the Gawler Range volcanics in the Toondulya Bluff area and U-Pb dating of the Yardea Dacite at Lake Acraman. *Honours Thesis (Unpublished)*, University of Adelaide

Le Maitre, R.W., Streckeisen, A., Zanettin, B., Le Bas, M.J., Bonin, B., Bateman, P., Bellieni, G., Dudek, A., Efremova, S., Keller, J., Lameyre, J., Sabine, P.A., Schmid, R., Sørensen, H., & Woolley, A.R. (2002). Igneous Rocks: A Classification and Glossary of Terms. Cambridge, United Kingdom: Cambridge University Press. ISBN: 978-1-13-914621-0

Li, W., Liang, X., An, P., Feng, X., Tan, W., Qiu, G., Yin, H., & Liu, F. (2016). Mechanisms on the morphology variation of hematite crystals by Al substitution: The modification of Fe and O reticular densities. *Scientific Reports, 6*, 35960. doi: 10.1038/srep35960

Mann, A.W., Birrell, R.D., Mann, A.T., Humphreys, D.B., & Perdrix, J.L. (1998). Application of the mobile metal ion technique to routine geochemical exploration. *Journal of Geochemical Exploration, 61*, 87-102. doi: 10.1016/s0375-6742(97)00037-x

McQueen, K.G. (2009). Regolith geochemistry. In K.M. Scott, & C.F. Pain (Eds.), *Regolith Science* (pp. 103-145): CSIRO Publishing. ISBN: 978-0-64-309826-8

Nesbitt, H.W., & Young, G.M. (1984). Prediction of some weathering trends of plutonic and volcanic rocks based on thermodynamic and kinetic considerations. *Geochimica et Cosmochimica Acta, 48*, 1523-1534. doi: 10.1016/0016-7037(84)90408-3

Nesbitt, H.W., & Young, G.M. (1989). Formation and Diagenesis of Weathering Profiles. *The Journal of Geology, 97*, 129-147. doi: 10.1086/629290

Nicolson, B., Reid, A., McAvaney, S., Keeling, J., Fraser, G., & Vasconcelos, P. (2017). A Mesoproterozoic advanced argillic alteration system: $^{40}Ar/^{39}Ar$ thermochronology from Nankivel Hill, Gawler Craton. Adelaide, South Australia: Department of Premier and Cabinet. Geological Survey of South Australia. Document Number: Report Book 2017/00011

Paul, M.W., Cook, N.J., Ciobanu, C.L., Anderson, J., & Murray, J. (2015). Preliminary mineralogical investigations of the Paris silver deposit, northern Eyre Peninsula, South Australia. In, *Society for Geology Applied to Mineral Deposits 13th Biennial Meeting* (pp. 181-184). Nancy, France: Society for Geology Applied to Mineral Deposits

Pollard, P.J. (2000). Evidence of a magmatic fluid and metal source for Iron oxide-Cu-Au mineralisation. In T.M. Porter (Ed.), *Hydrothermal Iron Oxide Copper-Gold and Related Deposits: A Global Perspective* (pp. 27-41). Adelaide, Australia: Porter GeoConsultancy Publishing. ISBN: 978-0-95-805740-0

Reimann, C. (2005). Geochemical mapping: technique or art? *Geochemistry: Exploration, Environment, Analysis, 5*, 359-370. doi: 10.1144/1467-7873/03-051

Roache, M.W. (1996). The geology, timing of mineralisation, and genesis of the Menninnie Dam Zn-Pb-Ag deposit, Eyre Peninsula, South Australia. *PhD Thesis (Unpublished),* University of Tasmania

Rudnick, R.L., & Gao, S. (2003). Composition of the Continental Crust. In R.L. Rudnick (Ed.), *Treatise on Geochemistry, Volume 3: The Crust* (pp. 1-64). Oxford, UK: Elsevier - Pergamon. ISBN: 978-0-08-044847-3

Salama, W., Anand, R.R., & Verrall, M. (2016). Mineral exploration and basement mapping in areas of deep transported cover using indicator heavy minerals and paleoredox fronts, Yilgarn Craton, Western Australia. *Ore Geology Reviews, 72*, 485-509. doi: 10.1016/j.oregeorev.2015.07.014

Scott, A.D., & Smith, S.J. (1987). Sources, Amounts and Forms of Alkali Elements in Soils. In B.A. Stewart (Ed.), *Advances in Soil Science* (pp. 101-147). New York, USA: Springer-Verlag. ISBN: 978-1-46-129112-1

Scott, K.M., & Howard, R.W. (2001). Hydrothermal alteration and geochemical dispersion in the regolith at Panglo, Eastern Goldfields, Western Australia. *Geochemistry: Exploration, Environment, Analysis, 1*, 313-322. doi: 10.1144/geochem.1.4.313

Spearman, C. (1904). The proof and measurement of association between two things. *The American Journal of Psychology, 15*, 72-101. doi: 10.2307/1412159

Stewart, K.P. (1994). High temperature felsic volcanism and the role of mantle magmas in Proterozoic crustal growth: The Gawler Range Volcanic Province. *PhD Thesis (Unpublished),* University of Adelaide

Tiddy, C.J., Hill, S.M., Giles, D., van der Hoek, B.G., Normington, V.J., Anand, R.R., Baudet, E., Custance, K., Hill, R., Johnson, A., McLennan, S., Mitchell, C., Zivak, D., Salama, W., Stoate, K., & Wolff, K. (2019). Utilising geochemical data for the identification and characterisation of mineral exploration sample media within cover sequence materials. *Australian Journal of Earth Sciences*, 1-29. doi: 10.1080/08120099.2019.1673484

Wade, C.E., McAvaney, S.O., Gordon, G.A., & Keeling, J.L. (2014). Epithermal-style textures, brecciation, veining and alteration, southern Gawler Ranges margin, South Australia. Adelaide, South Australia: Department of State Development. Geological Survey of South Australia. Document Number: Report Book 2014/00009

Wolff, K., Tiddy, C., Giles, D., & Hill, S.M. (2018). Pedogenic carbonate sampling for Cu exploration on the Yorke Peninsula, South Australia. *Journal of Geochemical Exploration, 194*, 239-256. doi: 10.1016/j.gexplo.2018.08.007

Chapter 5

INTEGRATING SOIL GEOCHEMISTRY, HYPERSPECTRAL MINERALOGY AND OBJECTIVE REGOLITH - LANDFORM MAPPING

5.1 Introduction

Sources of information that can be integrated to assist mineral exploration include geophysics, geochemistry, mineralogy and remote sensing (e.g. Schodde 2017; Hollis *et al.* 2019). In areas with surface geological exposures, multispectral remote sensing can provide interpretation of the regional landscape and the potential alteration mineralogy present in these exposures (e.g. Abrams *et al.* 1983; Duuring *et al.* 2012; Lampinen *et al.* 2017). However a majority of basement rock in Australia is covered by highly weathered regolith dominated terrains (RDTs) that provide a challenge for ongoing mineral exploration (e.g. Hillis *et al.* 2014). Remotely sensed products have also been useful for identifying variations of regolith in a landscape (e.g. Craig 2001; Mulder *et al.* 2011; Caruso *et al.* 2018).

It is well known that regolith profiles can preserve signatures of primary and secondary geochemical dispersion of bedrock or buried ore deposits (Aspandiar *et al.* 2008; Morris 2013; González-Álvarez *et al.* 2016; Anand *et al.* 2019). There has been extensive use of the regolith profile for geochemical sampling, with exploration generally targeting a specific horizon for the most favourable results (e.g. Salama *et al.* 2016). However, the top of regolith profiles has been used to identify surface expressions of buried mineralisation (de Caritat *et al.* 2016). A majority of lateral pathfinder distribution research is generally at depth using high resolution drill core data (e.g. Fabris *et al.* 2013; Halley *et al.* 2015; Baudet *et al.* 2018).

The aim of this chapter is to map the surface expression of geochemical and mineralogical signatures that may potentially be related to buried mineralisation in the southern Gawler Ranges through integration of results from previous chapters including objective regolith-landform mapping, hyperspectral alteration mapping, geochemistry and mineralogy. The landscape processes resulting in signature dispersion in this region and the impact on future mineral exploration sampling is then discussed. Background geology for the study area is given in Chapter 1.

5.2 Methodology

Surface expressions of geochemical and mineralogical signatures that may be related to buried mineralisation were examined by integrating objective regolith-landform mapping (Chapter 2), hyperspectral alteration mapping (Chapter 3) and assessment of the spatial distribution of pathfinder geochemistry (Chapter 4). Detailed methodology for generation of these data sets are given in the previous chapters.

5.2.1 Geochemical Data

Geochemical analysis was conducted on 57 rock exposure and soil samples collected during field work in 2017, the specific details of this analysis and interpretation is described in Chapter 4.

5.2.1.1 Distribution of Pathfinder Elements

The spatial distribution of pathfinder elements was assessed in relation to the hyperspectral alteration mapping to characterise a potential mineralogical and geochemical footprint of buried porphyry mineralisation. The distribution of pathfinder elements in relation to objective regolith-landform mapping was also used to interpret landscape processes and potential benefit for future geochemical sampling.

5.2.2 Mineralogical Data

5.2.2.1 Hyperspectral Alteration Mineral Mapping

Hyperspectral imagery was collected by HyVista Corporation in 2011 for the South Australian Geological Survey. The HyMap sensor obtained ten swaths of imagery, each approximately 2.5 km wide which when mosaicked, covered the extent of this study at 415 km^2 (Hussey 2015) (Figure 5.1). Further information of the configuration, pre-processing and analysis of this hyperspectral imagery can be found in Caruso *et al.* (in review) (Chapter 3). That research produced alteration mineral maps for the different types of alteration related to porphyry mineralisation in this area.

5.2.2.2 X-Ray Diffraction

Semi-quantitative X-ray diffraction (XRD) analysis was conducted on 57 field rock and soil samples from the study area (Caruso *et al.* in review) (Chapter 3). This analysis identified mineralogy somewhat consistent with the advanced argillic alteration style at Nankivel Hill, with the presence of alunite, pyrophyllite and dickite in some samples. It also assisted with landscape process interpretation by examining the mineralogical composition of rock and soil samples. Further interpretation and validation of mineralogy is presented in Chapters 3 and 4 with raw qualitative and semi-quantitative data available in Appendices A and B.

5.2.3 Geospatial Data

Chapter 2 used three freely available remotely sensed and geospatial products to create a regional objective regolith-landform map over an area of 3866 km^2 (Figure 5.1). This area is substantially larger than the study area for this chapter and was selected to demonstrate the potential use of these methods in a regional setting.

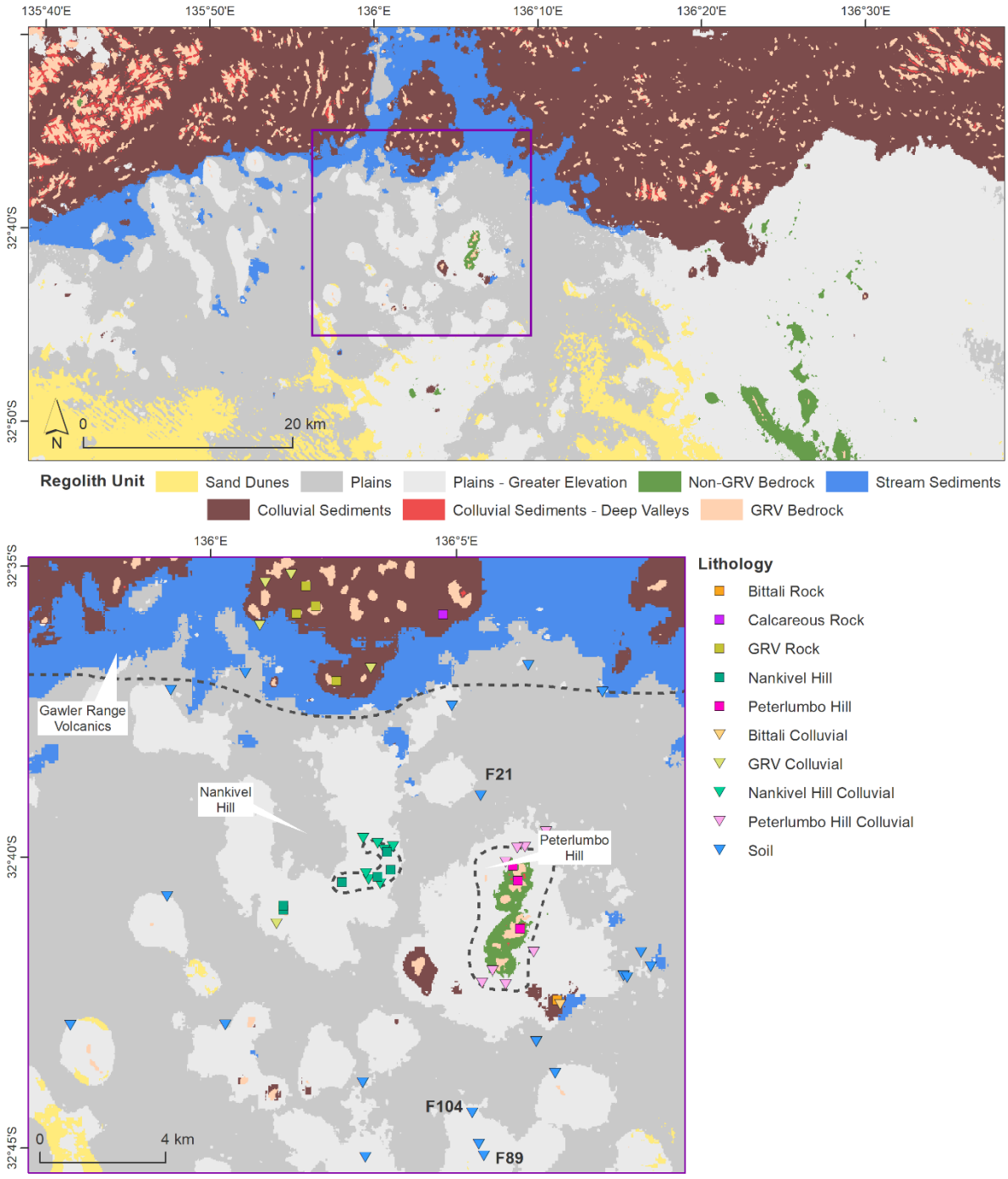

Figure 5.1: Top - Objective regolith landform map illustrating extent of the study area for this chapter, modified from Caruso *et al.* (2018); Bottom - The study area for this chapter with sample points delineated by lithology defined in Chapter 4; black lines indicate major landscape features.

5.3 Results

5.3.1 Major Elements

The variation of the major element chemistry for each regolith-landform unit can be seen in Figure 5.2 and Table 5.1. Colluvial Sediments contains a range of Al_2O_3 and CaO + Na_2O concentrations from 40 – 70 wt% and 10 – 60 wt% respectively while K_2O remains relatively consistent at 30 – 40 wt%, excluding one sample with very little K_2O (Figure 5.2A). The three GRV Bedrock samples contain 20 – 30 wt% K_2O, 50 – 67 wt% Al_2O_3 and 5 – 30 wt% CaO + Na_2O (Figure 5.2A). Non-GRV Bedrock contains limited range of Al_2O_3 at 75 wt%, CaO + Na_2O at 5 wt% and between 29 – 35 wt% K_2O. The Plains unit contains a wide range of Al_2O_3 from 30 – 90 wt%, CaO + Na_2O from 0 – 60 wt% but a limited range of K_2O concentrations of 0 – 30 wt% (Figure 5.2A). Plains – Greater Elevation has a similar range of major elements to the Plains unit but contains more samples with variable K_2O concentrations (Figure 5.2A).

Figure 5.2B shows the variation of Al_2O_3 at 25 – 75 wt%, CaO + Na_2O + K_2O at 8 – 50 wt% for the Plains unit, while FeO + MgO is generally consistent (20 – 30 wt%) with some samples ranging from 10 – 20 wt% and one sample at approximately 70 wt% FeO + MgO. Plains – Greater Elevation contains similar concentrations as the Plains unit, although a smaller range of Al_2O_3 concentrations (25 – 50 wt%) (Figure 5.2B). Non-GRV Bedrock has high Al_2O_3 concentrations of 55 – 70 wt% with low to moderate concentrations of both CaO + Na_2O + K_2O and FeO + MgO of approximately 20 wt% and 10 – 25 wt% respectively (Figure 5.2B). GRV Bedrock has a range of Al_2O_3 concentrations of 37 – 50 wt%, CaO + Na_2O + K_2O concentrations of 25 – 40 wt% but similar concentrations for FeO + MgO of 20 – 30 wt% (Figure 5.2B). The Colluvial Sediments have a wider range of Al_2O_3 and CaO +Na_2O + K_2O compared to GRV Bedrock (30 – 50 wt%, 20 – 50 wt%) but a similar range of FeO + MgO concentrations at 17 – 30 wt% (Figure 5.2B). Overall, the greatest variation of major element geochemistry is within the Plains unit (Figure 5.2).

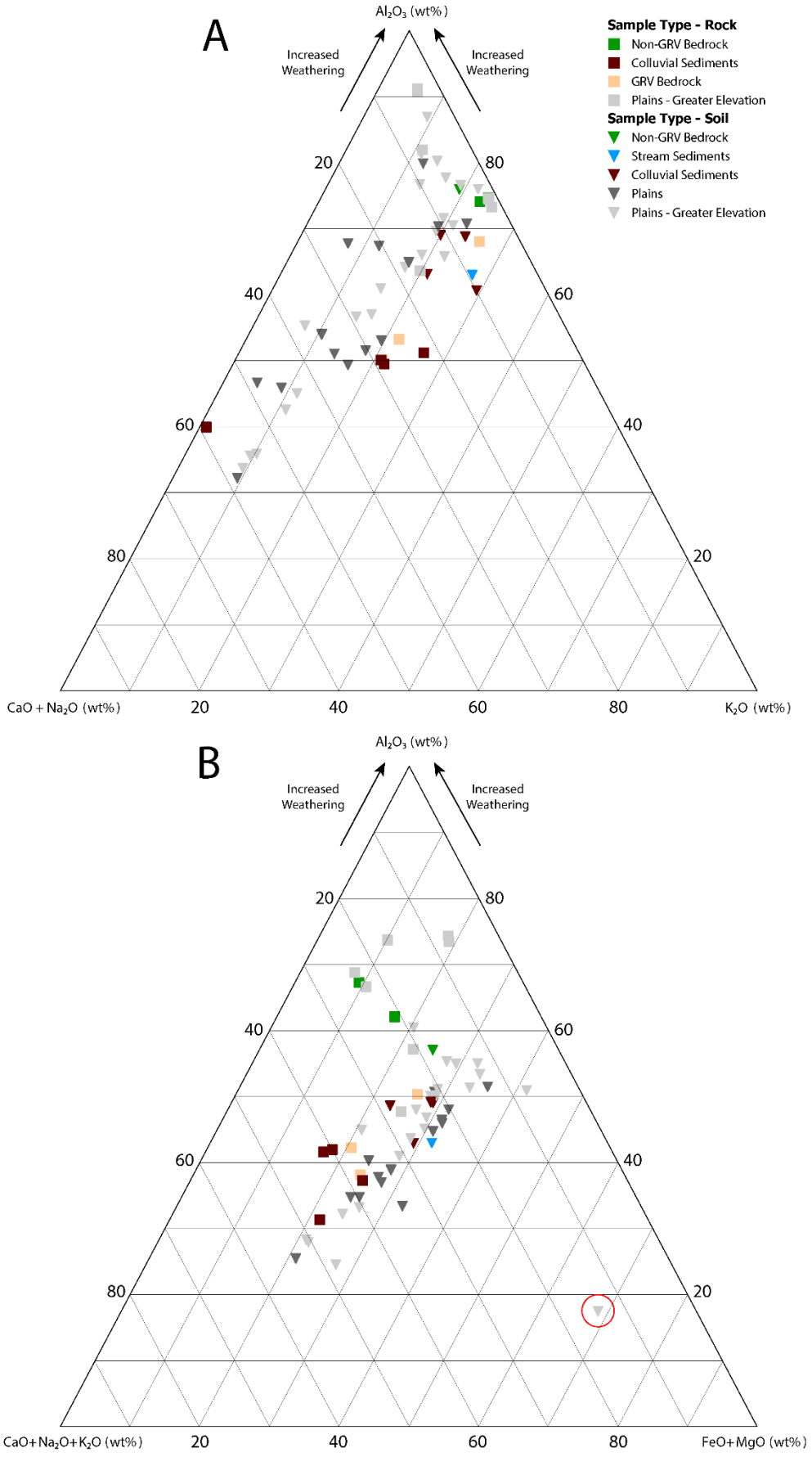

Figure 5.2: A: A-CN-K, B: A-CNK-FM diagram both defined by (Nesbitt and Young 1984, 1989). Red circle highlights sample F89.

Table 5.1: Summary statistics of major elements for objective regolith-landform units.

Objective Regolith-Landform Unit and Statistic, N = 59	**SiO_2 (%)**	**TiO_2 (%)**	**Al_2O_3 (%)**	**Fe_2O_3 (%)**	**MnO (%)**	**MgO (%)**	**CaO (%)**	**Na_2O (%)**	**K_2O (%)**	**P_2O_5 (%)**
GRV Bedrock: Minimum (*n* = 3)	66.53	0.09	1.78	0.66	0.00	0.03	0.07	0.63	0.02	0.01
GRV Bedrock: Maximum	94.34	0.66	13.37	4.99	0.10	0.57	1.33	5.10	2.85	0.15
GRV Bedrock: Mean	76.37	0.46	9.19	3.39	0.06	0.30	0.86	3.52	1.78	0.10
GRV Bedrock: Median	68.24	0.62	12.44	4.52	0.07	0.29	1.17	4.84	2.48	0.14
GRV Bedrock: Standard Deviation	15.59	0.32	6.44	2.38	0.05	0.27	0.69	2.51	1.54	0.08
Non-GRV Bedrock: Minimum (*n* = 3)	80.65	0.14	5.64	0.94	0.01	0.06	0.02	1.32	0.03	0.01
Non-GRV Bedrock: Maximum	93.06	0.24	9.86	1.60	0.02	0.17	0.10	2.85	0.20	0.03
Non-GRV Bedrock: Mean	85.86	0.18	7.09	1.20	0.01	0.10	0.05	1.96	0.11	0.02
Non-GRV Bedrock: Median	83.86	0.17	5.76	1.06	0.01	0.09	0.03	1.71	0.10	0.02
Non-GRV Bedrock: Standard Deviation	6.44	0.05	2.40	0.35	0.01	0.06	0.05	0.79	0.09	0.01
Plains: Minimum (*n* = 15)	62.47	0.19	4.61	1.80	0.01	0.15	0.07	0.81	0.09	0.02
Plains: Maximum	89.42	0.50	12.62	5.10	0.05	1.25	8.06	2.62	1.42	0.06
Plains: Mean	74.63	0.35	8.03	3.22	0.03	0.66	2.41	1.68	0.30	0.04
Plains: Median	72.95	0.34	8.35	3.53	0.03	0.68	1.98	1.72	0.17	0.04
Plains: Standard Deviation	7.64	0.09	2.04	0.98	0.01	0.29	2.06	0.48	0.34	0.01
Plains - Greater Elevation: Minimum (*n* = 29)	54.77	0.06	4.08	0.73	0.00	0.02	0.05	0.43	0.05	0.02
Plains - Greater Elevation: Maximum	91.13	0.43	14.28	23.16	0.07	0.93	6.06	4.24	0.67	0.20
Plains - Greater Elevation: Mean	77.83	0.27	8.16	2.97	0.02	0.43	1.27	1.80	0.16	0.06
Plains - Greater Elevation: Median	79.80	0.27	6.97	2.23	0.02	0.39	0.34	1.66	0.14	0.04
Plains - Greater Elevation: Standard Deviation	7.82	0.09	3.08	3.93	0.01	0.26	1.77	1.01	0.12	0.05
Colluvial Sediments: Minimum (*n* = 8)	44.93	0.30	7.55	2.92	0.01	0.18	0.17	0.34	0.10	0.02
Colluvial Sediments: Maximum	75.30	0.64	15.78	4.99	0.11	2.57	11.97	6.22	3.43	0.16
Colluvial Sediments: Mean	67.12	0.49	12.01	3.82	0.05	0.71	2.19	3.85	1.43	0.07
Colluvial Sediments: Median	71.35	0.52	11.75	3.77	0.05	0.47	0.75	3.43	0.85	0.05
Colluvial Sediments: Standard Deviation	10.18	0.11	2.62	0.68	0.04	0.78	4.00	1.93	1.24	0.06
Stream Sediments (*n* = 1)	81.51	0.34	7.04	3.56	0.02	0.27	0.18	2.85	0.44	0.03

5.3.2 Pathfinder Elements

5.3.2.1 Spatial Distribution of Pathfinders

The pathfinder element suite used here was defined in Chapter 4 and includes elevated Pb, Sn and Ta ± As, Bi, Cs, In, Mo, S, Sb and W and depleted Ni, Co ± Cu, Sc, Sr. The spatial distribution of all pathfinder elements across the study area indicates some key areas with the highest concentrations (Figure 5.3). The Nankivel Hill region accounts for most of the higher concentrations of all pathfinders apart from Ni, Co and Sc (Figure 5.3). Peterlumbo Hill also has high concentrations of Ta, Cs and W (Figure 5.3). One sample north of Peterlumbo Hill (Sample F21) contains high concentrations of Ni, Co, Cu and Sc (Figure 5.3). Elsewhere in the study area, there are moderate to low concentrations of pathfinder elements although there is a sample in the south of the area (Sample F89) that has the highest concentrations of As, Bi, In, Mo, and W and another (Sample F104) that contains high Ni with moderate Bi and S (Figure 5.3).

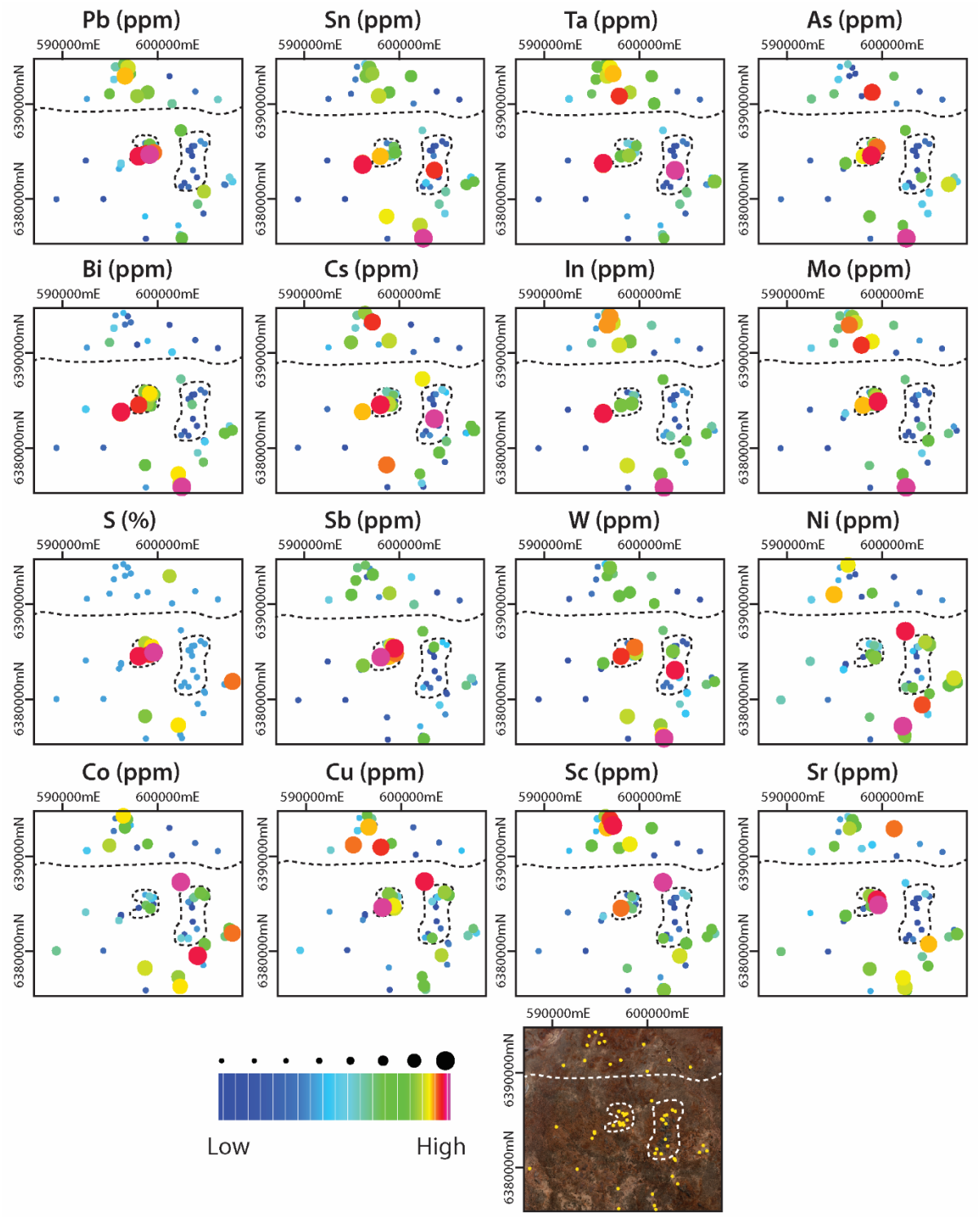

Figure 5.3: Spatial distribution of the pathfinder elements; black lines indicate the main landscape features of Nankivel Hill, Peterlumbo Hill and the Gawler Range Volcanics.

5.3.2.2 Spatial Distribution with Hyperspectral Alteration Mapping

Comparing the spatial distribution of the pathfinder elements with the hyperspectral alteration mineral mapping highlights some co-occurrence between these two data sets. For advanced argillic alteration, the highest concentrations of As are associated with pyrophyllite in the central area of Nankivel Hill (Figure 5.4A). Bismuth has high concentrations on the south western edge of Nankivel Hill and these extend to the south west, but they do not necessarily coincide with any of this mineralogy (Figure 5.4B). The highest values for Cu do not appear to spatially correlate with any of the advanced argillic mineralogy at Nankivel or Peterlumbo Hill (Figure 5.4C). Lead dominates across the southern section of Nankivel Hill and moderate concentrations are somewhat spatially associated with dickite (Figure 5.4D) while Sb is associated with the eastern segment of Nankivel Hill, approximately co-located with pyrophyllite (Figure 5.4E). Moderate concentrations of Cs are associated with the edges of Nankivel Hill but these are not associated with any particular advanced argillic alteration mineralogy (Figure 5.4F). However, there are moderate or high concentrations of Cs and Ta south west of Nankivel Hill that are associated with dickite (Figure 5.4F, G).

Some samples around Peterlumbo Hill contain moderate or high concentrations of Cu but these are not related to advanced argillic alteration mineralogy (Figure 5.4C). Caesium, Ta and W all have higher concentrations associated with dickite at Peterlumbo Hill within one sample (F21) (Figure 5.4F, G, H). The other samples at Peterlumbo Hill and east of Peterlumbo Hill have low concentrations of these elements and have no spatial associations with mineralogy for this alteration style.

For the argillic alteration style, there are spatial relationships of As, Bi and Sb with illite and kaolinite, south west of Nankivel Hill (Figure 5.5A, B, E). High As concentrations are also spatially associated illite at Nankivel Hill (Figure 5.5A). Copper has some spatial association with montmorillonite to the north and on the southern portion of Nankivel Hill (Figure 5.5C). Lead has associations with kaolinite (Figure 5.5D) while Sb is associated with montmorillonite at Nankivel Hill, similar to Cu and Pb. However, the highest concentration of Sb present at Nankivel Hill is spatially associated with kaolinite (Figure 5.5E). Moderate or high concentrations of Cs and Ta are also present at Nankivel Hill: Cs is associated with montmorillonite and illite while Ta is more closely associated with illite and kaolinite (Figure 5.5F, G). Notably, both of these elements contain high concentrations associated with dickite and illite south west of Nankivel Hill (Figure 5.5F, G). High concentrations of W at Nankivel Hill do not directly correlate with any of the argillic alteration minerals, although the low concentrations of this element do appear to correlate with illite (Figure 5.5H). Nickel, Co and Sc do not show any specific associations with the argillic alteration mineralogy (Figure 5.6) but moderate concentrations of Sc are associated with illite at Nankivel Hill (Figure 5.6C).

There is some association of Cu with kaolinite at Peterlumbo Hill, although the samples with high concentrations of Cu north of Peterlumbo Hill are not associated with any particular alteration mineralogy (Figure 5.5C). Caesium, Ta and W all contain moderate to high concentrations at Peterlumbo Hill, within one sample (F21) which has some association with kaolinite (Figure 5.5F, G, H). Some samples to the south east and east of Peterlumbo Hill with moderate concentrations of Cs have some associations with kaolinite (Figure 5.5F). Notable concentrations and associations are present at Peterlumbo Hill for Ni, Co and Sc (Figure 5.6). Sc is somewhat associated with kaolinite at Peterlumbo Hill (Figure 5.6C) while the other moderate or high concentrations are not associated with any particular mineralogy.

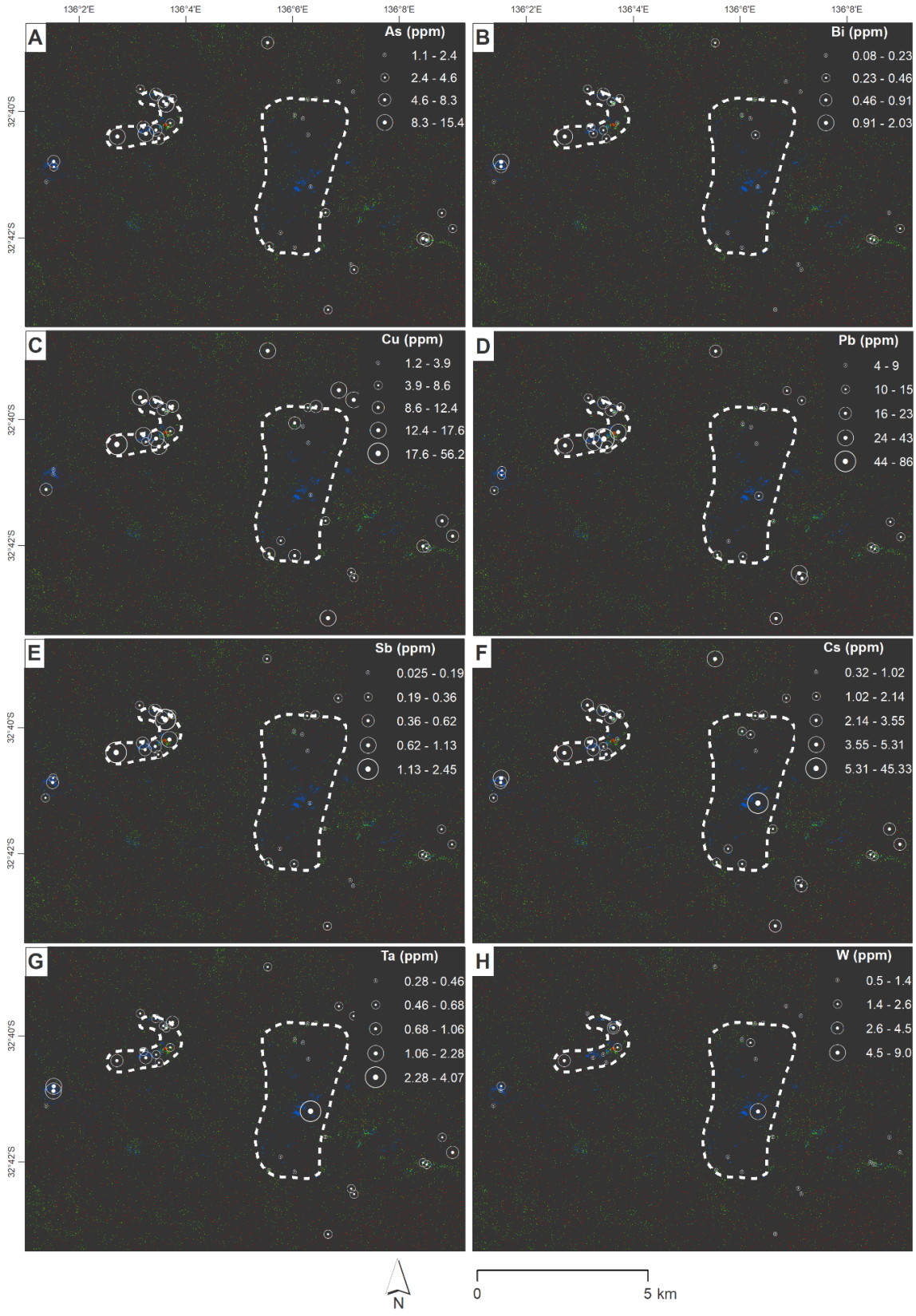

Figure 5.4: Spatial distribution of pathfinder elements at Nankivel and Peterlumbo Hills overlying the advanced argillic alteration mineral mapping from hyperspectral image analysis. A: As (ppm), B: Bi (ppm), C: Cu (ppm), D: Pb (ppm), E: Sb (ppm), F: Cs (ppm), G: Ta (ppm), H: W (ppm). Background image: advanced argillic alteration mineralogy (Red: Alunite, Green: Pyrophyllite, Blue: Dickite), black indicates no minerals present, white outline indicates location of Nankivel and Peterlumbo Hills. Modified from Caruso *et al.* (in review).

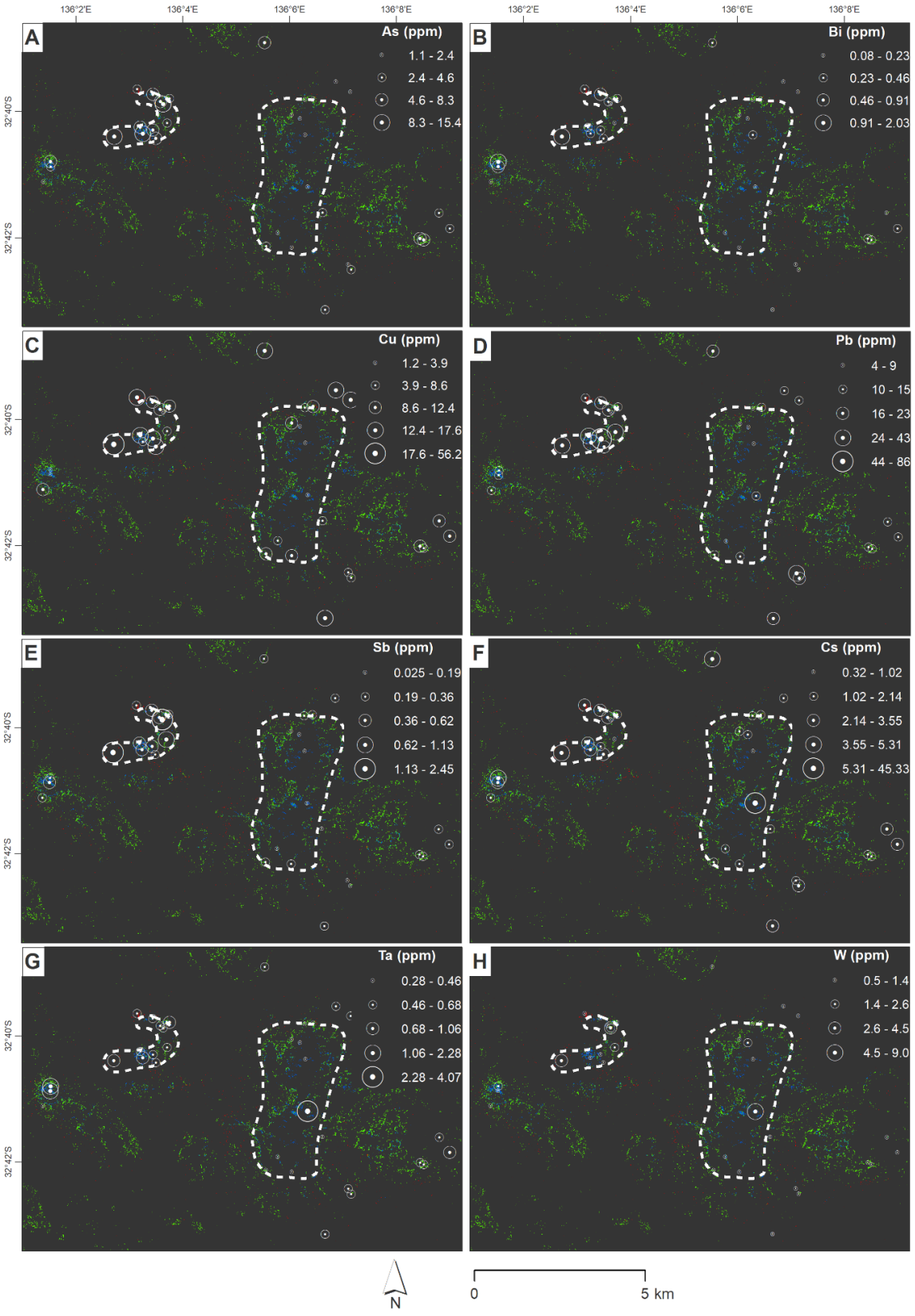

Figure 5.5: Spatial distribution of pathfinder elements at Nankivel and Peterlumbo Hills overlying the advanced argillic alteration mineral mapping from hyperspectral image analysis. A: As (ppm), B: Bi (ppm), C: Cu (ppm), D: Pb (ppm), E: Sb (ppm), F: Cs (ppm), G: Ta (ppm), H: W (ppm). Background image: argillic alteration mineralogy (Red: Montmorillonite, Green: Kaolinite, Blue: Illite), black indicates no minerals present, white outline indicates location of Nankivel and Peterlumbo Hills. Modified from Caruso *et al.* (in review).

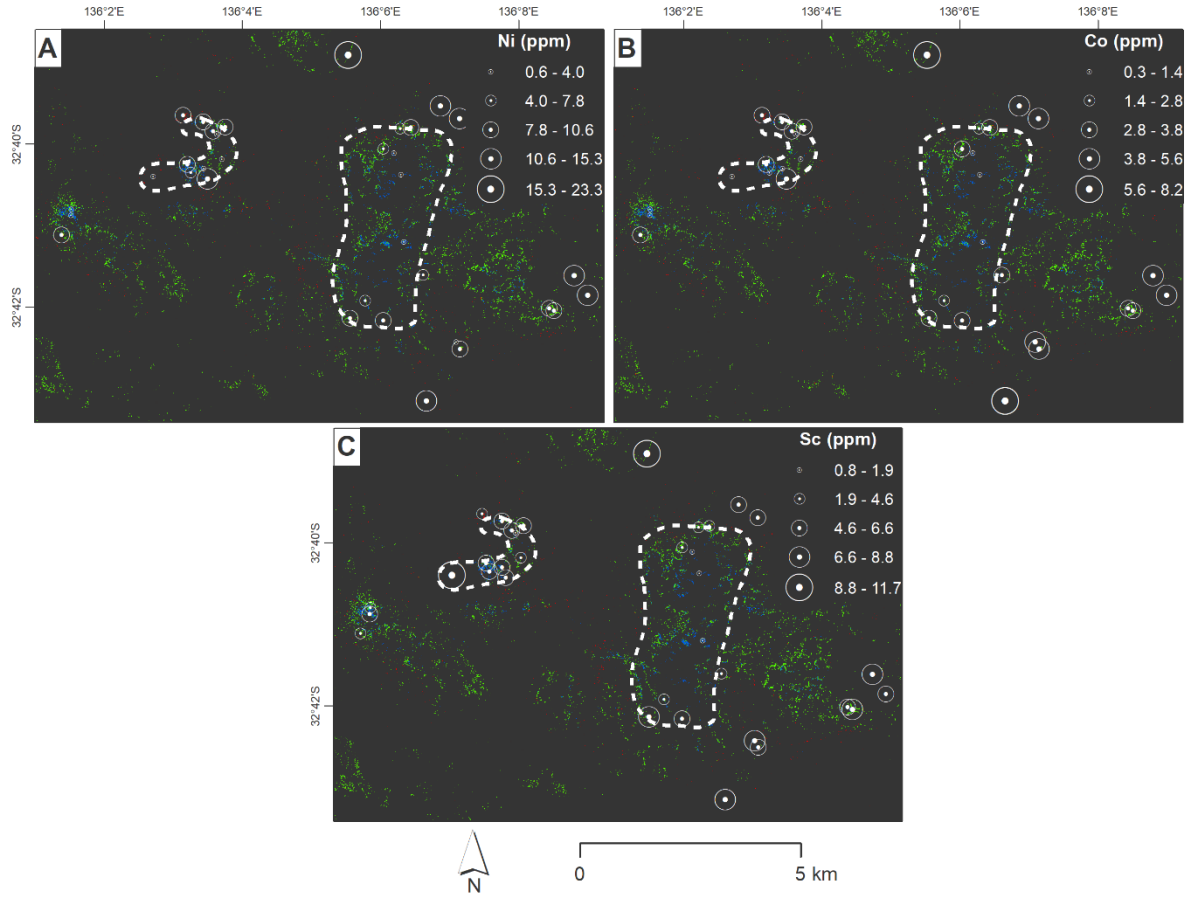

Figure 5.6: Spatial distribution of pathfinder elements at Peterlumbo Hill; pathfinder elements overlie the Argillic Alteration mineral mapping from hyperspectral image analysis. A: Ni (ppm), B: Co (ppm), C: Sc (ppm). Background image: argillic alteration mineralogy (Red: Montmorillonite, Green: Kaolinite, Blue: Illite), black indicates no minerals present, white outline indicates location of Peterlumbo Hill. Modified from Caruso *et al.* (in review).

5.3.2.3 Pathfinder Distribution within Objective Regolith Landform Units

The spatial distribution of the pathfinder elements in the context of the objective regolith-landform map is demonstrated in Figure 5.7. Mean concentrations and summary statistics for these pathfinder elements (Table 5.2 and 5.3) provide an overview of their abundance and distribution within the regolith-landform units.

Patterns emerge for some pathfinder elements across the landscape from Figure 5.7. Across all pathfinder elements, there are similar values for both Plains and Plains – Greater Elevation units with wider ranges of concentrations generally within Plains – Greater Elevation unit (Figure 5.7; Table 5.2 and 5.3). Plains – Greater Elevation contains at least one outlier for most elements (Figure 5.7), and it contains higher mean concentrations of Pb, Sn, Ta, As, Bi, In, Mo, S, Sb, W and Sr compared to the Plains unit (Table 5.2 and 5.3). However, the Plains unit contains higher mean concentrations of Cs, Co, Cu and Sc (Table 5.2 and 5.3). Non-GRV Bedrock contains some of the lowest concentrations of Sn, Ta, As, Bi, In, Mo, Sb, Ni, Co, Cu, Sc and Sr but contains some of the highest concentrations of Sn,

Ta, Cs, and W (Figure 5.7; Table 5.2 and 5.3). Stream Sediments only contains one sample (F17) but it has moderate concentrations of most pathfinder elements and a low concentration of Sn, S, and W (Table 5.2). Colluvial Sediments predominantly contains high concentrations of most pathfinder elements with a wide range of concentrations for As, Mo, Sb and Ni (Figure 5.7; Table 5.2). Similarly to Non-GRV Bedrock, GRV Bedrock contains a wide range of concentrations. Some of the highest concentrations for Pb, In, Mo, Co, Cu and Sc are within GRV Bedrock (Figure 5.7) as well as some of the lowest for Pb, As, Cs, Sb, Ni, Co, Cu, Sc and Sr (Table 5.2).

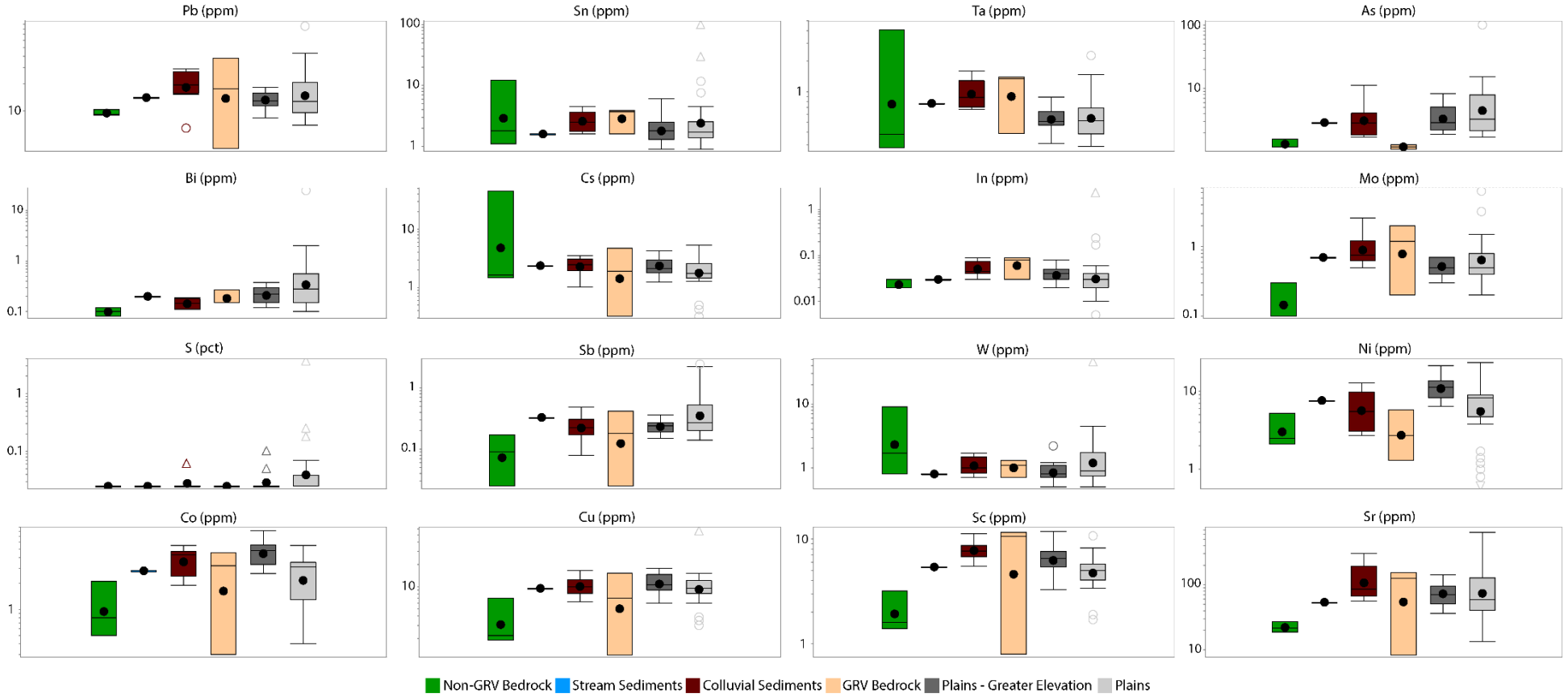

Figure 5.7: Pathfinder element Tukey box plots (logged) coloured by objective regolith-landform mapping units derived from Caruso *et al.* (2018). Open circles indicate outlier 1.5 x the Interquartile Range, open triangles indicate 3 x the Interquartile Range.

Table 5.2: Summary statistics of elevated pathfinder elements for objective regolith-landform units.

Objective Regolith-Landform Unit and Statistic, N = 59	**Pb (ppm)**	**Sn (ppm)**	**Ta (ppm)**	**As (ppm)**	**Bi (ppm)**	**Cs (ppm)**	**In (ppm)**	**Mo (ppm)**	**S (%)**	**Sb (ppm)**	**W (ppm)**
GRV Bedrock: Minimum (*n* = 3)	3.9	1.6	0.39	1.1	0.15	0.32	0.03	0.2	0.025	0.025	0.7
GRV Bedrock: Maximum	38	3.9	1.4	1.3	0.27	4.69	0.09	2	0.025	0.42	1.3
GRV Bedrock: Mean	19.83	3.07	1.04	1.20	0.19	2.31	0.07	1.13	0.03	0.21	1.03
GRV Bedrock: Median	17.6	3.7	1.34	1.2	0.15	1.91	0.08	1.2	0.025	0.18	1.1
GRV Bedrock: Standard Deviation	17.16	1.27	0.57	0.10	0.07	2.21	0.03	0.90	0.00	0.20	0.31
Non-GRV Bedrock: Minimum (*n* = 3)	9	1.1	0.28	1.2	0.08	1.47	0.02	0.1	0.025	0.025	0.8
Non-GRV Bedrock: Maximum	10.4	12.3	4.07	1.6	0.12	45.33	0.03	0.3	0.025	0.17	9
Non-GRV Bedrock: Mean	9.53	5.07	1.58	1.33	0.10	16.14	0.02	0.17	0.03	0.10	3.83
Non-GRV Bedrock: Median	9.2	1.8	0.38	1.2	0.1	1.63	0.02	0.1	0.025	0.09	1.7
Non-GRV Bedrock: Standard Deviation	0.76	6.27	2.16	0.23	0.02	25.28	0.01	0.12	0.00	0.07	4.50
Plains: Minimum (*n* = 15)	8.4	0.9	0.31	1.9	0.12	1.25	0.02	0.3	0.025	0.15	0.5
Plains: Maximum	18.2	6.1	0.89	8.3	0.38	4.29	0.08	0.7	0.1	0.36	2.2
Plains: Mean	13.47	2.05	0.55	3.67	0.22	2.49	0.04	0.53	0.03	0.24	0.91
Plains: Median	12.9	1.8	0.51	2.9	0.22	2.13	0.04	0.5	0.025	0.24	0.8
Plains: Standard Deviation	2.65	1.29	0.14	1.90	0.08	0.89	0.02	0.13	0.02	0.06	0.42
Plains - Greater Elevation: Minimum (*n* = 29)	7	0.9	0.29	1.7	0.1	0.32	0.005	0.2	0.025	0.14	0.5
Plains - Greater Elevation: Maximum	85.7	99.8	2.28	101.1	24.94	5.31	2.37	6.3	3.68	2.45	45.4
Plains - Greater Elevation: Mean	18.53	6.71	0.62	8.33	1.26	2.06	0.12	0.89	0.17	0.53	2.79
Plains - Greater Elevation: Median	12.8	1.7	0.52	3.3	0.28	1.76	0.03	0.5	0.025	0.27	0.9
Plains - Greater Elevation: Standard Deviation	16.51	18.75	0.41	18.20	4.57	1.06	0.44	1.18	0.68	0.63	8.25
Colluvial Sediments: Minimum (*n* = 8)	6.5	1.6	0.67	1.7	0.11	1.02	0.03	0.5	0.025	0.08	0.7
Colluvial Sediments: Maximum	29.2	4.5	1.61	11.2	0.19	3.55	0.09	2.6	0.06	0.49	1.7
Colluvial Sediments: Mean	19.80	2.76	1.00	3.78	0.15	2.42	0.05	1.03	0.03	0.25	1.13
Colluvial Sediments: Median	19.45	2.55	0.88	2.85	0.145	2.47	0.045	0.75	0.025	0.225	1
Colluvial Sediments: Standard Deviation	7.44	1.06	0.34	3.13	0.04	0.79	0.02	0.68	0.01	0.12	0.37
Stream Sediments (*n* = 1)	14.1	1.6	0.77	2.9	0.2	2.37	0.03	0.7	0.025	0.33	0.8

Table 5.3: Summary statistics of depleted pathfinder elements for objective regolith-landform units.

Objective Regolith-Landform Unit and Statistic, N = 59	**Ni (ppm)**	**Co (ppm)**	**Cu (ppm)**	**Sc (ppm)**	**Sr (ppm)**
GRV Bedrock: Minimum (*n* = 3)	1.3	0.3	1.2	0.8	8.24
GRV Bedrock: Maximum	5.8	4.5	15.2	11.5	154.37
GRV Bedrock: Mean	3.27	2.67	7.80	7.63	96.38
GRV Bedrock: Median	2.7	3.2	7	10.6	126.54
GRV Bedrock: Standard Deviation	2.30	2.15	7.03	5.93	77.59
Non-GRV Bedrock: Minimum (*n* = 3)	2.1	0.5	1.9	1.4	18.66
Non-GRV Bedrock: Maximum	5.2	2.1	7	3.2	26.98
Non-GRV Bedrock: Mean	3.27	1.13	3.70	2.07	22.33
Non-GRV Bedrock: Median	2.5	0.8	2.2	1.6	21.36
Non-GRV Bedrock: Standard Deviation	1.69	0.85	2.86	0.99	4.24
Plains: Minimum (*n* = 15)	6.4	2.6	6	3.3	36.17
Plains: Maximum	21.3	8.2	17.6	11.7	141.34
Plains: Mean	11.39	4.68	11.31	6.57	78.95
Plains: Median	11.2	4.8	10.6	6.5	70.6
Plains: Standard Deviation	3.95	1.66	3.33	2.14	33.27
Plains - Greater Elevation: Minimum (*n* = 29)	0.6	0.4	3	1.7	13.28
Plains - Greater Elevation: Maximum	23.3	5.5	56.2	10.7	639.62
Plains - Greater Elevation: Mean	7.34	2.70	10.94	5.03	120.03
Plains - Greater Elevation: Median	8.2	3.1	9.5	5	58.66
Plains - Greater Elevation: Standard Deviation	4.54	1.40	9.31	1.79	151.57
Colluvial Sediments: Minimum (*n* = 8)	2.7	1.9	6.3	5.5	56.28
Colluvial Sediments: Maximum	12.8	5.5	16.4	11.2	303.59
Colluvial Sediments: Mean	6.63	3.76	10.48	7.89	127.85
Colluvial Sediments: Median	5.75	4.25	10	7.65	86.67
Colluvial Sediments: Standard Deviation	3.85	1.28	3.19	1.69	88.33
Stream Sediments (*n* = 1)	7.6	2.8	9.5	5.4	53.73

5.3.3 Spatial Distribution of Mineralogy

Average proportions of minerals identified from semi-quantitative XRD of samples within the objective regolith-landform units are displayed in Table 5.4. Non-GRV Bedrock and Stream Sediments contain limited mineralogy, while the other four units display diverse mineralogy. GRV Bedrock is comprised predominantly of quartz, albite, chamosite, microcline and muscovite with some phengite, calcite and hematite. Non-GRV Bedrock contains limited mineralogy dominated by quartz and phengite with some muscovite and kaolinite.

Colluvial Sediments contains a large proportion of dickite and quartz with moderate proportions of feldspars and white micas including orthoclase, microcline, albite, oligoclase, muscovite and illite with calcareous minerals such as calcite and dolomite also present. This unit also contains a unique mineral in actinolite. The Plains unit contains a large proportion of quartz followed by white micas, clays and feldspars. It also contains calcite, dolomite and some hematite. Plains – Greater Elevation contains the greatest mineralogical diversity with 17 minerals. This unit exclusively contains alunite, pyrophyllite and phlogopite as well as feldspars, clays, quartz and calcareous mineralogy. The one sample that comprises Stream Sediments contains mostly quartz, orthoclase, muscovite, kaolinite, albite and hematite.

Table 5.4: Average X-ray diffraction mineralogy for objective regolith-landform map units.

		Objective Regolith-Landform Unit					
Mineral	**Chemical Formula**	**GRV Bedrock (n = 3)**	**Non-GRV Bedrock (n = 3)**	**Plains (n = 15)**	**Plains - Greater Elevation (n = 29)**	**Colluvial Sediments (n = 8)**	**Stream Sediments (n = 1)**
Actinolite (%)	$Ca_2Mg_{2.5}Fe_{2.5}[Si_8O_{22}](OH_2)$	-	-	-	-	4.1	-
Albite (%)	$NaAlSi_3O_8$	24.6	-	2.9	4.6	17	5
Alunite (%)	$K_2Al_6(OH)_{12}(SO_4)_4$	-	-	-	12.5	-	-
Calcite (%)	$CaCO_3$	2.1	-	6.0	4.9	10.2	-
Chamosite (%)	$(Fe^{2+})_{10}Al_2[Al_2Si_6O_{20}](OH)_{16}$	18.8	-	-	-	14.4	-
Dickite (%)	$Al_2Si_2O_5(OH)_4$	-	-	-	7.6	45.8	-
Dolomite (%)	$CaMg(CO_3)_2$	-	-	0.9	1	3.2	-
Hematite (%)	Fe_2O_3	0.5	-	0.8	0.6	1.3	1.3
Illite (%)	$K_{1.5\text{-}1}Al_4[Si_{6.5\text{-}7}Al_{1.5\text{-}1}O_{20}] (OH)_4$	-	-	19.4	22.1	18.1	-
Jarosite (%)	$KFe^{3+}{}_3(OH)_6(SO_4)_2$	0	-	-	1	-	-
Kaolinite (%)	$Al_2Si_2O_5(OH)_4$	-	7.8	12.1	8.1	10.3	7.2
Microcline (%)	$KAlSi_3O_8$	14.4	-	9.8	6.1	22.4	-
Muscovite (%)	$K_2Al_4[Si_6Al_2O_{20}](OH,F)_4$	14.7	13	15.6	17.8	10.1	9.4
Oligoclase (%)	$Na_{0.8}Ca_{0.2}Al_{1.2}Si_{2.8}O_8$	-	-	2.1	3	12.9	-
Orthoclase (%)	$KAlSi_3O_8$	-	-	11.1	8.6	28	16
Phengite (%)	$K(AlMg)_2(OH)_2(SiAl)_4O_{10}$	6.6	22.7	21.3	15.9	-	-
Phlogopite (%)	$K_2Mg_6[Al_2Si_6O_{20}](OH)_4$	-	-	-	3.4	-	-
Pyrophyllite (%)	$Al_4[Si_8O_{20}](OH)_4$	-	-	-	50.4	-	-
Quartz (%)	SiO_2	49.9	78	58.6	62.5	37	61.1

5.4 Discussion

5.4.1 Geochemical and Mineralogical Footprint

The lateral spatial distribution of pathfinder elements derived by Halley *et al.* (2015) highlighted Tl, As, Sb, Li ± Bi and Bi-Se-Te ± Mo to be present above a porphyry mineralised zone with advanced argillic alteration. Arsenic, Sb, Bi and Mo are within the region-specific pathfinder suite defined in Chapter 4. Selenium and Te were not assessed due to the high proportion of below detection limit data.

Nankivel and Peterlumbo Hill rock exposures have previously been demonstrated to preserve high concentrations of pathfinder elements (Chapter 4). The pathfinder element suite for the region includes elevated Pb, Sn and Ta ± As, Bi, Cs, In, Mo, S, Sb and W and depleted Ni, Co ± Cu, Sc, Sr. There is a zonation of pathfinder geochemistry, for all elevated pathfinder elements along with Sr containing high concentrations at Nankivel Hill (Figure 5.3). Another prominent region approximately 2 km south west of Nankivel Hill also contains a number of elevated pathfinder elements including Sn, Ta, Bi and In (Figure 5.3). Advanced argillic alteration was previously identified at Nankivel Hill (Geratikeys 1996; Nicolson *et al.* 2017a; Caruso *et al.* in review), and pathfinder elements associated with this alteration included As, Bi, Cu, Pb, Sb (Figure 5.4). Therefore the proximal footprint consists of Pb, Sn, Ta, As, Bi, Cs, In, Mo, S, Sb, W and Sr and a mineralogical expression of alunite, pyrophyllite and dickite (Figure 5.8). Some elements are present at Nankivel Hill while others appear to the south west.

At, or north of, Peterlumbo Hill low concentrations of Ni, Co, Cu, Sc were identified, coupled with high concentrations of Sn, Ta, Cs and W (Figure 5.3). There is extensive spatial distribution of dickite, illite and kaolinite in the same area characterised in the hyperspectral alteration mapping (Figure 5.4 and 5.5). There was also definition of potential chloritic alteration south of Peterlumbo Hill (Caruso *et al.* in review), signifying this area is distal to a potential ore deposit (e.g. Sillitoe 2010). Therefore, these geochemical and mineralogical expressions indicate that the Peterlumbo Hill area is distal to potential mineralisation.

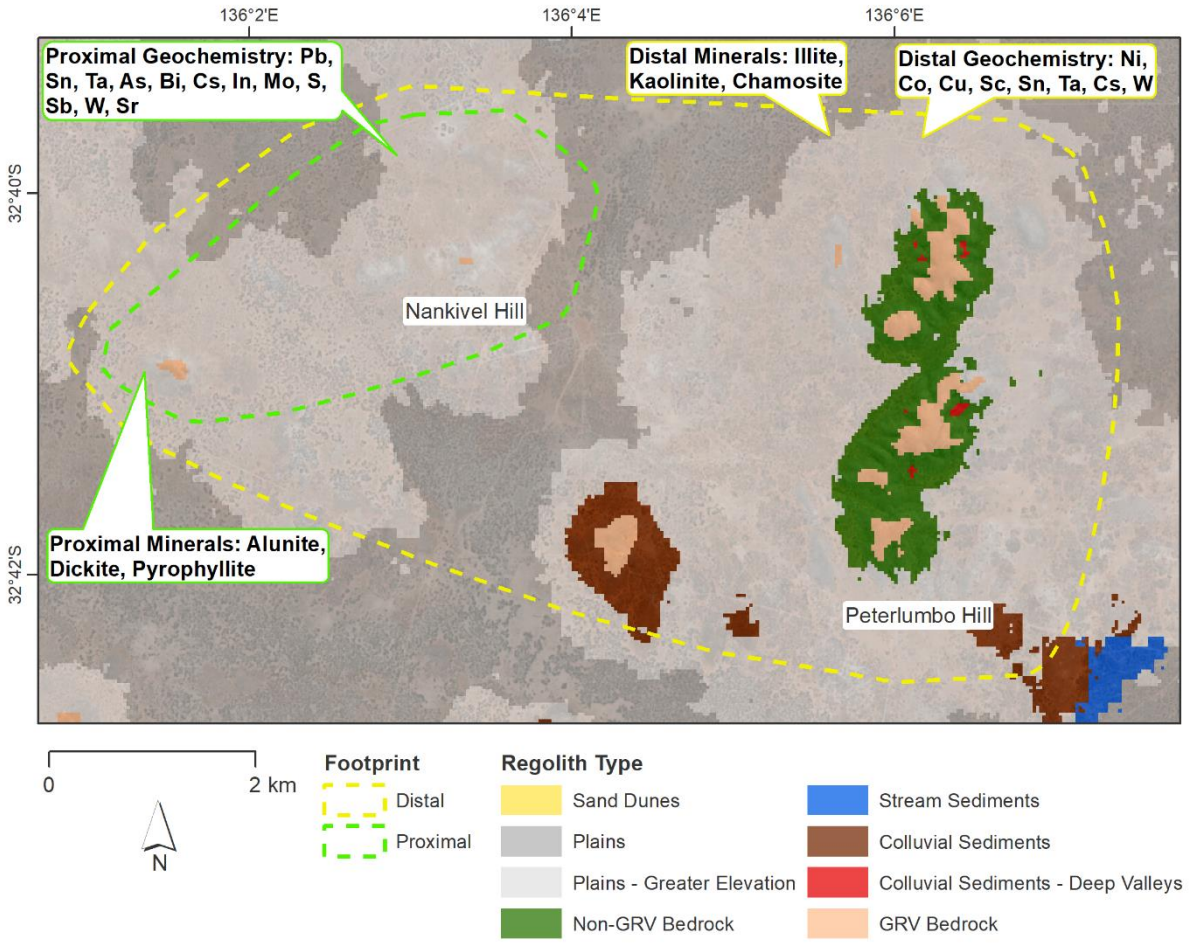

Figure 5.8: Approximate definition of the proximal and distal footprint for porphyry mineralisation based on geochemical and mineralogical interpretation. Background image: objective regolith-landform map laid over Sentinel 2A satellite true colour image.

5.4.2 Pathfinder Elements and Regolith Units

Mineralogical deportment of pathfinder elements in rock and cover sequence material was assessed in Chapter 4. This section will discuss the mineralogical deportment of pathfinder elements in relation to the objective regolith-landform map using the lithologies defined in Chapter 4 (Figure 5.1). It should be noted that most of the regolith-landform units contain both rock and soil samples (Figure 5.1) because of the coarse resolution of this mapping and that multiple lithologies are within some regolith units (Table 5.5). The Stream Sediments unit is not included in this discussion as it only contains one sample. Manganese Oxide (MnO) has very low concentrations in all regolith units (Table 5.1) and as in Chapter 4, it is excluded from this discussion.

Table 5.5: The spatial distribution of the defined lithologies from Chapter 4 and the regolith-landform units they are within from Figure 5.1.

Regolith-Landform Unit (Chapter 5)	**Defined Lithology (Chapter 4)**
Plains – Greater Elevation	Nankivel Hill Nankivel Hill Colluvial Peterlumbo Hill Peterlumbo Hill Colluvial GRV Colluvial Soil
Non- GRV Bedrock	Peterlumbo Hill
Plains	Peterlumbo Hill Colluvial Soil
GRV Rock	GRV Rock
Colluvial Sediments	GRV Colluvial Bittali Rock Bittali Colluvial Calcareous Rock

Figure 5.1 illustrates the lithologies defined in Chapter 4 in terms of their distribution across the objective regolith-landform map. This highlights the significant number of samples that are contained with the Plains – Greater Elevation regolith-landform unit. Most samples defined within the Peterlumbo Hill Colluvial and Soil lithologies and all samples from Nankivel Hill and Nankivel Hill Colluvial are within the Plains – Greater Elevation regolith unit (Figure 5.1, Table 5.5). The remaining Soil lithology samples are within the Plains regolith-landform unit which also includes two Peterlumbo Hill Colluvial samples. GRV Rock, Bittali Rock, GRV Colluvial and Bittali Colluvial primarily occur within the Colluvial Sediments and GRV Bedrock regolith-landform units (Table 5.5). There is one GRV Colluvial sample which was classed as Stream Sediment sample in the north of the study area. The Peterlumbo Hill lithology is divided across both GRV Bedrock and Non-GRV Bedrock regolith-landform units (Figure 5.1, Table 5.5). This is likely associated with the type of slope classified at Peterlumbo Hill during the objective regolith-landform mapping.

The spatial distribution of Nankivel Hill, Nankivel Hill Colluvial and Peterlumbo Hill Colluvial lithologies across Plains – Greater Elevation regolith unit supports the presence of alunite, jarosite, pyrophyllite and dickite within this regolith-landform unit. However, the distributions of these minerals appear to be spatially restricted to the Nankivel Hill rock exposure (Chapter 3, Figure 5.4) and are therefore not representative of the broader mineralogy within the Plains - Greater Elevation regolith unit. The three lithologies within Plains – Greater Elevation unit suggested mineralogical deportment of all pathfinder elements, excluding W, with carbonates, micas, clays, feldspars and hematite (Chapter 4). Therefore, minerals that would represent this regolith unit are broadly hematite, clays, feldspars and

micas. Due to the diverse mineralogy in the Plains – Greater Elevation regolith unit (Table 5.4) and the interpreted mineralogical deportment of pathfinder elements (Chapter 4), it would be expected that most pathfinder elements would be seen to some degree across the study area. There is the potential that some mineralogy preferentially hosts particular pathfinder elements, and some of those elements may also be hosted within multiple minerals in this regolith unit.

There are no rock exposure samples within the Plains unit and the soil samples are from two different lithologies meaning that there are two different sources of inferred mineralogical deportment for this regolith unit. The Soil lithology identified Cs, Co and Sc possibly hosted within kaolinite, phengite, phlogopite and hematite or kaolinite (Chapter 4) while the Peterlumbo Hill Colluvial lithology contained Pb, Cs, Sr, Ta, Ni, Co and Sc potentially hosted within minerals such as illite, kaolinite, microcline, muscovite, orthoclase, calcite, dolomite and hematite (Chapter 4). Therefore, it could be expected that Cs, Co and Sc would be prominent across the Plains regolith unit based on their interpreted mineralogical deportment from the Soil and Peterlumbo Hill Colluvial lithologies. The highest concentrations of Ni, Co, Cu and Sc are evident in the Plains unit (Figure 5.7), and it could be proposed that these elements are concentrated and preserved in the Plains regolith unit within micas, feldspars and hematite (Chapter 4).

GRV Rock and GRV Colluvium are mostly within the Colluvial Sediments unit and mineralogical deportment is within minerals such as chamosite, hematite, illite, microcline, muscovite, orthoclase and albite which host In, Pb, Sb, Ni, Co, Sc, Cu, Mo, As, Ta, Cs, W and Sr (Chapter 4). Figure 5.7 demonstrates that As, In, Cu, Sc and Sr are mostly preserved in this regolith unit. Due to the limited number of samples in this unit (Figure 5.1), a comprehensive geochemical or mineralogical description is not given. Albite, hematite, microcline, muscovite, orthoclase and quartz are the common minerals between these two lithologies, and therefore, would be representative of the Colluvial Sediments regolith unit.

The Non-GRV Bedrock regolith unit contains samples from the Peterlumbo Hill lithology and the mineralogy includes hematite, microcline, phengite and quartz with microcline and hematite identified to potentially host Sb, Ni, Co, Sc, Pb, Cs, W, Cu and Sr (Chapter 4). There are also Peterlumbo Colluvial lithology samples within this regolith unit, and it is more mineralogically diverse with illite, kaolinite, microcline, muscovite, orthoclase, calcite, dolomite and hematite potentially hosting Pb, Cs, Sr, Ta, Ni, Co and Sc. Common pathfinder elements between these lithologies includes Pb, Cs, Sr, Ni, Co and Cu with only Cs a common pathfinder with a high concentration (Figure 5.7). Tin, Ta and W also have high concentrations in the Non-GRV Bedrock unit (Figure 5.7). Due to the origins of these lithologies, there are few minerals representing this unit other than hematite and microcline. The potential hosts of pathfinders within this regolith unit is limited by minerals identified at Peterlumbo Hill.

The GRV Rock and Peterlumbo Hill lithologies have formed from different protolith materials and processes, meaning that the geochemical and mineralogical interpretation of the GRV Bedrock regolith unit should be examined with caution. The GRV Rock lithology contained potential mineralogical deportment of In, Pb, Ta, Sb, Ni, Co, Sr, Mo, Cu and Sn within feldspars, micas, hematite and chamosite. Peterlumbo Hill had microcline and hematite possibly hosting Sb, Ni, Co, Sc, Pb, Cs, W, Cu and Sr (Chapter 4). Although there are lithological differences, they do host similar pathfinder elements including Pb, Sb, Ni, Co, Sr and Cu. These pathfinders primarily contain a range of concentrations with particularly high concentrations for Sc and Pb within this regolith unit (Figure 5.7). Therefore the representative pathfinder elements would be Pb, Sb, Ni, Co, Sr and Cu while representative mineralogy would likely include feldspars, micas, hematite and chamosite, although the limited number of samples influences this result.

5.4.3 Pathfinder Elements and Landscape Processes

This section discusses the pathfinder elements, their possible mineralogical deportment and how this relates to landscape processes in the study area. The key pathfinder element suite has been identified as Pb, Sn and Ta ± As, Bi, Cs, In, Mo, S, Sb and W and depleted Ni, Co ± Cu, Sc, Sr and is best seen around the Nankivel Hill and Peterlumbo Hill exposures. Appreciable concentrations of the pathfinder element suite are preserved within the GRV, however the link with the potential buried mineralisation is less clear (Chapter 4). Therefore, only distribution of pathfinder elements in the landscape around Nankivel Hill and Peterlumbo Hill will be considered here.

5.4.3.1 Nankivel Hill

Although Nankivel Hill is not clearly defined within the objective regolith landform map due to scale, it is still a major feature of the landscape.

At Nankivel Hill, key minerals were identified from XRD as alunite, muscovite, microcline, orthoclase and hematite that hosted pathfinder elements. There was a difference in minerals between the rock exposure and the colluvium. Hematite, microcline, orthoclase and muscovite are inferred to continue hosting pathfinder elements from the rock exposure into the colluvium and illite and phengite were identified as potential new deportment for pathfinders (Table 5.4). Pathfinder elements of interest at Nankivel Hill included Ta, Bi, Cs, In, S, Sb, Pb, Ni, Cu and Sr. Within the colluvium As, Sc, Cu, Mo, Sb and Sn had correlations with major elements. As there are less pathfinders within the colluvium than the rock exposure, it can be suggested that a landscape process such as weathering has affected the mineralogical deportment of pathfinder elements at Nankivel Hill.

The hyperspectral analysis (Chapter 3) identified the presence of advanced argillic alteration at Nankivel Hill and this is corroborated in Chapter 4. However, these three key alteration minerals are not found in the colluvium and the pathfinders associated with these minerals include Pb, Bi, As, S and Sb have lower concentrations in the colluvium (Chapter 4,Figure 5.3). The Plains – Greater Elevation regolith-landform unit contains a reduced concentration of Pb and Bi (Table 5.2) although this unit also contains a sample with a significant concentration Bi (Sample F89, Soil lithology).

Copper contains a greater median concentration in the Plains unit compared to the Plains – Greater Elevation unit (Table 5.3). This implies that there is a landscape process influencing the host of Cu and causing enrichment of this pathfinder element. It is suggested that Cu is hosted within alunite or jarosite at Nankivel Hill, and as these minerals are not present in the colluvium, it can be suggested that Cu is dispersed from the Plains – Greater Elevation unit into the Plains unit and is potentially concentrated within calcite (Table 5.4). It is also possible that this change in concentration of Cu could be associated with transported material. From Table 5.2, there is a greater concentration of Sb in the Plains – Greater Elevation unit compared to the Plains unit, this indicates that the host of Sb, hematite, is not being transported or weathered from the unit with higher topography. The higher concentration of hematite in the Plains unit could be associated with other material being transported into this area.

5.4.3.2 Peterlumbo Hill

The Peterlumbo Hill exposure is comprised of microcline and hematite as the key minerals, possibly hosting pathfinder elements including Pb, Cs, W, Cu, Sr, Sb, Ni, Co, Sc and Sb. The Peterlumbo Hill colluvium was more mineralogically diverse with calcite, dolomite, albite, hematite, illite, microcline, muscovite, orthoclase, kaolinite potentially hosting pathfinder elements. A smaller number of pathfinders were hosted in the colluvium including Pb, Cs, Sr, Ni, Co and Cu however, there is similarity between the rock exposure and the colluvium regarding the pathfinder elements. There is a limited surface expression of argillic alteration from the hyperspectral mapping as shown in Figures 5.4 – 5.6. From Chapter 4, alteration at Peterlumbo Hill could be considered silicic due to the significant proportion of SiO_2 in the rock samples from this geological exposure.

There are higher concentrations associated with the colluvium for Ni, Co, Cu and Sc (Figure 5.7). These four pathfinder elements also contain greater concentrations within the Plains regolith-landform unit compared to the Plains – Greater Elevation unit (Table 5.3), indicating a process that is transporting material hosting these pathfinders away from Peterlumbo Hill. Within the Soil lithology, only hematite, kaolinite, phengite or phlogopite may host pathfinder elements. More specifically, these minerals are suggested to host a limited number of pathfinder elements including Cs, Co and Sc (Chapter 4). More pathfinder elements are inferred to be hosted within the Peterlumbo Hill colluvium, indicating that the

minerals hosting Cs, Co and Sc persist and are transported in the landscape away from the potential source. This is corroborated by the higher concentration of these three pathfinder elements in the Plains regolith unit compared to Plains – Greater Elevation (Table 5.3). It is known that minerals that potentially contain these pathfinder elements (e.g. hematite) can survive prolonged weathering (Anand 2005; McQueen 2009).

Peterlumbo Hill is a significant landscape feature reaching elevations of 400 m AMSL with steep valleys on its eastern and western sides (Chapter 1). Although there are steep slopes, the pathfinders that were identified in the colluvium and surrounding soils, Cs, Co and Sc, should still be considered for mineral exploration and geochemical analysis as prior research has used Co and Ni for base metal deposits (Smith *et al.* 2000). This study area is known to contain the Paris Ag-Pb-Zn deposit north west of Nankivel Hill (Nicolson *et al.* 2017b) and the Menninnie Dam Pb-Zn deposit is also east of this area within the southern Gawler Ranges (Roache 1996).

The hyperspectral analysis identifies a broad spatial distribution of clays around Peterlumbo Hill, and kaolinite is known to persist in the landscape and form following the weathering of feldspars (Anand 2005). Illite was identified in the hyperspectral alteration mapping at Peterlumbo Hill but was not validated in the XRD analysis (Caruso *et al.* in review; Chapter 3). However, illite is identified in the colluvial material around Peterlumbo Hill (Chapter 4) and it is also identified in the Plains – Greater Elevation and Plains regolith-landform units (Table 5.4).

5.4.3.3 Distal Soils

The Soil lithology from Chapter 4 spans both the Plains and Plains – Greater Elevation regolith units (Figure 5.1). Within the Soil lithology, the main minerals suggested to host pathfinder elements included kaolinite, phengite, phlogopite and hematite. The pathfinder elements associated with these minerals was limited to Cs, Co, and Sc (Chapter 4). Overall, concentrations of pathfinder elements are low within the distal soil samples (Figure 5.1, Chapter 4). Exceptions to this includes Sample F89 that has significantly high concentrations of Sn, As, Bi, In, Mo, W and Sample F104 containing high Ni and moderate Bi and S (Figure 5.3). These samples are notable due to the significant concentrations of pathfinder elements, unusual for surface soils in this region. These samples are near each other in the south of the study area (Figure 5.1), possibly indicating a different process or source for these materials.

Figure 5.7 demonstrates the range of the two Plains regolith units across the landscape and highlights the elements with the highest concentrations within these units and any significant outliers. The concentrations for Pb, Sn, As, Bi, In, Mo, S, Sb, W, Ni, Co, Cu and Sr for these two units indicates that these pathfinders are generally preserved within these units. There are notable outliers for Pb, Sn, As, Bi, In, Mo, S, Sb, W and Cu, indicating specific samples containing high concentrations of those elements

in these units. This also highlights the variability of these units, as they are so spatially extensive, there are numerous potential landscape processes taking place.

Caesium, Co and Sc are also identified in the Soil lithology with very small expressions of these pathfinder elements associated with Nankivel and Peterlumbo Hills expressed in the Plains unit. Comparing median pathfinder element concentrations of Plains to Plains – Greater Elevation regolith units, Cs, Ni, Co, Cu and Sc have higher median concentrations in the Plains unit (Table 5.2 and 5.3). This indicates that these elements are persisting through landscape processes through their inferred mineralogical hosts within the Plains unit and demonstrate a small expression of alteration from Nankivel and Peterlumbo Hills. These hosts are potentially hematite, kaolinite, phengite and phlogopite.

The hyperspectral alteration mapping indicated the dominance of clay minerals, primarily kaolinite, in the broader landscape with the advanced argillic alteration minerals, alunite, dickite and pyrophyllite, only identified at Nankivel Hill. Therefore, it is interpreted that these minerals are easily weathered and any remnant minerals, such as pyrophyllite in Nankivel Hill colluvium, do not persist into the distal soils. Another possible interpretation is that these materials are transported and are not related to the underlying geology.

5.4.4 Application to Mineral Exploration

5.4.4.1 Selection of Appropriate Sample Media

Linking pathfinder elements with landscape position has resulted in identification of potentially appropriate sampling media for exploration. In this region, there is an advantage to sampling Plains and Plains – Greater Elevation units as key minerals are preserved and these host relevant pathfinder elements such as Cs, Sc, Co and Ni for exploration in this region. Developing an objective regolith-landform map prior to reconnaissance sampling in a region may assist in identifying the location of these pathfinders in the landscape and therefore development of target sample areas. In a similar terrain, targeting these areas may allow for easier recognition of these geochemical signatures at the surface.

Non-GRV Bedrock and Colluvial Sediments could also be useful sampling media to classify and characterise landscape processes and interpret any weathering of the adjacent geological exposures that has occurred. However, distal soils within the Soil lithology are less likely to be a useful sample media due to the variability of source material and the requirement to conduct further mineralogical and geochemical analysis. For a first pass method, this lithology would not be beneficial.

Further input data to focus the objective regolith-landform mapping could classify units more explicitly to assist with selection of sample media and landscape interpretation. This could be of particular benefit to Plains and Plains – Greater Elevation units that are spatially extensive and encompass a majority of this

study area. Higher spatial resolution imagery or DEMs could assist in mapping features such as Nankivel Hill, which is currently not discriminated in the objective regolith-landform mapping.

5.4.4.2 Data Integration for Mineral Exploration

Exploration geochemistry databases commonly combine multiple generations of geochemical methods and sampling approaches. This may maximise identification of geochemical anomalies but the various datasets may not be comparable. Hence, integrating multiple sources of information, such as regolith-landform mapping, hyperspectral alteration mapping and mineralogy can allow for a thorough desktop study to assist the exploration geologist with planning a geochemical sampling campaign. The outcomes of this may include target ranking, selection of sample media and identification of landscape positions for sampling.

The advantage of using several methods and sources of information is to provide greater confidence and assurance of indications of an ore deposit, whether it be relatively surficial or buried under highly weathered regolith. Data integration for mineral exploration is increasing in its use as awareness grows of the benefits that this integrated approach has on positive exploration outcomes. There is also a wealth of geoscientific data available through state and federal government organisations (e.g. Geological Survey of South Australia, Geoscience Australia) that can contribute to a comprehensive desktop study of the geology of a region. Financially, studies such as these this can benefit an exploration company by investing limited time and money prior to conducting expensive field campaigns with significant personnel and equipment requirements.

5.5 Conclusions

Overall, it was expected that there would be a significant influence of broad landscape processes on the geochemical and mineralogical surface expressions considering the weathered and transported nature of this landscape with limited geological exposures. Caesium, Co, Sc and Ni were inferred to be hosted within minerals that survived weathering in the landscape, or were adsorbed onto other minerals following weathering processes, and the expression of alteration that survived into the colluvium and soil material around Nankivel and Peterlumbo Hills. This means that the Plains – Greater Elevation and Plains units are likely the most valuable sample media in this region to identify potential vectors to alteration and mineralisation. Distal soils and the Soil lithology are not likely to be a useful sample media due to the variety of potential source material. Conducting a comprehensive desktop study would likely positively influence potential sampling methodologies and planning field reconnaissance campaigns.

5.6 References

Abrams, M.J., Brown, D., Lepley, L., & Sadowski, R. (1983). Remote Sensing for Porphyry Copper Deposits in Southern Arizona. *Economic Geology, 78*, 591-604. doi: 10.2113/gsecongeo.78.4.591

Anand, R.R. (2005). Weathering history, landscape evolution and implications for exploration. In R.R. Anand, & P. De Broekert (Eds.), *Regolith Landscape Evolution Across Australia: A Compilation of Regolith Landscape Case Studies With Regolith Landscape Evolution Models* (pp. 2-40): CRC LEME. ISBN: 978-1-92-103928-7

Anand, R.R., Hough, R.M., Salama, W., Aspandiar, M.F., Butt, C.R.M., González-Álvarez, I., & Metelka, V. (2019). Gold and pathfinder elements in ferricrete gold deposits of the Yilgarn Craton of Western Australia: A review with new concepts. *Ore Geology Reviews, 104*, 294-355. doi: 10.1016/j.oregeorev.2018.11.003

Aspandiar, M.F., Anand, R.R., & Gray, D.J. (2008). Geochemical dispersion mechanisms through transported cover: implications for mineral exploration in Australia. Perth, Australia. CRC LEME. Document Number: Open File Report 246

Baudet, E., Giles, D., Tiddy, C., & Hill, S. (2018). Evaluation of cover sequence geochemical exploration sample media through assessment of element migration processes. *Ore Geology Reviews, 102*, 449-473. doi: 10.1016/j.oregeorev.2018.09.017

Caruso, A.S., Clarke, K.D., Tiddy, C.J., Delean, S., & Lewis, M.M. (2018). Objective regolith-landform mapping in a regolith dominated terrain to inform mineral exploration. *Geosciences, 8*, 318. doi: 10.3390/geosciences8090318

Caruso, A.S., Clarke, K.D., Tiddy, C.J., & Lewis, M.M. (in review). Airborne hyperspectral characterisation of hydrothermal alteration in a regolith dominated terrain, southern Gawler Ranges, SA.

Craig, M.A. (2001). Regolith mapping for geochemical exploration in the Yilgarn Craton, Western Australia. *Geochemistry: Exploration, Environment, Analysis, 1*, 383-390. doi: 10.1144/geochem.1.4.383

de Caritat, P., Main, P.T., Grunsky, E.C., & Mann, A.W. (2016). Recognition of geochemical footprints of mineral systems in the regolith at regional to continental scales. *Australian Journal of Earth Sciences*, 1-11. doi: 10.1080/08120099.2017.1259184

Duuring, P., Hagemann, S.G., Novikova, Y., Cudahy, T., & Laukamp, C. (2012). Targeting Iron Ore in Banded Iron Formations Using ASTER Data: Weld Range Greenstone Belt, Yilgarn Craton, Western Australia. *Economic Geology, 107*, 585-597. doi: 10.2113/econgeo.107.4.585

Fabris, A.J., Halley, S., van der Wielen, S., Keeping, T., & Gordon, G. (2013). IOCG-style mineralisation in the central eastern Gawler Craton, SA; characterisation of alteration, geochemical associations and exploration vectors. Adelaide, South Australia: Department of Manufacturing,

Innovation, Trade, Resources and Energy. Geological Survey of South Australia. Document Number: Report Book 2013/0014

Gerakiteys, C. (1996). Technical Report No. 2718, EL 1841 "Mt Ive Gate". Adelaide, Australia. MIM Exploration. Document Number: R96/02406

González-Álvarez, I., Boni, M., & Anand, R.R. (2016). Mineral exploration in regolith-dominated terrains: Global considerations and challenges. *Ore Geology Reviews, 73, Part 3*, 375-379. doi: 10.1016/j.oregeorev.2015.11.017

Halley, S., Dilles, J., & Tosdal, R. (2015). Footprints: hydrothermal alteration and geochemical dispersion around porphyry copper deposits. *Society of Economic Geologists Newsletter, 100*, 12-17

Hillis, R.R., Giles, D., Van Der Wielen, S.E., Baensch, A., Cleverley, J.S., Fabris, A., Halley, S.W., Harris, B.D., Hill, S.M., Kanck, P.A., Kepic, A., Soe, S.P., Stewart, G., & Uvarova, Y. (2014). Coiled Tubing Drilling and Real-Time Sensing-Enabling Prospecting Drilling in the 21st Century? In K.D. Kelley, & H.C. Golden (Eds.), *Society of Economic Geologists Special Publication Number 18* (pp. 243-259): Society of Economic Geologists. ISBN: 978-1-62-949637-5

Hollis, S.P., Podmore, D., James, M., Mole, D.R., Turner, O., Kneeshaw, A., & Beaton, R. (2019). Targeting VHMS mineralization at Erayinia in the Eastern Goldfields Superterrane using lithogeochemistry, soil chemistry and HyLogger data. *Journal of Geochemical Exploration, 207*, 106379. doi: 10.1016/j.gexplo.2019.106379

Hussey, M. (2015). March 2011 Peterlumbo area HyMap survey. Mineral maps Data Package. Adelaide, South Australia: Department of State Development. Document Number: GDP00028

Lampinen, H.M., Laukamp, C., Occhipinti, S.A., Metelka, V., & Spinks, S.C. (2017). Delineating Alteration Footprints from Field and ASTER SWIR Spectra, Geochemistry, and Gamma-Ray Spectrometry above Regolith-Covered Base Metal Deposits—An Example from Abra, Western Australia. *Economic Geology, 112*, 1977-2003. doi: 10.5382/econgeo.2017.4537

McQueen, K.G. (2009). Regolith geochemistry. In K.M. Scott, & C.F. Pain (Eds.), *Regolith Science* (pp. 103-145): CSIRO Publishing. ISBN: 978-0-64-309826-8

Morris, P.A. (2013). Fine fraction regolith chemistry from the East Wongatha area, Western Australia: tracing bedrock and mineralization through thick cover. *Geochemistry: Exploration Environment Analysis, 13*, 21-40. doi: 10.1144/geochem2012-141

Mulder, V.L., de Bruin, S., Schaepman, M.E., & Mayr, T.R. (2011). The use of remote sensing in soil and terrain mapping - A review. *Geoderma, 162*, 1-19. doi: 10.1016/j.geoderma.2010.12.018

Nesbitt, H.W., & Young, G.M. (1984). Prediction of some weathering trends of plutonic and volcanic rocks based on thermodynamic and kinetic considerations. *Geochimica et Cosmochimica Acta, 48*, 1523-1534. doi: 10.1016/0016-7037(84)90408-3

Nesbitt, H.W., & Young, G.M. (1989). Formation and Diagenesis of Weathering Profiles. *The Journal of Geology, 97*, 129-147. doi: 10.1086/629290

Nicolson, B., Reid, A., McAvaney, S., Keeling, J., Fraser, G., & Vasconcelos, P. (2017a). A Mesoproterozoic advanced argillic alteration system: $^{40}Ar/^{39}Ar$ thermochronology from Nankivel Hill, Gawler Craton. Adelaide, South Australia: Department of Premier and Cabinet. Geological Survey of South Australia. Document Number: Report Book 2017/00011

Nicolson, B.E., Reid, A., McAvaney, S., Keeling, J., Fraser, G., & Vasconcelos, P.M. (2017b). Timing of advanced argillic alteration at Nankivel Hill, SE of Paris silver deposit, northern Eyre Peninsula. *MESA Journal, 83*, 20-26

Roache, M.W. (1996). The geology, timing of mineralisation, and genesis of the Menninnie Dam Zn-Pb-Ag deposit, Eyre Peninsula, South Australia. *PhD Thesis (Unpublished),* University of Tasmania

Salama, W., Anand, R.R., & Verrall, M. (2016). Mineral exploration and basement mapping in areas of deep transported cover using indicator heavy minerals and paleoredox fronts, Yilgarn Craton, Western Australia. *Ore Geology Reviews, 72*, 485-509. doi: 10.1016/j.oregeorev.2015.07.014

Schodde, R.C. (2017). Challenges of Exploring Under Deep Cover. In, *AMIRA International's 11th Biennial Exploration Managers Conference* (p. 43). Healesville, Australia: MinEx Consulting

Sillitoe, R.H. (2010). Porphyry Copper Systems. *Economic Geology, 105*, 3-41. doi: 10.2113/gsecongeo.105.1.3

Smith, R.E., Anand, R.R., & Alley, N.F. (2000). Use and implications of paleoweathering surfaces in mineral exploration in Australia. *Ore Geology Reviews, 16*, 185-204. doi: 10.1016/S0169-1368(99)00030-X

Chapter 6

DISCUSSION & CONCLUSIONS

6.1 Discussion

The overarching aim of this thesis was to use and integrate spatial and spectral methods to advance the understanding of the landscape to enhance mineral exploration outcomes, intending to reduce risk and cost. This aim was addressed in three component studies that demonstrate a suite of methods with potential to enhance mineral exploration in the southern Gawler Ranges, South Australia, a regolith dominated terrain within the central Gawler Craton.

Chapter 2 created an objective regolith-landform map using a DEM and gamma-ray spectrometry using an unsupervised classification and hierarchical clustering. This objective map was statistically evaluated against a traditionally derived regolith map using the 'Mapcurves' Goodness-of-Fit algorithm in *R*. This resulted in a Goodness of Fit score of 26.4 % indicating the positive statistical relationship between the objective regolith-landform map and the traditionally derived map. This approach was most successful for Sandplains/dunes and Gawler Range Volcanics when compared with their corresponding objective regolith-landform mapping class but was least successful for Lake/Palaeochannel Sediments and its associated objective regolith-landform map class.

As an alternative to current methods, this outcome illustrated the potential of using freely available remote sensing and geospatial data and repeatable analyses to create this type of map for initial exploration campaigns. For example, this approach is very achievable across most of Australia due to the high quality DEM and the airborne gamma-ray spectrometry coverage across all or a majority of the continent. Internationally, there is global coverage of both DEMs and varied coverage of gamma-ray spectrometry, and in regions where regolith, or cover, is a particular problem, mapping such as this would offer a reproducible product that could be easily interpreted.

Although there are subtle slope and landscape features not identified using the particular geospatial products used in this research, there is scope to amend the resolution and scale of the geospatial products used as inputs to compile a regolith-landform map. As suggested by Weiss (2001), the directionally weighted Topographic Position Index (TPI) may assist in resolving similarities of landform slope, potentially beneficial for the interpretation of weathering processes in flat landscapes. There are algorithms to interpolate DEMs, attracting their own accuracy concerns, which may be used with the TPI algorithm at finer scales than 300 m as used in **Chapter 2**. This particular resolution was chosen because of the regional scale of the map being produced; in other more localised contexts, the TPI may be applied at 100 or 50 m.

There is also scope to integrate other remote sensing products including ASTER mineral indices (e.g. Cudahy *et al.* 2016), Landsat imagery and indices or other traditional data such as airborne magnetic or gravity geophysics and interpolated soil geochemistry surfaces into this workflow to create a map that is

based on a wider range of information, delivering more information for particular locations. For example, Cracknell *et al.* (2015) incorporated geophysical datasets such as magnetics and Bouguer gravity with remotely sensed mineral indices to create a continental-scale regolith map using machine learning algorithms. This work specifically examined in the Yilgarn Craton identifying regolith characteristics that related to prospectivity of nickel or uranium to use for future mineral exploration (Cracknell *et al.* 2015).

Therefore, the method created in **Chapter 2** provides a rational argument to increase the use of desktop studies to provide a wider landscape assessment with remote sensing and digital geospatial data prior to conducting expensive field campaigns. This method can provide a faster first-pass alternative to traditional regolith-landform mapping. The statistical evaluation has provided confidence in the application of this method in this research phase but would not be necessary in operational contexts. Although this method cannot replace the traditional 'boots-on-ground' field assessment, it can direct these field efforts by providing a preliminary overview of the landscape for the purpose of mineral exploration, quick and easy identification of appropriate sample media and minimising the requirement for such extensive traditional mapping.

Chapter 3 characterised surface expressions of mineralogy by integrating two independent approaches in a regolith dominated terrain. Airborne hyperspectral imagery was used to map diagnostic absorption features of alteration minerals associated with alteration types for Cu-Au mineralisation. This successfully identified advanced argillic and argillic alteration in the study area, primarily at Nankivel Hill. X-ray diffraction (XRD) provided semi-quantitative mineralogical data for 57 field samples, validating key alteration mineralogy, proximal to the hyperspectral mineral mapping results. From this, identification of placement within a porphyry-epithermal mineral system was suggested, indicating an approximate location of potential buried mineralisation. This component of the research has demonstrated that transported colluvial surface material can still be useful to examine the surface expression of mineralisation and that hyperspectral remote sensing can detect signatures of alteration minerals within this material.

Collecting traditional geological data at a similar spatial extent to the airborne HyMap imagery used in this research would require considerable time and financial investment. For example, Hewson *et al.* (2006) compared the acquisition of HyMap data as approximately 40 times cheaper than the $120/line km for geophysical airborne electromagnetic surveys. Therefore, **Chapter 3** provides another motivation to use desktop studies for landscape assessment prior to conducting field campaigns. Hyperspectral alteration mineral maps could also be used as another useful input when creating objective regolith-landform maps, possibly defining mineralogy within classes and assisting with initial landscape interpretation. Obtaining and interpreting data such as this is valuable for mineral exploration as it

highlights the use of the surface, rather than sub-surface soil horizons, for mineralogical examination. In practice, this approach could assist with assessment of regions of interest for mineral exploration. For example, even if there had been no field knowledge prior to this research, the hyperspectral image analysis pointed to the Nankivel Hill and Gawler Range Volcanics regions as important focal areas for subsequent field campaigns. Noting the limitations of spatial resolution and vegetation cover, there is still a strong case to use airborne hyperspectral imagery to collect mineralogical information of the landscape surface. This work provides an approach to remote and isolated regions when access and funding is limited.

Although the benefits using HyMap imagery for this research have been demonstrated, there are also limitations that were discussed in **Chapter 3**, primarily spatial resolution in regard to removing vegetation for analysis of the surface and successful identification of geological exposures. The Normalised Difference Vegetation Index (NDVI) identified green vegetation in this landscape which was used to mask pixels prior to spectral analysis. Dry vegetation is also prevalent in arid Australian landscapes. **Chapter 3** discusses dry vegetation spectral features that overlap with mineral absorption features at 2090 nm and 2400 nm (Elvidge 1990). Although not masked in this research, a band ratio, such as that derived by van Ruitenbeek *et al.* (2006), or unmixing of pixels known to contain non-photosynthetic vegetation, may better account for the influence of non-photosynthetic vegetation (e.g. Roberts *et al.* 1998; Asner and Heidebrecht 2002; Haest *et al.* 2013).

Pixels below the NDVI threshold still contained a proportion of vegetation and a vegetation spectral signature at the 4.4 m spatial resolution of this imagery, influencing the results of the mineral mapping. A possible solution to this is acquisition of higher spatial resolution imagery by Unmanned Aerial Vehicles (UAVs) that are currently used for environmental and agricultural applications (e.g. Rango *et al.* 2006; Capolupo *et al.* 2015; Iost Filho *et al.* 2020) with some research being undertaken for geological applications (e.g. Micklethwaite *et al.* 2012; Micklethwaite 2018; Dering *et al.* 2019). There are a number of hyperspectral sensors suitable for operation on UAVs spanning the VNIR (approx. 400 – 900 nm) or SWIR (approx. 1000 – 2500 nm) that can also be co-aligned for imagery acquisition e.g. Micro-Hyperspec®, HySpex Mjolnir S-620 (Headwall Photonics 2018; Harris Aerial 2019).

Considering the technical advances for UAVs made in approximately a decade, it would be expected that an all-in-one multi-detector sensor system similar to the spectral range of HyMap would be possible on a UAV system in the coming years. This could mean that UAVs are used as a complementary system to obtain very high resolution imagery over particular prospective areas with airborne sensors conducting broad scale image acquisitions.

Chapter 4 examined geochemical data from 57 soil and geological exposure field samples collected in 2017 from the southern Gawler Ranges study area. This research aimed to examine the

lithogeochemistry of these samples, generate a pathfinder element suite that may be related to potential regional mineralisation and understand mineralogical deportment of these elements. Following the interpretation that the published pathfinder element suite for porphyry deposits was not suitable in this region, this chapter identified thresholds to define a region-specific pathfinder element suite that included elevated Pb, Sn and Ta ± As, Bi, Cs, In, Mo, S, Sb and W and depleted Ni, Co ± Cu, Sc, Sr. Pathfinder element abundances and distributions were combined with semi-quantitative XRD data presented in **Chapter 3** to identify their potential mineralogical deportment and any influence of weathering by comparing rock, their associated colluvium and distal soils. This identified kaolinite, hematite and phengite as the main constituents that survived or were formed due to prolonged weathering, and hence, most likely to contain the pathfinder elements.

Chapter 5 integrated results of the hyperspectral alteration mapping, semi-quantitative XRD analysis (**Chapter 3**), surface geochemistry (**Chapter 4**) and objective regolith-landform mapping (**Chapter 2**) to identify the surface expression of both mineralogical and geochemical signatures potentially related to buried mineralisation. Geochemical and mineralogical footprints indicating proximal and distal regions were identified around Nankivel Hill and Peterlumbo Hill respectively. This interpretation incorporated the hyperspectral alteration mapping and geochemistry results from **Chapters 3** and **4**. The rock, colluvial and soil lithologies at Nankivel and Peterlumbo Hills from **Chapter 4** were interpreted in terms of the objective regolith-landform map, highlighting the preservation of Cs, Sc, Co and Ni pathfinder elements within hematite, kaolinite and white micas from the rock exposures to the colluvium and then distal soils. From this interpretation, the regolith-landform units of most benefit to exploration are Plains and Plains – Greater Elevation. These contain the highest concentrations of Cs, Sc, Co and Ni and would be beneficial for further sampling. Although this is a regolith dominated terrain, the geochemical and mineralogical surface expression of alteration has not been impeded by the weathered and transported nature of this landscape.

Data integration using geochemistry and mineralogy is an approach that is gaining interest (e.g. Laakso *et al.* 2016; Lampinen *et al.* 2017). These methods could also integrate other regional-scale information such as a wider range of geophysical data and regional geology to create a product such as a mineral prospectivity map for specific ore deposit types. **Chapter 5** was focused at a tenement scale although this approach could be extrapolated to regional scales to infer which units may contain interesting mineralogy and hence elevated or depleted geochemistry. This can therefore assist with reconnaissance exploration planning in a new region by conducting substantial desktop studies by providing detailed landscape information and interpretation.

The collection of geochemical data for mineral exploration is an expensive process and the interpretation of results are often under-interpreted by explorers. Using these additional sources of information could

also save time and money by sampling less extensively across units that provide limited benefit for exploration. These savings could instead be used to select a different analytical method or suite of elements, producing a more targeted and appropriate geochemical dataset. Integrating multiple sources of information may assist with identification of specific regions for future exploration campaigns and sampling efforts. The overall implication for mineral exploration in a regolith dominated terrain using geochemical and mineralogical hyperspectral data is to provide independent lines of evidence of a nearby porphyry deposit by highlighting regions of interest from geochemical and mineralogical interpretation.

In a region where regolith cover dominates, these associations are encouraging as the use of such integrated methods could provide positive outcomes in other similar environments. Using the regolith-landform mapping with any historical surface geochemical data could reduce incorrect interpretations of potential buried mineralisation by interpreting landscape processes and position. This can be beneficial when no field work can be conducted and field campaign planning is based on desktop studies.

Together, these components may be considered a collection of alternative methods for the mineral exploration toolkit. The methods developed in this thesis can be integrated with traditional forms of data to reduce the potential risk of mineral exploration and long term financial investment. This toolkit would be most valuable during the early stages of exploration, when exploring a new region that has limited field or historical data. They could also be implemented after basic desktop studies as additional methods to enhance interpretation of the landscape and any potential surface expressions of mineralisation. Application of these methods in regolith dominated terrains is valuable as the requirement to explore deeper is increasing. The need to use the regolith as a tool for exploration is also increasing and this work has indicated constructive and first pass outcomes can be enhanced with other lines of evidence but are also as useful with the current data available. Field work and associated sampling campaigns can be targeted more appropriately for the landscape which will reduce expense and allow funds to be appropriately distributed for ongoing exploration. This is beneficial for junior explorers with limited budgets who contribute over 60 % of exploration in the western world (Schodde 2019).

The methods presented here are cheaper than extensive exploration campaigns and drilling. The spatial extent they offer is broader than traditional exploration methods and demonstrates the potential benefit of interpreting land surface information. There is the ability to provide rapid turnaround compared to traditional drilling or field methods and requires far less 'people power'. Therefore, the financial outlay is also reduced to generate results and identify regions of interest. Overall, these methods are flexible with existing or historical data and are able to assist with the reduction of overall risk and cost of ongoing exploration in buried terrains.

6.2 Future Research

From this thesis, there are a number of avenues that could address remaining research gaps. These include the use of machine learning, statistical geochemical methods and subsurface mineralogical and geochemical data.

Machine learning and prospectivity mapping is a research area that is being developed for mineral exploration (e.g. Rodriguez-Galiano *et al.* 2015). These methods use supervised classifications of multivariate data to identify patterns, but unlike unsupervised classification, machine learning requires training data to train, validate and test the accuracy of the algorithm. There has been increasing interest in machine learning for a variety of geological applications, one of the most recent of which is the Explorer Challenge run by OZ Minerals and Unearthed (Unearthed Solutions 2019). In this scenario, the project was designed to bring new perspectives to existing company and state government data to identify potential new drill targets in the Mt Woods Inlier in the northern Gawler Craton. Most submissions developed mineral prospectivity maps using a combination of machine learning algorithms and geological interpretation. Although these methods could be applicable in a number of mineral exploration situations, they should be used with caution as reproducibility and inaccurate predictions are common without proper examination of what the methods achieve (Japkowicz 2006). In the southern Gawler Ranges, prospectivity mapping using machine learning algorithms could potentially provide useful interpretation of regional scale features using geophysics, lithology and structural interpretation to assist with further assessment of the prospectivity for different ore deposit styles.

However, machine learning may not be the most appropriate method in this particular study area due to the limited amount of data available as well as the quality of historical data collected by Investigator Resources. In particular, data available in the tenement area from mineral exploration companies is currently insufficient for algorithm training and validation. Furthermore, the use of multivariate analysis for soil geochemistry (e.g. Grunsky 2010; Gazley *et al.* 2015; Levitan *et al.* 2015; Grunsky and de Caritat 2019) is more appropriate due to the statistically robust nature of the approach: even with a dataset limited in number of elements or samples, it is possible to identify patterns within the data.

The concept of integrating geochemical and mineralogical data sets could be expanded in spatial scope to examine subsurface alteration and mineralisation to broaden the interpretation the mineral system in this region. Integrating subsurface mineralogical information from instruments such as the HyLogger™ spectral drill core logger has been used to produce a high resolution mineralogical model of subsurface alteration in the Hamersley Province in Western Australia and the eastern Gawler Craton (e.g. Haest *et al.* 2012; van der Wielen *et al.* 2013) and can complement geochemical interpretation. Research integrating mineralogical and geochemical data in the eastern Gawler Craton has mapped IOCG mineral

systems and identified other prospective regions in the subsurface (Fabris *et al.* 2013). Across the main study area of the thesis, there are a number of diamond and reverse circulation drill holes and some of these at Paris have been scanned with a HyLogger™ (Gordon *et al.* 2016) to identify mineralogy present at the deposit. However, there are recently drilled holes proximal to Nankivel Hill (Investigator Resources 2017) that could be spectrally scanned for mineralogical examination and combined with geochemistry collected from drill core. Data such as this, when integrated with surficial interpretations of mineralogy and geochemistry, could provide a broader picture of the processes that lead to the formation of buried mineralisation such as those described by Halley *et al.* (2015).

6.3 Conclusions

There is a suite of traditional methods used in mineral exploration including geochemistry, geophysics and geological mapping. However, the integration of alternative remote sensing and geospatial methods used in this thesis has demonstrated the benefits of multiple approaches using surficial data. This thesis developed or applied new and existing alternative methods and has shown their benefits for mineral exploration in the vegetated and regolith dominated terrain of the southern Gawler Ranges, a prospective region within the Gawler Craton. Due to the significant regolith cover across much of the Australian continent, the approaches developed and demonstrated here have wider potential for mineral exploration and discovery of deposits under cover.

6.4 References

Asner, G.P., & Heidebrecht, K.B. (2002). Spectral unmixing of vegetation, soil and dry carbon cover in arid regions: Comparing multispectral and hyperspectral observations. *International Journal of Remote Sensing, 23*, 3939-3958. doi: 10.1080/01431160110115960

Capolupo, A., Pindozzi, S., Okello, C., Fiorentino, N., & Boccia, L. (2015). Photogrammetry for environmental monitoring: The use of drones and hydrological models for detection of soil contaminated by copper. *Science of The Total Environment, 514*, 298-306. doi: 10.1016/j.scitotenv.2015.01.109

Cracknell, M.J., Reading, A.M., & de Caritat, P. (2015). Multiple influences on regolith characteristics from continental-scale geophysical and mineralogical remote sensing data using Self-Organizing Maps. *Remote Sensing of Environment, 165*, 86-99. doi: 10.1016/j.rse.2015.04.029

Cudahy, T., Caccetta, M., Thomas, M., Hewson, R., Abrams, M., Kato, M., Kashimura, O., Ninomiya, Y., Yamaguchi, Y., Collings, S., Laukamp, C., Ong, C., Lau, I., Rodger, A., Chia, J., Warren, P., Woodcock, R., Fraser, R., Rankine, T., Vote, J., de Caritat, P., English, P., Meyer, D., Doescher, C., Fu, B.H., Shi, P.L., & Mitchell, R. (2016). Satellite-derived mineral mapping and monitoring of weathering, deposition and erosion. *Scientific Reports, 6*. doi: 10.1038/srep23702

Dering, G.M., Micklethwaite, S., Thiele, S.T., Vollgger, S.A., & Cruden, A.R. (2019). Review of drones, photogrammetry and emerging sensor technology for the study of dykes: Best practises and future potential. *Journal of Volcanology and Geothermal Research, 373*, 148-166. doi: 10.1016/j.jvolgeores.2019.01.018

Elvidge, C.D. (1990). Visible and near infrared reflectance characteristics of dry plant materials. *International Journal of Remote Sensing, 11*, 1775-1795. doi: 10.1080/01431169008955129

Fabris, A.J., Halley, S., van der Wielen, S., Keeping, T., & Gordon, G. (2013). IOCG-style mineralisation in the central eastern Gawler Craton, SA; characterisation of alteration, geochemical associations and exploration vectors. Adelaide, South Australia: Department of Manufacturing, Innovation, Trade, Resources and Energy. Geological Survey of South Australia. Document Number: Report Book 2013/0014

Gazley, M., Collins, K., Roberston, J., Hines, B., A Fisher, L., & McFarlane, A. (2015). Application of principal component analysis and cluster analysis to mineral exploration and mine geology. In, *AusIMM New Zealand Branch Annual Conference 2015*. Dunedin, New Zealand: Australasian Institute of Mining and Metallurgy

Gordon, G., Murray, J., & Mauger, A. (2016). Infrared analysis of drill cores from the Paris Silver Prospect, South Australia. In, *AESC 2016 - Australian Earth Sciences Convention*. Adelaide, Australia: Geological Society of Australia

Grunsky, E.C. (2010). The interpretation of geochemical survey data. *Geochemistry: Exploration Environment Analysis, 10*, 27-74. doi: 10.1144/1467-7873/09-210

Grunsky, E.C., & de Caritat, P. (2019). State-of-the-Art Analysis of Geochemical Data for Mineral Exploration. *Geochemistry: Exploration, Environment, Analysis*, 34. doi: 10.1144/geochem2019-031

Haest, M., Cudahy, T., Laukamp, C., & Gregory, S. (2012). Quantitative Mineralogy from Infrared Spectroscopic Data. II. Three-Dimensional Mineralogical Characterization of the Rocklea Channel Iron Deposit, Western Australia. *Economic Geology, 107*, 229-249. doi: 10.2113/econgeo.107.2.229

Haest, M., Cudahy, T., Rodger, A., Laukamp, C., Martens, E., & Caccetta, M. (2013). Unmixing the effects of vegetation in airborne hyperspectral mineral maps over the Rock lea Dome iron-rich palaeochannel system (Western Australia). *Remote Sensing of Environment, 129*, 17-31. doi: 10.1016/j.rse.2012.10.011

Halley, S., Dilles, J., & Tosdal, R. (2015). Footprints: hydrothermal alteration and geochemical dispersion around porphyry copper deposits. *Society of Economic Geologists Newsletter, 100*, 12-17

Harris Aerial (2019). Hyspex Mjolnir S-620 Hyperspectral Camera, https://www.harrisaerial.com/solutions-applications/hyspex-mjolnir-s-620-hyperspectral-camera/: Harris Aerial. Access Date: October 2019

Headwall Photonics, Inc (2018). Micro-Hyperspec Imaging Sensors Product Data Sheet, https://cdn2.hubspot.net/hubfs/145999/June%202018%20Collateral/MicroHyperspec0418.pdf: Headwall Photonics, Inc. Access Date: October 2019

Hewson, R.D., Cudahy, T.J., Drake-Brockman, J., Meyers, J., & Hashemi, A. (2006). Mapping geology associated with manganese mineralisation using spectral sensing techniques at Woodie Woodie, East Pilbara. *Exploration Geophysics, 37*, 389-400. doi: 10.1071/eg06389

Investigator Resources (2017). New drilling and advanced exploration techniques upgrade porphyry copper target at Nankivel. In J. Anderson, & J. Murray (Eds.). Adelaide, South Australia: Investigator Resources

Iost Filho, F.H., Heldens, W.B., Kong, Z., & de Lange, E.S. (2020). Drones: Innovative Technology for Use in Precision Pest Management. *Journal of Economic Entomology*, *113*, 1-25. doi: 10.1093/jee/toz268

Japkowicz, N. (2006). Why question machine learning evaluation methods. In, *AAAI workshop on evaluation methods for machine learning* (pp. 6-11)

Laakso, K., Peter, J.M., Rivard, B., & White, H.P. (2016). Short-Wave Infrared Spectral and Geochemical Characteristics of Hydrothermal Alteration at the Archean Izok Lake Zn-Cu-Pb-Ag

Volcanogenic Massive Sulfide Deposit, Nunavut, Canada: Application in Exploration Target Vectoring. *Economic Geology, 111*, 1223-1239. doi: 10.2113/econgeo.111.5.1223

Lampinen, H.M., Laukamp, C., Occhipinti, S.A., Metelka, V., & Spinks, S.C. (2017). Delineating Alteration Footprints from Field and ASTER SWIR Spectra, Geochemistry, and Gamma-Ray Spectrometry above Regolith-Covered Base Metal Deposits—An Example from Abra, Western Australia. *Economic Geology, 112*, 1977-2003. doi: 10.5382/econgeo.2017.4537

Levitan, D.M., Zipper, C.E., Donovan, P., Schreiber, M.E., Seal, R.R., Engle, M.A., Chermak, J.A., Bodnar, R.J., Johnson, D.K., & Aylor, J.G. (2015). Statistical analysis of soil geochemical data to identify pathfinders associated with mineral deposits: An example from the Coles Hill uranium deposit, Virginia, USA. *Journal of Geochemical Exploration, 154*, 238-251. doi: 10.1016/j.gexplo.2014.12.012

Micklethwaite, S. (2018). Drones in mining- the new possible. In, *AusIMM Bulletin* (pp. 32-36): The Australasian Institute of Mining and Metallurgy

Micklethwaite, S., Turner, D., Vasuki, Y., Kovesi, P., Holden, E.-J., & Lucieer, A. (2012). Mapping from an Armchair: Rapid, High-Resolution Mapping Using UAV and Computer Vision Technology. In, *Proceedings of Structural Geology and Resources 2012* (pp. 130-133). Kalgoorlie, WA: Australian Institute of Geoscientists

Rango, A., Laliberte, A., Stelle, C., Herrick, J.E., Bestelmeyer, B., Schmugge, T., Roanhorse, A., & Jenkins, V. (2006). Using Unmanned Aerial Vehicles for Rangelands: Current Applications and Future Potentials. *Environmental Practice, 8*, 159-168. doi: 10.1017/S1466046606060224

Roberts, D.A., Gardner, M., Church, R., Ustin, S., Scheer, G., & Green, R.O. (1998). Mapping Chaparral in the Santa Monica Mountains Using Multiple Endmember Spectral Mixture Models. *Remote Sensing of Environment, 65*, 267-279. doi: 10.1016/S0034-4257(98)00037-6

Rodriguez-Galiano, V., Sanchez-Castillo, M., Chica-Olmo, M., & Chica-Rivas, M. (2015). Machine learning predictive models for mineral prospectivity: An evaluation of neural networks, random forest, regression trees and support vector machines. *Ore Geology Reviews, 71*, 804-818. doi: 10.1016/j.oregeorev.2015.01.001

Schodde, R.C. (2019). Trends in exploration. In, *International Mining and Resource Conference* (p. 30). Melbourne, Australia: MinEx Consulting

Unearthed Solutions (2019). Explorer Challenge, https://unearthed.solutions/u/competitions/explorer-challenge: Unearthed Solutions. Access Date: September 2019

van der Wielen, S., Fabris, A., Keeling, J., Mauger, A., Gordon, G., Keeping, T., Heath, P., Reed, G., Katona, L., Fairclough, M., Hill, S., Giles, D., & Halley, S. (2013). Integrated 3D mineral systems maps for iron oxide copper gold (IOCG) Deposits, Eastern Gawler Craton, South Australia. In E. Jonsson

(Ed.), *12th SGA Biennial Meeting - "Mineral Deposit Research for a High-Tech World"* (pp. 108-111). Uppsala, Sweden: Society of Geology Applied to Mineral Deposits

van Ruitenbeek, F.J.A., Debba, P., van der Meer, F.D., Cudahy, T., van der Meijde, M., & Hale, M. (2006). Mapping white micas and their absorption wavelengths using hyperspectral band ratios. *Remote Sensing of Environment, 102*, 211-222. doi: 10.1016/j.tse.2006.02.012

Weiss, A.D. (2001). Topographic Position and Landforms Analysis. In, *ESRI User Conference*. San Diego, USA: The Nature Conservancy

Appendix A

QUALITIATIVE X-RAY DIFFRACTION OUTPUTS

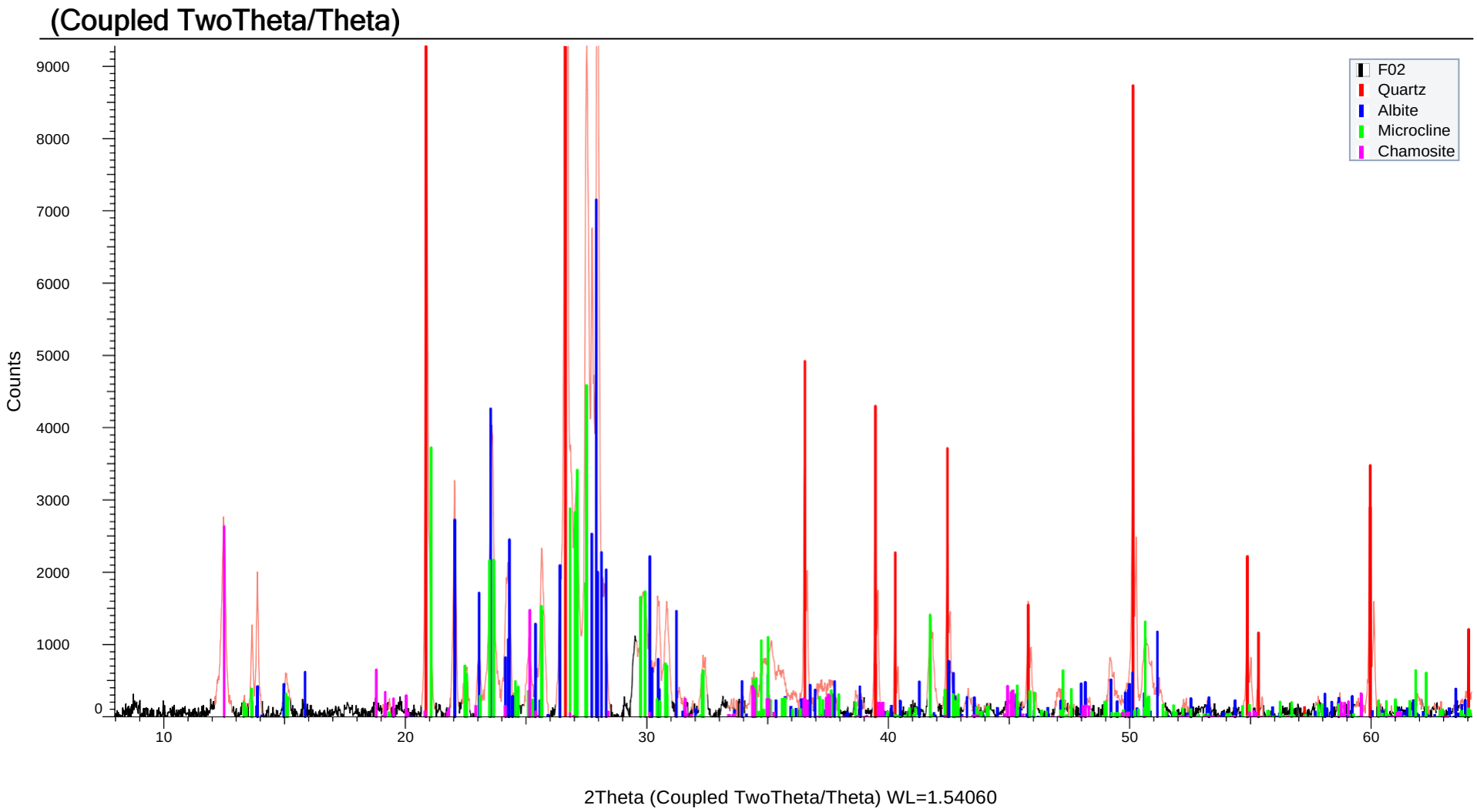
(Coupled TwoTheta/Theta)
F02
Quartz
Albite
Microcline
Chamosite
Counts
9000
8000
7000
6000
5000
4000
3000
2000
1000
0
10
20
30
40
50
60
2Theta (Coupled TwoTheta/Theta) WL=1.54060

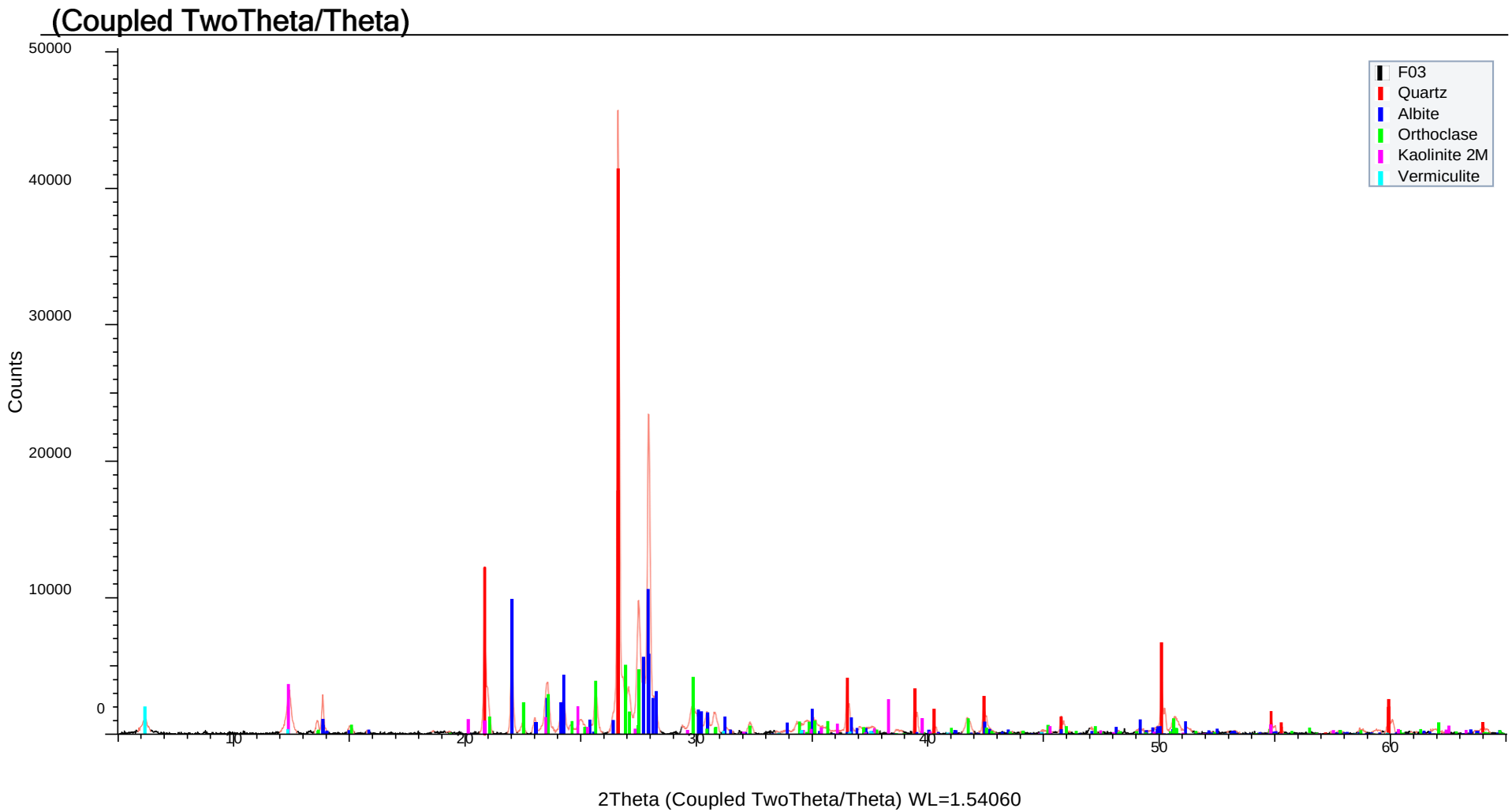
(Coupled TwoTheta/Theta)
50000
40000
30000
20000
10000
0
Counts
10
20
30
40
50
60
2Theta (Coupled TwoTheta/Theta) WL=1.54060
F03
Quartz
Albite
Orthoclase
Kaolinite 2M
Vermiculite

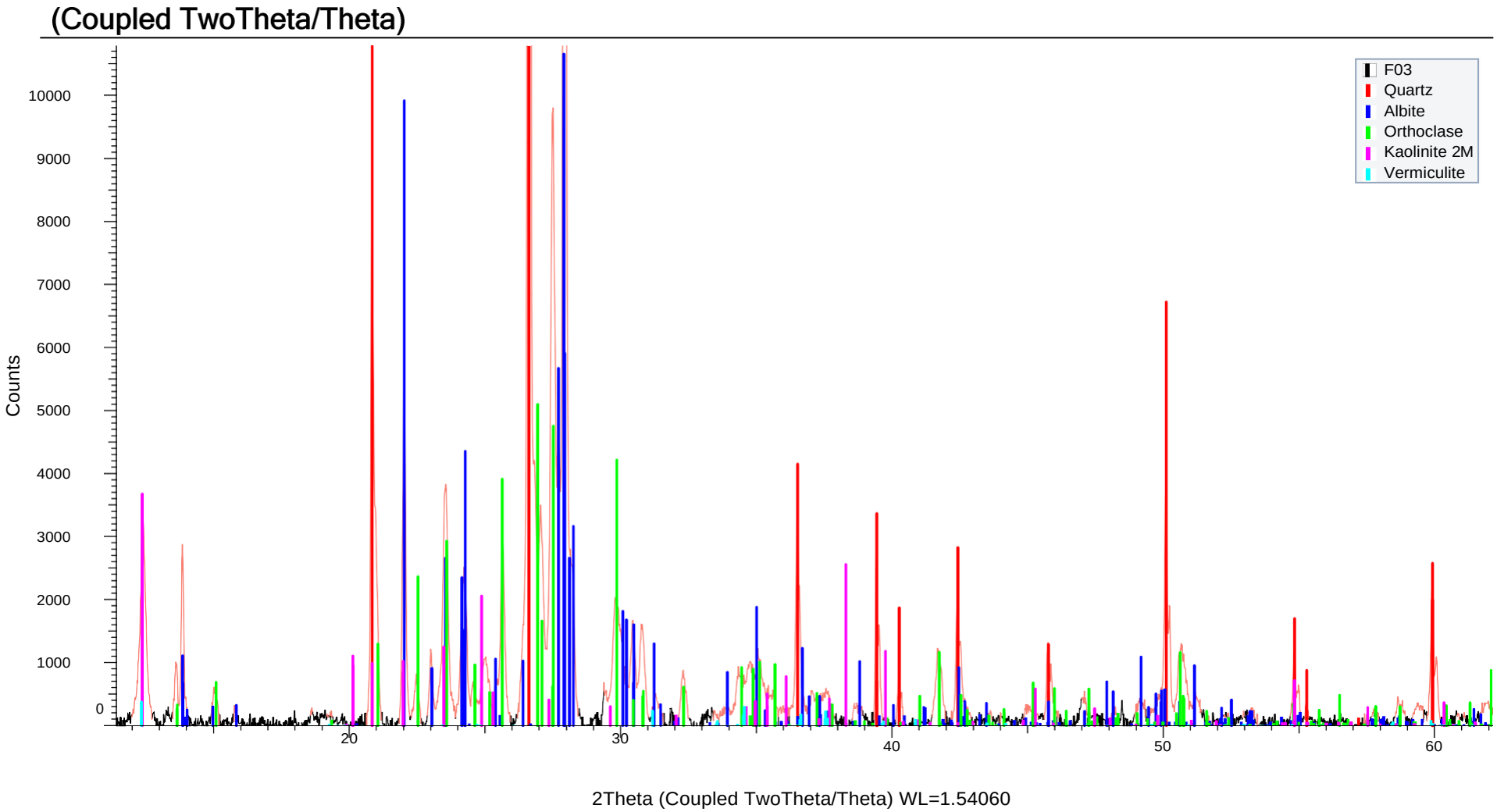
(Coupled TwoTheta/Theta)
F03
Quartz
Albite
Orthoclase
Kaolinite 2M
Vermiculite
Counts
10000
9000
8000
7000
6000
5000
4000
3000
2000
1000
0
20
30
40
50
60
2Theta (Coupled TwoTheta/Theta) WL=1.54060

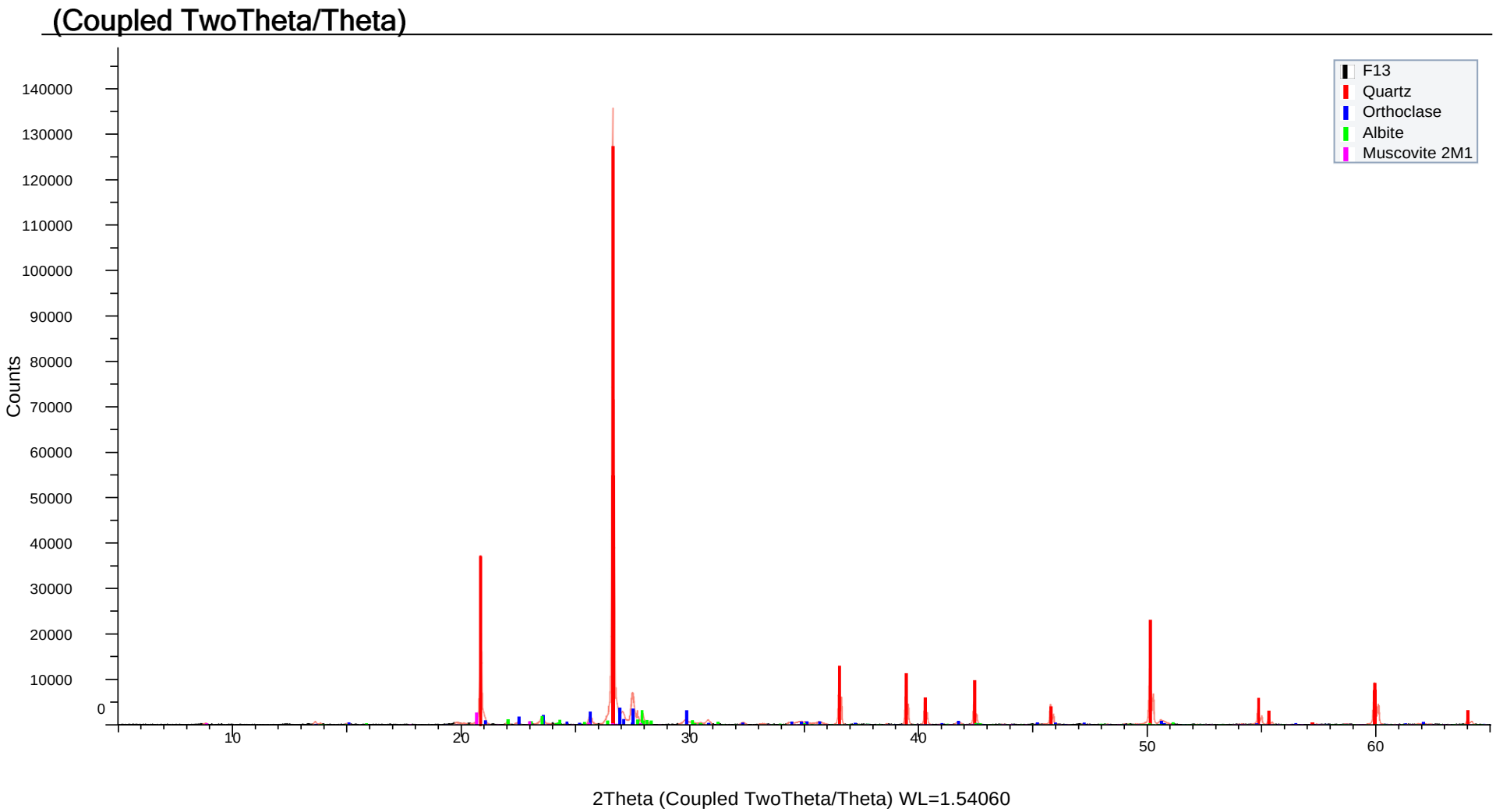
(Coupled TwoTheta/Theta)
F13
Quartz
Orthoclase
Albite
Muscovite 2M1
Counts
140000
130000
120000
110000
100000
90000
80000
70000
60000
50000
40000
30000
20000
10000
0
10
20
30
40
50
60
2Theta (Coupled TwoTheta/Theta) WL=1.54060

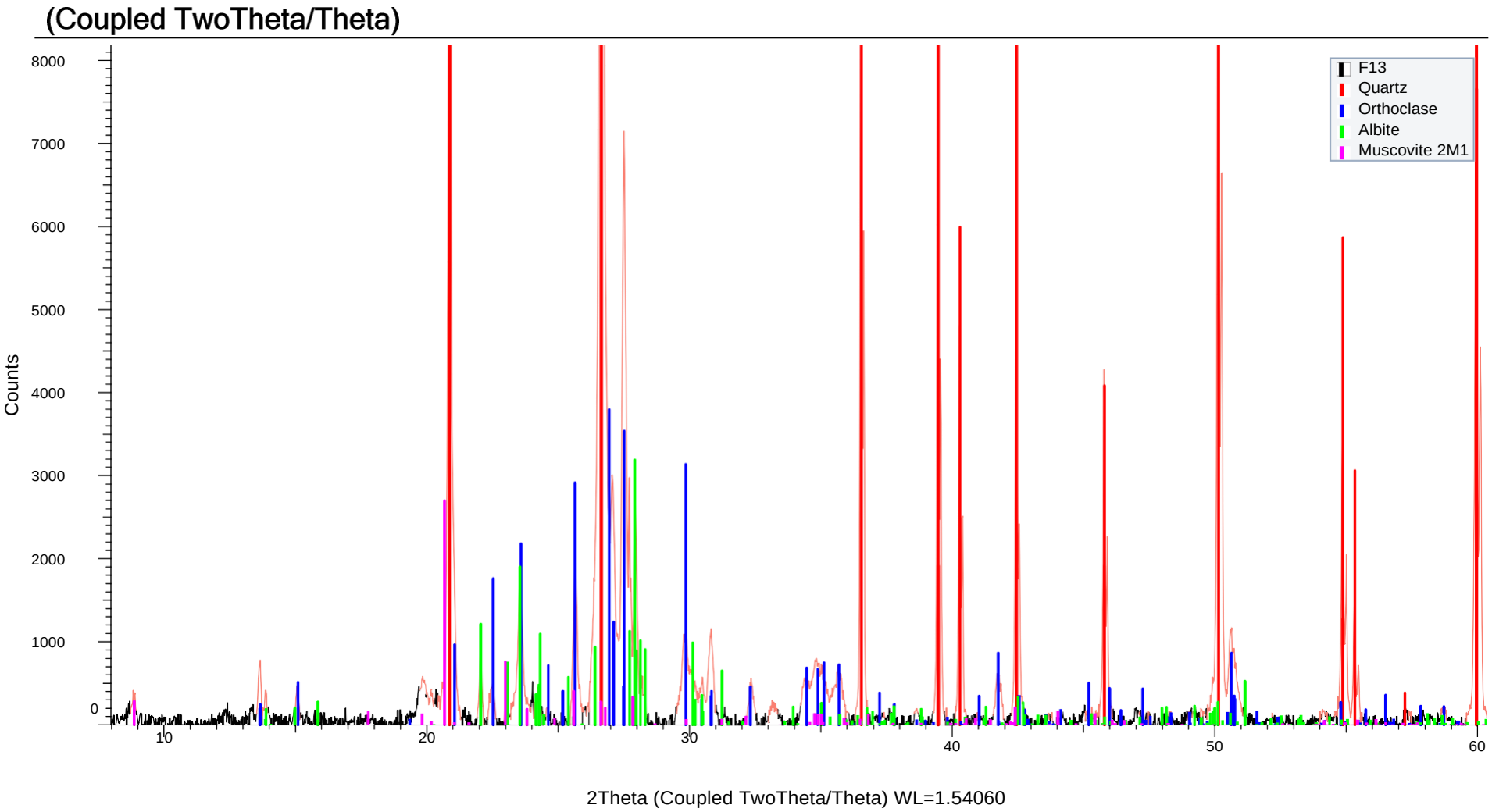
(Coupled TwoTheta/Theta)
F13
Quartz
Orthoclase
Albite
Muscovite 2M1
Counts
8000
7000
6000
5000
4000
3000
2000
1000
0
10
20
30
40
50
60
2Theta (Coupled TwoTheta/Theta) WL=1.54060

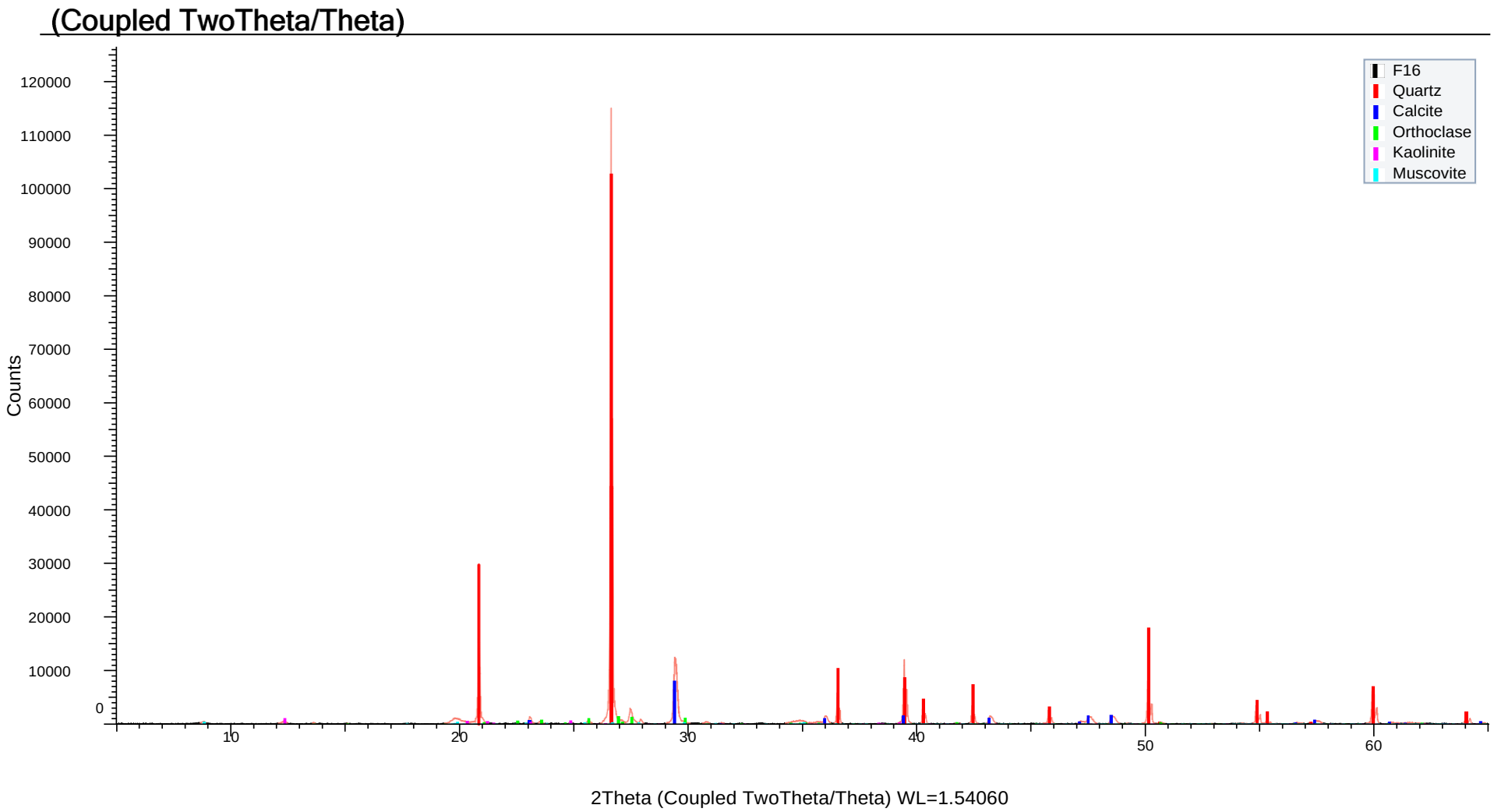
(Coupled TwoTheta/Theta)
F16
Quartz
Calcite
Orthoclase
Kaolinite
Muscovite
Counts
120000
110000
100000
90000
80000
70000
60000
50000
40000
30000
20000
10000
0
10
20
30
40
50
60
2Theta (Coupled TwoTheta/Theta) WL=1.54060

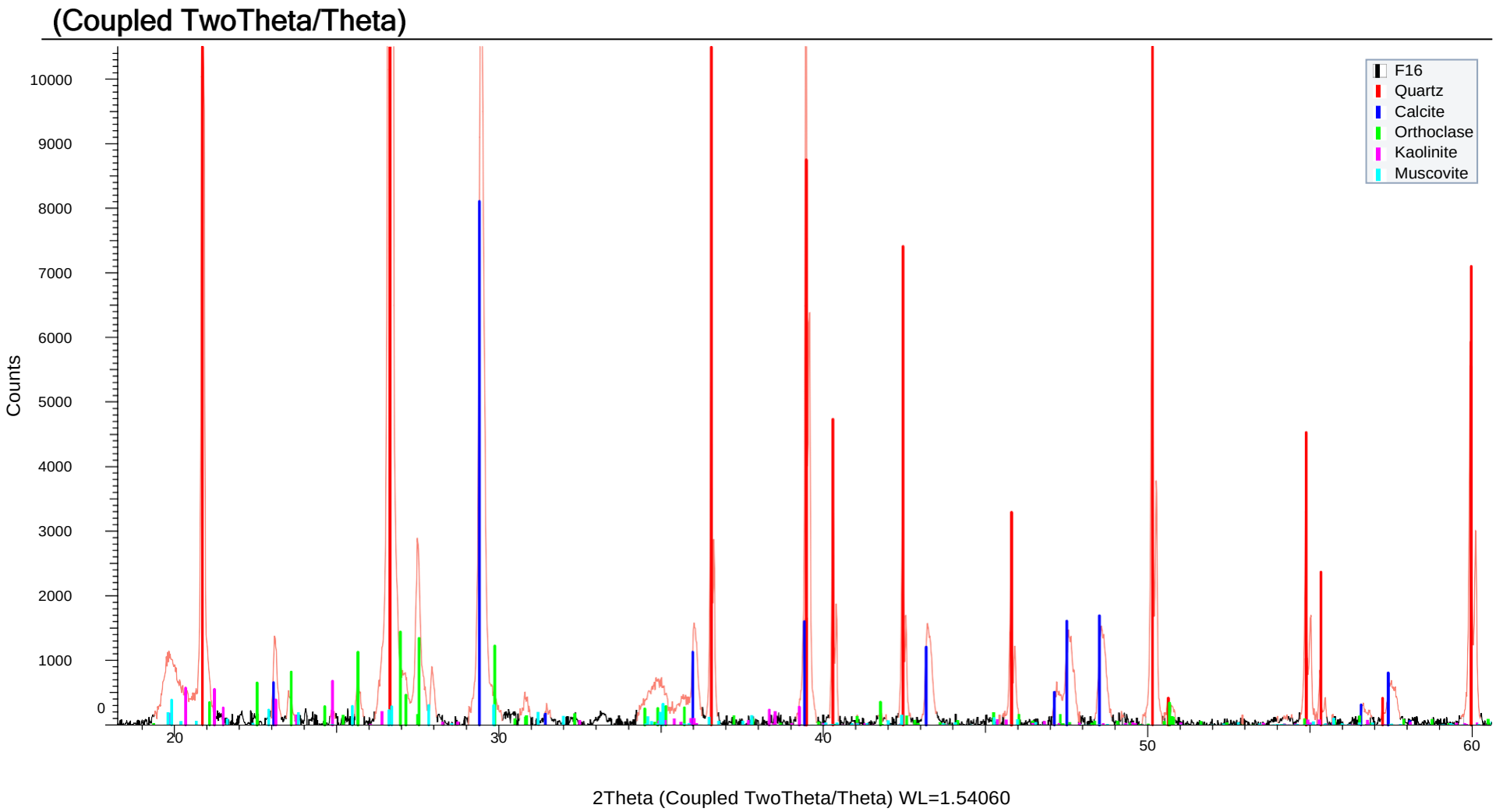
(Coupled TwoTheta/Theta)
F16
Quartz
Calcite
Orthoclase
Kaolinite
Muscovite
Counts
10000
9000
8000
7000
6000
5000
4000
3000
2000
1000
0
20
30
40
50
60
2Theta (Coupled TwoTheta/Theta) WL=1.54060

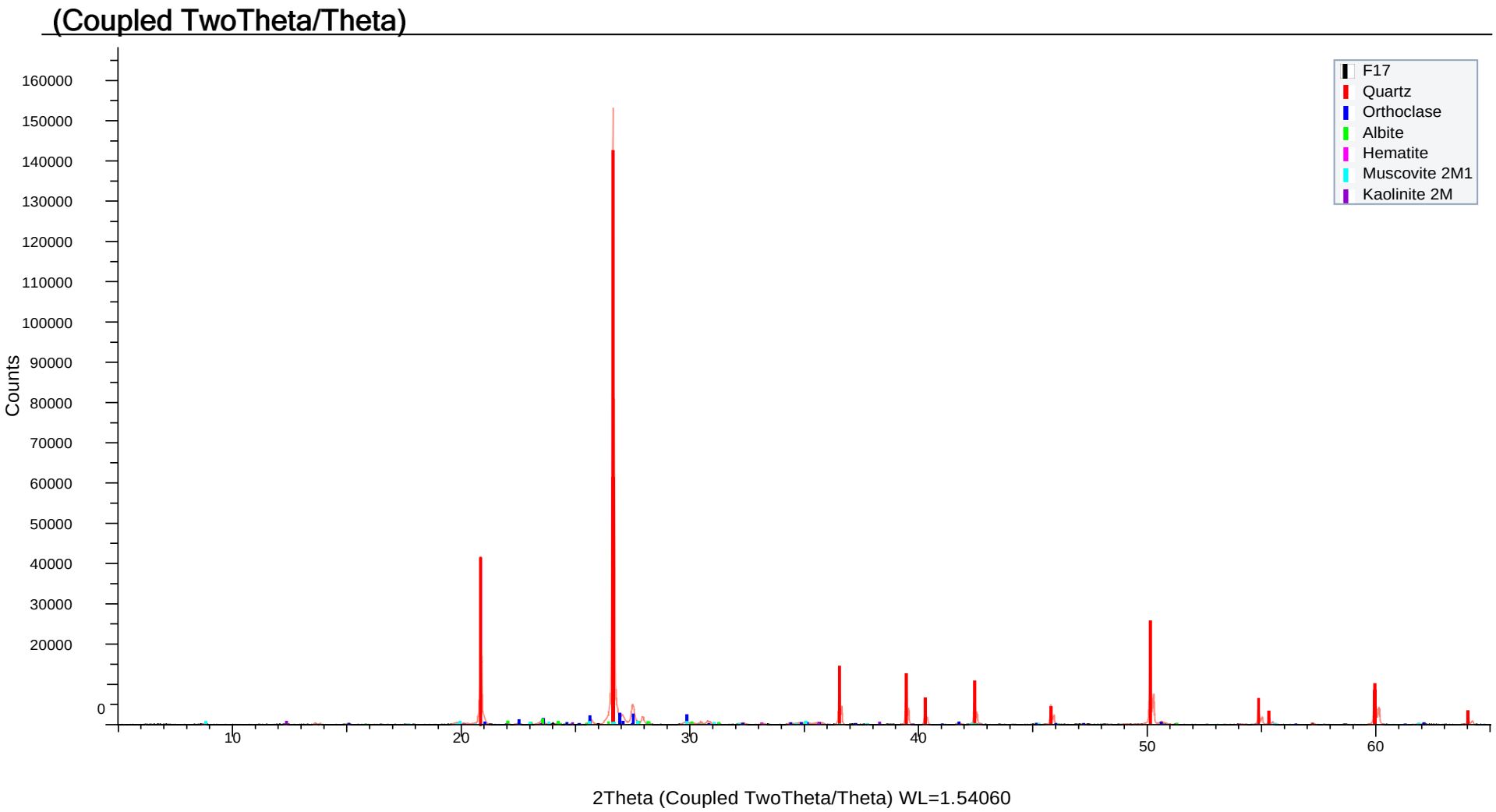
(Coupled TwoTheta/Theta)
F17
Quartz
Orthoclase
Albite
Hematite
Muscovite 2M1
Kaolinite 2M
Counts
160000
150000
140000
130000
120000
110000
100000
90000
80000
70000
60000
50000
40000
30000
20000
0
10
20
30
40
50
60
2Theta (Coupled TwoTheta/Theta) WL=1.54060

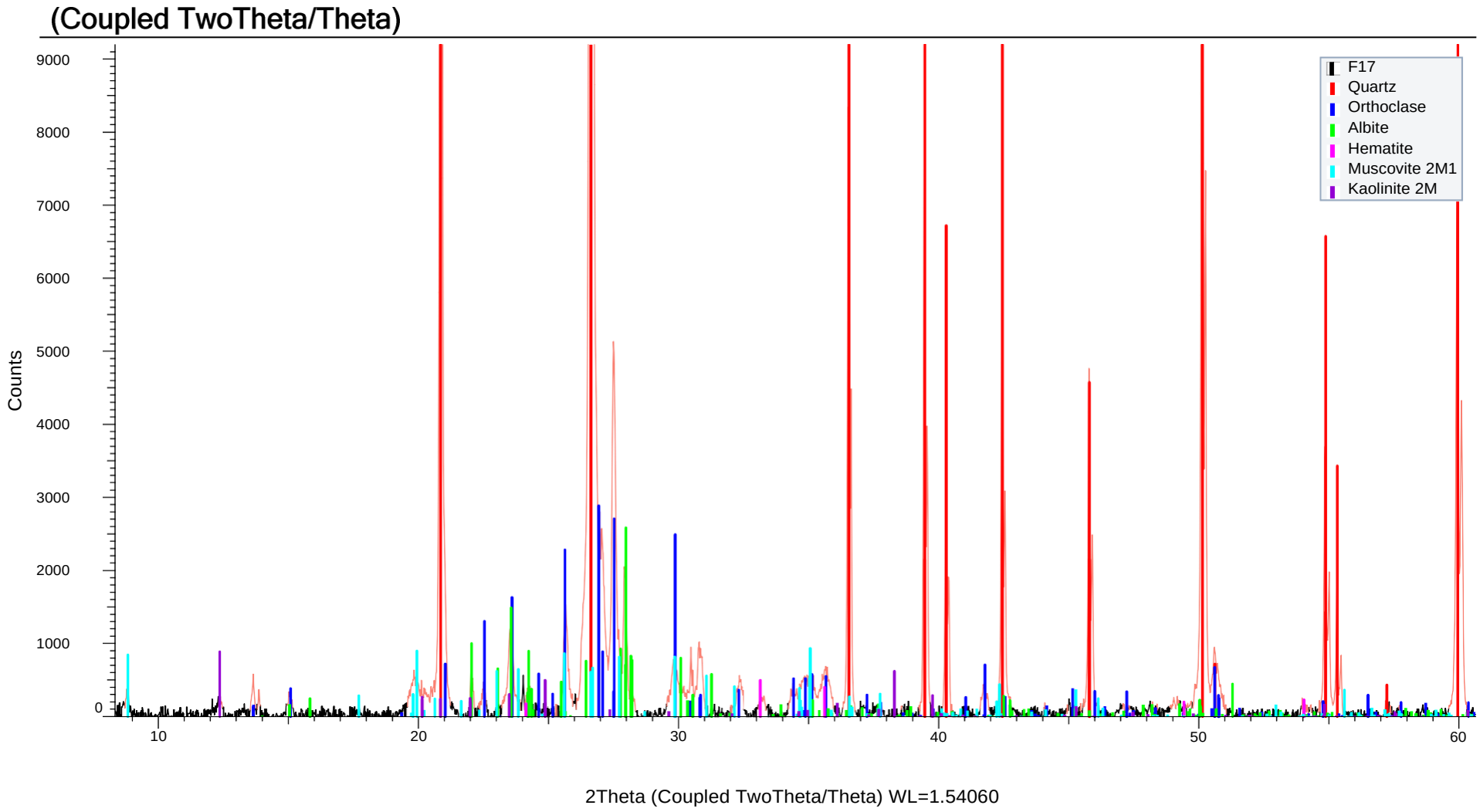
(Coupled TwoTheta/Theta)
Counts
9000
8000
7000
6000
5000
4000
3000
2000
1000
0
10
20
30
40
50
60
F17
Quartz
Orthoclase
Albite
Hematite
Muscovite 2M1
Kaolinite 2M
2Theta (Coupled TwoTheta/Theta) WL=1.54060

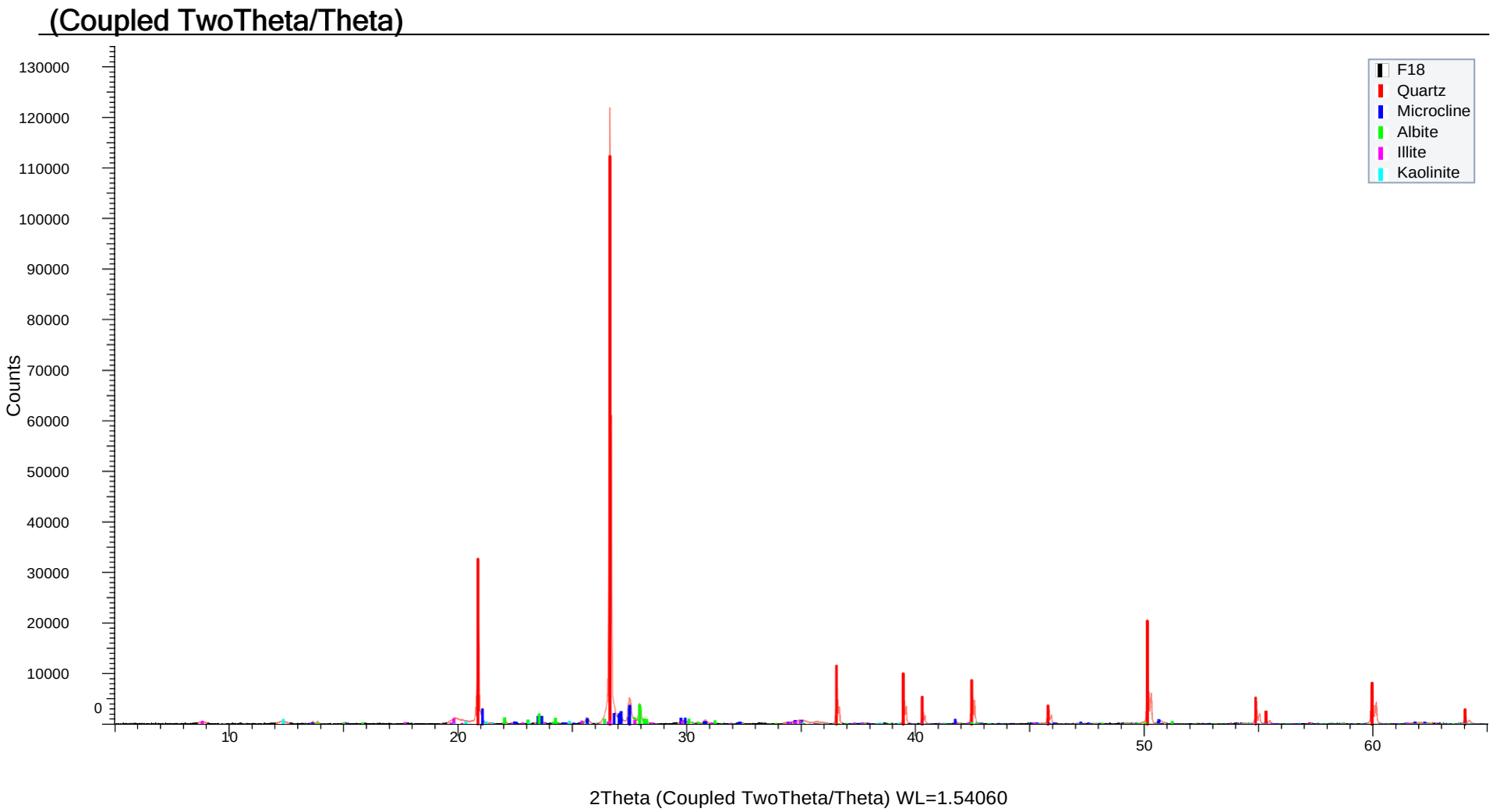
(Coupled TwoTheta/Theta)
130000
120000
110000
100000
90000
80000
70000
60000
50000
40000
30000
20000
10000
0
Counts
10
20
30
40
50
60
2Theta (Coupled TwoTheta/Theta) WL=1.54060
F18
Quartz
Microcline
Albite
Illite
Kaolinite

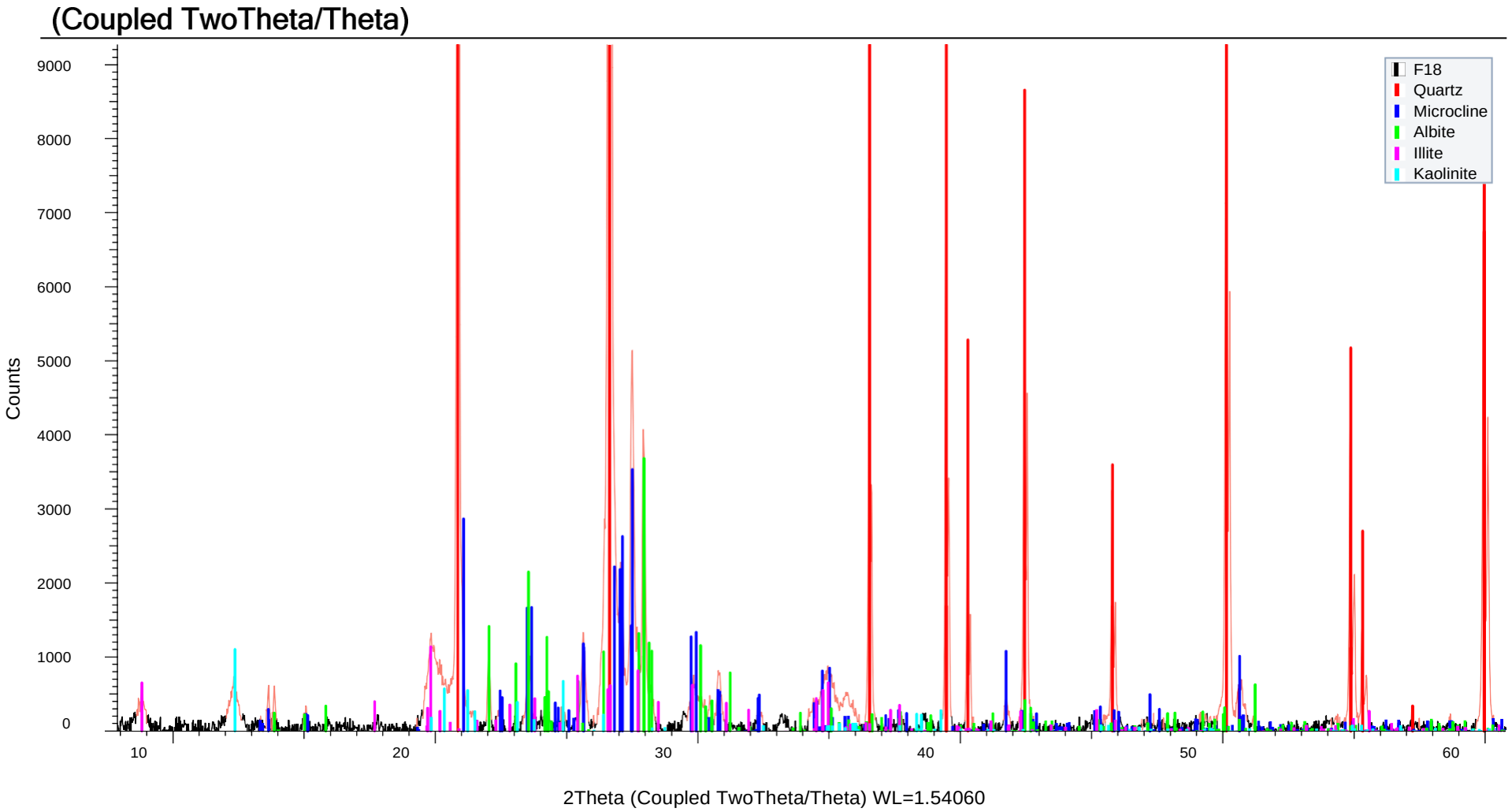
(Coupled TwoTheta/Theta)
F18
Quartz
Microcline
Albite
Illite
Kaolinite
Counts
9000
8000
7000
6000
5000
4000
3000
2000
1000
0
10
20
30
40
50
60
2Theta (Coupled TwoTheta/Theta) WL=1.54060

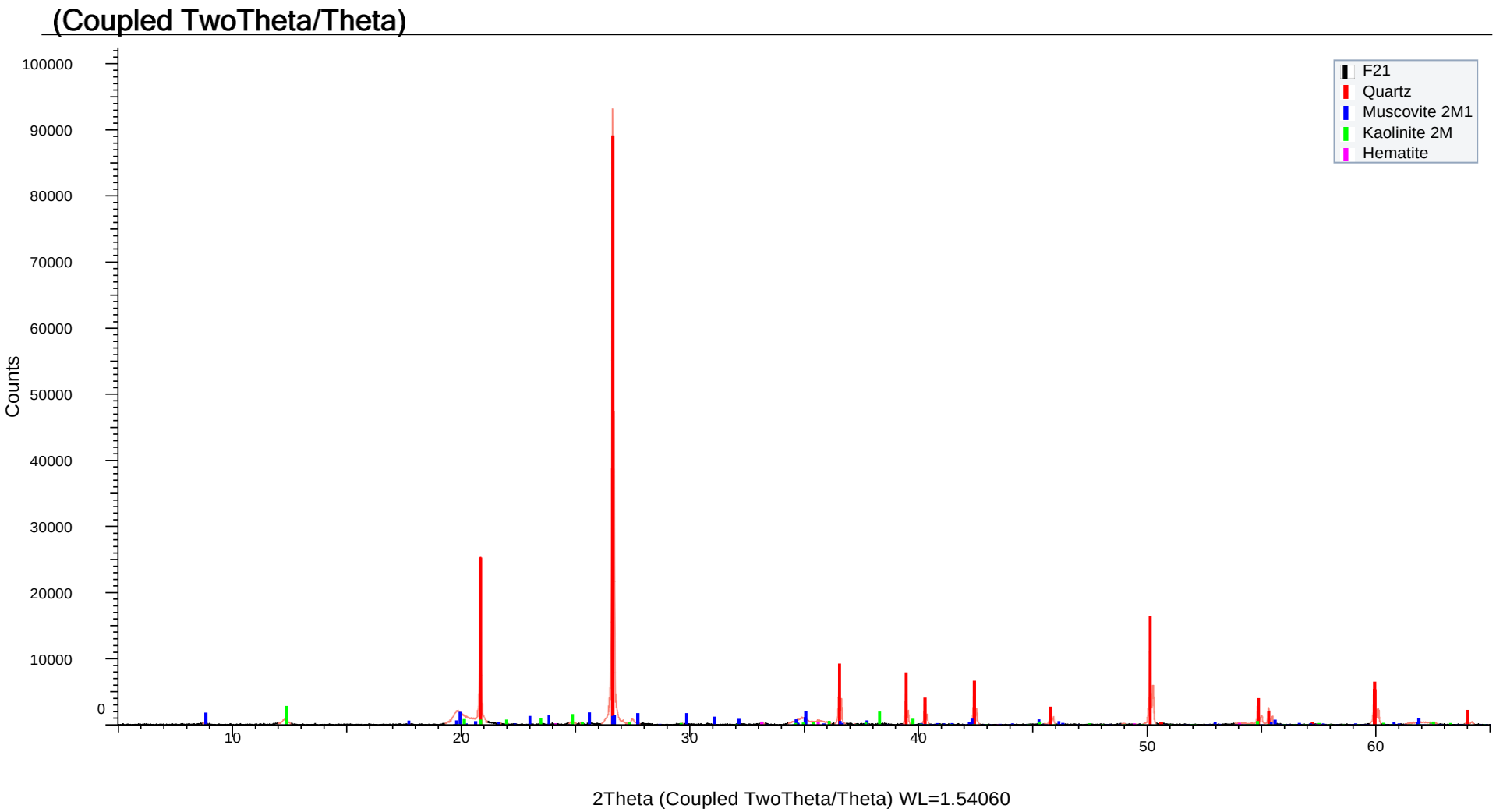
(Coupled TwoTheta/Theta)
F21
Quartz
Muscovite 2M1
Kaolinite 2M
Hematite
Counts
100000
90000
80000
70000
60000
50000
40000
30000
20000
10000
0
10
20
30
40
50
60
2Theta (Coupled TwoTheta/Theta) WL=1.54060

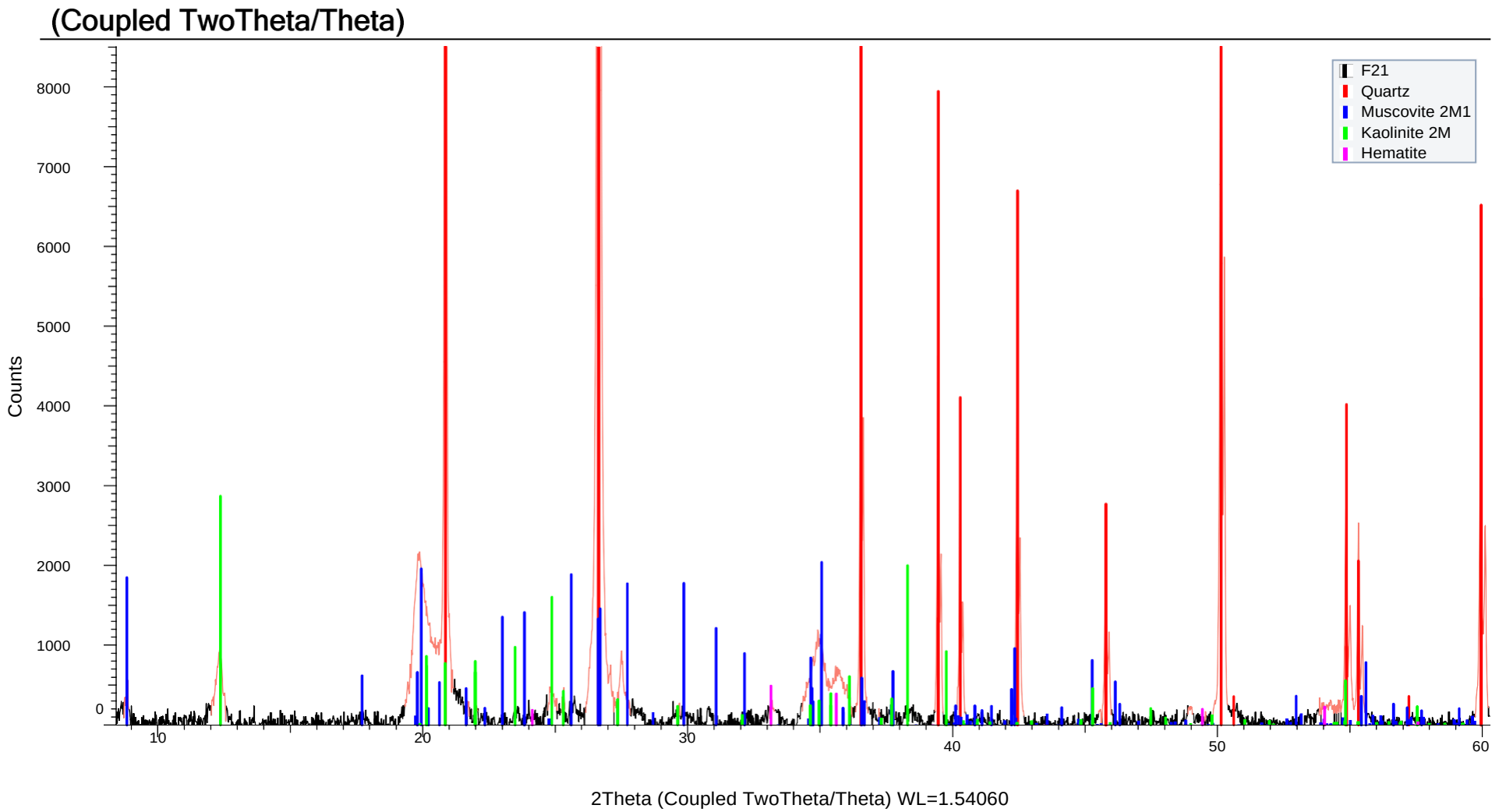
(Coupled TwoTheta/Theta)
F21
Quartz
Muscovite 2M1
Kaolinite 2M
Hematite
Counts
8000
7000
6000
5000
4000
3000
2000
1000
0
10
20
30
40
50
60
2Theta (Coupled TwoTheta/Theta) WL=1.54060

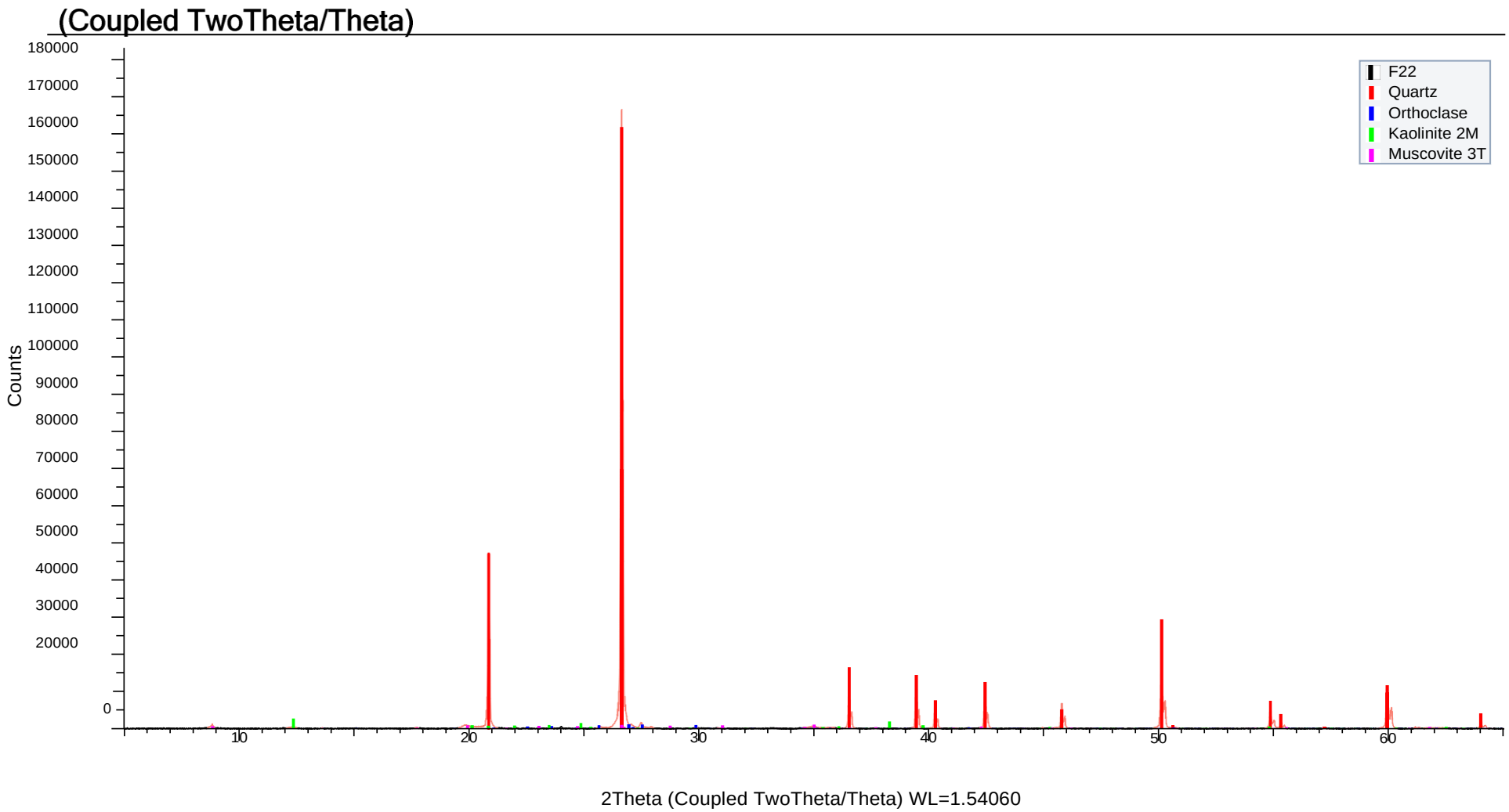
(Coupled TwoTheta/Theta)
Counts
180000
170000
160000
150000
140000
130000
120000
110000
100000
90000
80000
70000
60000
50000
40000
30000
20000
0
10
20
30
40
50
60
F22
Quartz
Orthoclase
Kaolinite 2M
Muscovite 3T
2Theta (Coupled TwoTheta/Theta) WL=1.54060

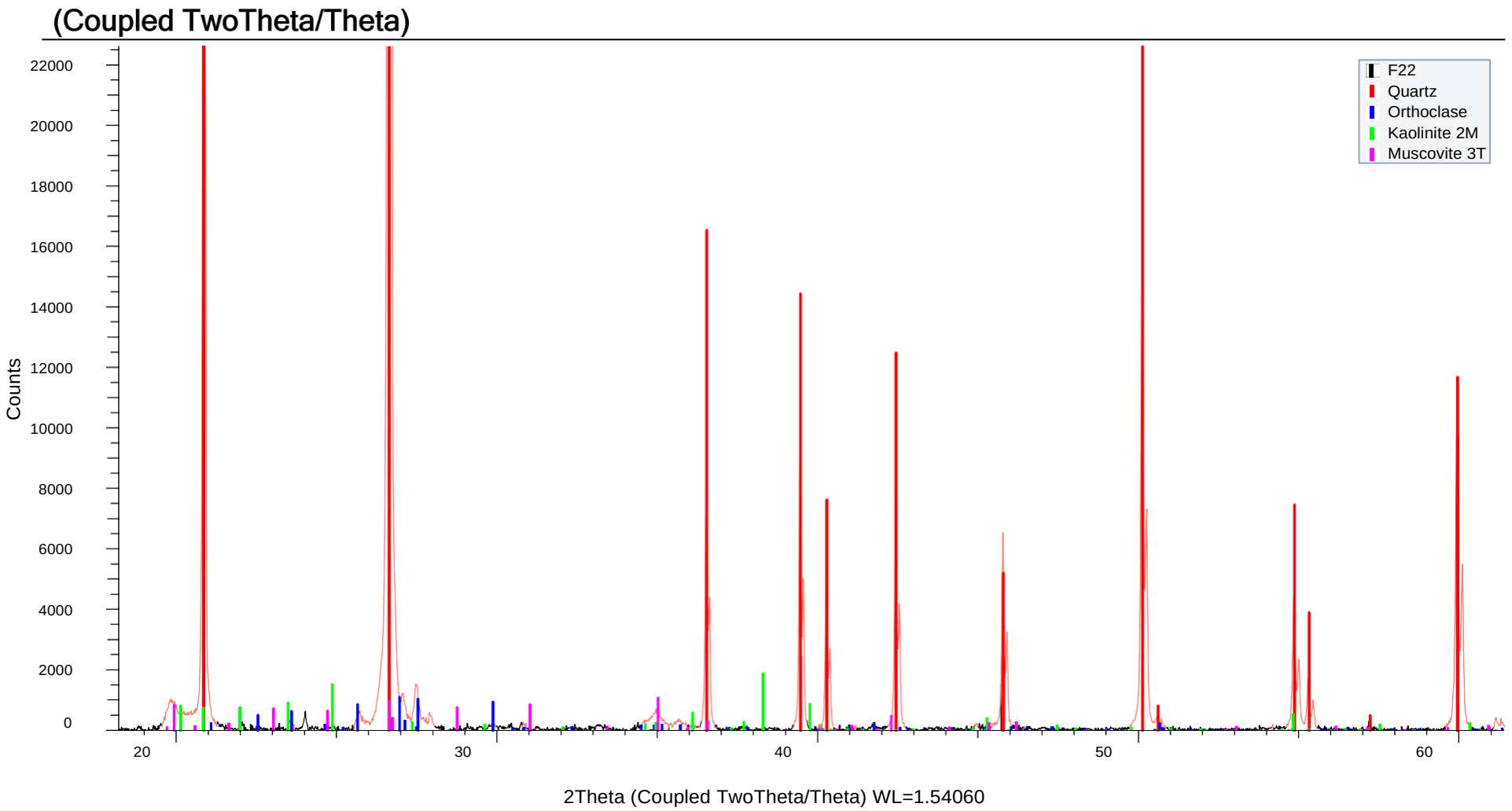
(Coupled TwoTheta/Theta)
F22
Quartz
Orthoclase
Kaolinite 2M
Muscovite 3T
Counts
22000
20000
18000
16000
14000
12000
10000
8000
6000
4000
2000
0
20
30
40
50
60
2Theta (Coupled TwoTheta/Theta) WL=1.54060

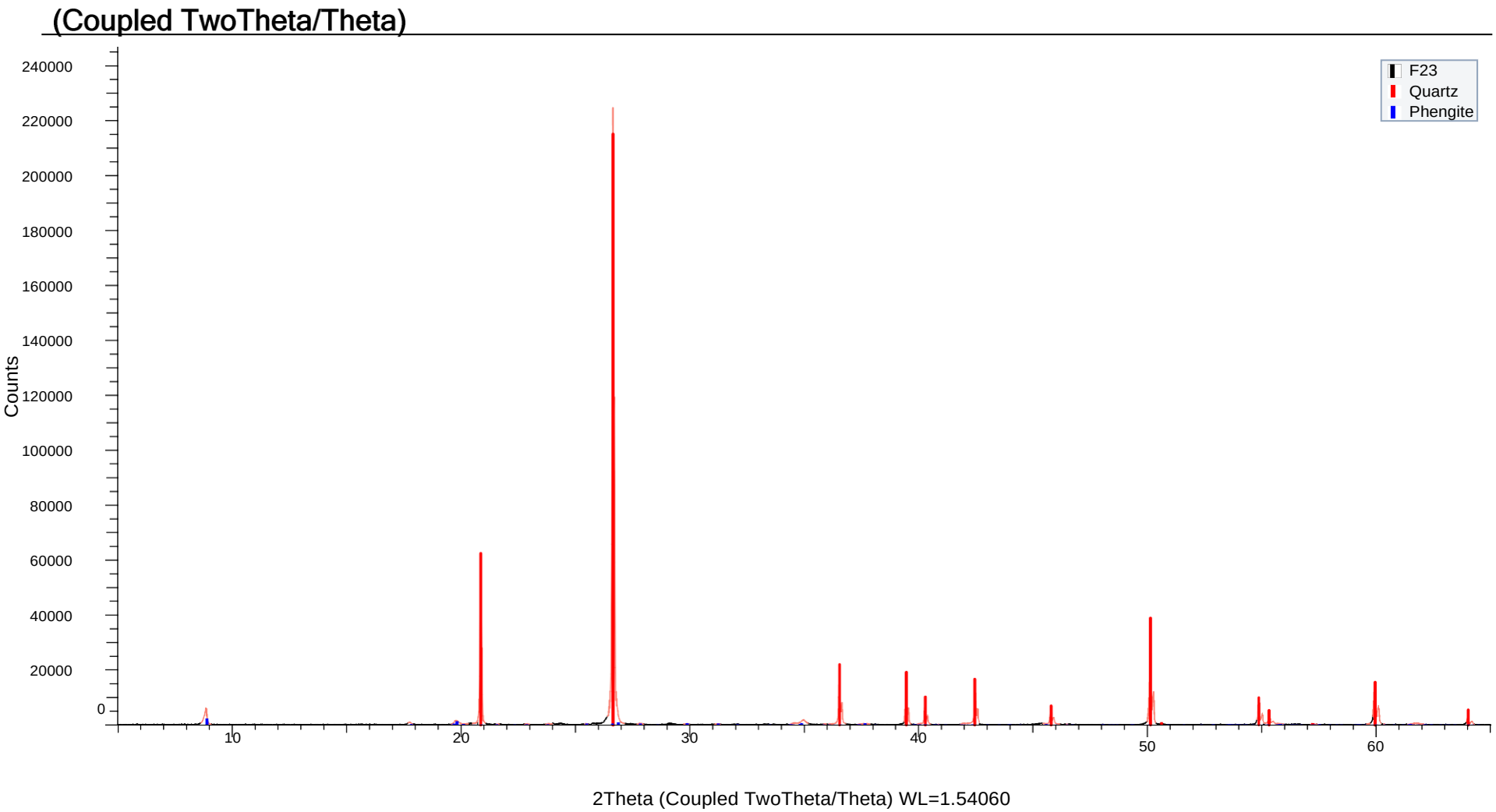
(Coupled TwoTheta/Theta)
F23
Quartz
Phengite
Counts
240000
220000
200000
180000
160000
140000
120000
100000
80000
60000
40000
20000
0
10
20
30
40
50
60
2Theta (Coupled TwoTheta/Theta) WL=1.54060

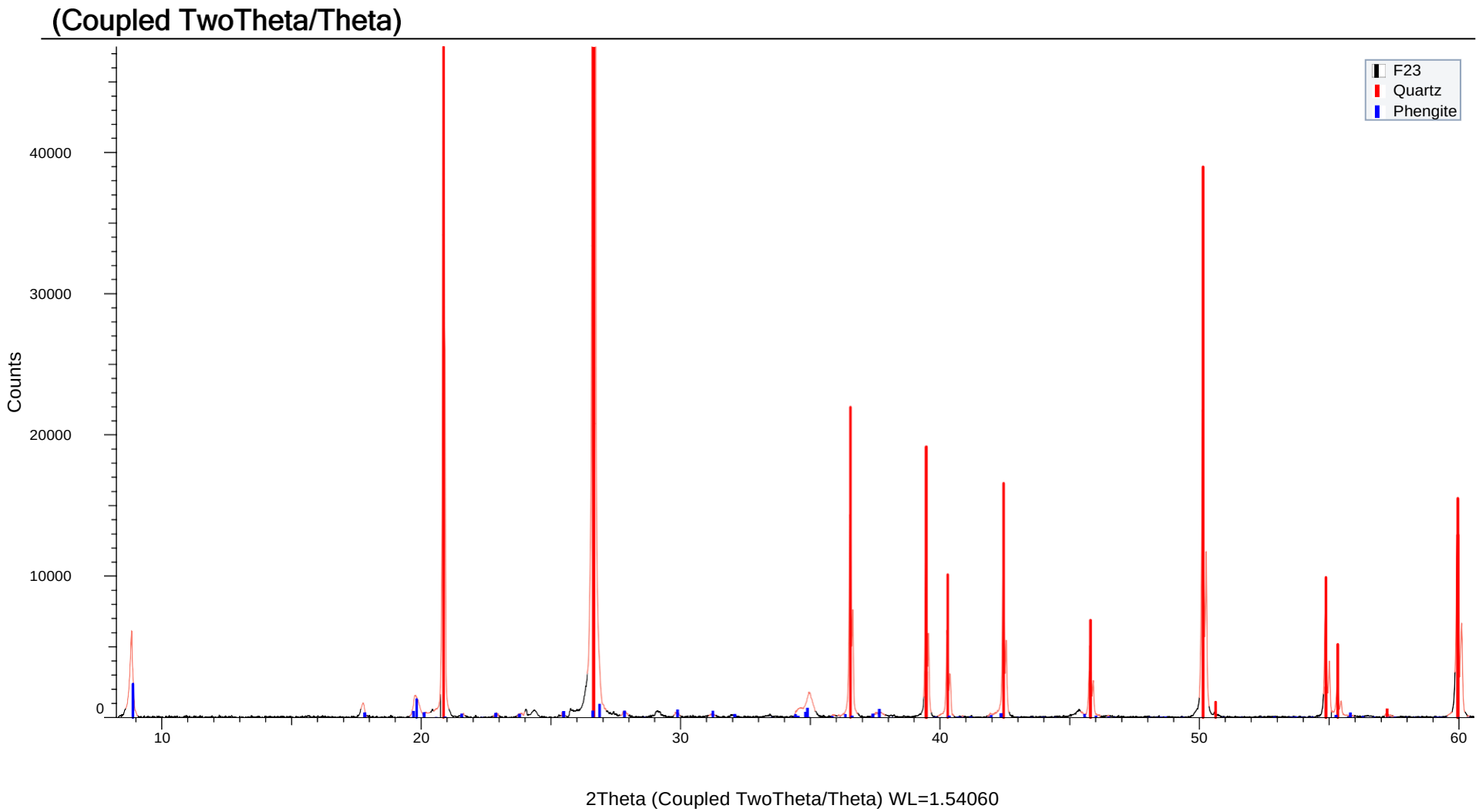
(Coupled TwoTheta/Theta)
F23
Quartz
Phengite
Counts
40000
30000
20000
10000
0
10
20
30
40
50
60
2Theta (Coupled TwoTheta/Theta) WL=1.54060

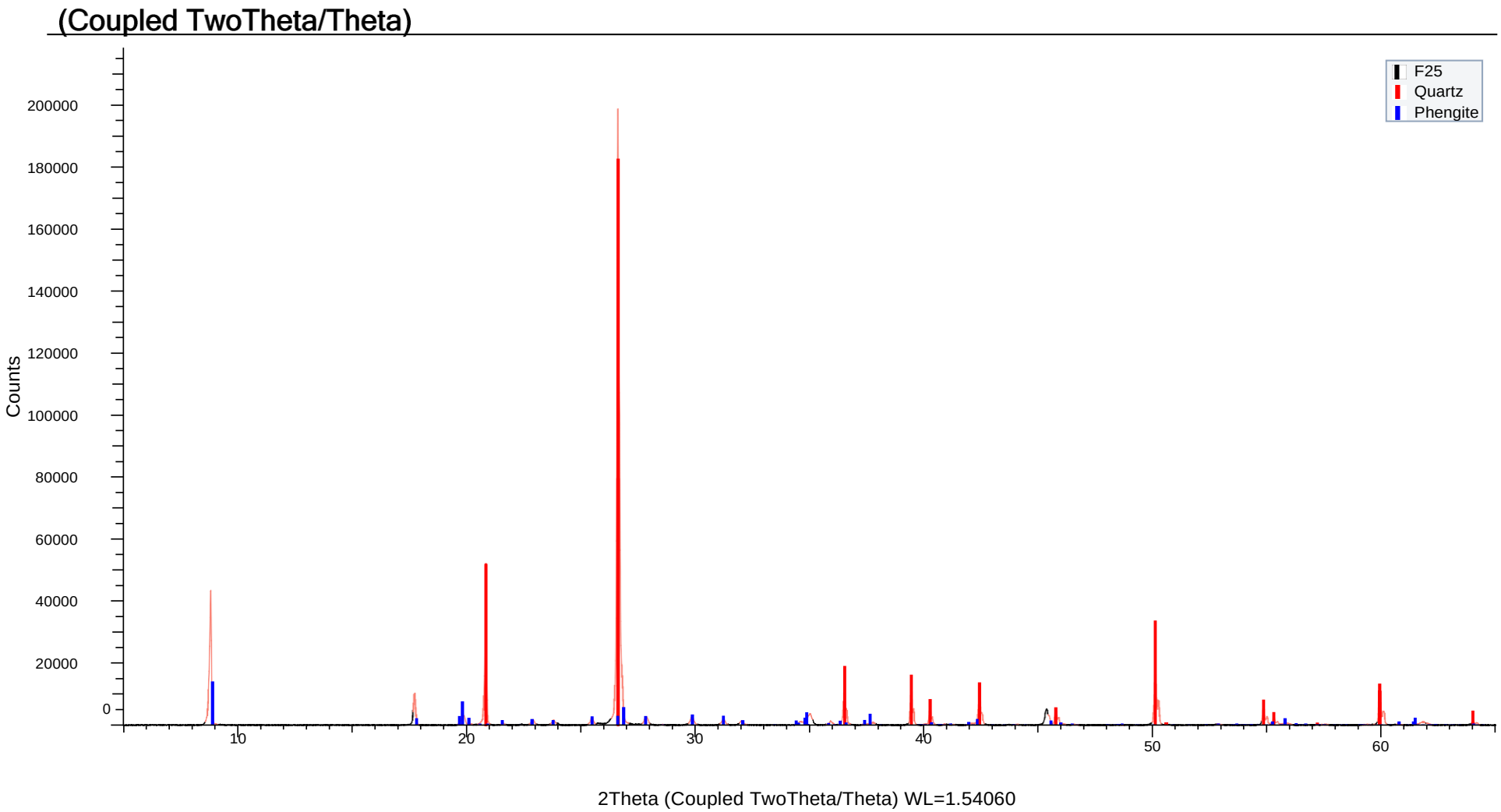
(Coupled TwoTheta/Theta)
F25
Quartz
Phengite
Counts
200000
180000
160000
140000
120000
100000
80000
60000
40000
20000
0
10
20
30
40
50
60
2Theta (Coupled TwoTheta/Theta) WL=1.54060

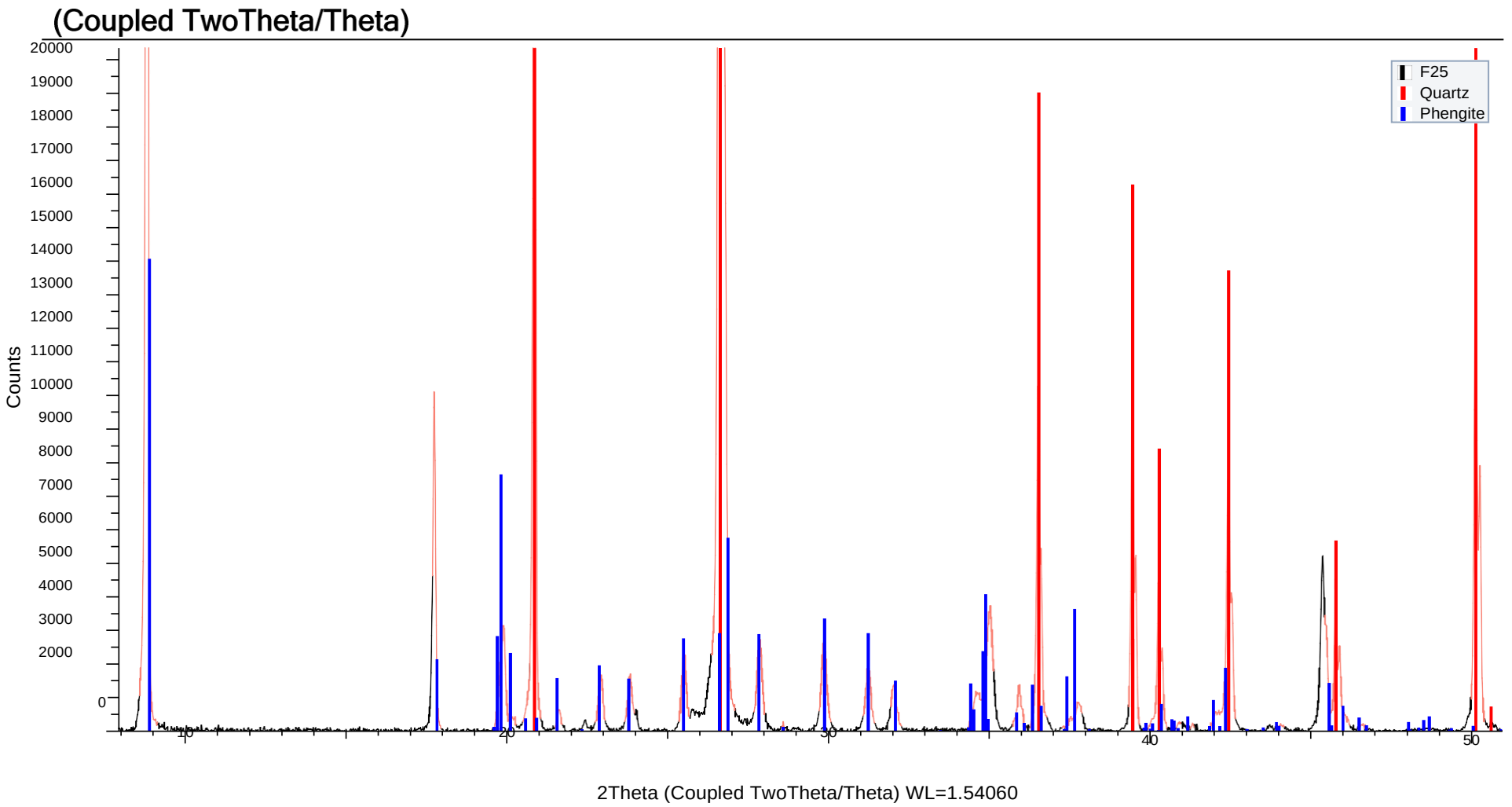
(Coupled TwoTheta/Theta)
Counts
20000
19000
18000
17000
16000
15000
14000
13000
12000
11000
10000
9000
8000
7000
6000
5000
4000
3000
2000
0
10
20
30
40
50
F25
Quartz
Phengite
2Theta (Coupled TwoTheta/Theta) WL=1.54060

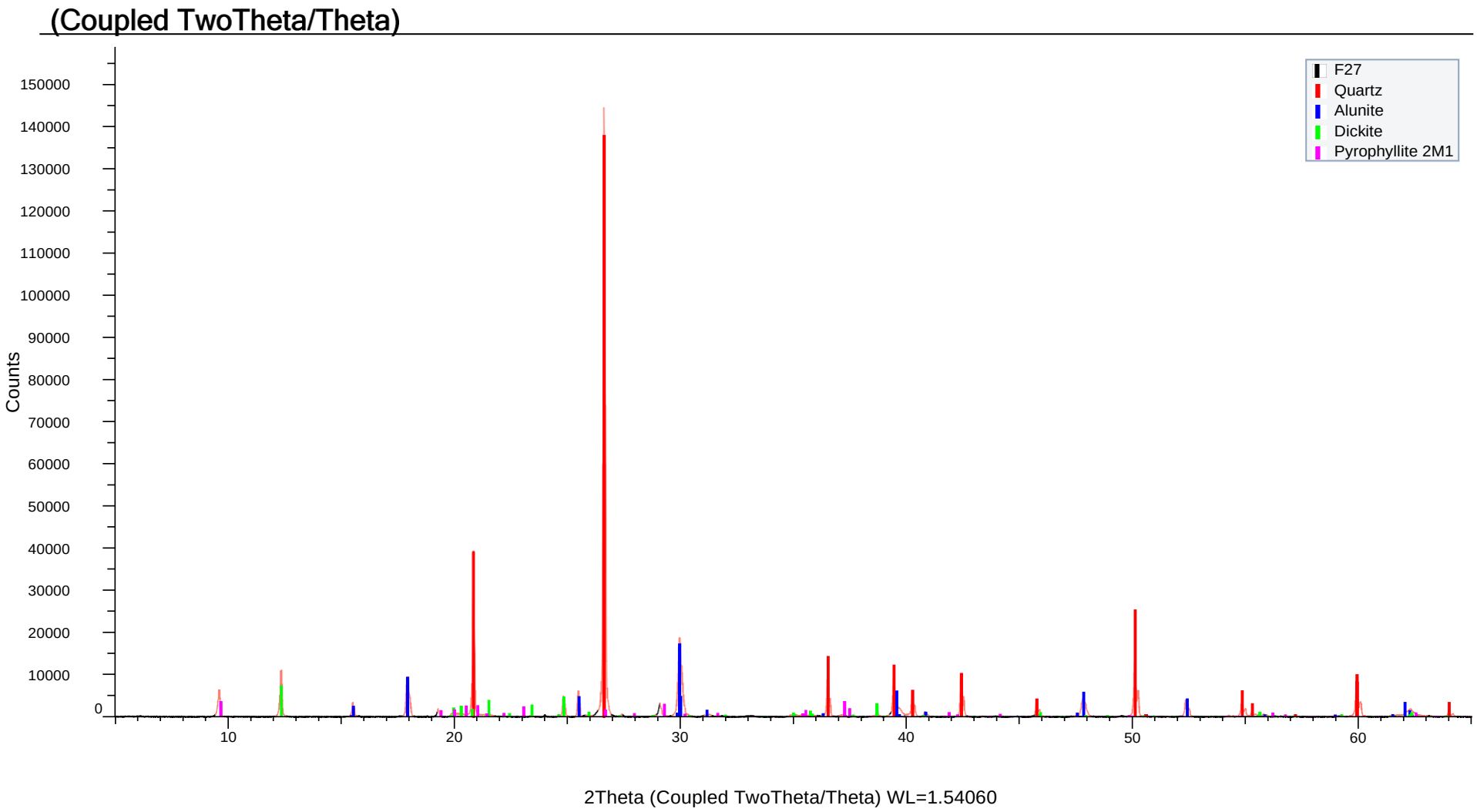
(Coupled TwoTheta/Theta)
F27
Quartz
Alunite
Dickite
Pyrophyllite 2M1
Counts
150000
140000
130000
120000
110000
100000
90000
80000
70000
60000
50000
40000
30000
20000
10000
0
10
20
30
40
50
60
2Theta (Coupled TwoTheta/Theta) WL=1.54060

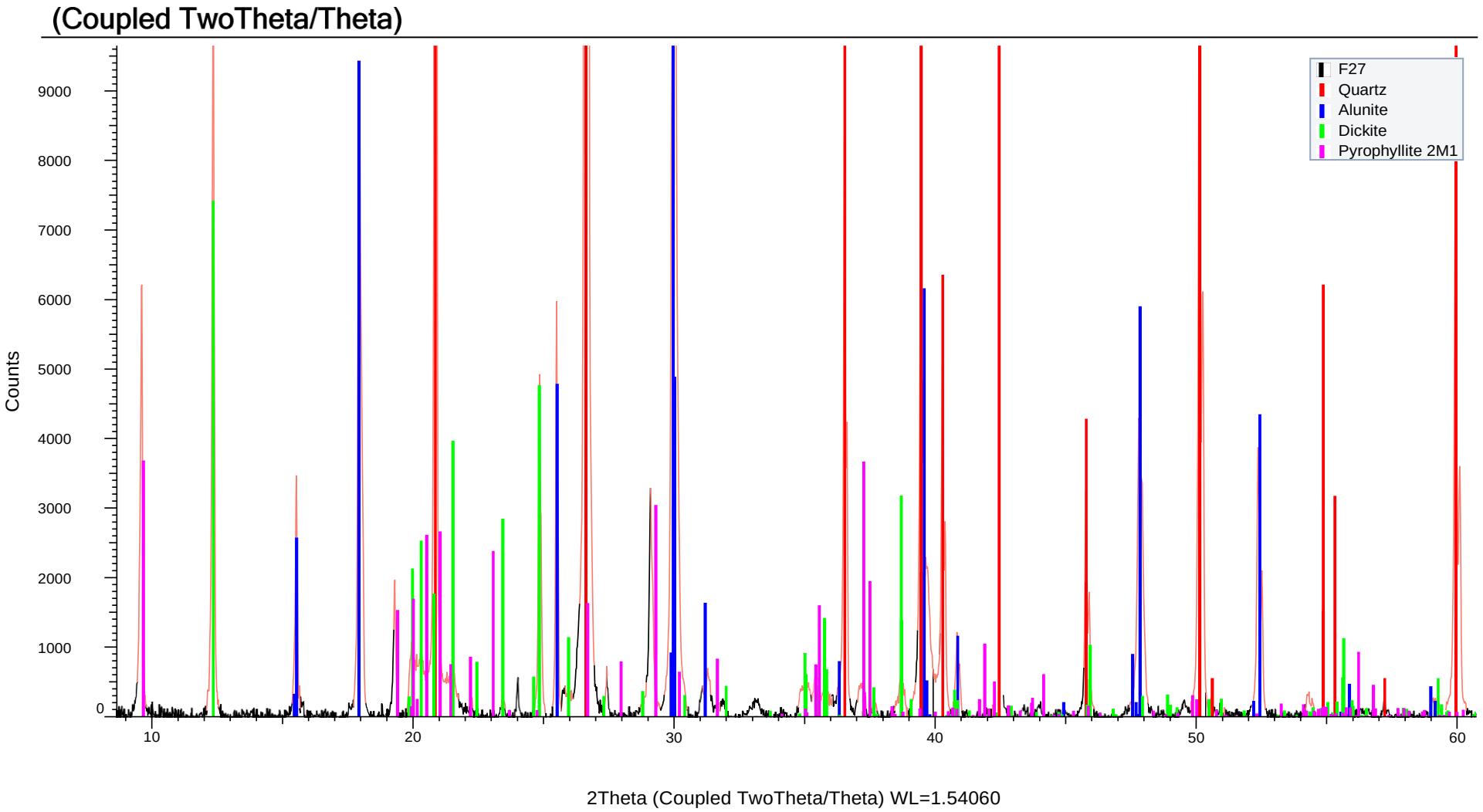
(Coupled TwoTheta/Theta)
F27
Quartz
Alunite
Dickite
Pyrophyllite 2M1
Counts
0
1000
2000
3000
4000
5000
6000
7000
8000
9000
10
20
30
40
50
60
2Theta (Coupled TwoTheta/Theta) WL=1.54060

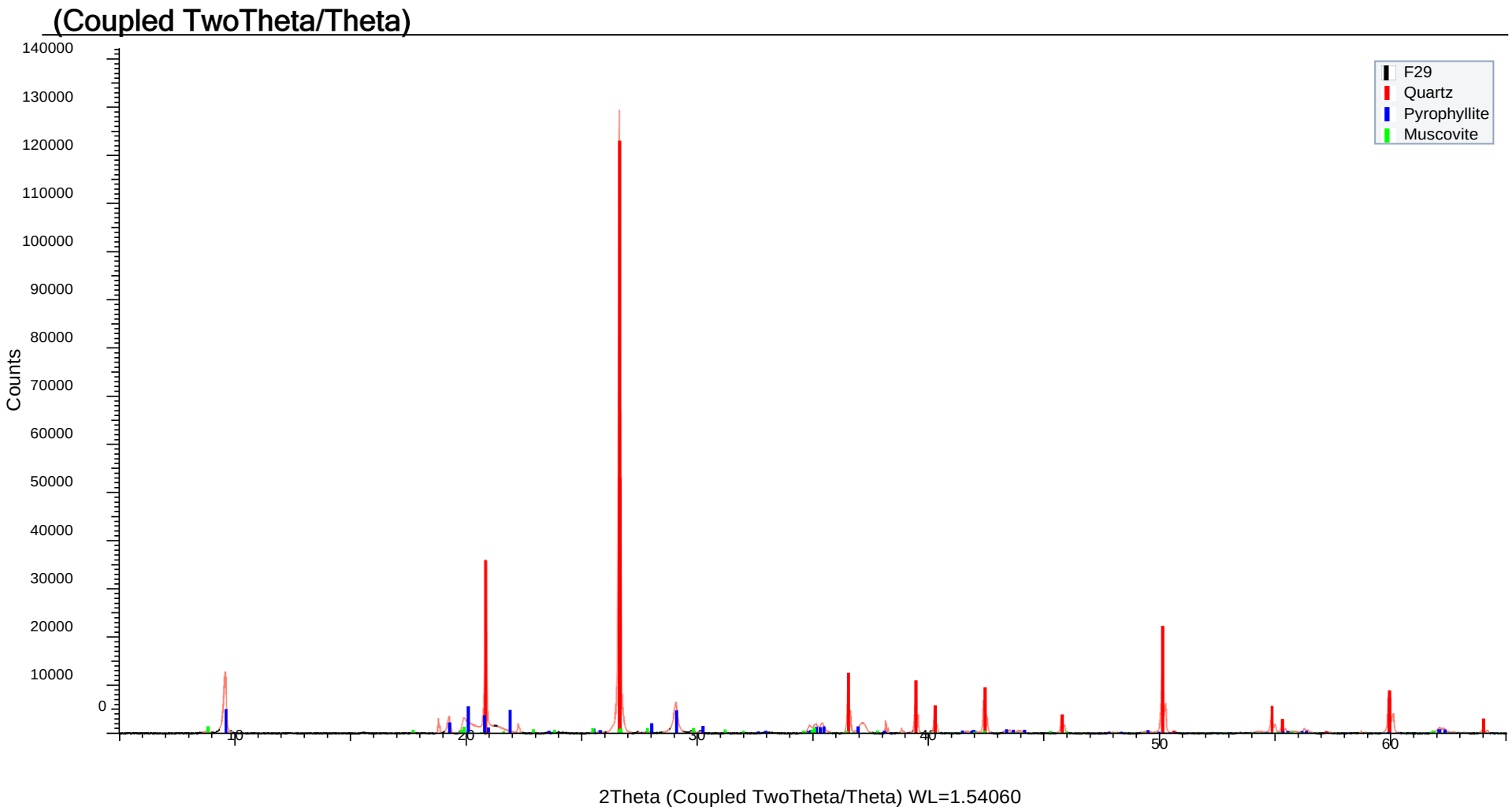
(Coupled TwoTheta/Theta)
F29
Quartz
Pyrophyllite
Muscovite
Counts
140000
130000
120000
110000
100000
90000
80000
70000
60000
50000
40000
30000
20000
10000
0
10
20
30
40
50
60
2Theta (Coupled TwoTheta/Theta) WL=1.54060

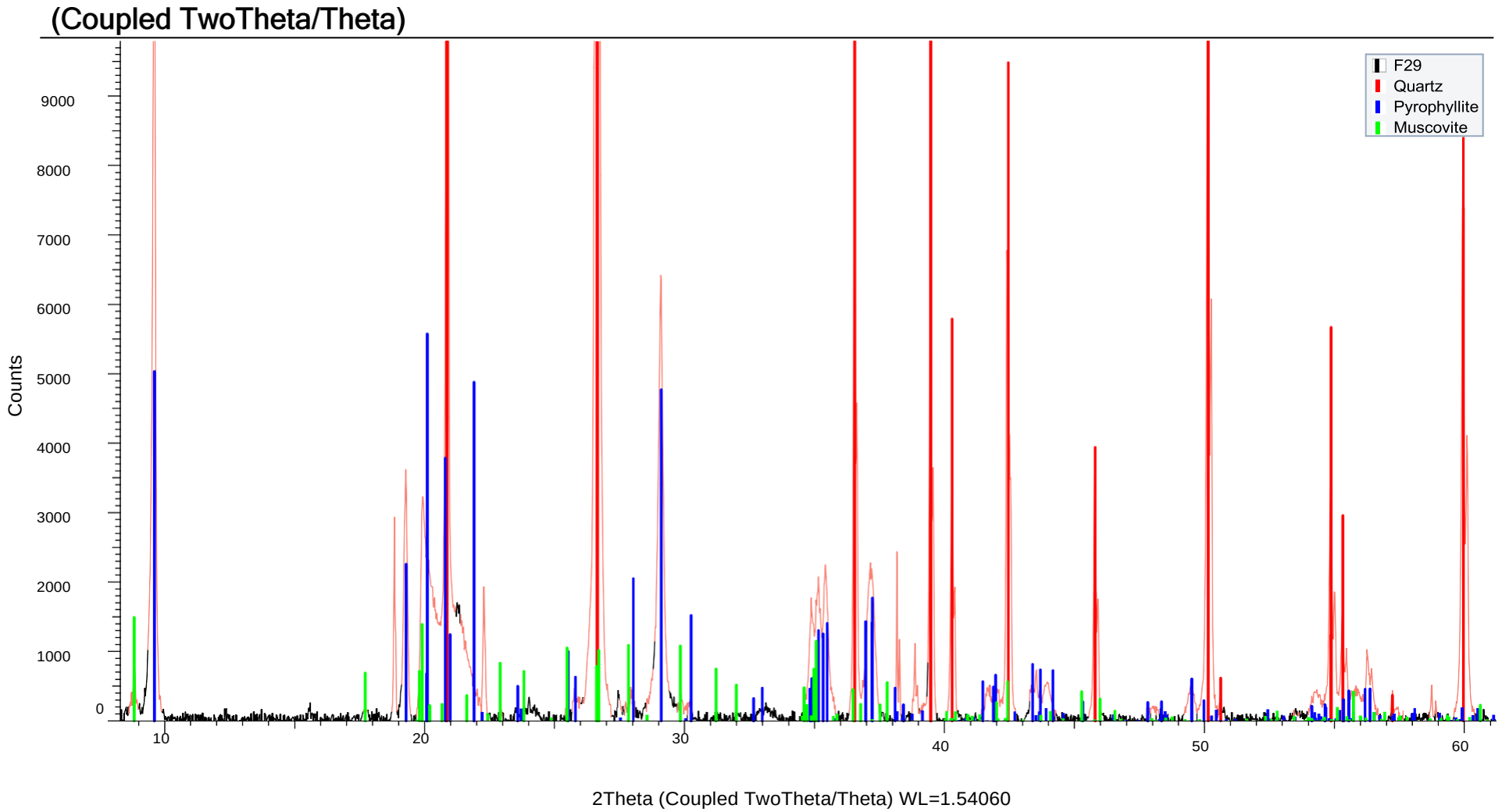
(Coupled TwoTheta/Theta)
F29
Quartz
Pyrophyllite
Muscovite
Counts
9000
8000
7000
6000
5000
4000
3000
2000
1000
0
10
20
30
40
50
60
2Theta (Coupled TwoTheta/Theta) WL=1.54060

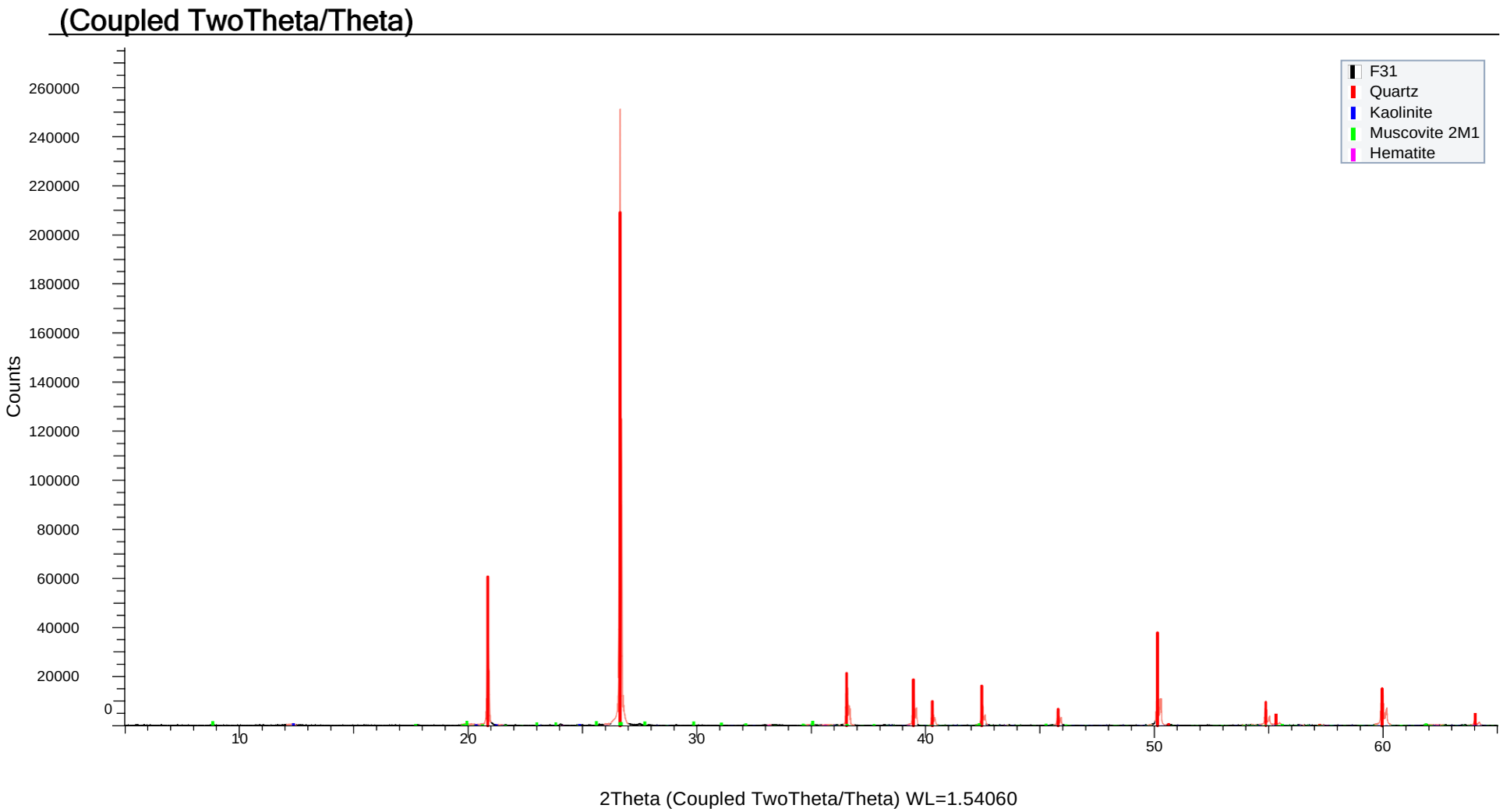
(Coupled TwoTheta/Theta)
F31
Quartz
Kaolinite
Muscovite 2M1
Hematite
Counts
260000
240000
220000
200000
180000
160000
140000
120000
100000
80000
60000
40000
20000
0
10
20
30
40
50
60
2Theta (Coupled TwoTheta/Theta) WL=1.54060

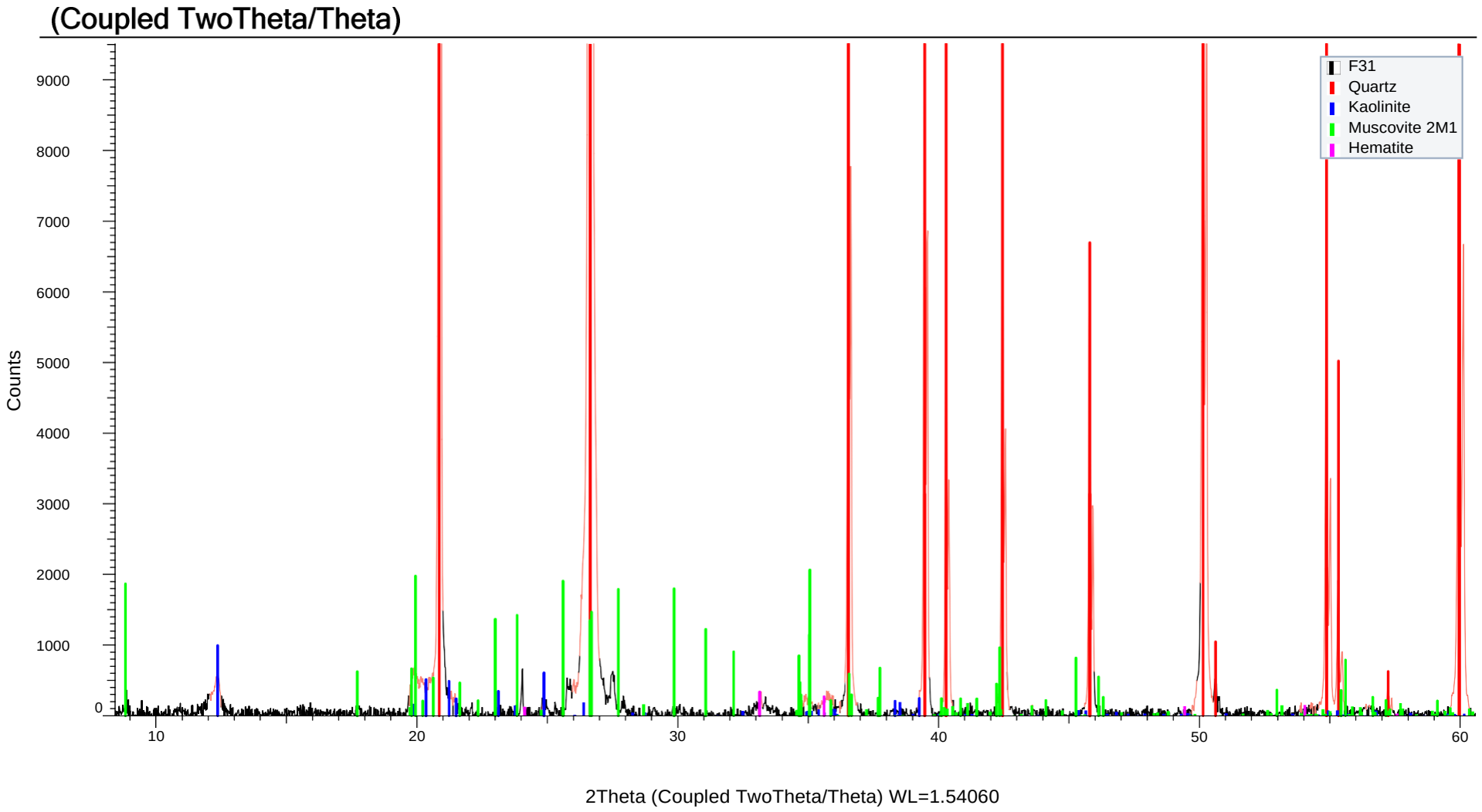
(Coupled TwoTheta/Theta)
F31
Quartz
Kaolinite
Muscovite 2M1
Hematite
Counts
9000
8000
7000
6000
5000
4000
3000
2000
1000
0
10
20
30
40
50
60
2Theta (Coupled TwoTheta/Theta) WL=1.54060

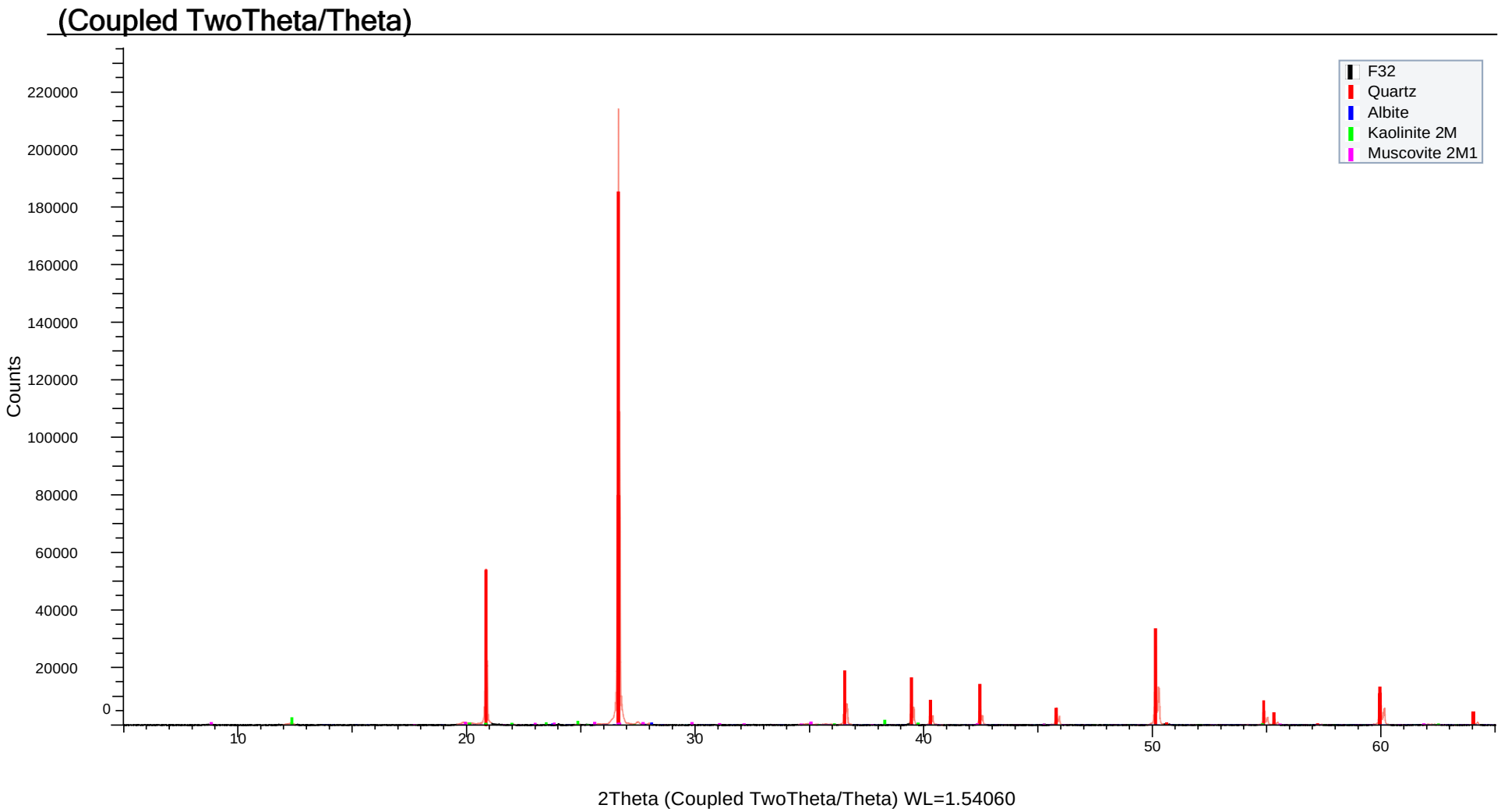
(Coupled TwoTheta/Theta)
F32
Quartz
Albite
Kaolinite 2M
Muscovite 2M1
Counts
220000
200000
180000
160000
140000
120000
100000
80000
60000
40000
20000
0
10
20
30
40
50
60
2Theta (Coupled TwoTheta/Theta) WL=1.54060

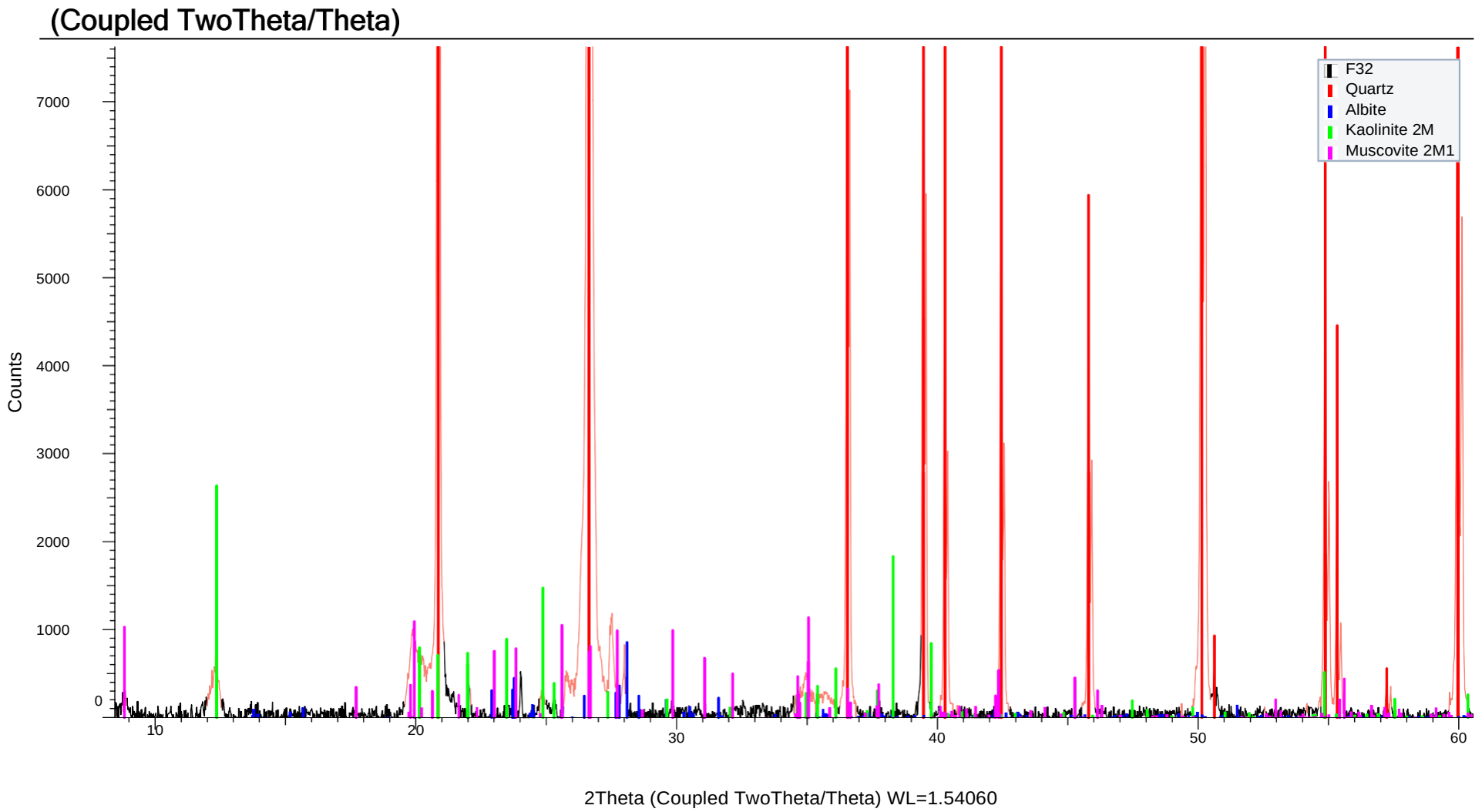
(Coupled TwoTheta/Theta)
F32
Quartz
Albite
Kaolinite 2M
Muscovite 2M1
Counts
7000
6000
5000
4000
3000
2000
1000
0
10
20
30
40
50
60
2Theta (Coupled TwoTheta/Theta) WL=1.54060

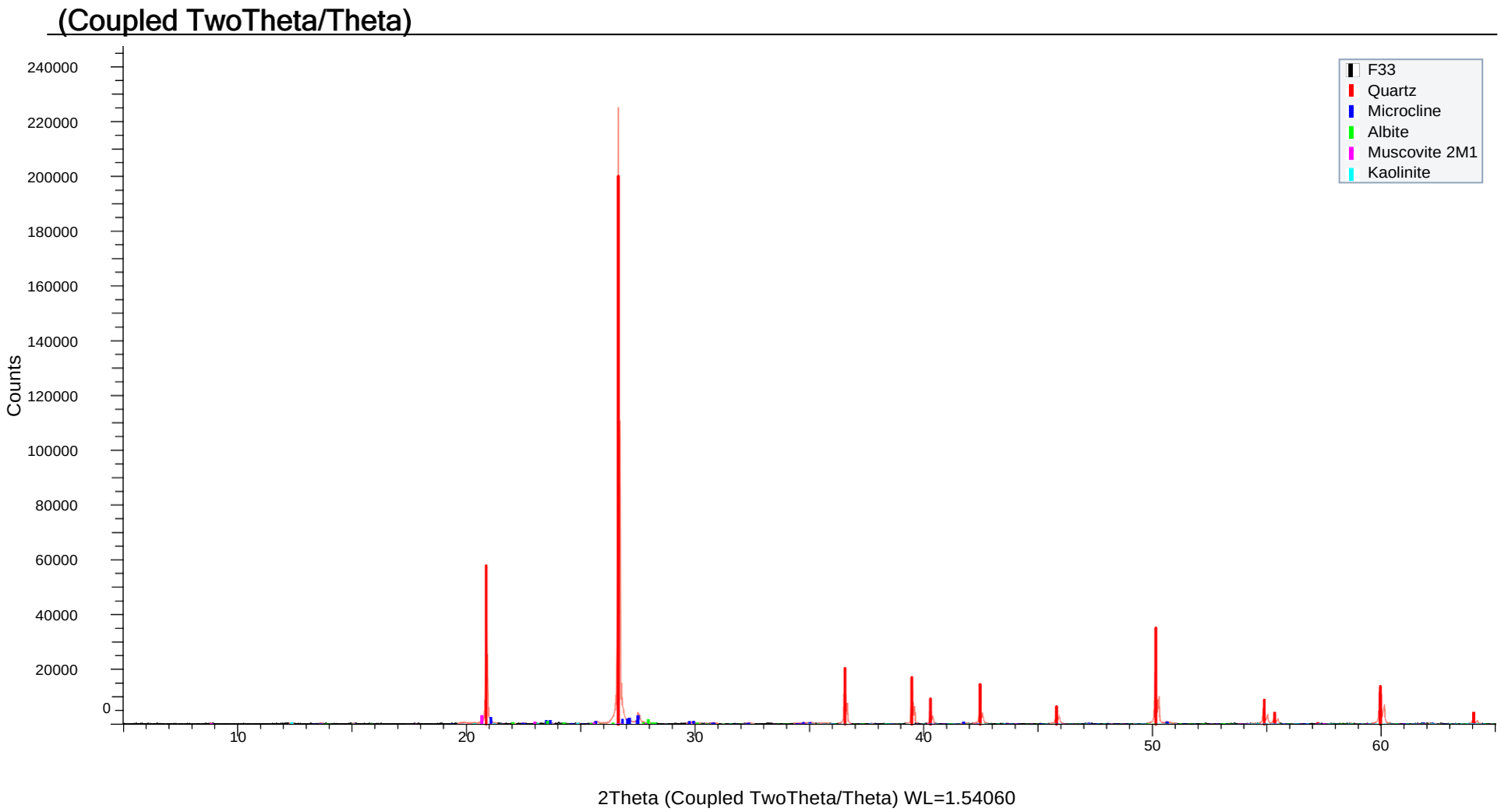
(Coupled TwoTheta/Theta)
F33
Quartz
Microcline
Albite
Muscovite 2M1
Kaolinite
Counts
240000
220000
200000
180000
160000
140000
120000
100000
80000
60000
40000
20000
0
10
20
30
40
50
60
2Theta (Coupled TwoTheta/Theta) WL=1.54060

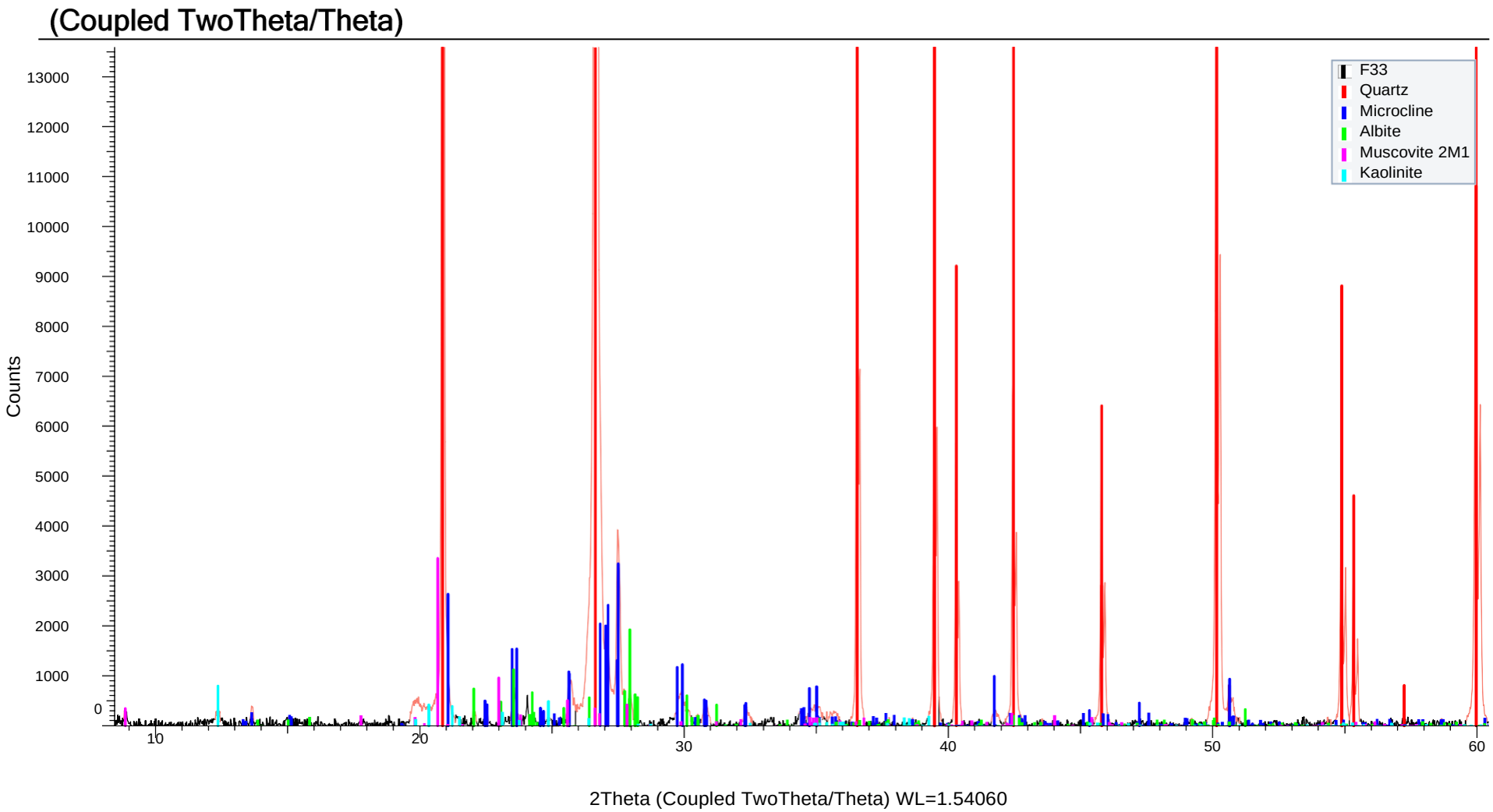
(Coupled TwoTheta/Theta)
Counts
13000
12000
11000
10000
9000
8000
7000
6000
5000
4000
3000
2000
1000
0
10
20
30
40
50
60
F33
Quartz
Microcline
Albite
Muscovite 2M1
Kaolinite
2Theta (Coupled TwoTheta/Theta) WL=1.54060

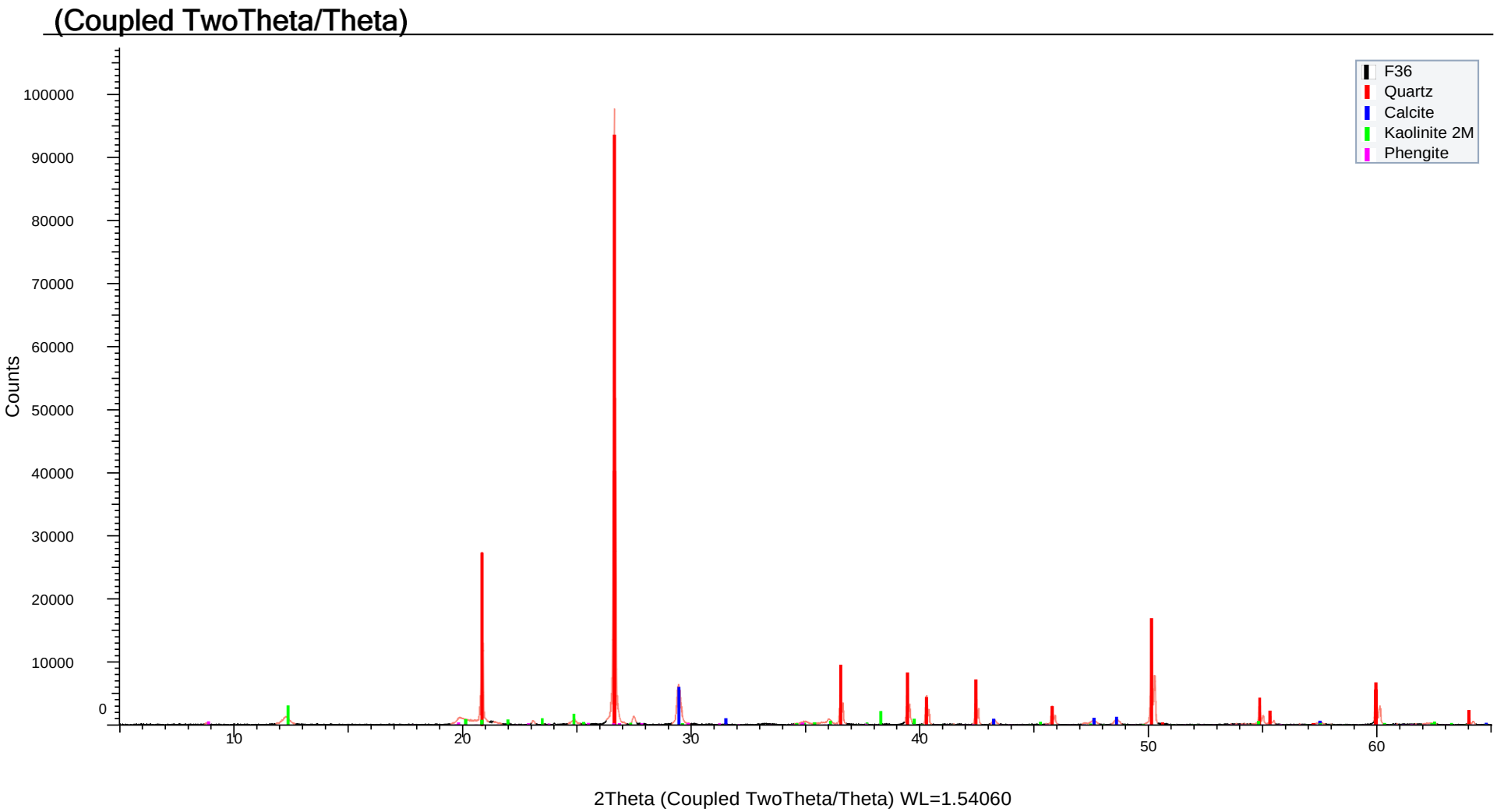
(Coupled TwoTheta/Theta)
F36
Quartz
Calcite
Kaolinite 2M
Phengite
Counts
100000
90000
80000
70000
60000
50000
40000
30000
20000
10000
0
10
20
30
40
50
60
2Theta (Coupled TwoTheta/Theta) WL=1.54060

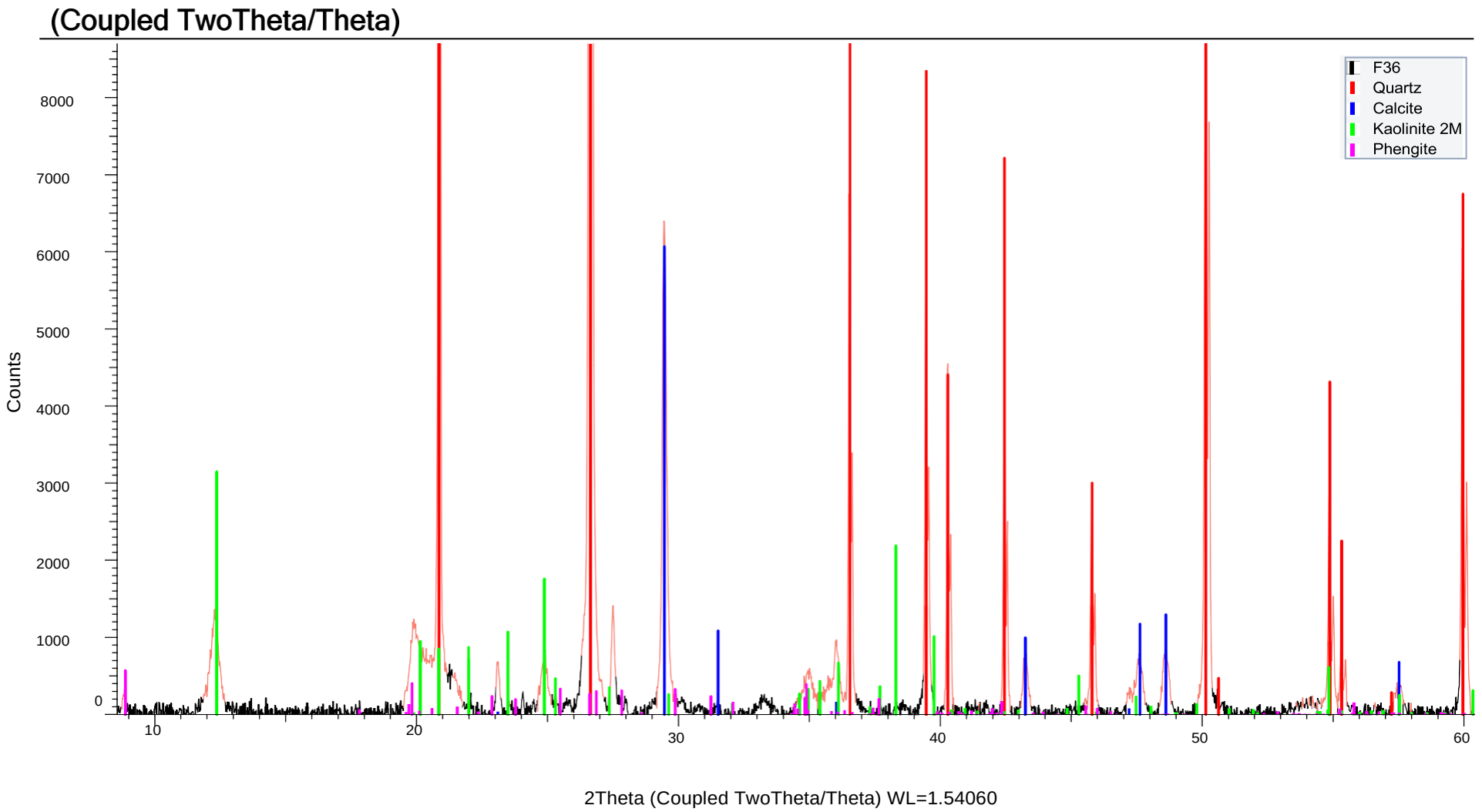
(Coupled TwoTheta/Theta)
F36
Quartz
Calcite
Kaolinite 2M
Phengite
Counts
8000
7000
6000
5000
4000
3000
2000
1000
0
10
20
30
40
50
60
2Theta (Coupled TwoTheta/Theta) WL=1.54060

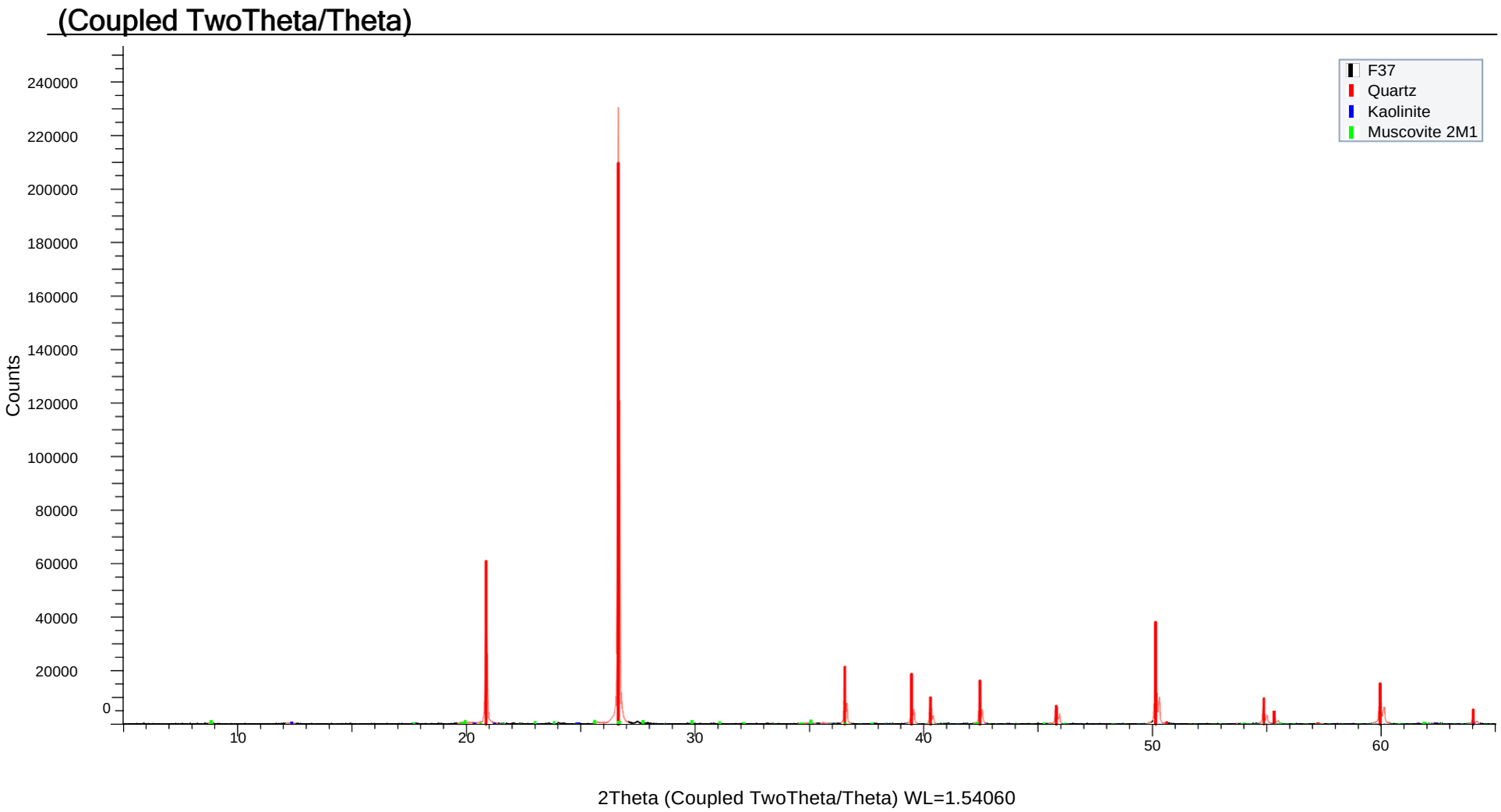
(Coupled TwoTheta/Theta)
F37
Quartz
Kaolinite
Muscovite 2M1
Counts
240000
220000
200000
180000
160000
140000
120000
100000
80000
60000
40000
20000
0
10
20
30
40
50
60
2Theta (Coupled TwoTheta/Theta) WL=1.54060

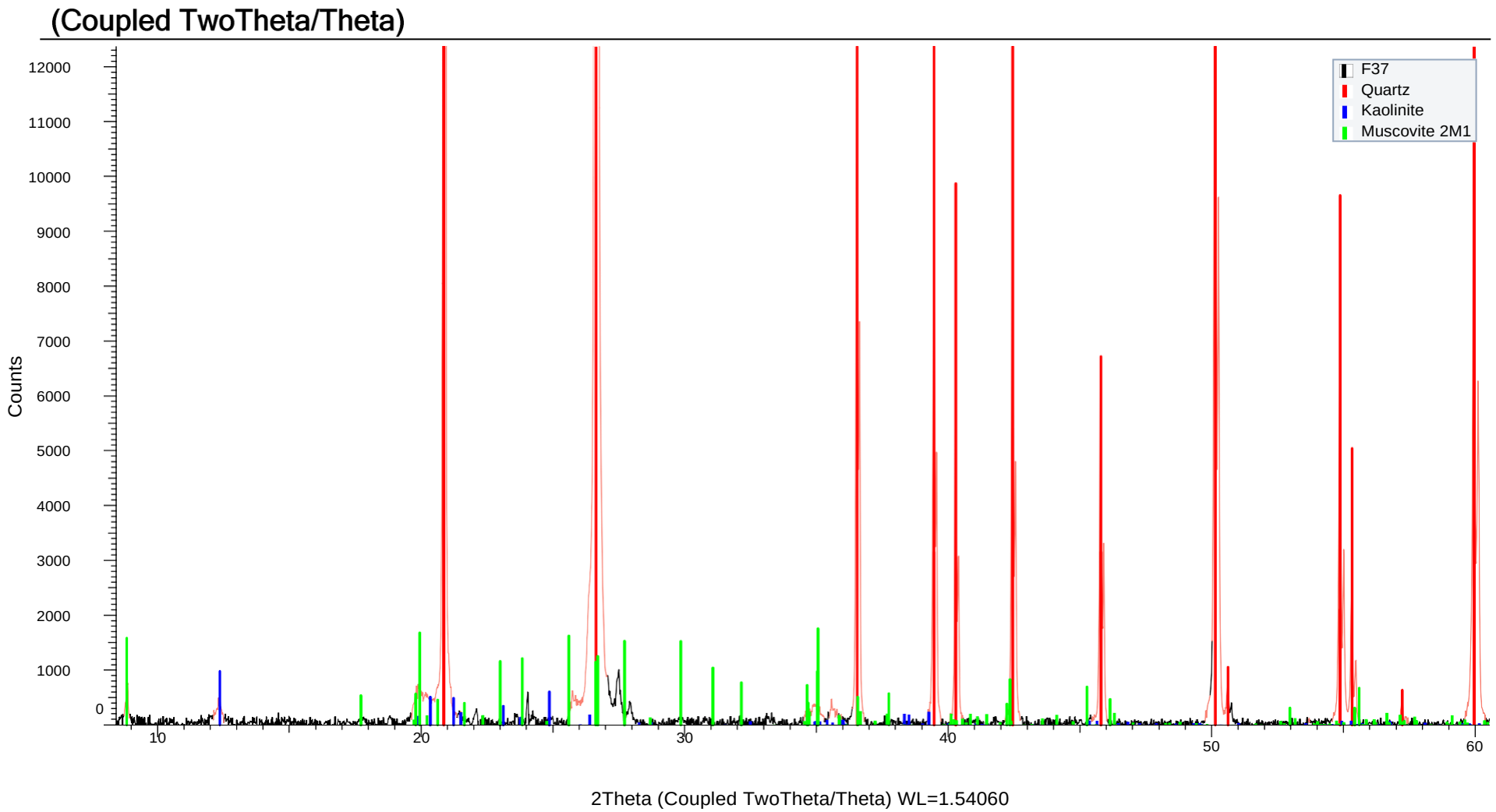
(Coupled TwoTheta/Theta)
F37
Quartz
Kaolinite
Muscovite 2M1
Counts
12000
11000
10000
9000
8000
7000
6000
5000
4000
3000
2000
1000
0
10
20
30
40
50
60
2Theta (Coupled TwoTheta/Theta) WL=1.54060

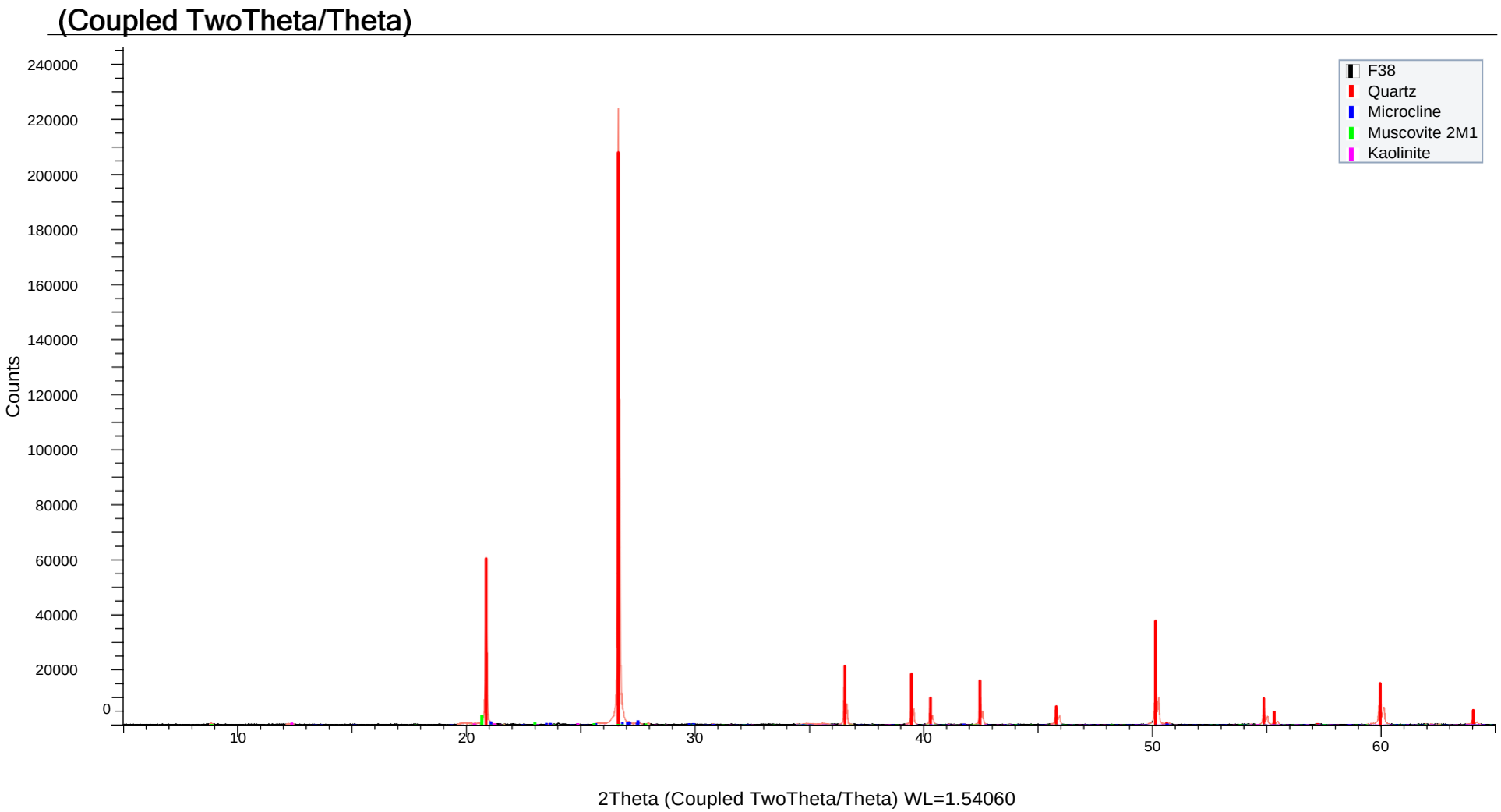
(Coupled TwoTheta/Theta)
F38
Quartz
Microcline
Muscovite 2M1
Kaolinite
Counts
240000
220000
200000
180000
160000
140000
120000
100000
80000
60000
40000
20000
0
10
20
30
40
50
60
2Theta (Coupled TwoTheta/Theta) WL=1.54060

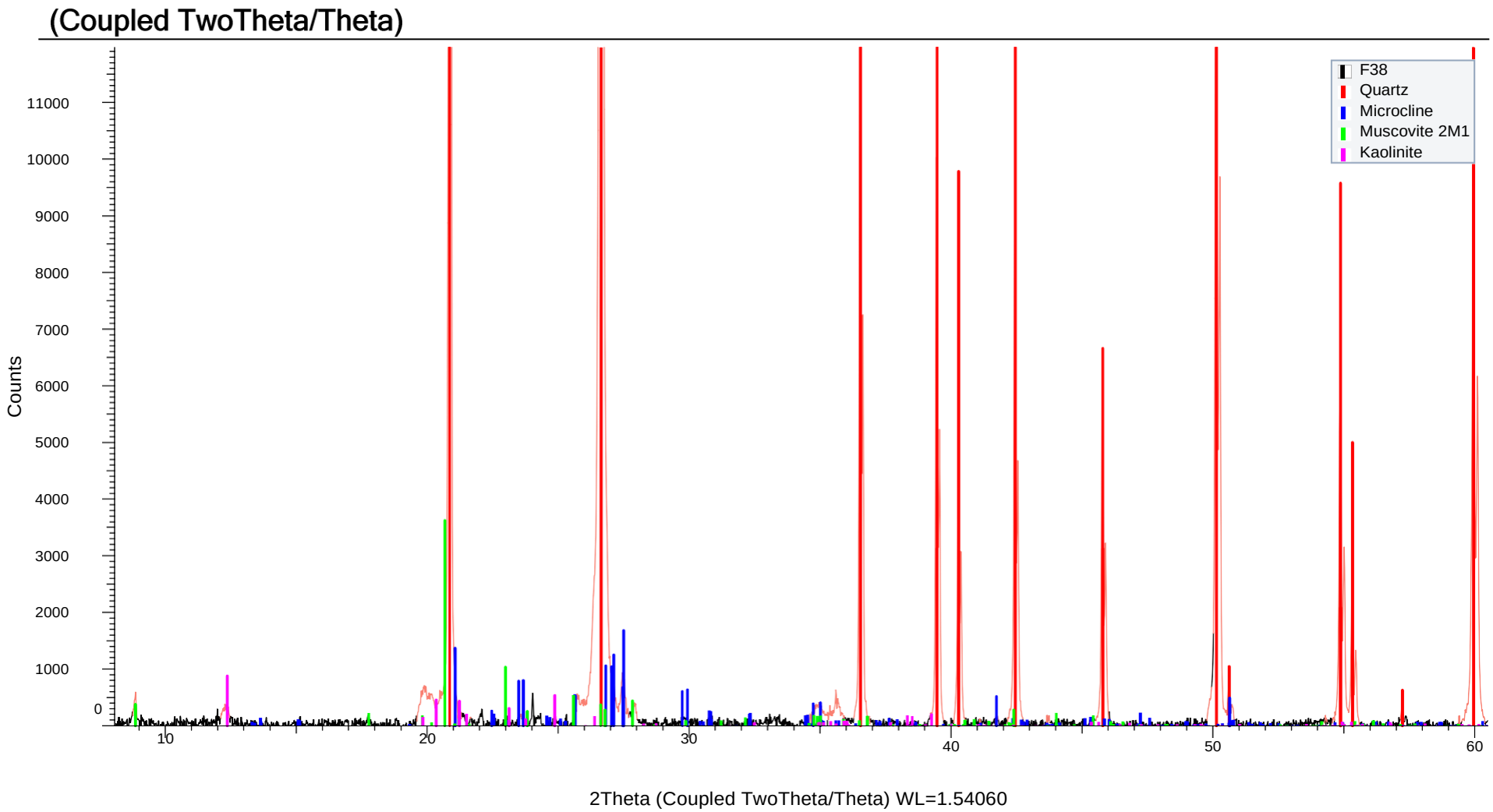
(Coupled TwoTheta/Theta)
F38
Quartz
Microcline
Muscovite 2M1
Kaolinite
Counts
11000
10000
9000
8000
7000
6000
5000
4000
3000
2000
1000
0
10
20
30
40
50
60
2Theta (Coupled TwoTheta/Theta) WL=1.54060

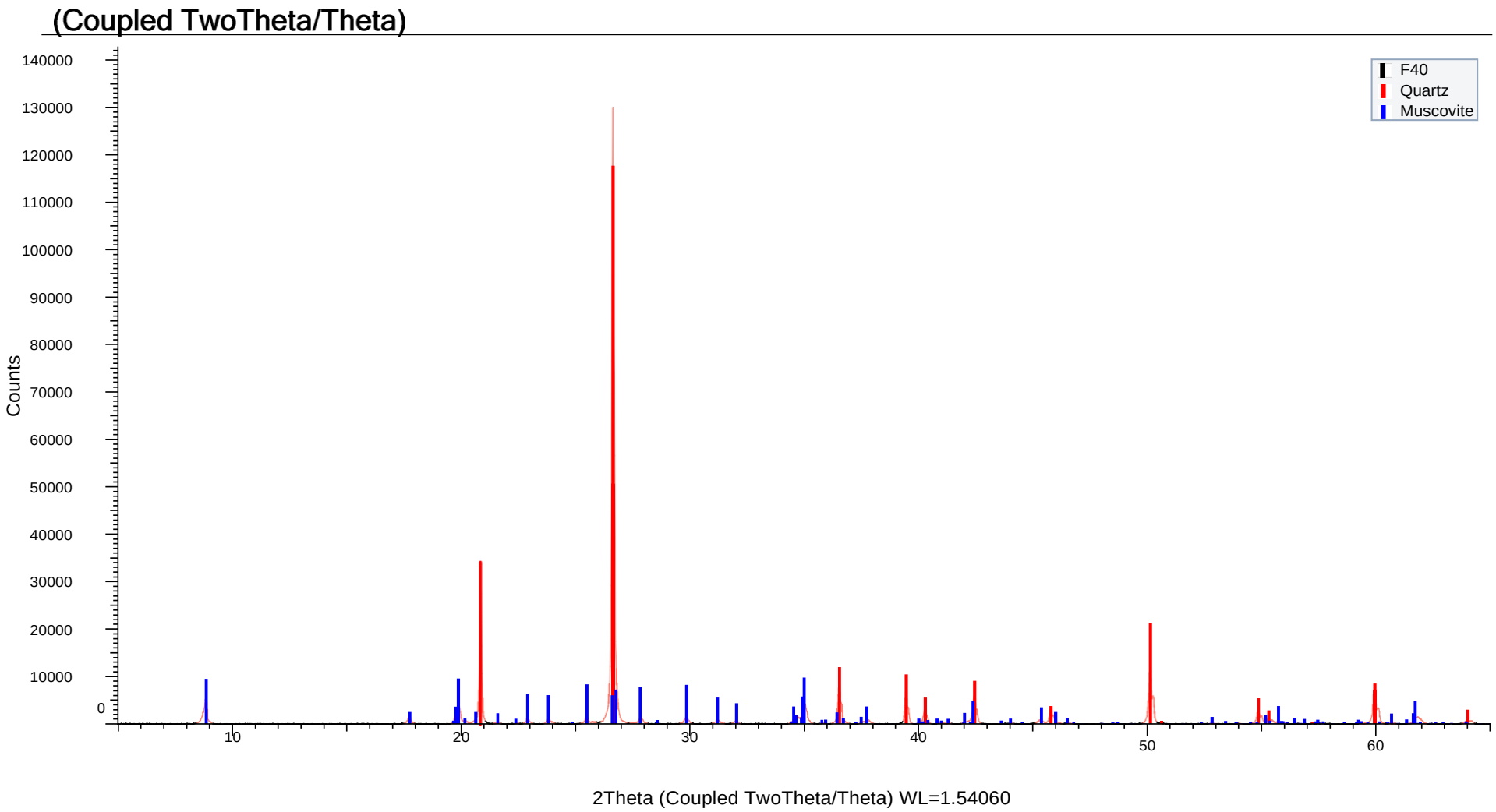
(Coupled TwoTheta/Theta)
F40
Quartz
Muscovite
Counts
140000
130000
120000
110000
100000
90000
80000
70000
60000
50000
40000
30000
20000
10000
0
10
20
30
40
50
60
2Theta (Coupled TwoTheta/Theta) WL=1.54060

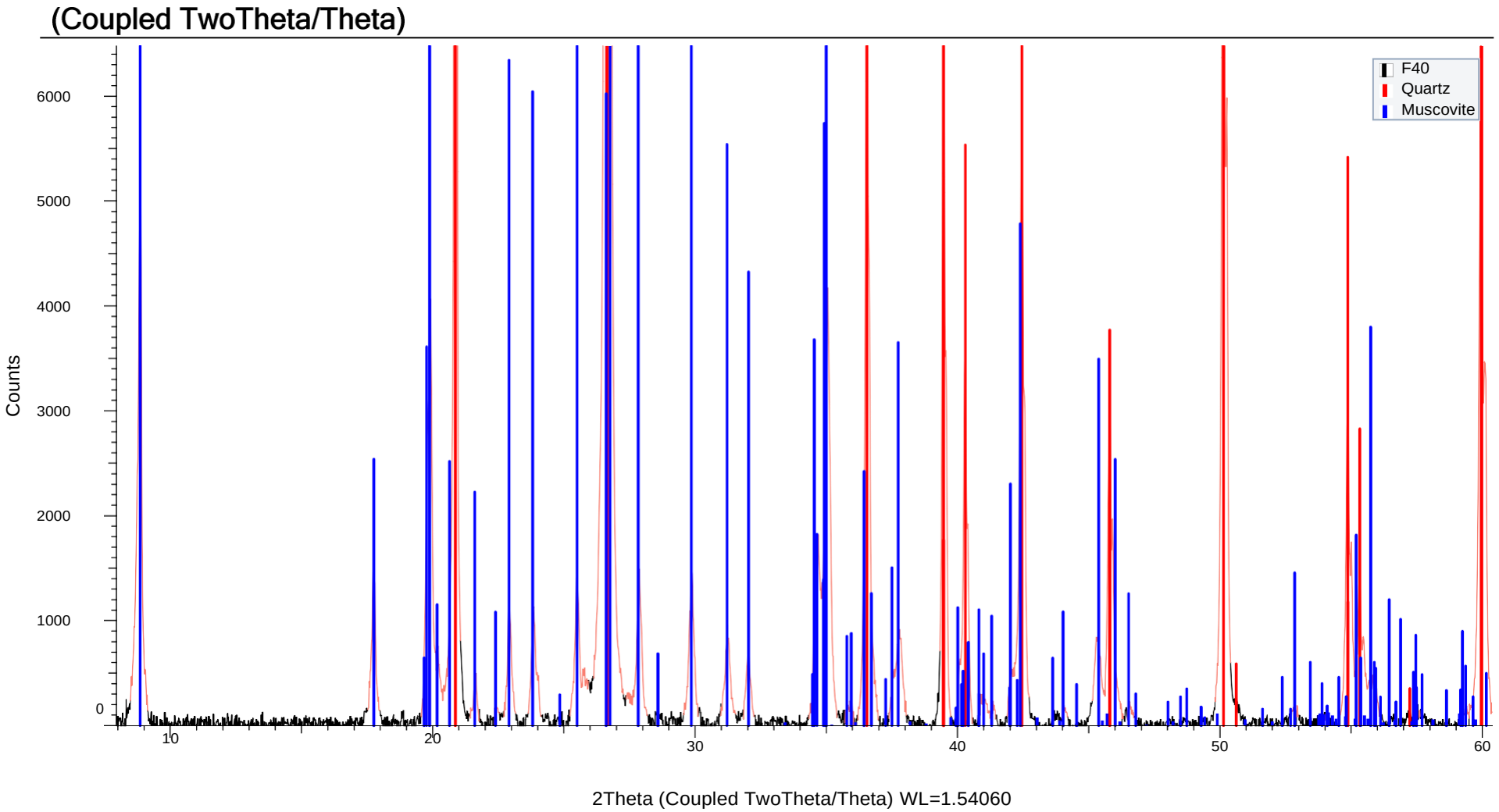
(Coupled TwoTheta/Theta)
F40
Quartz
Muscovite
Counts
6000
5000
4000
3000
2000
1000
0
10
20
30
40
50
60
2Theta (Coupled TwoTheta/Theta) WL=1.54060

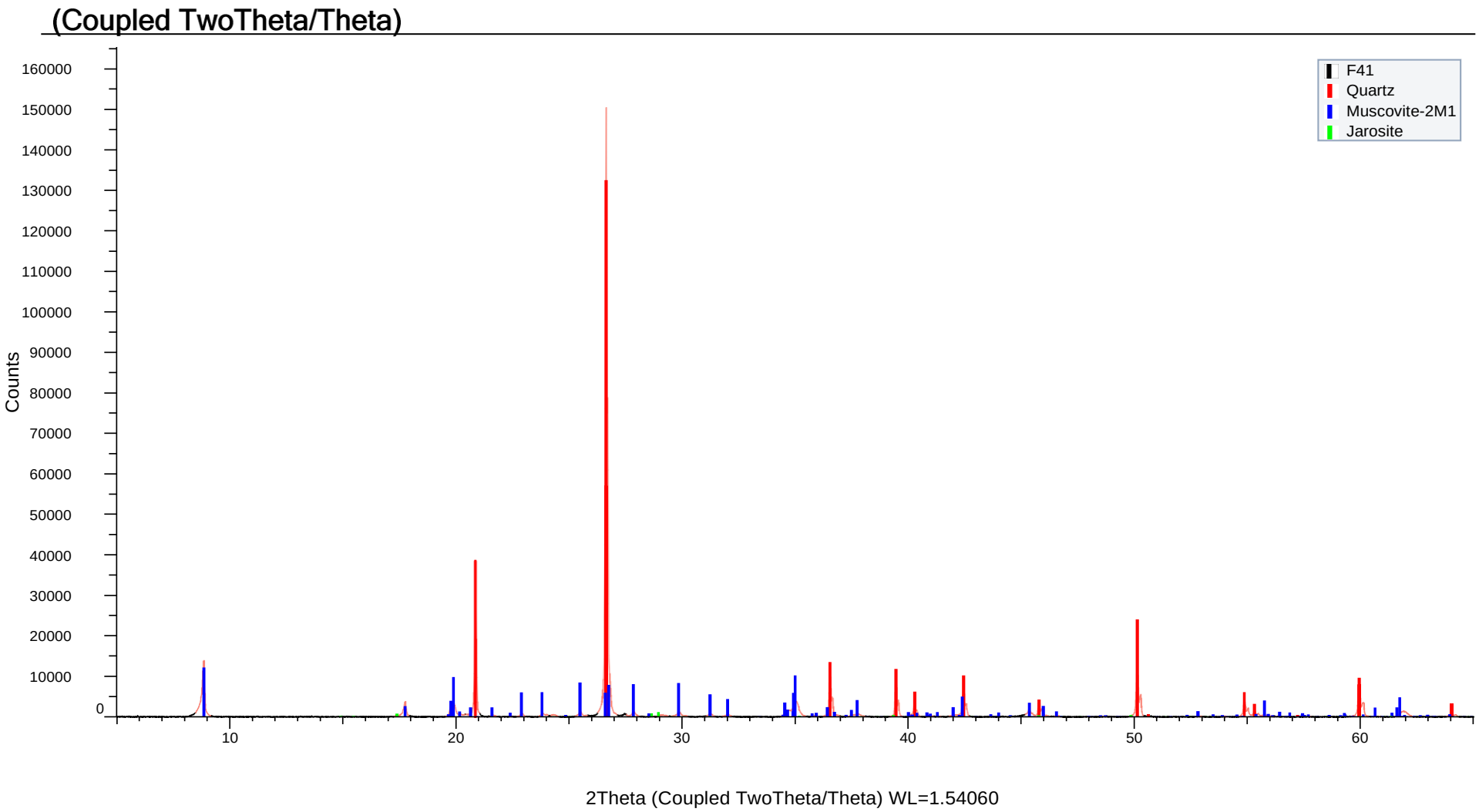
(Coupled TwoTheta/Theta)
F41
Quartz
Muscovite-2M1
Jarosite
Counts
160000
150000
140000
130000
120000
110000
100000
90000
80000
70000
60000
50000
40000
30000
20000
10000
0
10
20
30
40
50
60
2Theta (Coupled TwoTheta/Theta) WL=1.54060

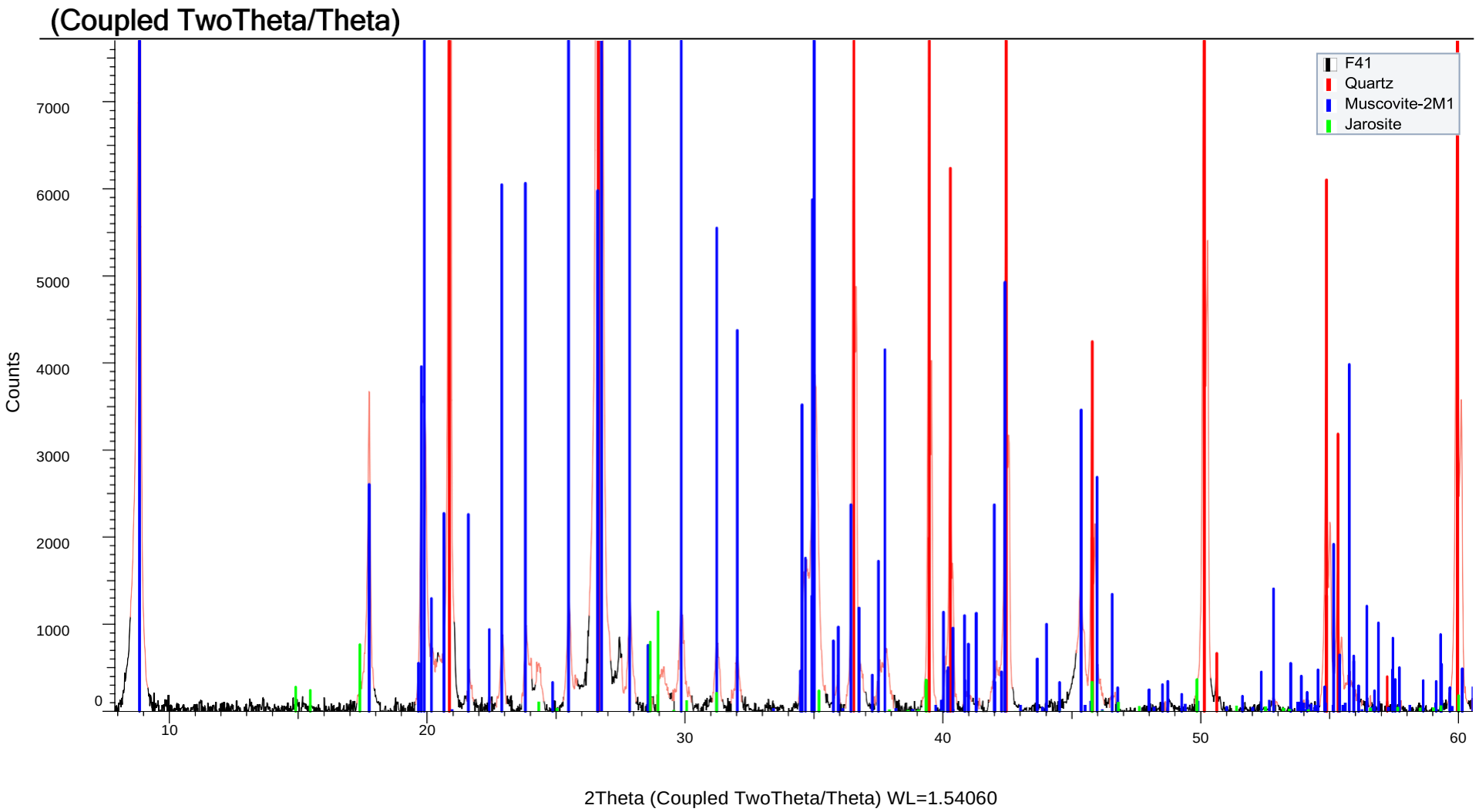
(Coupled TwoTheta/Theta)
F41
Quartz
Muscovite-2M1
Jarosite
Counts
0
1000
2000
3000
4000
5000
6000
7000
10
20
30
40
50
60
2Theta (Coupled TwoTheta/Theta) WL=1.54060

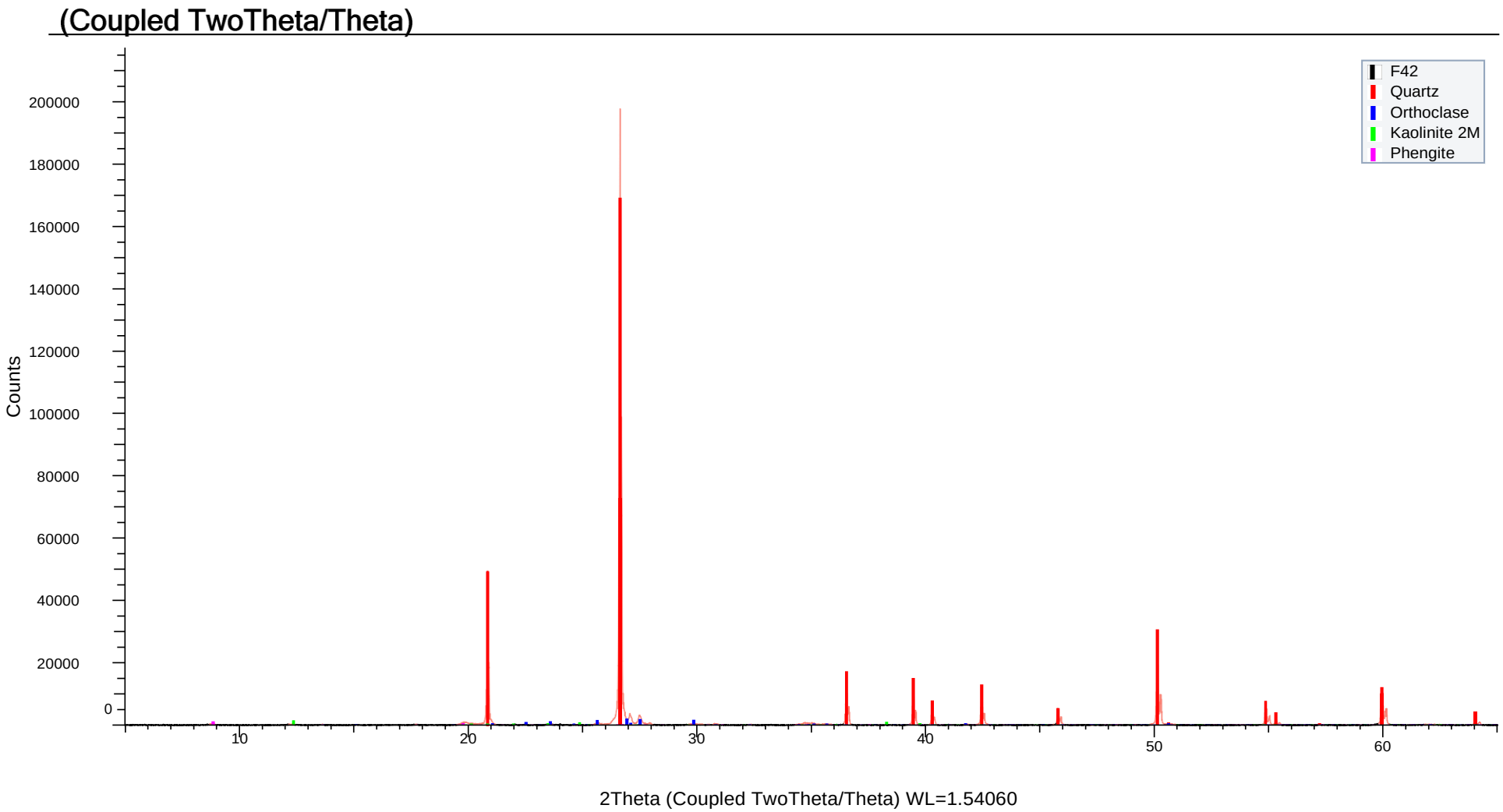
(Coupled TwoTheta/Theta)
F42
Quartz
Orthoclase
Kaolinite 2M
Phengite
Counts
200000
180000
160000
140000
120000
100000
80000
60000
40000
20000
0
10
20
30
40
50
60
2Theta (Coupled TwoTheta/Theta) WL=1.54060

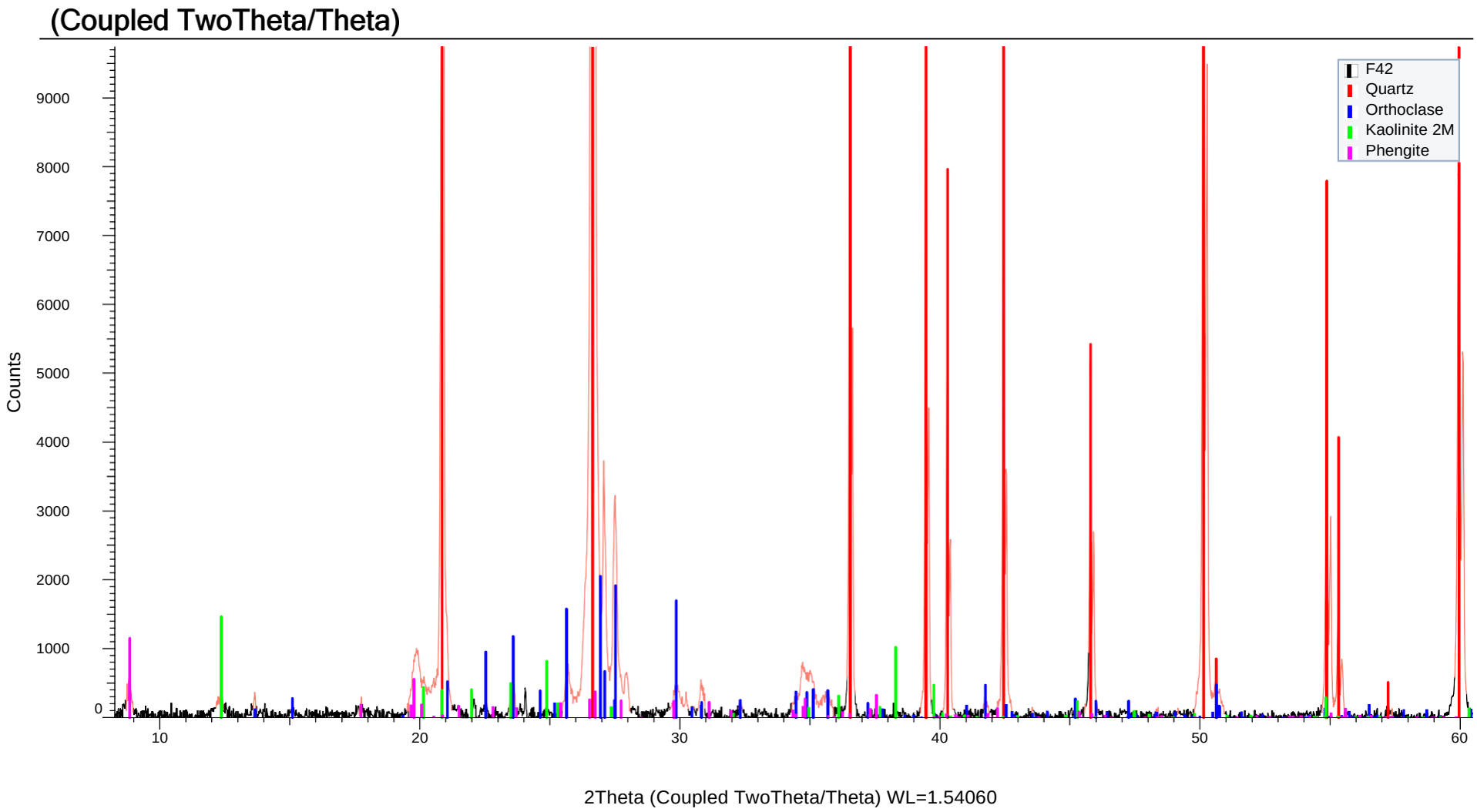
(Coupled TwoTheta/Theta)
F42
Quartz
Orthoclase
Kaolinite 2M
Phengite
Counts
9000
8000
7000
6000
5000
4000
3000
2000
1000
0
10
20
30
40
50
60
2Theta (Coupled TwoTheta/Theta) WL=1.54060

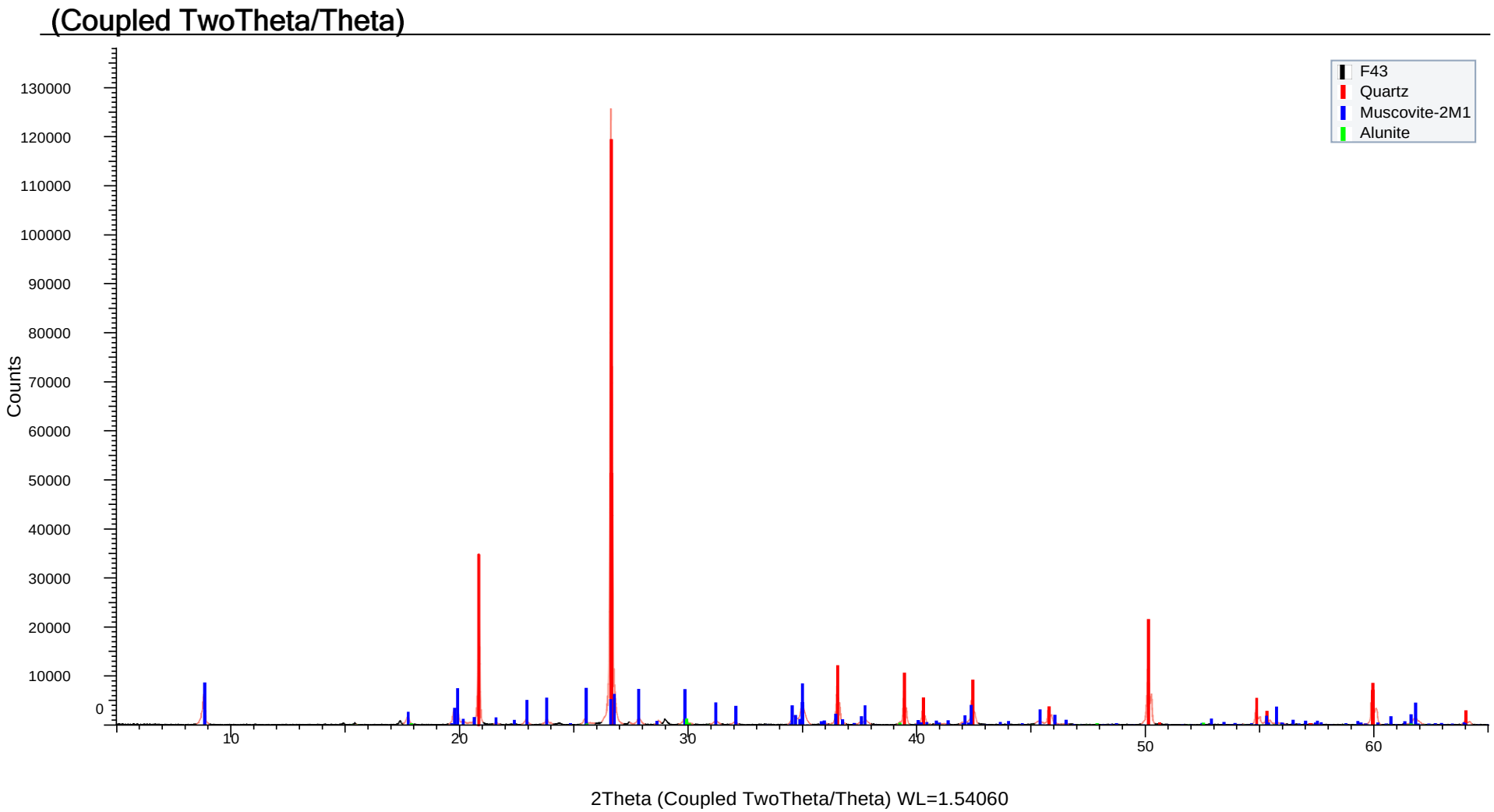
(Coupled TwoTheta/Theta)
F43
Quartz
Muscovite-2M1
Alunite
Counts
130000
120000
110000
100000
90000
80000
70000
60000
50000
40000
30000
20000
10000
0
10
20
30
40
50
60
2Theta (Coupled TwoTheta/Theta) WL=1.54060

(Coupled TwoTheta/Theta)

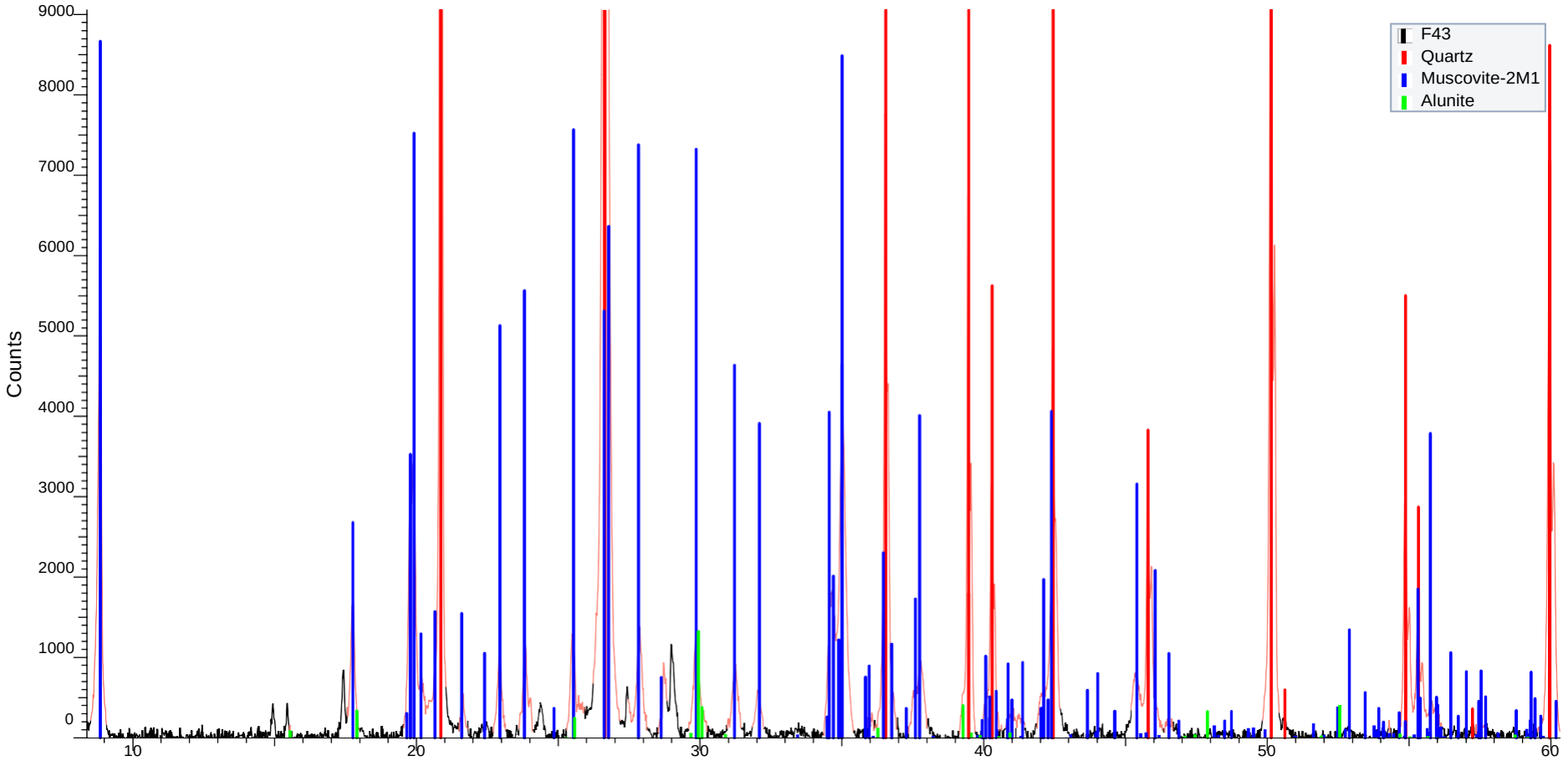

(Coupled TwoTheta/Theta)

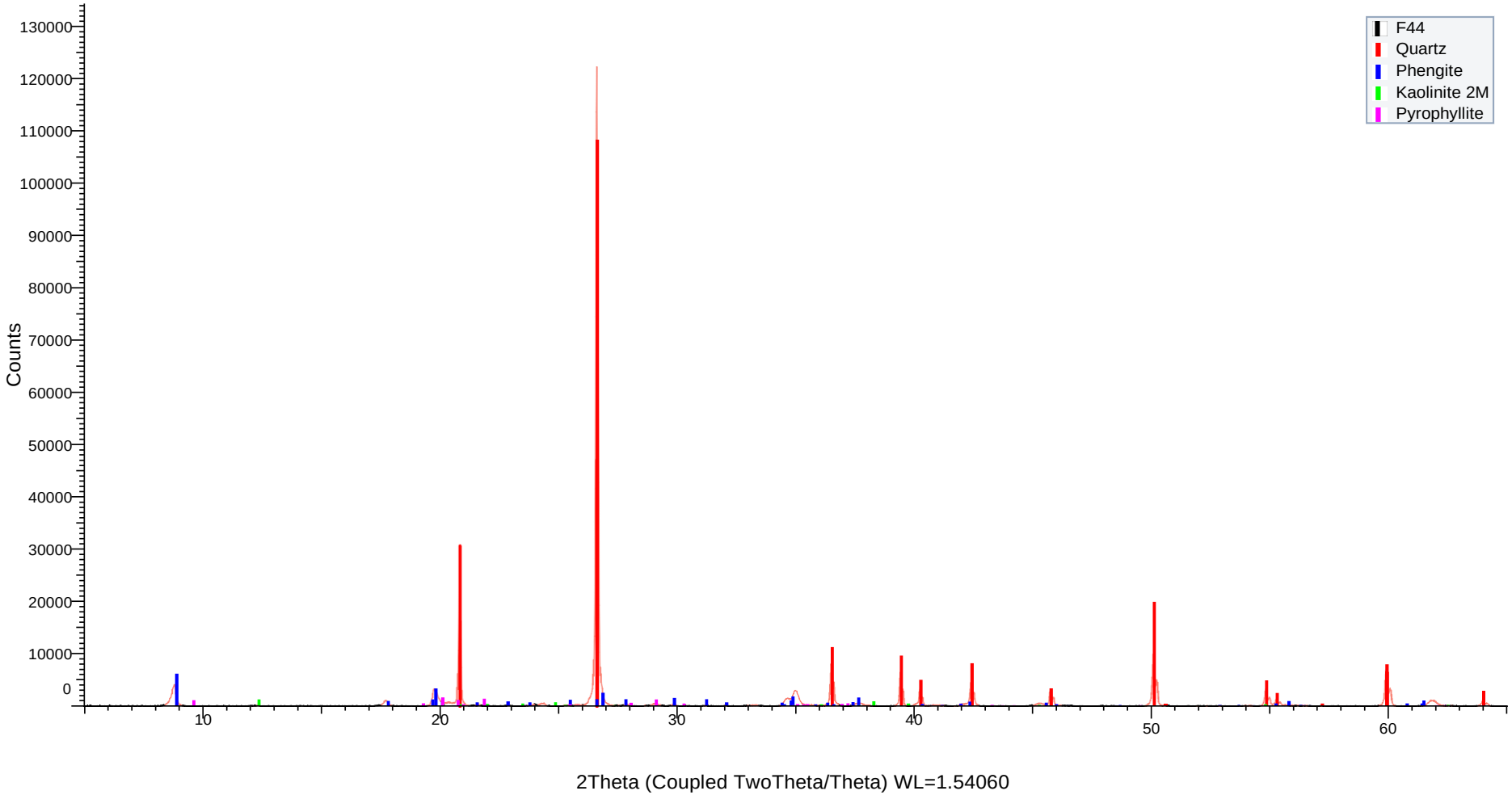

(Coupled TwoTheta/Theta)

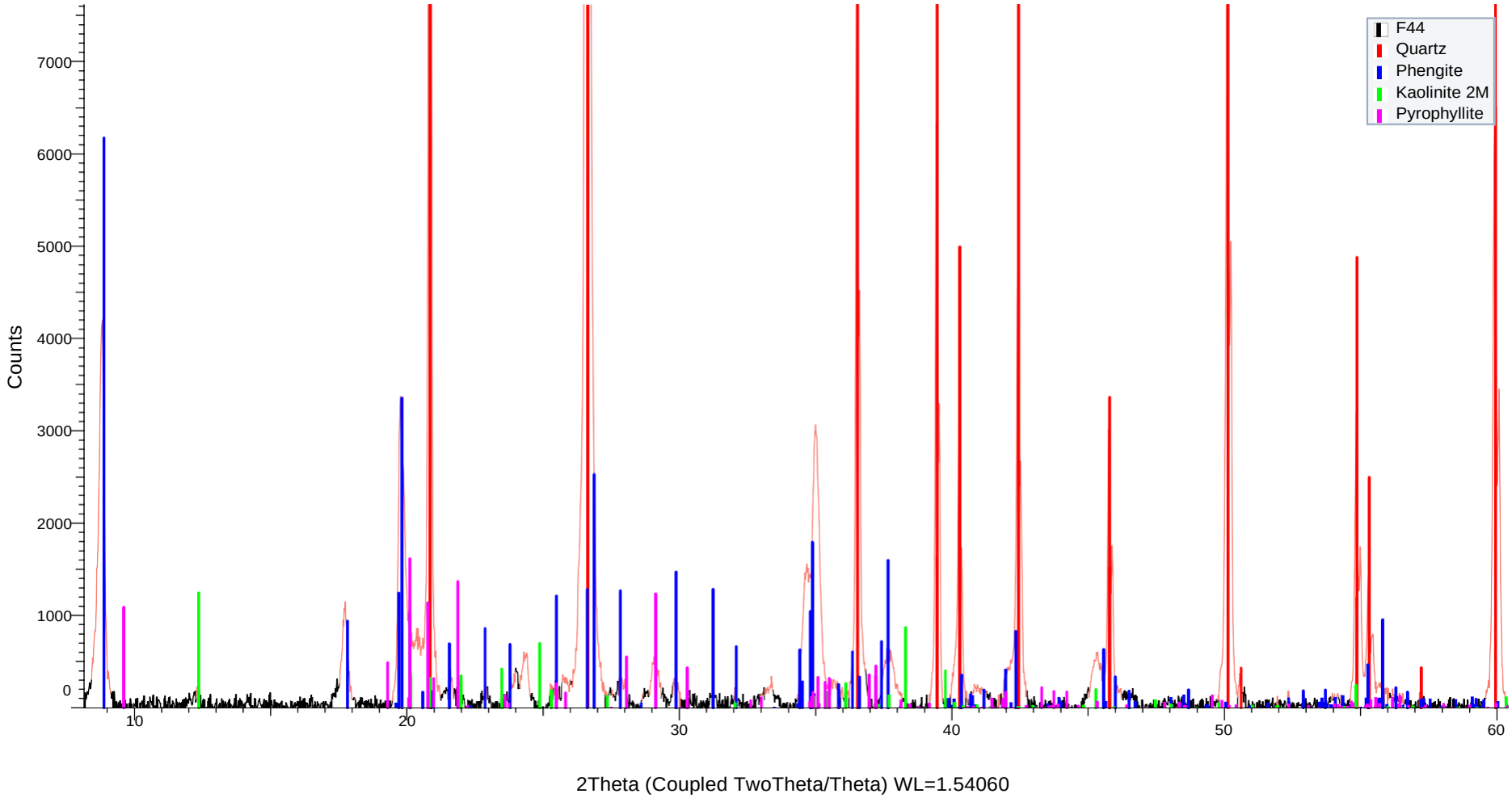

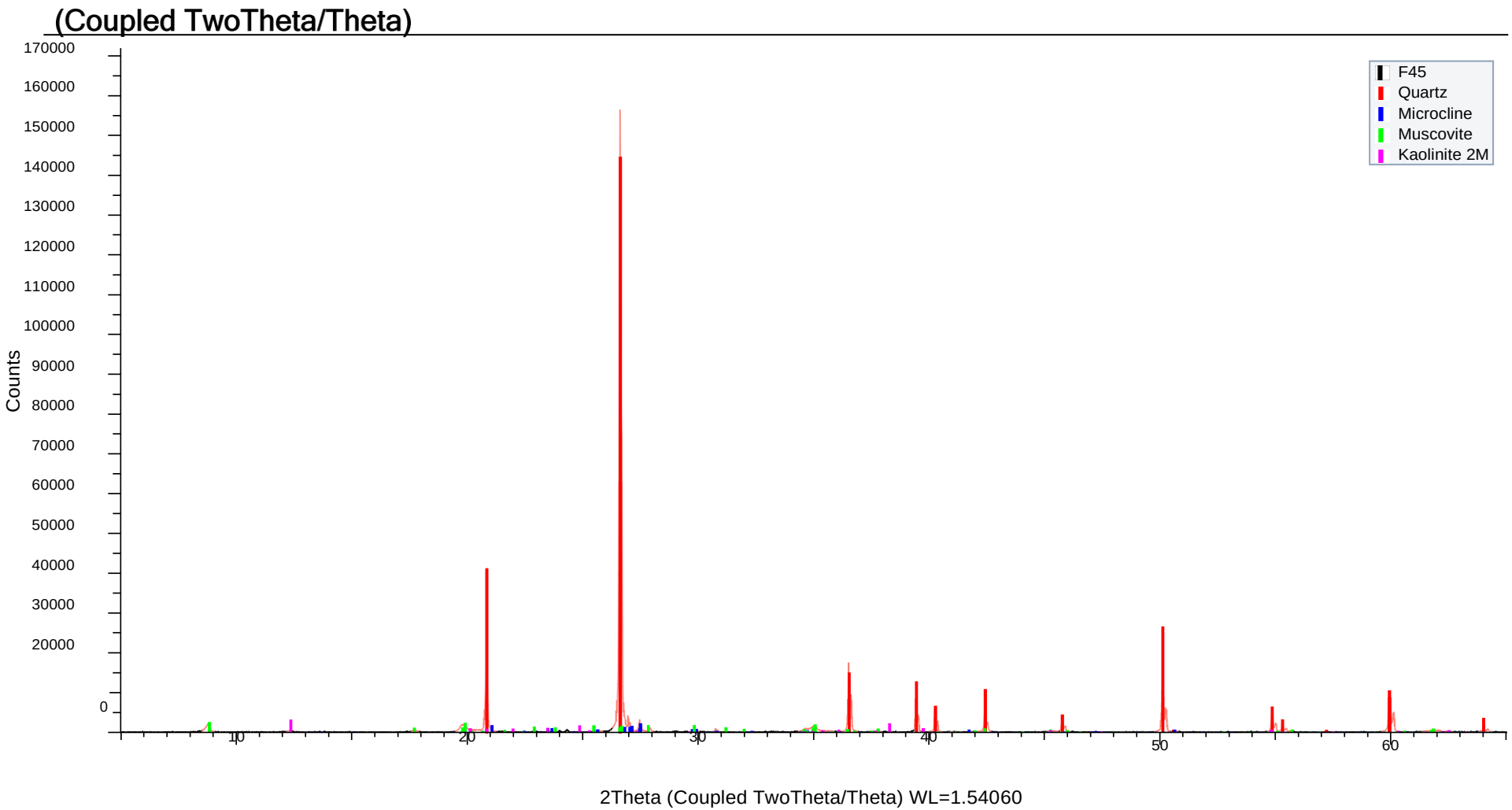
(Coupled TwoTheta/Theta)
Counts
170000
160000
150000
140000
130000
120000
110000
100000
90000
80000
70000
60000
50000
40000
30000
20000
0
10
20
30
40
50
60
F45
Quartz
Microcline
Muscovite
Kaolinite 2M
2Theta (Coupled TwoTheta/Theta) WL=1.54060

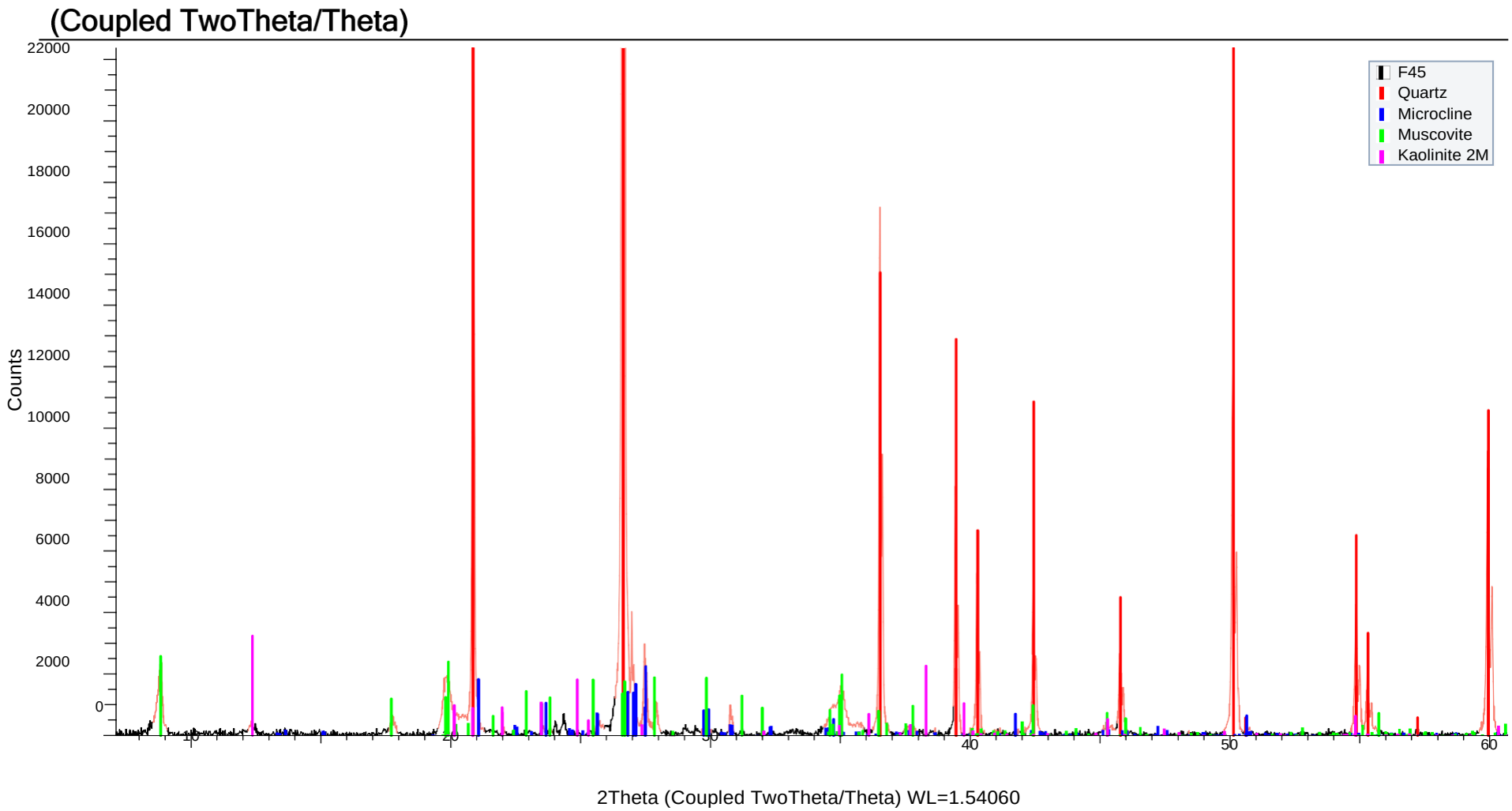
(Coupled TwoTheta/Theta)
Counts
22000
20000
18000
16000
14000
12000
10000
8000
6000
4000
2000
0
10
20
30
40
50
60
F45
Quartz
Microcline
Muscovite
Kaolinite 2M
2Theta (Coupled TwoTheta/Theta) WL=1.54060

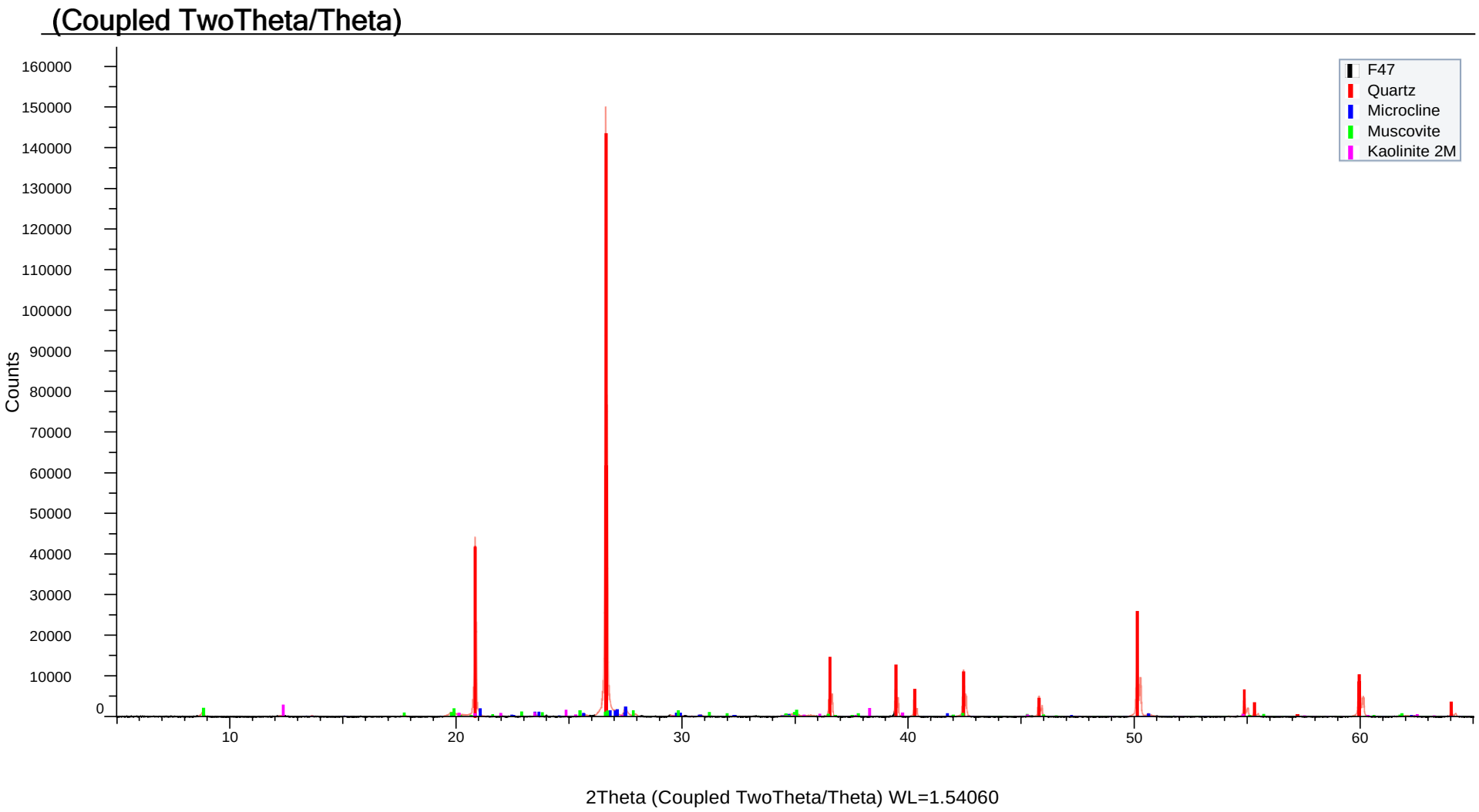
(Coupled TwoTheta/Theta)
F47
Quartz
Microcline
Muscovite
Kaolinite 2M
Counts
160000
150000
140000
130000
120000
110000
100000
90000
80000
70000
60000
50000
40000
30000
20000
10000
0
10
20
30
40
50
60
2Theta (Coupled TwoTheta/Theta) WL=1.54060

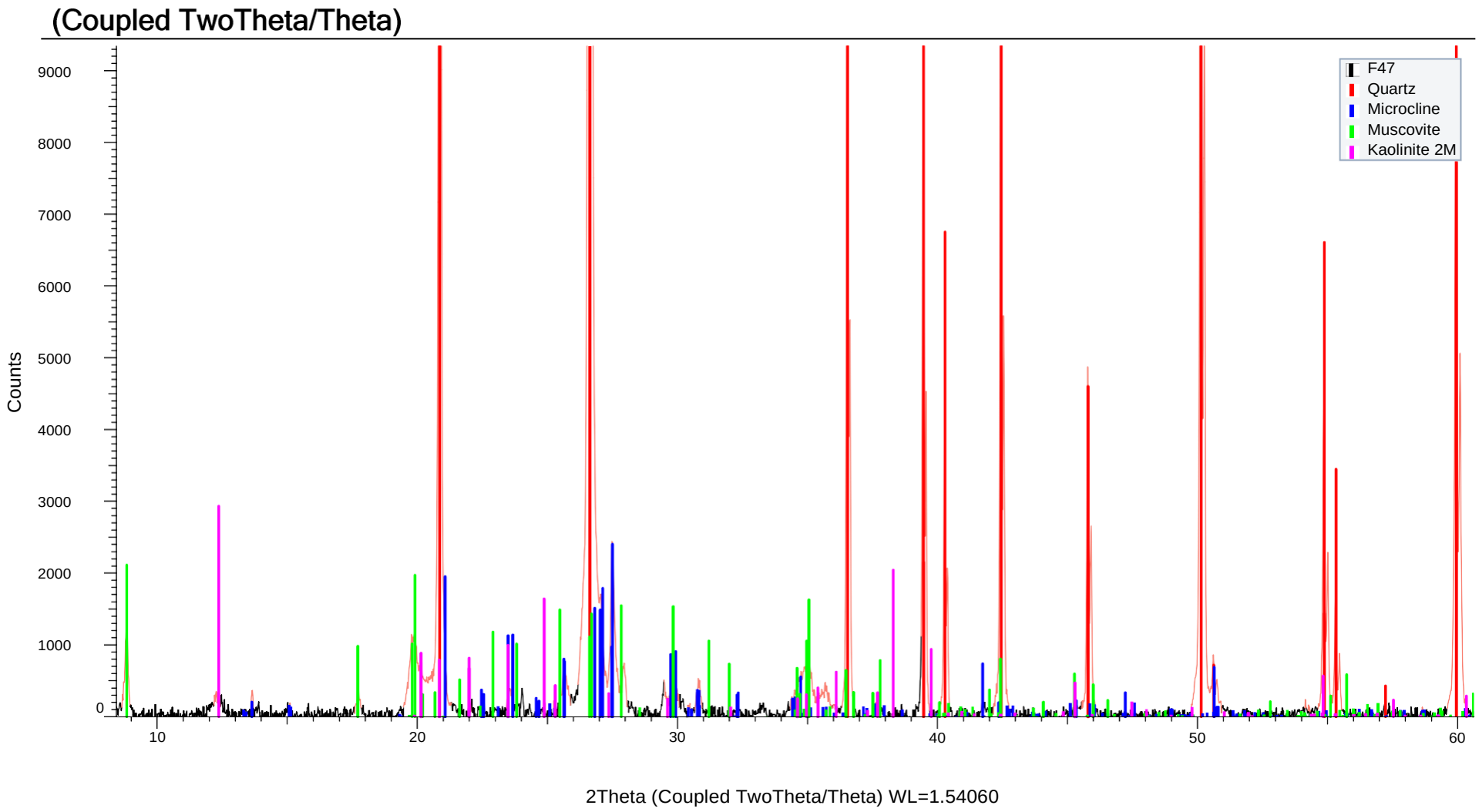
(Coupled TwoTheta/Theta)
F47
Quartz
Microcline
Muscovite
Kaolinite 2M
Counts
9000
8000
7000
6000
5000
4000
3000
2000
1000
0
10
20
30
40
50
60
2Theta (Coupled TwoTheta/Theta) WL=1.54060

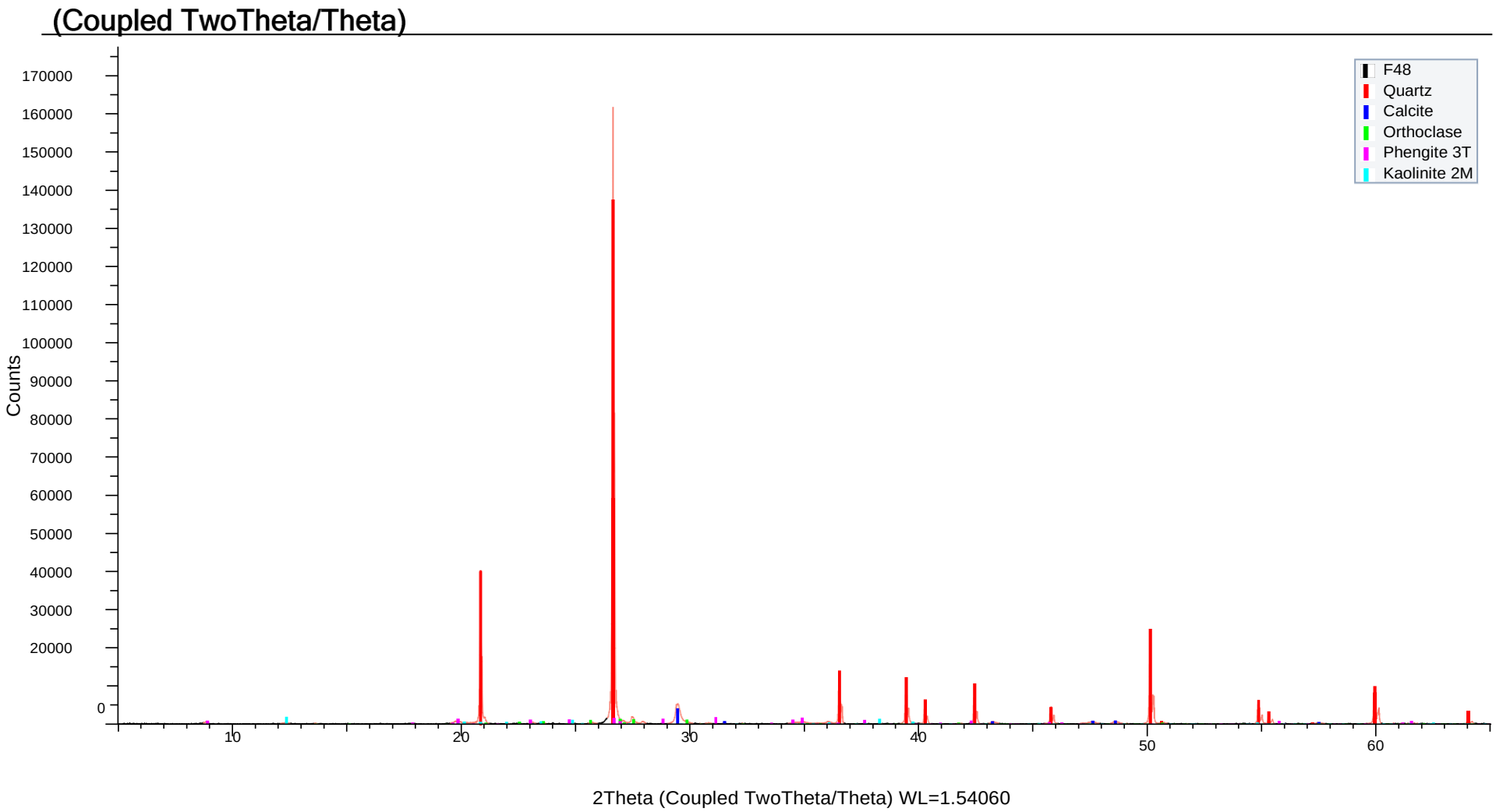
(Coupled TwoTheta/Theta)
F48
Quartz
Calcite
Orthoclase
Phengite 3T
Kaolinite 2M
Counts
170000
160000
150000
140000
130000
120000
110000
100000
90000
80000
70000
60000
50000
40000
30000
20000
0
10
20
30
40
50
60
2Theta (Coupled TwoTheta/Theta) WL=1.54060

(Coupled TwoTheta/Theta)

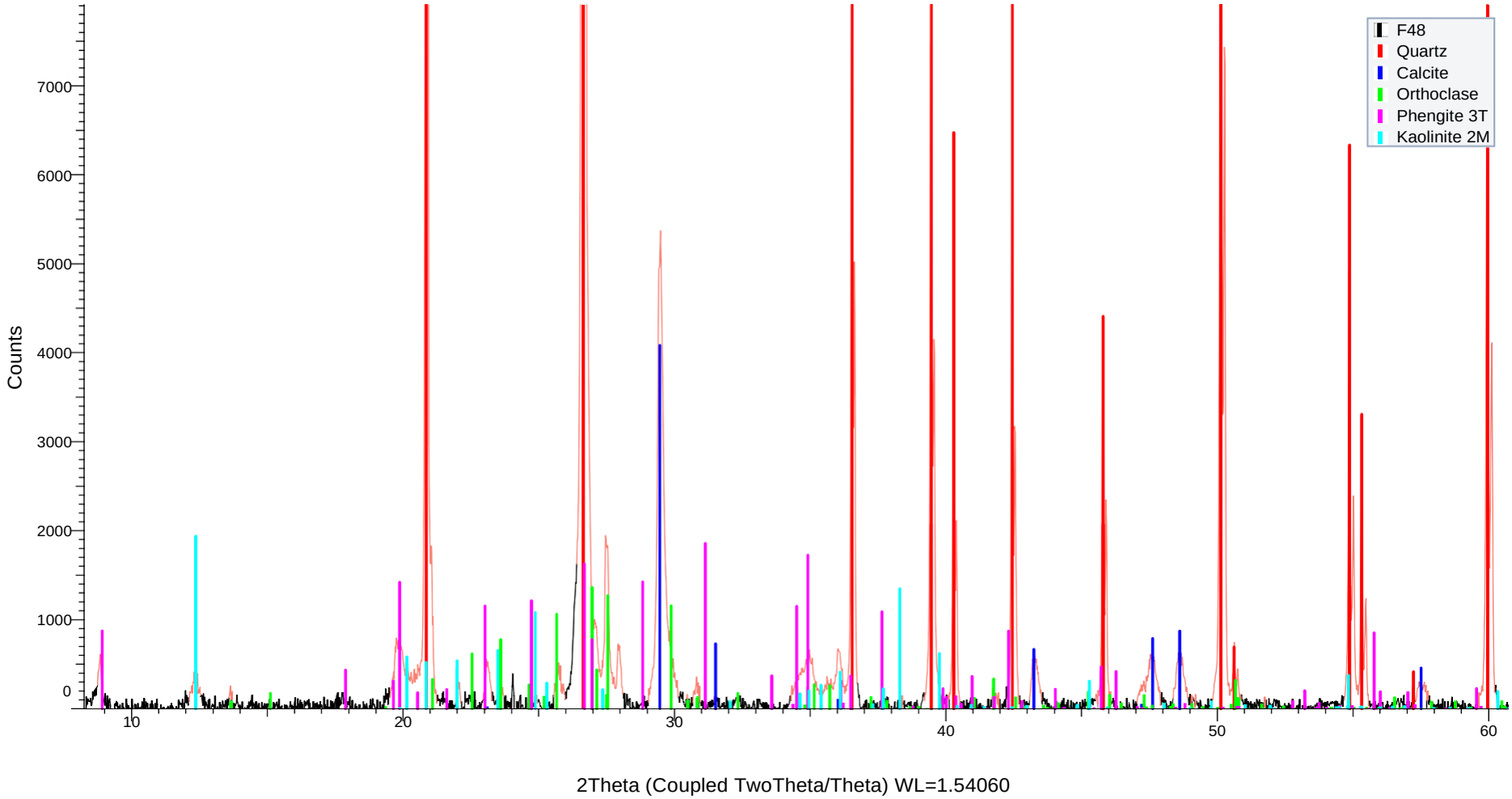

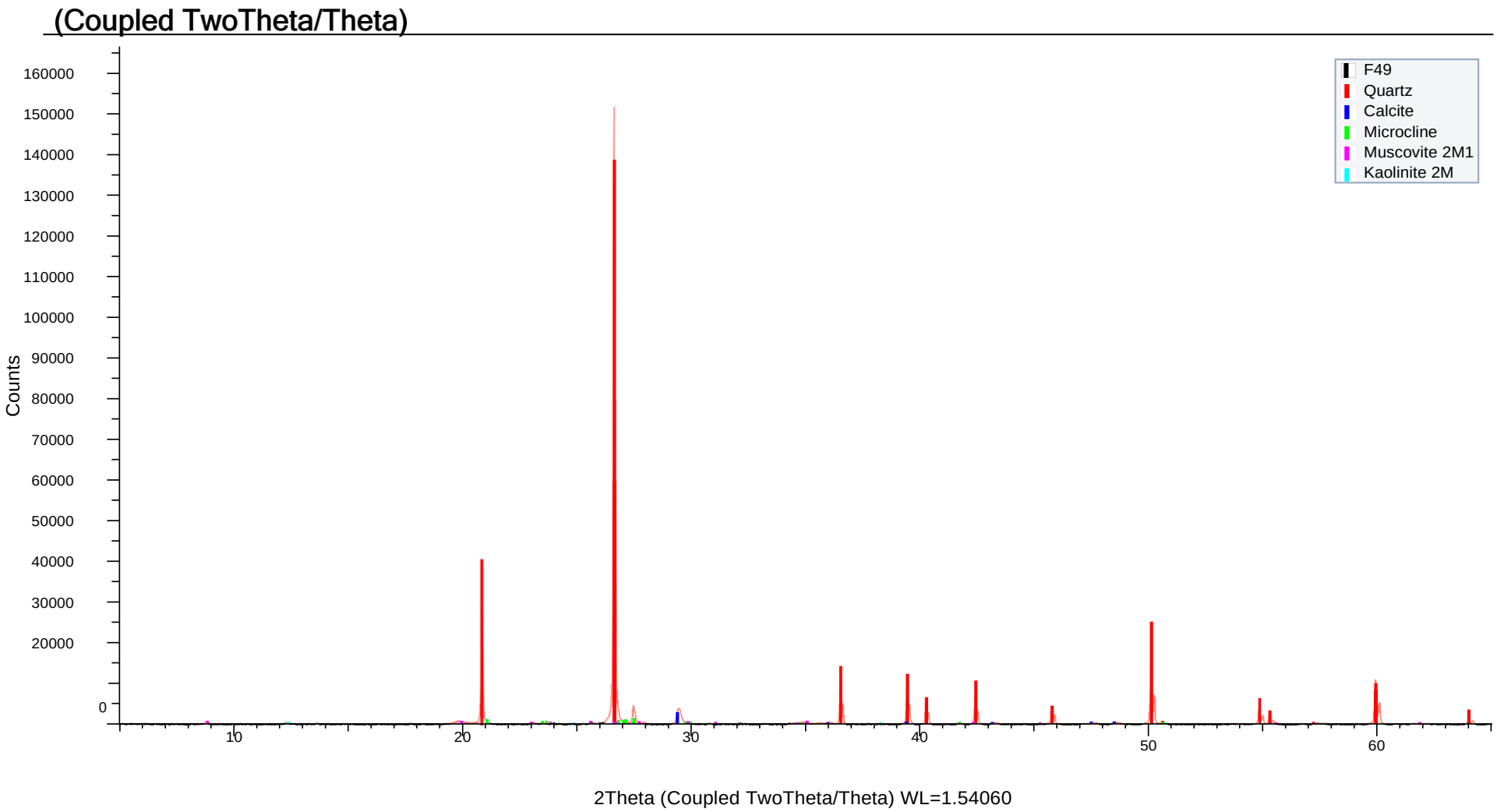
(Coupled TwoTheta/Theta)
Counts
160000
150000
140000
130000
120000
110000
100000
90000
80000
70000
60000
50000
40000
30000
20000
0
10
20
30
40
50
60
2Theta (Coupled TwoTheta/Theta) WL=1.54060
F49
Quartz
Calcite
Microcline
Muscovite 2M1
Kaolinite 2M

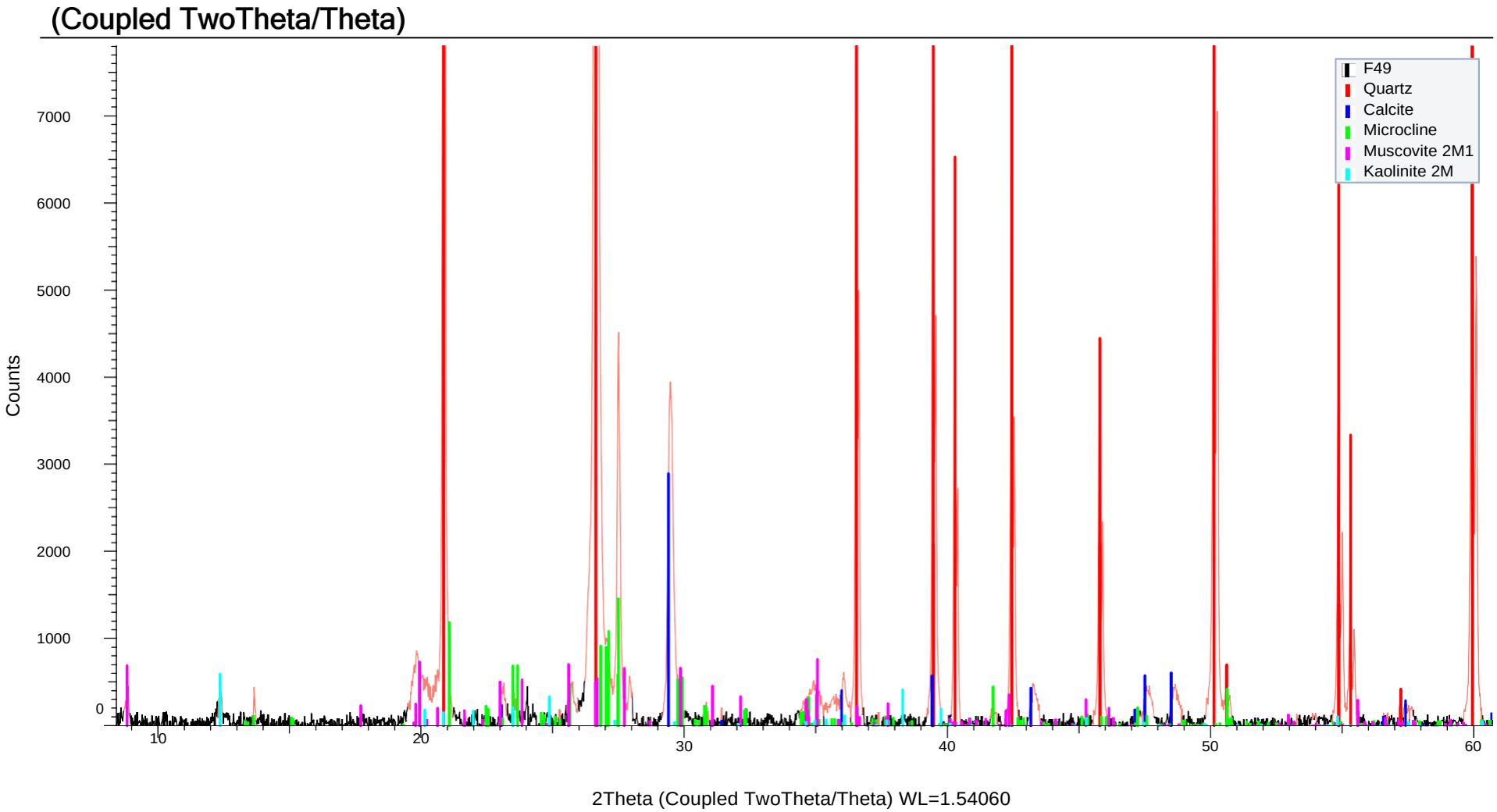
(Coupled TwoTheta/Theta)
F49
Quartz
Calcite
Microcline
Muscovite 2M1
Kaolinite 2M
Counts
0
1000
2000
3000
4000
5000
6000
7000
10
20
30
40
50
60
2Theta (Coupled TwoTheta/Theta) WL=1.54060

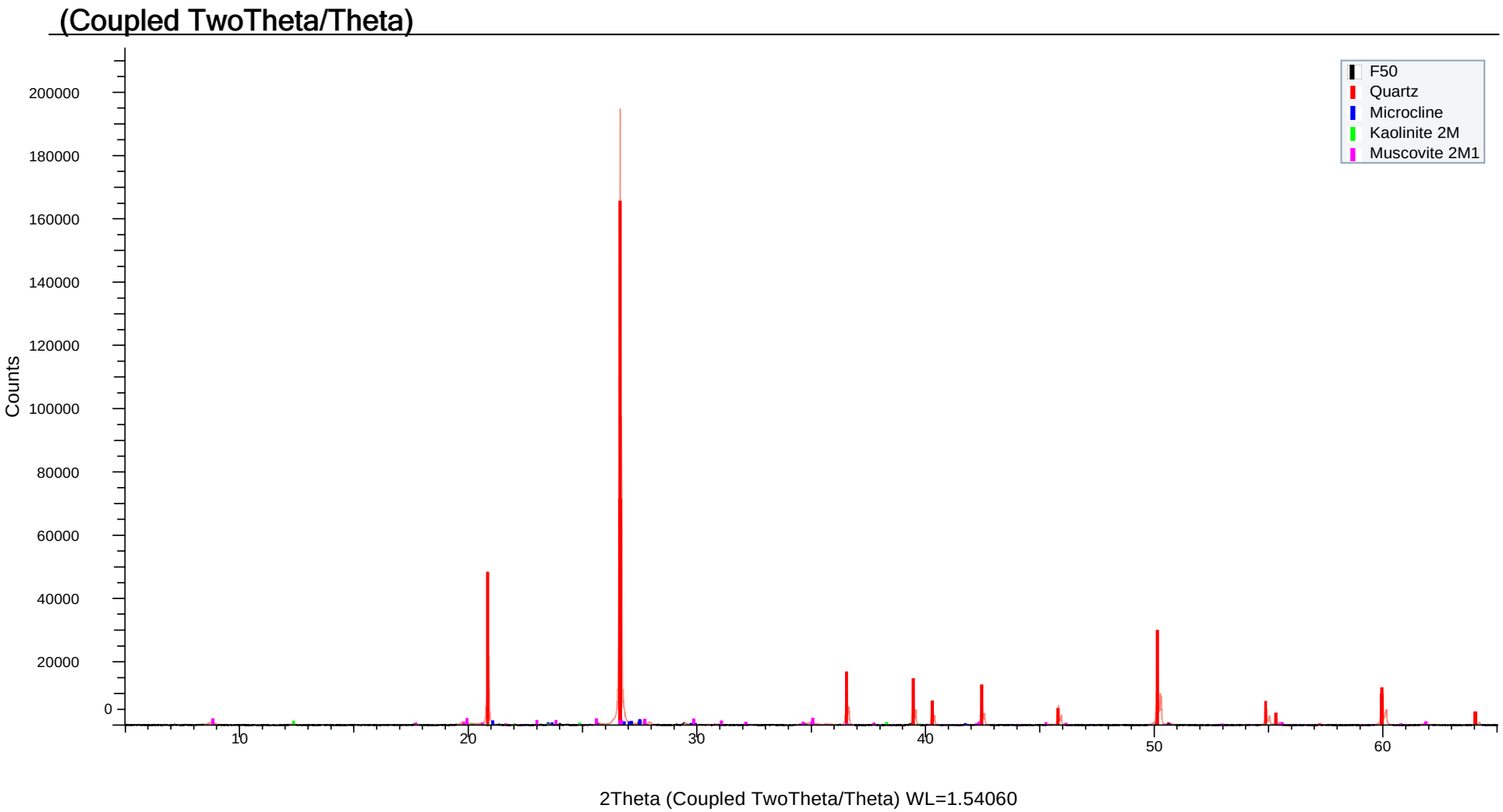
(Coupled TwoTheta/Theta)
F50
Quartz
Microcline
Kaolinite 2M
Muscovite 2M1
Counts
200000
180000
160000
140000
120000
100000
80000
60000
40000
20000
0
10
20
30
40
50
60
2Theta (Coupled TwoTheta/Theta) WL=1.54060

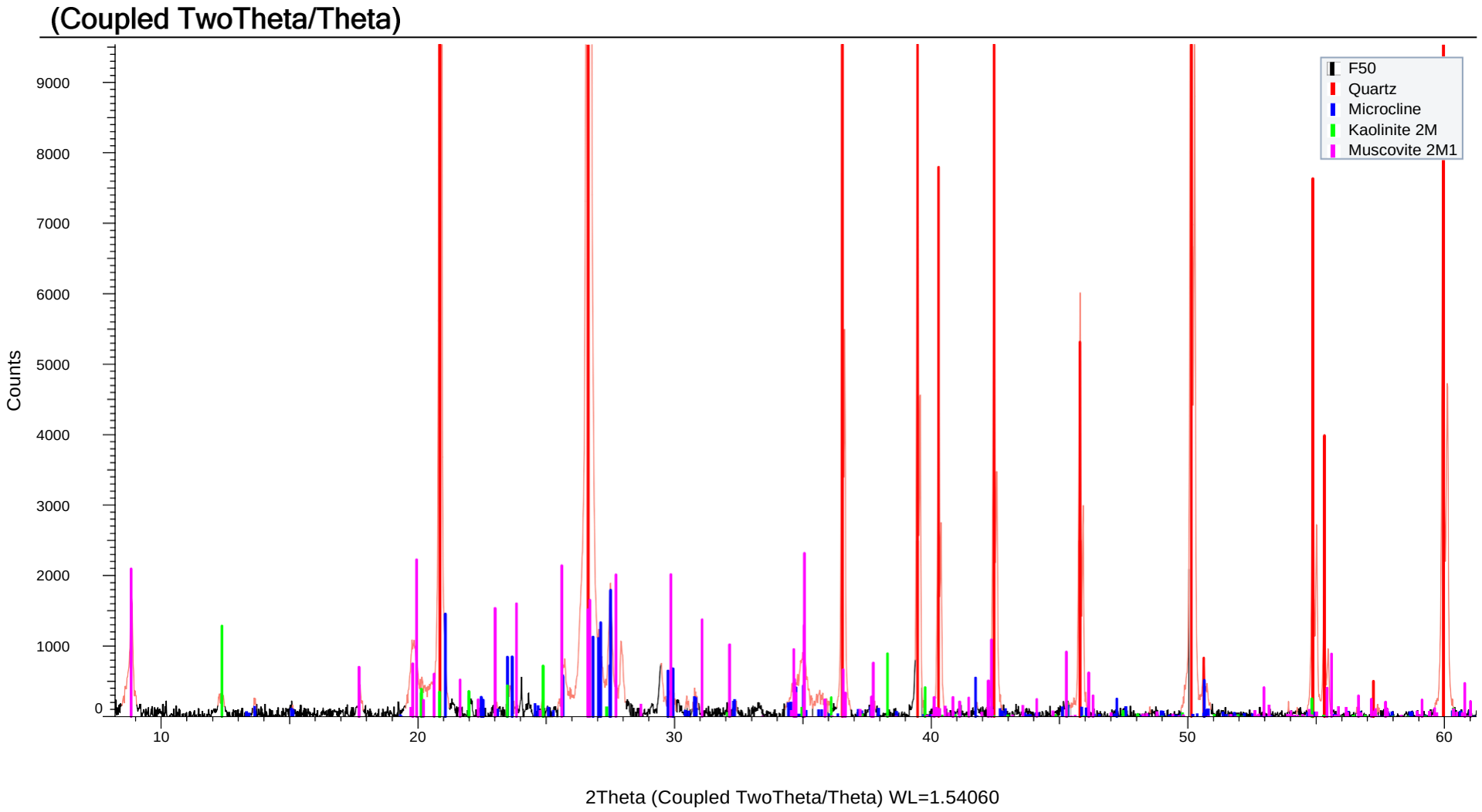
(Coupled TwoTheta/Theta)
F50
Quartz
Microcline
Kaolinite 2M
Muscovite 2M1
Counts
9000
8000
7000
6000
5000
4000
3000
2000
1000
0
10
20
30
40
50
60
2Theta (Coupled TwoTheta/Theta) WL=1.54060

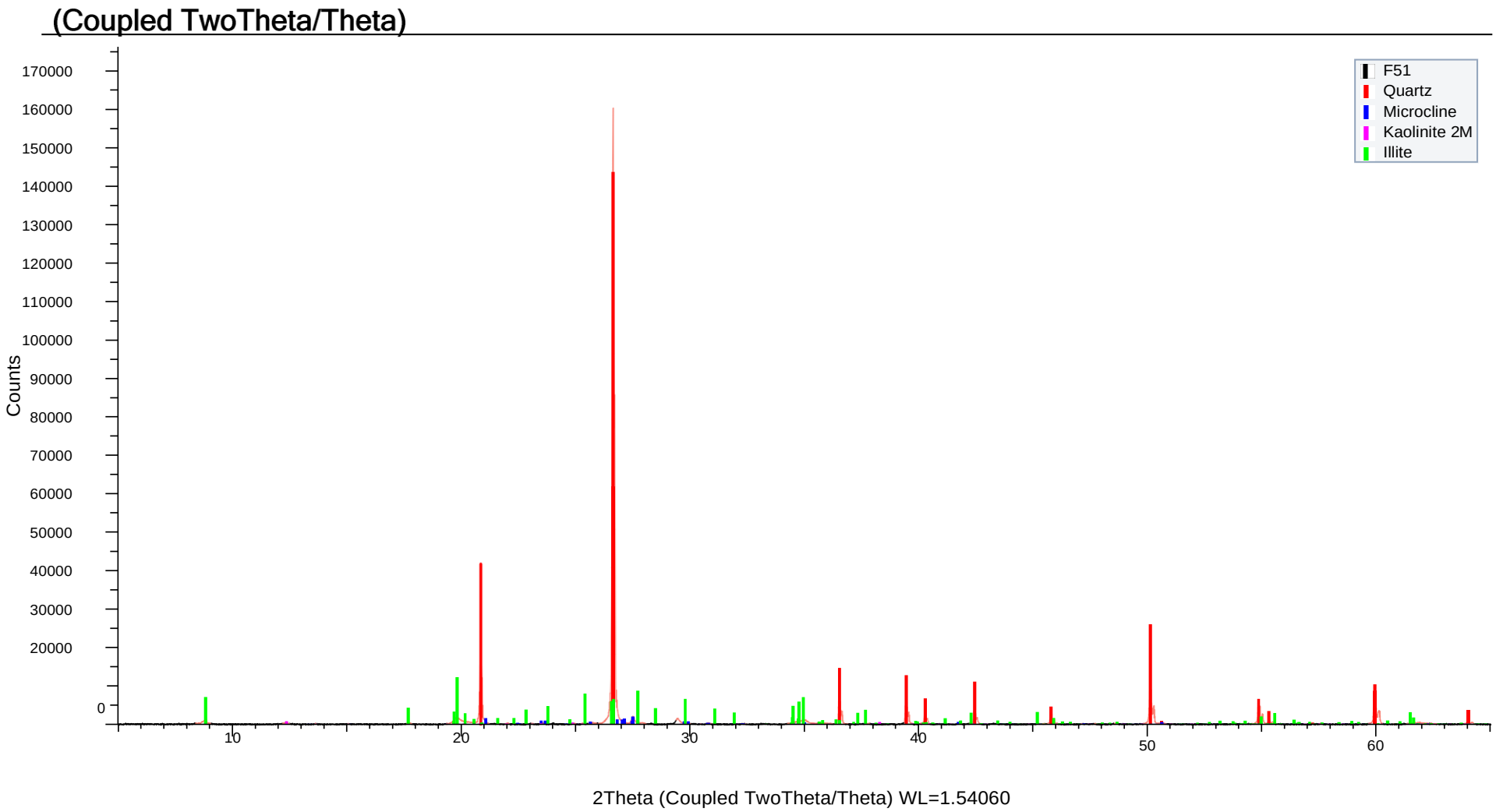
(Coupled TwoTheta/Theta)
F51
Quartz
Microcline
Kaolinite 2M
Illite
Counts
170000
160000
150000
140000
130000
120000
110000
100000
90000
80000
70000
60000
50000
40000
30000
20000
0
10
20
30
40
50
60
2Theta (Coupled TwoTheta/Theta) WL=1.54060

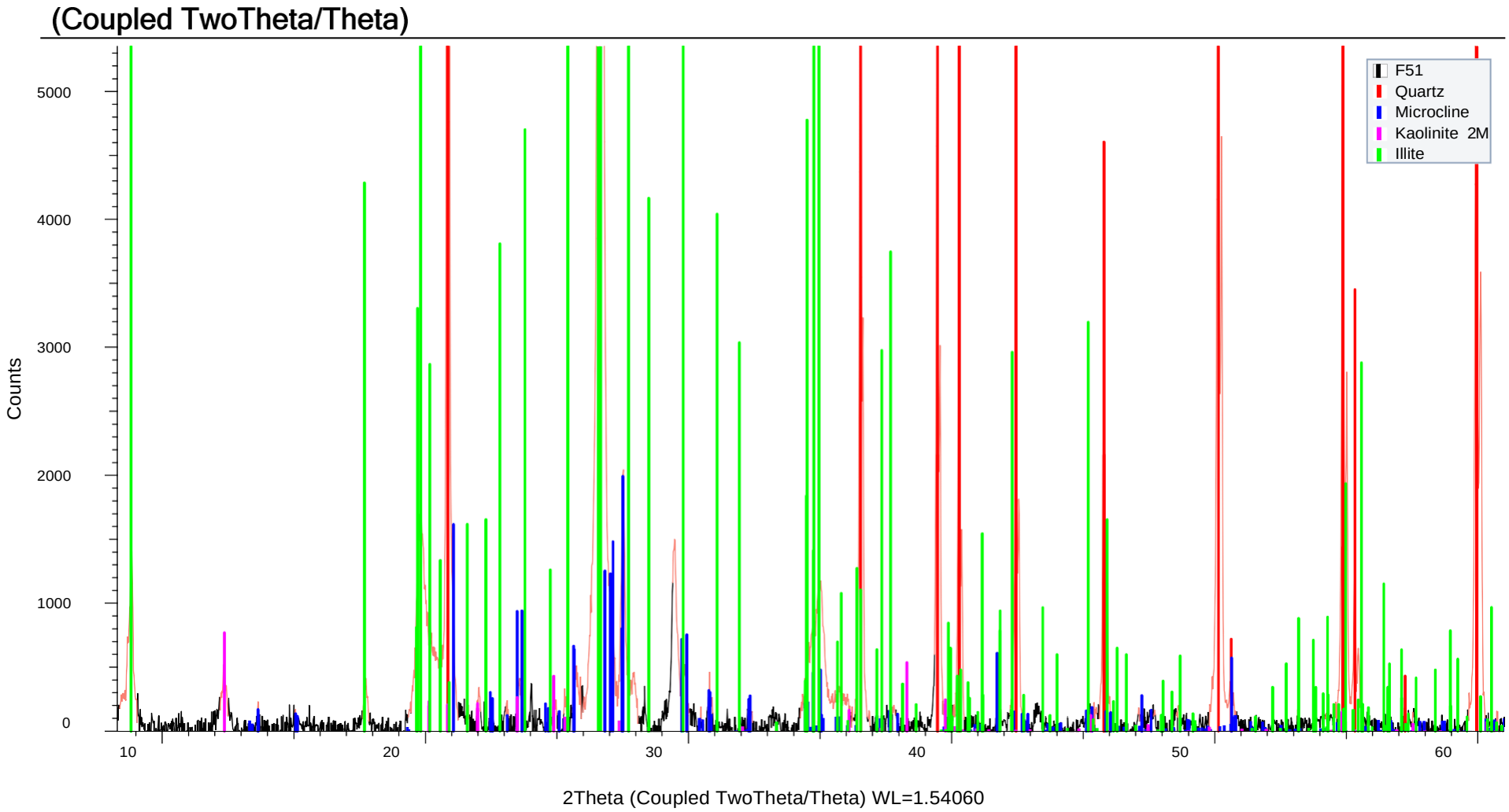
(Coupled TwoTheta/Theta)
F51
Quartz
Microcline
Kaolinite 2M
Illite
Counts
5000
4000
3000
2000
1000
0
10
20
30
40
50
60
2Theta (Coupled TwoTheta/Theta) WL=1.54060

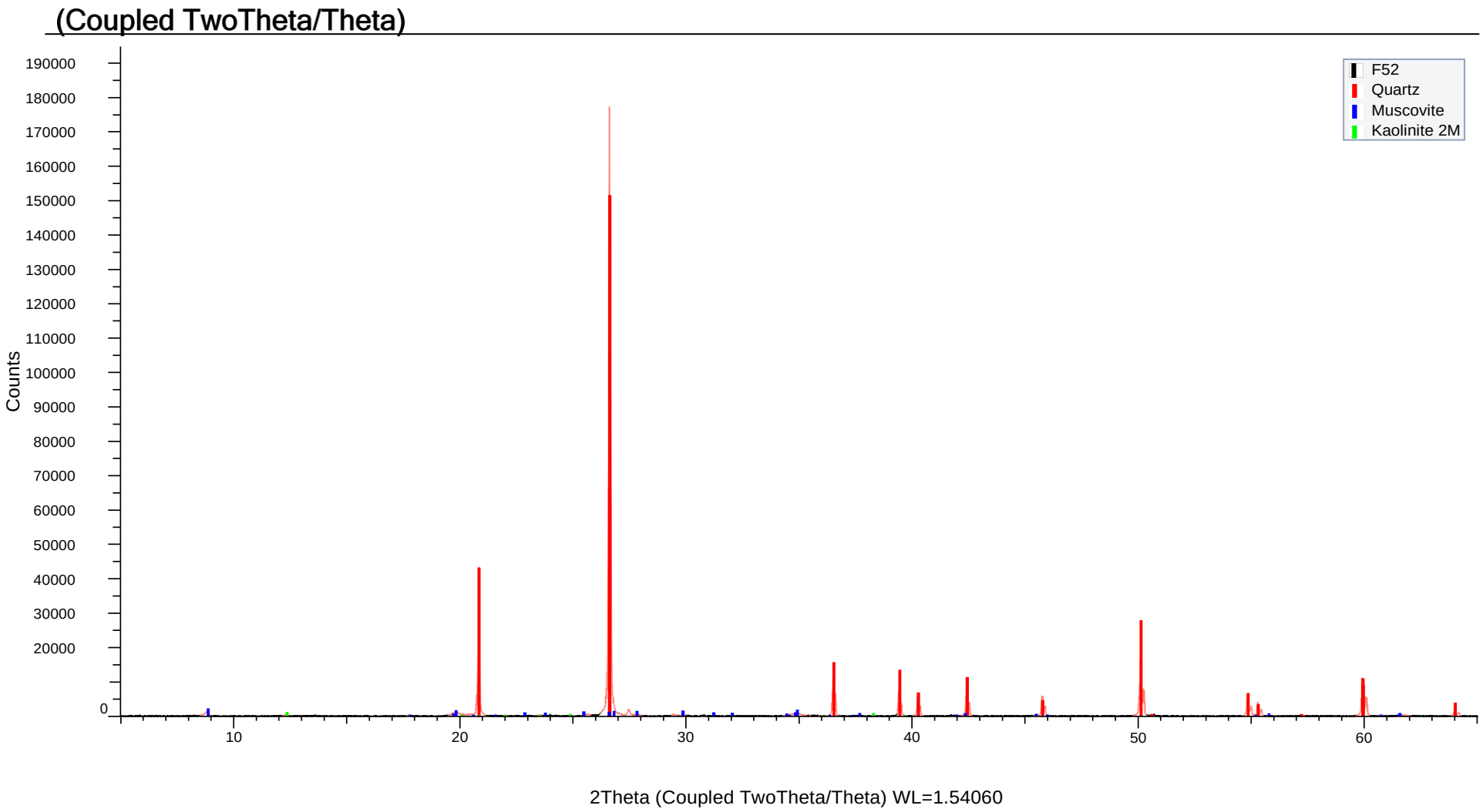
(Coupled TwoTheta/Theta)
F52
Quartz
Muscovite
Kaolinite 2M
Counts
190000
180000
170000
160000
150000
140000
130000
120000
110000
100000
90000
80000
70000
60000
50000
40000
30000
20000
0
10
20
30
40
50
60
2Theta (Coupled TwoTheta/Theta) WL=1.54060

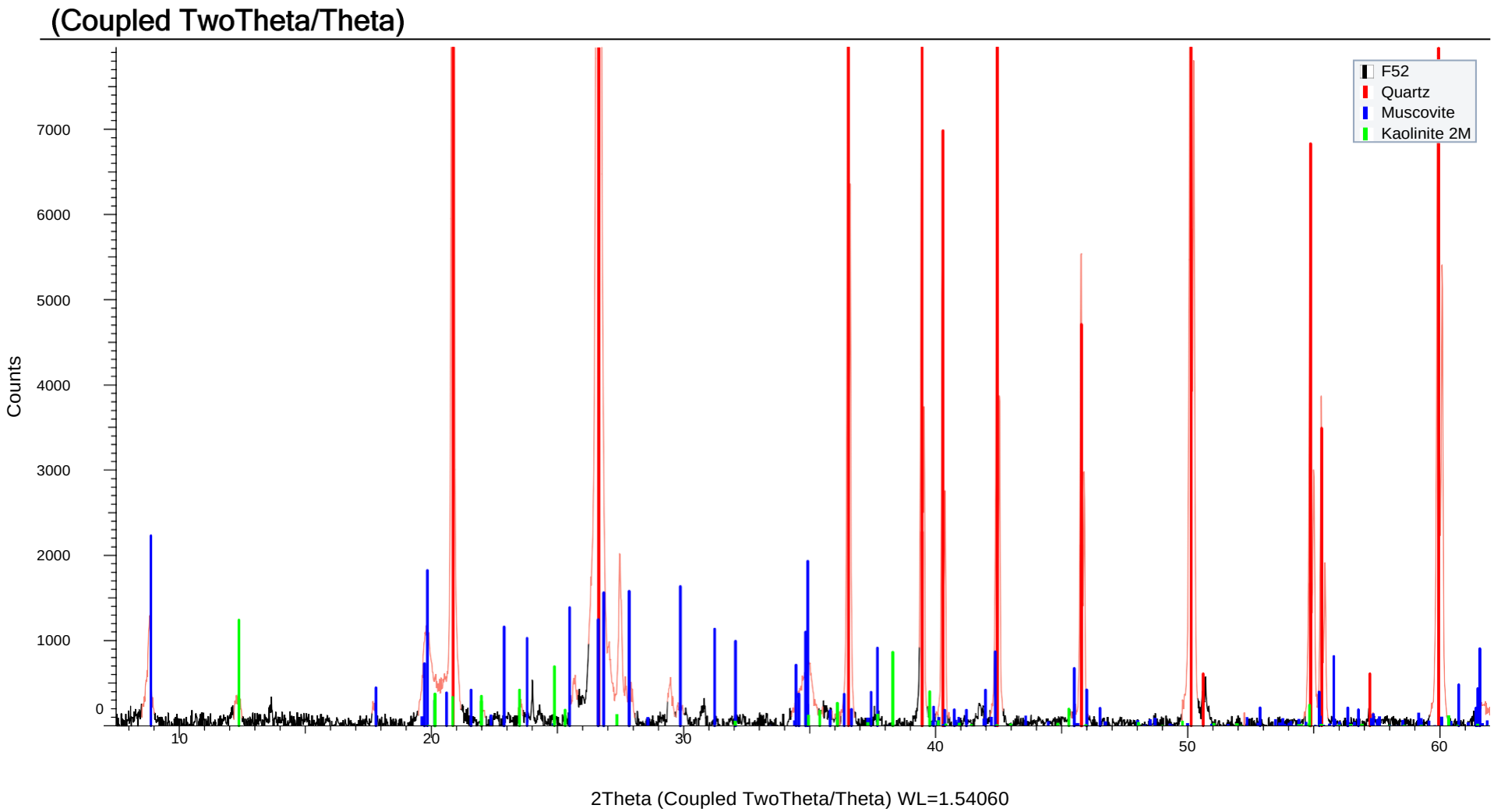
(Coupled TwoTheta/Theta)
F52
Quartz
Muscovite
Kaolinite 2M
Counts
7000
6000
5000
4000
3000
2000
1000
0
10
20
30
40
50
60
2Theta (Coupled TwoTheta/Theta) WL=1.54060

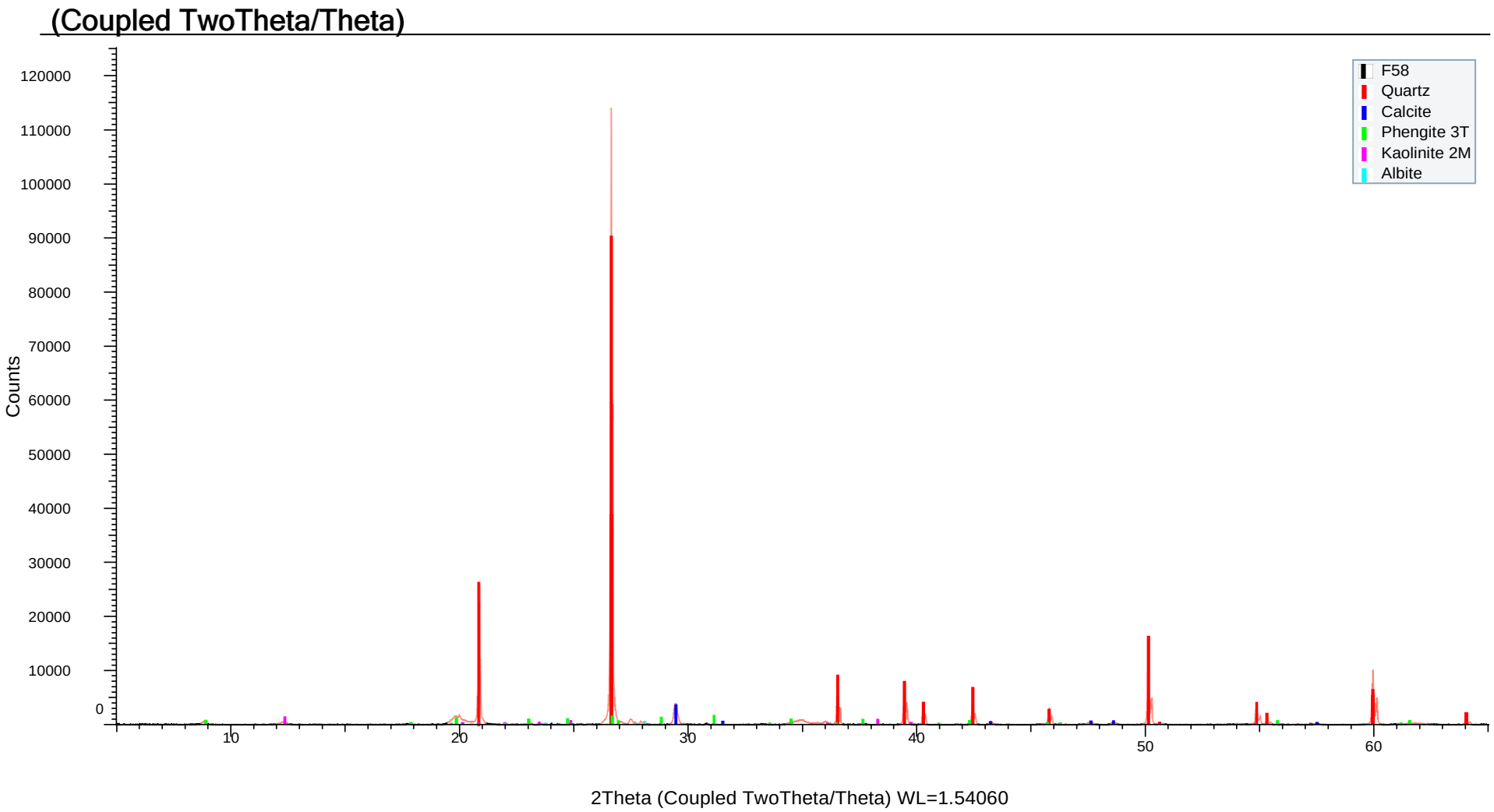
(Coupled TwoTheta/Theta)
F58
Quartz
Calcite
Phengite 3T
Kaolinite 2M
Albite
Counts
120000
110000
100000
90000
80000
70000
60000
50000
40000
30000
20000
10000
0
10
20
30
40
50
60
2Theta (Coupled TwoTheta/Theta) WL=1.54060

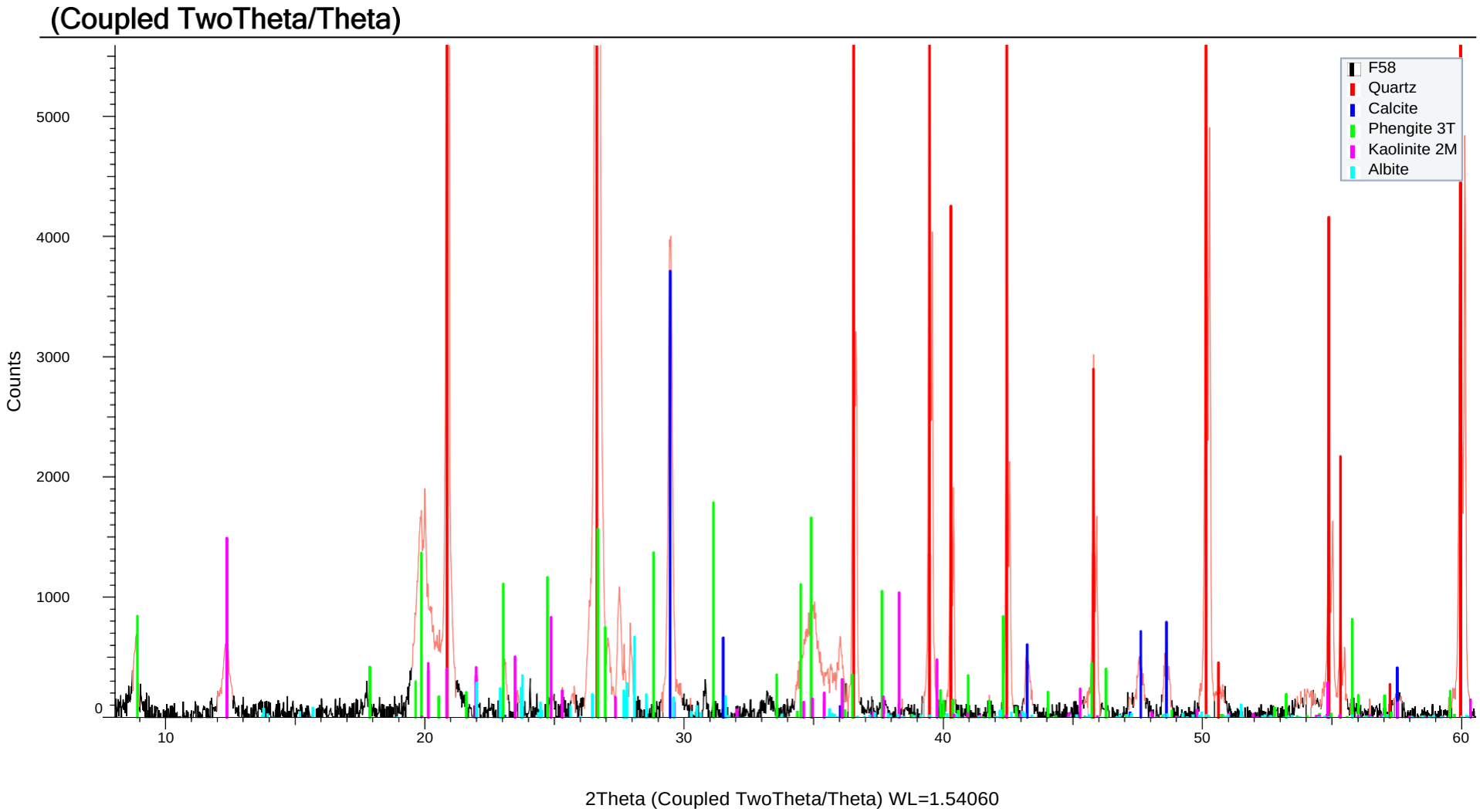
(Coupled TwoTheta/Theta)
F58
Quartz
Calcite
Phengite 3T
Kaolinite 2M
Albite
Counts
0
1000
2000
3000
4000
5000
10
20
30
40
50
60
2Theta (Coupled TwoTheta/Theta) WL=1.54060

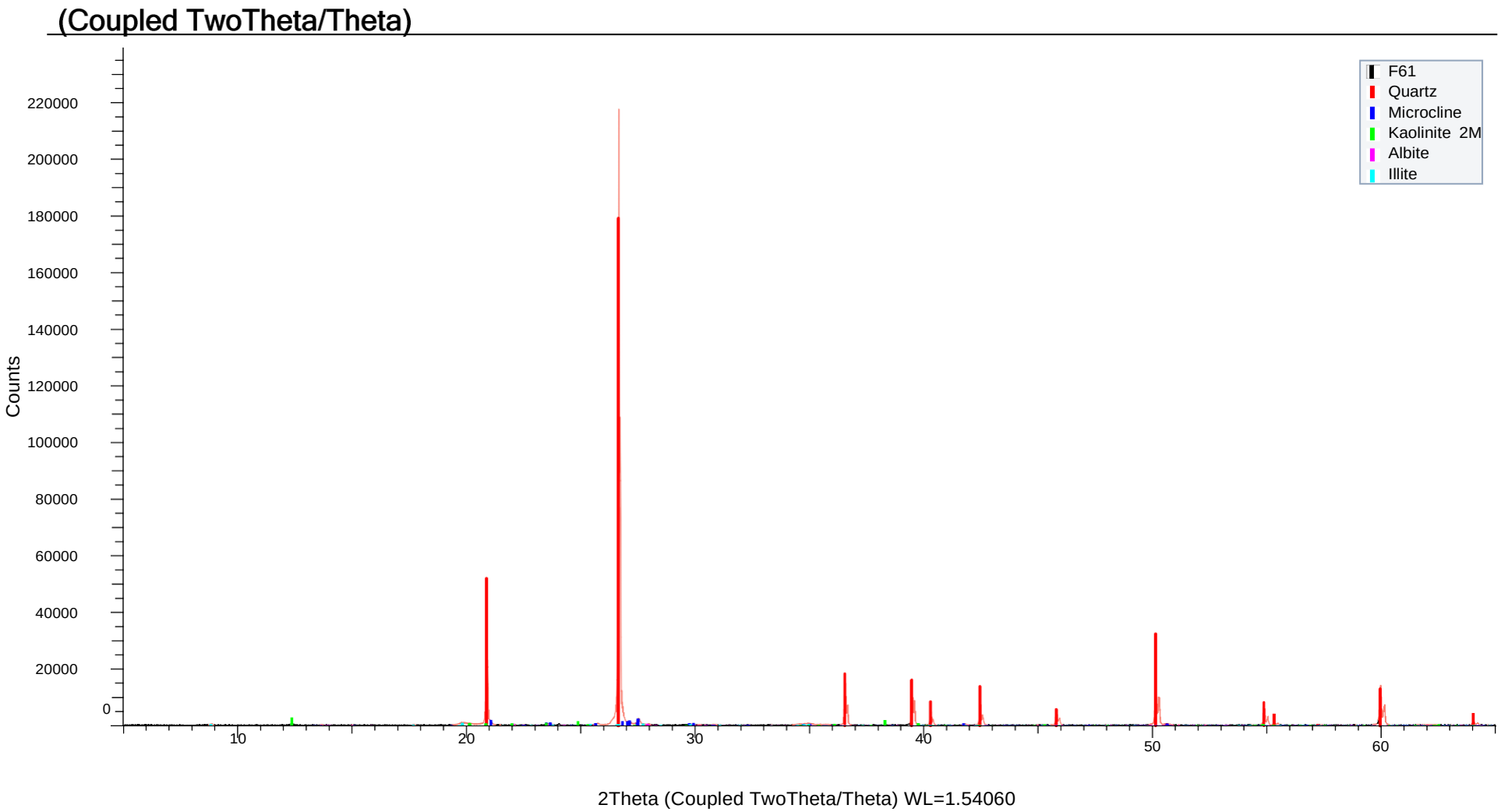
(Coupled TwoTheta/Theta)
F61
Quartz
Microcline
Kaolinite 2M
Albite
Illite
Counts
220000
200000
180000
160000
140000
120000
100000
80000
60000
40000
20000
0
10
20
30
40
50
60
2Theta (Coupled TwoTheta/Theta) WL=1.54060

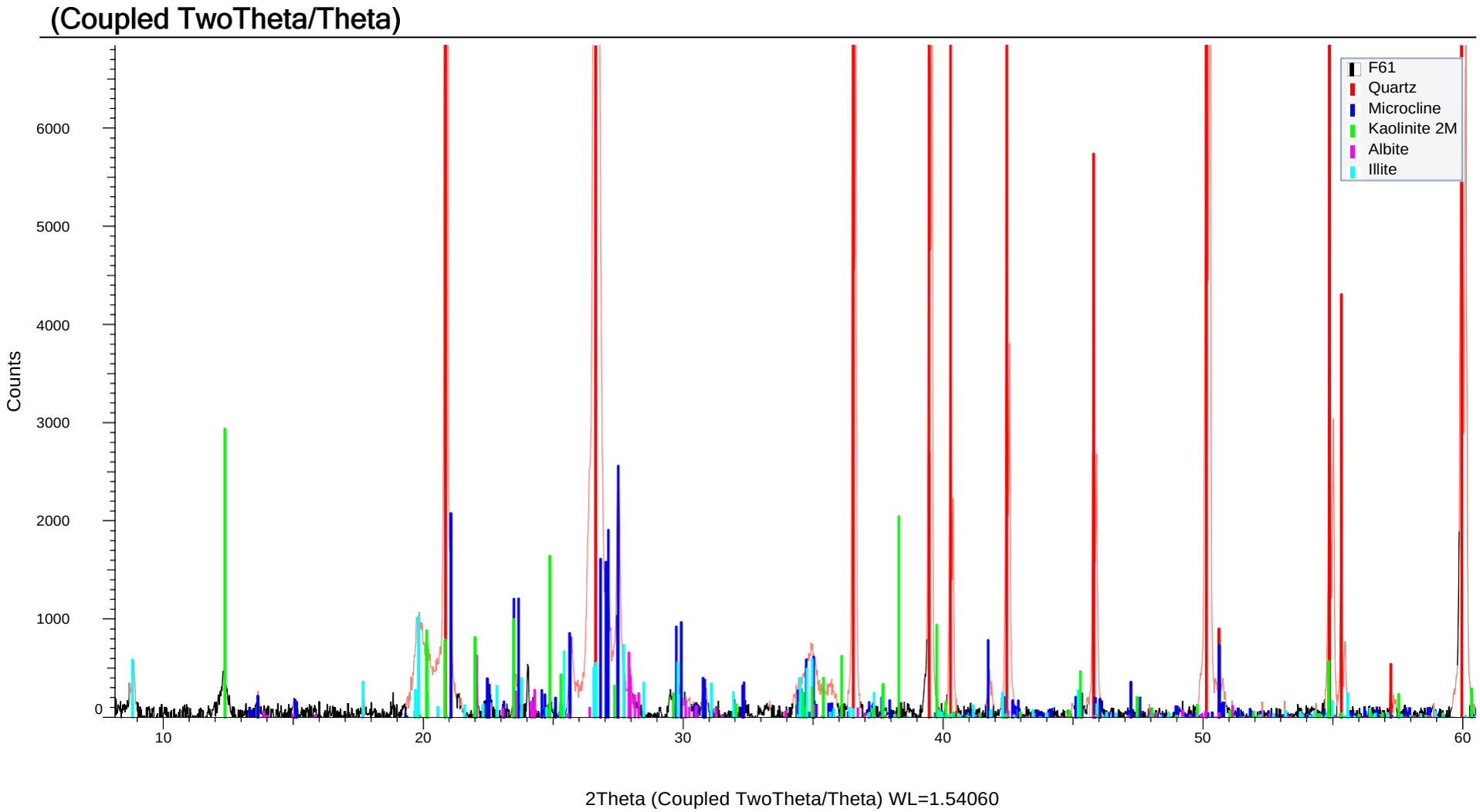
(Coupled TwoTheta/Theta)
F61
Quartz
Microcline
Kaolinite 2M
Albite
Illite
Counts
0
1000
2000
3000
4000
5000
6000
10
20
30
40
50
60
2Theta (Coupled TwoTheta/Theta) WL=1.54060

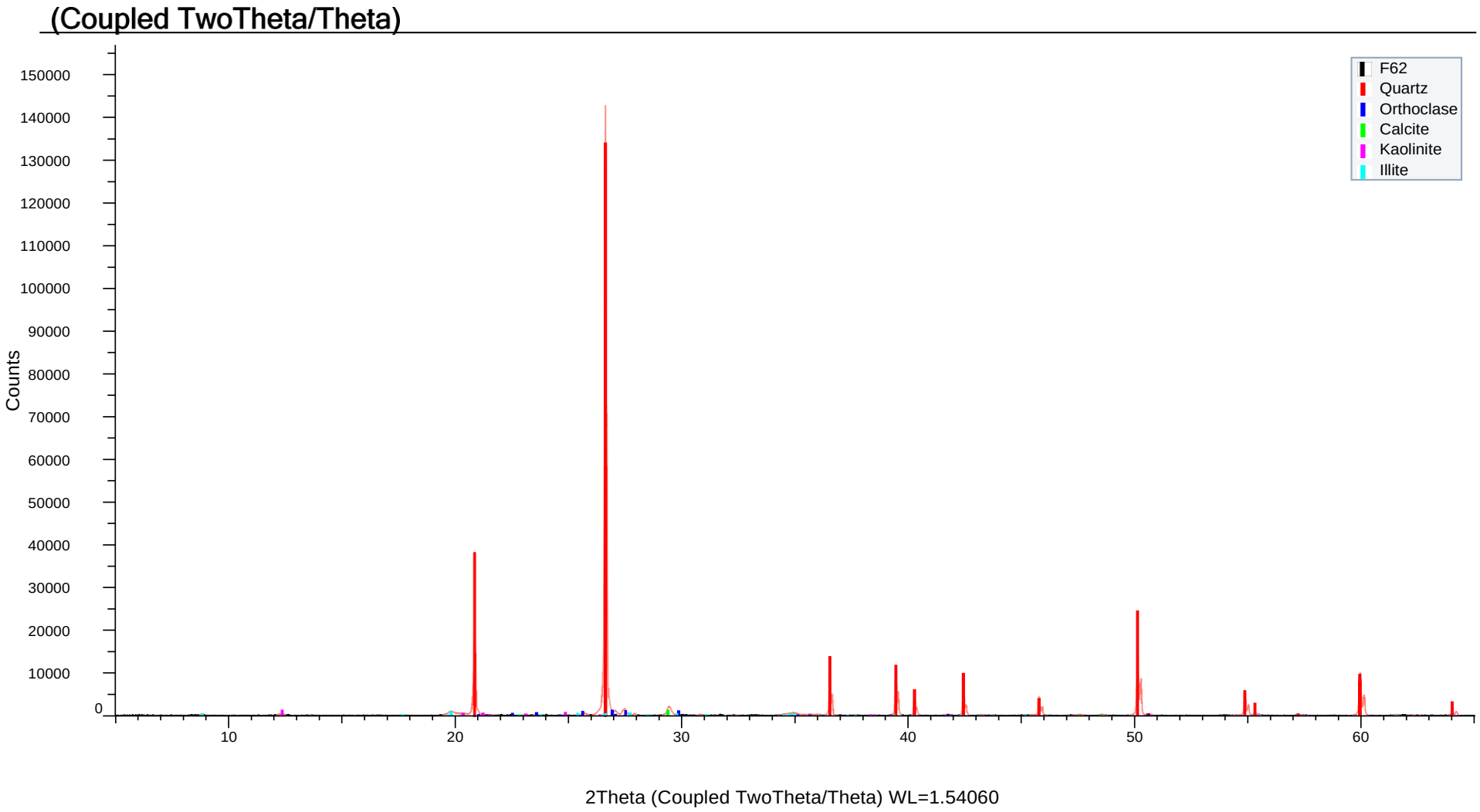
(Coupled TwoTheta/Theta)
F62
Quartz
Orthoclase
Calcite
Kaolinite
Illite
Counts
150000
140000
130000
120000
110000
100000
90000
80000
70000
60000
50000
40000
30000
20000
10000
0
10
20
30
40
50
60
2Theta (Coupled TwoTheta/Theta) WL=1.54060

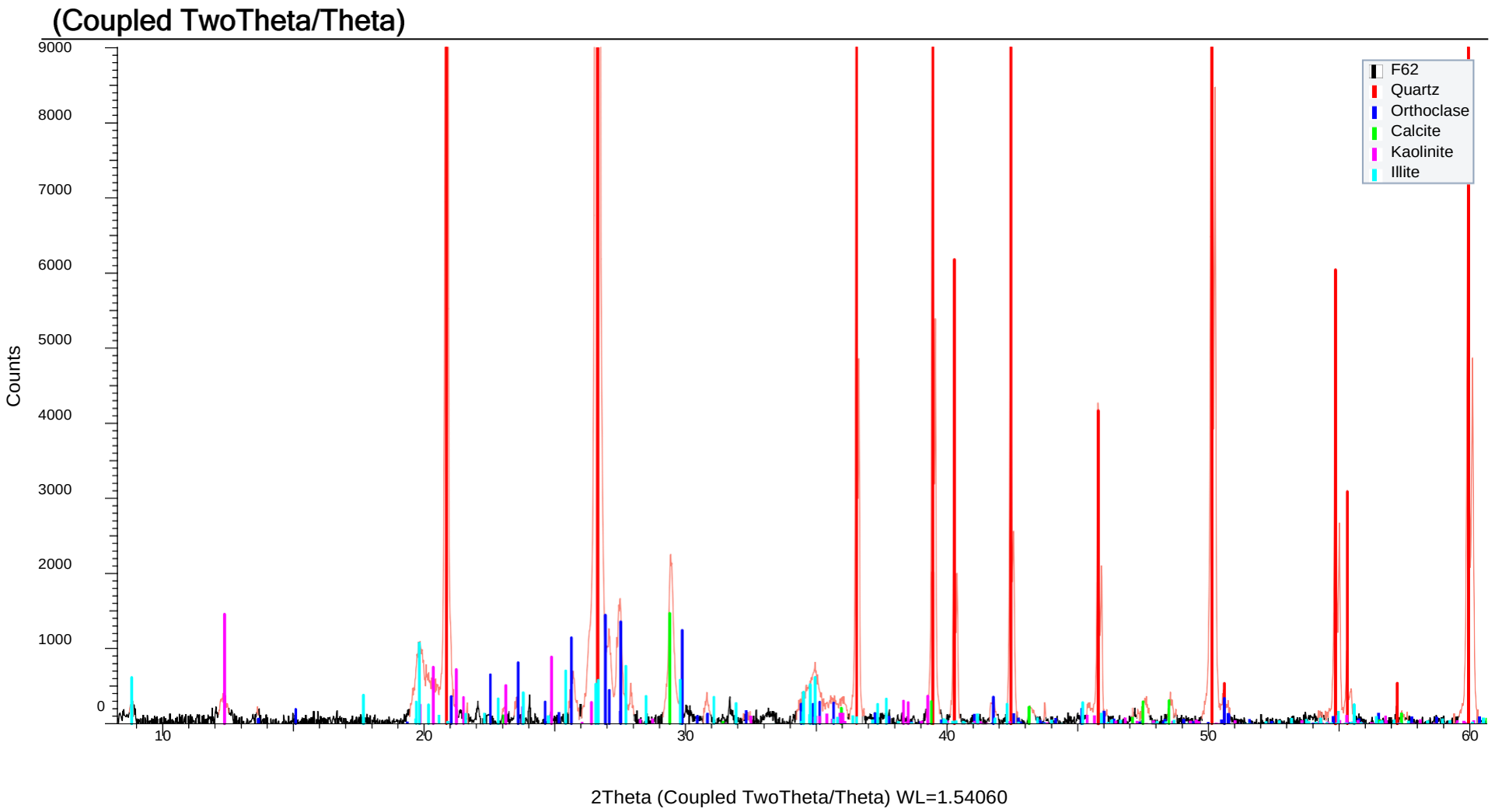
(Coupled TwoTheta/Theta)
Counts
9000
8000
7000
6000
5000
4000
3000
2000
1000
0
10
20
30
40
50
60
F62
Quartz
Orthoclase
Calcite
Kaolinite
Illite
2Theta (Coupled TwoTheta/Theta) WL=1.54060

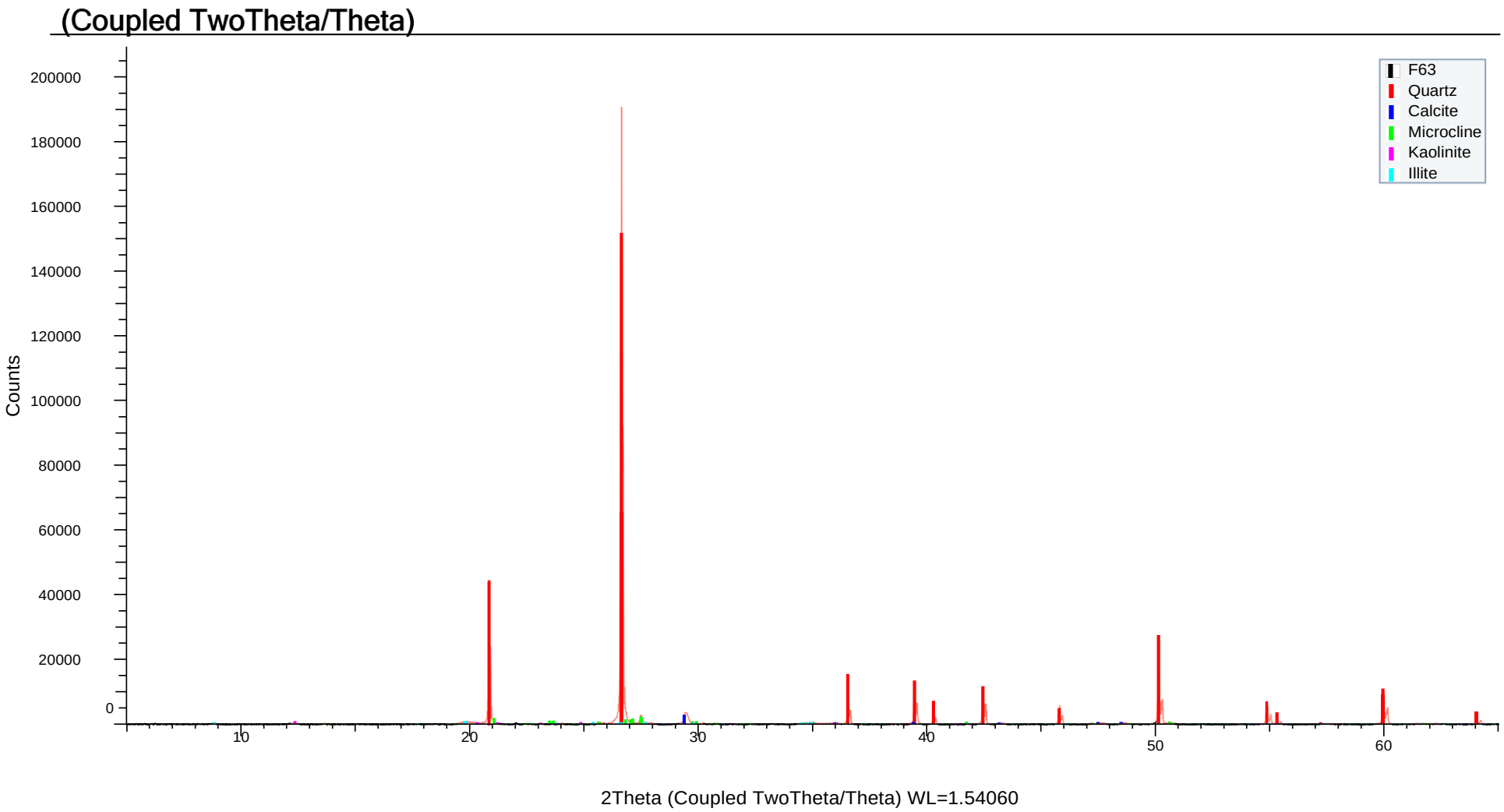
(Coupled TwoTheta/Theta)
F63
Quartz
Calcite
Microcline
Kaolinite
Illite
Counts
200000
180000
160000
140000
120000
100000
80000
60000
40000
20000
0
10
20
30
40
50
60
2Theta (Coupled TwoTheta/Theta) WL=1.54060

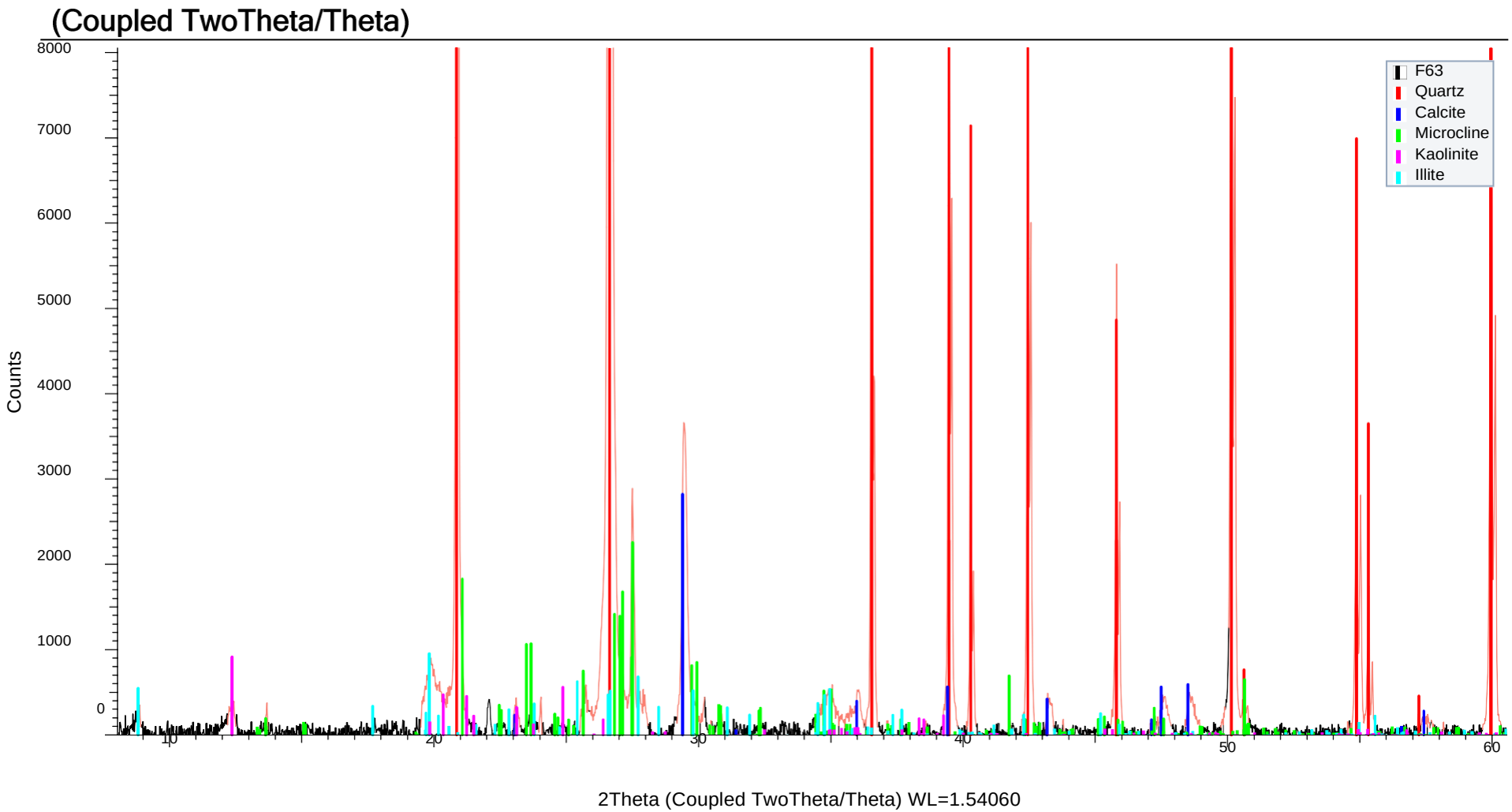
(Coupled TwoTheta/Theta)
Counts
8000
7000
6000
5000
4000
3000
2000
1000
0
10
20
30
40
50
60
F63
Quartz
Calcite
Microcline
Kaolinite
Illite
2Theta (Coupled TwoTheta/Theta) WL=1.54060

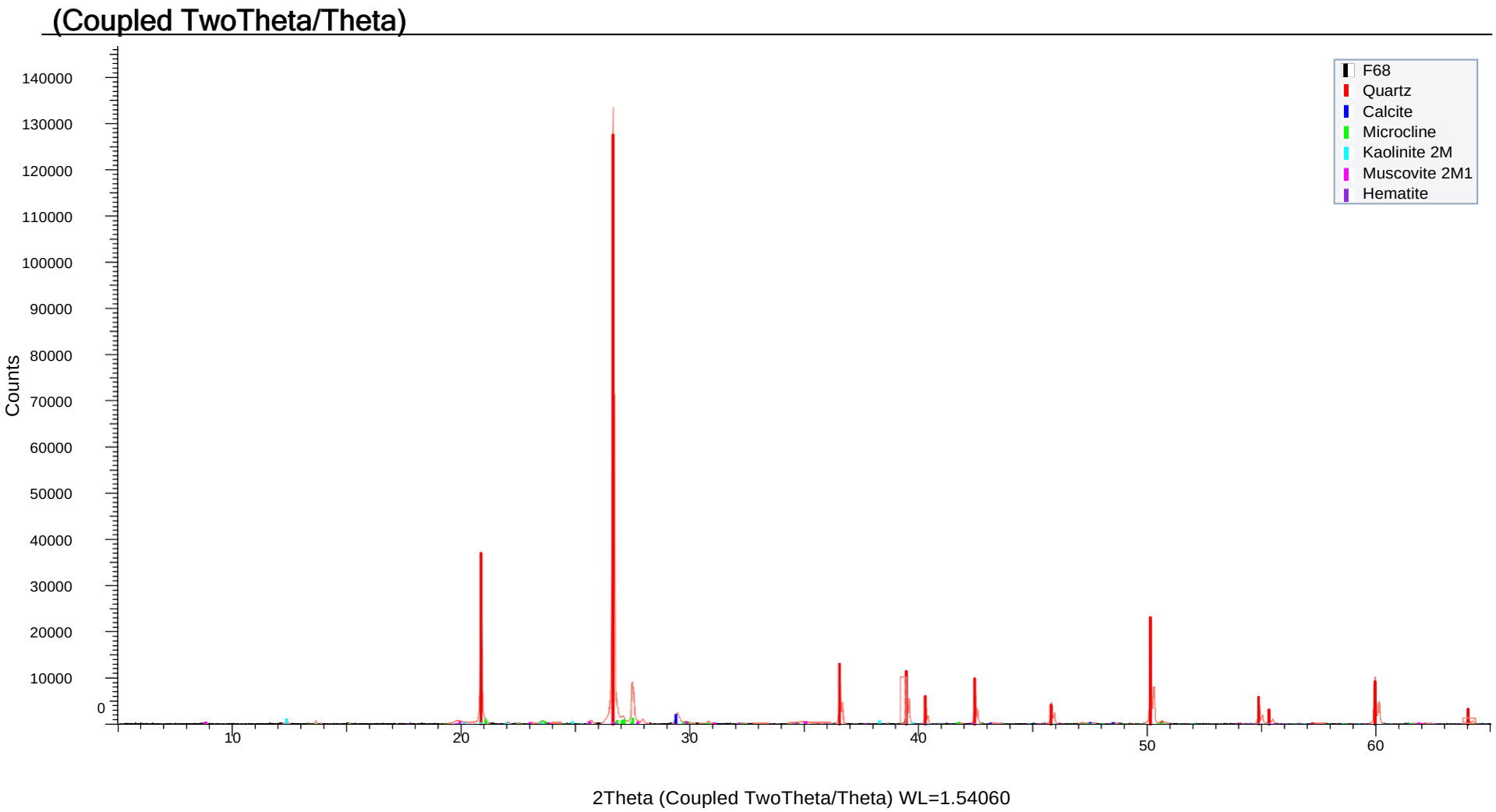
(Coupled TwoTheta/Theta)
F68
Quartz
Calcite
Microcline
Kaolinite 2M
Muscovite 2M1
Hematite
Counts
140000
130000
120000
110000
100000
90000
80000
70000
60000
50000
40000
30000
20000
10000
0
10
20
30
40
50
60
2Theta (Coupled TwoTheta/Theta) WL=1.54060

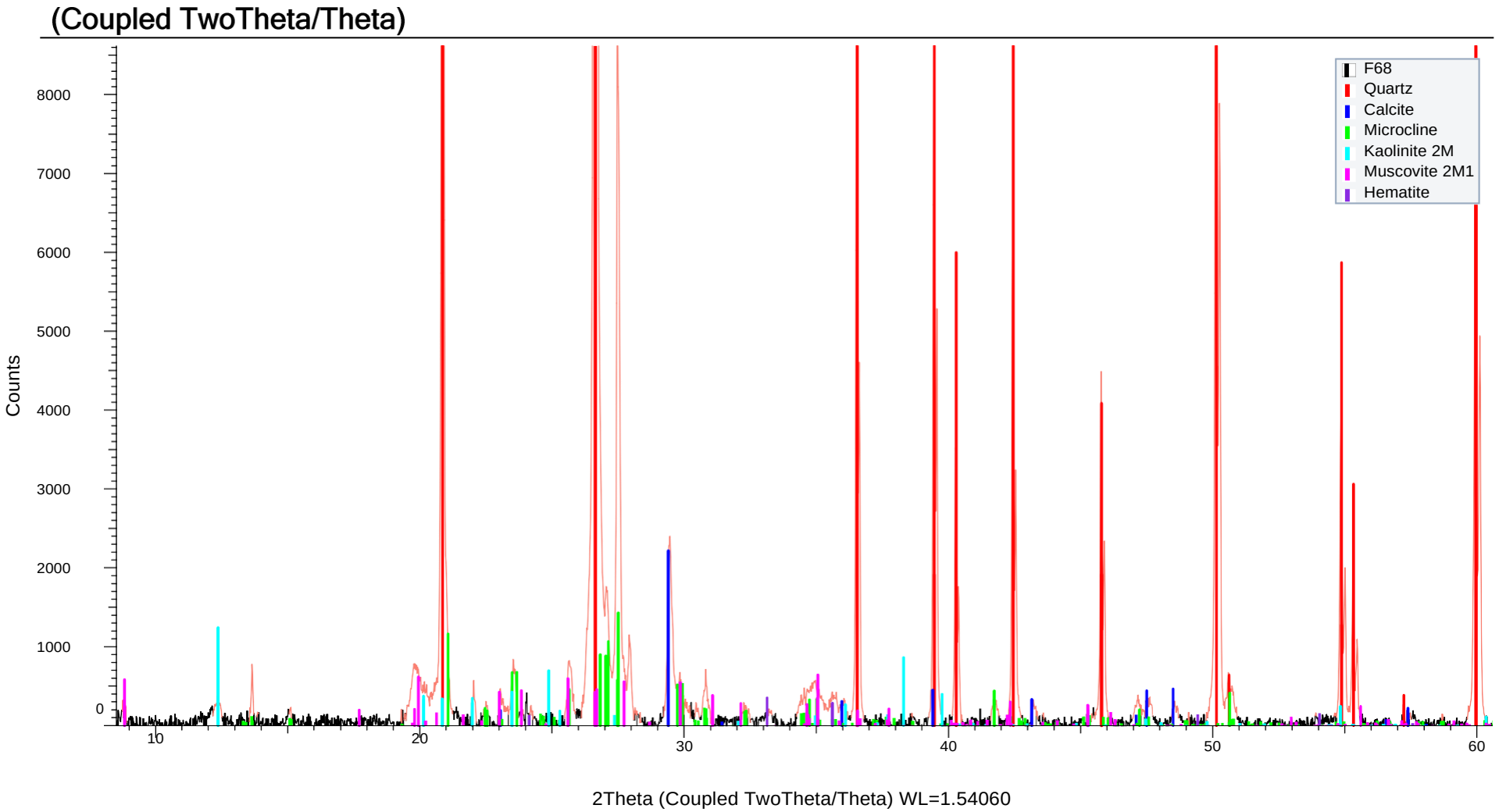
(Coupled TwoTheta/Theta)
F68
Quartz
Calcite
Microcline
Kaolinite 2M
Muscovite 2M1
Hematite
Counts
8000
7000
6000
5000
4000
3000
2000
1000
0
10
20
30
40
50
60
2Theta (Coupled TwoTheta/Theta) WL=1.54060

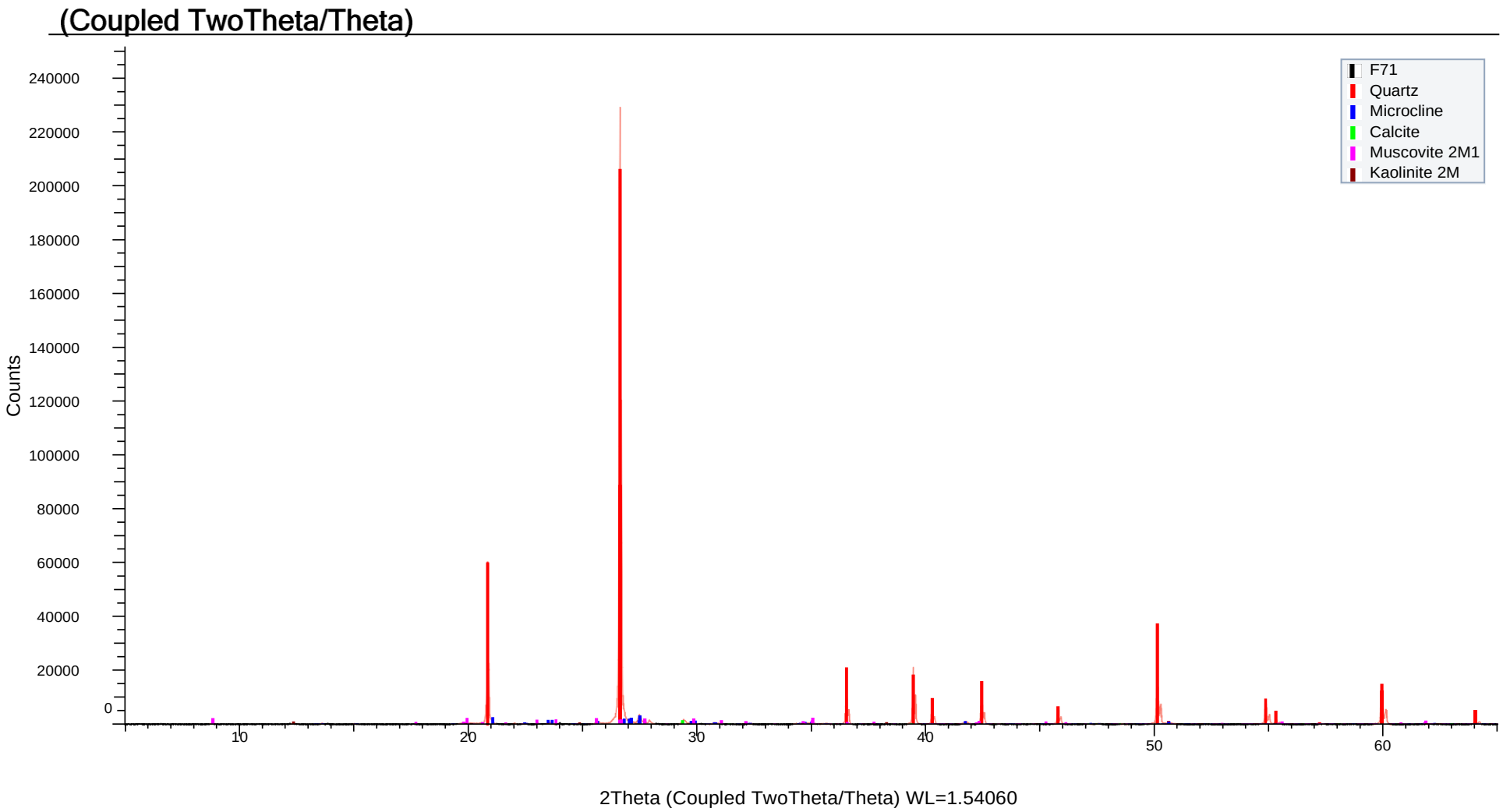
(Coupled TwoTheta/Theta)
F71
Quartz
Microcline
Calcite
Muscovite 2M1
Kaolinite 2M
Counts
240000
220000
200000
180000
160000
140000
120000
100000
80000
60000
40000
20000
0
10
20
30
40
50
60
2Theta (Coupled TwoTheta/Theta) WL=1.54060

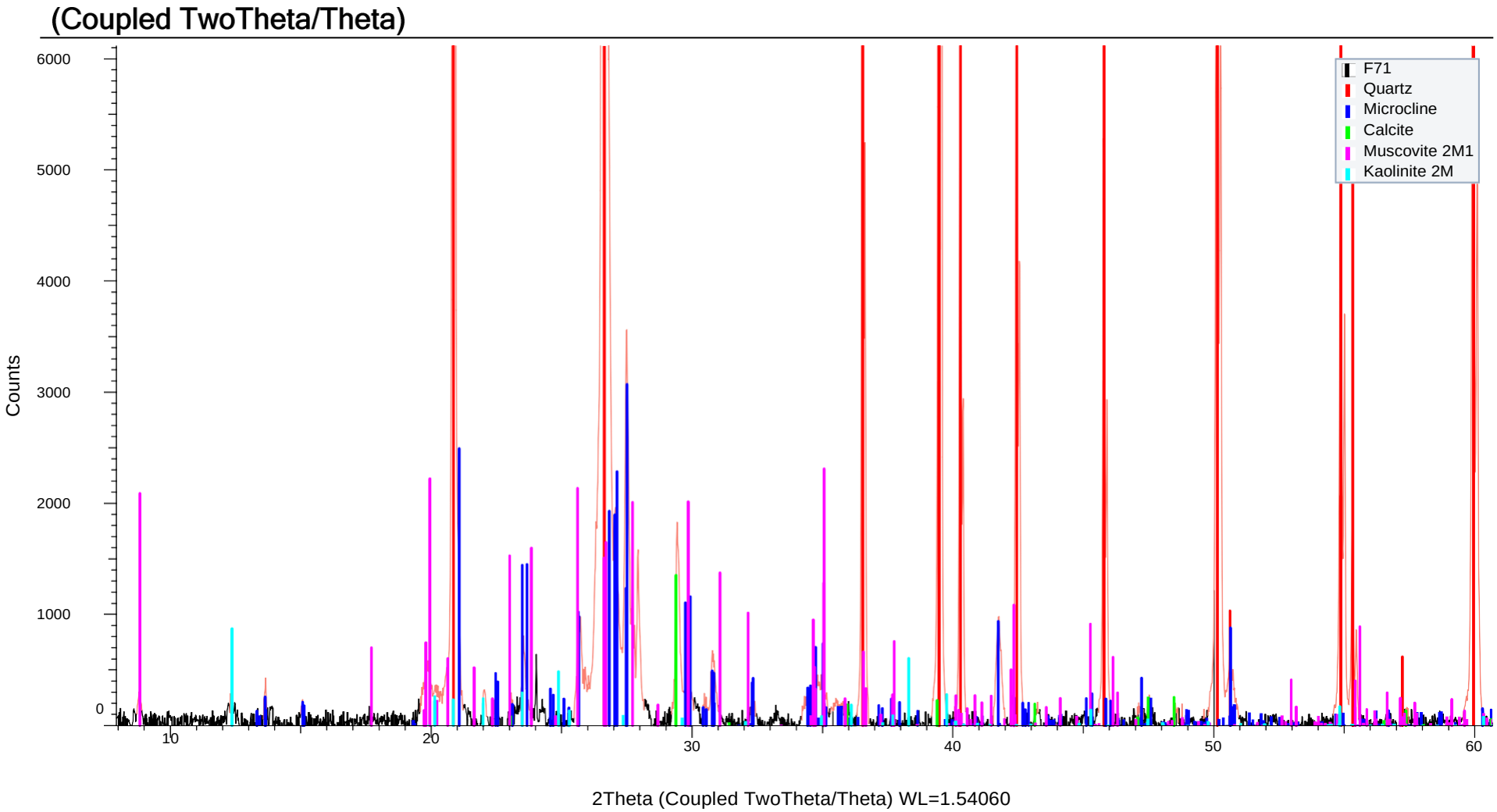
(Coupled TwoTheta/Theta)
Counts
6000
5000
4000
3000
2000
1000
0
10
20
30
40
50
60
F71
Quartz
Microcline
Calcite
Muscovite 2M1
Kaolinite 2M
2Theta (Coupled TwoTheta/Theta) WL=1.54060

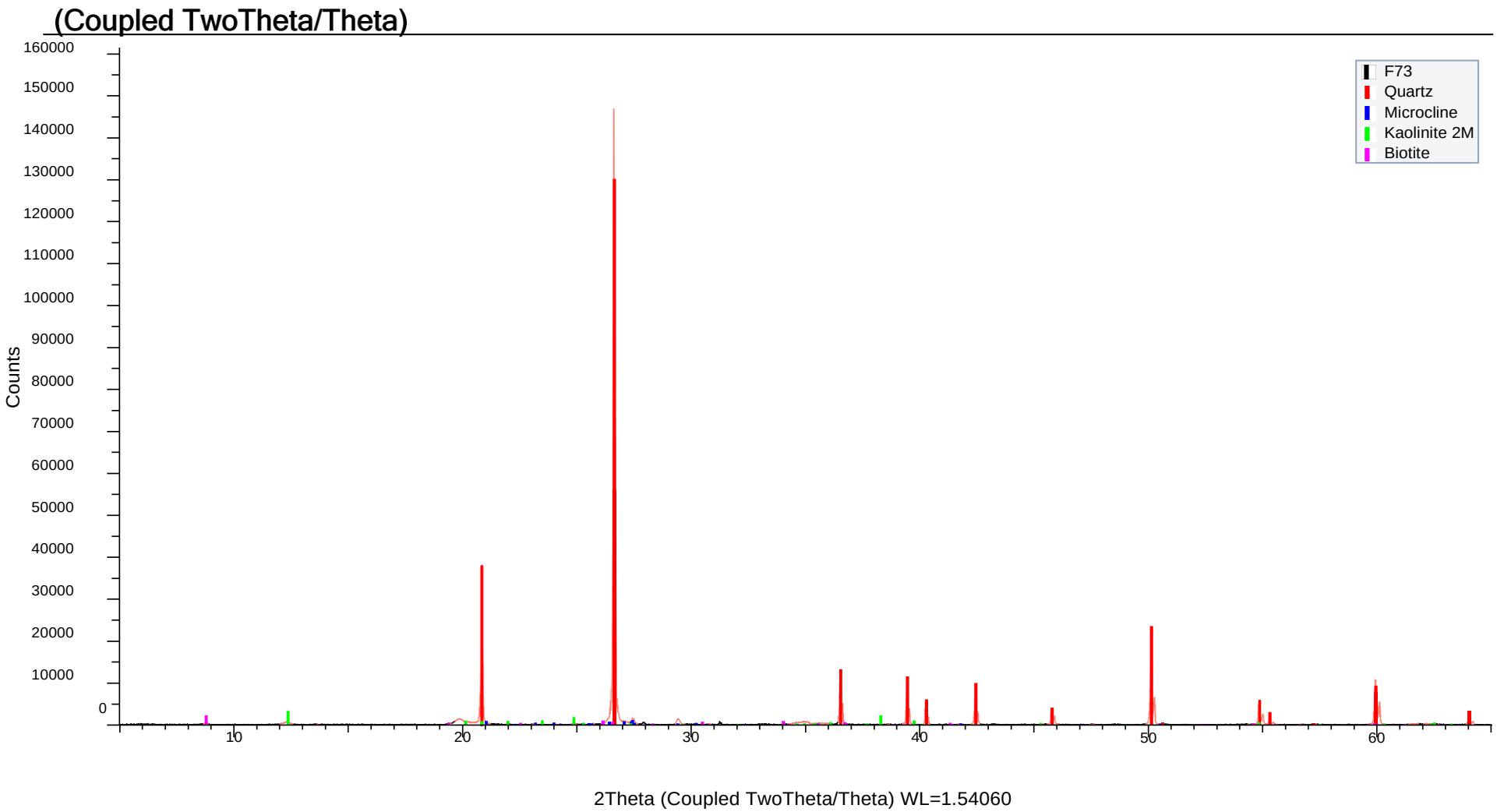
(Coupled TwoTheta/Theta)
160000
150000
140000
130000
120000
110000
100000
90000
80000
70000
60000
50000
40000
30000
20000
10000
0
Counts
10
20
30
40
50
60
2Theta (Coupled TwoTheta/Theta) WL=1.54060
F73
Quartz
Microcline
Kaolinite 2M
Biotite

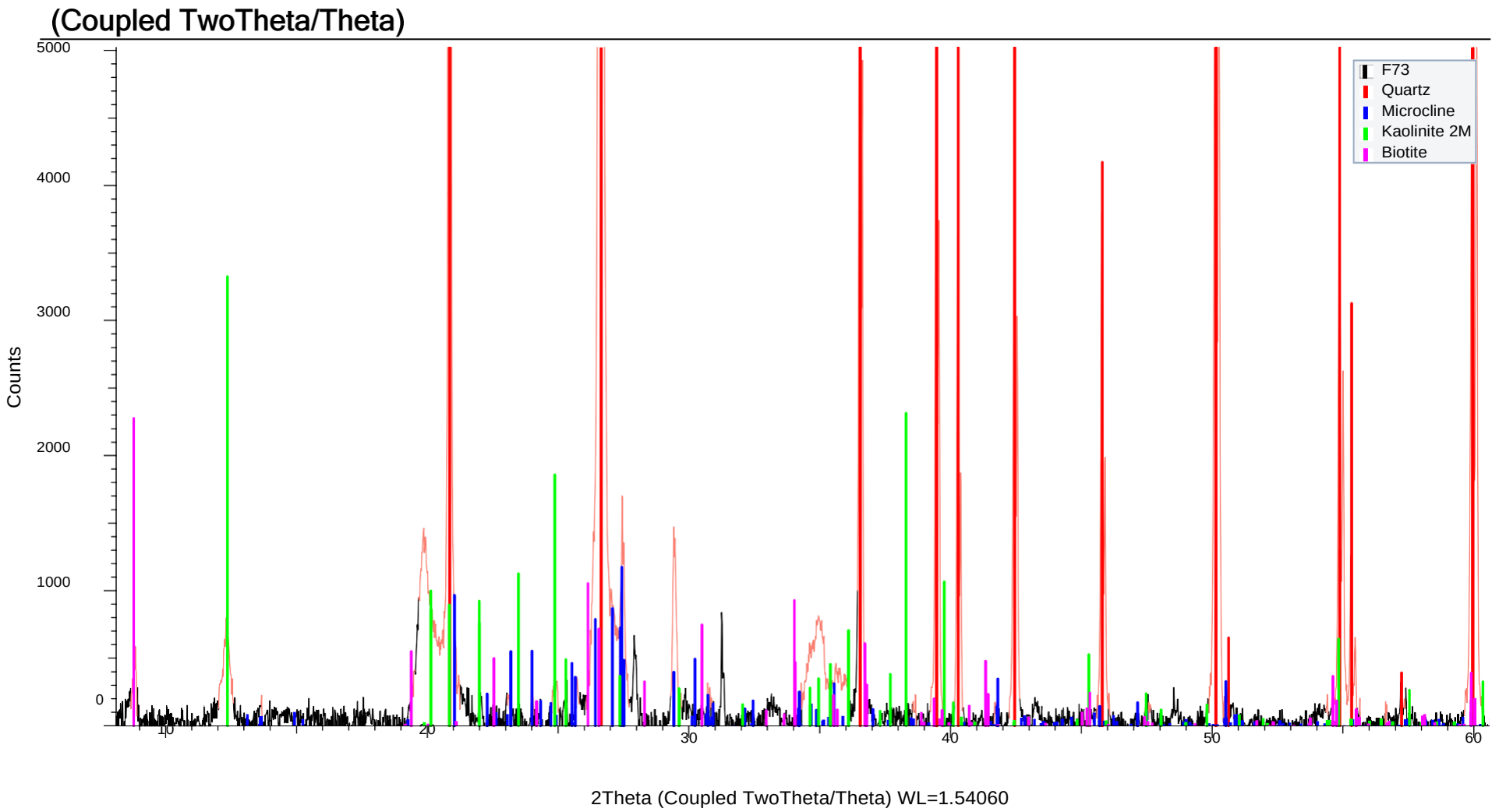
(Coupled TwoTheta/Theta)
Counts
5000
4000
3000
2000
1000
0
10
20
30
40
50
60
F73
Quartz
Microcline
Kaolinite 2M
Biotite
2Theta (Coupled TwoTheta/Theta) WL=1.54060

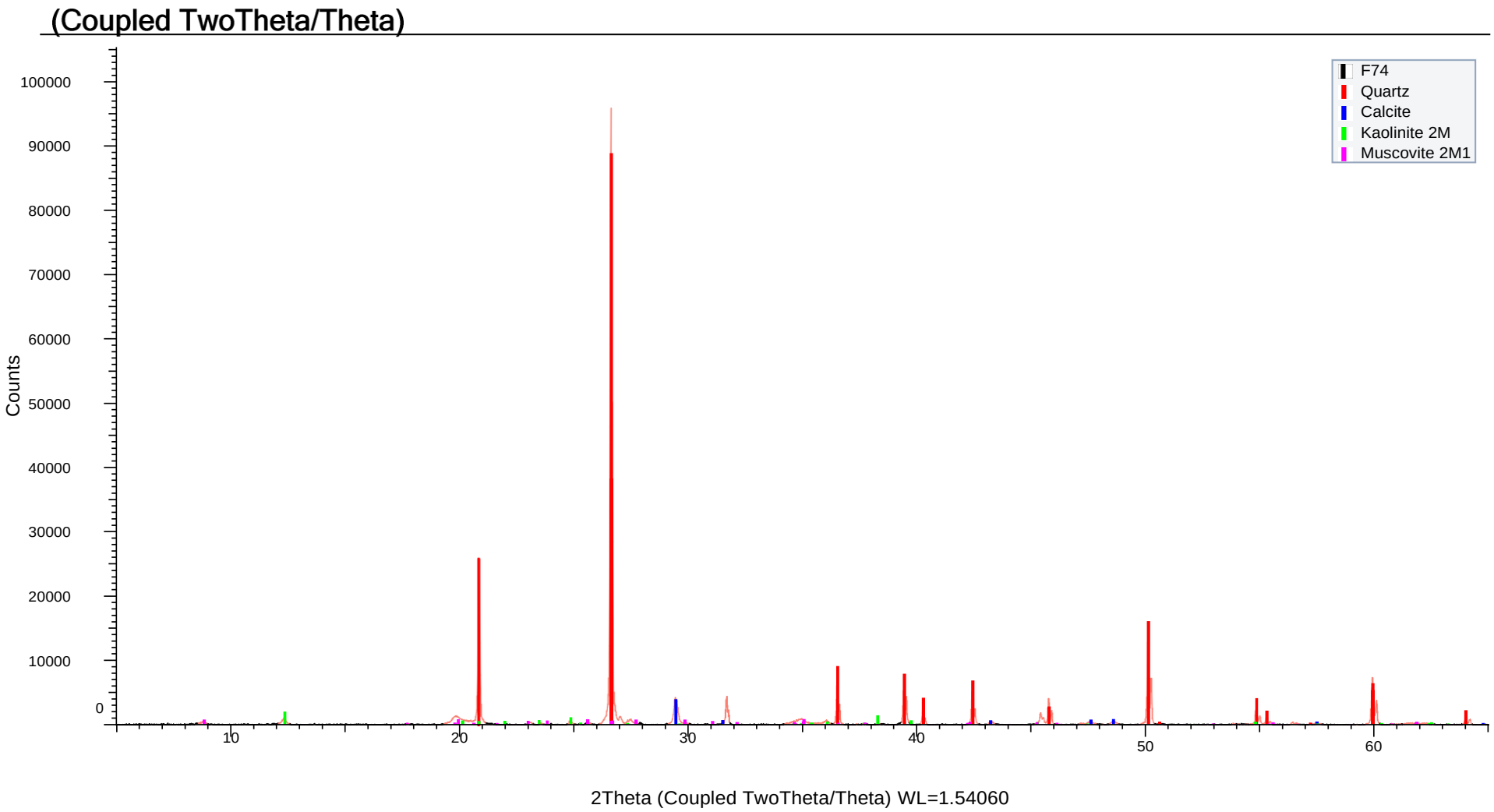
(Coupled TwoTheta/Theta)
F74
Quartz
Calcite
Kaolinite 2M
Muscovite 2M1
Counts
100000
90000
80000
70000
60000
50000
40000
30000
20000
10000
0
10
20
30
40
50
60
2Theta (Coupled TwoTheta/Theta) WL=1.54060

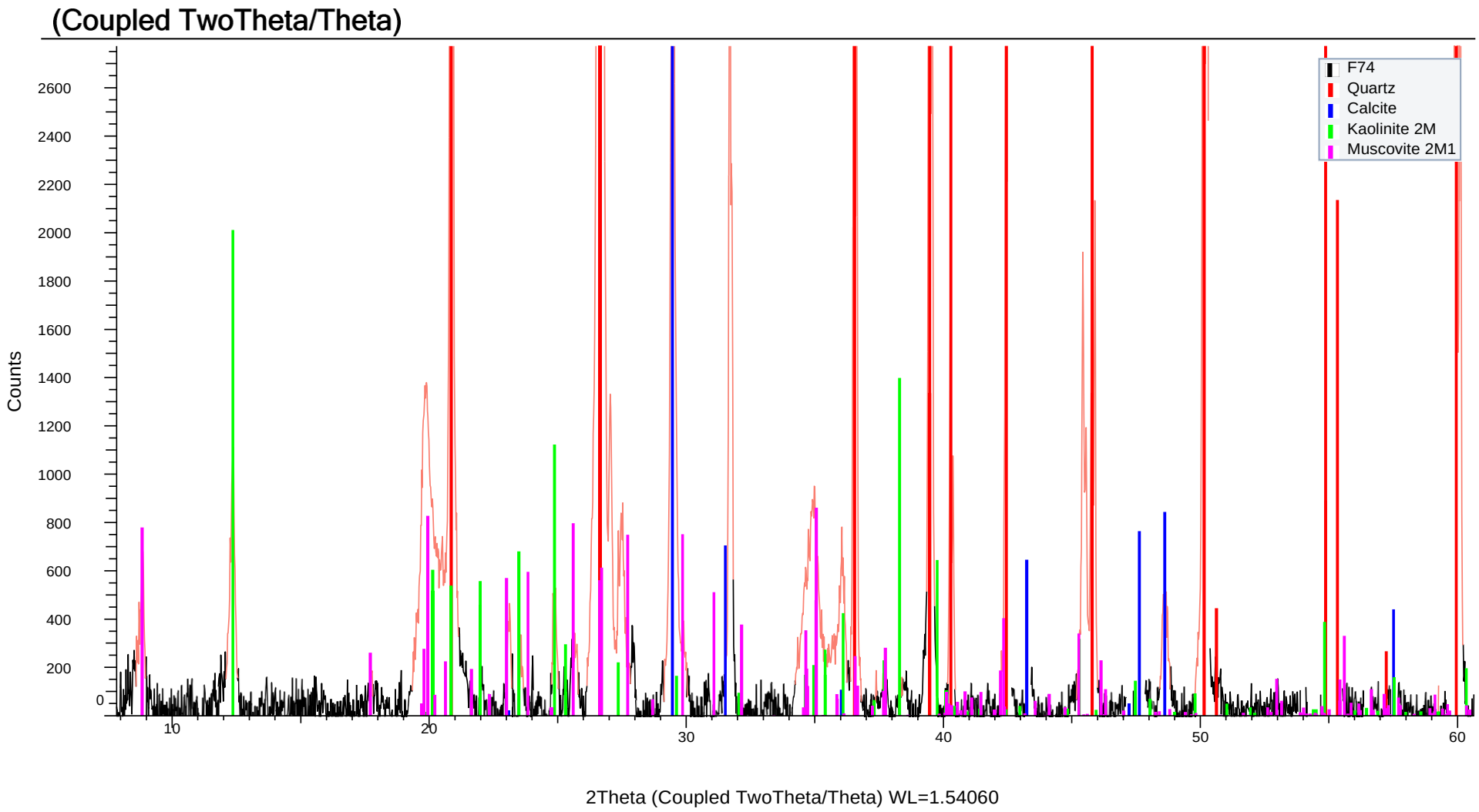
(Coupled TwoTheta/Theta)
F74
Quartz
Calcite
Kaolinite 2M
Muscovite 2M1
Counts
0
200
400
600
800
1000
1200
1400
1600
1800
2000
2200
2400
2600
10
20
30
40
50
60
2Theta (Coupled TwoTheta/Theta) WL=1.54060

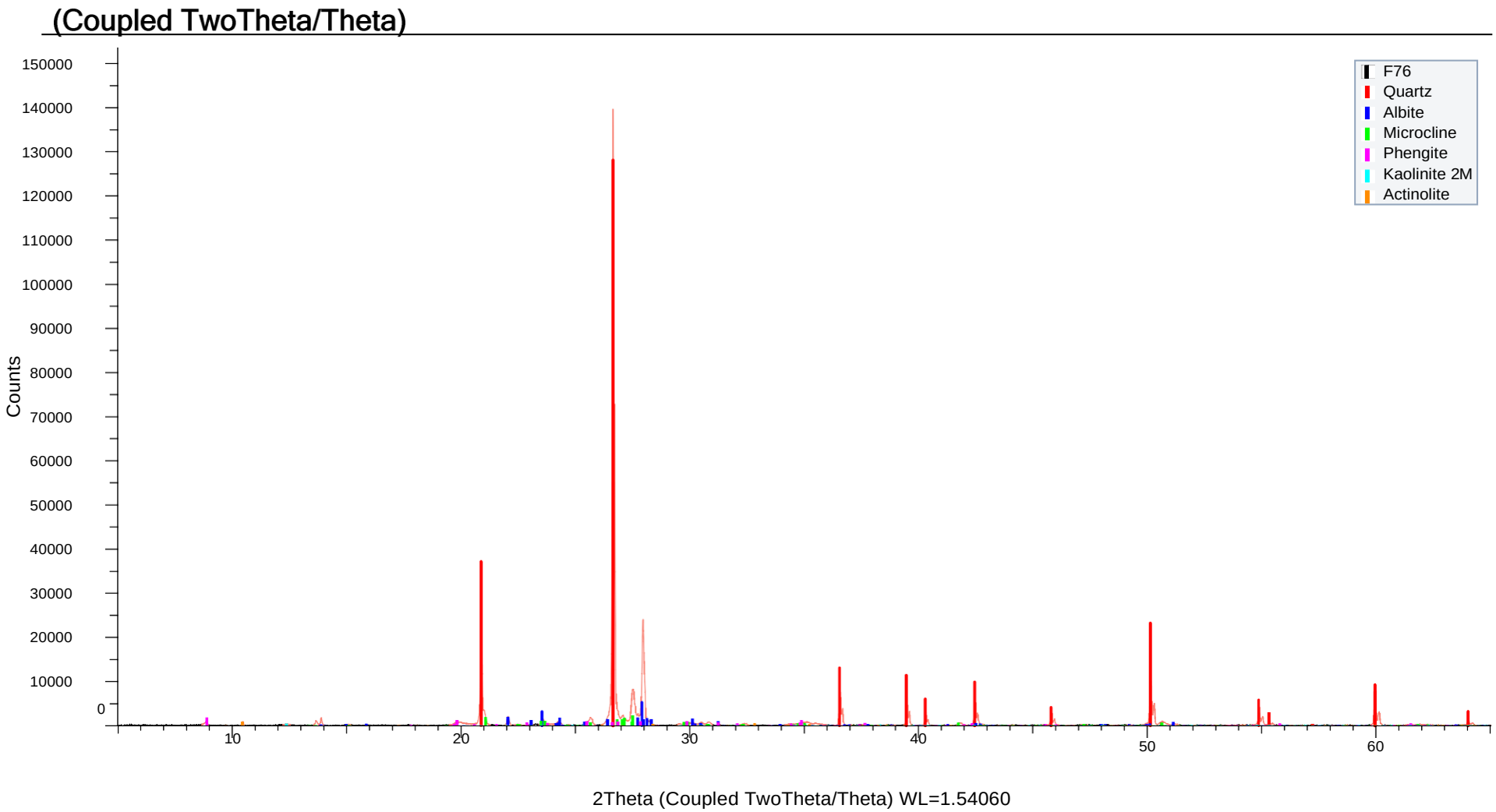
(Coupled TwoTheta/Theta)
Counts
150000
140000
130000
120000
110000
100000
90000
80000
70000
60000
50000
40000
30000
20000
10000
0
10
20
30
40
50
60
F76
Quartz
Albite
Microcline
Phengite
Kaolinite 2M
Actinolite
2Theta (Coupled TwoTheta/Theta) WL=1.54060

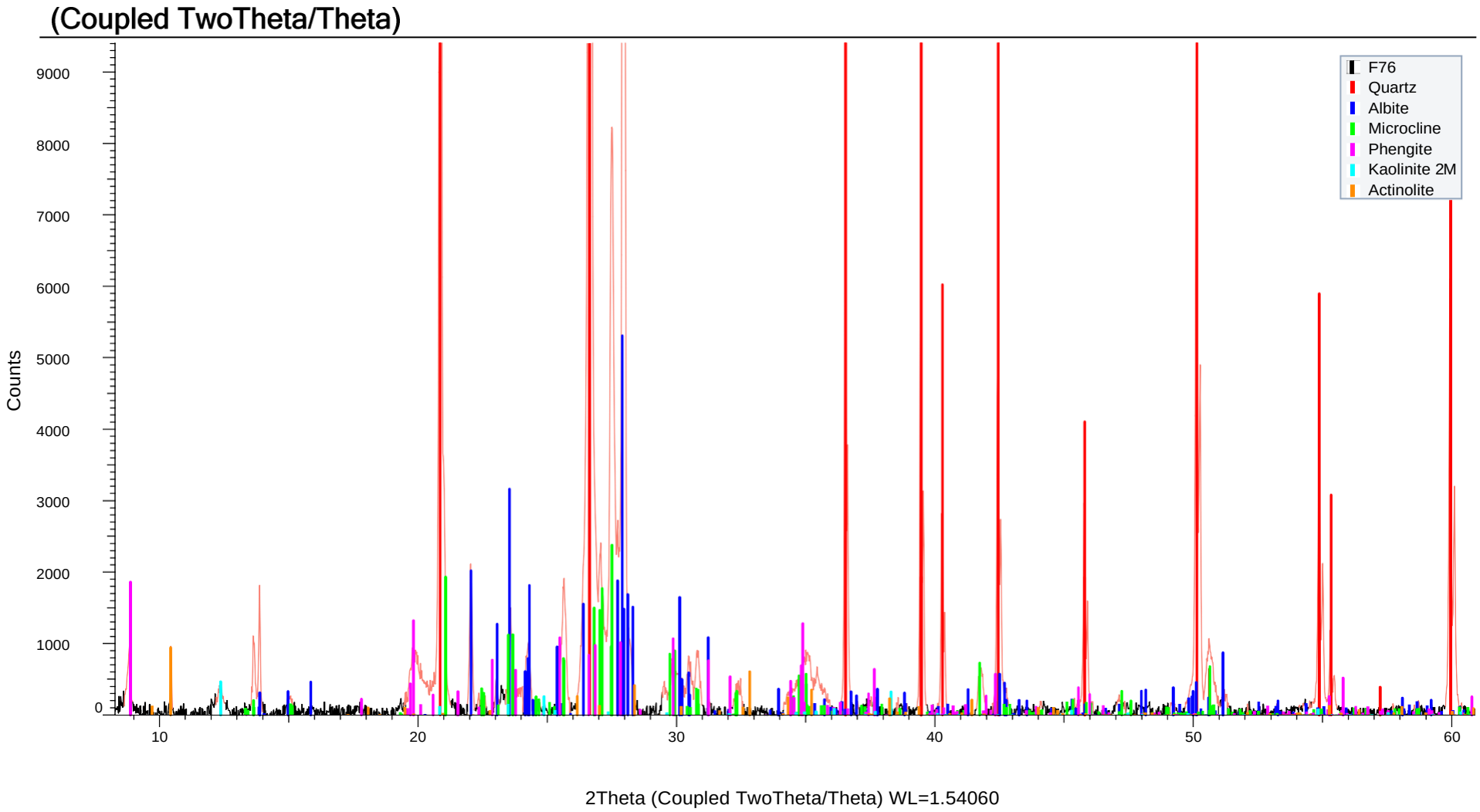
(Coupled TwoTheta/Theta)
F76
Quartz
Albite
Microcline
Phengite
Kaolinite 2M
Actinolite
Counts
9000
8000
7000
6000
5000
4000
3000
2000
1000
0
10
20
30
40
50
60
2Theta (Coupled TwoTheta/Theta) WL=1.54060

(Coupled TwoTheta/Theta)

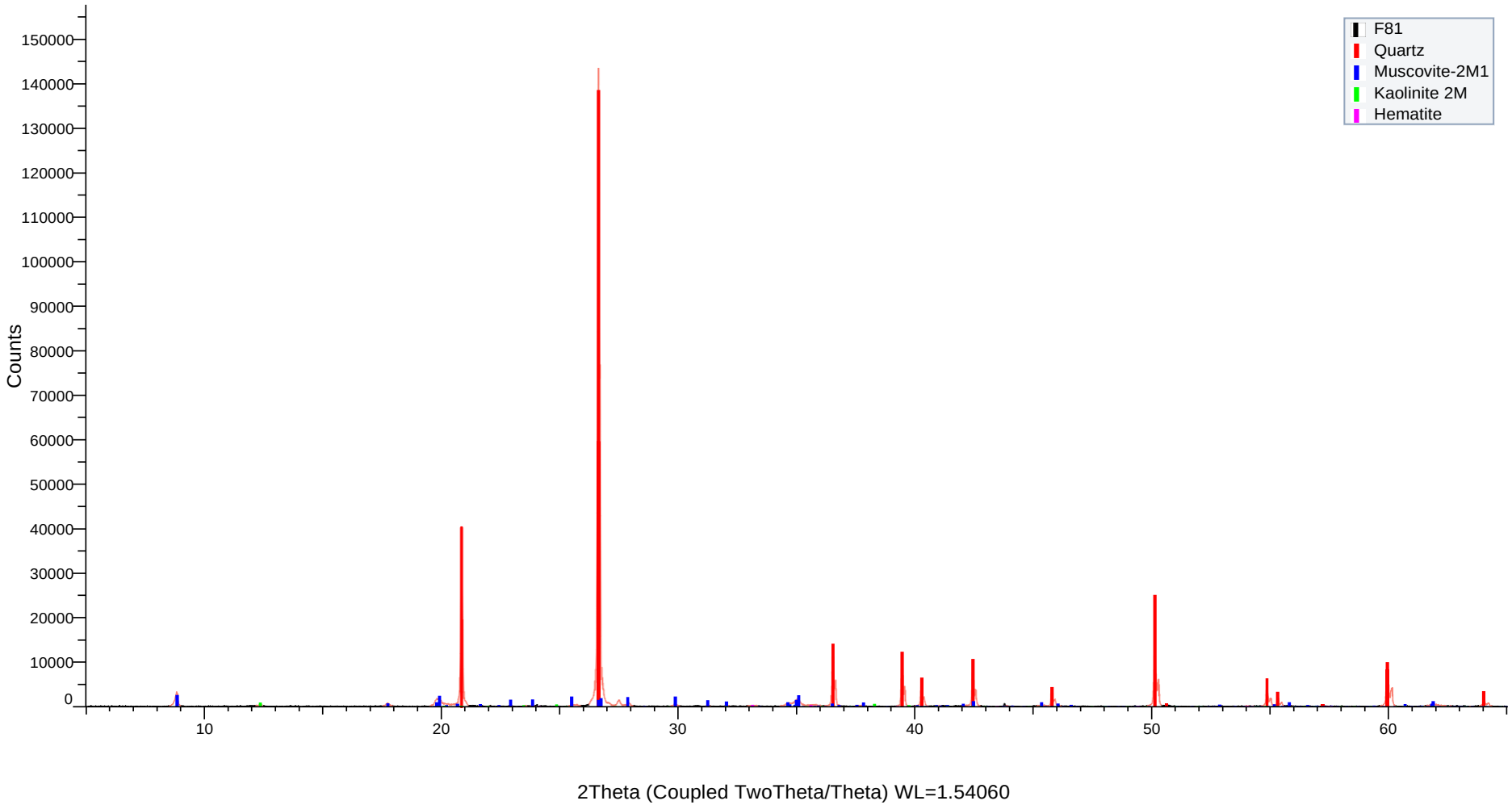

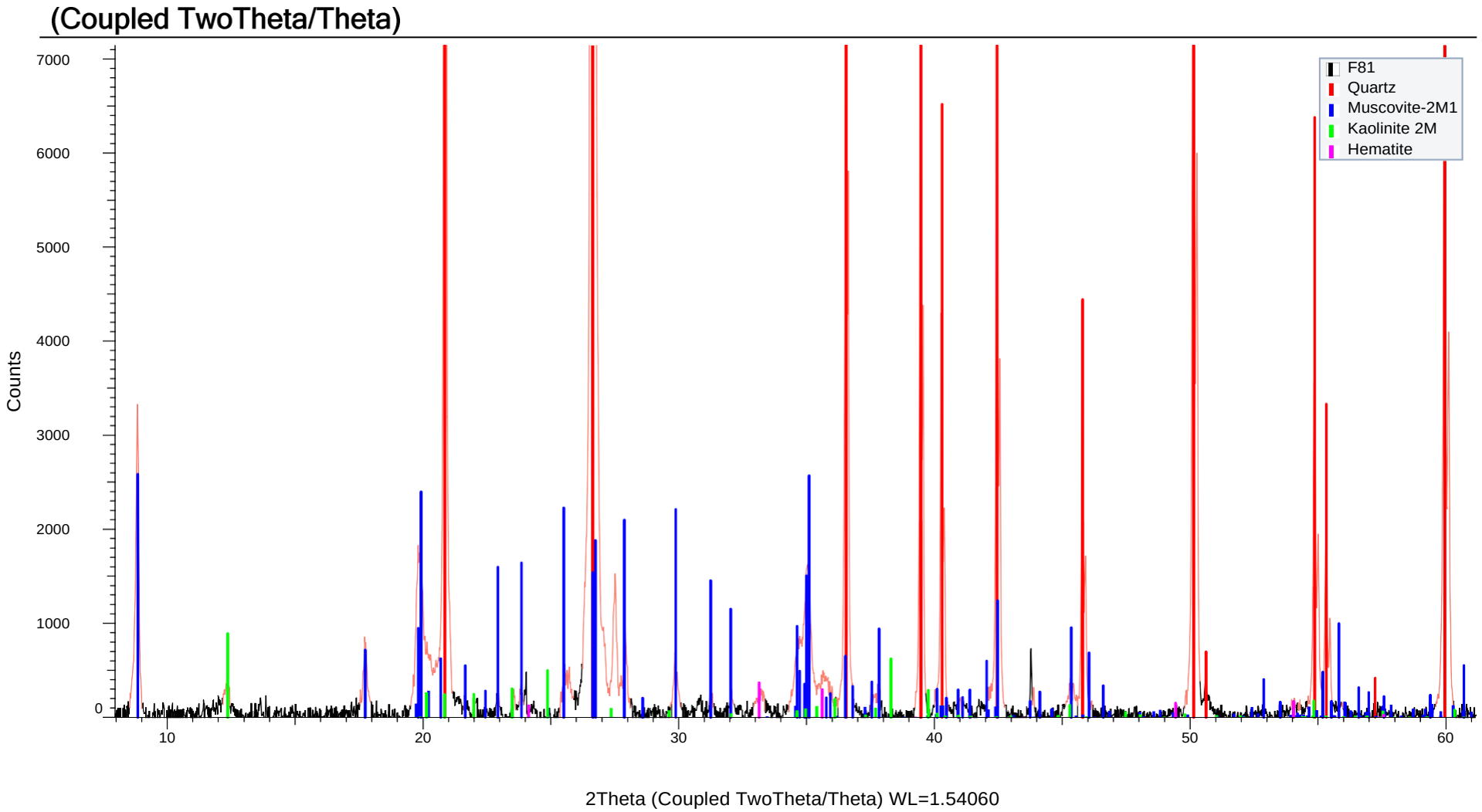
(Coupled TwoTheta/Theta)
Counts
7000
6000
5000
4000
3000
2000
1000
0
10
20
30
40
50
60
F81
Quartz
Muscovite-2M1
Kaolinite 2M
Hematite
2Theta (Coupled TwoTheta/Theta) WL=1.54060

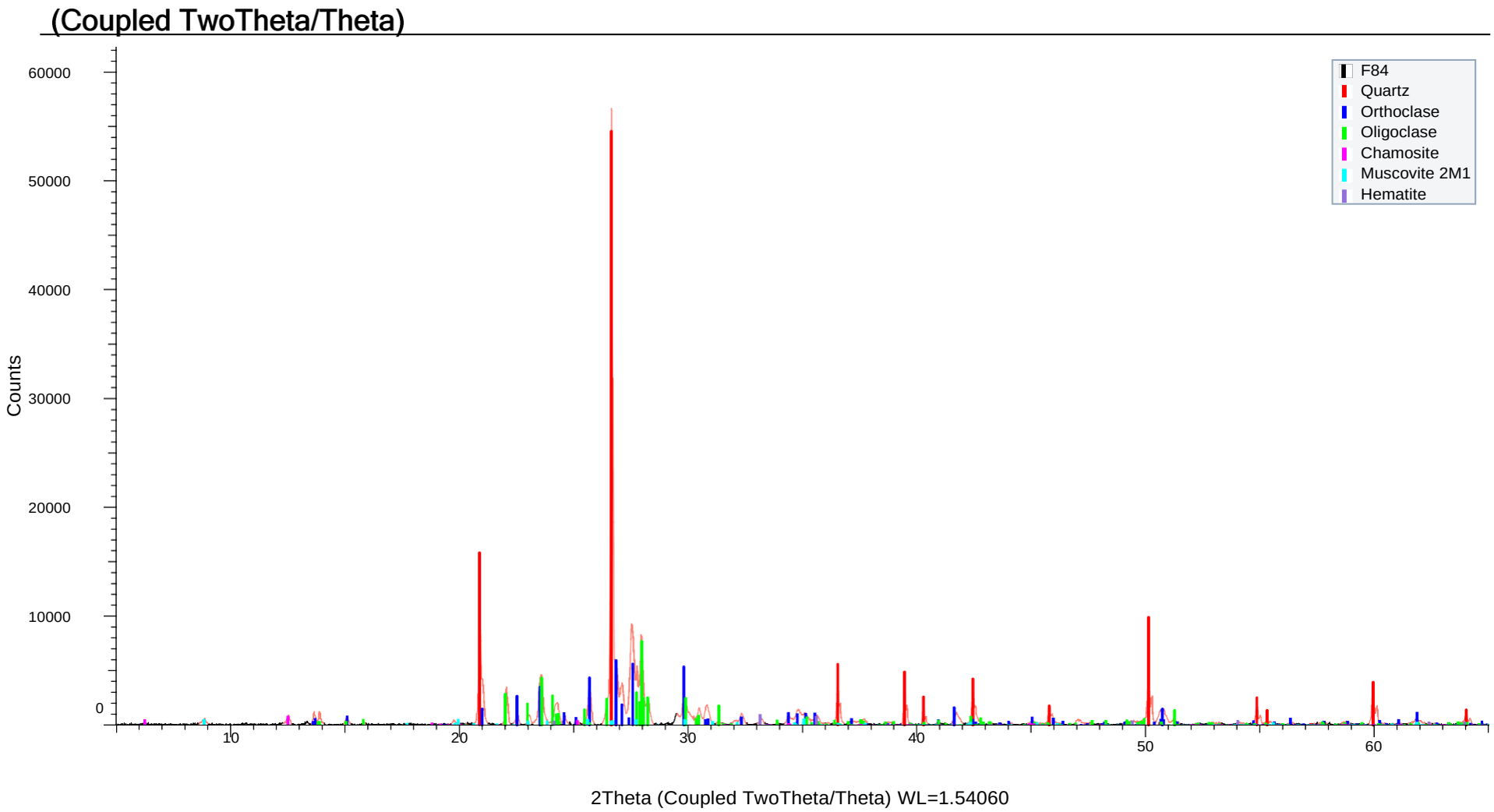
(Coupled TwoTheta/Theta)
F84
Quartz
Orthoclase
Oligoclase
Chamosite
Muscovite 2M1
Hematite
Counts
60000
50000
40000
30000
20000
10000
0
10
20
30
40
50
60
2Theta (Coupled TwoTheta/Theta) WL=1.54060

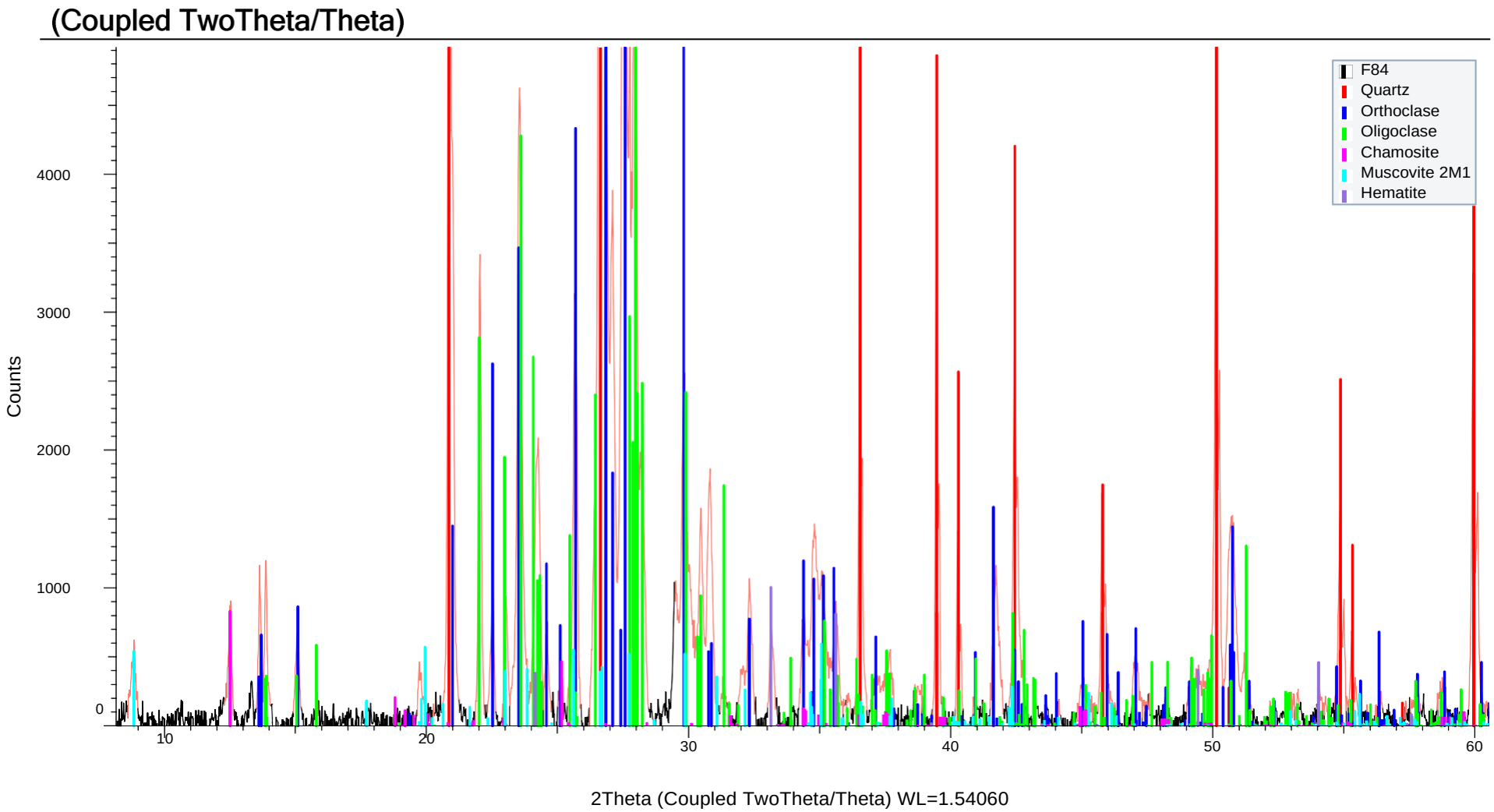
(Coupled TwoTheta/Theta)
F84
Quartz
Orthoclase
Oligoclase
Chamosite
Muscovite 2M1
Hematite
Counts
0
1000
2000
3000
4000
10
20
30
40
50
60
2Theta (Coupled TwoTheta/Theta) WL=1.54060

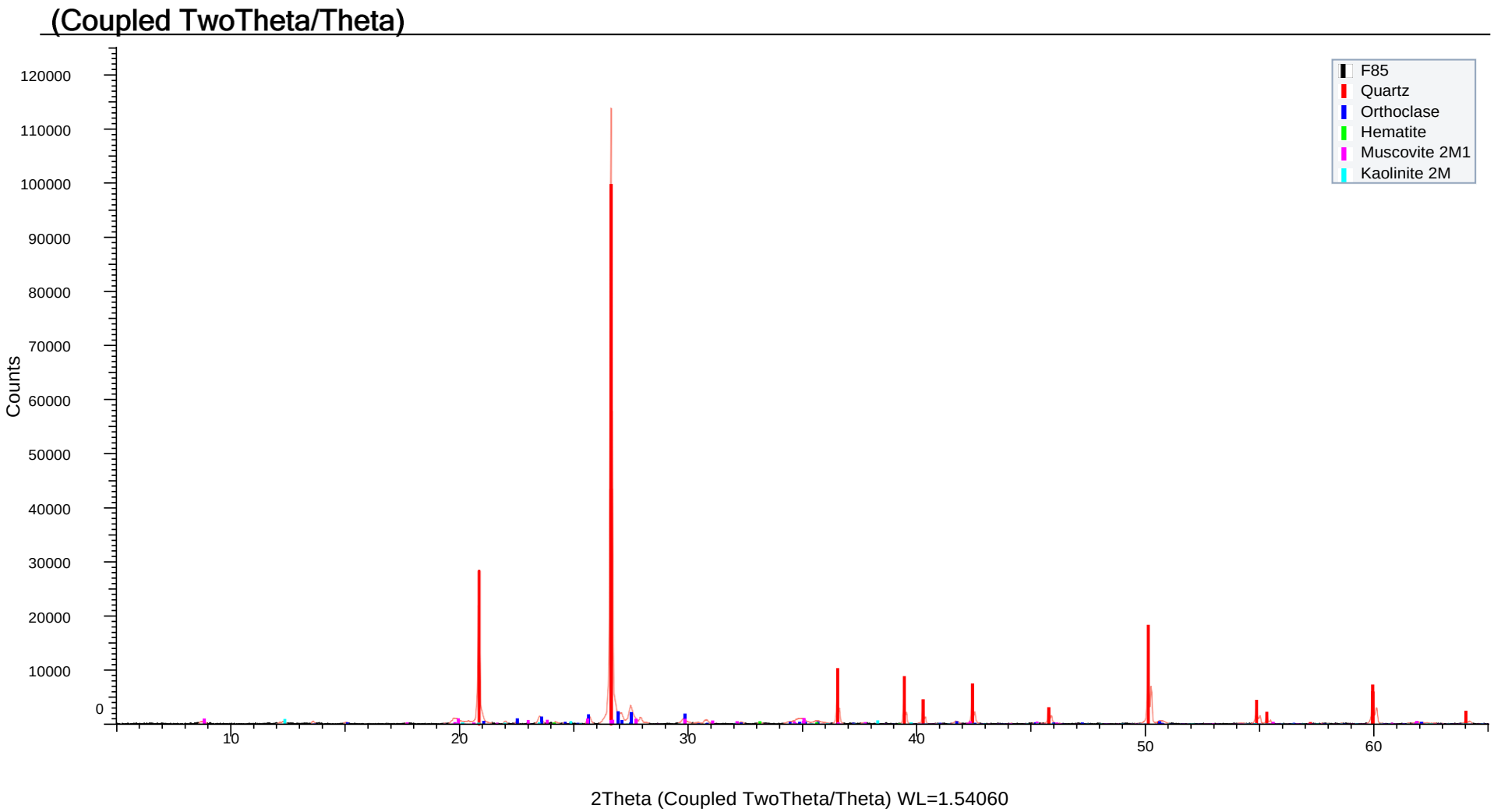
(Coupled TwoTheta/Theta)
F85
Quartz
Orthoclase
Hematite
Muscovite 2M1
Kaolinite 2M
Counts
120000
110000
100000
90000
80000
70000
60000
50000
40000
30000
20000
10000
0
10
20
30
40
50
60
2Theta (Coupled TwoTheta/Theta) WL=1.54060

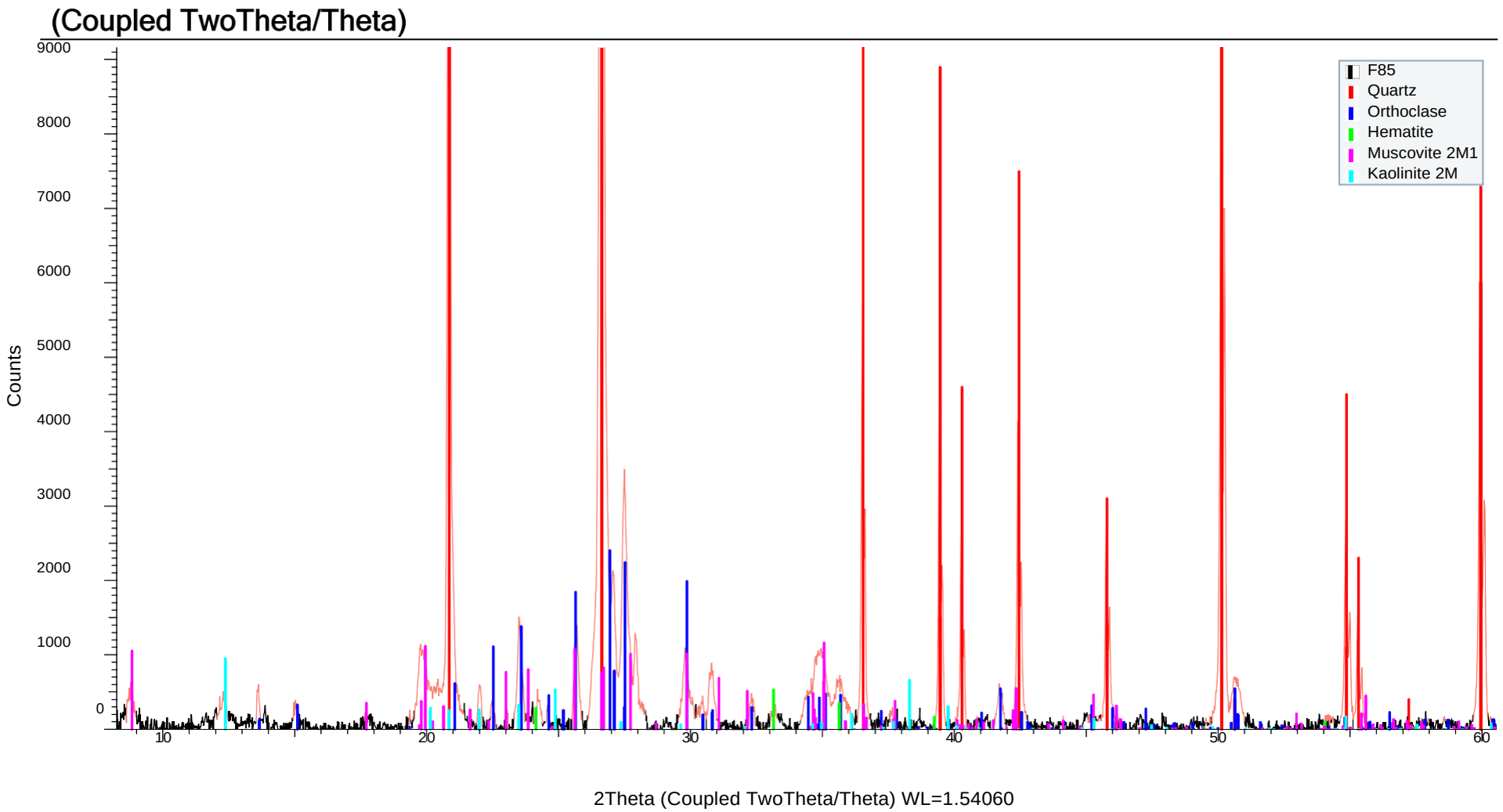
(Coupled TwoTheta/Theta)
Counts
9000
8000
7000
6000
5000
4000
3000
2000
1000
0
10
20
30
40
50
60
F85
Quartz
Orthoclase
Hematite
Muscovite 2M1
Kaolinite 2M
2Theta (Coupled TwoTheta/Theta) WL=1.54060

(Coupled TwoTheta/Theta)

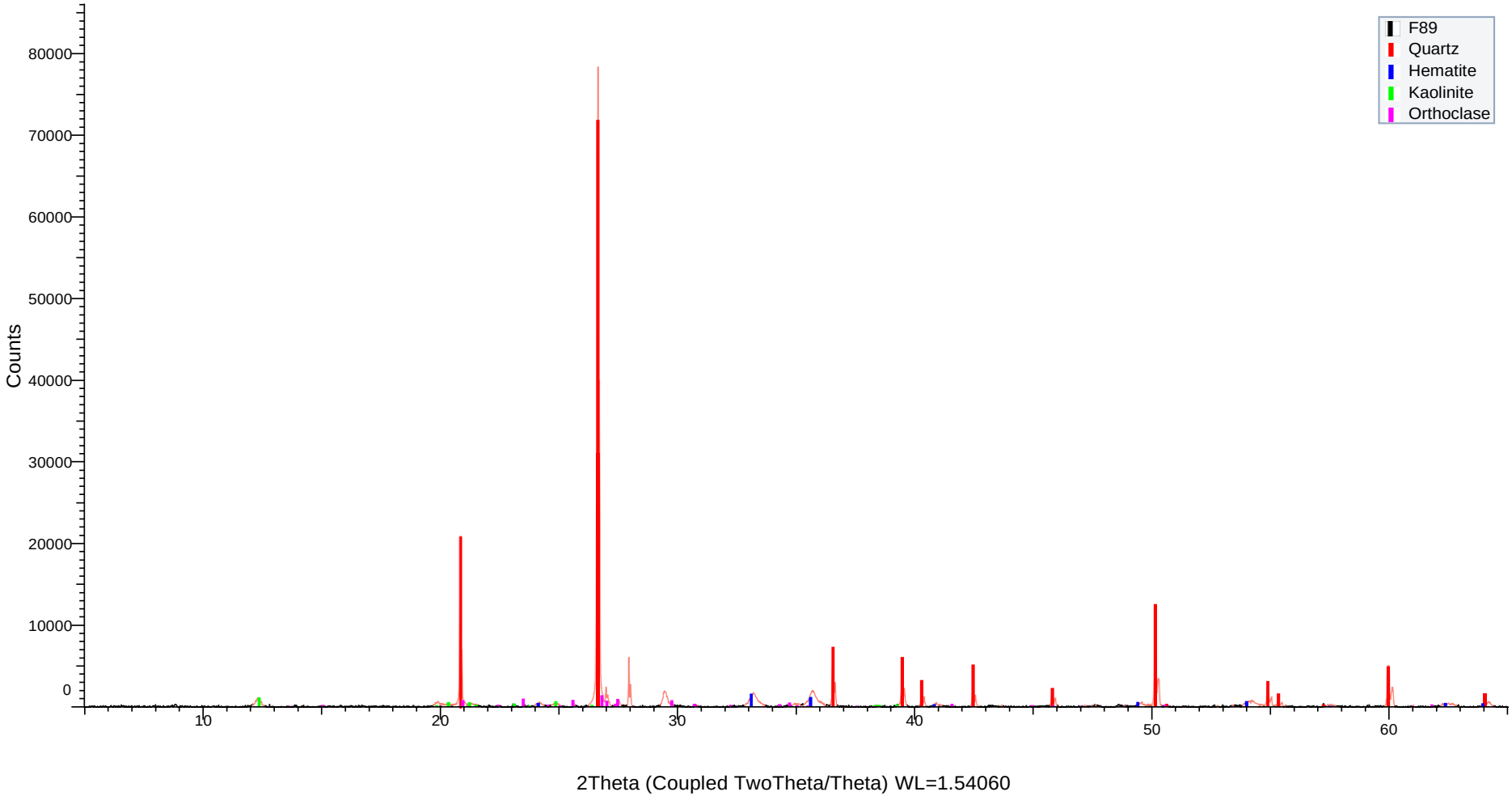

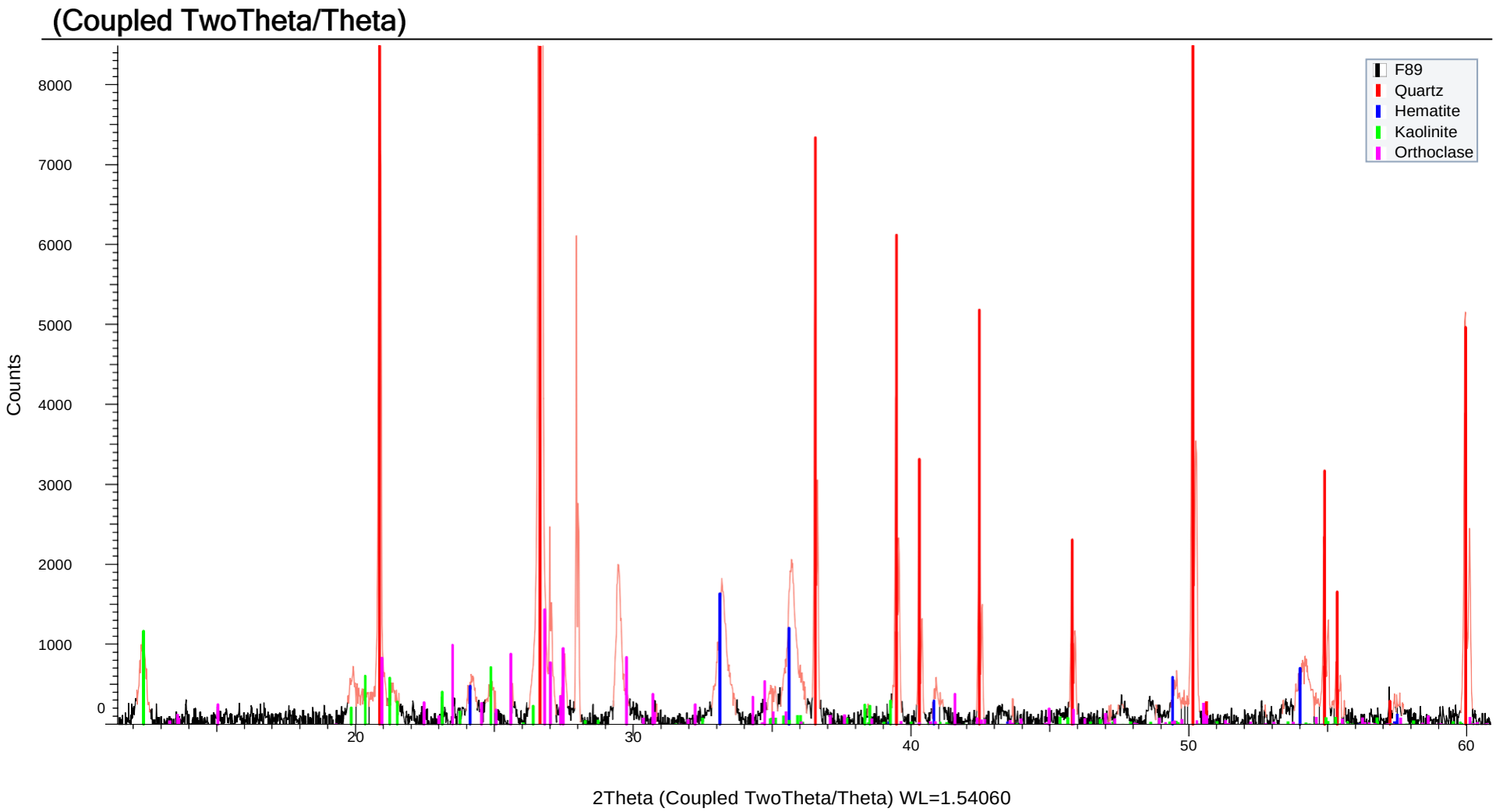
(Coupled TwoTheta/Theta)
F89
Quartz
Hematite
Kaolinite
Orthoclase
Counts
8000
7000
6000
5000
4000
3000
2000
1000
0
20
30
40
50
60
2Theta (Coupled TwoTheta/Theta) WL=1.54060

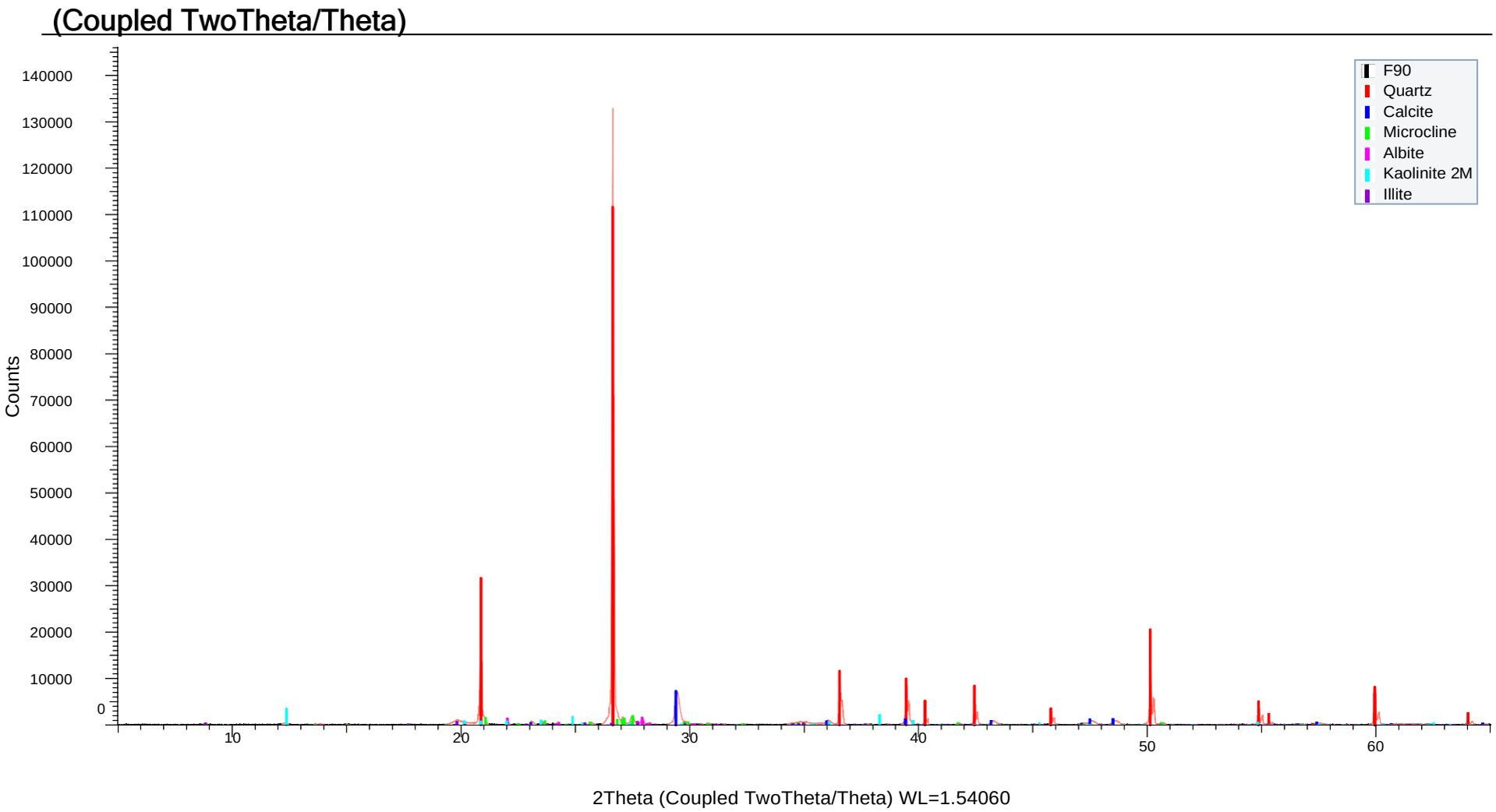
(Coupled TwoTheta/Theta)
F90
Quartz
Calcite
Microcline
Albite
Kaolinite 2M
Illite
Counts
140000
130000
120000
110000
100000
90000
80000
70000
60000
50000
40000
30000
20000
10000
0
10
20
30
40
50
60
2Theta (Coupled TwoTheta/Theta) WL=1.54060

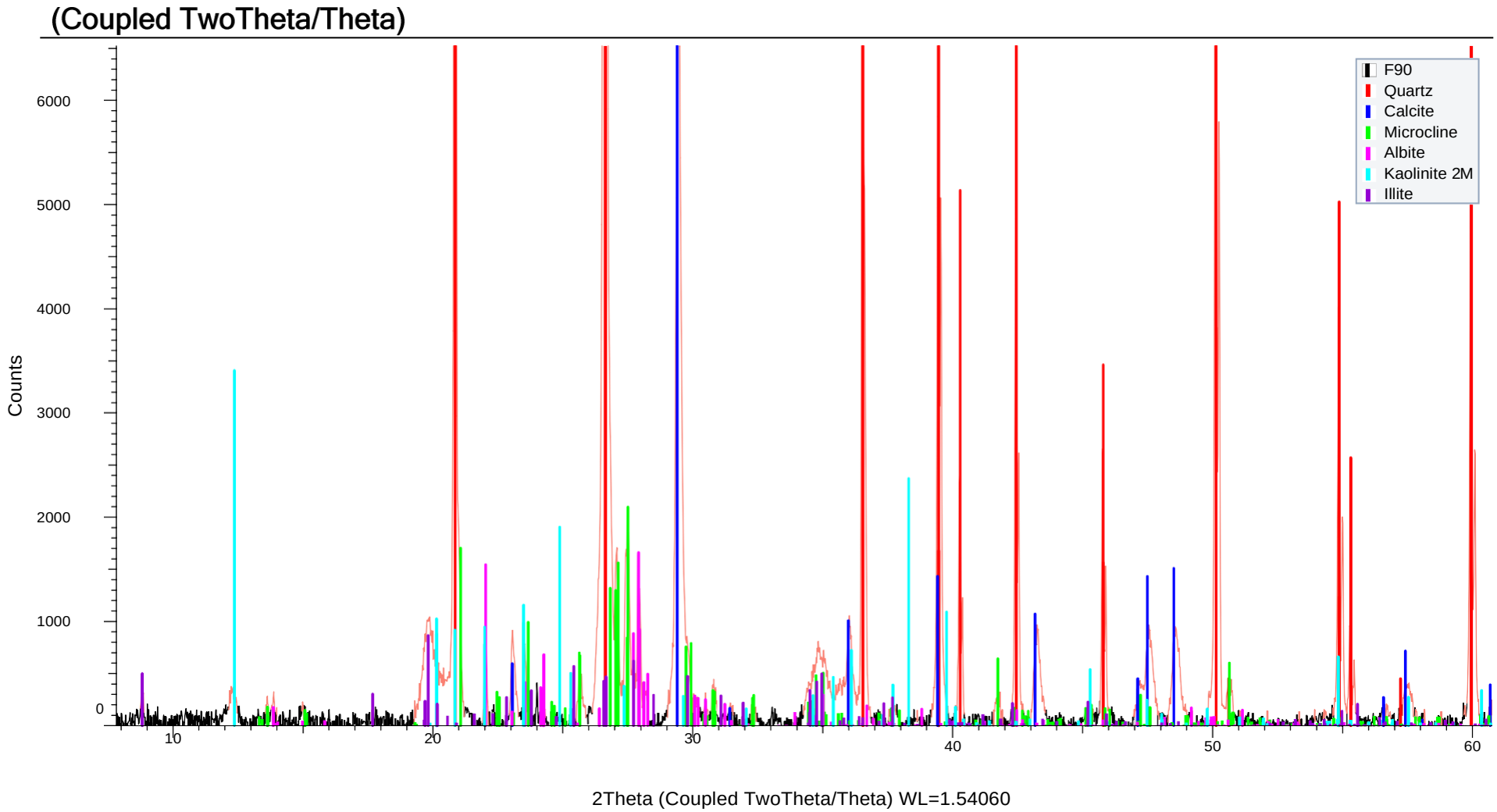
(Coupled TwoTheta/Theta)
F90
Quartz
Calcite
Microcline
Albite
Kaolinite 2M
Illite
Counts
6000
5000
4000
3000
2000
1000
0
10
20
30
40
50
60
2Theta (Coupled TwoTheta/Theta) WL=1.54060

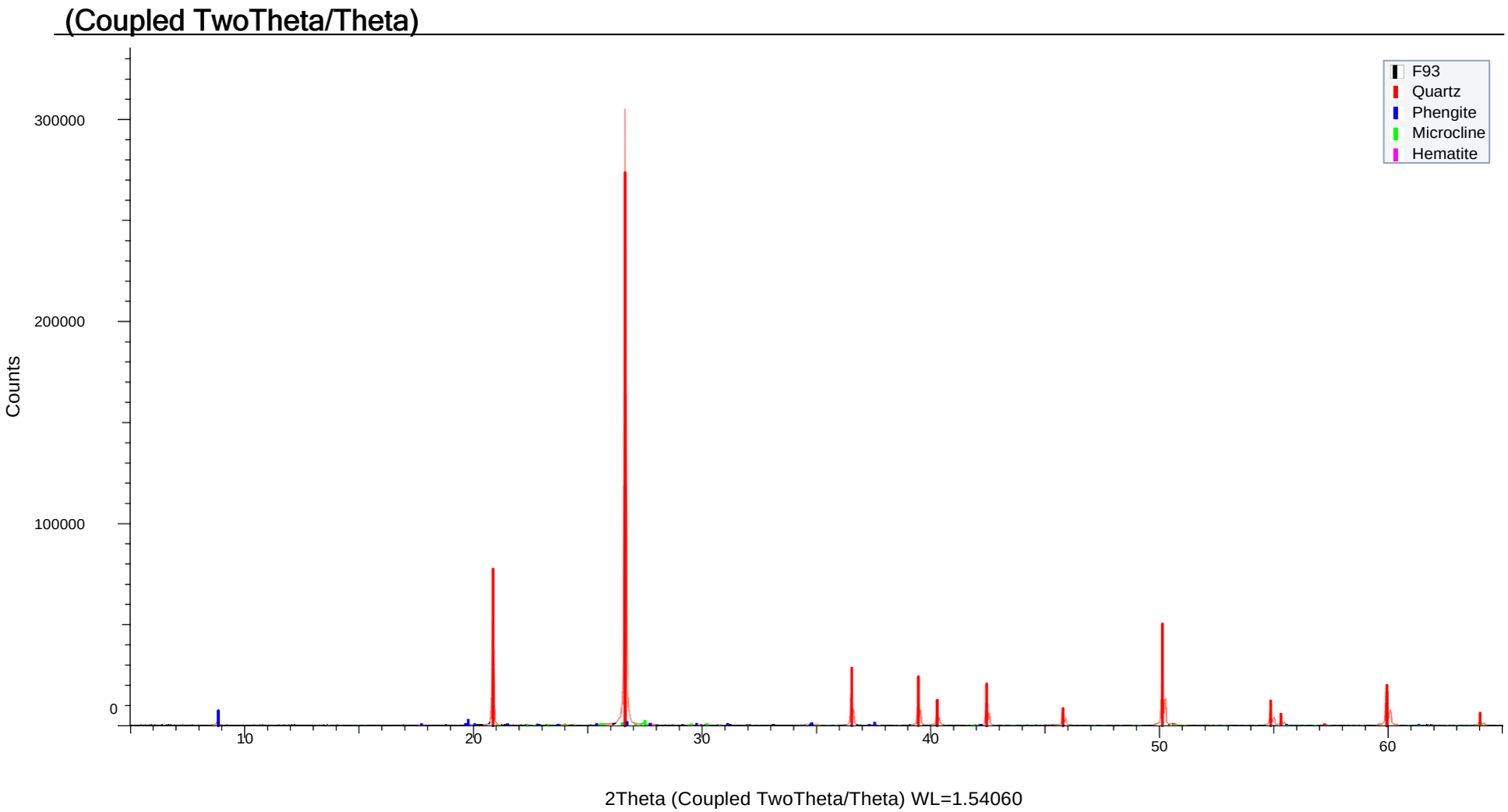
(Coupled TwoTheta/Theta)
F93
Quartz
Phengite
Microcline
Hematite
300000
200000
100000
0
Counts
10
20
30
40
50
60
2Theta (Coupled TwoTheta/Theta) WL=1.54060

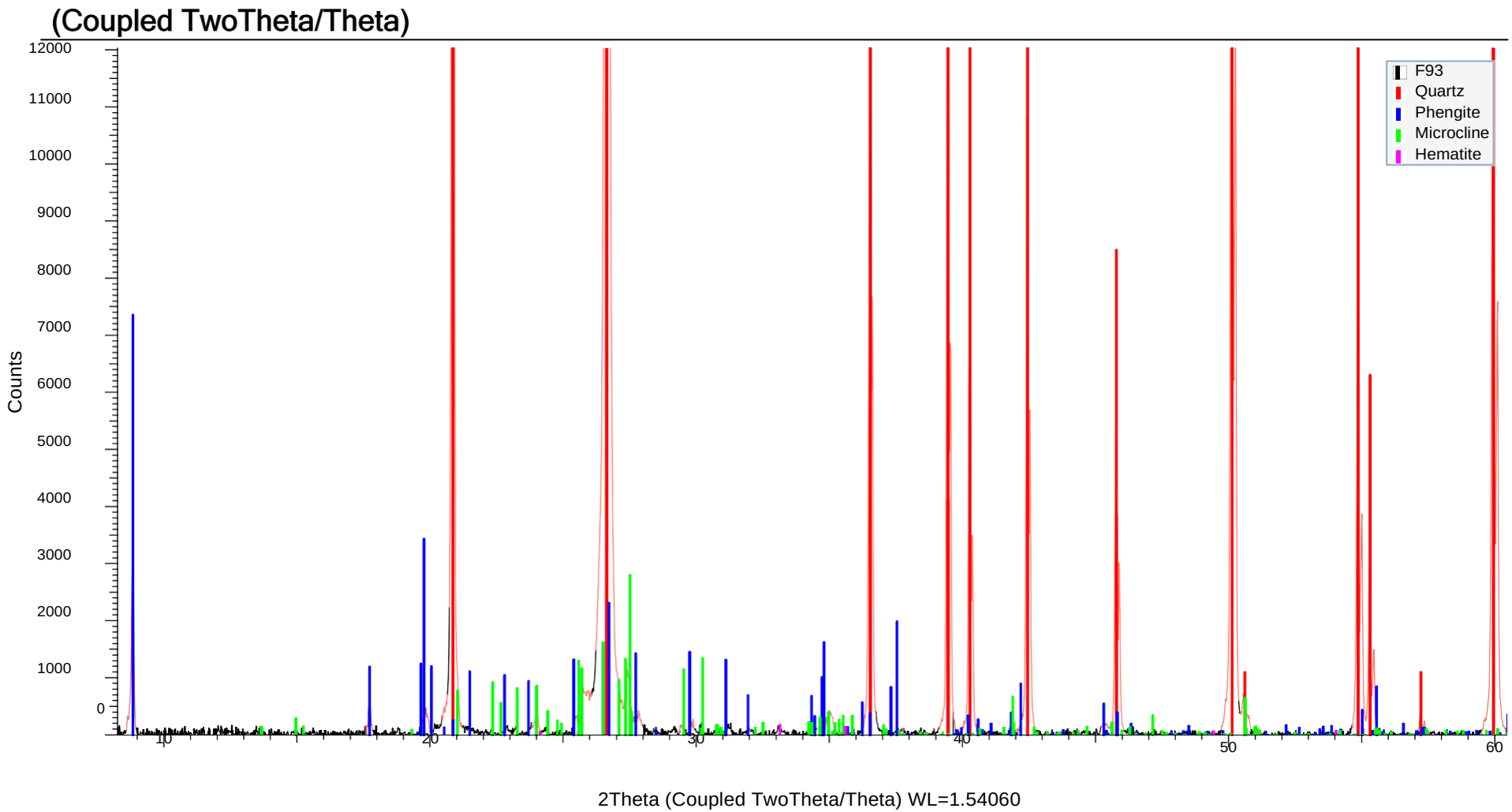
(Coupled TwoTheta/Theta)
Counts
12000
11000
10000
9000
8000
7000
6000
5000
4000
3000
2000
1000
0
10
20
30
40
50
60
F93
Quartz
Phengite
Microcline
Hematite
2Theta (Coupled TwoTheta/Theta) WL=1.54060

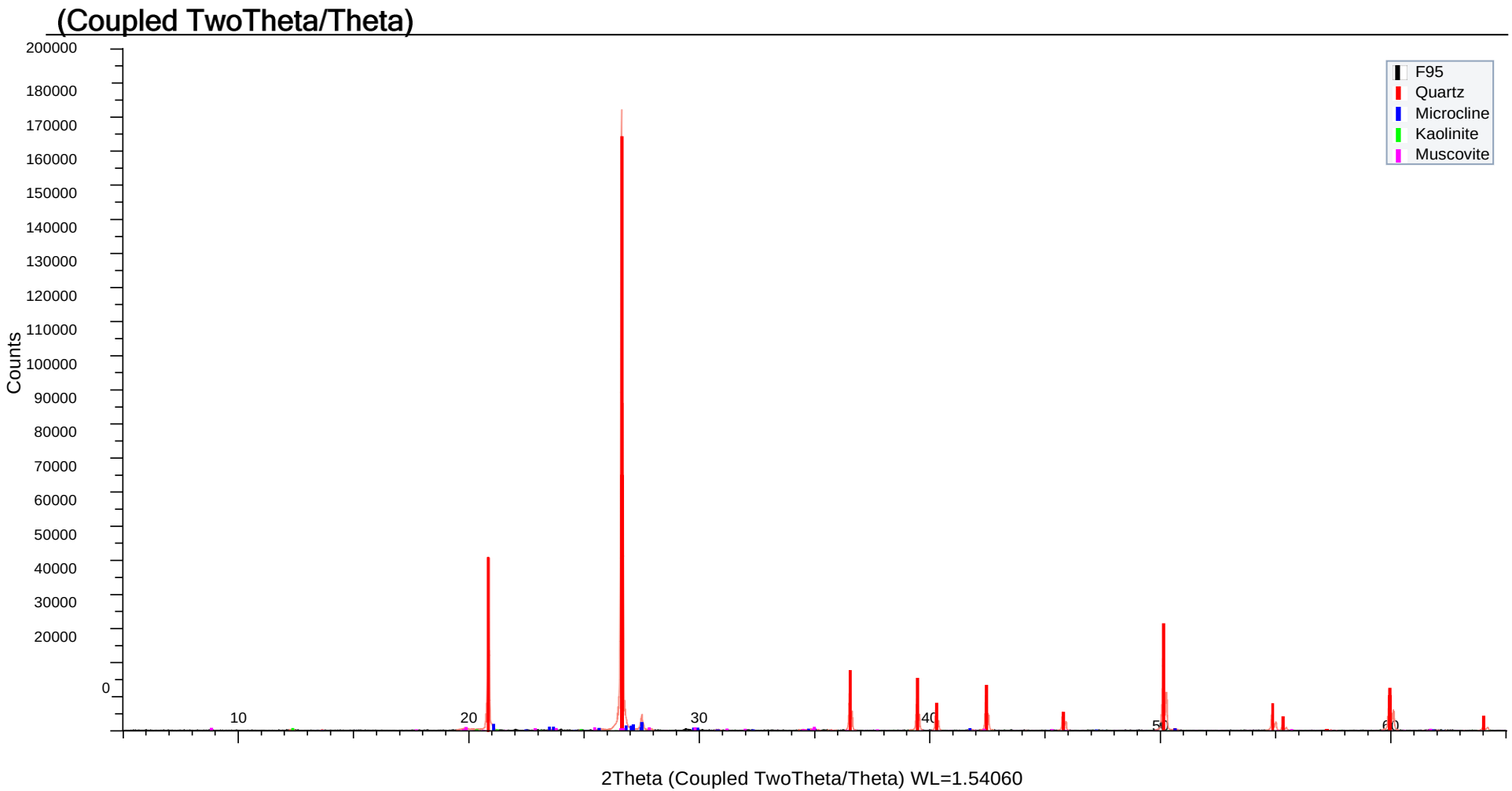
(Coupled TwoTheta/Theta)
Counts
200000
180000
170000
160000
150000
140000
130000
120000
110000
100000
90000
80000
70000
60000
50000
40000
30000
20000
0
10
20
30
40
50
60
F95
Quartz
Microcline
Kaolinite
Muscovite
2Theta (Coupled TwoTheta/Theta) WL=1.54060

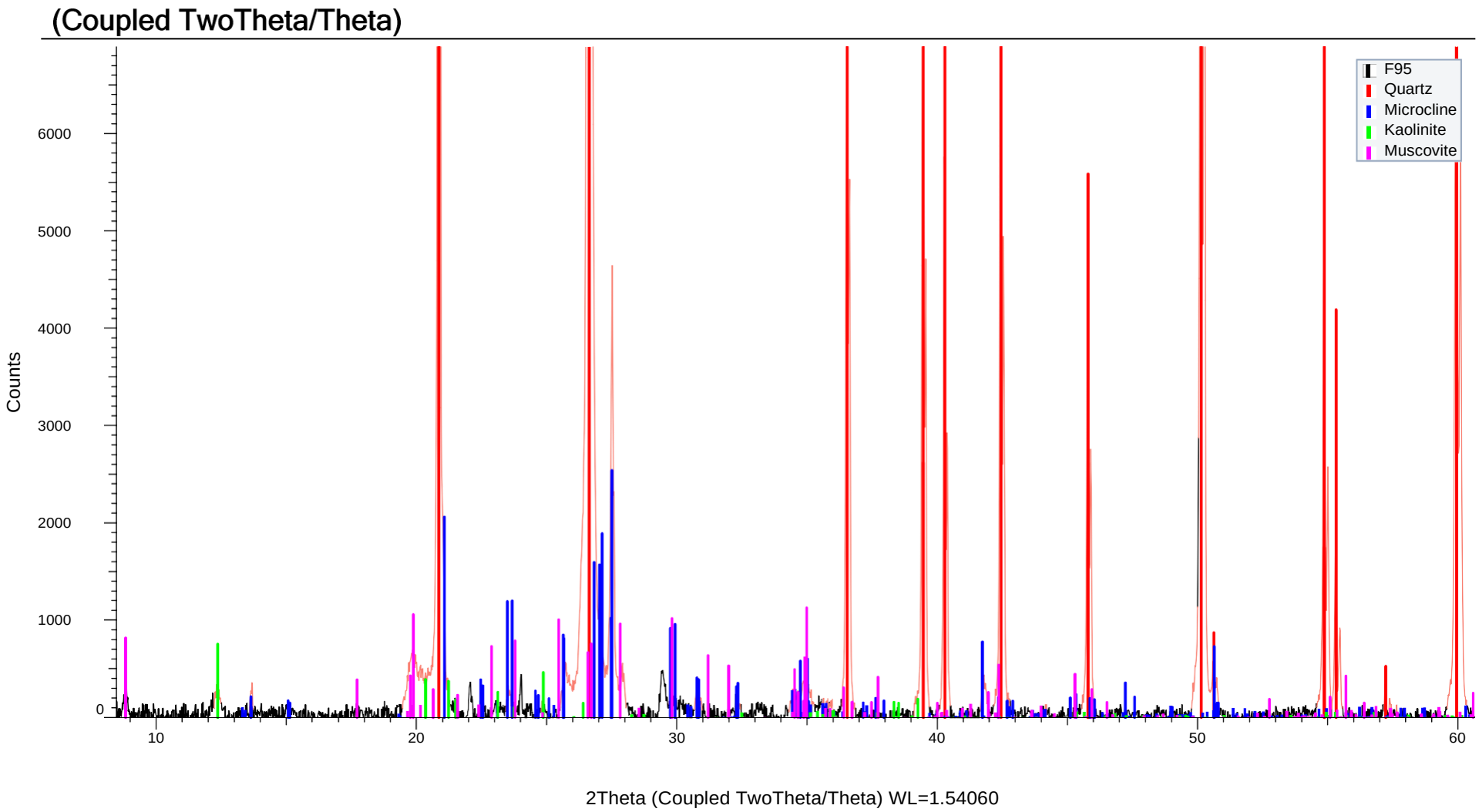
(Coupled TwoTheta/Theta)
F95
Quartz
Microcline
Kaolinite
Muscovite
Counts
0
1000
2000
3000
4000
5000
6000
10
20
30
40
50
60
2Theta (Coupled TwoTheta/Theta) WL=1.54060

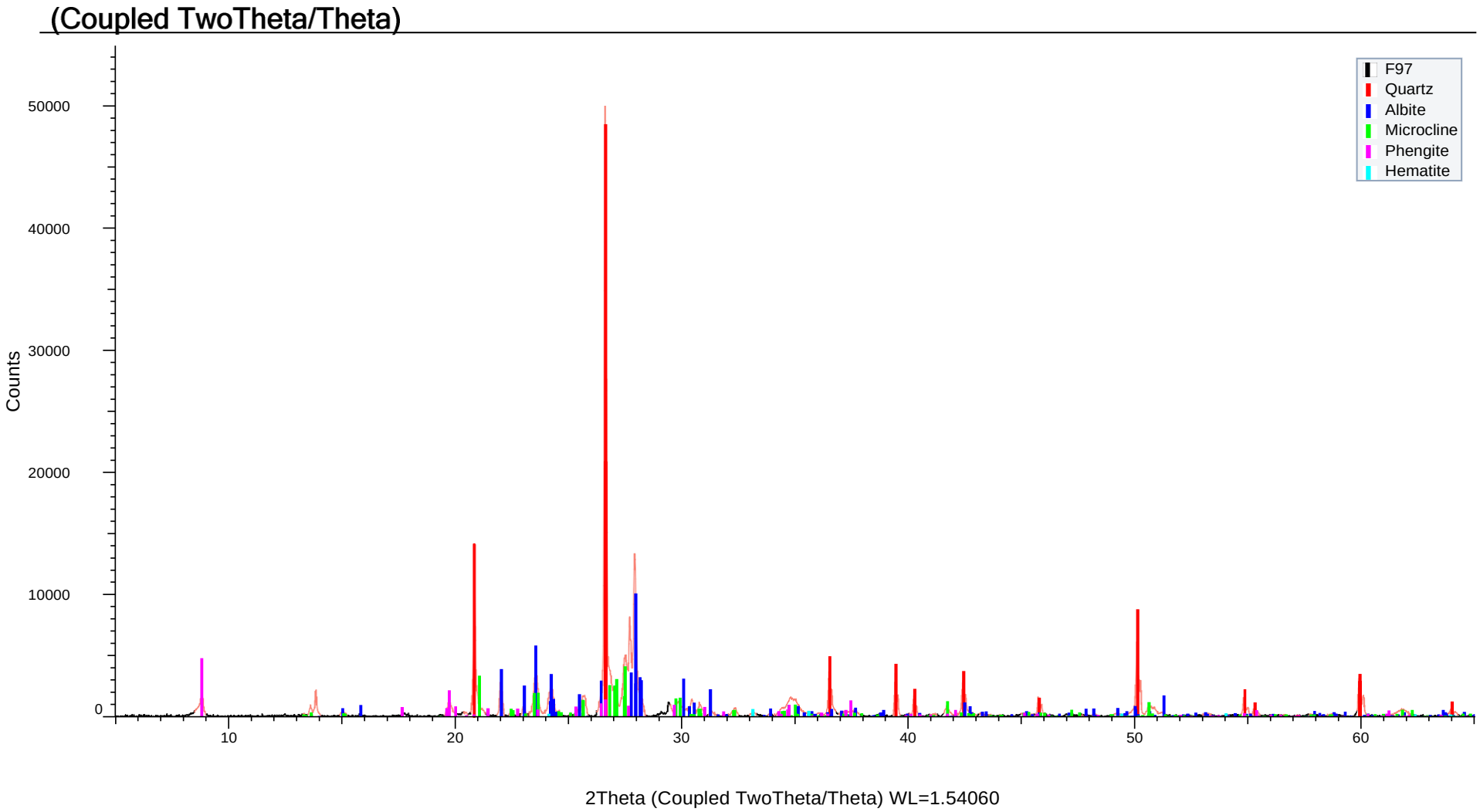
(Coupled TwoTheta/Theta)
F97
Quartz
Albite
Microcline
Phengite
Hematite
Counts
50000
40000
30000
20000
10000
0
10
20
30
40
50
60
2Theta (Coupled TwoTheta/Theta) WL=1.54060

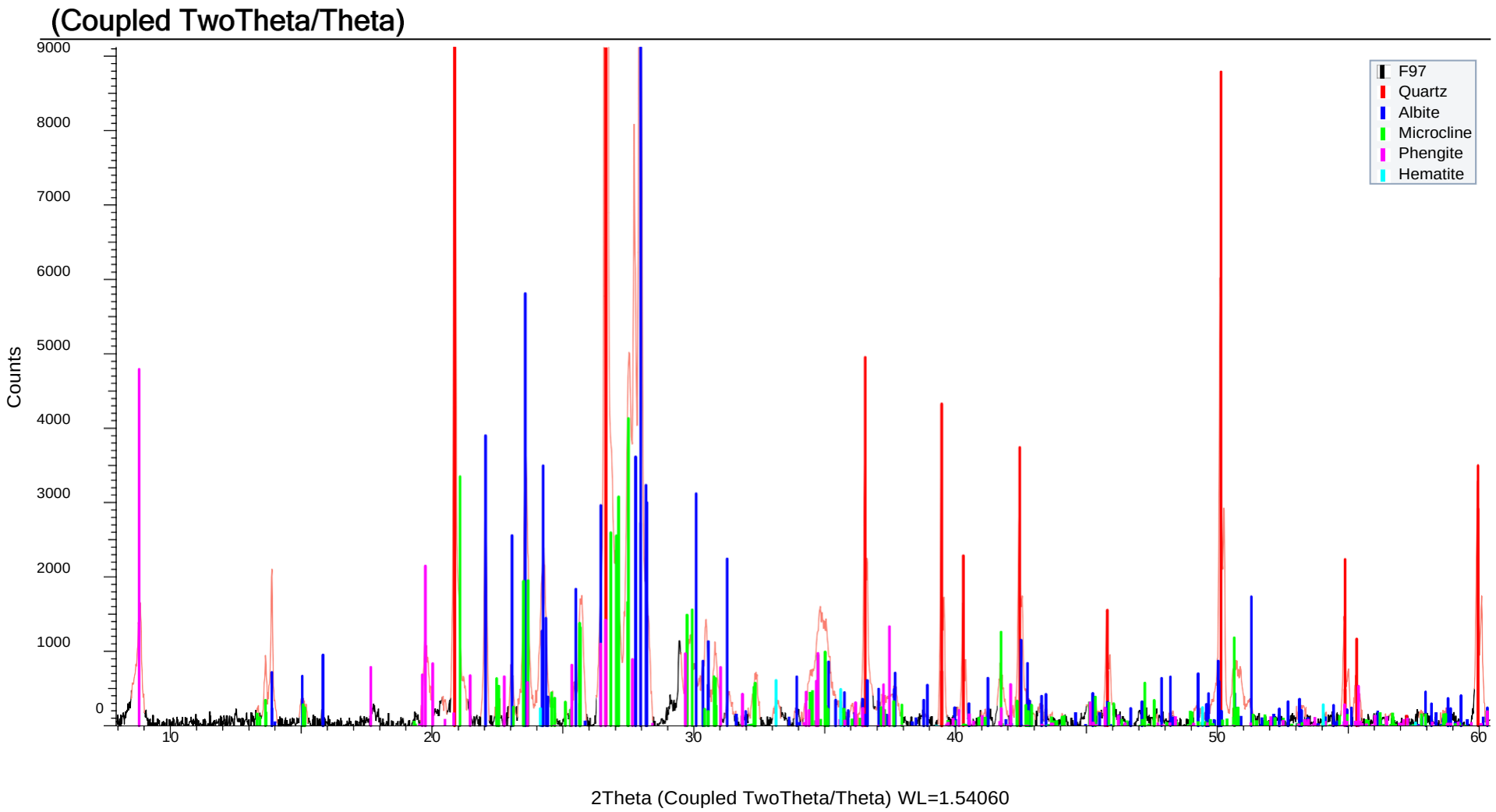
(Coupled TwoTheta/Theta)
Counts
9000
8000
7000
6000
5000
4000
3000
2000
1000
0
10
20
30
40
50
60
F97
Quartz
Albite
Microcline
Phengite
Hematite
2Theta (Coupled TwoTheta/Theta) WL=1.54060

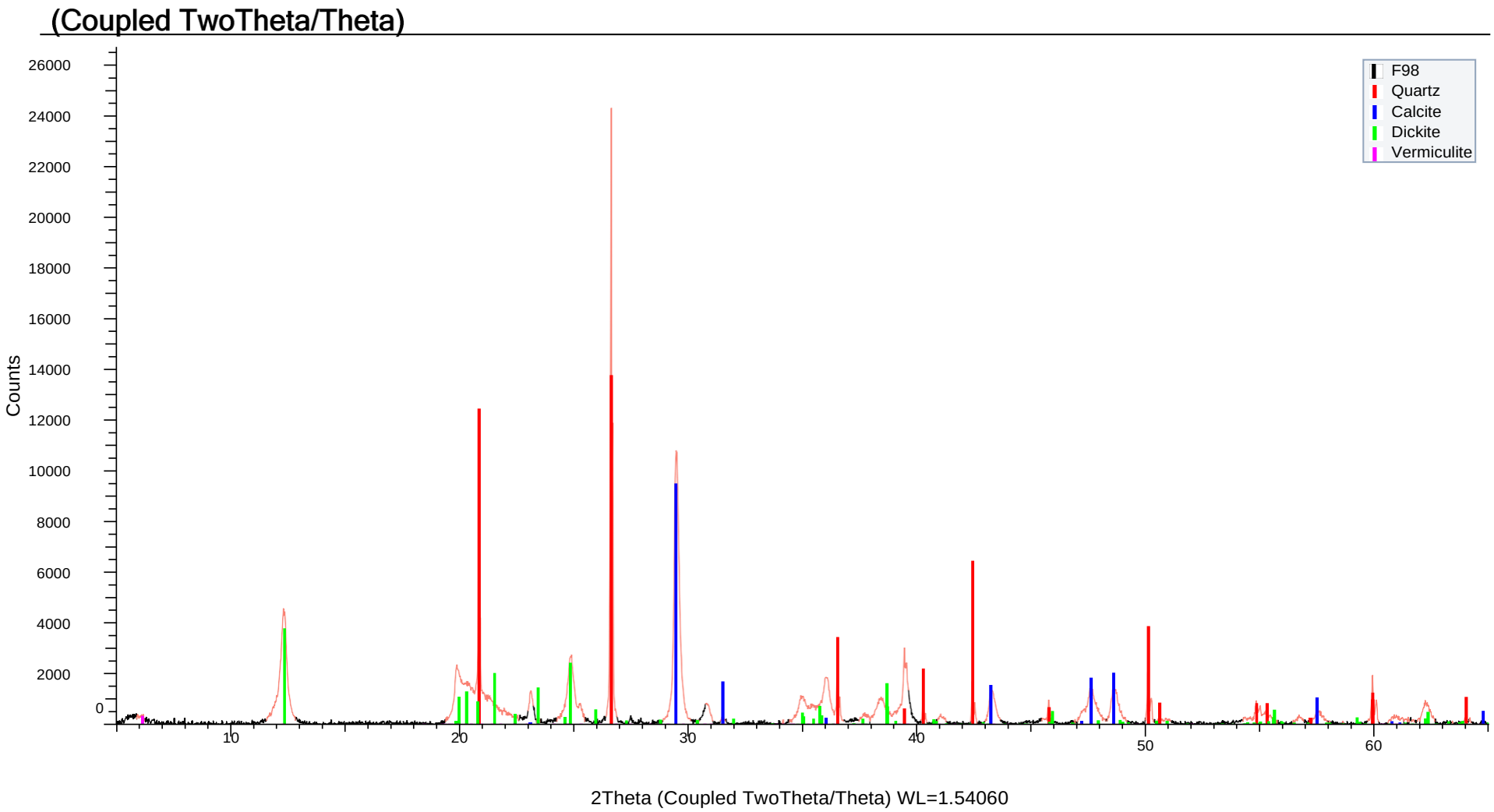
(Coupled TwoTheta/Theta)
F98
Quartz
Calcite
Dickite
Vermiculite
Counts
26000
24000
22000
20000
18000
16000
14000
12000
10000
8000
6000
4000
2000
0
10
20
30
40
50
60
2Theta (Coupled TwoTheta/Theta) WL=1.54060

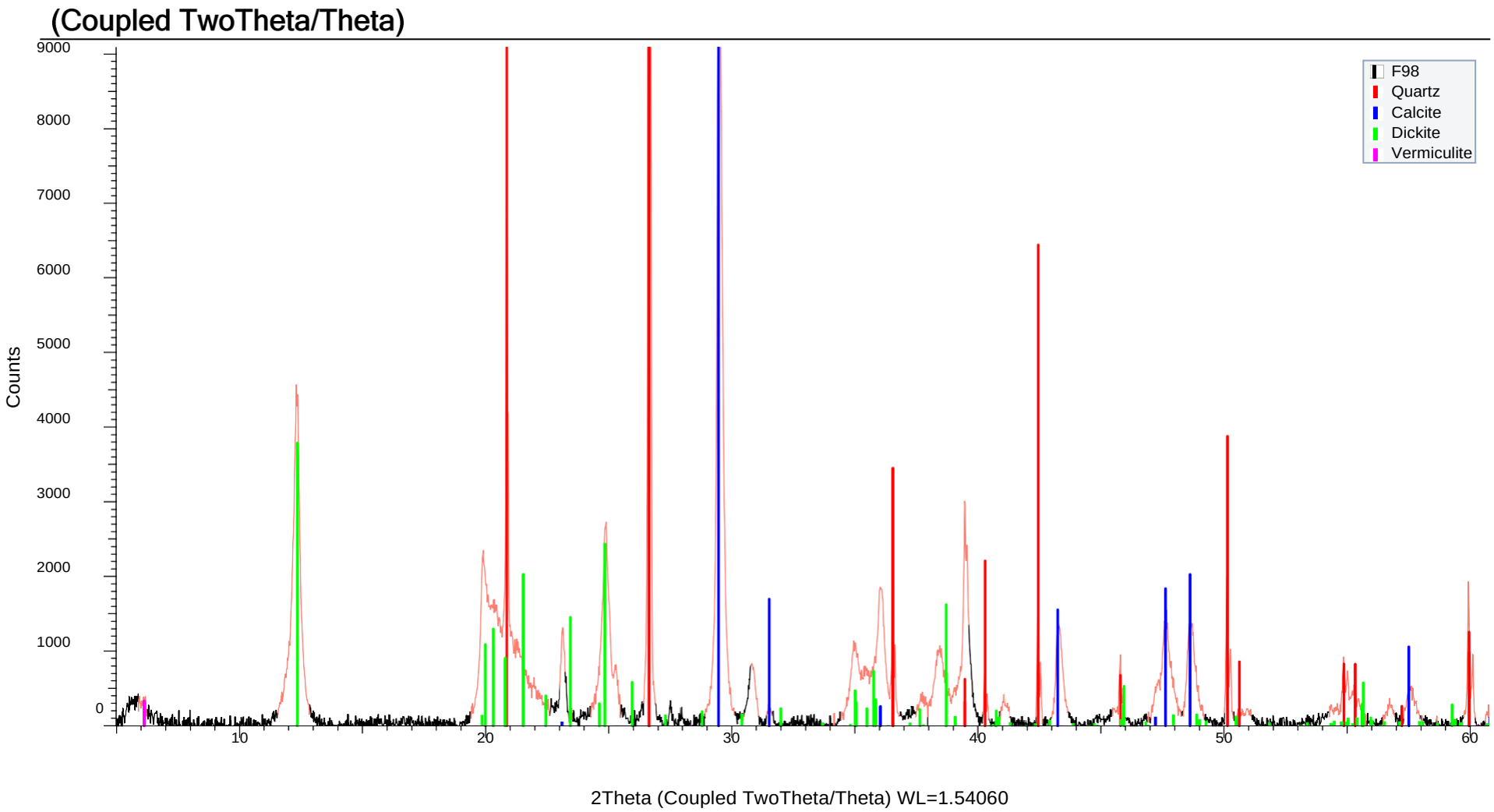
(Coupled TwoTheta/Theta)
Counts
9000
8000
7000
6000
5000
4000
3000
2000
1000
0
10
20
30
40
50
60
F98
Quartz
Calcite
Dickite
Vermiculite
2Theta (Coupled TwoTheta/Theta) WL=1.54060

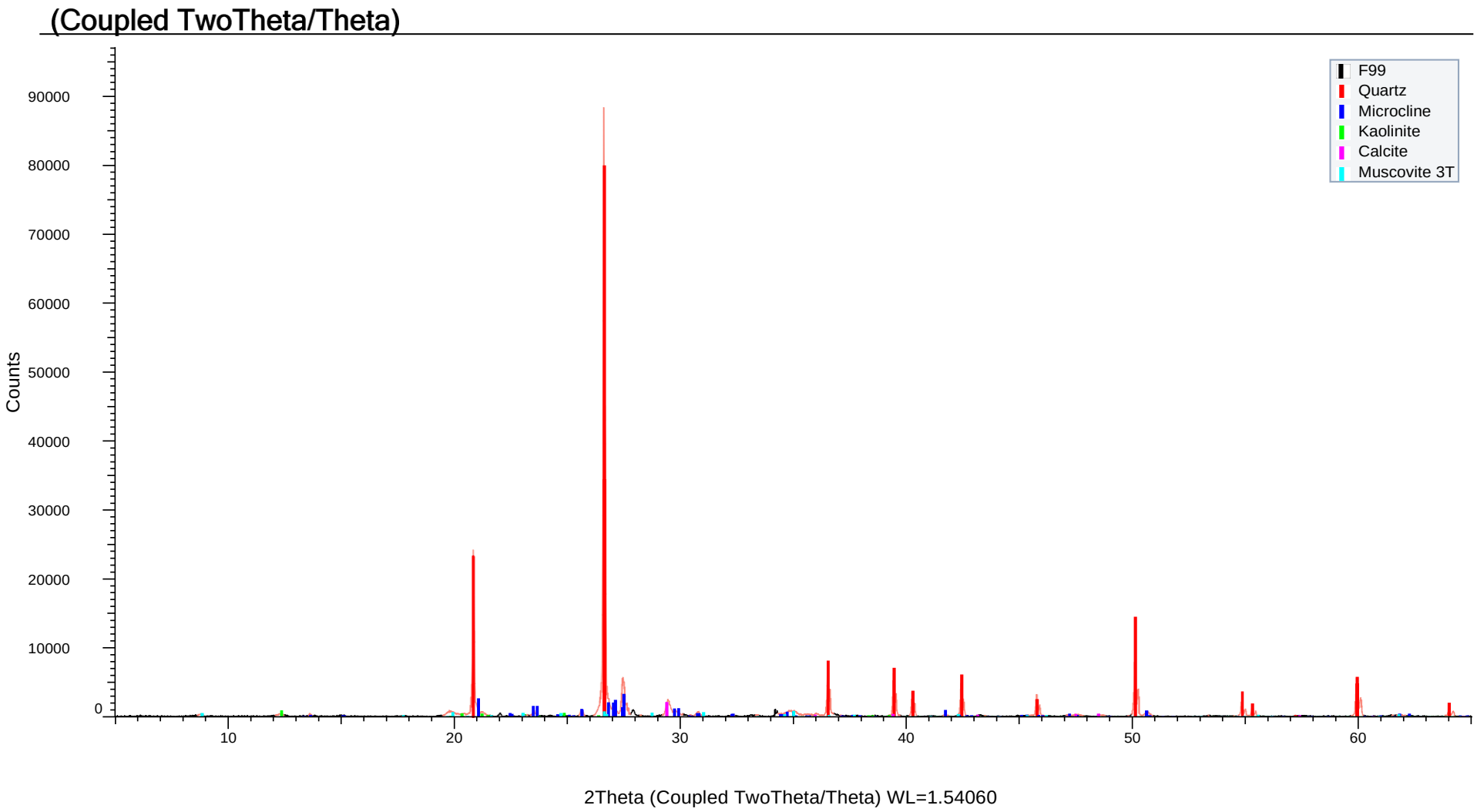
(Coupled TwoTheta/Theta)
F99
Quartz
Microcline
Kaolinite
Calcite
Muscovite 3T
Counts
90000
80000
70000
60000
50000
40000
30000
20000
10000
0
10
20
30
40
50
60
2Theta (Coupled TwoTheta/Theta) WL=1.54060

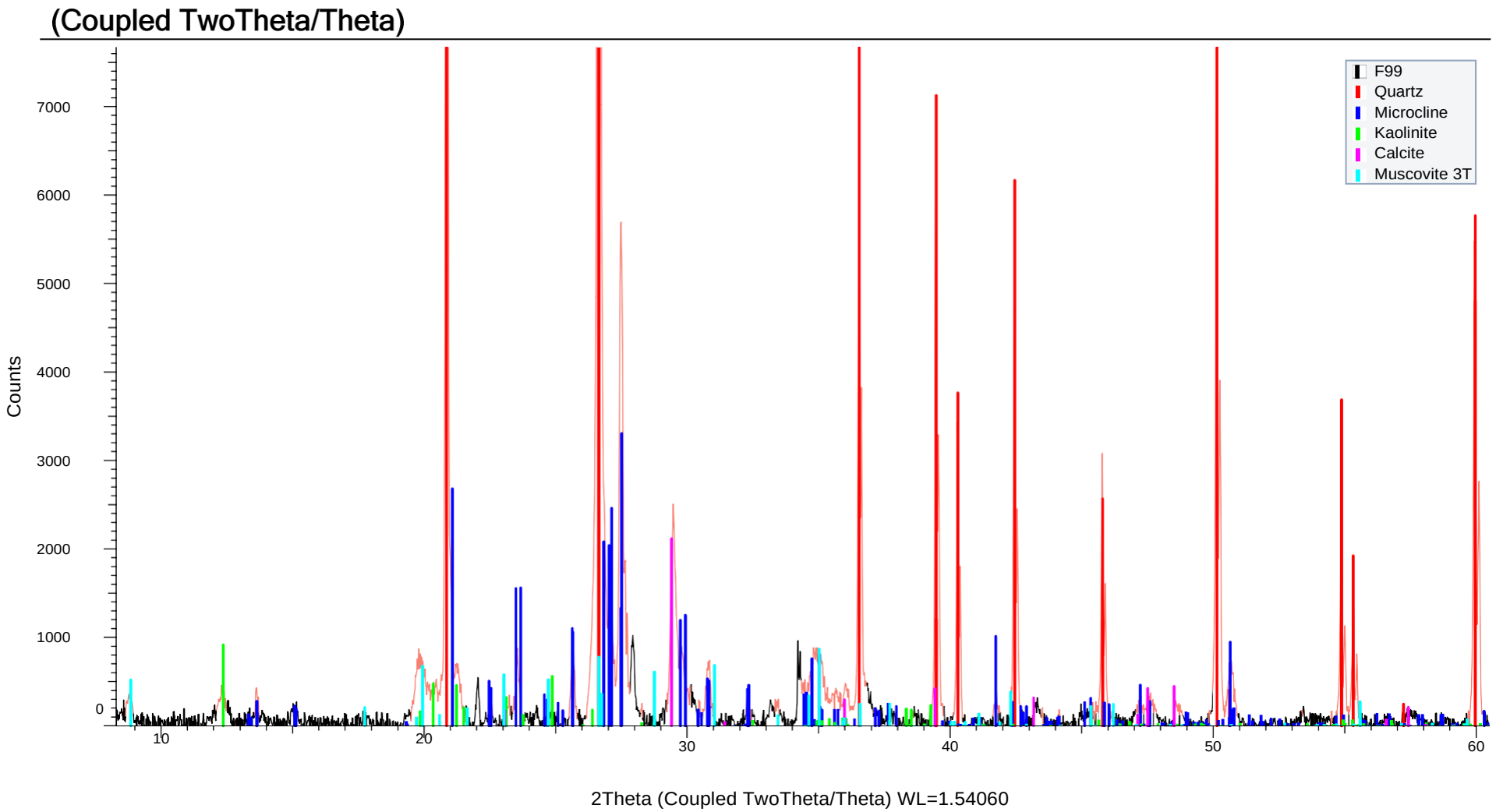
(Coupled TwoTheta/Theta)
F99
Quartz
Microcline
Kaolinite
Calcite
Muscovite 3T
Counts
7000
6000
5000
4000
3000
2000
1000
0
10
20
30
40
50
60
2Theta (Coupled TwoTheta/Theta) WL=1.54060

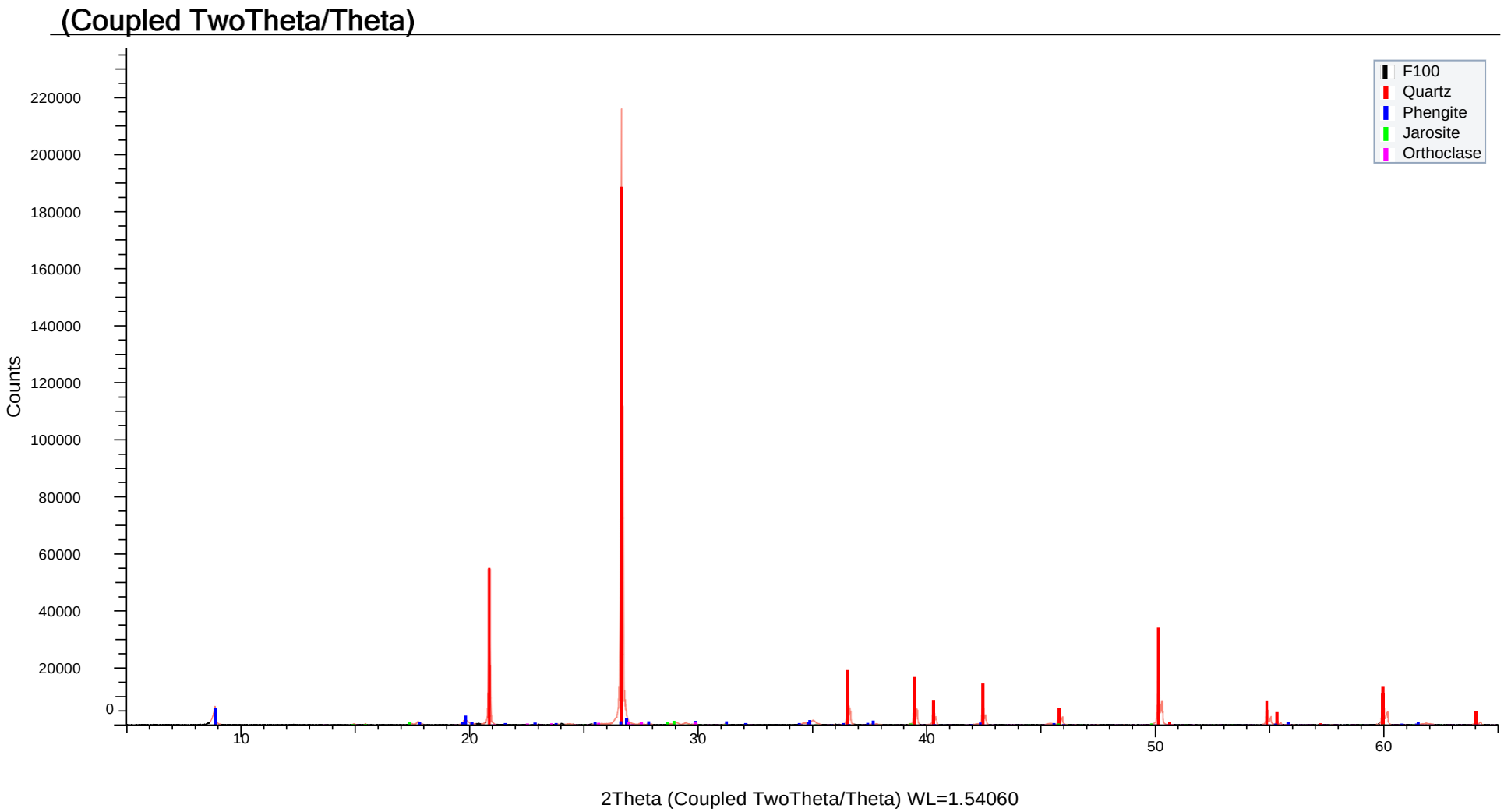
(Coupled TwoTheta/Theta)
F100
Quartz
Phengite
Jarosite
Orthoclase
Counts
220000
200000
180000
160000
140000
120000
100000
80000
60000
40000
20000
0
10
20
30
40
50
60
2Theta (Coupled TwoTheta/Theta) WL=1.54060

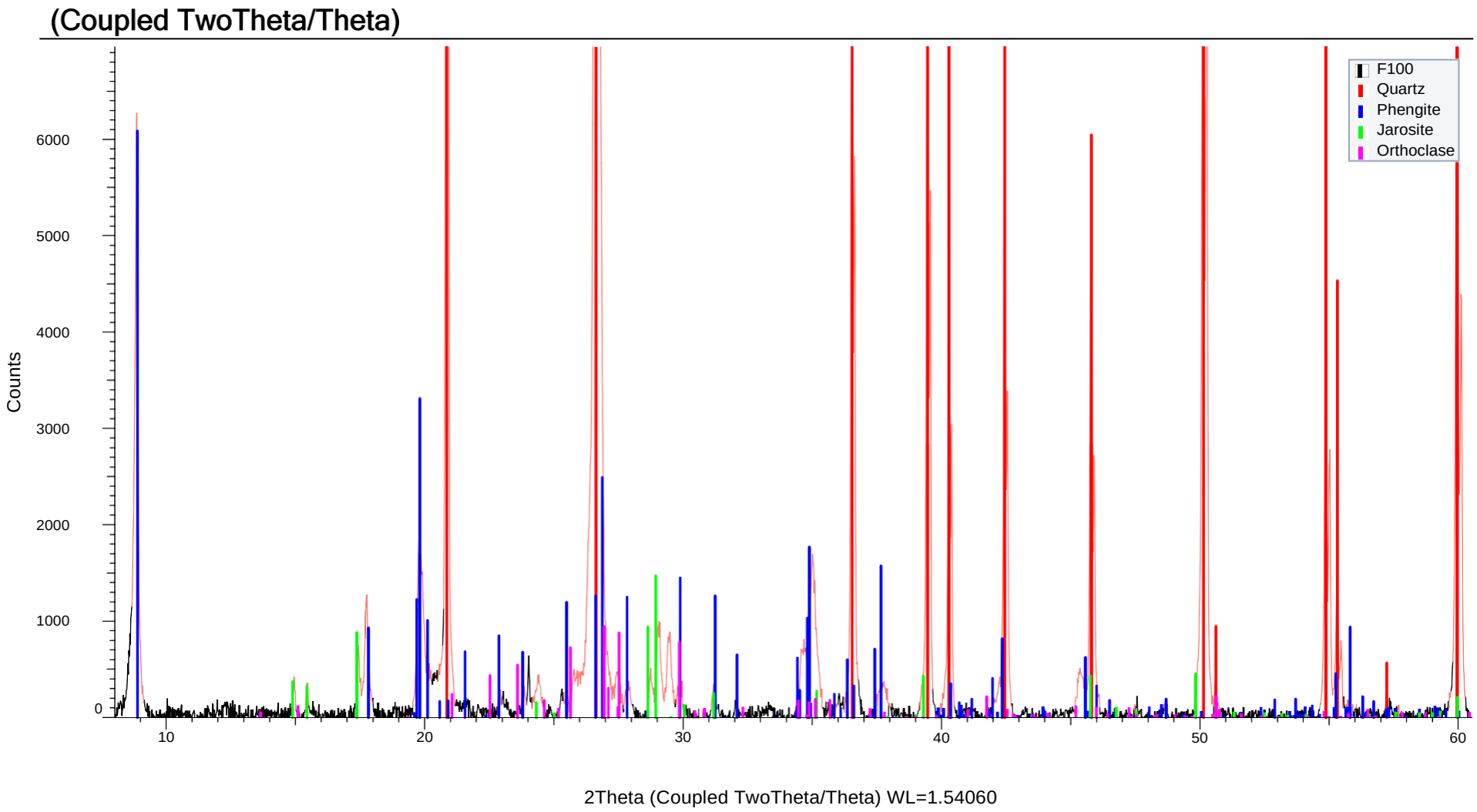
(Coupled TwoTheta/Theta)
F100
Quartz
Phengite
Jarosite
Orthoclase
Counts
0
1000
2000
3000
4000
5000
6000
10
20
30
40
50
60
2Theta (Coupled TwoTheta/Theta) WL=1.54060

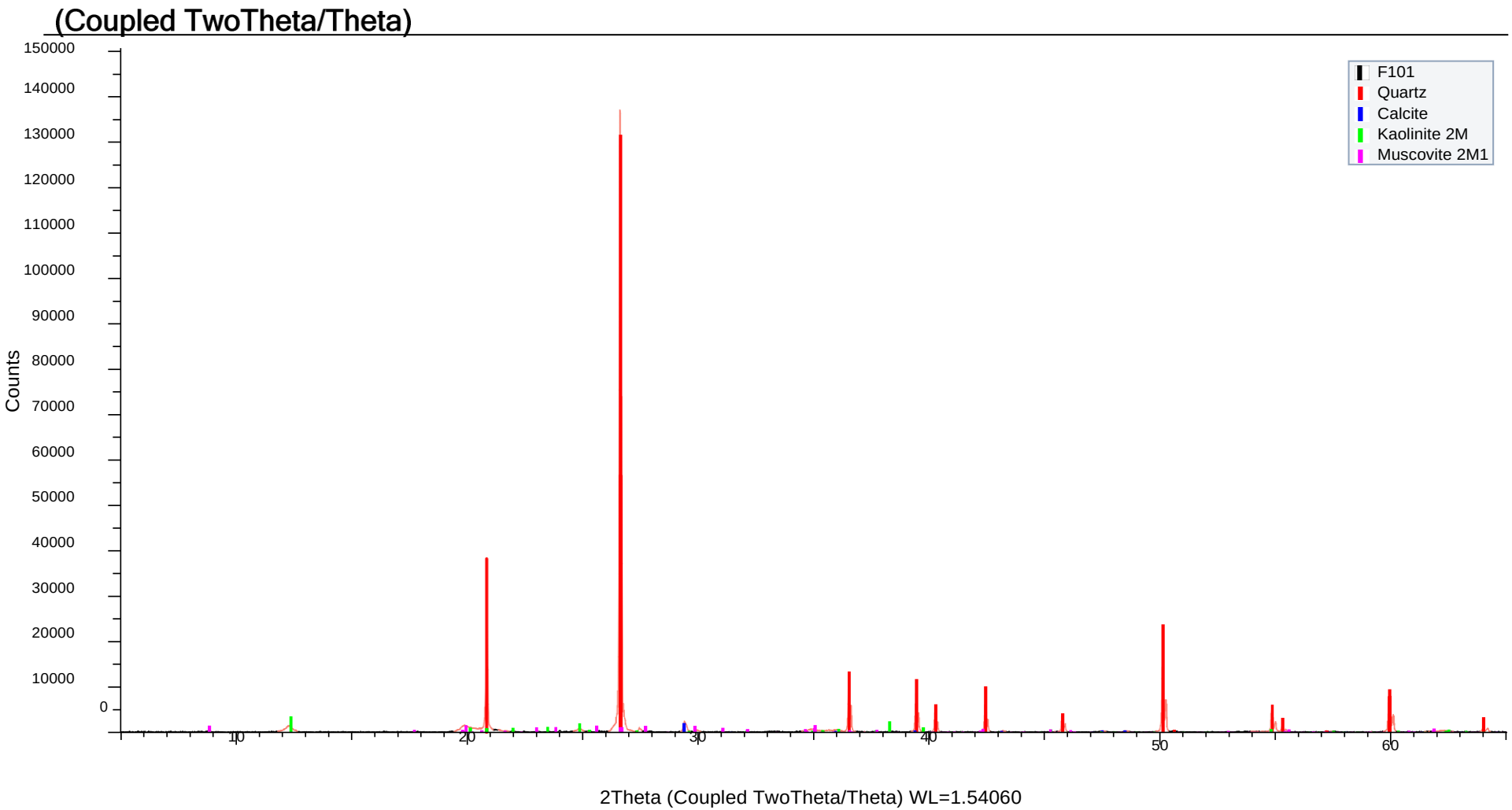
(Coupled TwoTheta/Theta)
150000
140000
130000
120000
110000
100000
90000
80000
70000
60000
50000
40000
30000
20000
10000
0
Counts
10
20
30
40
50
60
2Theta (Coupled TwoTheta/Theta) WL=1.54060
F101
Quartz
Calcite
Kaolinite 2M
Muscovite 2M1

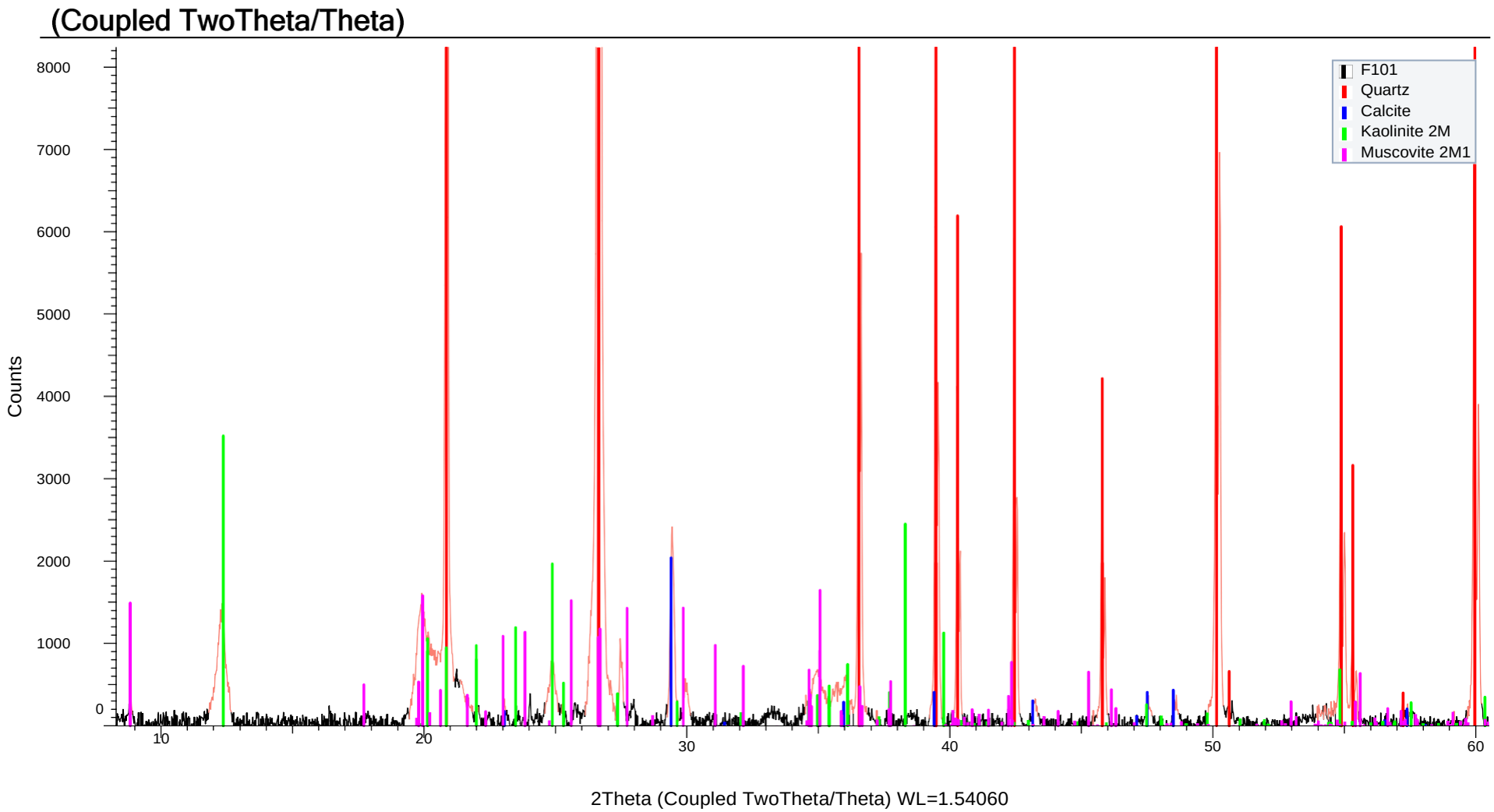
(Coupled TwoTheta/Theta)
F101
Quartz
Calcite
Kaolinite 2M
Muscovite 2M1
Counts
8000
7000
6000
5000
4000
3000
2000
1000
0
10
20
30
40
50
60
2Theta (Coupled TwoTheta/Theta) WL=1.54060

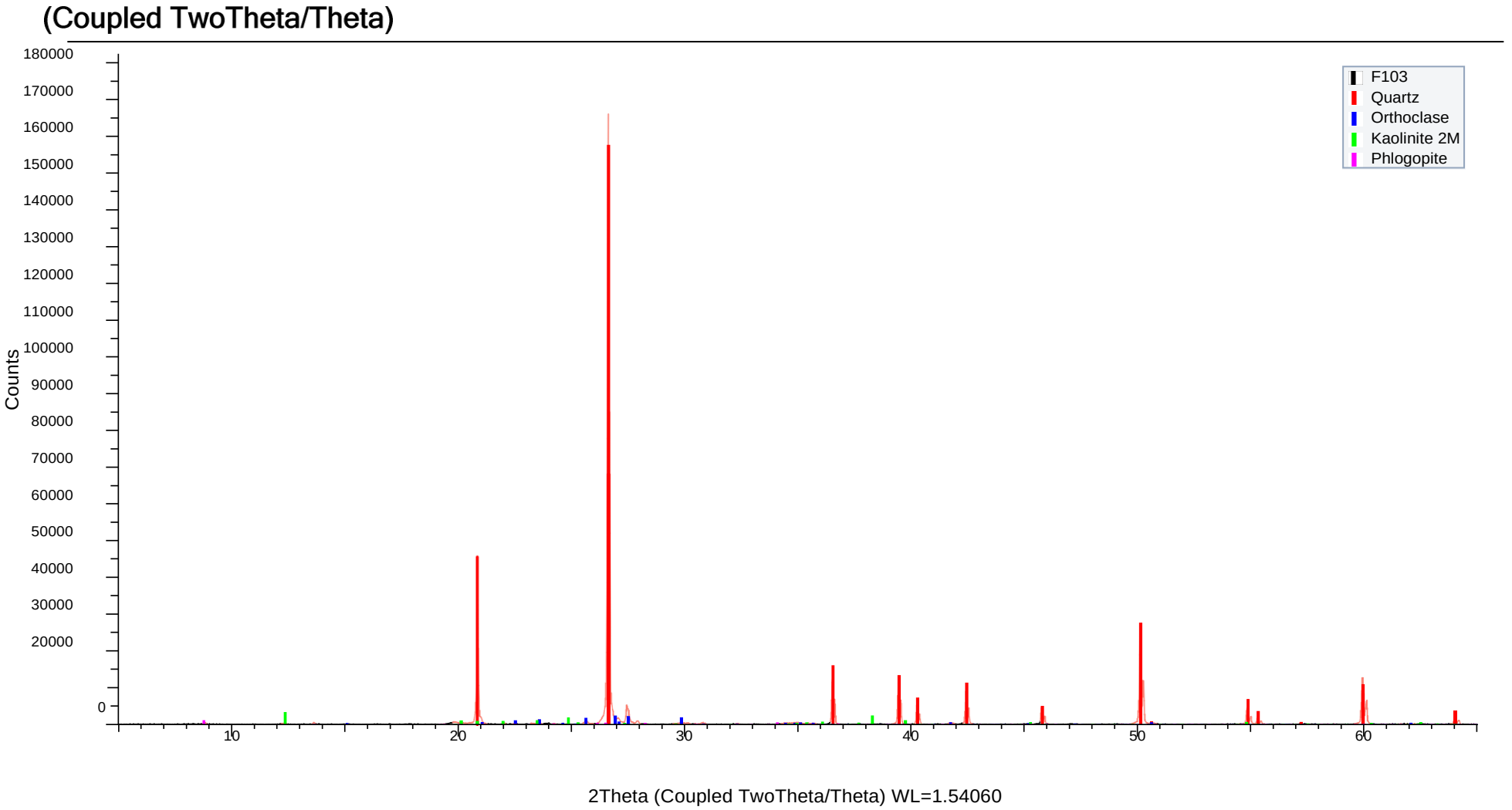
(Coupled TwoTheta/Theta)
F103
Quartz
Orthoclase
Kaolinite 2M
Phlogopite
Counts
180000
170000
160000
150000
140000
130000
120000
110000
100000
90000
80000
70000
60000
50000
40000
30000
20000
0
10
20
30
40
50
60
2Theta (Coupled TwoTheta/Theta) WL=1.54060

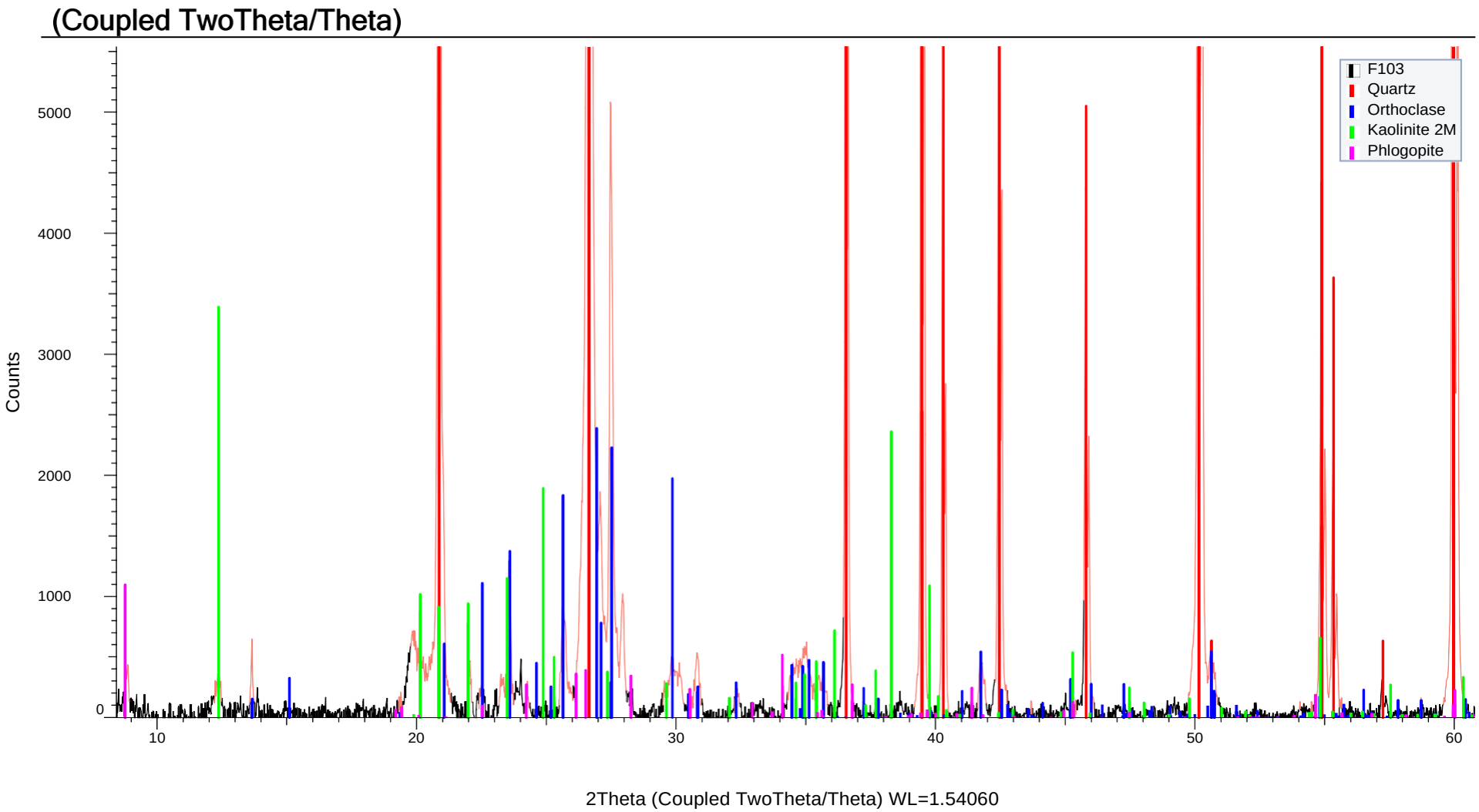
(Coupled TwoTheta/Theta)
F103
Quartz
Orthoclase
Kaolinite 2M
Phlogopite
Counts
5000
4000
3000
2000
1000
0
10
20
30
40
50
60
2Theta (Coupled TwoTheta/Theta) WL=1.54060

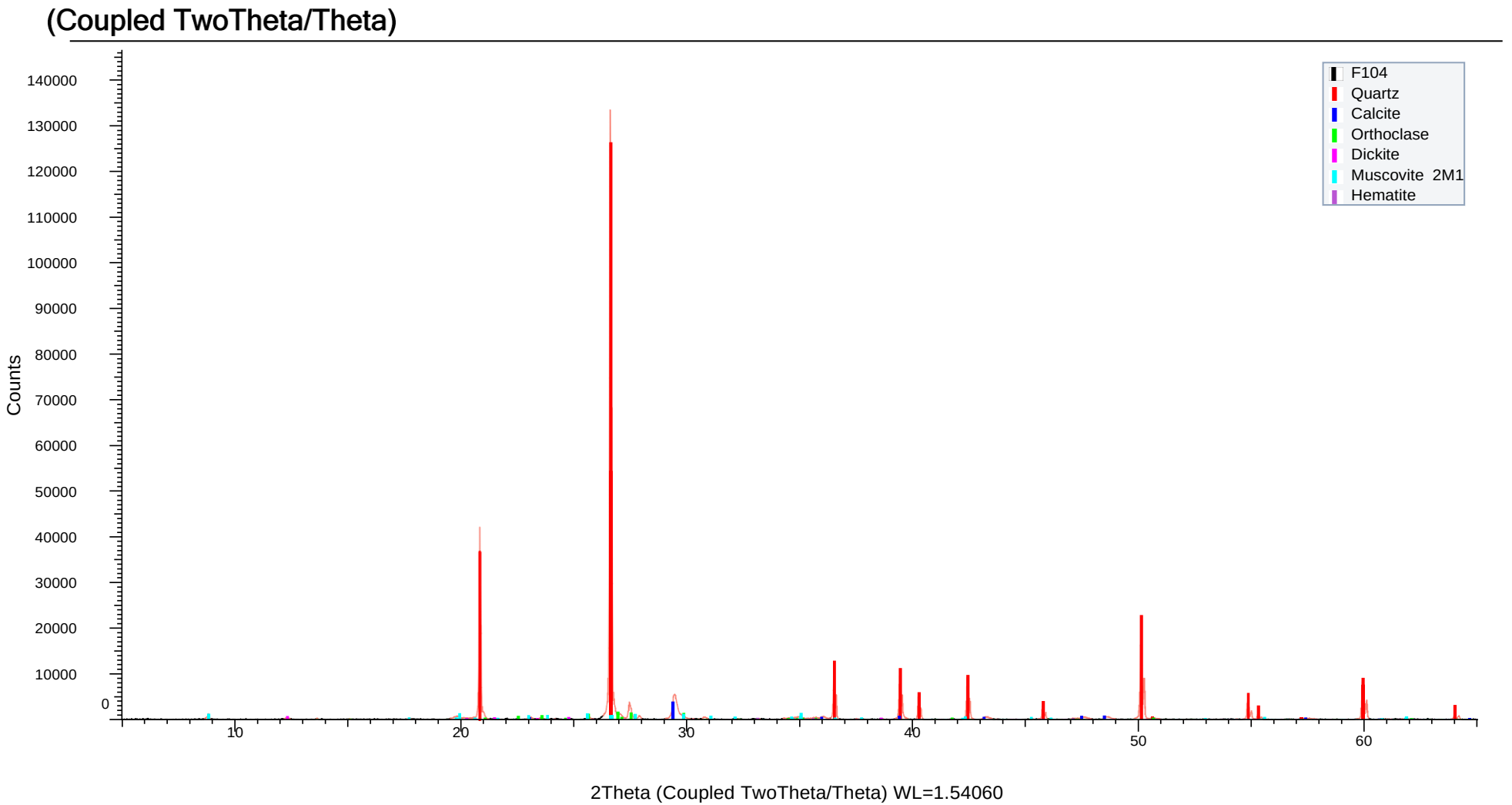
(Coupled TwoTheta/Theta)
F104
Quartz
Calcite
Orthoclase
Dickite
Muscovite 2M1
Hematite
Counts
140000
130000
120000
110000
100000
90000
80000
70000
60000
50000
40000
30000
20000
10000
0
10
20
30
40
50
60
2Theta (Coupled TwoTheta/Theta) WL=1.54060

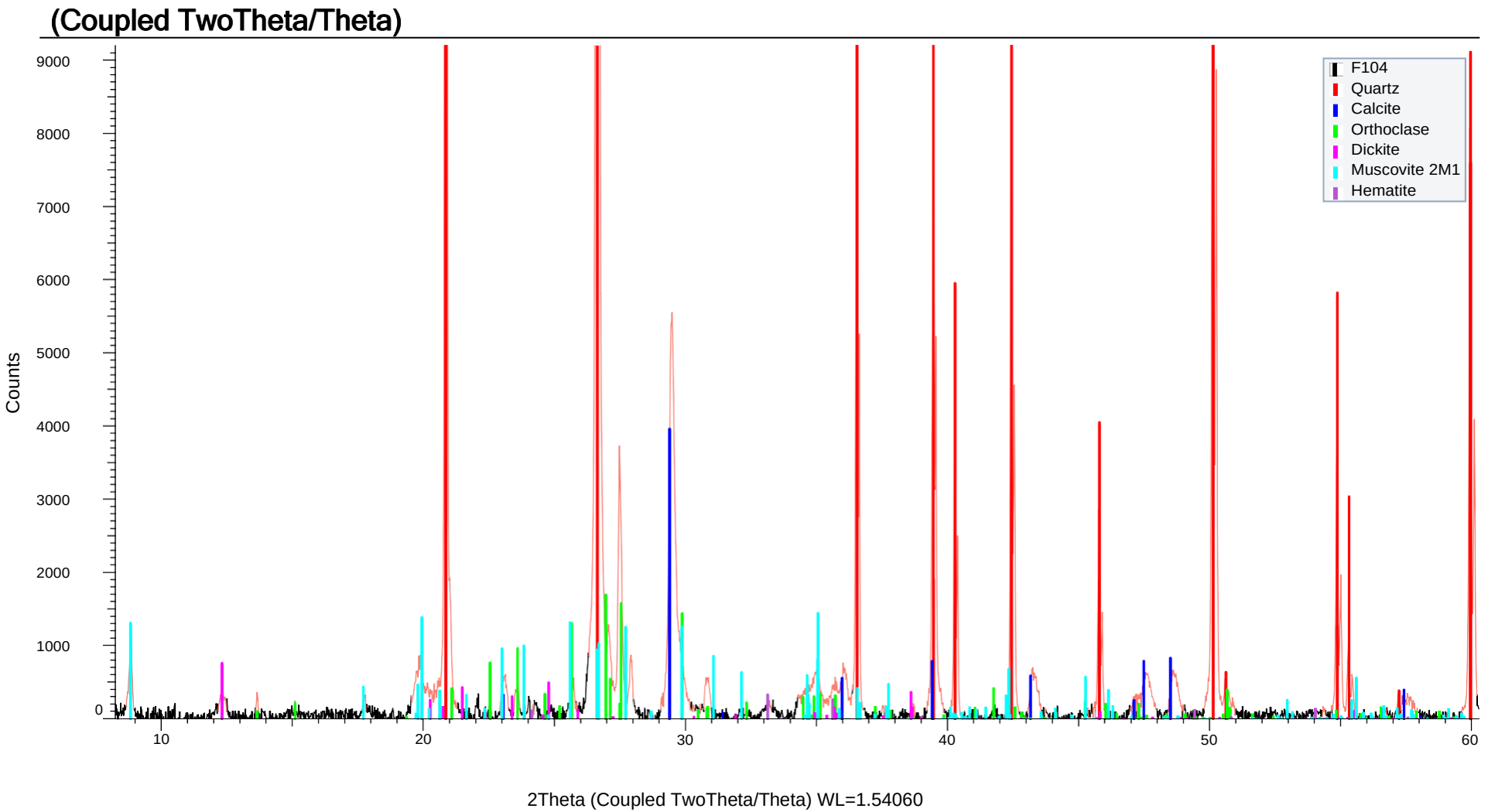
(Coupled TwoTheta/Theta)
F104
Quartz
Calcite
Orthoclase
Dickite
Muscovite 2M1
Hematite
Counts
9000
8000
7000
6000
5000
4000
3000
2000
1000
0
10
20
30
40
50
60
2Theta (Coupled TwoTheta/Theta) WL=1.54060

Appendix B

RAW SEMI-QUANTITATIVE X-RAY DIFFRACTION DATA

Sample Number	Easting	Northing	Actinolite (%)	Albite (%)	Alunite (%)	Calcite (%)	Chamosite (%)	Dickite (%)	Dolomite (%)
F02	596585.3142	6393013.532	-	22.5	-	-	18.8	-	-
F03	596879.9037	6393897.492	-	28.9	-	0.6	22.3	-	-
F13	595585.9085	6393985.062	-	5.3	-	-	-	-	-
F16	594953.1819	6391115.917	-	-	-	17.1	-	-	-
F17	595414.5067	6392639.608	-	5	-	-	-	-	-
F18	596409.9373	6394257.869	-	7.6	-	-	-	-	-
F21	602436.8138	6387226.754	-	-	-	-	-	-	-
F22	603850.9153	6385589.393	-	-	-	-	-	-	-
F23	603471.039	6385004.821	-	-	-	-	-	-	-
F25	603695.4458	6382998.535	-	-	-	-	-	-	-
F27	599577.1909	6384873.184	-	-	24	-	-	7.6	-
F29	599462.7805	6385440.893	-	-	0.9	-	-	-	-
F31	604128.5479	6382245.286	-	-	-	-	-	-	-
F32	602481.2224	6381265.082	-	3.4	-	-	-	-	-
F33	603956.4972	6391367.521	-	2.3	-	-	-	-	-
F36	606986.2956	6381490.253	-	-	-	10.5	-	-	-
F37	603228.2185	6385101.869	-	-	-	-	-	-	-
F38	603611.9974	6385559.348	-	-	-	-	-	-	-
F40	596162.937	6383597.585	-	-	-	-	-	-	-
F41	596167.3026	6383738.873	-	-	-	-	-	-	-
F42	595951.3338	6383148.584	-	-	-	-	-	-	-
F43	598023.8258	6384481.04	-	-	-	-	-	-	-
F44	598868.6289	6384565.138	-	-	-	-	-	-	-
F45	598798.5508	6384749.996	-	-	-	-	-	-	-
F47	599647.9653	6385599.17	-	-	-	-	-	-	-
F48	598695.3641	6385858.782	-	-	-	8.8	-	-	-
F49	604809.5308	6378397.161	-	-	-	5.8	-	-	-
F50	601519.8075	6390079.101	-	-	-	1.2	-	-	-
F51	599247.9317	6384419.448	-	-	-	2.7	-	-	-
F52	603233.3533	6381221.331	-	-	-	1.3	-	-	1.2

Sample Number	Easting	Northing	Actinolite (%)	Albite (%)	Alunite (%)	Calcite (%)	Chamosite (%)	Dickite (%)	Dolomite (%)
F53	592464.7568	6384022.243	-	-	-	2.1	-	-	-
F58	604210.1487	6379394.878	-	4.5	-	6.4	-	-	-
F61	604949.0676	6385784.19	-	2.2	-	-	-	-	-
F62	604522.479	6386073.697	-	2.4	-	3.6	-	-	-
F63	589384.0267	6379921.34	-	-	-	5.4	-	-	0.8
F68	592585.2303	6390574.64	-	-	-	3.6	-	-	-
F71	606317.6783	6390518.148	-	-	-	2.5	-	-	-
F73	607545.5524	6382237.135	-	-	-	-	-	-	-
F74	607853.2714	6381783.935	-	-	-	7.6	-	-	-
F76	604965.2548	6380575.979	4.2	12	-	-	-	-	-
F76B	604878.38	6380726.58	3.9	31	-	-	11.3	-	-
F77	602818.5933	6381656.817	-	-	-	-	-	-	-
F80	599160.5626	6385709.792	-	-	-	-	-	-	-
F81	599381.8341	6385498.231	-	-	-	-	-	-	-
F84	597851.5509	6390870.039	-	-	-	1.7	9.7	-	-
F85	598947.8806	6391275.135	-	-	-	-	-	-	-
F89	602542.8257	6375769.217	-	-	-	5.6	-	-	-
F90	602371.1967	6376139.516	-	5.7	-	10.4	-	-	-
F93	603629.3626	6384525.627	-	-	-	-	-	-	-
F95	594314.9808	6379931.888	-	-	-	0.9	-	-	0.9
F97	597197.1325	6393264.172	-	26.6	-	2.1	-	-	-
F98	601249.0185	6392986.498	-	-	-	28.4	-	45.8	3.2
F99	598687.7938	6378092.966	-	-	-	4	-	-	-
F100	599162.1958	6384658.274	-	-	-	1.8	-	-	-
F101	607096.2656	6381436.665	-	-	-	3.9	-	-	-
F103	598770.7474	6375720.862	-	-	-	-	-	-	-
F104	602178.7105	6377134.464	-	-	-	9.4	-	-	-

Sample Number	Easting	Northing	Hematite (%)	Illite (%)	Jarosite (%)	Kaolinite (%)	Microcline (%)	Muscovite (%)
F02	596585.3142	6393013.532	-	-	0.003	-	24.3	5.2
F03	596879.9037	6393897.492	-	-	-	-	24.5	-
F13	595585.9085	6393985.062	-	-	-	-	-	12.5
F16	594953.1819	6391115.917	1.2	-	-	11.4	-	14
F17	595414.5067	6392639.608	1.3	-	-	7.2	-	9.4
F18	596409.9373	6394257.869	-	18.1	-	10.3	13.2	-
F21	602436.8138	6387226.754	1.4	-	-	23.3	-	25.5
F22	603850.9153	6385589.393	-	-	-	9.4	-	11.8
F23	603471.039	6385004.821	-	-	-	-	-	-
F25	603695.4458	6382998.535	-	-	-	-	-	-
F27	599577.1909	6384873.184	-	-	-	-	-	-
F29	599462.7805	6385440.893	0.7	-	-	-	-	0
F31	604128.5479	6382245.286	0.6	-	-	5.8	-	8.3
F32	602481.2224	6381265.082	-	-	-	10.4	-	10.3
F33	603956.4972	6391367.521	-	-	-	7.4	9.5	7
F36	606986.2956	6381490.253	1	-	-	18.7	6.1	14.3
F37	603228.2185	6385101.869	-	-	-	7.1	-	10.9
F38	603611.9974	6385559.348	-	-	-	7.9	4.3	8.4
F40	596162.937	6383597.585	-	-	-	-	-	39.2
F41	596167.3026	6383738.873	-	-	-	-	2.5	38.6
F42	595951.3338	6383148.584	-	-	-	9.6	-	-
F43	598023.8258	6384481.04	0.3	-	0.6	-	1.4	38.7
F44	598868.6289	6384565.138	0.7	-	-	7.1	-	-
F45	598798.5508	6384749.996	-	-	-	10.2	4	21.5
F47	599647.9653	6385599.17	-	-	-	7.2	7.6	16.4
F48	598695.3641	6385858.782	-	-	-	11.1	-	-
F49	604809.5308	6378397.161	-	-	-	8.2	9.4	12.1
F50	601519.8075	6390079.101	0.5	-	-	7.9	6.1	14
F51	599247.9317	6384419.448	-	30	-	6.2	7	-
F52	603233.3533	6381221.331	-	-	-	11	-	16.1

Sample Number	Easting	Northing	Hematite (%)	Illite (%)	Jarosite (%)	Kaolinite (%)	Microcline (%)	Muscovite (%)
F53	592464.7568	6384022.243	0.5	-	-	5.9	7.1	11.5
F58	604210.1487	6379394.878	0.9	-	-	15	-	-
F61	604949.0676	6385784.19	-	18.5	-	4.7	6.1	-
F62	604522.479	6386073.697	0.8	20.3	-	6.5	-	-
F63	589384.0267	6379921.34	-	18.8	-	5.5	7	-
F68	592585.2303	6390574.64	0.6	-	-	7.9	14.7	14.1
F71	606317.6783	6390518.148	0.5	-	-	7.3	9.4	7.7
F73	607545.5524	6382237.135	0.8	-	-	13.1	7.4	19.4
F74	607853.2714	6381783.935	-	-	-	17.8	-	25.3
F76	604965.2548	6380575.979	-	-	-	8.1	18.2	12.3
F76B	604878.38	6380726.58	-	-	-	-	33.5	6.5
F77	602818.5933	6381656.817	-	-	-	7.8	-	13
F80	599160.5626	6385709.792	0.9	-	-	9.8	5	22.5
F81	599381.8341	6385498.231	0.8	-	-	9.6	5.3	22.3
F84	597851.5509	6390870.039	1.3	-	-	-	-	5.9
F85	598947.8806	6391275.135	1.2	-	-	12.5	-	13.4
F89	602542.8257	6375769.217	7.3	-	-	19	-	-
F90	602371.1967	6376139.516	-	17.4	-	4.5	7.3	-
F93	603629.3626	6384525.627	0.3	-	-	-	2.4	-
F95	594314.9808	6379931.888	0.3	-	-	6.6	8.3	10
F97	597197.1325	6393264.172	0.7	-	-	-	16.6	24.1
F98	601249.0185	6392986.498	-	-	-	-	-	-
F99	598687.7938	6378092.966	-	-	-	11	16.7	16.5
F100	599162.1958	6384658.274	-	-	1.4	-	-	-
F101	607096.2656	6381436.665	-	-	-	19	-	17.6
F103	598770.7474	6375720.862	-	-	-	8.5	-	3.5
F104	602178.7105	6377134.464	0.8	-	-	7.9	11	13.7

Sample Number	Easting	Northing	Oligoclase (%)	Orthoclase (%)	Phengite (%)	Phlogopite (%)	Pyrophyllite (%)
F02	596585.3142	6393013.532	-	-	-	-	-
F03	596879.9037	6393897.492	-	-	-	-	-
F13	595585.9085	6393985.062	-	21.6	-	-	-
F16	594953.1819	6391115.917	-	11.1	-	-	-
F17	595414.5067	6392639.608	-	16	-	-	-
F18	596409.9373	6394257.869	-	-	-	-	-
F21	602436.8138	6387226.754	-	-	-	-	-
F22	603850.9153	6385589.393	-	6.9	-	-	-
F23	603471.039	6385004.821	-	-	16.8	-	-
F25	603695.4458	6382998.535	-	-	28.6	-	-
F27	599577.1909	6384873.184	-	-	-	-	30.7
F29	599462.7805	6385440.893	-	-	-	-	98.4
F31	604128.5479	6382245.286	-	-	-	-	-
F32	602481.2224	6381265.082	-	-	-	-	-
F33	603956.4972	6391367.521	-	-	-	-	-
F36	606986.2956	6381490.253	-	-	-	-	-
F37	603228.2185	6385101.869	-	-	-	-	-
F38	603611.9974	6385559.348	-	-	-	-	-
F40	596162.937	6383597.585	-	-	-	-	-
F41	596167.3026	6383738.873	-	-	-	-	-
F42	595951.3338	6383148.584	-	10.3	11.8	-	-
F43	598023.8258	6384481.04	-	-	-	-	-
F44	598868.6289	6384565.138	-	-	26.5	-	22
F45	598798.5508	6384749.996	-	-	-	-	-
F47	599647.9653	6385599.17	-	-	-	-	-
F48	598695.3641	6385858.782	-	8.6	9.3	-	-
F49	604809.5308	6378397.161	-	-	-	-	-
F50	601519.8075	6390079.101	-	-	-	-	-
F51	599247.9317	6384419.448	-	-	-	-	-
F52	603233.3533	6381221.331	-	-	-	-	-

Sample Number	Easting	Northing	Oligoclase (%)	Orthoclase (%)	Phengite (%)	Phlogopite (%)	Pyrophyllite (%)
F53	592464.7568	6384022.243	2.4	-	-	-	-
F58	604210.1487	6379394.878	-	-	21.3	-	-
F61	604949.0676	6385784.19	-	-	-	-	-
F62	604522.479	6386073.697	-	-	-	-	-
F63	589384.0267	6379921.34	-	-	-	-	-
F68	592585.2303	6390574.64	-	-	-	-	-
F71	606317.6783	6390518.148	-	-	-	-	-
F73	607545.5524	6382237.135	-	-	-	-	-
F74	607853.2714	6381783.935	-	-	-	-	-
F76	604965.2548	6380575.979	-	-	-	-	-
F76B	604878.38	6380726.58	-	-	-	-	-
F77	602818.5933	6381656.817	-	-	-	-	-
F80	599160.5626	6385709.792	-	-	-	-	-
F81	599381.8341	6385498.231	-	-	-	-	-
F84	597851.5509	6390870.039	12.9	41.8	-	-	-
F85	598947.8806	6391275.135	-	20.6	-	-	-
F89	602542.8257	6375769.217	5.6	11.2	-	-	-
F90	602371.1967	6376139.516	-	-	-	-	-
F93	603629.3626	6384525.627	-	-	6.6	-	-
F95	594314.9808	6379931.888	-	-	-	-	-
F97	597197.1325	6393264.172	-	-	-	-	-
F98	601249.0185	6392986.498	-	-	-	-	-
F99	598687.7938	6378092.966	2.1	-	-	-	-
F100	599162.1958	6384658.274	-	3.3	-	-	-
F101	607096.2656	6381436.665	-	-	-	-	-
F103	598770.7474	6375720.862	3.5	13.7	-	3.4	-
F104	602178.7105	6377134.464	-	-	-	-	-

Sample Number	Easting	Northing	Quartz (%)	Fit Score
F02	596585.3142	6393013.532	29.1	0.0971
F03	596879.9037	6393897.492	23.6	0.111
F13	595585.9085	6393985.062	60.6	0.1404
F16	594953.1819	6391115.917	45.2	0.1258
F17	595414.5067	6392639.608	61.1	0.1431
F18	596409.9373	6394257.869	50.8	0.1186
F21	602436.8138	6387226.754	49.7	0.1015
F22	603850.9153	6385589.393	71.9	0.173
F23	603471.039	6385004.821	83.2	0.23553
F25	603695.4458	6382998.535	71.4	0.2071
F27	599577.1909	6384873.184	37.7	0.2026
F29	599462.7805	6385440.893	0	0.1537
F31	604128.5479	6382245.286	85.4	0.1923
F32	602481.2224	6381265.082	76	0.186
F33	603956.4972	6391367.521	73.8	0.1967
F36	606986.2956	6381490.253	49.5	0.1143
F37	603228.2185	6385101.869	82	0.2067
F38	603611.9974	6385559.348	79.3	0.2021
F40	596162.937	6383597.585	60.8	0.1558
F41	596167.3026	6383738.873	58.9	0.18243
F42	595951.3338	6383148.584	68.3	0.1782
F43	598023.8258	6384481.04	58.9	0.1376
F44	598868.6289	6384565.138	43.8	0.13084
F45	598798.5508	6384749.996	64.3	0.1581
F47	599647.9653	6385599.17	68.8	0.1611
F48	598695.3641	6385858.782	62.2	0.16454
F49	604809.5308	6378397.161	64.5	0.165
F50	601519.8075	6390079.101	70.2	0.1734
F51	599247.9317	6384419.448	54.1	0.1464
F52	603233.3533	6381221.331	70.5	0.18

Sample Number	Easting	Northing	Quartz (%)	Fit Score
F53	592464.7568	6384022.243	70.4	0.18835
F58	604210.1487	6379394.878	51.9	0.12915
F61	604949.0676	6385784.19	68.4	0.1714
F62	604522.479	6386073.697	60	0.14272
F63	589384.0267	6379921.34	62.5	0.1757
F68	592585.2303	6390574.64	59	0.15
F71	606317.6783	6390518.148	72.6	0.2078
F73	607545.5524	6382237.135	59.2	0.1417
F74	607853.2714	6381783.935	49.4	0.1538
F76	604965.2548	6380575.979	45.1	0.14947
F76B	604878.38	6380726.58	13.8	0.1283
F77	602818.5933	6381656.817	79.3	0.2047
F80	599160.5626	6385709.792	61.8	0.1429
F81	599381.8341	6385498.231	61.9	0.1425
F84	597851.5509	6390870.039	26.7	0.09834
F85	598947.8806	6391275.135	52.4	0.1064
F89	602542.8257	6375769.217	51.3	0.0435
F90	602371.1967	6376139.516	54.8	0.151
F93	603629.3626	6384525.627	90.7	0.28899
F95	594314.9808	6379931.888	73	0.18851
F97	597197.1325	6393264.172	29.9	0.10129
F98	601249.0185	6392986.498	22.6	0.13515
F99	598687.7938	6378092.966	49.7	0.0985
F100	599162.1958	6384658.274	73	0.19406
F101	607096.2656	6381436.665	59.5	0.1304
F103	598770.7474	6375720.862	67.3	0.1831
F104	602178.7105	6377134.464	57.2	0.1476

Appendix C

RAW GEOCHEMICAL DATA

Sample Number	Easting	Northing	Au (ppb)	Au (ppb) Rpt	Ag (ppm)	Al (ppm)	As (ppm)	Ba (ppm)	Be (ppm)
F02	596585.3142	6393013.532	<1		<0.05	65818	1.1	1420.4	3.17
F03	596879.9037	6393897.492	<1		<0.05	66269	1.7	1387.3	3.39
F13	595585.9085	6393985.062	<1		<0.05	39970	2.8	983.6	1.18
F16	594952	6391116	2		0.05	43950	4.1	471.1	1.28
F17	595414.5067	6392639.608	<1		<0.05	37261	2.9	817.3	1.1
F18	596409.9373	6394257.869	<1		<0.05	55446	3	706.9	1.77
F21	602436.8138	6387226.754	2		0.05	66776	5.1	282.8	1.58
F22	603853	6385589	<1		<0.05	32292	1.8	230.7	0.75
F23	603471.5712	6385004.102	<1		<0.05	30487	1.2	112	0.5
F25	603699	6382997	<1		<0.05	52189	1.2	66.9	3.58
F27	599577.1909	6384873.184	<1		<0.05	75602	3.4	481.5	0.73
F29	599462.7805	6385440.893	1		<0.05	60266	11.1	269.3	0.81
F29.R	599462.7805	6385440.893	2		<0.05	56268	10.9	260	0.84
F31	604129	6382245	<1		<0.05	23402	4.6	96.2	0.65
F32	602481.2224	6381265.082	<1		<0.05	31377	2.9	198.8	0.86
F33	603955	6391367	<1		<0.05	27619	1.9	492.9	1.45
F36	606990	6381490	1		<0.05	44173	8.3	224.8	0.9
F37	603232.3188	6385105.171	<1		<0.05	24655	1.8	155.9	0.66
F38	603611.9974	6385559.348	<1		<0.05	21593	1.9	150.1	0.6
F40	596162.937	6383597.585	<1		0.43	64153	2.7	127.5	5.99
F41	596167.3026	6383738.873	<1		0.06	75368	6.8	127	5.08
F42	595951.3338	6383148.584	<1		<0.05	32619	2	374.3	1.24
F43	598028	6384478	1		0.2	66932	10.6	1214.1	1.42
F44	598868.6289	6384565.138	<1		0.05	68948	15.4	530.7	2.17
F45	598798.5508	6384749.996	<1		0.06	54586	7.8	420.7	1.42
F47	599649	6385600	<1		<0.05	38291	2.9	436	1.11
F48	598699	6385865	<1		<0.05	33424	2.8	373.8	0.93
F49	604806	6378392	<1		<0.05	28386	2.9	393.8	0.84
F50	601519.8075	6390079.101	<1		<0.05	32548	2.6	327.9	0.92
F51	599247.9317	6384419.448	<1		<0.05	50188	6.6	400.8	1.39

Sample Number	Easting	Northing	Au (ppb)	Au (ppb) Rpt	Ag (ppm)	Al (ppm)	As (ppm)	Ba (ppm)	Be (ppm)
F52	603233.3533	6381221.331	<1		<0.05	32804	1.7	255	1.06
F53	592464.7568	6384022.243	<1		<0.05	30848	2	382.6	0.84
F58	604207	6379398	<1		<0.05	50591	2.8	268.2	1.37
F58.R	604207	6379398	<1		<0.05	50516	2.9	265.9	1.39
F61	604950	6385785	<1		<0.05	37913	2.2	393.6	1.05
F62	604522	6386077	<1		<0.05	37569	2.2	374.2	1.1
F63	589383	6379921	<1		<0.05	30027	2.2	272.2	0.87
F68	592585	6390574	<1		<0.05	36682	3.5	672.8	0.92
F71	606317	6390515	<1		<0.05	28767	2.2	585.9	1.09
F73	607545	6382235	<1		<0.05	47562	3	243.4	1
F74	607854	6381785	<1		0.09	48886	2.9	238	1.84
F76	604966	6380576	<1		<0.05	58055	2.9	997.1	1.4
F76B	604878	6380727	<1		0.06	83516	2.4	1898.1	1.75
F77	602818.5933	6381656.817	<1		<0.05	29860	1.6	200.9	0.74
F80	599160.5626	6385709.792	<1		0.08	51535	8.1	414.9	1.51
F81	599381.8341	6385498.231	55	37	0.23	56298	8.2	523.7	1.35
F84	597854	6390873	<1		<0.05	68721	1.7	1477.9	3.69
F85	598947.8806	6391275.135	<1		0.05	57880	11.2	877	2.29
F89	602542	6375770	<1		0.07	42499	101.1	348.9	2.92
F90	602375	6376138	<1		<0.05	39877	3.3	544.1	1.5
F93	603628	6384523	2		<0.05	9399	1.3	72.4	0.18
F95	594315	6379932	<1		<0.05	24418	2	263.9	0.65
F97	597197.1325	6393264.172	<1		<0.05	70746	1.2	2284.8	3.39
F98	601249	6392991	3		<0.05	78560	4.5	543.3	0.46
F99	598687	6378092	<1		<0.05	44589	6.8	1508.8	1.69
F100	599162.1958	6384658.274	<1		0.07	36873	6.1	406.5	0.96
F101	607096	6381438	<1		<0.05	47741	5.1	207.2	0.86
F103	598771	6375722	<1		<0.05	29135	2.1	606.2	0.71
F104	602176	6377135	<1		<0.05	32374	5.3	587.9	1.53

Sample Number	Bi (ppm)	Ca (ppm)	Cd (ppm)	Ce (ppm)	Co (ppm)	Cr (ppm)	Cs (ppm)	Cu (ppm)	Dy (ppm)	Er (ppm)
F02	0.15	9488	<0.02	142.32	4.5	18	1.91	15.2	10.08	6.03
F03	0.13	10472	0.13	156.33	4.2	14	2.49	10.8	10.44	6.24
F13	0.16	1247	0.03	46.22	2.8	40	2.45	9.2	5.53	3.71
F16	0.27	57599	0.07	39.21	5.1	50	3.11	15.3	3.47	2.21
F17	0.2	1275	0.04	35.13	2.8	45	2.37	9.5	4.36	2.89
F18	0.18	2672	0.05	57.77	5.5	41	3.31	12.2	4.78	3.1
F21	0.26	4207	0.03	46.77	8.2	51	4.14	17.6	3.41	2
F22	0.12	912	0.03	44.05	3.6	34	1.76	9.5	2.38	1.27
F23	0.08	192	<0.02	65.47	0.8	18	1.63	1.9	1.57	0.57
F25	0.1	132	<0.02	71.08	0.5	8	45.33	2.2	2.15	0.7
F27	0.11	446	0.03	109.11	0.5	49	0.32	8.1	0.99	0.71
F29	0.21	724	<0.02	60.99	0.4	14	0.5	3.5	1.73	0.95
F29.R	0.23	767	0.02	60.66	0.4	14	0.42	3.9	1.69	0.9
F31	0.12	420	<0.02	22.31	3	45	1.41	8.1	1.32	0.75
F32	0.15	1589	0.04	30.15	3.5	48	1.74	9.1	2.16	1.35
F33	0.13	506	0.03	28.25	2.7	30	1.65	8	2.33	1.51
F36	0.3	33404	0.03	22.92	3.5	36	1.79	10.6	1.54	0.88
F37	0.13	723	0.02	25.32	3	37	1.49	9.7	1.55	0.86
F38	0.1	1582	<0.02	23.37	2.5	34	1.27	8.2	1.46	0.81
F40	0.91	374	<0.02	31.99	0.7	19	2.79	3.9	1.92	1.13
F41	2.03	516	<0.02	23.8	0.7	14	4.22	3	1.15	0.57
F42	0.18	1750	<0.02	27.97	3.5	24	1.73	8.9	2.1	1.34
F43	1.39	439	<0.02	98.82	0.7	42	5.31	56.2	2.73	1.04
F44	0.44	889	0.03	84.71	1.4	21	3.55	8.5	3.3	1.9
F45	0.4	3423	0.03	59.16	3.8	38	2.58	13.2	2.8	1.69
F47	0.31	3473	0.03	29.13	3.2	36	2.14	9.6	2.17	1.3
F48	0.41	36087	0.06	27.89	3.1	41	2.44	14.2	2.09	1.28
F49	0.28	22038	0.06	24.52	3.1	42	1.59	8.6	1.7	1.08
F50	0.19	4465	<0.02	48.2	2.3	39	1.67	6	2.46	1.33
F51	0.38	12716	0.05	42.56	4.4	44	3.1	15	2.65	1.57

Sample Number	Bi (ppm)	Ca (ppm)	Cd (ppm)	Ce (ppm)	Co (ppm)	Cr (ppm)	Cs (ppm)	Cu (ppm)	Dy (ppm)	Er (ppm)
F52	0.13	6233	<0.02	39.78	3.4	35	1.78	12	3.19	1.41
F53	0.19	9759	0.04	23.84	3.5	26	1.71	9	2.04	1.23
F58	0.22	23590	0.06	48.01	6.7	50	2.94	14.9	3.24	1.82
F58.R	0.22	23713	0.06	52.33	6.8	48	2.99	13.4	3.25	1.88
F61	0.15	3142	0.04	33.19	4.4	44	2.07	12.8	2.84	1.75
F62	0.15	16248	0.04	36.58	4.8	39	2.13	14.6	2.96	1.84
F63	0.15	20651	0.05	24.27	3.6	32	1.63	9.5	1.81	1.03
F68	0.17	14137	0.04	31.63	3.3	37	1.98	10.1	3.32	2.04
F71	0.12	9508	0.02	39.17	2.8	32	1.59	9.4	2.91	1.74
F73	0.21	9914	0.05	34	4.8	45	2.61	11.2	2.25	1.27
F74	0.3	26669	0.03	39.15	5.6	41	2.8	9.5	2.37	1.31
F76	0.19	3659	0.03	52.86	4.8	36	2.52	8.6	2.87	1.67
F76B	0.11	13579	0.09	147.58	4.3	10	2.09	6.3	4.67	2.52
F77	0.12	717	0.03	35.76	2.1	30	1.47	7	1.53	0.78
F80	0.75	1084	0.03	49.68	3.5	41	2.43	11.7	2.55	1.52
F81	0.46	20731	0.05	73.93	3.3	29	2.56	10.2	2.83	1.58
F84	0.11	7093	0.04	144.15	2.3	10	1.91	16.4	10.21	6.54
F85	0.18	1216	<0.02	82.38	4.3	38	3.55	12.4	6.64	4.28
F89	24.94	20263	<0.02	23.9	3.3	66	1.35	10.9	1.68	1.03
F90	0.68	43335	0.05	37.54	5.5	34	2.13	13.4	3.23	2.01
F93	0.27	478	<0.02	32.21	0.3	11	0.32	1.2	1.02	0.3
F95	0.14	4101	0.03	23.07	2.6	31	1.25	6	1.45	0.86
F97	0.15	8391	0.07	151.23	3.2	10	4.69	7	10.53	6.33
F98	0.11	85527	0.04	15.17	1.9	17	1.02	7.9	2.47	1.85
F99	0.38	18889	0.05	38.67	5.2	35	4.29	9	2.22	1.35
F100	0.3	6616	0.03	56.57	1.2	55	2.08	15.1	2.23	1.34
F101	0.3	12387	0.07	24.92	3.7	39	2.07	7.3	1.63	0.98
F103	0.17	2417	<0.02	18.59	2.3	23	1.37	6.2	1.2	0.69
F104	0.75	39248	0.07	39.29	4.9	47	2.6	12.1	2.05	1.06

Sample Number	Eu (ppm)	Fe (pct)	Ga (ppm)	Gd (ppm)	Ge (ppm)	Hf (ppm)	Ho (ppm)	In (ppm)	K (ppm)	La (ppm)
F02	2.36	3.49	20.74	10.52	1.2	10.29	2.1	0.09	40153	69.89
F03	2.38	3.49	19.95	10.92	1.1	10.01	2.18	0.09	42071	77.69
F13	1.08	2.43	9.78	4.53	0.8	5.63	1.22	0.03	28067	23.53
F16	0.77	2.63	10.7	3.64	0.4	3.18	0.75	0.04	18376	19.76
F17	0.86	2.49	9.18	3.53	0.9	4.44	0.94	0.03	23664	18.25
F18	1.16	2.73	13.12	4.62	0.9	4.97	1.02	0.04	23322	29.17
F21	0.88	3.57	16.26	3.82	1.1	2.91	0.71	0.05	14678	23.41
F22	0.62	1.46	7.19	3.06	0.9	2.64	0.45	0.02	9893	21.99
F23	0.5	0.74	6.94	3.21	0.8	3.28	0.24	0.02	14190	32.52
F25	0.34	0.66	12.85	4.3	1.6	3.5	0.33	0.02	23640	32.39
F27	0.4	1.04	14.87	1.35	0.7	5.2	0.22	<0.01	14710	66.93
F29	0.66	1.51	17.73	2.6	1.6	5.07	0.31	<0.01	5350	28.86
F29.R	0.66	1.47	16.32	2.61	1.2	4.96	0.32	<0.01	5261	28.84
F31	0.35	1.82	6.6	1.44	0.9	3.25	0.25	0.02	3578	10.9
F32	0.58	1.56	7.73	2.53	0.9	3.23	0.45	0.03	6220	12.98
F33	0.49	1.39	5.89	2.22	0.8	2.44	0.49	0.03	12974	16.35
F36	0.35	2.7	11.37	1.67	0.9	2.42	0.31	0.05	6758	10.16
F37	0.39	1.34	5.79	1.8	0.8	2.36	0.3	0.01	6204	12.18
F38	0.36	1.21	5.24	1.74	0.8	2.35	0.28	0.02	5392	11.01
F40	0.24	0.51	43.47	2.27	0.9	4.82	0.37	0.24	30220	13.68
F41	0.16	0.62	20.74	1.06	1.3	1.91	0.21	0.17	35167	14.96
F42	0.49	1.49	7.4	2.22	0.9	2.09	0.44	0.02	14130	13.44
F43	0.86	1.71	18.28	4.56	1.7	4.3	0.4	0.06	33368	51.78
F44	0.89	1.71	18.09	4.07	1.1	5.07	0.66	0.03	28822	43.52
F45	0.69	2.14	13.4	2.97	1.1	3.67	0.57	0.03	21205	30.26
F47	0.49	1.7	8.78	2.1	1	2.57	0.45	0.03	15198	14.64
F48	0.5	1.53	7.51	2.15	0.9	2.01	0.45	0.02	13810	13.56
F49	0.44	1.55	6.49	1.89	0.8	1.62	0.36	0.03	10681	11.79
F50	0.53	1.61	7.09	3.08	0.9	4.19	0.45	0.02	13452	24.11
F51	0.69	2.1	11.81	2.96	1.1	2.76	0.53	0.04	18487	21.34

Sample Number	Eu (ppm)	Fe (pct)	Ga (ppm)	Gd (ppm)	Ge (ppm)	Hf (ppm)	Ho (ppm)	In (ppm)	K (ppm)	La (ppm)
F52	0.68	1.46	7.49	3.18	0.9	2.06	0.51	0.04	12868	19.6
F53	0.52	1.57	7.09	2.02	0.9	1.83	0.43	0.01	12658	11.92
F58	0.86	2.47	11.73	3.84	1	2.3	0.65	0.05	14259	23.83
F58.R	0.86	2.48	11.6	4.05	1	2.48	0.64	0.05	14272	26.15
F61	0.68	1.83	8.78	2.96	1	2.47	0.58	0.03	14926	16.67
F62	0.73	1.84	8.58	3.83	0.8	2.96	0.63	0.03	14713	18.4
F63	0.46	1.58	7.19	1.99	0.8	1.5	0.35	0.02	11044	12.56
F68	0.66	1.99	8.17	3	0.9	3.15	0.68	0.03	18610	16.43
F71	0.71	1.38	6.44	3.13	0.9	2.28	0.65	0.02	15334	18.44
F73	0.55	2.47	11.14	2.52	1	2.15	0.45	0.04	12325	16.59
F74	0.62	1.81	11.46	3.15	1	2.21	0.49	0.03	13592	18.54
F76	1.24	2.21	12.88	3.51	1	3.23	0.58	0.04	28092	26.07
F76B	2.48	2.54	18.99	6.62	1.1	6.45	0.9	0.05	50559	77.56
F77	0.37	1.12	6.53	2.11	0.9	2.16	0.29	0.03	10960	17.53
F80	0.66	2.14	12.76	2.99	1.2	3.28	0.53	0.03	18663	25.19
F81	0.81	1.97	14.62	3.45	1	3.88	0.55	0.04	20302	40.38
F84	1.85	2.81	20.78	9.92	1.4	11.79	2.17	0.08	51598	71.57
F85	1.4	3.1	15.29	6.29	1.1	6.86	1.44	0.06	28886	40.84
F89	0.36	16.2	17.3	1.71	0.7	3.36	0.37	2.37	8302	10.95
F90	0.63	2.03	9.37	3.46	0.8	2.2	0.66	0.04	15300	17.56
F93	0.25	0.46	2.43	1.8	0.7	2.74	0.15	0.03	5217	15.94
F95	0.35	1.26	5.6	1.65	0.7	1.29	0.3	0.02	9568	11.59
F97	2.41	3.16	21.4	10.95	1.3	9.82	2.17	0.08	42301	75.87
F98	0.3	2.04	20.95	1.5	0.8	7.23	0.57	0.04	2818	7.75
F99	0.99	3.27	9.77	2.67	0.9	2.2	0.45	0.08	21715	18.46
F100	0.56	1.37	9.76	2.42	1	6.9	0.45	0.06	16611	28.51
F101	0.4	2.66	12.32	1.89	1	2.43	0.33	0.04	7550	12.08
F103	0.37	1.26	5.89	1.37	0.7	1.09	0.24	0.02	14244	9.45
F104	0.6	2.52	7.54	2.39	0.7	1.57	0.39	0.06	13013	18.04

Sample Number	Li (ppm)	Lu (ppm)	Mg (ppm)	Mn (ppm)	Mo (ppm)	Na (ppm)	Nb (ppm)	Nd (ppm)	Ni (ppm)	P (ppm)
F02	16.6	0.83	3433	763	2	21139	20.51	60.41	5.8	622
F03	21.3	0.84	4604	875	1	20693	21.04	65.41	2.9	670
F13	12.1	0.52	1683	194	0.7	4146	11.17	20.53	7.5	110
F16	23.4	0.3	4956	325	0.7	1844	8.1	17.96	13.6	244
F17	13.8	0.41	1602	170	0.7	3259	9.91	15.89	7.6	150
F18	23.9	0.42	2875	357	0.6	4388	11.29	25.7	12.8	236
F21	33.2	0.27	5258	275	0.7	846	7.81	21.3	21.3	184
F22	14.3	0.15	1411	182	0.5	1008	5.04	18.91	8.5	118
F23	3.9	0.05	527	50	0.1	209	3.47	26.44	2.5	59
F25	14.1	0.07	359	87	0.1	1480	12.11	31.52	2.1	86
F27	3.3	0.14	128	36	3.2	4980	6.32	25.66	1.4	893
F29	7.7	0.17	177	64	0.9	933	7.77	28.13	0.8	669
F29.R	7.6	0.16	177	63	0.8	902	3.98	28.72	0.6	754
F31	11.3	0.1	662	109	0.7	401	5.07	9.41	7.6	132
F32	16.8	0.2	1526	119	0.4	649	5.43	13.56	9	121
F33	14.2	0.22	914	109	0.5	1518	5.85	11.01	6.4	104
F36	21.2	0.12	2888	139	0.7	699	5.94	9.38	10.5	227
F37	12.1	0.12	1135	123	0.4	677	4.44	10.57	7.8	107
F38	11.1	0.12	996	141	0.4	587	4.11	10.08	6.9	132
F40	8.2	0.18	2366	109	0.6	493	16.46	13.01	1	66
F41	16.3	0.06	1194	85	0.2	518	11.88	9.82	1.2	242
F42	16.5	0.19	1975	153	0.4	1291	6.07	11.86	7.9	117
F43	10.2	0.16	4180	134	1.5	618	10.38	38.54	1.7	218
F44	10.8	0.24	3079	122	0.8	546	14.48	32.53	6.2	188
F45	16.2	0.22	4454	196	0.6	2056	8.48	23.23	10.4	201
F47	15.5	0.2	2278	157	0.5	1293	8.1	12.35	8.5	138
F48	13	0.18	4560	160	0.5	1320	6.28	11.63	8.2	177
F49	14.4	0.14	2949	143	0.4	1031	4.92	10.26	8.2	145
F50	11.4	0.19	2112	142	0.4	1200	8.62	19.87	6.7	130
F51	17.5	0.21	5617	208	0.6	1900	6.85	18	11.6	178

Sample Number	Li (ppm)	Lu (ppm)	Mg (ppm)	Mn (ppm)	Mo (ppm)	Na (ppm)	Nb (ppm)	Nd (ppm)	Ni (ppm)	P (ppm)
F52	14.4	0.19	3373	146	0.4	876	4.76	19.28	9.7	696
F53	14.9	0.18	2723	151	0.4	1152	5.14	10.73	8.8	150
F58	25.1	0.24	5601	307	0.6	1105	7.03	21.68	15.3	213
F58.R	26.1	0.25	5636	304	0.5	1102	7.53	23.76	15.3	211
F61	17.8	0.24	3318	188	0.4	1253	6.55	15.23	11.6	104
F62	18.7	0.25	4625	192	0.4	3378	6.63	17.07	11.9	133
F63	15	0.14	3834	158	0.4	1002	4.47	11.4	8.8	176
F68	13.3	0.3	3057	168	0.6	2206	7.9	14.39	8.3	170
F71	17.1	0.24	1750	419	0.4	1739	5.84	17.64	6.9	108
F73	20.8	0.17	4093	229	0.5	980	6.46	14.49	12.2	182
F74	20.6	0.18	7517	308	0.4	10530	7.04	18.27	11.2	169
F76	19.1	0.22	2769	361	0.5	8155	10.32	22.36	9.7	191
F76B	16.4	0.32	4275	660	0.8	25455	12.87	58.89	4	708
F77	8.5	0.1	1004	130	0.3	769	4.78	15.82	5.2	115
F80	17.2	0.22	2341	194	0.8	1186	7.39	19.23	8.9	183
F81	14.6	0.23	3167	142	1.1	908	6.8	27.62	8.4	256
F84	7.5	0.89	1085	559	2.6	17291	24.68	56.54	2.7	218
F85	15.7	0.61	1685	215	1.3	3966	15.96	34.17	9.8	222
F89	12.4	0.16	4441	562	6.3	1109	10.96	9.24	9.6	182
F90	18.7	0.25	5093	244	0.5	2629	8.62	17.6	11.6	161
F93	1.6	0.03	191	33	0.2	138	3.65	13.22	1.3	58
F95	12.2	0.11	2172	110	0.3	913	4.12	9.84	6.5	122
F97	8	0.86	1777	572	1.2	18366	21.5	65.67	2.7	641
F98	16.9	0.31	15473	39	0.7	755	13.22	4.98	3.6	78
F99	16.2	0.17	5261	277	0.7	4497	7.27	16.78	9.3	259
F100	7	0.2	2765	82	1	574	5.25	23.28	3.8	125
F101	21.1	0.13	3028	169	0.6	668	6.33	10.6	10.6	159
F103	12.4	0.09	1911	150	0.4	1735	4.43	7.93	5.8	165
F104	18	0.14	5258	379	0.8	1537	8.93	15.51	23.3	186

Sample Number	Pb (ppm)	Pr (ppm)	Rb (ppm)	Re (ppm)	S (pct)	Sb (ppm)	Sc (ppm)	Se (ppm)	Si (pct)	Sm (ppm)
F02	38	16.14	199.22	<0.002	<0.05	0.18	10.6	<0.5	31.9	11.12
F03	29.2	17.63	208.84	<0.002	<0.05	0.21	11.2	<0.5	31.4	12.29
F13	15.2	5.54	140.02	<0.002	<0.05	0.29	5.5	<0.5	33.5	4.31
F16	17.5	4.76	89.5	<0.002	<0.05	0.36	7.6	<0.5	29.2	3.55
F17	14.1	4.38	119.49	<0.002	<0.05	0.33	5.4	<0.5	38.1	3.43
F18	17	6.91	126.12	<0.002	<0.05	0.31	8.4	<0.5	35.2	5
F21	18.2	5.6	86.21	<0.002	<0.05	0.32	11.7	<0.5	31.8	4.15
F22	10.3	5.15	53.06	<0.002	<0.05	0.2	4.4	<0.5	39.1	3.64
F23	9	7.41	71.41	<0.002	<0.05	0.09	1.6	<0.5	43.5	4.63
F25	10.4	8.29	403.85	<0.002	<0.05	<0.05	1.4	<0.5	39.2	6.11
F27	38.9	9.38	6.48	<0.002	3.68	1.13	4	4.5	30.6	2.59
F29	7.3	7.45	27.86	<0.002	<0.05	2.24	1.7	3.4	36.7	4.4
F29.R	7.1	7.43	27.07	<0.002	<0.05	1.98	1.9	3.2	37.9	4.28
F31	7.7	2.49	24.42	<0.002	<0.05	0.18	4.4	<0.5	40.2	1.86
F32	9.7	3.4	36.94	<0.002	<0.05	0.22	7	<0.5	40.1	2.75
F33	11.3	3.18	68.92	<0.002	<0.05	0.16	3.7	<0.5	41.8	2.14
F36	11.4	2.49	35.22	<0.002	<0.05	0.29	6.4	<0.5	32.9	1.85
F37	9.2	2.87	35.05	<0.002	<0.05	0.16	4.1	<0.5	39.6	1.95
F38	7	2.62	31.34	<0.002	<0.05	0.33	3.7	<0.5	42.6	2
F40	13.8	3.79	263.19	<0.002	<0.05	0.47	5.8	0.6	37.7	2.78
F41	14.1	3.03	260.77	<0.002	<0.05	0.2	3.4	<0.5	36.5	1.64
F42	12.7	3.22	74.99	<0.002	<0.05	0.2	4.3	<0.5	38.6	2.3
F43	43.3	11.03	219.27	<0.002	0.25	2.45	10.7	4	34.7	6.23
F44	33.7	9.32	151.89	<0.002	<0.05	0.62	5.6	1.4	34.6	5.51
F45	41.2	6.58	100.94	<0.002	0.06	0.45	6.6	1	33	3.95
F47	13.2	3.33	80.63	<0.002	<0.05	0.33	5.1	<0.5	38.6	2.43
F48	12	3.16	73.25	<0.002	0.06	0.27	4.3	<0.5	36.4	2.34
F49	9.7	2.77	51.94	<0.002	<0.05	0.21	4.1	<0.5	37.8	2.07
F50	15.5	5.45	70.66	<0.002	<0.05	0.28	3.8	<0.5	41.4	3.84
F51	20.6	4.87	93.6	<0.002	<0.05	0.25	6.6	<0.5	35.2	3.43

Sample Number	Pb (ppm)	Pr (ppm)	Rb (ppm)	Re (ppm)	S (pct)	Sb (ppm)	Sc (ppm)	Se (ppm)	Si (pct)	Sm (ppm)
F52	11.1	5.06	63.74	<0.002	<0.05	0.2	5.1	<0.5	35.1	3.76
F53	9.5	2.81	61.56	<0.002	<0.05	0.16	4.6	<0.5	32.3	2.17
F58	15.7	5.81	73.93	<0.002	<0.05	0.24	8.4	<0.5	31.6	4.27
F58.R	15.7	6.29	74.98	<0.002	<0.05	0.24	8.7	<0.5	33.3	4.57
F61	12.1	4.04	74.44	<0.002	<0.05	0.23	6.1	<0.5	39.6	2.92
F62	12.1	4.45	73.11	<0.002	<0.05	0.23	6	<0.5	37.1	3.33
F63	10.3	3.04	51.01	<0.002	<0.05	0.17	5	<0.5	38.8	2.18
F68	12.4	3.9	89.26	<0.002	<0.05	0.25	5.4	<0.5	35.1	2.89
F71	15	4.71	78.14	<0.002	<0.05	0.19	3.9	<0.5	36	3.43
F73	14.4	3.98	64.71	<0.002	<0.05	0.27	7.1	<0.5	35.2	2.96
F74	14	4.76	71.93	<0.002	0.1	0.21	6.5	<0.5	32.6	3.62
F76	17.7	6.02	106.52	<0.002	<0.05	0.16	6.6	<0.5	33.8	4.26
F76B	28.5	16.16	124.86	<0.002	<0.05	0.08	7.6	<0.5	28.1	8.77
F77	9.2	4.12	64.54	<0.002	<0.05	0.17	3.2	<0.5	37.7	2.85
F80	20.9	5.41	97.89	<0.002	<0.05	0.57	6.6	0.6	37.3	3.38
F81	15.8	7.96	109.26	<0.002	0.07	0.58	5.7	2.8	34.3	4.8
F84	23.1	15.79	242.89	<0.002	<0.05	0.21	7.7	<0.5	33.2	10.73
F85	21.2	9.23	156.36	<0.002	<0.05	0.49	8.8	<0.5	34.8	6.45
F89	20.8	2.51	50.78	<0.002	<0.05	0.34	8.2	1.7	25.6	1.83
F90	15	4.5	84.47	<0.002	<0.05	0.2	5.5	<0.5	31.4	3.82
F93	3.9	3.7	21.89	<0.002	<0.05	<0.05	0.8	<0.5	44.1	2.43
F95	8.4	2.65	43.44	<0.002	<0.05	0.15	3.3	<0.5	40.5	1.88
F97	17.6	17.44	224.25	<0.002	<0.05	0.42	11.5	<0.5	31.1	12.07
F98	6.5	1.47	15.74	<0.002	0.06	0.24	7.3	<0.5	21	1.22
F99	12.9	4.52	93.52	<0.002	0.05	0.19	6.6	<0.5	32.5	3.22
F100	85.7	6.34	98.3	<0.002	0.18	0.49	5.3	1.1	38.9	3.54
F101	11	2.9	39.95	<0.002	<0.05	0.26	7.1	<0.5	34.1	2.08
F103	8.6	2.19	56.24	<0.002	<0.05	0.14	3.4	<0.5	37.8	1.48
F104	12.8	4.25	66.55	<0.002	0.07	0.22	5.1	<0.5	32.3	3.06

Sample Number	Sn (ppm)	Sr (ppm)	Ta (ppm)	Tb (ppm)	Te (ppm)	Th (ppm)	Ti (ppm)	Tl (ppm)	Tm (ppm)	U (ppm)
F02	3.7	154.37	1.34	1.55	<0.2	27.8	3701	1.01	0.85	6.12
F03	3.7	136.64	1.38	1.68	<0.2	28.6	3824	1	0.88	6.12
F13	1.6	56.28	0.88	0.79	<0.2	17.91	1793	0.74	0.55	2.81
F16	1.5	105.94	0.72	0.55	<0.2	11.8	2114	0.49	0.31	1.57
F17	1.6	53.73	0.77	0.63	<0.2	15.24	2009	0.61	0.41	2.24
F18	2	72.89	0.8	0.73	<0.2	14.85	3003	0.65	0.43	2.26
F21	2.1	66.1	0.61	0.55	<0.2	11.7	3004	0.47	0.28	1.15
F22	1.1	34.66	0.36	0.43	<0.2	11.58	1773	0.3	0.16	1.39
F23	1.1	18.66	0.28	0.36	<0.2	13.07	1020	0.54	0.06	2.04
F25	12.3	21.36	4.07	0.48	<0.2	28.89	818	1.89	0.08	3.35
F27	3.5	639.62	0.63	0.16	0.3	13.53	960	0.08	0.12	3.01
F29	2.5	482.57	0.58	0.31	0.3	7.06	657	0.27	0.13	2.56
F29.R	1.7	479.59	0.29	0.32	0.2	6.99	344	0.28	0.14	2.55
F31	1	23.63	0.39	0.23	<0.2	7.69	1640	0.16	0.1	0.96
F32	1.4	29.73	0.42	0.37	<0.2	8.26	1920	0.23	0.19	0.83
F33	0.9	54.62	0.43	0.35	<0.2	7.99	1391	0.37	0.21	2.53
F36	2.5	96.09	0.47	0.25	<0.2	17.13	1826	0.22	0.13	1.14
F37	1	27.21	0.33	0.25	<0.2	6.9	1504	0.21	0.12	0.95
F38	0.9	25.42	0.33	0.25	<0.2	7	1434	0.19	0.12	0.78
F40	29.9	13.28	1.49	0.29	0.3	22.85	710	2.21	0.17	3.78
F41	11.7	129.75	2.28	0.18	<0.2	6.92	512	1.89	0.08	3.31
F42	1.7	40.04	0.46	0.33	<0.2	8.6	1506	0.43	0.19	1.38
F43	7.6	44.63	0.85	0.5	0.3	20.86	2044	2.52	0.14	3.17
F44	2.4	41.42	1.04	0.57	0.4	16.05	1504	1.71	0.26	3.11
F45	2.1	104.56	0.62	0.44	<0.2	12.11	2063	0.76	0.23	1.91
F47	1.5	47.8	0.74	0.32	<0.2	8.54	2090	0.47	0.21	1.15
F48	1.6	143.51	0.63	0.32	<0.2	7.29	1485	0.45	0.19	1.01
F49	2	114.94	0.43	0.27	<0.2	7.21	1514	0.36	0.15	0.87
F50	1.6	42.7	0.82	0.42	<0.2	15.72	2161	0.46	0.19	1.7
F51	2	93.72	0.52	0.42	<0.2	9.96	2113	0.57	0.21	1.28

Sample Number	Sn (ppm)	Sr (ppm)	Ta (ppm)	Tb (ppm)	Te (ppm)	Th (ppm)	Ti (ppm)	Tl (ppm)	Tm (ppm)	U (ppm)
F52	1.6	53.12	0.38	0.46	<0.2	9.47	1606	0.43	0.21	1
F53	1.1	63.82	0.42	0.33	<0.2	6.79	1596	0.32	0.18	0.9
F58	2	94.78	0.64	0.53	<0.2	10.61	2544	0.44	0.24	1.07
F58.R	2.2	95.48	0.67	0.55	<0.2	10.4	2655	0.45	0.25	1.12
F61	1.4	47.63	0.47	0.42	<0.2	9.3	2015	0.39	0.24	1.16
F62	1.3	92.09	0.48	0.47	<0.2	9.57	1984	0.37	0.26	1.21
F63	1	96.11	0.34	0.3	<0.2	6.28	1643	0.28	0.14	0.91
F68	1.5	70.6	0.59	0.46	<0.2	11.87	1757	0.47	0.29	1.68
F71	1	51.02	0.44	0.47	<0.2	8.49	1340	0.42	0.23	1.28
F73	1.8	52.24	0.53	0.36	<0.2	9.86	2290	0.36	0.18	1
F74	2.8	137.53	0.89	0.42	<0.2	9.64	1995	0.39	0.19	1.57
F76	1.7	100.45	0.67	0.5	<0.2	11.27	3265	0.63	0.24	1.66
F76B	2.2	215.67	0.68	0.8	<0.2	16.56	3320	0.74	0.33	2.68
F77	1.8	26.98	0.38	0.27	<0.2	9.78	1422	0.47	0.12	1.14
F80	1.5	40.1	0.55	0.43	<0.2	11.83	1998	0.65	0.21	1.59
F81	2.3	92.3	0.49	0.48	0.3	11.52	1686	0.95	0.22	1.78
F84	4.5	72.83	1.61	1.55	<0.2	32.29	2309	1.18	0.9	7.43
F85	2.9	64.45	1.06	1.01	<0.2	19.69	3488	0.79	0.63	3.26
F89	99.8	125.46	0.79	0.26	<0.2	22.62	2592	0.6	0.15	1.21
F90	2.6	160.78	0.65	0.54	<0.2	11.72	2197	0.54	0.27	1.15
F93	1.6	8.24	0.39	0.22	<0.2	8.75	540	0.15	0.04	1.08
F95	0.9	36.17	0.31	0.23	<0.2	5.75	1167	0.26	0.12	0.76
F97	3.9	126.54	1.4	1.64	<0.2	27.87	3957	1.05	0.87	5.65
F98	3.5	303.59	0.88	0.32	<0.2	21.93	2625	0.14	0.29	2.9
F99	6.1	141.34	0.51	0.37	<0.2	8.02	2924	0.93	0.17	1.18
F100	1.7	58.66	0.48	0.35	0.3	14.53	1606	0.83	0.19	2.79
F101	2.8	42.56	0.5	0.27	<0.2	15.27	2025	0.25	0.14	0.98
F103	1.4	56.82	0.29	0.19	<0.2	4.91	1397	0.37	0.1	0.71
F104	4.5	175.04	0.52	0.36	<0.2	8.13	2060	0.48	0.16	1.04

Sample Number	V (ppm)	W (ppm)	Y (ppm)	Yb (ppm)	Zn (ppm)	Zr (ppm)
F02	18	1.3	55.66	5.76	94	360.7
F03	17	1.7	56.09	5.97	101	351
F13	44	0.8	32.3	3.94	28	196.1
F16	62	0.8	19.9	2.18	56	109
F17	49	0.8	25.53	2.93	27	168.8
F18	47	0.9	26.54	3	49	168.3
F21	79	1.1	17.97	1.9	47	96.5
F22	30	0.6	12.17	1.1	23	92.8
F23	17	1.7	5.51	0.38	7	107.4
F25	10	9	8.09	0.48	13	111.2
F27	36	2.2	5.26	0.92	4	165.7
F29	11	3.3	8.61	1.04	8	171.7
F29.R	10	2.6	8.22	1	9	165.3
F31	46	0.9	6.58	0.77	12	93.3
F32	34	0.8	11.34	1.33	18	106.3
F33	31	0.5	13.61	1.47	17	80.7
F36	86	1.1	7.99	0.86	22	81.3
F37	28	0.5	7.88	0.88	17	83.6
F38	25	0.8	7.29	0.81	16	82
F40	19	1.1	10.45	1.31	4	90.1
F41	7	1.6	6.45	0.48	7	50.8
F42	30	0.5	11.71	1.36	22	75.3
F43	52	4.5	9.62	1.01	10	140.2
F44	21	1	18.28	1.8	12	176.7
F45	38	0.7	15.44	1.67	30	124.8
F47	38	0.9	12.11	1.37	24	91
F48	33	0.8	11.7	1.27	25	70
F49	39	0.9	9.77	1.02	21	56.4
F50	36	1.2	11.65	1.34	21	143
F51	48	1	14.36	1.51	32	93.3

Sample Number	V (ppm)	W (ppm)	Y (ppm)	Yb (ppm)	Zn (ppm)	Zr (ppm)
F52	29	0.8	13.8	1.36	25	71.3
F53	35	0.5	11.53	1.23	24	63.4
F58	52	0.9	16.68	1.63	43	77
F58.R	49	1	17.77	1.78	43	84
F61	37	0.7	15.2	1.71	31	86.5
F62	35	0.7	16.75	1.73	32	95.9
F63	38	0.5	9.25	0.91	27	49.9
F68	51	0.7	18.77	2.06	28	116.2
F71	31	0.5	16.51	1.66	25	77.5
F73	55	0.8	12.1	1.24	33	71.3
F74	46	1.2	13.85	1.25	38	75
F76	43	0.9	15.11	1.47	36	107.9
F76B	24	0.7	23.16	2.25	68	231.8
F77	25	0.8	7.35	0.71	16	72.1
F80	40	0.9	13.6	1.52	26	109.1
F81	33	1	15.07	1.53	22	131.1
F84	8	1.4	58.19	6.16	81	433.1
F85	45	1.5	37.46	4.11	75	236.7
F89	71	45.4	8.64	1.07	61	105.4
F90	41	2.6	17.76	1.74	35	72.1
F93	7	0.7	3.5	0.22	3	88.9
F95	28	0.5	7.71	0.78	18	46.7
F97	18	1.1	58.8	5.86	74	354.5
F98	19	1.1	14.36	2.13	7	252.5
F99	54	2.2	12.11	1.14	41	75.3
F100	33	0.9	12.65	1.37	16	237.9
F101	67	0.9	8.42	0.92	22	78.2
F103	30	0.6	6.31	0.66	22	38
F104	57	1.9	10.34	1.01	36	55.5